

RADIOSTEREOMETRIC ANALYSIS ORIGIN STYLES:  
THEIR IMPACT ON THE ACCURACY AND PRECISION IN THE  
ASSESSMENT OF SPINAL FUSION SUCCESS

By

**Alan J. Spurway**

Submitted in partial fulfillment of the requirements  
for the degree of Master of Applied Science

at

**Dalhousie University**  
Halifax, Nova Scotia  
April 2012

DALHOUSIE UNIVERSITY  
School of Biomedical Engineering

The undersigned hereby certify that they have read and recommend the Faculty of Graduate Studies for acceptance a thesis entitled “*Radiostereometric Analysis Origin Styles: Their Impact on the Accuracy and Precision in the Assessment of Spinal Fusion Success*” by Alan J. Spurway in partial fulfillment of the degree of Master of Applied Science.

Dated: April 24, 2012

Supervisor: \_\_\_\_\_

Readers: \_\_\_\_\_

\_\_\_\_\_

\_\_\_\_\_

External Examiner: \_\_\_\_\_

DALHOUSIE UNIVERSITY

Date: April 24, 2012

AUTHOR: Alan J. Spurway

TITLE: *Radiostereometric Analysis Origin Styles: Their Impact on the Accuracy and Precision in the Assessment of Spinal Fusion Success*

DEPARTMENT OR SCHOOL: School of Biomedical Engineering

DEGREE: MASC                      CONVOCATION: October                      YEAR: 2012

Permission is herewith granted to Dalhousie University to circulate and to have copied for non-commercial purposes, at its discretion, the above title upon request of individuals or institutions. I understand that my thesis will be electronically available to the public.

The author reserves other publication rights, and neither thesis nor extensive extracts from it may be printed or otherwise reproduced without the author's written permission.

The author attests that permission has been obtained for the use of any copyrighted material appearing in the thesis (other than the brief excerpts requiring only proper acknowledgement in scholarly writing), and that all such use is clearly acknowledged.

---

Signature of Author

# Table of Contents

<b>LIST OF TABLES .....</b>	<b>viii</b>
<b>LIST OF FIGURES .....</b>	<b>x</b>
<b>ABSTRACT .....</b>	<b>xv</b>
<b>LIST OF ABBREVIATIONS USED .....</b>	<b>xvi</b>
<b>GLOSSARY .....</b>	<b>xviii</b>
<b>ACKNOWLEDGEMENTS .....</b>	<b>xxi</b>
<b>CHAPTER 1 - INTRODUCTION .....</b>	<b>1</b>
1.1    BACKGROUND .....	1
1.1.1 <i>Spinal Anatomy and Physiology</i> .....	1
1.1.2 <i>Adolescent Idiopathic Scoliosis</i> .....	4
1.1.3 <i>Medical Treatment</i> .....	12
1.1.4 <i>Radiostereometric Analysis</i> .....	20
1.1.5 <i>RSA Markers</i> .....	30
1.1.6 <i>Migration Assessment</i> .....	33
1.2    PREVIOUS WORK .....	40
1.2.1 <i>Previous Project Outcomes</i> .....	40
1.2.2 <i>Previous Limitations</i> .....	45
<b>CHAPTER 2 - THESIS OBJECTIVES .....</b>	<b>48</b>
2.1    OBJECTIVE #1: RSA SIMULATION PRECISION VALIDATION.....	48
2.2    OBJECTIVE #2: ASSESSMENT OF NOVEL RSA ORIGIN STYLES USED FOR SPINAL FUSION SUCCESS ANALYSIS .....	49
<b>CHAPTER 3 - THESIS OBJECTIVE #1: RSA SIMULATION PRECISION VALIDATION.....</b>	<b>51</b>
3.1    INTRODUCTION .....	51
3.2    SIMULATION PRECISION VALIDATION METHODOLOGY .....	53
3.2.1 <i>Computer Simulated Spine Model</i> .....	53
3.2.2 <i>Radiostereometric Simulation</i> .....	63
3.2.3 <i>Simulated RSA Environment</i> .....	66
3.2.4 <i>Radiostereometric Analysis</i> .....	72
3.2.5 <i>Simulation Precision Validation</i> .....	79



3.3	SIMULATION PRECISION VALIDATION RESULTS .....	95
3.3.1	<i>Image Simulation</i> .....	95
3.3.2	<i>Precision Results</i> .....	99
3.3.3	<i>Precision Comparison</i> .....	100
3.4	SIMULATION PRECISION VALIDATION DISCUSSION .....	104
3.4.1	<i>Spinal Fusion Precision Comparison</i> .....	108
3.4.2	<i>Limitations</i> .....	109
3.4.3	<i>Conclusion</i> .....	112
<b>CHAPTER 4 - THESIS OBJECTIVE #2: ASSESSMENT OF NOVEL RSA ORIGIN STYLES USED FOR SPINAL FUSION SUCCESS ANALYSIS .....</b>		<b>113</b>
4.1	INTRODUCTION .....	113
4.1.1	<i>RSA Origin Styles</i> .....	115
4.2	ORIGIN STYLE ASSESSMENT METHODOLOGY.....	123
4.2.1	<i>Accuracy Assessment</i> .....	123
4.2.2	<i>Precision Assessment Methodology</i> .....	134
4.3	ORIGIN STYLE ASSESSMENT RESULTS.....	138
4.3.1	<i>Accuracy Assessment Results</i> .....	138
4.3.2	<i>Precision Assessment Results</i> .....	149
4.4	ORIGIN STYLE ASSESSMENT DISCUSSION.....	163
4.4.1	<i>Origin Style Assessment</i> .....	166
4.4.2	<i>Origin Style Selection</i> .....	172
4.4.3	<i>Limitations</i> .....	176
4.4.4	<i>Conclusion</i> .....	177
<b>CHAPTER 5 - DISCUSSION.....</b>		<b>178</b>
5.1	THESIS IMPACT .....	178
5.1.1	<i>RSA Research</i> .....	178
5.1.2	<i>Spinal Fusion Assessment</i> .....	180
5.2	LIMITATIONS .....	185
5.2.1	<i>Simulation Limitations</i> .....	185
5.3	FUTURE WORK .....	187
5.3.1	<i>Image Simulation Improvements</i> .....	187
5.3.2	<i>Complete Simulation Validation</i> .....	188
5.3.3	<i>Patient Specific Anatomical Information</i> .....	189
5.3.4	<i>Vertebral Marking Protocols</i> .....	191

5.4	SUMMARY AND CONCLUSION .....	193
<b>BIBLIOGRAPHY .....</b>		<b>195</b>
<b>APPENDIX A - CAD DRAWINGS .....</b>		<b>202</b>
<b>APPENDIX B - THESIS COORDINATE SYSTEMS .....</b>		<b>206</b>
B.1	VERTEBRAL COORDINATE SYSTEMS.....	206
B.2	T8 ROTATIONAL COORDINATE SYSTEM .....	207
B.3	SPINAL COORDINATE SYSTEM .....	208
B.3.1	<i>Precision Movement Coordinate Systems</i> .....	209
B.4	RSA ORIGIN STYLE COORDINATE SYSTEMS .....	211
B.4.1	<i>Caudal Coordinate System</i> .....	212
B.4.2	<i>Apex Coordinate System</i> .....	213
B.4.3	<i>Dual Coordinate System</i> .....	214
B.5	RSA COORDINATE SYSTEM.....	215
<b>APPENDIX C - SIMULATION PROCESS.....</b>		<b>217</b>
C.1	PROGRAMS USE .....	217
C.2	RSA SETUP.....	217
C.3	MODEL CONSTRUCTION AND PLACEMENT .....	219
C.4	PLACEMENT IN THE RSA ENVIRONMENT.....	220
C.5	FILE CONVERSION .....	221
C.6	POV-RAY PROCESSING .....	222
C.7	RS ASSESSMENT.....	224
<b>APPENDIX D - PROGRAMMING CODE .....</b>		<b>225</b>
D.1	POV-RAY CODE.....	225
D.1.1	<i>RSA Image Code</i> .....	225
D.1.2	<i>Material Attenuation Properties</i> .....	232
D.2	MATLAB CODE.....	233
D.2.1	<i>RSA Calculations – Global Reference Frame</i> .....	233
D.2.2	<i>Apex Rotation Calculation</i> .....	241
D.2.3	<i>LocalMigration Function</i> .....	244

<b>APPENDIX E - TABULATED DATA .....</b>	<b>247</b>
E.1 SIMULATION PRECISION VALIDATION DATA .....	247
E.2 PRECISION VALIDATION CALCULATIONS.....	254
E.3 ACCURACY DATA .....	258
E.4 PREDICTION INTERVAL ACCURACY CALCULATIONS .....	309
E.5 PRECISION DATA .....	319
E.6 PRECISION CALCULATIONS.....	330
<b>APPENDIX F - PLOTS .....</b>	<b>333</b>
F.1 SIMULATION VALIDATION.....	333
<i>F.1.1 Check for Normalcy.....</i>	<i>333</i>
<i>F.1.2 Variance Comparison.....</i>	<i>349</i>
F.2 ACCURACY PLOTS .....	357
<i>F.2.1 X Accuracy.....</i>	<i>358</i>
<i>F.2.2 Y Accuracy.....</i>	<i>359</i>
<i>F.2.3 Z Accuracy.....</i>	<i>360</i>
<i>F.2.4 Rx Accuracy.....</i>	<i>361</i>
<i>F.2.5 Ry Accuracy.....</i>	<i>362</i>
<i>F.2.6 Rz Accuracy.....</i>	<i>363</i>
<i>F.2.7 Translational Accuracy Comparison.....</i>	<i>364</i>
<i>F.2.8 Rotational Accuracy Comparison .....</i>	<i>364</i>
F.3 PRECISION PLOTS.....	365
<i>F.3.1 Check for Normalcy.....</i>	<i>365</i>
<i>F.3.2 Variance Comparison.....</i>	<i>389</i>
<b>APPENDIX G - ORIGINAL THESIS WORK.....</b>	<b>399</b>
<b>APPENDIX H - PERMISSION FOR PUBLICATION .....</b>	<b>402</b>

# List of Tables

TABLE 1.1: SCOLIOSIS POPULATION DEMOGRAPHICS .....	5
TABLE 1.2: PROBABILITY OF CURVE PROGRESSION DEPENDANT ON DETECTION AGE AND CURVE MAGNITUDE.....	12
TABLE 1.3: SUMMARY OF THE ACCURACY RESULTS FROM MADANAT ET AL. (2007) [59].....	36
TABLE 1.4: PRECISION RESULT SUMMARY FROM ALLEN ET AL (2004) [63].....	39
TABLE 1.5: AVERAGE ACCURACY RESULTS REPORTED BY FRANCIS (2009) [27].....	45
TABLE 2.1: LIMITS OF CLINICAL SIGNIFICANCE. ....	50
TABLE 3.1: ACRONYMS USED FOR ANATOMICAL DIMENSIONS FOR THE VERTEBRAL MODEL.....	55
TABLE 3.2: ANATOMICAL MEASUREMENTS OF THE SIMULATED VERTEBRAL MODELS .....	55
TABLE 3.3: SPECIFICATIONS OF THE SIMULATED SPINE MODEL .....	57
TABLE 3.4: PEDICLE SCREW SIZES USED IN THE SIMULATED SPINAL MODEL.....	59
TABLE 3.5: LOCATION OF RSA RIGID BODY MARKERS WITHIN THE VERTEBRAL MODELS .....	61
TABLE 3.6: POSITIONS OF THE CENTERS OF THE RSA RIGID BODY MARKERS LOCATED WITHIN THE VERTEBRAL MODELS .....	62
TABLE 3.7: SIMULATED ATTENUATION COEFFICIENTS .....	71
TABLE 3.8: PEDICLE SCREW SIZES USED IN THE SIMULATED SPINAL MODEL.....	82
TABLE 3.9: NOMINAL DIMENSIONS OF THE PHANTOM MODEL COMPARED TO THOSE OF THE FULL-SIZE SIMULATED SPINAL MODEL. ....	83
TABLE 3.10: LOCATIONS OF THE RSA MARKERS AS DETERMINED FROM THE ASSEMBLED PHANTOM CT SCAN .....	86
TABLE 3.11: GLOBAL MOVEMENTS OF THE FUSION MODEL.....	91
TABLE 3.12: REGIONS OF INTEREST FOR THE PHYSICAL PHANTOM IMAGE ASSESSMENT .....	95
TABLE 3.13: PHYSICAL IMAGE PROPERTIES .....	96
TABLE 3.14: REGIONS OF INTEREST IN THE SIMULATE REFERENCE IMAGE.....	97
TABLE 3.15: SIMULATED IMAGE PROPERTIES .....	98
TABLE 3.16: SUPERIOR PRECISIONS GENERATED BY THE PHANTOM AND SIMULATED MODEL ASSESSMENTS .....	99
TABLE 3.17: INFERIOR PRECISIONS GENERATED BY THE PHANTOM AND SIMULATED MODEL ASSESSMENTS .....	100

TABLE 3.18: DISTRIBUTION OF THE PRECISION DATASETS.....	101
TABLE 3.19: SUMMARY OF THE RESULTS OF THE ASSESSMENT OF EQUAL VARIANCE BETWEEN THE PHYSICAL AND SIMULATED MODELS. ....	103
TABLE 4.1: MANIPULATIONS USED TO ASSESS TRANSLATIONAL ACCURACY OF ONE CARDINAL DIRECTION .....	127
TABLE 4.2: ROTATIONS INDUCED DURING ROTATIONAL ACCURACY ASSESSMENT .....	129
TABLE 4.3: TRANSLATIONAL AND ROTATIONAL LIMITS OF CLINICAL SIGNIFICANCE.....	133
TABLE 4.4: GLOBAL MOVEMENTS USED TO ASSESS SYSTEM PRECISION .....	135
TABLE 4.5: SUPERIOR AND INFERIOR MIGRATION SETS USED IN THE THREE ORIGIN STYLES.....	138
TABLE 4.6: MIGRATION DATA RECORDED FOR THE SUPERIOR ASPECT OF THE CAUDAL ORIGIN STYLE UNDERGOING A SIMULATED FAILURE OF THE SUPERIOR SECTION OF THE SPINE .....	139
TABLE 4.7: ACCURACY IN THE X DIRECTION CALCULATED FOR THE CAUDAL ORIGIN STYLE.....	140
TABLE 4.8: TRANSLATIONAL ACCURACIES OF THE THREE PRINCIPLE DIRECTIONS OF THE THREE ORIGIN STYLES COMPARED TO THE LIMITS OF CLINICAL SIGNIFICANCE .....	141
TABLE 4.9: CALCULATED ROTATIONAL ACCURACIES OF THE THREE ORIGIN STYLES .....	143
TABLE 4.10: MEASUREMENT BIAS OF THE THREE ORIGIN STYLES.....	148
TABLE 4.11: BIAS ERROR PERCENTAGE OF RESPECTIVE LIMIT OF CLINICAL SIGNIFICANCE .....	148
TABLE 4.12: MIGRATING AND ORIGIN VERTEBRAE OF THE TWO ASPECTS OF PRECISION FOR EACH ORIGIN STYLE.....	149
TABLE 4.13: PRECISION DATA FOR THE SUPERIOR ASPECT .....	150
TABLE 4.14: PRECISION OUTCOMES FOR THE INFERIOR ASPECT .....	151
TABLE 4.15: ASSESSMENT OF THE NORMALCY OF THE SUPERIOR PRECISION DATASETS FOR EACH PRINCIPAL DIRECTION.....	154
TABLE 4.16: ASSESSMENT OF THE NORMALCY OF THE INFERIOR PRECISION DATASETS FOR EACH PRINCIPAL DIRECTION .....	154
TABLE 4.17: SUMMARY OF THE STATISTICAL OUTCOME OF THE PRECISION COMPARISON TESTS.....	156
TABLE 4.18: EFFECTIVE DOSE TISSUE WEIGHTING FACTORS. ....	175

# List of Figures

FIGURE 1.1: ANTERIOR VIEW OF A NORMAL ADULT SPINE .....	1
FIGURE 1.2: SAGITTAL CURVATURES OF THE SPINE .....	2
FIGURE 1.3: COMMON STRUCTURES OF THE VERTEBRAE.....	4
FIGURE 1.4: COBB MEASUREMENT OF THE SCOLIOTIC CURVATURE .....	8
FIGURE 1.5: SUMMARY OF THE LENKE CURVE CLASSIFICATION.....	10
FIGURE 1.6: POSTERIOR SPINAL FUSION IMPLANTS .....	14
FIGURE 1.7: POST-OPERATIVE DIAGNOSTIC IMAGING AND ASSESSMENT TREE .....	17
FIGURE 1.8: PARTS OF A MODERN RSA SYSTEM.....	22
FIGURE 1.9: RSA IMAGING SET-UPS .....	23
FIGURE 1.10: OBJECT MAGNIFICATION DEPENDANT ON DISTANCE FROM DETECTOR PLANE.....	28
FIGURE 1.11: DEFINITION OF THE CROSSING LINE DISTANCE.....	31
FIGURE 1.12: PREVIOUSLY DEVELOPED SIMULATION PROCESS .....	41
FIGURE 1.13: THE CAUDAL ORIGIN STYLE UTILIZED BY FRANCIS (2009) [27].....	42
FIGURE 1.14: MARKER PLACEMENT PROTOCOL.....	44
FIGURE 1.15: THE APEX AND DUAL ORIGIN STYLES FOR MEASURING INTERVERTEBRAL MIGRATION .....	47
FIGURE 3.1: ORTHOGONAL VIEWS OF THE THORACIC VERTEBRA .....	54
FIGURE 3.2: CAD MODEL OF THE T8 VERTEBRA. ....	56
FIGURE 3.3: DIMENSIONS AND COORDINATE SYSTEM OF THE ASSEMBLED FULL SIZE CAD SIMULATED SPINAL MODEL.....	58
FIGURE 3.4: MONOAXIAL PEDICLE SCREW USED IN THE L1 VERTEBRA. ....	59
FIGURE 3.5: PLACEMENT OF THE #4 RSA MARKER IN THE T4 VERTEBRA .....	61
FIGURE 3.6: AXIAL VIEW OF T8 VERTEBRA SHOWING THE MARKER PLACEMENT WITHIN THE VERTEBRAE. ....	62
FIGURE 3.7: RSA SUITE AT THE HALIFAX INFIRMARY. ....	63
FIGURE 3.8: ALIGNMENT OF THE RSA AND SPINAL COORDINATE SYSTEMS.....	65
FIGURE 3.9: MODEL SPINE IN THE CAD RSA ENVIRONMENT.....	67
FIGURE 3.10: RSA SIMULATION PROCESS AS DEVELOPED BY FRANCIS (2009) [27].....	70

FIGURE 3.11: SURFACE ATTENUATION TECHNIQUE COMPARED TO A PHANTOM MODEL IMAGE .....	71
FIGURE 3.12: LINEAR ATTENUATION SIMULATION METHOD COMPARED TO A PHANTOM MODEL.....	72
FIGURE 3.13: SAMPLE DATA OUTPUT FROM THE MB-RSA SOFTWARE .....	73
FIGURE 3.14: PROCESS FLOW CHART OF THE PARALLEL SIMULATION PRECISION VALIDATION.....	80
FIGURE 3.15: MODIFIED T8 VERTEBRAL MODEL .....	81
FIGURE 3.16: NOMINAL DIMENSIONS AND COORDINATE SYSTEM OF THE PHANTOM SPINAL MODEL .....	83
FIGURE 3.17: PHANTOM MODEL ON ITS PLEXIGLAS BACKING .....	84
FIGURE 3.18: A SLICE FROM THE CT SCAN PERFORMED ON THE ASSEMBLED PHANTOM MODEL SHOWING THE T8 VERTEBRAL MODEL AND IMPLANTED COMPONENTS.....	85
FIGURE 3.19: SIMULATED MODEL MARKER DISTRIBUTION .....	87
FIGURE 3.20: COMPARISON OF PHYSICAL AND SIMULATED IMAGES OF THE L1 VERTEBRAL MODELS.....	88
FIGURE 3.21: TRANSLATIONAL PRECISION MOVEMENT.....	89
FIGURE 3.22: ROTATIONAL PRECISION MOVEMENT.....	90
FIGURE 3.23: ETCHED PHANTOM PRECISION ROTATION CENTER. ....	91
FIGURE 3.24: PHYSICAL PHANTOM REFERENCE IMAGE PAIR WITH ASSESSED REGIONS OF INTEREST .....	96
FIGURE 3.25: SIMULATED PHANTOM LEFT REFERENCE IMAGE WITH ASSESSED REGIONS OF INTEREST .....	97
FIGURE 3.26: CALCULATED SUPERIOR PRECISION .....	99
FIGURE 3.27: CALCULATED INFERIOR PRECISION. ....	100
FIGURE 3.28: TEST FOR EQUAL VARIANCE OF THE RX DIRECTION FOR THE INFERIOR ASPECT. ....	102
FIGURE 3.29: SIMULATED PHOTON ATTENUATION TECHNIQUES .....	106
FIGURE 3.30: MAGNIFICATION BLURRING .....	107
FIGURE 3.31: A COMPARISON OF T4 VERTEBRAE SHOWING THE X-RAY ATTENUATION TECHNIQUES .....	112
FIGURE 4.1: PROCESS FLOW CHART OF THE TESTING OF THE THREE ORIGIN STYLES.....	114
FIGURE 4.2: THE CAUDAL ORIGIN STYLE AND CAUDAL COORDINATE SYSTEM .....	116
FIGURE 4.3: THE APEX ORIGIN STYLE AND ASSOCIATED APEX COORDINATE SYSTEM.....	118
FIGURE 4.4: COMPARISON OF THE IMAGE SETS REQUIRED FOR THE CAUDAL ORIGIN STYLE AND APEX ORIGIN STYLE.....	119
FIGURE 4.5: THE DUAL ORIGIN STYLE AND DUAL COORDINATE SYSTEMS .....	122

FIGURE 4.6: EXAMPLE SHOWING THE 95% PREDICTION INTERVALS VERSUS 95% CONFIDENCE INTERVALS .....	124
FIGURE 4.7: INDUCED DISPLACEMENTS USED TO ASSESS SYSTEM TRANSLATIONAL ACCURACY.....	125
FIGURE 4.8: SUPERIOR FUSION FAILURE TRANSLATIONAL ACCURACY MOVEMENT.....	126
FIGURE 4.9: INFERIOR FUSION FAILURE TRANSLATIONAL ACCURACY MOVEMENT .....	126
FIGURE 4.10: ROTATIONAL ORIGIN OF THE T8 VERTEBRA.....	128
FIGURE 4.11: ROTATIONAL ACCURACY MOVEMENT .....	129
FIGURE 4.12: ALIGNMENT OF THE MIGRATION AND REFERENCE SCENES IN MB-RSA .....	131
FIGURE 4.13: TRANSLATIONAL PRECISION MOVEMENT.....	134
FIGURE 4.14: ROTATIONAL PRECISION MOVEMENT.....	135
FIGURE 4.15: COMPARISON OF THE TRANSLATIONAL ACCURACIES OF THE THREE ORIGIN TECHNIQUES COMPARED TO THE LIMITS OF CLINICAL SIGNIFICANCE .....	141
FIGURE 4.16: COMPARISON OF THE ROTATIONAL ACCURACIES OF THE THREE ORIGIN TECHNIQUES. ....	143
FIGURE 4.17: COMPARISON OF THE ROTATIONAL ACCURACIES OF THE THREE ORIGIN STYLES WITHOUT THE LIMITS OF CLINICAL SIGNIFICANCE INDICATORS. ....	144
FIGURE 4.18: BLAND-ALTMAN PLOT SHOWING THE ACCURACY OF THE CAUDAL ORIGIN TECHNIQUE IN THE X DIRECTION .....	145
FIGURE 4.19: BLAND-ALTMAN PLOT SHOWING THE ACCURACY OF THE APEX ORIGIN TECHNIQUE IN THE X DIRECTION .....	145
FIGURE 4.20: BLAND-ALTMAN PLOT SHOWING THE ACCURACY OF THE DUAL ORIGIN TECHNIQUE IN THE X DIRECTION .....	146
FIGURE 4.21: COMPARISON OF THE TRANSLATIONAL ACCURACY BLAND-ALTMAN PLOTS LIMITS OF AGREEMENT.....	147
FIGURE 4.22: COMPARISON OF THE ROTATIONAL ACCURACY BLAND-ALTMAN PLOTS LIMITS OF AGREEMENT.....	147
FIGURE 4.23: GRAPHICAL DISPLAY OF THE PRECISION OF THE SUPERIOR ASPECT OF THE THREE ORIGIN STYLES. ....	150
FIGURE 4.24: GRAPHICAL DISPLAY OF THE PRECISION OF THE INFERIOR ASPECT FOR THE THREE ORIGIN STYLES .....	151
FIGURE 4.25: PROBABILITY PLOT FOR THE PRECISION RESULTS OF THE SUPERIOR ASPECT OF THE APEX ORIGIN STYLE.....	152
FIGURE 4.26: PROBABILITY PLOT FOR THE PRECISION RESULTS OF THE INFERIOR ASPECT OF THE CAUDAL ORIGIN STYLE .....	153



FIGURE 4.27: EXAMPLE OF ONE OF THE TEN VARIANCE COMPARISONS WITH NO STATISTICAL DIFFERENCE .....	155
FIGURE 4.28: VARIANCE COMPARISON SHOWING STATISTICAL DIFFERENCE PRESENT IN THE Y DIRECTION FOR THE SUPERIOR ASPECT OF THE SPINE PRECISION .....	157
FIGURE 4.29: COMPARISON OF THE SUPERIOR Y PRECISION OF THE APEX AND DUAL ORIGIN STYLES.....	158
FIGURE 4.30: VARIANCE COMPARISON SHOWING STATISTICAL DIFFERENCE PRESENT IN THE Z DIRECTION FOR THE SUPERIOR ASPECT OF THE SPINE PRECISION .....	159
FIGURE 4.31: VARIANCE COMPARISON SHOWING STATISTICAL DIFFERENCE PRESENT IN THE X DIRECTION FOR THE SUPERIOR ASPECT OF THE SPINE PRECISION .....	160
FIGURE 4.32: COMPARISON OF THE INFERIOR X PRECISION OF THE APEX AND DUAL ORIGIN STYLES .....	161
FIGURE 4.33: VARIANCE COMPARISON SHOWING STATISTICAL DIFFERENCE PRESENT IN THE RY DIRECTION FOR THE SUPERIOR ASPECT OF THE SPINE PRECISION .....	161
FIGURE 4.34: X-RAY IMAGES COMPRISING THE REFERENCE EXAM FOR THE CAUDAL ORIGIN STYLE.....	163
FIGURE 4.35: X-RAY IMAGE SETS COMPRISING THE REFERENCE EXAMS FOR THE APEX AND DUAL ORIGIN STYLES .....	164
FIGURE 4.36: A POSTERIOR-ANTERIOR VIEW OF THE SIMULATED SPINE ASSEMBLY SHOWING THE RESIDUAL 20° RIGHT MAIN THORACIC CURVE.....	165
FIGURE 4.37: COMPARISON OF THE THREE EXAMINED ORIGIN STYLES .....	166
FIGURE 4.38: VECTOR ADDITION OF THE TRANSLATIONAL ACCURACIES FOR THE THREE ORIGIN STYLES ....	168
FIGURE 5.1: T4 VERTEBRA WITH MARKER MOVEMENT .....	182
FIGURE 5.2: SECTIONAL ORIGIN STYLE.....	192
FIGURE B.1: VERTEBRAL COORDINATE SYSTEMS.....	206
FIGURE B.2: T8 ROTATIONAL COORDINATE SYSTEM.....	207
FIGURE B.3: SPINAL COORDINATE SYSTEM .....	208
FIGURE B.4: LOCATION OF THE TRANSLATED ORIGIN USED FOR THE ROTATIONAL PRECISION ASSESSMENT OF THE PHANTOM SPINAL MODEL .....	210
FIGURE B.5: LOCATION OF THE TRANSLATED ORIGIN USED FOR THE ROTATIONAL PRECISION ASSESSMENT OF THE SIMULATED SPINAL MODEL.....	211
FIGURE B.6: THE CAUDAL COORDINATE SYSTEM.....	212
FIGURE B.7: APEX COORDINATE SYSTEM .....	213
FIGURE B.8: THE SUPERIOR AND INFERIOR COORDINATE SYSTEMS WHICH MAKE UP THE DUAL COORDINATE SYSTEM.....	215
FIGURE B.9: FRONT VIEW OF THE RSA COORDINATE SYSTEM.....	216

FIGURE B.10: BOTTOM VIEW OF THE RSA COORDINATE SYSTEM. .... 216

FIGURE C.1: CALIBRATION BOX AND IMAGING AREA IN THE CAD ENVIRONMENT..... 218

FIGURE C.2: IMAGE OF THE FULLY ASSEMBLED SPINE MODEL..... 219

FIGURE C.3: PLANES USED TO LOCATE MODEL TO BE IMAGED. .... 220

FIGURE C.4: SIMULATED MODEL LOCATED WITHIN RSA ENVIRONMENT. .... 220

## **Abstract**

The goal of this thesis was to assess the validity of a computer simulated Radiostereometric Analysis (RSA) environment and assess the use of novel migration origin styles for use in the assessment of spinal fusion success in post-surgical adolescent idiopathic scoliosis patients.

A parallel precision study was conducted with a physical phantom and identical computed simulated spinal fusion model. This study was used to conduct a precision validation of the simulate RSA environment. The origin style assessment was done in comparison with the translational and rotational Limits of Clinical Significance defined by Pape et al (2002) and Johnsson et al (2002) respectively [1], [2].

This thesis concluded that the use of a simulated environment is an acceptable method for the creation of phantom RSA research studies. It was also shown that both the Apex and Dual Origin Styles equally accurate and precise.

## List of Abbreviations Used

IAN	-	Lenke Classification of Scoliotic Curve [3]: 1- Main Thoracic Curve, A- Center Sacral Vertebral Line falls between Lumbar Pedicles N- Normal Thoracic Sagittal Profile
AIS	-	Adolescent Idiopathic Scoliosis
BA	-	Bland-Altman
CAD	-	Computer Aided Design, referring to the Solid Edge package developed by Siemens, Germany
CN	-	Condition Number
CNR	-	Contrast to Noise Ratio
CT	-	Computed Tomography
GCS	-	Global Coordinate System
HBI	-	Halifax Biomedical Inc <sup>©</sup>
L1	-	The First Lumbar Vertebra
LLA	-	Lower Limit of Agreement
LoCS	-	Limit of Clinical Significance
MB-RSA	-	Model Based RSA Software by Medis specials bv.
MRI	-	Magnetic Resonance Imaging
MTPM	-	Maximum Total Point Motion
PA	-	Posterior-Anterior
PI	-	Prediction Interval
POV-Ray	-	Persistence of Vision Raytracer developed by Persistence of Vision Raytracer Pty. Ltd.
RCS	-	Relative Coordinate System
RSA	-	Radiostereometric Analysis or Roentgen Stereogrammetric Analysis

RS	-	Radiostereometric
S1	-	The First Sacral Vertebra
SD	-	Standard Deviation
SNR	-	Signal to Noise Ratio
SP	-	Spinous Process
T4	-	The Fourth Thoracic Vertebra
T8	-	The Eighth Thoracic Vertebra
TP	-	Transverse Process
ULA	-	Upper Limit of Agreement

## Glossary

- Accuracy - An assessment of the closeness of a measurement to the true value.
- Adolescent Idiopathic Scoliosis - Three-dimensional deformity of the spine with no defined cause.
- Bartlett's Test - Test for equal variances when all data sets tested are normally distributed.
- Bland-Altman Plot - Difference plot developed by Bland and Altman (Lancet 1986) [4]. Also known as a Tukey Difference Plot.
- Caudal - Pertaining to the inferior of the spinal column.
- Centroid - The geometric center of an object or group of objects.
- Condition Number - A measurement of the linearity of a distribution of RSA markers.
- Control Markers - The markers in the calibration box that make up the control plane. Used to determine the three dimensional location of the x-ray foci.
- Cranial - Pertaining to the superior of the spinal column.
- Crossing Line Distance - The length of the shortest perpendicular connection line between a pair of projection lines.
- Absorbed Dose / Effective Dose - The energy imparted by ionizing radiation per unit mass of irradiated material (Gy) / A measure of equivalent dose which is weighted for the biological sensitivity of the exposed tissues, relative to the whole body (Sv).
- Fiducial Markers - The markers in the calibration box that make up the fiducial plane. Used to define the global coordinate system of the RSA environment.
- Fixation Rod - Titanium or Cobalt-Chrome rod implanted into the back immobilize and provide initial support to the fused section of the spine.

Functional Integrity	- The rigidity of the fused spine section.
Global Coordinate System	- The coordinate system used in the RSA environment.
Inferior Aspect	- Pertaining to the Inferior section of the spine. A measurement including the L1 vertebra.
Inferior Failure	- A simulated failure condition where both the T4 and T8 vertebrae are moved in relation to the L1 vertebra.
Kyphosis	- An anterior concavity of the spine in the sagittal plane.
Levene's Test	- Test for equal variances when one or more data sets tested are not normally distributed.
Lordosis	- A posterior concavity of the spine in the sagittal plane.
Lumbar Spine	- The third region of the spine made up of vertebrae L1 through L5. This section makes up the lower back.
Marked Vertebrae	- Vertebrae into which RSA markers have been implanted.
Marker Cluster	- The three-dimensional distribution of RSA markers that define the pose of a rigid body.
Marker Model	- A model that represents the rigid body generated from the markers matched in both the left and right image.
Matched Markers	- Markers which are matched in both the left and right image of an RSA exam which have a parallel crossing line distance below 0.1mm.
#Matched Markers (RSA Output)	- The number of markers in a marker model matched between two RSA exams.
Maximum Total Point Motion	- The length of the translation vector of the marker in a marker cluster that has the greatest migration.
Origin Style / Origin Technique	- One of the three conditions used to measure intervertebral migration.

Phantom Model	- A physical anatomical model built for research or equipment testing.
Pose	- The three dimensional position and orientation of and object.
Precision	- A measurement of the system repeatability. The degree which repeated measurements under identical conditions produce the same results.
Rigid Body Error	- The mean difference in the relative distances between markers from one exam to the subsequent exam.
RSA Marker	- Tantalum beads used as radio opaque objects for use in RS assessment. Usually of standard diameter or 0.5, 0.8 or 1.0mm [5].
Simulated Model	- A computer simulated anatomical model used for research.
Structural Stability	- The osseointegration of the implant into the bone.
Superior Aspect	- Pertaining to the Superior section of the spine. A measurement including the T4 vertebra.
Superior Failure	- A simulated failure condition where only the T4 vertebra is moved in relation to the T8 and L1 vertebrae.
Thoracic Spine	- The second region of the spine made up of vertebrae T1 through T12. The section of the spine where the rib cage attaches.
Vertebra/Vertebrae	- Boney segments that makes up the vertebral column or spine.



## Acknowledgements

I would like to thank my supervisory committee, my supervisor Dr. Ron El-Hawary (Department of Surgery), Dr Michael Dunbar (Department of Surgery), Dr. Steven Beyea (Department of Physics and Atmospheric Science), and Dr. Andrew Warkentin (Department of Mechanical Engineering) for their knowledge, time, and advice. I enjoyed my work with the committee and without their support and experience this project would not have been possible.

I would like to thank Elise Laende, James Edwards, and Allan Hennigar for their invaluable help with the RSA and statistical aspects of the project, and for taking the time out of their day to answer all my questions and offer their welcome advice. I would like to acknowledge Jason Fong for his early assistance with anatomical structure modeling. I would also like to thank Dr. Waleed Kishta for his help in the assembly of the phantom model and the IWK and NRC CT imaging groups for their time and equipment.

I would like to thank DePuy Spine™ for providing financial and technical support, specifically the use of the AIS implant CAD models, Halifax Biomedical Inc<sup>®</sup> for use of the Halifax Infirmary RSA suite and calibration box data and the Dalhousie Mechanical Engineering Department for use of their rapid prototyper.

I would also like to thank the School of Biomedical Engineering community for their guidance and support. I would especially like to thank Sandy Mansfield for everything that she has helped me with during my time in graduate studies.

Lastly, I would like to acknowledge my family and friends for their continued support throughout my time spent pursuing my master's degree.

# Chapter 1 - Introduction

## 1.1 Background

### 1.1.1 Spinal Anatomy and Physiology

One of the distinguishing characteristics of vertebrates is the spine, a segmented anatomical structure which runs the length of the back. It provides support necessary for an upright posture while providing flexibility allowing motion in six degrees of freedom; extension (forward bending), flexion (backward bending), side-to-side bending, as well as left and right rotation. This support/flexibility relationship is created through the interactions of rigid vertebral bones, flexible intervertebral discs, and surrounding muscular structures [6], [7].

The spine is made up of thirty-three vertebrae separated into four sections based on vertebral shape. They are the Cervical, Thoracic, Lumbar, and Sacrococcygeal regions, Figure 1.1. The Cervical Spine consists of the seven vertebrae (C1–C7) which support the skull and make up the neck. Inferior to C7 vertebra, the Thoracic Spine consists of twelve vertebrae (T1–T12). These vertebrae are where the ribs posteriorly attach, creating the structural unit of the rib cage. The third section of the spine, located inferior to the thoracic

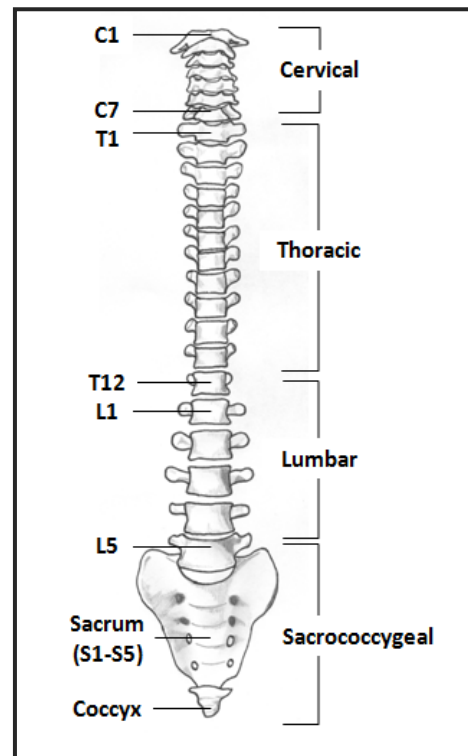


Figure 1.1: Anterior view of a normal adult spine. Adapted from Gray's Anatomy: the Anatomical Basis of Clinical Practice 40th Anniversary Edition (2008) [6]

region, is that of the Lumbar Spine. This section consists of five vertebrae (L1-L5) which make up the lower back. This section provides the majority of the flexibility found in the back. The fourth and most inferior section, the sacrococcygeal region consists of two sections of the spine: the Sacrum and the Coccyx. The Sacrum is composed of five fused vertebrae and the Coccyx is composed of a separate group of three fused vertebrae, commonly known as the tailbone [6], [7].

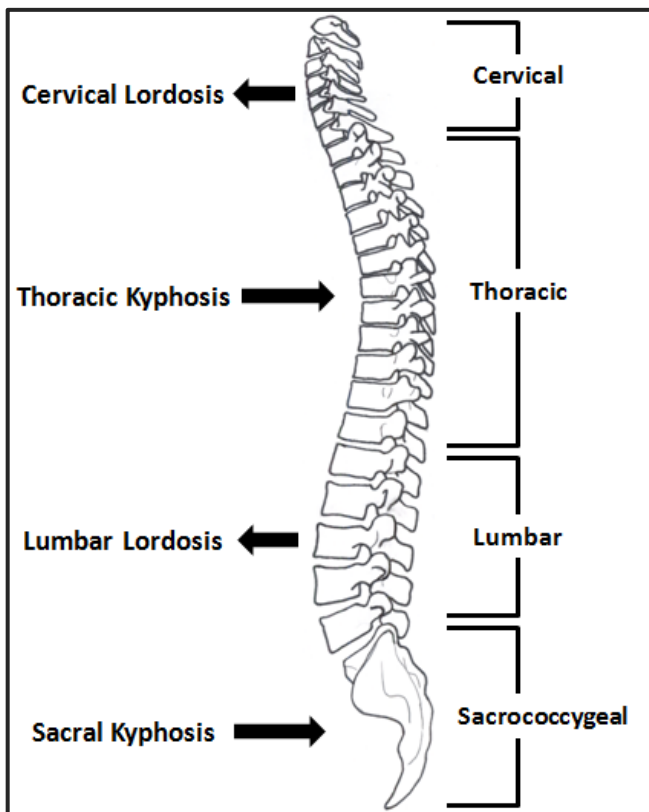


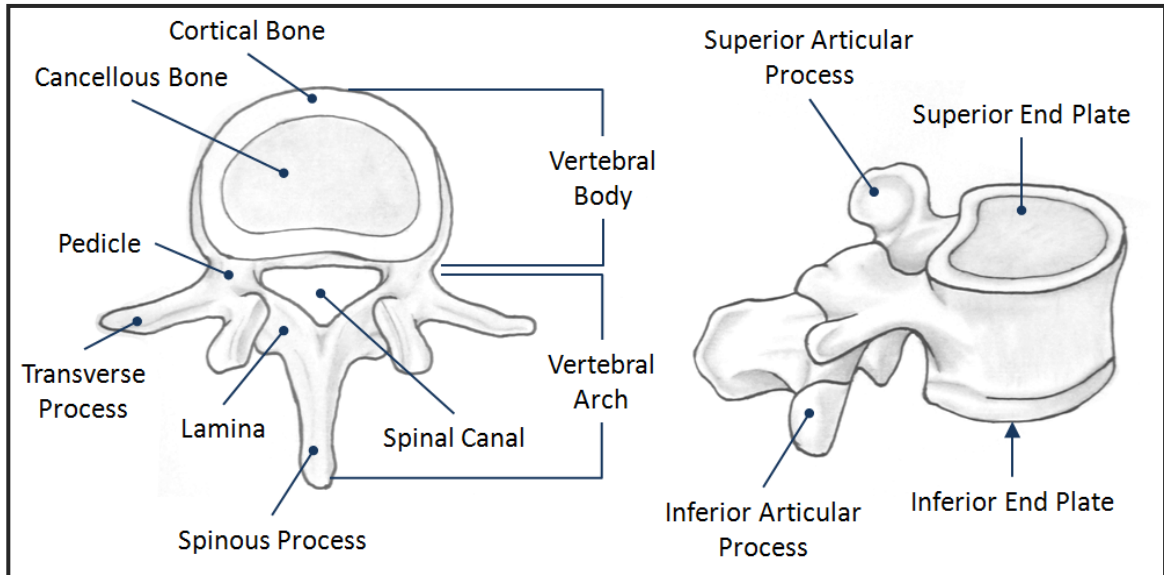
Figure 1.2: Sagittal curvatures of the spine. Adapted from Gray's Anatomy: the Anatomical Basis of Clinical Practice 40th Anniversary Edition (2008) [6]

The sections of the spine also delineate the four lateral curves of the normal adult spine: two in kyphosis and two in lordosis, Figure 1.2. A kyphosis is an anterior concavity or curvature in the sagittal plane with a frontward concavity. Conversely a lordosis is a posterior concavity having a rearward concavity [7]. A normal cervical spine has a lordosis ranging from 20° to 40° [7]. This is mirrored by the kyphosis present in a normal thoracic

spine which also has a general range of 20° to 40° [7]. A normal lumbar spine has a lordosis in the range of 30° to 50° [7]. The range of the sacral kyphosis varies greatly between individuals [7].

Due to the proximity to the skull, the first two vertebrae of the cervical spine differ in their anatomical structure to compensate for their different anatomical loading. Their unique anatomy is not discussed in this thesis. The remaining twenty-two vertebrae that make up the cervical, thoracic, and lumbar sections of the spine all share similar anatomy. The general anatomy is shown in Figure 1.3. Each vertebra consists of two sections: the vertebral body and the vertebral arch. The vertebral body is a disk shaped structure made of an outer ring of cortical bone surrounding an area of cancellous bone. Adjacent to the superior and inferior plates of the vertebral body are the intervertebral discs. The intervertebral discs are collagenous structures that allow for movement between two adjacent vertebrae. Attached to the posterior of the vertebral body is the structure known as the vertebral arch. The vertebral arch is made of two pedicles, two laminae, two transverse processes, one spinous process, and four articular processes. This structure encompasses the spinal cord providing protection for the vital nerve cord. The pedicles are two, round post like structures which extend posteriorly from vertebral body. The laminae are flat structures that extend medially from the pedicles, coming together in the center. Attached to the union of the two laminae is the spinous process. The spinous process is a structure which extends posteriorly from the vertebral arch. The transverse processes extend laterally from the posterior ends of the pedicles. Both the spinous and transverse processes act as attachment points for tendons and ligaments. The four articular processes exist as two pairs: the superior and inferior articular processes. They extend superiorly and inferiorly from the union of the pedicles and lamina. The superior articular process creates an interface with inferior articular process from the superior vertebrae creating the facet joints. The facet joints are lubricated with synovial fluid allowing for movement between the two processes. The structures of the articular

processes create movement constraints between the two adjacent vertebrae, limiting how the spine can flex between the two adjacent vertebrae [6], [7].



**Figure 1.3: Common structures of the vertebrae. (Adapted from Gray's Anatomy for Students 2<sup>nd</sup> Edition (2009)) [8].**

Each vertebra gets progressively larger the more inferior their placement in the vertebral column. This is due to the increased axial loading present at each descending level. The overall geometry of the spine provides additional resilience to axial loads through the use of the alternating lordoses and kyphoses allowing for the upright posture present in humans keeping the line of gravity over the pelvis [6], [7].

### **1.1.2 Adolescent Idiopathic Scoliosis**

The etymology of the word scoliosis is that it was derived from the Greek word *Skoliōsis* which means “a crookedness” [7], [9], [10]. Scoliosis is defined as “a lateral deviation of the normal vertical line of the spine which, when measured on a radiograph, is greater than 10°” [10]. A scoliotic curve is considered an Adolescent Scoliotic curve if it is developed after the age of 10 [11]. The etiology of the typical Adolescent Scoliosis

remains unknown and therefore is apt to the moniker idiopathic. Adolescent Idiopathic Scoliosis (AIS) is the most common type of scoliosis [11]. AIS accounts for over 80% of surgical cases for scoliosis correction [7].

The prevalence of scoliosis in the general adolescent population is small with only 1.5 to 3 percent of the population having curves greater than 10° when measured on a standing Postero-Anterior (PA) radiograph [10]. The demographics of the scoliotic population as reported by the *Tachdjian's Pediatric Orthopaedics* and *The Pediatric Spine* text books are presented in Table 1.1.

**Table 1.1: Scoliosis Population Demographics. Data taken from *Tachdjian's Pediatric Orthopaedics* [10] and *The Pediatric Spine* [12]. \*indicates female-male patient ratio requiring surgical intervention.**

Curve Magnitude	Tachdjian's Pediatric Orthopaedics [10]		The Pediatric Spine [12]	
	Population Prevalence (%)	Female-Male Ratio	Population Prevalence (%)	Female-Male Ratio
>10°	1.5-3	1.4:1	2-3	1.4-2:1
>20°	0.3-0.5	5.4:1 (7.2:1*)	0.3-0.5	5.4:1
>30°	0.2-0.3		0.1-0.3	10:1
>40°			<0.1	

Scoliotic curves are named for the section of the spine in which they form. For example a thoracic curve is present in the thoracic region of the spine. Scoliotic curves can be broken down into two sub groups: structural and non-structural. Structural curves are the largest curves present and do not bend when imaged in side bending radiographs. Non-structural curves are the smaller curves present in the spine and are shown to bend in side bending radiographs. Non-structural curves are also called compensatory curves as they often appear as an attempt to maintain trunk alignment. As such non-structural curves often resolve after correction of the main structural curves [7].

The existence of scoliosis in a patient can have several adverse effects on that patient. Among these include psychosocial effects, respiratory function impairment, rib prominence, back pain and trunk imbalance. It has been found that the mortality rate of patients who have AIS is comparable to that of the average population [10], [12].

Respiratory function impairment is directly correlated to thoracic curve magnitude. As curve magnitude increases, the impairment also increases. Curves in the lumbar spine do not affect pulmonary function [11]. It has been shown that cardiopulmonary impairment often does not occur in patients with curve magnitudes less than  $100^{\circ}$  [10]. No patient who has had adolescent onset idiopathic scoliosis has died due to respiratory failure caused by AIS [11].

There has been no correlation between scoliosis curve magnitude or location and the psychosocial effects that the condition has on the patients. In fact patients who have larger curves are often more accepting of their deformity, experiencing less focus on the cosmetic effects of the deformity than those with lesser magnitude curvatures [11].

A trunk imbalance is the lateral shifting of the line of gravity away from its normal position over the center of the pelvis. Interestingly, smaller magnitude single curves can create larger imbalances than comparably larger magnitude compound curve structures. Compound curves can rebalance the spine producing less of a decompensation and less of a cosmetic impact [11], [12].

### **1.1.2.1 Patient Assessment**

The assessment for scoliosis severity varies from patient to patient but includes forward bending tests, plumb line, skin assessment, leg length assessment and radiographic assessment [7], [10–12].

Forward bending tests look for a rib prominence using a scoliometer. A patient is asked to bend forward until the spine is level. If scoliosis is present one side of the back will be raised above the other. The scoliometer is an inclinometer which gives a clinical measurement to this test [7], [10–12].

A plumb line test examines the spine for trunk decompensation. On a standing patient a plumb-bob is used to drop a plumb line from the C7 vertebra straight down the back. This test will indicate whether the trunk is centered over the pelvis or to what degree the trunk is decompensated [7], [11].

The skin is assessed for indicators of underlying conditions. Café au lait spots and axillary freckles indicate possible neurofibromatosis. Dimpling or a hairy patch in the lumbosacral region may indicate a spinal dysraphism. Connective disorders like Marfan syndrome may be indicated by excessive skin or joint laxity [11].

Discrepancies in leg length are also an indicator of scoliosis [7], [10], [11]. Leg lengths are measured from the anterior superior iliac spine or the umbilicus to the medial malleolus for both legs [7].



### 1.1.2.1.1 Radiographic Curve Measurement

The primary method for assessing the magnitude of a scoliotic deformity has been the Cobb Method. This method uses the Cobb Angle which uses a PA radiograph to assess the lateral magnitude of scoliotic curves. The Cobb Method uses lines drawn perpendicular to the endplates of the cranial and caudal vertebrae of the scoliotic curve to determine the radius of curvature. The angle of this intersection is the Cobb Angle for the curve [7], [10–12]. Figure 1.4 shows the determination of the Cobb Angle from a PA view.

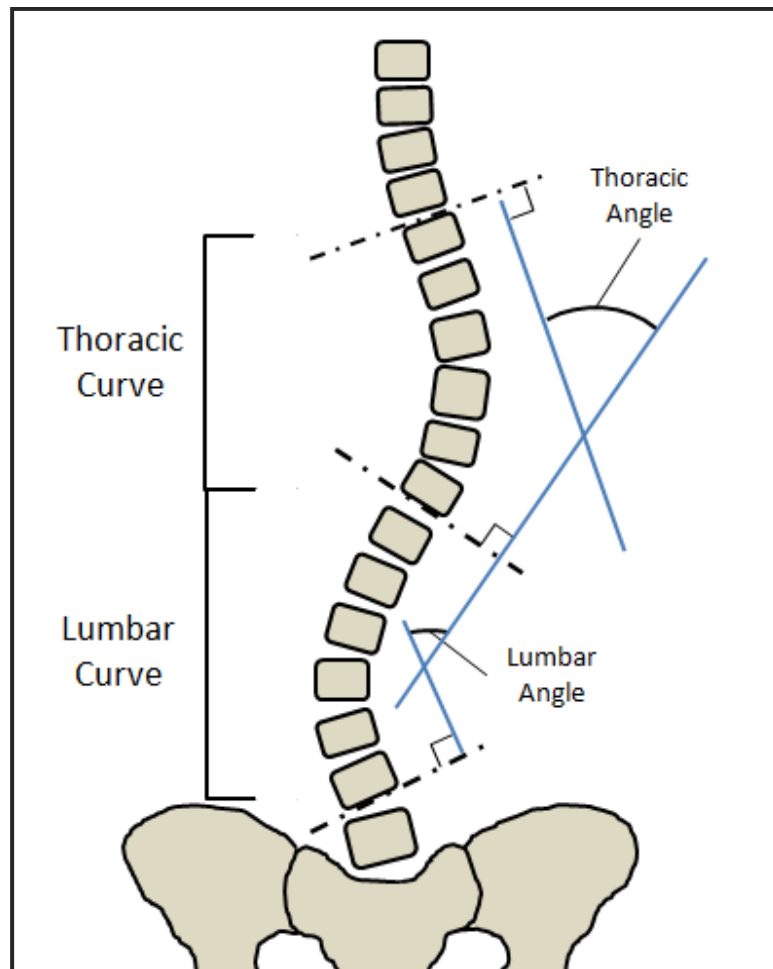


Figure 1.4: Cobb Measurement of the Scoliotic Curvature. Adapted from Tachdjian's *Pediatric Orthopaedics* 3<sup>rd</sup> Edition (2002) [10].

### **1.1.2.2 Curve Classifications**

There have been several methods for the classification of scoliotic curve structures. This thesis utilized the Lenke radiographic classification which is summarized here [3], [7], [12]. This thesis deals with a spinal deformity corrected to a 20° right 1AN Lenke classified curve.

#### *1.1.2.2.1 Curve Type*

The spine column is broken into three regions: The Proximal Thoracic (PT), the Main Thoracic (MT) and the Thoracolumbar/Lumbar (TL/L). From these six curve types are created [3], [7], [12].








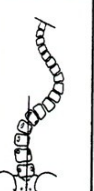



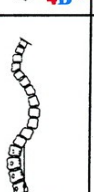
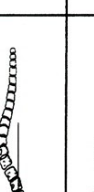



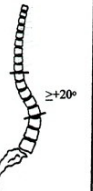
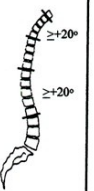
- Type 1 Main Thoracic (MT)
- Type 2 Double Thoracic (DT)
- Type 3 Double Major (DM)
- Type 4 Triple Major (TM )
- Type 5 Thoracolumbar/Lumbar (TL/L)
- Type 6 Thoracolumbar/Lumbar, Main Thoracic (TL/L-MT)

#### *1.1.2.2.2 Lumbar Spine Modifier*

The lumbar modifier is a measurement of the position of the lumbar vertebra with respect to the center vertical sacral line (CVSL) [3], [7], [12]. They are classed as follows:

- Modifier A The CSVL runs between the pedicles all the way to the stable vertebra.
- Modifier B The CSVL lies between the medial border of the concave pedicle and the concave margin of the vertebral body at the apex of the lumbar curve.
- Modifier C The CSVL lies completely medial to the concave margin of the apex vertebra of the lumbar curve.

Figure 1.5 shows a summary of the Lenke (2001) classification [3].

<b>Lumbar Spine Modifier</b>	<b>Curve Type (1 - 6)</b>					
	<b>Type 1 (Main Thoracic)</b>	<b>Type 2 (Double Thoracic)</b>	<b>Type 3 (Double Major)</b>	<b>Type 4 (Triple Major)</b>	<b>Type 5 (TL/L)</b>	<b>Type 6 (TL/L - MT)</b>
<b>A (No to Minimal Curve)</b>	 1A*	 2A*	 3A*	 4A*		
<b>B (Moderate Curve)</b>	 1B*	 2B*	 3B*	 4B*		
<b>C (Large Curve)</b>	 1C*	 2C*	 3C*	 4C*	 5C*	 6C*
<b>Possible Sagittal structural criteria (To determine specific curve type)</b>	 Normal	 PT Kyphosis	 TL Kyphosis	 PT + TL Kyphosis		

- : <10°  
\* T5-12 sagittal alignment modifier: -, N, or + N : 10-40°  
+ : >40°

Figure 1.5: Summary of the Lenke Curve Classification. The 1AN curve was modeled for this thesis. Reproduced with permission from Lenke et al (2001)<sup>1</sup> [3].

<sup>1</sup> Lenke, L. G., Betz, R. R., Harms, J., Bridwell, K. H., Clements, D. H., Lowe, T. G., & Blanke, K. (2001). Adolescent idiopathic scoliosis: a new classification to determine extent of spinal arthrodesis. *The Journal of Bone and Joint Surgery. American volume*, 83-A(8), 1169-81.

#### 1.1.2.2.3 Thoracic Sagittal Alignment Modifier

The thoracic sagittal alignment modifier is an indicator of the sagittal alignment of the spine. Three symbols are used to define this quantity. A (+) indicates a hyperkyphotic ( $>40^\circ$ ) thoracic spine while a (-) indicates a hypokyphotic thoracic spine ( $<10^\circ$ ). A (N) indicates a normal kyphotic curve of the thoracic spine [3], [7], [12].

#### 1.1.2.3 Curve Progression

The risk of curve progression is dependent on many factors. Among these factors include family history, curve size, detection age, length of time until skeletal maturity and gender [7], [10–12]. It has been noticed that adolescent idiopathic scoliosis occurs more frequently in members of the same family. Male patients have approximately one tenth the chance of curve progression than similar female patients [12].

The threshold which defines curve progression has been reported. *Tachdjian's* defines curve progression as an increase of  $5-6^\circ$  [10] while others define curve progression as a curve increase over time. *Lovell and Winter's Pediatric Orthopaedics* define curve progression as a more than  $1^\circ$  increase over a period of a month [11], while *Basic Anatomy and Pathology of the Spine* by Medtronic defines curve progression as an increase in curvature of more than  $5^\circ$  in a six month period [7].

Detection age is a significant factor in assessing whether a scoliotic curve will progress. For example a curve under  $19^\circ$  detected in a 16 year old patient has a progression potential of 0% while a  $30^\circ-59^\circ$  curve detected in a 10-12 year old patient has a 90% chance of progression [12]. *The Pediatric Spine* reports the probability of progression of scoliotic curves as shown in Table 1.2 [12].

**Table 1.2: Probability of Curve Progression Dependant on Detection Age and Curve Magnitude as reported by The Pediatric Spine [12].**

Curve Magnitude at Detection (Deg)	Detection Age		
	10-12	13-15	16
< 19	25%	10%	0%
20-29	60%	40%	10%
30-59	90%	70%	30%
> 60	100%	90%	70%

The length of time until a patient reaches skeletal maturity is another factor for assessing the risk of curve progression. A patient undergoing the early stages of their puberal growth spurt is at the risk of a crankshaft phenomenon [10], [11]. Any curve increasing by more than 1° per month during this early period is likely to be progressive and will require treatment. Curve increases during this early period of more than 0.5° per month should be monitored closely while increases of less than 0.5° per month are considered mild [11]. After they reach their peak height velocity, the risk of crankshaft decreases [10].

### **1.1.3 Medical Treatment**

The treatment required for scoliosis varies from patient to patient. The treatment path decided upon is determined by curve magnitude, curve classification, health effects and patient psychosocial characteristics [7], [10–12].

#### **1.1.3.1 Observation**

For deformities under 20° observation of curve progression is often undertaken [7], [10–12]. *Lovell and Winter's Pediatric Orthopaedics* recommends that curves under 25° should be radiographically monitored every four to six months and patients who grow to skeletal maturity with curve magnitudes less than 30° should be monitored every five

years [11]. Schnuerer (2003) recommends watching for curve magnitude increases of 5-10° in a six month period indicating curve progression [7].

### **1.1.3.2 Bracing**

The next level of medical intervention for the treatment of scoliosis is the prescription of an orthopaedic brace. These braces, worn 16-18 hours a day [7], produce stagnation in the progression of scoliotic curves [7], [10–12]. Braces are designed to arrest curve progression while a patient reaches skeletal maturity and are not a form of permanent correction [7], [10–12].

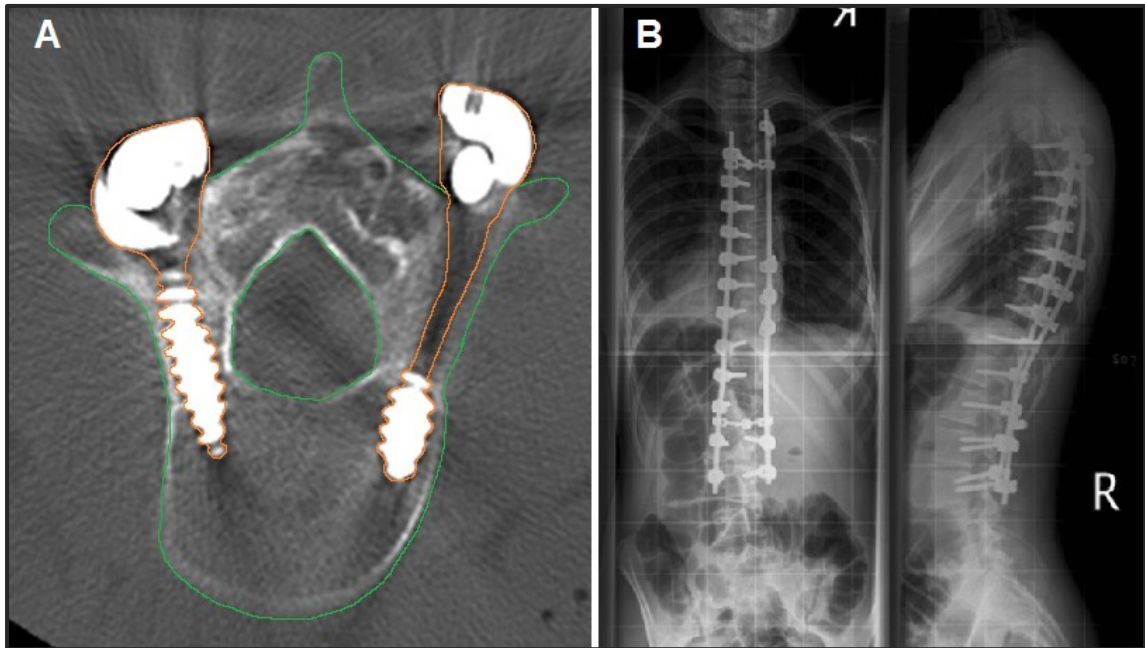
The use of bracing is indicated if a curve severity is between 30° and 45° or with patients who have curves 20 to 30° who have undergone a curve progression over 5° [10], [12]. The use of bracing has an upper functionality limit of around 45° as these curves cannot be controlled with bracing as well as the brace having a detrimental cosmetic effect [10–12].

Bracing has been found to be successful at halting curve progression (less than a 5° increase in curve severity) in around 70% of treated patients [11], [13], [14].

### **1.1.3.3 Surgical Intervention**

The choice to undergo a surgical intervention for scoliosis treatment is a complex multifaceted one. The goal of a surgical treatment is to improve alignment of the spine and restore balance while preventing further curve progression. This is done through creating a solid arthrodesis or rigid fusion of a multi-level spine section [10–12]. To create a spinal fusion, rigid implants are used to secure the spine and provide corrective forces. There are several fusion stabilization techniques but this thesis focuses on the use

of a system of pedicle screws and rigid fixation rods implanted using a posterior approach. These screws and rods can be seen implanted in Figure 1.6.



**Figure 1.6: Posterior Spinal Fusion Implants A) An image taken from a CT scan showing a vertebra (green outline) implanted with pedicle screws (orange outline). B) Post-operative bi-planar x-rays of a patient who received a spinal fusion using posterior implants.**

The implanted screws and rods are there to provide structure while the fusion occurs. The resulting solid fusion is created by bridging bony growths of the posterior region of the vertebrae. These growths form over the facet joints and implanted bone auto and allograft tissue, removing the freedom of movement of the fused sections. This region is expected to perform similar to natural bone, demonstrating standard stiffness and strength properties.

The options for implants used come in a variety of metals including: Stainless Steels, Titanium alloys and Cobalt-Chrome alloys. They are selected for their strength and biocompatibility properties. The fixation rods are machined as long cylinders with diameters of around 5-6mm. They are bent and cut to length in the operating room and

implanted into the patient. The rods are connected firmly to the pedicle screws and are connected to one another using cross-connectors. The cross-connections create a box configuration (Figure 1.6 B) which strengthens the implant system. However, the fixation rods are not designed to withstand the full loading of the spine and allow for some bending before a full fusion has taken place. Therefore if a solid fusion does not occur then the stress imparted on the immobilization system will eventually fatigue the rods and they will fail, leading to a loss of correction [11].

There are many considerations that go into selecting a spinal fusion. These considerations include: Curve magnitude (Cobb Angle), Decompensation, Rotation, Proximity to Skeletal Maturity, Progression Despite Bracing, Pulmonary Function, and Psychosocial Considerations [12]. Curves with magnitudes of 40-50°, for skeletally immature patients, or over 50° for skeletally mature patients are good candidates for spinal fusions [7], [10–12]. In less than 1% of surgical cases, the required intervention was due to the presence of back pain [12].

The right thoracic curve pattern, like the one used during the course of this research study, is the most common curve pattern seen clinically [11]. The right thoracic curves are most often corrected using a posterior approach [11]. Anterior approaches are undertaken when required but they will result in decreased pulmonary function, at least temporarily, when undertaken for thoracic fusions [11].

The length of the spinal fusions are kept to a minimum as to impinge as little as possible on patient mobility while providing adequate correction [10], [11]. Normally one level proximal to the stable vertebrae is selected [11].



#### **1.1.3.4 Diagnostic Follow-Up**

It has been estimated that between 20 and 40% of patients who undergo surgical intervention report that the surgery has failed to relieve their symptoms. In many of these cases, a pseudoarthrosis or non-union has occurred [15]. Therefore it is important that a patient who has undergone a spinal fusion undergo routine follow-up diagnostic assessment. Accurate measures of the arthrodesis is important, especially for those patients who remain symptomatic after surgical intervention [16]. There are currently no universally accepted radiographic assessment criteria for determining fusion success but there are several methods used to attempt to assess the fusion success [16]. Spinal fusions are assessed for two characteristics: structural stability and functional integrity. Structural stability is the assessment of whether the implants have integrated into the vertebrae, or the osseointegration of the implants [1], [17]. The functional integrity is the assessment of the arthrodesis itself; wither or not the fusion acts as a single rigid body or not [1], [17].

The general process in which diagnostic imaging is conducted post-operatively was summarized by Hilibrand et al (1998) [15]. In their diagnostic process all post-operative patients undergo plain radiographs. Those who have suspected non-unions as determined from the plain radiographs are assessed for symptoms. If these patients exhibit pseudoarthrosis symptoms they are imaged using CT imaging. If apparent union is shown but symptoms persist MR imaging is undertaken.

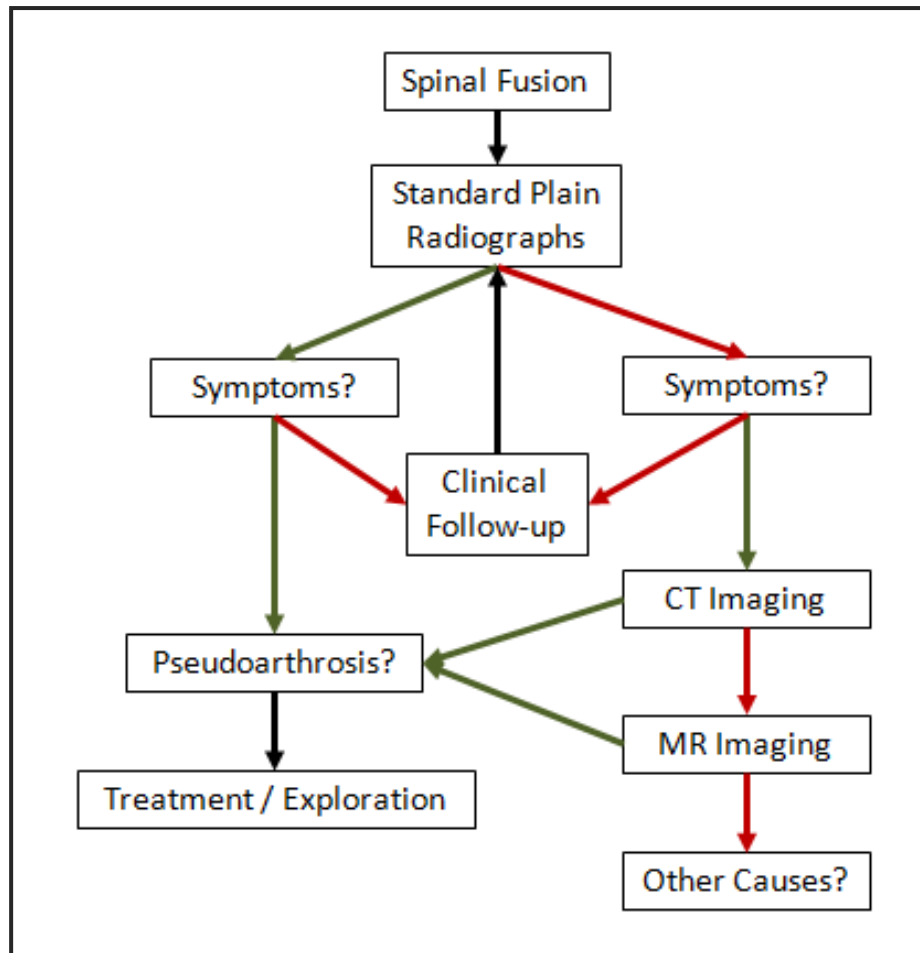


Figure 1.7: Post-operative diagnostic imaging and assessment tree. Adapted from Hilibrand et al (1998) [15]. Green arrows indicate that the patient is positive for non-union assessment. Red arrows indicate that patients do not exhibit non-union characteristics.

#### 1.1.3.4.1 Radiographic Imaging

The most prevalent method for assessing the success of spinal fusion is the use of standard radiographs [15], [16]. These radiographs are used as an initial screening for non-union or delayed union and it is recommended that a non-symptomatic patient comply with a radiographic regime of at least two years [15]. Movement of the fused spine is normally assessed using lateral flexion-extension radiographs [18], [19]. It is been widely accepted that criteria for positive fusion is translational movement of the fusion of less than 2mm [15], [18].

Lam et al (2008) in an analysis of a collection of various studies found that radiographic assessment of spinal fusions carries with it significant error. They reported that translational error is  $\pm 2\text{mm}$  while rotational measurement error can be as high as  $\pm 5^\circ$  [20]. The rotational error characteristic is alarming since most non-unions show rotational movements of  $2\text{-}4^\circ$  in helical CT scans [16]. Santos et al (2003) concluded that the use of plain radiographs indicate a higher rate of fusions than helical CT scans due to their inability to detect fine gaps indicating pseudoarthrosis. They concluded that static radiographs are unable to detect non-unions present in spinal fusions [16].

#### *1.1.3.4.2 Computed Tomography*

The next level of diagnostic assessment for spinal fusions is the use of Computed Tomography or CT scans. These scans provide increased resolution of the imaging area over that of the plain radiograph [15]. This increased resolution allows for CT scans to assess patients who appear to have solid fusions in radiographic assessment but still exhibit symptoms [15].

The use of CT imaging comes with several drawbacks. Chief among those is the high radiation dose administered to the patient [11], [20]. A study by Huda et al (1997) determined that the effective dose experienced by a pediatric patient undergoing a abdominal CT scan is 3.1 to 5.3mSv [21]. Patients who undergo surgical treatment for scoliosis are often young and are vulnerable to these high radiation dosages during their growth period [20]. More over the use of CT imaging requires more time and expense than traditional plain radiographic imaging [20]. Another drawback for the use of CT imaging is that the non-unions often occur in the axial plane. Even with high resolution imaging having image slices spaced 1-3mm apart, these pseudoarthrosis may still be

missed [15]. CT imaging also shows an increased inaccuracy in the measurement of the rotation of vertebrae inclined in the sagittal and coronal planes [20]. Since scoliosis is a three-dimensional deformity, vertebrae are often rotated in several planes leading the rotational measurements recorded by CT scans to be misleading [20]. Due to the high amount of dense implants located in a spinal fusion surgical site large artifacts can be produced during CT imaging [15]. Newer CT software and the use of titanium as an implant material have reduced these artifacts [15].

The nature of CT imaging precludes it from being able to assess the functional integrity of a spinal fusion. It is however able to adequately assess the structural stability of the fusion [17].

#### *1.1.3.4.3 Magnetic Resonance Imaging*

The third modality of diagnostic imaging used to assess spinal fusion success is Magnetic Resonance Imaging or MRI. MRIs do not have as high a resolution as CT scans but are better able to assess patients who experience mechanical instabilities where both plain radiographs and CT imaging show a solid fusion [15]. This is an assessment of the functional integrity of the spinal fusion [17]. Unfortunately due to the signal generation and acquisition technique, MR imaging is not able to assess the composition of the bone surrounding the implanted surgical screws. This leads to a poor assessment of the structural stability of the spinal fusion [17].

Unlike the two nuclear imaging modalities, MR imaging does not expose patients to radiological doses. Although the use of MR imaging is normally counter indicated where metal is concerned, the use of non-ferrous metals in surgical implants mean that

they are safely imaged using an MRI scanner [15]. MR imaging is associated with high costs compared to standard plain radiographs.

#### *1.1.3.4.4 Surgical Exploration*

Surgical exploration, as stated by the Bosworth dictum, is the only way to be certain that a spinal fusion has occurred [22]. As such it is considered the “gold standard” for surgical fusion assessment as no other modality can match the assessment accuracy achieved [1], [15]. The use of surgical exploration is not recommended for routine assessment of spinal fusions due to the fact that they are economically impractical, invasive and their associated morbidity [1], [15], [22].

### **1.1.4 Radiostereometric Analysis**

Radiostereometric Analysis or RSA is a method of using two registered x-ray images to determine the three dimensional position of marked structures of the body. It was originally developed shortly after the first use of x-rays in medical diagnostics, with the first published use in 1898 [23]. The modern use of RSA for medical diagnostics was pioneered by Selvik in Sweden in the 1970s [5], [23–29]. With the growing use of computers in medical imaging the use of RSA has expanded.

RSA is a highly accurate, three-dimensional measurement method with accuracy ten times over that of conventional radiography [5], [27–30]. Repeated RSA examinations provide low dose temporal assessment of marked body motion [5], [27–29], [31]. The most significant use of RSA has been the study of the micromotion of implanted joint replacements [5], [25], [28–34]. It has been shown that the continual motion of an implant is predictive of implant failure. In a seminal article, Ryd et al (1995) found that the

determination of long term implant performance could be predicted by assessing early implant stability [33]. They found that data recorded in the first two years predicted long term implant performance 85% of the time [28], [29], [33].

Due to these advantages, RSA has been used extensively in the literature to assess the motion of the spine [1], [2], [5], [24], [27], [35–45]. It has been found to be a good measurement tool to determine the intervertebral migration associated with determination of lumbar and cervical spine fusion success [1], [2], [35], [39], [41–43], [46–50]. With the high measurement resolution and low dosage characteristics RSA has the potential to accurately assess the three-dimensional complex migrations associated with multi-level spinal fusions performed for the treatment of adolescent idiopathic scoliosis [27].

#### ***1.1.4.1 RSA Equipment Setup***

All modern RSA equipment setups share common physical components. These common components include: a pair of synchronized x-ray tubes, a pair of image detectors and a calibration box [51]. The main components of an RSA set-up are shown in Figure 1.8. The term calibration cage is also used in the literature instead of calibration box [5], [23–25], [32], [51]. This thesis will use the term calibration box to define the rigid body used to calibrate the RSA images for analysis.

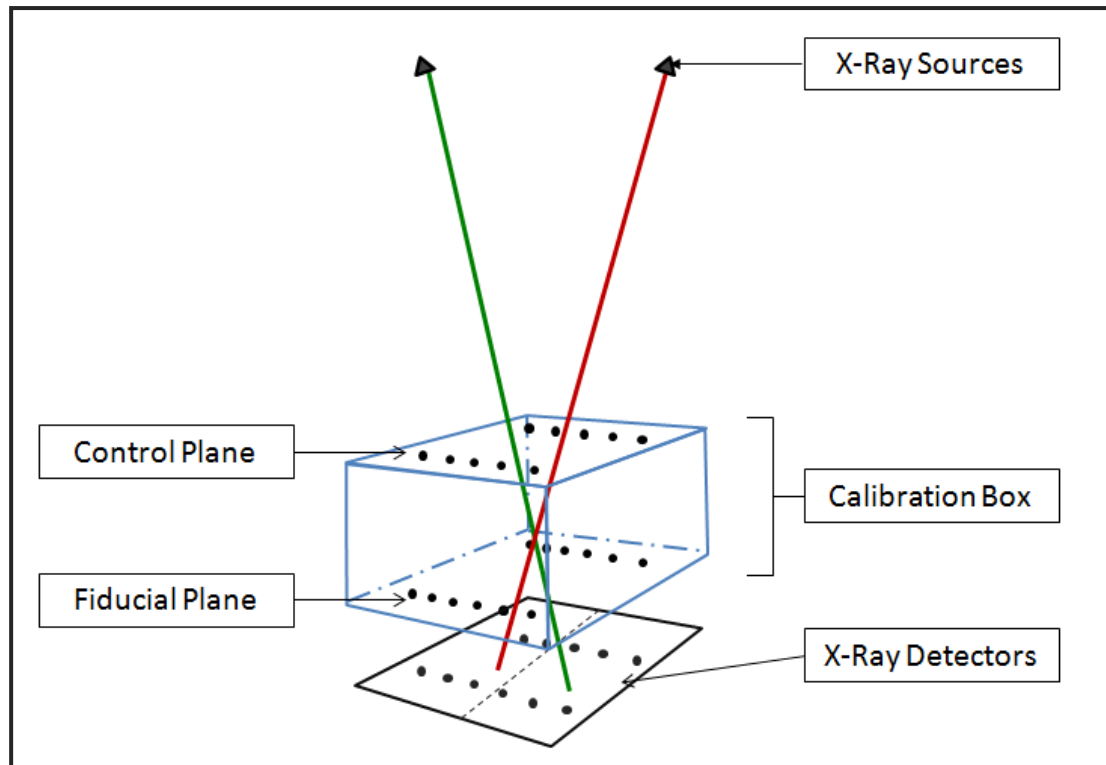


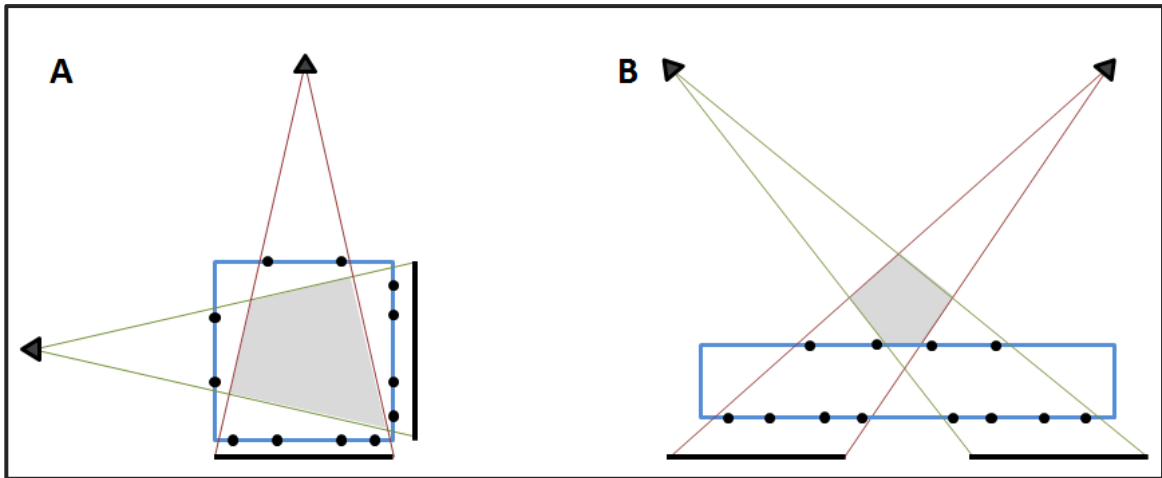
Figure 1.8: Parts of a modern RSA system. Adapted from Kärrholm (1989) [25]

The fiducial and control planes of the calibration box contain a grid work of imbedded markers called the fiducial and control markers. The fiducial markers are used to define the coordinate system of the calibration box. The control markers are used to determine the positions of the x-ray sources or foci [25].

The x-ray tubes provide a synchronized set of x-ray beams which are used to image the interested area at an identical time point. The images must be of an identical time point so that there is no movement of the patient between the images.

The arrangement of the RSA equipment setup is dependent on the required diagnostic information. There are two main equipment arrangements used in RSA studies [29], [52]. The first setup is a biplanar set up where the x-ray tubes and imaging detectors are positioned orthogonal to one another, Figure 1.9 A. In this RSA setup the calibration

cage surrounds the diagnostic imaging area, shown in grey. The second setup used is a uniplanar design, Figure 1.9 B. This design allows for easier patient placement options but has an increase in out-of-plane error [31], [53]. The uniplanar style is utilized by the Halifax Infirmary RSA suite.



**Figure 1.9: RSA Imaging Set-ups. A) Biplanar Imaging, B) Uniplanar Imaging. Triangles are x-ray sources, Black lines are x-ray detectors, Blue rectangles are calibration boxes with fiducial and control markers, and the shaded regions are areas of diagnostically important imaging.**

The placement of patients in the RSA imaging area during an RSA study should be done so that the patient anatomical directions align with the global coordinate system. For a series of examinations patient placement should be standardized as recommended by Valstar et al (2005) [5]. The alignment and standardization of the patient placement is done to produce measured migrations which are easily correlated with the spine coordinate system.



### ***1.1.4.2 Diagnostic Radiographs***

Diagnostic radiographs are created through the use of a form of electromagnetic radiation which has a shorter wavelength than visible light, x-rays. The first use of x-rays for medical use was in 1895 [7]. Since then their use has become prevalent in diagnostic medicine. An x-ray is generated using an x-ray tube, projected toward the target subject and imaging detector [7], [12]. These detectors can be either a traditional analog setup, the exposing of photographic style film or the newer style digital detectors. Digital radiography has become widely used in diagnostic medicine despite their higher initial cost and reduced resolution. Digital radiography does provide improvements in an improved contrast resolution, faster image development and post processing image enhancement opportunities. The use of digital radiography also subjects patients to a decreased radiological dose compared to traditional systems [11].

Image quality is a very important factor in the assessment of clinical radiographs. Without adequate image quality diagnostic assessments may be impossible and require the patient to undergo additional imaging, increasing their radiological dose. There are several aspects that go into the determination but for this thesis and the outcomes herein only three main image quality characteristics are discussed. They are: Image Noise, Image Contrast and Image Spatial Resolution.

#### ***1.1.4.2.1 Image Noise***

Image noise is an issue that can degrade image clarity, impacting spatial resolution and image contrast. Noise adds a random component to the photon signal measurement, adding or subtracting slight contrast variations over the detected imaging area [54], [55]. It is caused by several factors including scatter from the tissues of the patient interacting

with the x-rays (known as scatter), variations in the signal itself as well discrepancies in the photon amplification by the image detector [54], [55]. The standard equation for noise, as stated in *The Essential Physics of Medical Imaging (2<sup>nd</sup> Edition)* [56], is:

$$SNR = \frac{N}{\sigma_{bg}} = \frac{N}{\sqrt{N}} = \sqrt{N} \quad \text{Equation 1.1}$$

where SNR is the Signal-to-Noise Ratio,  $N$  is the average number of photons per pixel and  $\sigma_{bg}$  is the standard deviation of the photon count in the image background [56].

A method for increasing the SNR, as demonstrated by Equation 1.1, is to simply increase the number of photons hitting the image detector. This unfortunately leads to a proportional increase in radiological dose to the patient when the photons are generated at the same energy. If we wanted to increase the SNR by a factor of two, the patient would receive an increase dose on the order of 4 [56]. Due to the nature of RSA imaging, higher energy photons can be emitted for a decreased time duration compared to conventional radiography [41]. In this situation there is actually a decrease in number of emitted photons. With less photons emitted there is a decrease in  $N$  and thus a proportional decrease in the SNR. An SNR above 5 will almost always allow for the recognition of image objects [54].

The scatter produced by the interaction of x-rays with tissue degrades image performance. It is dealt with by the implementation of anti-scatter screens. These screens prohibit the ability of oblique x-rays produced during scatter from contacting the image detectors. Only the narrow beams emitted pass through the screens and contact the detectors, producing a detected signal [55]. RSA utilizes higher energy x-rays which

interact less with the patient tissue, therefore scatter is reduced over traditional radiography.

#### 1.1.4.2.2 Image Contrast

Image contrast is created by the differing absorption criteria of electromagnetic radiation by the various materials of the body. A denser material, like bone, absorbs higher energy x-rays than does a soft tissue, which has a lower density [7], [54]. The amount of attenuation created by a unit length of material is dependent on their respective attenuation coefficients [54], [55]. Along with density, material thickness variation also creates differences in image contrast. The more material that the x-rays pass through the more attenuation the signal undergoes, increasing image contrast [54], [55]. These differing absorption characteristics and tissue thicknesses allow x-ray technicians to distinguish the different anatomical structures of the body. A material which absorbs all x-rays and stops them from hitting the imaging film are called radio-opaque while materials which only partially absorb x-rays are called radio-lucent [7].

Due to the post-processing abilities inherent in digital radiography, basic image contrast present at the time of exposure is not a strong descriptor of the image contrast potential. The Contrast-to-Noise Ratio (CNR) becomes a more relevant description of the contrast potential. Therefore the noise level of the image becomes very important. As the noise level decreases the image display window can be more tightly refined allowing objects to become more perceptible [56]. The equation for CNR is defines as:

$$CNR = \frac{(\bar{X}_S - \bar{X}_{bg})}{\delta_{bg}} \quad \text{Equation 1.2}$$

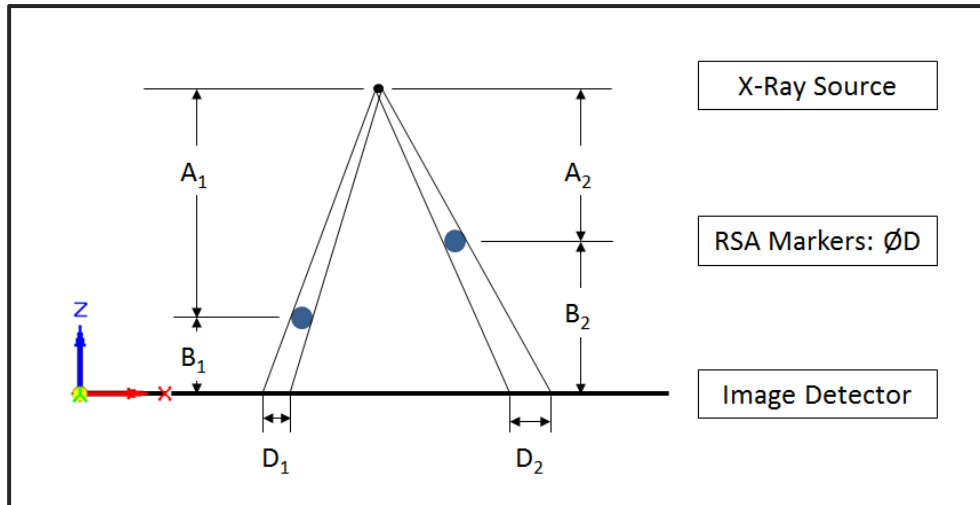
where  $\delta_{bg}$  is the standard deviation of the image background,  $\bar{X}_S$  is the signal of the source and  $\bar{X}_{bg}$  is the signal of the image background. The use of the CNR is most effective when used on image areas which general homogeneous signal strengths [54].

#### *1.1.4.2.3 Image Spatial Resolution*

Spatial resolution is the ability of an imaging modality to distinguish objects as they become smaller or closer together. High spatial resolution means that very small objects which are close together can still be distinguished as two separate, unique entities [56]. When two objects get so close so that their boundaries cannot be distinguished, this is considered the edge of the spatial resolution [56]. Spatial resolution is of particular importance in RSA, as the modality routinely deals with small, closely packed objects and minute relative motions. The accurate registration of the marker locations is dependent on the point spread function of the radiographic system.

Several factors affect the resultant spatial resolution of an imaging modality. These include: subject motion, defocus blur, and image noise [56]. Subject motion is not important in standard radiographic system due to the short image acquisition time. Motion blur becomes more of an issue in long acquisition time systems like during CT or MRI scans [56].

Another factor that impacts spatial resolution is the magnification of the image. Magnification is an unavoidable consequence for projection radiography due to the x-rays diverging from the central source [56]. The further an object is from the detection plane the more it is magnified [56]. An example of this is shown in Figure 1.10.



**Figure 1.10: Object magnification dependant on distance from detector plane.  $D < D_1 < D_2$**

The magnification of an object degrades the spatial resolution of the imaged object [56]. The edges are less defined due to the amplification of the projection shadow's area. This is very noticeable in RSA exams where the definition of marker boundaries and centers become more difficult as they are moved away from the image detectors. A clear example of this is the differences between the fiducial and control markers present in all RSA images. The fiducial markers appear smaller with more defined borders than their control marker counterparts.

Image magnification spatial resolution loss could have an impact in scoliosis spinal fusion success assessment as the distance between the detectors and the RSA markers implanted into the spine will vary due to the three-dimensional nature of the deformity. This will cause the positioning of less magnified marker clusters to be more accurate than others which undergo more magnification.

#### 1.1.4.2.4 Radiological Dose

Radiological dose in x-ray imaging is often reported as an effective dose in the units of Sievert (Sv). This unit is in Joules absorbed per kilogram of tissue (J/kg). The effective dose is a method of describing a radiation dose as subjected to the whole body by using weighting factors for the affected organs. The effective dose is defined by the equation:

$$E = X \times \sum W_t \quad \text{Equation 1.3}$$

where  $E$  is the effective whole body dose,  $X$  is the amount of radiation dose given to the patient during an x-ray image and  $W_t$  is the tissue weighting factor. For example a dose experienced by the gonads is given a weighting factor of 0.08 for the whole body subjected to a uniform energy field at the same energy. The tissue weighting factors was introduced in the 1970s and has been periodically updated by the International Commission on Radiological Protection (ICRP). The tissue weighting factors used in this thesis are from the most recent of these updates in 2007 published as ICRP report 103 and republished in *The Essential Physics of Medical Imaging* (3<sup>rd</sup> Edition) (2012) [54].

Unlike standard skeletal diagnostic imaging, RSA imaging is used to capture highly radio-opaque objects. This allows for the use of higher energy photons which would normally produce inadequate contrast in standard skeletal x-rays [41]. The use of the higher energy x-rays decreases the radiological dose experienced by the patient since these higher energy photons do not get absorbed as easily by the soft tissue of the body [41], [56]. Work by Greene-Donnelly et al (2008) found that using 141KVp photons for 11.6mS provided adequate contrast for RSA imaging of the lumbar spine. The use of this higher energy x-ray beam imparted only 0.304mSv to the patient per RSA image pair.

This resulted in a total dose of 1.52mSv per visit for a total of approximately 9.1mSv over the course of their two year study. This is a reduction of 91% compared to the 18mSv dose received by patients in another single diagnostic lumbar study [41].

### **1.1.5 RSA Markers**

RSA markers are almost exclusively spherical beads made from Tantalum (Ta), atomic number 73 [5]. Tantalum is a radio-opaque material with low reactivity in the body. Implanted Tantalum markers of the size of 0.5mm-1.0mm are excellent for use during RSA studies as they are well defined landmarks that provide high image contrast at the high x-ray energies used [5]. Valstar et al. (2005) recommends the use of 6-9 well distributed markers per examined rigid body to provide adequate marker occlusion redundancy [5]. The distribution of these marker should be kept as non-linear as possible [5].

#### ***1.1.5.1 Marker Location Determination***

The location of the markers in three-dimensional space is defined by the back projection of the marker shadows present on the radiographic film. The intersection of these projection lines defines the position of the individual marker. The equations for the determination of the back projection lines was reported by Selvik (1989) [24].

##### ***1.1.5.1.1 Crossing Line Distance***

Due to shadow location identification and calculation errors the projection lines of the rigid body markers rarely intersect in three-dimensional space [27–29], [57]. To compensate for this shortfall the center of the shortest perpendicular crossing line is used as marker location [27–29], [57]. This approximation is only acceptable if the crossing

line distance is less than 0.100mm. If the crossing line distance is over this threshold the projection line pair is not considered to be from the same marker projection. An example of this crossing line definition is shown in Figure 1.11.

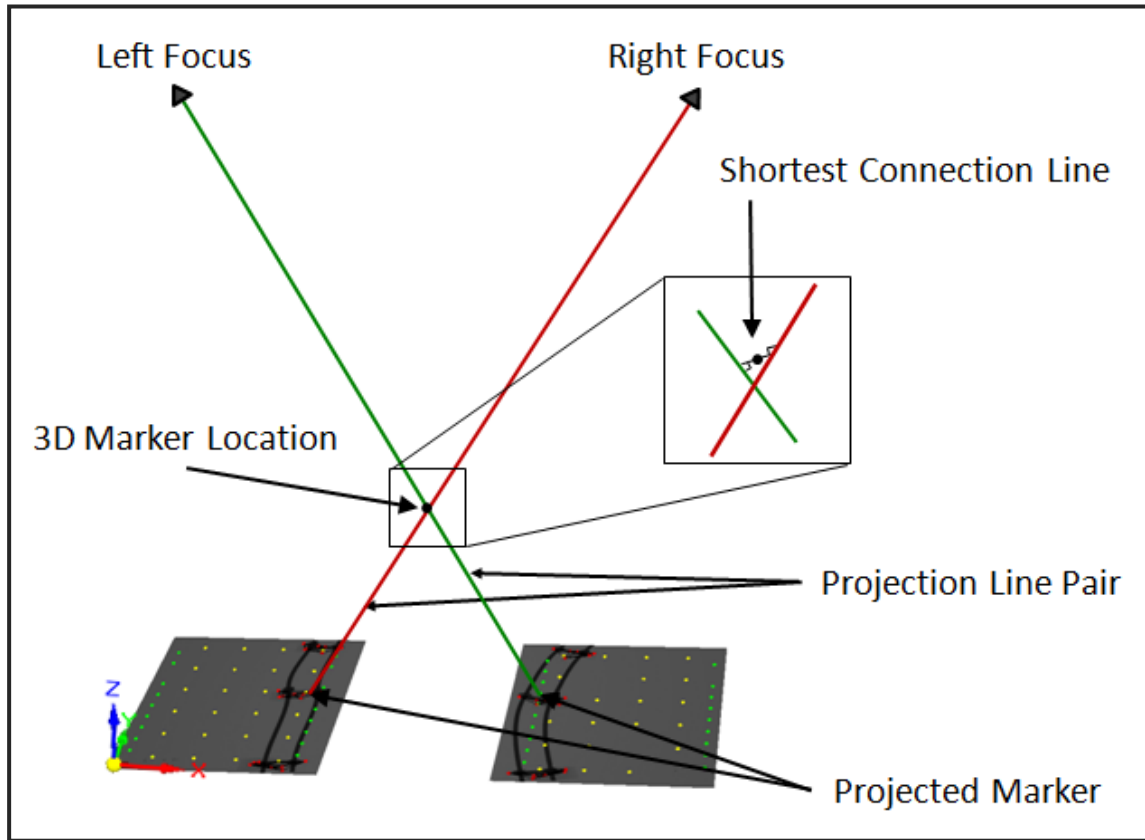


Figure 1.11: Definition of the crossing line distance. Adapted from Kaptein et al. (2005) [52] [27–29], [57]

#### 1.1.5.1.2 Marker Cluster Condition Number

Marker distribution is very important for the accurate assessment of motion using RSA. The Condition Number or CN is a method to measure the distribution the RSA marker clusters. The condition number is an important determinate of RSA performance. It is a measure of the linearity of the cluster. The more linear the marker cluster the less-accurate rotational data can be derived from its migrational assessment. The lower the condition number, the more distributed the marker cluster [5], [27–29], [53].



To derive the condition number, the distances of the markers from an arbitrary mathematical line is drawn through the marker cluster are determined. The three dimensional orientation of the line is driven mathematically so that the lowest condition number is achieved. The equation for the condition number of any given marker cluster is given by Equation 1.4 [5], [27–29], [53]

$$CN = \frac{1}{\sqrt{d_1^2 + d_2^2 + \dots + d_n^2}} \quad \text{Equation 1.4}$$

where  $d$  is the distance of the marker from the mathematical line and  $n$  is the number of markers in the cluster.

A well distributed marker cluster has a condition number less than 100 [5], [27]. In general, the lower the condition number, the better the marker cluster is for translational and rotational assessment.

#### *1.1.5.1.3 Marker Stability*

Marker stability is an assessment of the migration of the individual markers within the surrounding bone. A stable marker is one which forms a solid attachment to the surrounding bone, while an unstable marker fails to form this solid attachment and can migrate within the bone.

Marker stability is an important feature to examine when performing RS assessments. The stability of markers is assessed using the mean error of the rigid body marker cluster fitting [24]. In their RSA guidelines, Valstar et al. (2005) define the acceptable threshold for mean error for a marker cluster as 0.35mm [5].

### **1.1.6 Migration Assessment**

To assess the longitudinal migration of vertebrae involved in a spinal fusion, several post-operative RSA exams must be undertaken. The initial post-operative exam becomes the “Reference Scene” for all future examinations. Comparing the relative positions of the marked segments determined in the examinations taken at diagnostic time points to the relative positions in the reference scene, the intervertebral migration of the spinal fusion can be ascertained.

#### ***1.1.6.1 System Accuracy Assessment***

The dictionary defines accuracy as the “degree of conformity of a measure to a standard or a true value” [58]. In essence accuracy is an assessment of how close a measurement is to the true value produced. For a diagnostic technique to be applicable for use it must exceed the accuracy requirements of the clinical diagnostic threshold. These thresholds are called the Limits of Clinical Significance. For the assessment of the migrations of the spine using RSA Limits of Clinical Significance have been defined in the literature. In a study by Pape et al (2002) examining fusions of the L5 and S1 vertebrae, found that solid fusion can be assumed if observed translational movements are less than 0.3, 0.5, and 0.7mm in the transverse (X) (Left/Right), vertical (Y) (Axial along the spine) and sagittal (Z) (Anterio-posterior) spinal axes, respectively [1]. These thresholds were used as the translational Limits of Clinical Significance for this thesis. The rotational Limits of Clinical Significance were defined by Johnsson et al (2002) as 2.0°, 0.5° and 0.9° around the transverse (X), vertical (Y) and sagittal (Z) axes respectively [2]. These two sets of values were used as the Limits of Clinical Significance for this thesis. In their *Guidelines for Standardization of Radiostereometry (RSA) of*

*Implants*, Valstar et al (2005) state that the accuracy of a RSA system can be determined by comparing the RSA measurement with a method that has a much more substantial accuracy, on the order of  $\mu\text{m}$  [5].

Several studies published in the literature have conducted accuracy assessments of on phantom models. Most use a 95% Prediction Interval assessment to determine the accuracy of their respective RSA systems [28], [29], [34], [59–61]. Önsten et al (2001) [34] assessed the accuracy of a pair of human and canine femoral component phantom mode. The models were visually aligned with the calibration cages and 14 increments of the femoral component displacement were induced in all three principal directions. The range of these displacements was from zero to 0.5mm. This process was repeated 5 times for each specimen, for a total of 75 image pairs taken per specimen. The results from this study were an accuracy range for the human specimen of  $\pm 0.047\text{mm}$  to  $\pm 0.121\text{mm}$  and  $\pm 0.045\text{mm}$  to  $\pm 0.074\text{mm}$  for the canine model. This study also found that the longitudinal (along the axis of the femur) axis showed a higher accuracy than either the sagittal or transverse directions [34].

The study conducted by Bragdon et al. (2002) [26] was the only one presented in this section which did not calculate the system accuracy using a prediction interval method. They conducted a study on a hip arthroplasty phantom in which four displacements in each of the medial, posterior and superior directions were induced. The displacement range for any one displacement direction was from 0.05mm to 0.2mm. The induced displacements in this study were not performed independently of one another; therefore the final placement of the femoral component was 0.2mm, 0.2mm, 0.2mm (all medial increments, then all posteriorly increments, then all superior increments

respectively) from its original starting position. At each increment a RSA image set was taken. This procedure was repeated 5 times for a total of 85 image pairs per phantom model. The results for this study found that for an acetabular component with a condition number of 55 gave an accuracy range of  $\pm 0.0219\text{mm}$  to  $\pm 0.0861\text{mm}$  [26].

In 2005 Madanat et al [60] performed an accuracy study on the use of RSA in the assessment of distal radius fracture healing. They examined both the translational and rotational accuracy of the RSA system. To perform this study, a two section distal radius fracture phantom model was implanted with RSA markers. Into this model 7 migrations along the distal, medial and anterior axes of the range of 0.025mm to 5.0mm. An additional 5 migrations were induced in the proximal direction. These displacements were of the range from 0.025mm to 0.9mm. To assess rotational accuracy, 4 rotational displacements were induced around the longitudinal and transverse principal axes. The displacements were conducted in both the clockwise and anti-clockwise directions. The rotational migrations were of the range of  $1/6^\circ$  to  $2^\circ$ . This study found a translational accuracy range of  $\pm 0.006\text{mm}$  to  $\pm 0.029\text{mm}$  and a rotational accuracy range of  $\pm 0.073^\circ$  to  $\pm 0.187^\circ$  [60].

Two years later in 2007 the same research team (Madanat et al 2007) utilized a computer simulated distal radius fracture model to complete a similar RSA assessment study [59]. This study used both a two and three section distal radius fracture model to assess both the translational and rotational accuracy of the RSA system. Due to the unconstrained nature of the simulated environment, complex motions could be induced which were not able to be completed in a physical phantom model. The results from this

study are summarized in Table 1.3 [59]. This was the only study found to conduct an RS analysis in a simulated RSA environment.

**Table 1.3: Summary of the accuracy results from Madanat et al. (2007) [59]**

Accuracy Assessed	Fracture Model Accuracy Results	
	2-Part	3-Part
Translational (mm)	±0.001 to ±0.002	±0.003 to ±0.004
Rotational (deg)	±0.009 to ±0.015	±0.009 to ±0.031
Complex Translation (mm)		±0.005 to ±0.006
Complex Rotation (deg)		±0.017 to ±0.120

Also in 2007 Wilson assessed the accuracy of a knee arthroplasty phantom model, assessing both the use of standard RSA and model-based RSA migration assessment [28]. To do this the study induced six displacement increments along the three principal axes of the phantom model. The two migrational assessment techniques were both completed on this set of data. The translational accuracy of the traditional RSA measurement had a range of ±0.025mm to ±0.079mm while the model-based RSA measurement exhibited and accuracy range of ±0.020mm to ±0.063mm [28].

Laende et al. (2009) conducted an assessment of the use of a local coordinate system based on the tibial implant component used in a knee arthroplasty [61]. To assess the accuracy in this study 7 displacements in each direction were implemented. The range of these displacements was from 0.05mm to 3.0mm. The displacement directions were not tested independently. The displacements were implemented along the X-axis, then the Y-axis, then the Z-axis. This left the final positions of the tibial implant  $\langle 3, 3, 3 \rangle$  from its original reference position. Along with the translational accuracy, the rotational accuracy was also assessed. Around each axis the implant was rotated to six discrete displacements. The ranges for the displacements were  $1/6^\circ$  to  $6^\circ$  for the X and Z axes but

1/6° to 10° for the Y-axis. The rotations were not completed in combination. The results from the study found that translational accuracy ranged from ±0.025mm to ±0.075mm for the conventional RSA system to ±0.021 to ±0.048 for RSA using an implant based coordinate system. The rotational accuracy ranged from ±0.061o to ±0.153o [61].

### **1.1.6.2 System Precision Assessment**

Precision is an assessment of the repeatability of diagnostic system. Under identical conditions, multiple measurements of the same parameter should yield the same result. The variations of the recorded measurements yields the system's precision. For in vivo precision assessment Valstar et al (2005) and Makinen et al (2004) advocate the use of double examinations [5], [62]. Double examinations are a pair of RSA exams taken at a single time point, thus eliminating the migration that may occur between exams. This provides a set zero displacement exams from which system precision can be assessed.

Other researchers recommend the repeated measurements of a zero-displacement phantom model to assess system precision [26], [34], [63]. A zero-displacement phantom model is a model in which no inter-segmental movement is induced between RSA exams. These can be used like the in vivo double exams to assess system precision. Unlike the in vivo double exams, the number of zero displacement exams produced is not limited by subject radiological dose. This allows for the phantom precision datasets to have much larger populations than other precision studies.

In their 2001 article, Önsten et al performed a precision assessment on their cadaveric human and canine hip arthroplasty models [34]. Each model was consecutively imaged 5 times in the initial reference position. The models were then moved 0.200mm

along the three principal axes. At each point, the model was once again consecutively imaged 5 times for a total of 30 images per phantom model. The precision was calculated as the standard deviation of the zero-displacement exams. The longitudinal precision results from this study were: 0.03mm and 0.04mm for the human specimen and the canine model respectively [34].

In their study, Bragdon et al (2002) used the errors of the 79 accuracy data points to assess their system accuracy [26]. For the acetabular component with a condition number of 55 the system precision was found to be of the range 0.0055mm to 0.016mm [26].

The 2004 cemented canine total hip study conducted by Allen et al assessed three models for precision [63]. The three total hip models examined were a Plexiglas model, a canine simulant Sawbones model and four in vivo canine subjects. The three different models were expected to produce three levels of system precision with the most precise measurements taken on the Plexiglas model and the least precise measurements recorded from the in vivo subjects. The two phantom models were imaged four successive times, having been repositioned in between each image. The four in vivo canine subjects underwent double exams at four post-operative time points. The subjects were repositioned between each RSA exam [63]. The results from this study are summarized in Table 1.4.

**Table 1.4: Precision result summary from Allen et al (2004) [63].**

RSA Precision Assessment Model	Precision Assessed	
	Translational (mm)	Rotational (deg)
<b>Plexiglas</b>	0.0166 to 0.0188	0.009 to 0.040
<b>Sawbones</b>	0.0091 to 0.0426	0.062 to 0.421
<b>In Vivo Canine</b>	0.0162 to 0.0411	0.168 to 0.436

In the 2005 Madanat et al article, the distal radius fracture model was used to assess system precision as well as accuracy [60]. A single image RSA exam was completed with the model in the initial, reference position. The model was then moved within the global RSA environment 0.200mm along each of the three axes (distal displacement along the longitudinal axis, medial and lateral displacement along the transverse axis, and an anterior displacement along the sagittal axis). This study also induced a rotational displacement for precision assessment. The model was rotated 1/20 clockwise about the long axis of the radius. This totaled 26 image pairs used to assess the system precision using a standard deviation approach. The results from this study found that the translational precision was of the range 0.002mm-0.006mm and the rotational precision was of the range 0.025° to 0.096° [60].

Assessing a total knee arthroplasty, Wilson (2007) reported a standard RSA system translational precision of 0.03mm to 0.06mm and a rotational precision of 0.05° to 0.09° [28]. These precision were recorded from the assessment of 11 small movements of a zero-displacement phantom model [28].

Laende et al (2009) using a phantom of a tibial implant used in total knee arthroplasties assessed the precision of three different RSA migration assessment styles [61]. They conducted 12 zero-displacement exams with model relocations undertaken between each exam. The precision results presented in this study ranged from 0.017mm



to 0.044mm for the translational precision and 0.014° to 0.049° for the rotational precision [61].

## **1.2 Previous Work**

The use of RSA for examining the movement within spinal fusions is not a novel concept and it has been studied previously by various research groups [1], [39], [47–49], [64]. These studies focused on single level fusions performed on adult patients, determining fusion failure thresholds. After a review of the literature, to my knowledge, the use of RSA to assess the success of multi-level fusions utilized during the surgical treatment of scoliosis is unique to this research center.

The measurement of migration in spinal fusion in a scoliosis model using RSA is a unique challenge. The complex nature of the deformity extends in all three dimensions with vertebral rotations existing around all three axes. The use of pedicle screws and fixation rods introduce many metallic implants which easily occlude markers and limit the RSA field of view. Unlike other spinal fusion studies, the fusions used to treat scoliosis extend over multiple levels increasing intervertebral measurement distances.

### **1.2.1 Previous Project Outcomes**

Significant work has been performed by A. Francis (MASc) on the assessment of the implantation of RSA in the evaluation of spinal fusion success during his time with the Dalhousie School of Biomedical Engineering. His work has formed the foundation for the work performed for this thesis [27].

### 1.2.1.1 Computer Simulation

A right main thoracic curve was simulated using the Solid Edge CAD program developed by Siemens, Germany. Tantalum markers and AIS fixation implants were placed in the vertebrae. The Solid Edge assembly file was converted to a Persistence of Vision Raytracer imaging software (POV-Ray, created by Persistence of Vision Raytracer Pty. Ltd.) where a simulated radiographic exam was performed. The conversion was completed using Rhinoceros NURBS Modeling software (McNeel North America) as an intermediary file conversion tool. The resulting images were analyzed using the Model-Based RSA (MB-RSA) program produced by Medis specials bv. An overview of this process can be seen in Figure 1.12 [27].

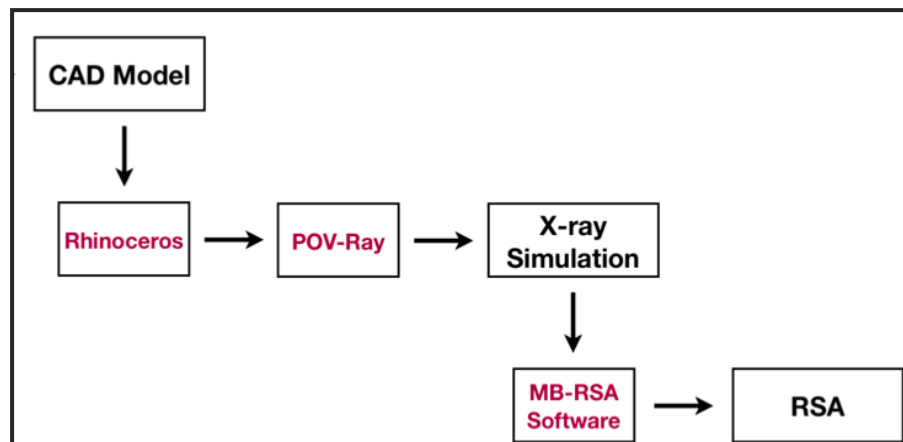


Figure 1.12: Previously developed simulation process. Reproduced with permission from A. Francis (2009) [27].

### 1.2.1.2 Origin Style

The origin style used in the previous work performed on this project was the standard used in the literature; the Caudal Origin Style. This style uses the inferior vertebrae of the fusion as the origin for assessing all migration between subsequent RSA exams. For the spine model used in the previous project the L1 vertebra was used as the

migration origin while the T4 and T8 vertebrae were the migrating marker clusters. This origin style is shown in Figure 1.13.

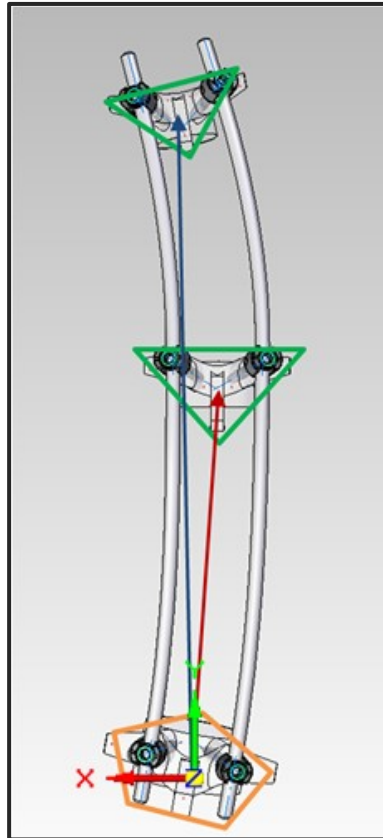


Figure 1.13: The Caudal Origin Style utilized by Francis (2009) [27]. Green triangles are the migratory vertebrae while the orange pentagon denotes the migration origin marker cluster.

### ***1.2.1.3 Marker Placement Protocol***

The primary objective of the previous thesis was to develop a marker placement protocol for RS analysis of the post-operative success of posterior spinal fusions performed in the treatment of thoracic adolescent idiopathic scoliosis. The developed protocol ensured that:

- Required accuracy and precision was maintained.
  - The placement protocol demonstrated a simulated accuracy of 0.3, 0.5, and 0.7mm in the respective transverse, sagittal, and vertical anatomical directions respectively [1], [43], [64].
- All markers were placed in optimal locations
  - The vertebrae selected for marker implantation were at the curve apex as well as superior and caudal ends of the curve deformity.
  - All are placed in positions are both easily accessible during surgery and not considered dangerous to the patient.
  - The markers are well distributed in the vertebrae so that they attain a condition number below 100 [5], [27], [53], [65].
  - All markers remain visible without being obscured by the AIS implants and without overlapping in a 30° RSA perspective.
  - Markers are implanted in locations where they will remain stable allowing for a mean error of rigid body fitting of less than 0.35mm [5], [27].

The resulting marker placement protocol consisted of seven markers distributed throughout the vertebrae. One was implanted at the end of each of the pedicle screw holes, one was implanted in each of the transverse processes, one was implanted in each of the lamina, and the final marker was implanted into the spinous process.[27] The marker placement protocol is shown in Figure 1.14.

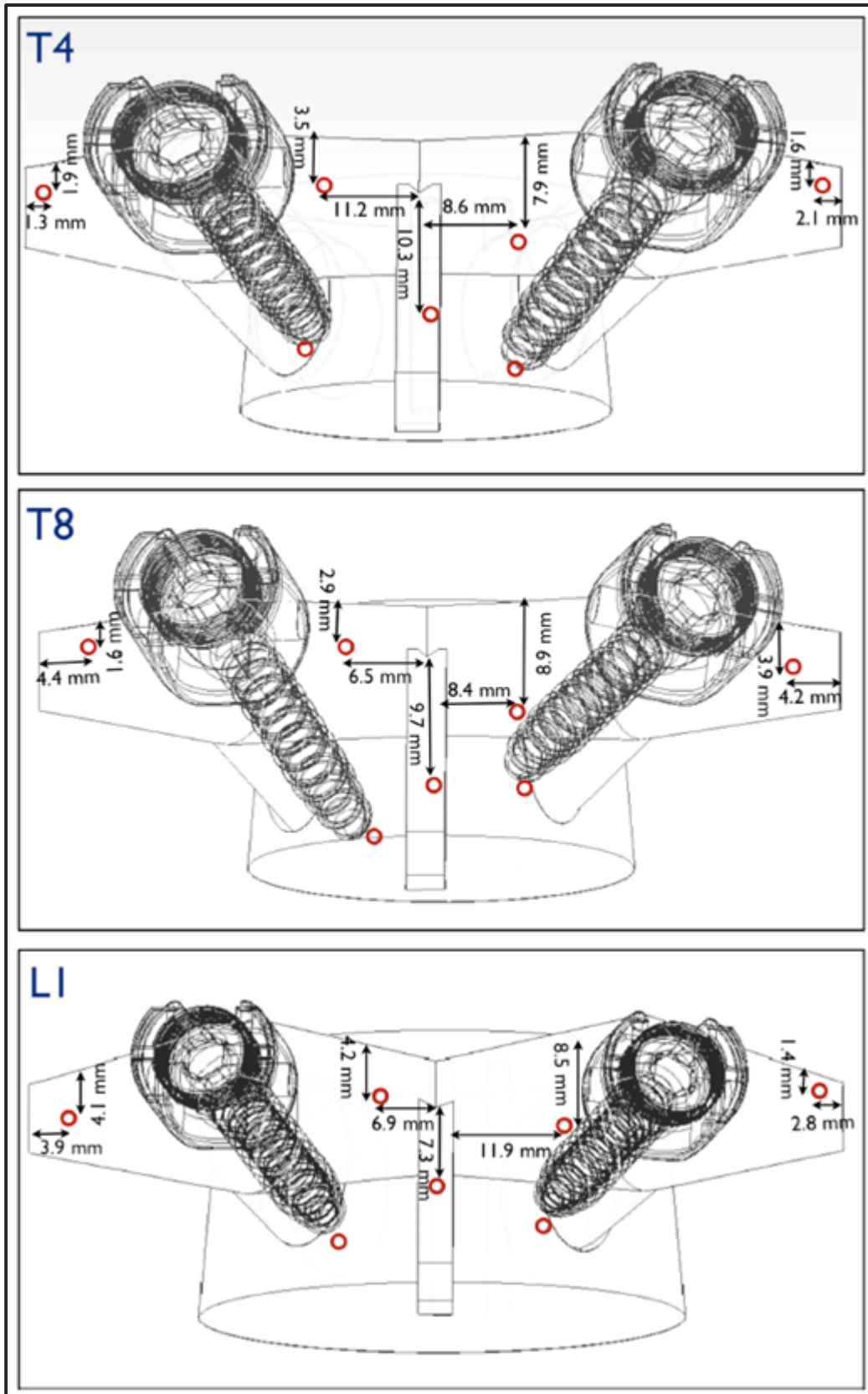


Figure 1.14: Marker Placement Protocol. Reproduced with permission from Francis (2009) [27].

This marker placement protocol and migrational measurement origin style demonstrated the required movement sensitivity as shown in Table 1.5.

**Table 1.5: Average accuracy results reported by Francis (2009) [27]**

	Transverse	Sagittal	Vertical
<b>Limits of Clinical Significance (mm) (from Pape et al. (2002)) [1]</b>	0.300	0.500	0.700
<b>CAD Simulation: Translation Error (mm)[27]</b>	0.156	0.014	-0.564
<b>CAD Simulation: Rotation Error (degrees)[27]</b>	0.1769	0.4319	-0.3965

### 1.2.2 Previous Limitations

Due to the novel nature of the work, the required scope of the previous work remained focused resulting in several limitations. The most significant limitation was that physical RSA setup restrictions could not be maintained. It was found that the physical size of the x-ray detectors at the Halifax Infirmary RSA suite are too small to accommodate a full length image of the spine. To compensate for this shortcoming, the equipment setup of the simulated environment was allowed to exceed the real-world physical size constraints by placing the x-ray sources further away from the detectors, thereby increasing available diagnostic imaging area. The end result was that the simulated spine model was able to fit within the area of the detectors [27]. The physical size restrictions are equipment dependant and thus may not affect patient populations examined at other institutions.

The restriction of patient size was mostly based on the nature of the origin style used to assess the intervertebral movement. The use of the Caudal Origin Style requires that the full length of the fusion fit within the diagnostic area. This requirement prohibits

the continued use of the Caudal Origin Style in our research, as it cannot be applied clinically.

To eliminate the full fusion image requirement, two additional origin styles have been suggested. These are the Apex and Dual Origin Styles. These origin styles use two sets of RSA images to section the fusion section into a superior and an inferior section. With the Apex Origin Style the marker cluster located at the apex of the scoliotic curve is used as the origin to assess the movements of the superior and inferior marker clusters. Conversely, the Dual Origin Style uses the superior and inferior marker clusters as the migration origins, assessing the movements of the central cluster. Both of these origin styles divide the spine into a superior and inferior aspect which can be separately imaged, effectively doubling the length of the diagnostic imaging area. These two origin styles are shown in Figure 1.15.

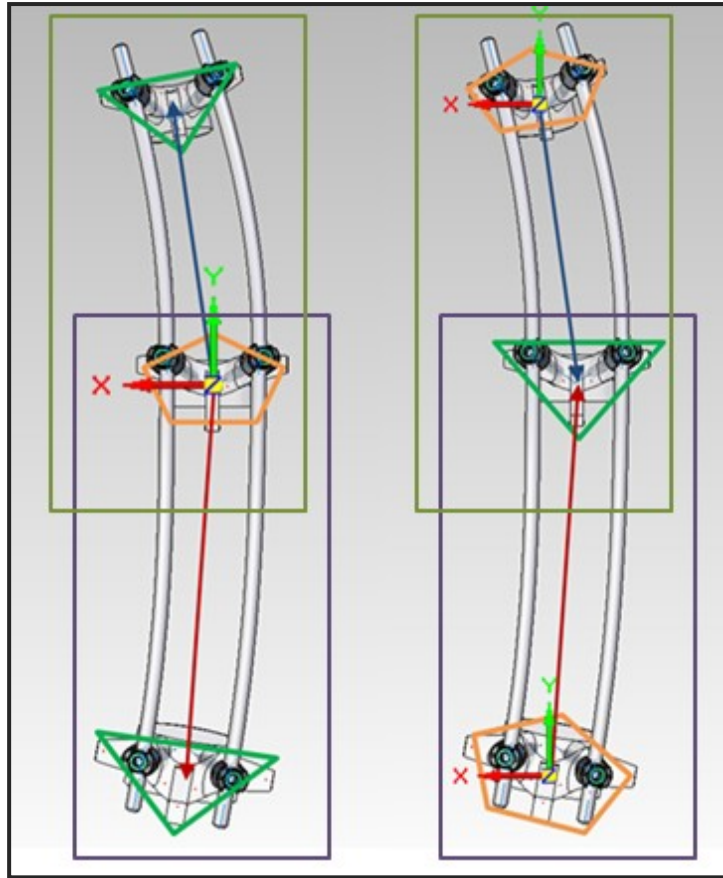


Figure 1.15: The Apex and Dual Origin Styles for measuring intervertebral migration. Left: Apex Origin Style, Right: Dual Origin Style. The green triangles denote the migratory vertebra while the orange pentagons denote the migration origins for each of the origin styles. The green rectangle shows the superior image area while the purple rectangle shows the inferior image area.



# Chapter 2 - Thesis Objectives

The overall goal of the project undertaken at the IWK Health Center is to utilize the highly accurate measurement available from Radiostereometric Analysis (RSA) to assess the success of spinal fusions performed during the treatment of Adolescent Idiopathic Scoliosis. There were two main objectives for the completion of this thesis:

*Objective 1:* To validate the use of the raytracing simulated RSA environment for use in the analysis of the applicability of RSA in the assessment of spinal fusion success.

*Objective 2:* To develop and analyze two novel migration origin styles used to remove the physical constraints of the RSA suite located at the Halifax Infirmary.

## 2.1 Objective #1: RSA Simulation Precision Validation

To this researcher's knowledge there has been no parallel study of a physical and simulated spinal phantom to validate the use of the simulated environment to assess the applicability of the use of the simulated RSA environment to assess the use of RSA in spinal fusion success assessment.

**Approach:** Complete a parallel precision comparison of identical phantom and computer simulated spinal fusion models to assess the validity of the simulated RSA environment. This will examine the system precision of the Halifax Infirmary's RSA suite and its simulated counterpart.

**Hypothesis:** The simulated RSA environment will accurately reflect the real world counterpart, yielding similar precision values.

**Rationale:** The use of a simulated RSA environment has been used previously at this institution and in the literature [27], [59]. In both cases, outcomes the accuracies recorded from manipulation of the simulated phantom model were congruent with the expected accuracy threshold of published phantom and clinical RSA research [27], [59].

By assessing the system precision of both environments, the simulation can be assessed for its realism and congruency to the physical RSA environment. If there is no statistical significance between the outcomes of the two environments the simulation can be said that it accurately reflects the systemic error associated with the physical RSA system environment.

## **2.2 Objective #2: Assessment of Novel RSA Origin Styles Used for Spinal Fusion Success Analysis**

Research performed by Francis (2009) found that the current setup of the RSA suite at the Halifax Infirmary severely limited the length of potential patients who could undergo RS assessment of spinal fusions [27]. The maximum allowable length at the current configuration was approximately 300mm.

**Approach:** Using a computer simulation of the Halifax Infirmary's RSA environment and a simulated phantom model, create and assess two novel origin styles which would allow for the assessment of spinal lengths over 300mm. The origin styles will be assessed based on their recorded accuracy and precision. To ensure that the migrational measurement performance is maintained, the novel origin styles will be compared with the Caudal Origin Style used in the literature and previously at this institution. The two novel origin styles introduced are the Apex and Dual Origin Styles.

**Hypothesis:** These novel origin styles will provide equivalent accuracy and precision outcomes to those of the traditional Caudal Origin Style.

**Rationale:** The length of the available imaging area prohibits the assessment of patients who have spinal fusions longer than 300mm. This work will increase the effective size of the imaging area, increasing the proportion of the patient population that can be assessed in the future using RS analysis.

**Action Plan:** Parallel accuracy and precision analyses will be performed on all three origin styles to assess their applicability for use in the assessment of spinal fusion success in future clinical research. The accuracy outcomes of the three origin styles will be compared to the translational and rotational Limits of Clinical Significance reported by Pape et al.(2002) and Johnsson et al.(2002) respectively [1], [2]. These Limits of Clinical Significance are shown in Table 2.1. The precision outcomes are expected to be congruent with various precision outcomes reported in the literature [26], [34], [60], [61], [63].

**Table 2.1: Limits of Clinical Significance.**

	X	Y	Z
<b>Translational (mm) [1]</b>	0.3000	0.5000	0.7000
<b>Rotational (deg) [2]</b>	2.0000	0.5000	0.9000

# Chapter 3 - Thesis Objective #1: RSA Simulation Precision Validation

## 3.1 Introduction

Raytracing software has been used in the literature for the assessment of RSA performance. Specifically, in 2007 Madanat et al utilized POV-Ray to simulate movements in a marked distal radius fracture simulation. In their assessment they found “...that a computer simulation model can be accurately used to replace phantom models in the simulation of RSA studies” [59]. The simulation was shown to have “very high correlation” between the induced migrations and the recorded RSA measurements [59]. They surmised that the simulated RSA environment provided an adequate research tool since the accuracy of the simulated system compared well to that of physical RSA systems.

The use of a simulated RSA environment has been previously used at this institution by Francis (2009) [27]. The simulated RSA environment was used to develop a marker placement protocol and to assess the use of RSA in the assessment of the success of spinal fusions.

The use of simulated RSA assessments provides an opportunity for the accurate creation of complex movements. The required use of micrometers and staging limit the movements that can be created on a traditional phantom model. The use of simulated RSA exams provide a vehicle for the further development of model based RSA, by creating a fast and cost-effective means to conduct RSA studies, requiring only

commercially available computing hardware [59]. In fact this entire thesis, except for the physical phantom model, was completed on an over-the-counter, mid to high range computer notebook.

The validation of the simulated RSA environment is a three component process to assess the simulation accuracy, precision and responsiveness. The Madanat et al (2007) study concluded that the use of the simulated system was acceptable due to the similarity of the recorded accuracy values with those previously obtained in separate distal radius fracture phantom studies [59]. The use of the simulated RSA environment has not yet gone through a parallel comparison study with a physical phantom counterpart. This thesis object has completed a parallel precision comparison of the simulated environment with an identical phantom model to validate the systemic errors inherent within the Simulated RSA Environment used clinical research at this institution.

## **3.2 Simulation Precision Validation Methodology**

This investigation of the implementation of Radiostereometric Analysis (RSA) for the assessment of spinal fusion success was completed through the use of simulated RSA exams performed on a simulated computer model consisting of three vertebrae and associated AIS implants. The construction of the simulated model and RSA environment are discussed below.

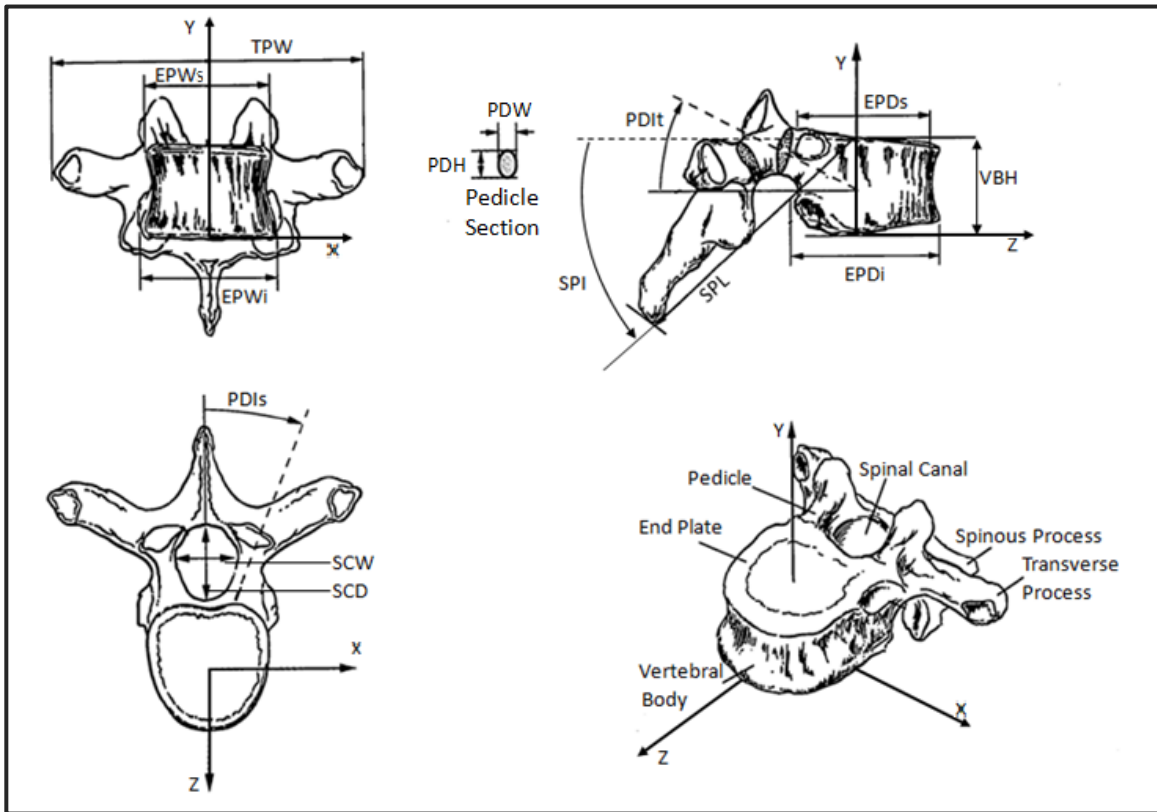
### **3.2.1 Computer Simulated Spine Model**

The process for the construction of a Computer Aided Design (CAD) spinal model was developed by D. Breglia of Ohio University (2006) [66]. This method was used previously in project development at this institution by A. Francis (2009) [27]. This section reports upon and details the improvements made to the processes developed by these two individuals.

#### ***3.2.1.1 Vertebral Models***

Using Solid Edge ST2 CAD software (Siemens, Germany) three vertebral models were constructed to represent the vertebrae at the superior and inferior ends of the scoliotic curve as well as the apex of the curve. The modeling technique used was adapted from Breglia (2006) [66] and used by Francis (2009) [59]. The anatomical measurements used for the vertebral models were adapted from two cadaveric studies performed by Panjabi et al (1991, 1992), who conducted studies on both the thoracic and lumbar spine of adult subjects collecting average measurements for both [67], [68]. Figure 3.1 shows the dimensions used to construct the CAD models used in this thesis. The measurements used for vertebral models used in this thesis can be found in Table 3.2 with the dimension

acronyms defined in Table 3.1. New CAD vertebral models were designed for this project to better emulate the data reported by Panjabi et al (1991, 1992) [67], [68]. The coordinate system definitions for each vertebra can be found in Appendix B.



**Figure 3.1: Orthogonal views of the thoracic vertebra showing the dimensions and the Vertebral Coordinate System used to construct the vertebral CAD models. (Adapted from and reproduced with permission from Panjabi et al (1991)<sup>2</sup>) [67]**

<sup>2</sup> Panjabi, M, K. Takata, V. Goel, et al “Thoracic Human Vertebrae Quantitative Three-Dimensional Anatomy” *Spine*, vol. 16, no. 8, pp. 888-901, 1991

**Table 3.1: Acronyms used for anatomical dimensions for the vertebral models from Panjabi et al (1991, 1992) [67], [68].**

Vertebral Part	Dimension	Acronym
Vertebral Body	End-Plate Width	EPW
	End-Plate Depth	EPD
	Vertebral Body Height	VBH
Spinal Canal	Spinal Canal Width	SCW
	Spinal Canal Depth	SCD
Pedicule	Pedicule Width	PDW
	Pedicule Height	PDH
	Pedicule Inclination	PDI
Spinous Process	Spinous Process Length	SPL
	Spinous Process Inclination	SPI
Transverse Process	Transverse Process Width	TPW
Suffixes	Superior (upper)	u
	Inferior (lower)	i
	Sagittal	s
	Transverse	t
	Right	r
	Left	l

**Table 3.2: Anatomical measurements of the simulated vertebral models from data reported by Panjabi et al (1991 and 1992) [67], [68].**

Vertebral Part	Linear Dimensions (mm)	Vertebrae		
		T4	T8	L1
Vertebral Body	EPWu	24.5	29.5	41.2
	EPWi	26.0	30.5	45.3
	EPDu	23.3	27.9	34.1
	EPDi	24.5	29.4	35.3
	VBH	16.2	18.7	23.8
Spinal Canal	SCW	17.0	17.7	23.7
	SCD	16.2	15.9	19.0
Pedicule	PDWr	5.5	6.7	8.0
	PDWi	7.0	6.7	9.2
	PDHr	11.9	12.5	15.9
	PDHi	12.2	12.5	15.8
Spinous Process	SPL	51.1	52.8	67.7
	SPI	32.5	32.3	20.6
Transverse Process	TPW	56.9	59.9	71.2
	TPD	6.25	6.5	8.3
<b>Angular Dimensions (deg)</b>				
Pedicule Angles	PDIsr	21.8	22.5	16.5
	PDIsl	17.2	16.7	12.4
	PDitr	6.4	12.1	2.2
	PDItl	10.5	11.1	2.9



The constructed T8 vertebra is shown in Figure 3.2. The articular processes of the vertebrae were not simulated as they are normally removed during implantation of the pedicle screws. The CAD drawings of the three vertebrae have been included in Appendix A.

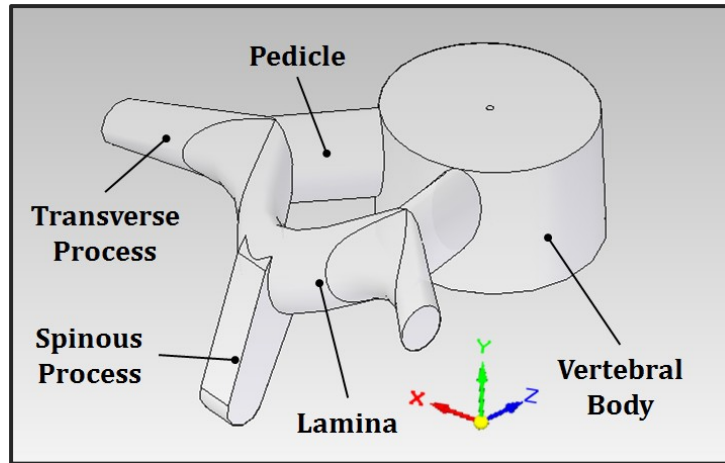


Figure 3.2: CAD model of the T8 vertebra.

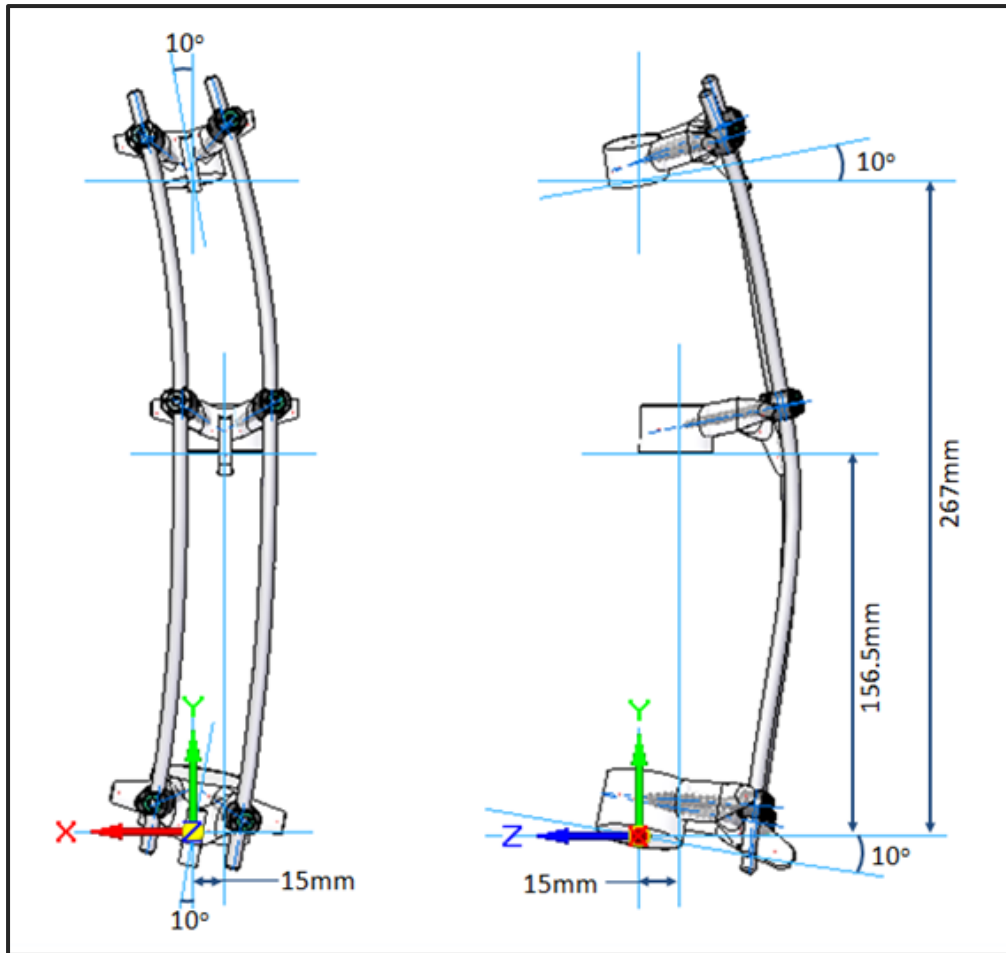
### 3.2.1.2 Simulated Spine Assembly

The simulated spine was designed to recreate a post-operative main thoracic scoliosis corrected to  $20^{\circ}$ , simulating a 1AN curve under the Lenke classifications [3]. The spinal dimensions used in the construction of the spine were previously used by Francis (2009) and represent average adult spine dimensions [27]. The simulated spine model extended from the T4 to the L1 vertebrae which make up the superior and inferior ends of the curve respectively. In total the model was approximately 290mm long. To simulate the curve, the T4 and L1 vertebrae were both rotated about their Z axes  $10^{\circ}$  and  $-10^{\circ}$  respectively. The T8 vertebra was moved -15mm along the X axis to simulate the displacement caused by the scoliotic curve. To recreate the normal kyphotic curve present, the T4 and L1 vertebrae were rotated  $-10^{\circ}$  and  $10^{\circ}$  respectively about their Z-axis while the T8 vertebra was translated -15mm along the Z-axis. For a full list of dimension

specifications of the spine refer to Table 3.3. The spine origin is located at the center of the inferior endplate of the L1 vertebra and is of the same orientation as the RSA Coordinate System. The Spine Coordinate System and RSA Coordinate System are defined in Appendix B. Figure 3.3 shows the final arrangement of the simulated spine model.

**Table 3.3: Specifications of the simulated spine model. All distances are measured from the spine origin to the vertebral origin. Rotations are about the vertebral axes.**

		Position (mm)	Rotation (deg)
<b>T4</b>	X	0.0	10
	Y	267.0	0
	Z	0.0	-10
<b>T8</b>	X	-15.0	0
	Y	156.5	0
	Z	-15.0	0
<b>L1</b>	X	0.0	-10
	Y	0.0	0
	Z	0.0	10



**Figure 3.3: Dimensions and Coordinate System of the assembled Full Size CAD simulated spinal model.**

#### 3.2.1.2.1 Pedicle Screw Implants

The monoaxial pedicle screws were implanted into the simulated vertebral models as single assemblies including the pedicle screw itself and the set screw companion, Figure 3.4. The CAD models of the screws were supplied by DePuy Spine™. The screw sizes used were matched with the size of the corresponding pedicle. The maximum diameter screw that still fit within the confines of the pedicle was used. The length of the pedicle screw was selected on its ability to pass through the vertebral arch and reach securely into the vertebral body. The sizes of the pedicle screws used are show in Table 3.4.

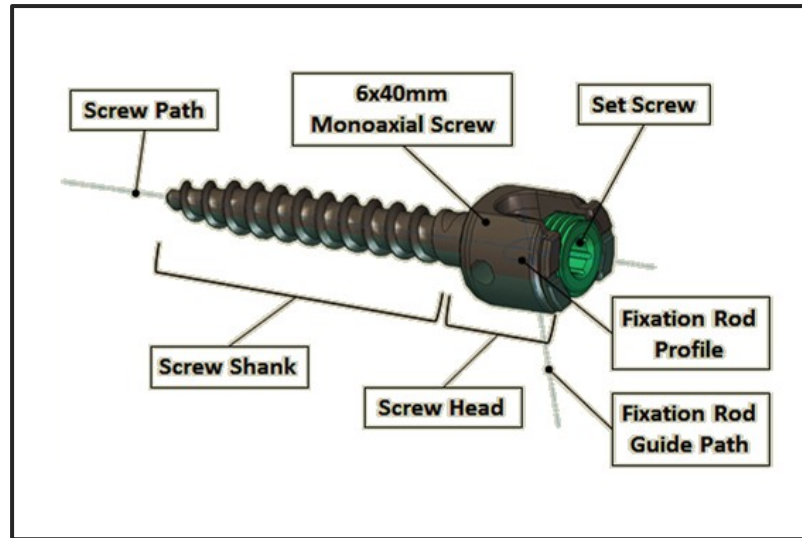


Figure 3.4: Monoaxial pedicle screw used in the L1 vertebra.

Table 3.4: Pedicle screw sizes used in the simulated spinal model

Vertebra	Screw Length (mm)	Diameter (mm)
T4	30	5
T8	35	5
L1	40	6

The pedicle screws were implanted the full length of their shank into the vertebrae to the union of the shank and the screw head. This placement simulates that of the screws driven into the vertebrae during actual surgical procedures.

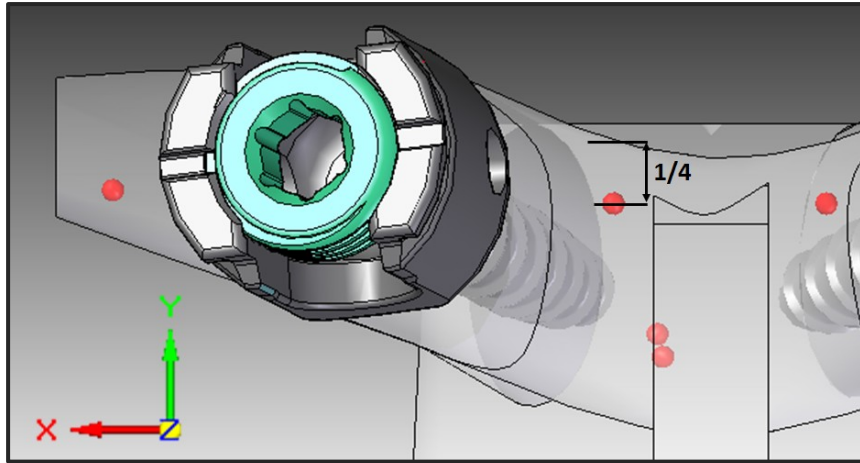
#### 3.2.1.2.2 Fixation Rod Construction

The models of the AIS fusion fixation rods were driven by the placement of the vertebral models. To create the unique configuration of the left and right fixation rods, three-dimensional curves were created running through the fixation rod grooves in pedicle screw heads. The rod paths were drawn in the full spine assembly using complex keypoint curves.

A swept protrusion was then created with a rod diameter of 5.5mm along the developed curve. The rod profile was defined by a circle located with the L1 pedicle screw assembly, Figure 3.4. To keep the rods from intersecting with the fixation screws, straight line segments were used at the union of the rod and screws protruding 6mm orthogonally from the center of the fixation rod groove in each pedicle screw head. At the superior and inferior ends of the spine, the rod was extended 15mm past the ends of the screw to simulate the full length of the rod in a patient, Figure 3.4. This method of fixation rod construction is novel to this thesis. The previous project work used a rod configuration which drove vertebral placement and created rod-screw interference conditions [27].

#### *3.2.1.2.3 Marker Placement*

The placement of the markers into the vertebral models was done using anatomical landmarks to attempt to simulate the implantation precision available to a surgeon in the operating room. This is a deviation from the work done previously, where each marker placement was precisely located [27]. The previously used placement style was overly accurate and not something that could be achieved in a surgical setting using dimensions which were accurate to a tenth of a millimeter. The dimensions used to place the markers in this study were fractions of distances of the vertebral model. For example, the #4 marker in the T4 vertebra is located approximately  $\frac{1}{4}$  of the way down from the superior edge of the lamina, Figure 3.5.



**Figure 3.5: Placement of the #4 RSA marker in the T4 vertebra. Fixation rod not depicted for clarity.**

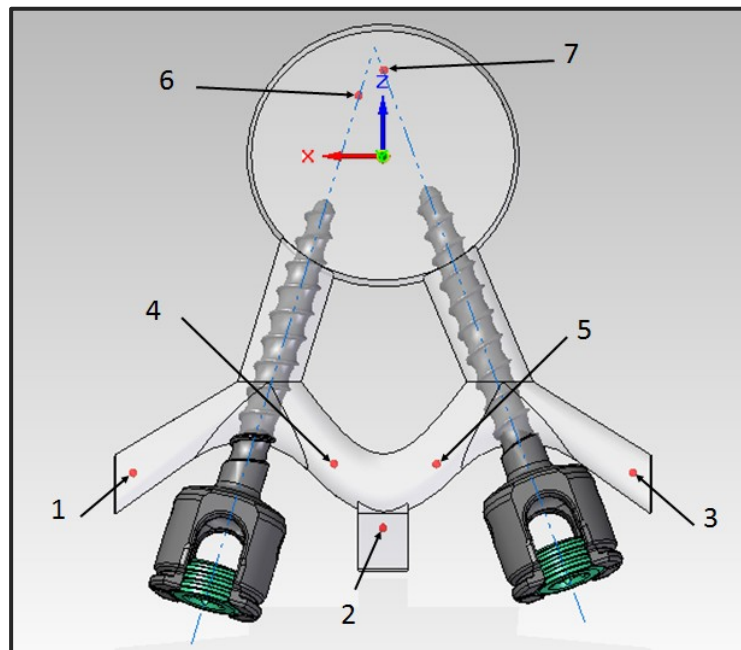
The positions of the markers were optimized for visibility through trial and error imaging of the reference spine model using the caudal origin style placement. The placement of all markers can be found in Table 3.5 and Table 3.6 as well as depicted in an axial view in Figure 3.6.

**Table 3.5: Location of RSA rigid body markers within the vertebral models. Locations are based on the anatomical references of the individual vertebral models.**

Marker Number	Vertebrae								
	T4			T8			L1		
	X	Y	Z	X	Y	Z	X	Y	Z
1	Lateral 1/4 of TP	Inferior 1/4 of TP	Center of TP	Lateral 1/4 of TP	Inferior 1/4 of TP	Center of TP	Lateral 1/4 of TP	Center of TP	Center of TP
2	Center of SP	Inferior 1/3 of SP	Center of SP	Center of SP	Inferior 1/3 of SP	Center of SP	Center of SP	Inferior 1/3 of SP	Center of SP
3	Lateral 1/4 of TP	Inferior 1/4 of TP	Center of TP	Lateral 1/4 of TP	Inferior 1/3 of TP	Center of TP	Lateral 1/4 of TP	Center of TP	Center of TP
4	Medial 1/3 of Lamina	Superior 1/4 of Lamina	Center of Lamina	Medial 1/3 of Lamina	Inferior 1/4 of Lamina	Center of Lamina	Midpoint of Lamina	Inferior 1/3 of Lamina	Center of Lamina
5	Medial 1/3 of Lamina	Superior 1/4 of Lamina	Center of Lamina	Midpoint of Lamina	Inferior 1/4 of Lamina	Center of Lamina	Midpoint of Lamina	Inferior 1/3 of Lamina	Center of Lamina
6	Along Screw Path		Anterior 1/4 of Vertebral Body	Along Screw Path		Anterior 1/4 of Vertebral Body	Along Screw Path		Anterior 1/4 of Vertebral Body
7	Along Screw Path		Anterior 1/8 of Vertebral Body	Along Screw Path		Anterior 1/5 of Vertebral Body	Along Screw Path		Anterior 1/3 of Vertebral Body

**Table 3.6: Positions of the centers of the RSA rigid body markers located within the vertebral models. Dimensions are based on the individual Vertebral Coordinate Systems. All dimensions are in mm.**

Marker Number		Vertebrae								
		T4			T8			L1		
		X	Y	Z	X	Y	Z	X	Y	Z
1	Left Transverse Process	26.00	15.75	-31.00	28.00	16.50	-35.50	33.00	18.00	-41.00
2	Spinous Process	0.00	-3.25	-40.00	0.00	-2.00	-41.75	0.00	3.25	-55.50
3	Right Transverse Process	-26.00	15.75	31.00	-28.00	16.50	-35.50	-33.00	18.00	-41.00
4	Left Lamina	4.00	9.00	-30.00	5.50	10.50	-34.50	6.50	10.00	-40.00
5	Right Lamina	-5.00	9.00	-30.00	-6.00	10.50	-34.50	-6.50	10.00	-40.00
6	Left Pedicle Screw Hole	4.25	8.00	1.00	4.00	9.00	2.25	1.25	14.50	15.50
7	Right Pedicle Screw Hole	-1.50	9.25	1.50	-2.50	9.50	3.00	-4.25	15.00	12.50



**Figure 3.6: Axial view of T8 vertebra showing the marker placement within the vertebrae.**

### 3.2.2 Radiostereometric Simulation

To analyze the application of RSA in the assessment of spinal fusion success this thesis utilized a process of creating computer simulated RSA exams. This process is similar to the use of phantom models which are standard in clinical research. The use of a computer based simulation provided the potential for extremely precise inputs and absolute control over the testing environment. Any implemented displacement or positioning of the model within the simulated environment was, in effect, perfect. This removed a source of error found in physical phantom models, where the input itself has a measurement error associated with it. The process for the simulation of RSA images was first developed at this institution by Francis (2009) forming the basis for the simulation method in this thesis [27].

#### 3.2.2.1 Physical Facilities

The simulation process was designed to mimic the set-up of the RSA suite available at the Halifax Infirmary, Figure 3.7. This equipment is a uniplanar RSA set-up using two x-ray sources, two digital detectors, and a single calibration box.

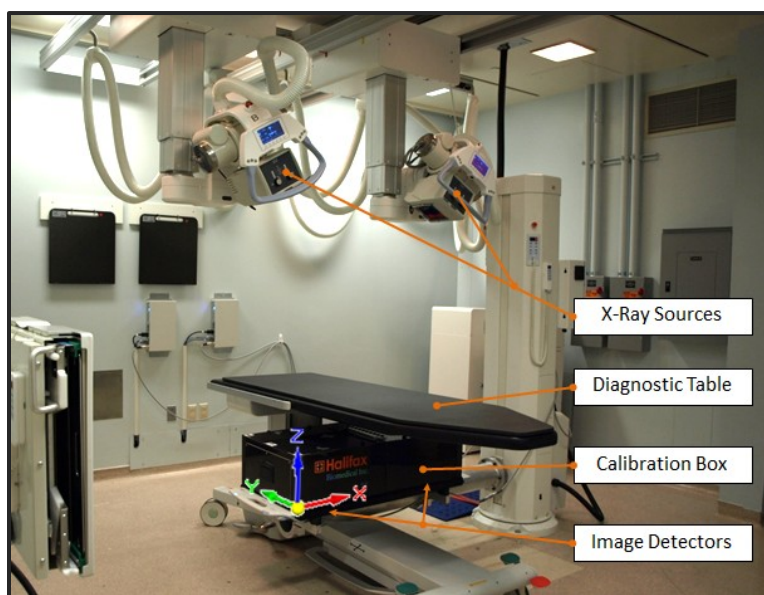


Figure 3.7: RSA Suite at the Halifax Infirmary.



The x-ray sources used are located above the patient during imaging. They can only be extended to a maximum of 1.6m above the image detectors due to ceiling height restrictions. The system is designed to operate with the x-ray sources being set at an angle of 30° to the image detectors, with equipment bulk prohibiting a more acute setting. During previous project work conducted by A. Francis (2009), to fit the spine model within the imaging area the simulated x-ray sources were artificially moved to 1.9m above the x-ray detectors [27]. As well the previous simulation tested an earlier RSA set-up which used a calibration box and x-ray source set up which utilized a configuration where the x-ray beam struck the image detectors at a 20° incident angle [27].

The RSA suite has been updated and now uses Canon CXDI-55C digital x-ray detectors. They have a detection area of 353x430mm with a resolution of 2208x2688 pixels, approximately 5.9 million pixels. The pixel size of the detectors is 160x160µm [69]. The two image detectors are located side-by side and are approximately 20mm below the fiducial plane of the calibration box.

The calibration box used was designed and built by Halifax Biomedical Inc. (HBI). The calibration box was designed to be used with off-planar x-ray images placed at an incident angle of 30°. The calibration box consists of 37 control markers and 45 fiducial markers spread over the right and left images. The calibration box also contains box identification marker clusters and left and right image identifiers. The placement of the markers is unique to the specific calibration box and is proprietary information of HBI.

### 3.2.2.2 Patient Placement

The placement of the patient was designed to reflect the probable clinical placement of a patient undergoing RS analysis. The placement of the patient was aligned with the global coordinate system and was standardized throughout the study in accordance with the recommendations of Valstar et al (2005) [5].

The model was placed in a supine position on a level plane. This simulated a patient lying flat on their back on a level examination table. The model was axially aligned with the RSA imaging area such that the Y axis of the spinal model ran parallel to the Y axis of the RSA environment. In this placement all model spinal axes are parallel to the corresponding RSA Coordinate System axes. This alignment of the coordinate systems is shown in Figure 3.8.

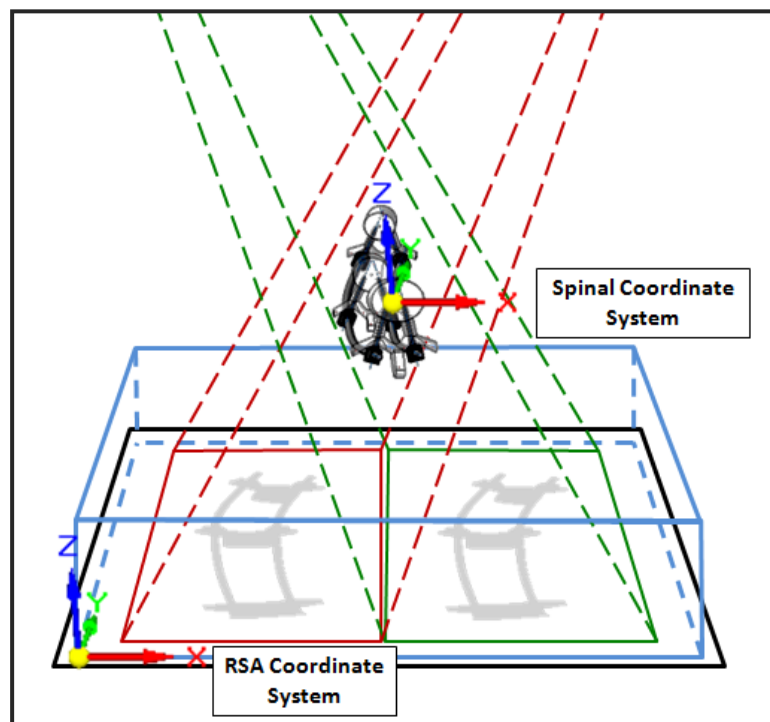


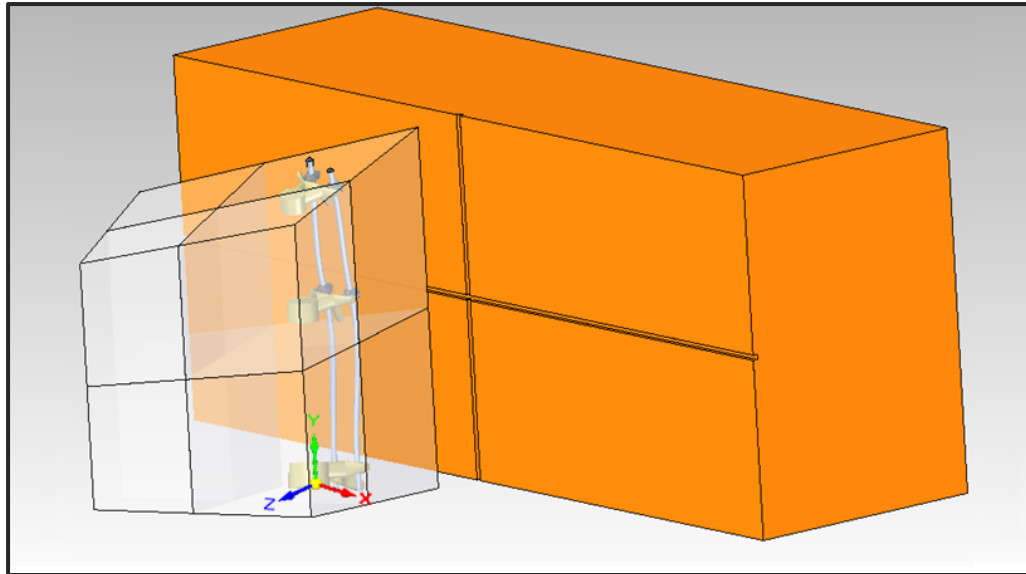
Figure 3.8: Alignment of the RSA and Spinal Coordinate Systems. Adapted from Kaptein et al (2006) [70].

In a clinical setting, this patient placement would be achieved by laying the patient on their back on a flat level examination table. The patient's superior/inferior axis would then be approximately aligned with the Y axis of the RSA equipment. Although alignment variations may occur between patients due to the unique configuration of their deformity, the individual patients should not experience significant misalignments of the two coordinate systems during the series of post-operative exams. Slight misalignments in patient placement are common between exams in all RSA applications as patient alignment is always approximated at time of examination. The use of relative motion between two rigid segments allows for the correction of this error.

The placement of the patient in this orientation within the RSA environment creates images in which the patient's left and right directions are reversed from image left and right. This is a departure from the normal fusion assessment coronal x-rays but is the standard convention for anteroposterior chest x-rays.

### **3.2.3 Simulated RSA Environment**

The simulated RSA environment was designed to mimic that of the physical system available at the Halifax Infirmary. The simulation environment was built in two sections: one in the Solid Edge CAD (Siemens, Germany) environment and one in the Persistence of Vision Raytracer (POV-Ray) (Persistence of Vision Raytracer Pty. Ltd.) environment.



**Figure 3.9: Model spine in the CAD RSA environment. Orange Box: Calibration box. White Prism: Diagnostically significant imaging area. The Spinal Coordinate System is shown.**

The CAD RSA environment consists of a mock-up of the calibration box and was used to locate the spine model within the diagnostic imaging area, Figure 3.9. The origin of the spine was placed so that the model is approximately centered within the imaging area.

The second simulated environment is that of the POV-Ray imaging environment. This environment contains the simulated calibration box, detector plates, and x-ray sources. The POV-Ray environment was the only environment of the project which used a left-handed coordinate system. To compensate for this discrepancy, the placement of the spine in the CAD environment was adjusted to align with the POV-Ray calibration box and light sources. A more detailed description of this adjustment appears in Appendix C.

The calibration box was constructed as a system of 1mm spheres placed in an identical layout as specified for the physical calibration box. It was processed as a separate POV-Ray .INC file, which eliminated the requirement of including every sphere in each image file. This allows for easy updates of the image environment for the future

use of new calibration boxes. As with the fiducial and control markers, the image and calibration box identifying markers were also simulated. The inclusion of these markers, although not vital to the calculation of RSA migration measurements, adds to the realism of the simulated RSA environment.

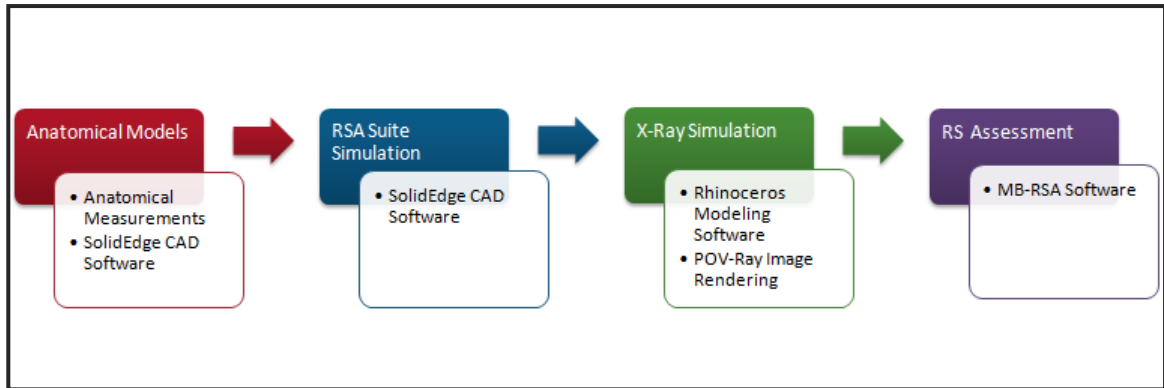
To simulate the detectors in the POV-Ray environment, two 353.3x430.1mm white planes were constructed to match the size and position of the detectors. The shadows of the simulated phantom model are projected onto these surfaces. Two cameras, or view points, were placed in front of the planes to capture the image of the shadows projected on to the planes. One camera was used for each image. The locations of the cameras within the RSA Coordinate System are  $\langle -105, 175, 633 \rangle$ mm and  $\langle 740, 175, 633 \rangle$ mm for the right and left images respectively. The field of view for these cameras was adjusted to view only the dimensions of the real world x-ray detectors. The rendered image was produced with a 2208x2688 pixel resolution to match that of the physical detectors.

The x-ray sources were simulated by the placement of the image light source within the POV-Ray environment. The focus of a physical x-ray source is not a singular point but an area source. To simulate this area source, grids of twenty-five individual point sources were arranged in a 3x3mm area. The locations of the x-ray foci were located 1.6m above at an angle of  $30^\circ$  to the detector planes. The positions of the foci in the RSA Coordinate System were  $\langle -184, 175, 1580 \rangle$ mm and  $\langle 1019, 175, 1580 \rangle$ mm for the right and left images respectively.

Due to the POV-Ray shadow process, the images produced are colour negatives of physical x-rays. For this thesis, an image showing white shadows on a black background denotes a real physical x-ray of a phantom model. Conversely, an image showing a black shadow on a white background denotes a simulated x-ray produced using the following method. This convention is maintained unless otherwise stated.

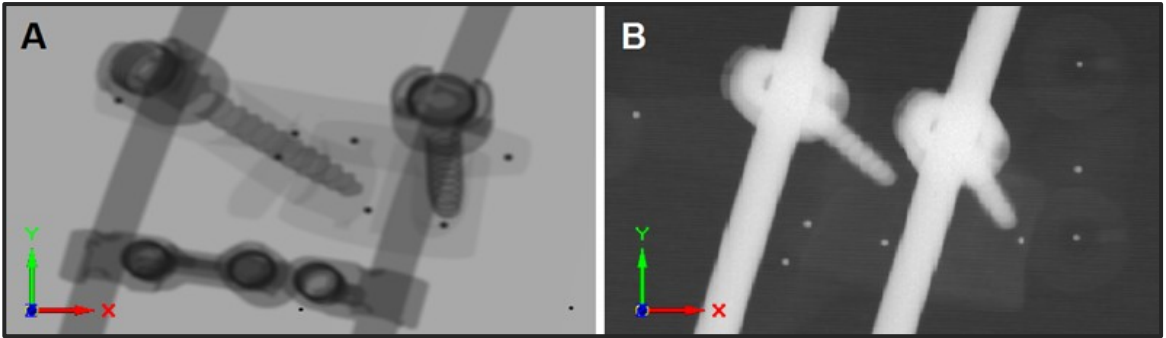
### ***3.2.3.1 Image Simulation***

The process for the simulation of RSA images was originally developed by Francis (2009) [27]. With the previously created simulation process, a CAD model of the spine and calibration box is created using Solid Edge CAD software (Siemens, Germany). This CAD model is converted into a single POV-Ray (Persistence of Vision Raytracer Pty. Ltd.) file through the intermediary program; Rhinoceros, a NURBs modeling software (McNeel North America, US). In the POV-Ray file, light sources, cameras and detector planes were created to simulate the RSA environment. The overview of the conversion process is depicted in Figure 3.10 with the step-by-step instructions for the current simulation process found in Appendix C.



**Figure 3.10: RSA Simulation Process as developed by Francis (2009) [27].**

Significant improvements were made to the image simulation process to better emulate the conditions found in actual radiographic images. Chief among the changes was the alteration of the x-ray signal attenuation method. The previous work focused on a surface attenuation technique to create different material contrasts [27]. With the surface attenuation method, whenever a simulated photon interacted with a surface, a percentage of the signal was blocked while the remainder was allowed to continue on toward the detector planes. The thickness of the material was not taken into consideration with this method. This created an over-definition of each surface which incorrectly increased the contrast of thin objects with many surface layers, and produced low contrast where thick objects had few surfaces for interaction. This issue was most noticeable in the area of the screw thread, shown in Figure A, when compared to a similar thread imaged in a physical phantom model, shown in Figure 3.11 B. The simulated x-ray images produced are colour negatives compared to traditional x-ray images.



**Figure 3.11: Surface attenuation technique (A) compared to a phantom model image (B).**

To improve the modeling technique, a novel material attenuation technique was implemented. Each material was given its own linear attenuation coefficient providing the required material contrast. The coefficients for the four simulated materials are listed in Table 3.7. Interface admittance is the percentage of the signal that is transmitted through the surface interface while the linear attenuation coefficient is the half-strength thickness used for the simulated material.

**Table 3.7: Simulated Attenuation Coefficients**

	Interface Admittance	Linear Attenuation Coefficient ( $\mu$ )
<b>Bone</b>	0.97	100.00mm
<b>Titanium</b>	0.90	4.20mm
<b>Cobalt-Chrome</b>	0.75	2.70mm
<b>Tantalum</b>	1.00	0.21mm

As the simulated photon passed through the objects of the simulated spine their signal strength was decreased linearly depending on the thickness of the object. The linear attenuation coefficients were qualitatively developed to match the contrast present in phantom model studies, an example of the visual matching is shown in Figure 3.12. This process recreates the depth contrast present in actual images as well as creating edge blurring.



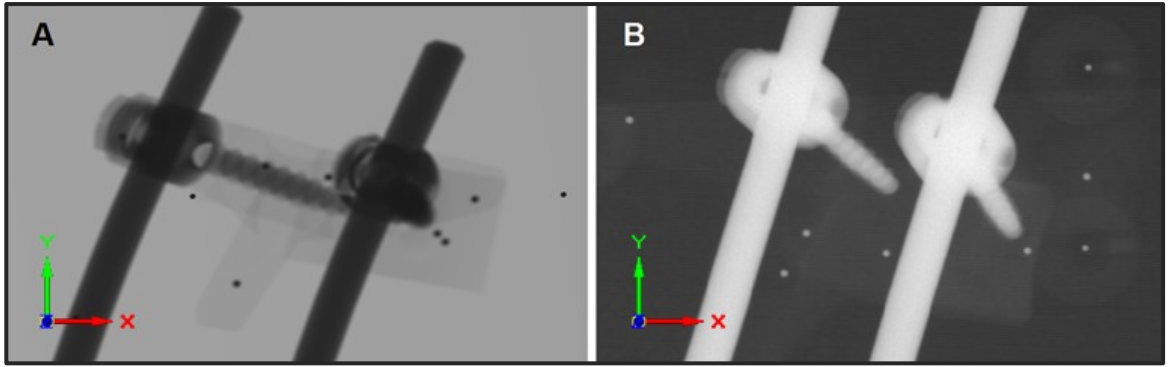


Figure 3.12: Linear attenuation simulation method (A) compared to a phantom model (B).

### 3.2.4 Radiostereometric Analysis

The simulated image pairs comprising the RSA exams were analyzed using Model-Based Radiostereometric Analysis v3.31 (MB-RSA software) developed by Medis specials bv. based in the Netherlands.

Marker identification was completed using a detection algorithm built into the MB-RSA software. Markers not identified by the algorithm were manually identified using a marker identification tool. The markers were also manually checked to confirm that the software correctly centered the identifier over the visual center of the marker shadow. This was most significant in locations where the marker was occluded by metal implants. The marker contrast was affected causing errors in location of marker centers during automatic marker identification.

Each marker cluster was assessed for marker visibility and cluster distribution in each reference RSA exam. To evaluate marker visibility, the number of matched markers in each cluster was assessed. A matched marker was classed as being visible in both the left and right images as well as having a crossing line distance of less than 0.1mm. Optimally, all seven markers implanted into each vertebra would be visible and matched.

Unfortunately, due to x-ray foci and pedicle screw placement, the marker #7 implanted in the L1 vertebrae was not able to be re-positioned to a location where it would be visible.

From the matched markers in each rigid body segments marker models were created. Marker models are vital in generating migration data. The MB-RSA software uses marker models to match marker clusters between follow-up exams. A matrix method for calculating the intervertebral migrations of the fused spine is shown in Section 3.2.4.1.

For each marker cluster the program calculates the CN, rigid body error, number of matched markers, the Maximum Total Point Motion (MTPM) and the translational vector and rotational matrix. A sample of this data is presented in Figure 3.13.

Model: T4															
Reference: L1															
Xref	Xmig	X	Y	Z	Rx	Ry	Rz	#Matched Markers	#Matched Reference Markers	Rigid Body Error	Rigid Body Error Reference	Condition Number	Condition Number Reference Model	Maximum Total Point Motion	
0	1	20.0235	-0.0143	0.1165	0.0881	0.0472	0.0225	7	6	0.1471	0.0099	18.5	19.8	20.1579	
0	2	-0.0391	19.9844	0.1162	0.0430	-0.0063	0.3203	3	6	0.0148	0.0240	34.4	19.8	19.9992	

**Figure 3.13: Sample Data output from the MB-RSA software. Data recorded from the 20mm inferior failure accuracy assessment.**

The markers of an individual cluster are not uniquely identified by the MB-RSA software between follow-up exams. To match the markers, the software calculates the distance from one marker to the remainder in the cluster for each exam. The program pairs markers between exams by which exhibit the least difference in intra-cluster distance using a least mean squares regression. The “# Matched Markers” result in Figure 3.13 indicates the number of markers in the marker model which were matched between the two RSA exams. Only markers in the marker models with a corresponding counterpart in both analyzed RSA exams are used to calculate the rigid body motion of the vertebral segment.

When computing migrations during in vivo situations, marker loosening can be a factor. The software uses a ‘Rigid Body Match Threshold’ to eliminate unstable markers. If the intra-cluster motion exceeds 0.5mm, then the migratory marker is excluded from use in rigid body migration calculations. Since there is no marker movement during testing in this thesis, the elimination of unstable markers was not observed.

‘Rigid Body Error’ is the mean difference in the calculated intra-cluster marker distances between one RSA exam and another. It is a measure of the overall stability of a marker cluster and should not exceed 0.35mm, as advised by Valstar et al (2005) [5]. The marker distribution within their respective marker models was assessed using the CN. A desirable distribution was one that had a resultant CN of less than 100 [5], [27]. A higher CN is an indicator of a poorly distributed marker cluster. A poorly distributed marker cluster provides less information than is required to derive the marker cluster pose matrix. This leads to higher measurement error associated with the calculated rigid body migration.

#### ***3.2.4.1 Global Migration Calculation***

The initial post-operative exam is used as the “Reference Scene” for subsequent follow-up examinations. Comparing the relative positions of the vertebral marker clusters with their positions in the reference scene, a longitudinal assessment of the intervertebral migration can be created.

All measured migration of the vertebrae is calculated from the centroids of the individual marker clusters. The centroid of the marker clusters are defined by Equation 3.1, Equation 3.2, and Equation 3.3.

$$X_c = \frac{x_1 + x_2 + \dots + x_n}{n} \quad \text{Equation 3.1}$$

$$Y_c = \frac{y_1 + y_2 + \dots + y_n}{n} \quad \text{Equation 3.2}$$

$$Z_c = \frac{z_1 + z_2 + \dots + z_n}{n} \quad \text{Equation 3.3}$$

$X_c$ ,  $Y_c$  and  $Z_c$  define the three dimensional coordinates of the marker cluster centroid with  $x_n$ ,  $y_n$  and  $z_n$  defining the positions of an individual marker.  $n$  is the number of markers in a marker cluster. The centroid is defined as: *Centroid* =  $\langle X_c, Y_c, Z_c \rangle$ .

The three marker clusters assessed during this project were located in the T4, T8 and L1 vertebra. The migration of these marker clusters is determined using the implementation of the following matrix equations published by Laende (2006) [29]. They were reproduced here with permission. The equation script was modified to reflect the use in the spine.

Variables:

$$[P_{Time}^{Vertebra}]_{Coordinate\ System}$$

**Pose Matrix** for a marker cluster

$$[T_{Time\ to\ Time}^{Vertebra}]_{Coordinate\ System}$$

**Transformation Matrix.** This represents the rotational transformation of a Pose Matrix between Time 1 and Time 2. It is in the form:

$$\begin{bmatrix} 1 & 0 & 0 & 0 \\ [X_c] & & & \\ [Y_c] & [R] & & \\ [Z_c] & & & \end{bmatrix}$$

$$[R] = \begin{bmatrix} \cos \beta & 0 & \sin \beta \\ 0 & 1 & 0 \\ \sin \beta & 0 & \cos \beta \end{bmatrix} \begin{bmatrix} \cos \gamma & -\sin \gamma & 0 \\ \sin \gamma & \cos \gamma & 0 \\ 0 & 0 & 1 \end{bmatrix} \begin{bmatrix} 1 & 0 & 0 \\ 0 & \cos \alpha & -\sin \alpha \\ 0 & \sin \alpha & \cos \alpha \end{bmatrix}$$

**Rotational Matrix** where  $\alpha$  is rotation about the x-axis,  $\beta$  is about the y-axis and  $\gamma$  is about the z-axis.

$$[MM_{Time,Corrected}^{Vertebra}]_{Coordinate\ System}$$

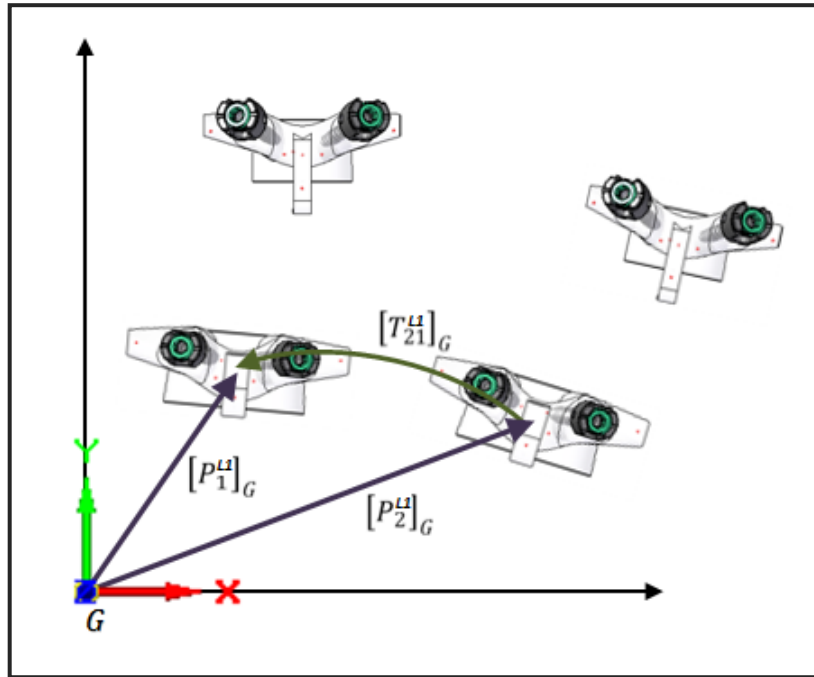
**Marker Matrix**

Where:	<i>Vertebra</i> =	T4, T8, or L1 vertebrae. The example shown here is of the T8 vertebra measured in reference to the L1 vertebra.
	<i>Time</i> =	Reference exam (1) or follow-up exam (2)
	<i>Coordinate System</i> =	RSA Coordinate System (G)
	<i>Corrected</i> =	Origin vertebra transformation applied to remove global misalignment between exams.
	<i>Shifted</i> =	Moved to origin of coordinate system

1) Determine the time 1-2 transformation for the reference marker cluster.

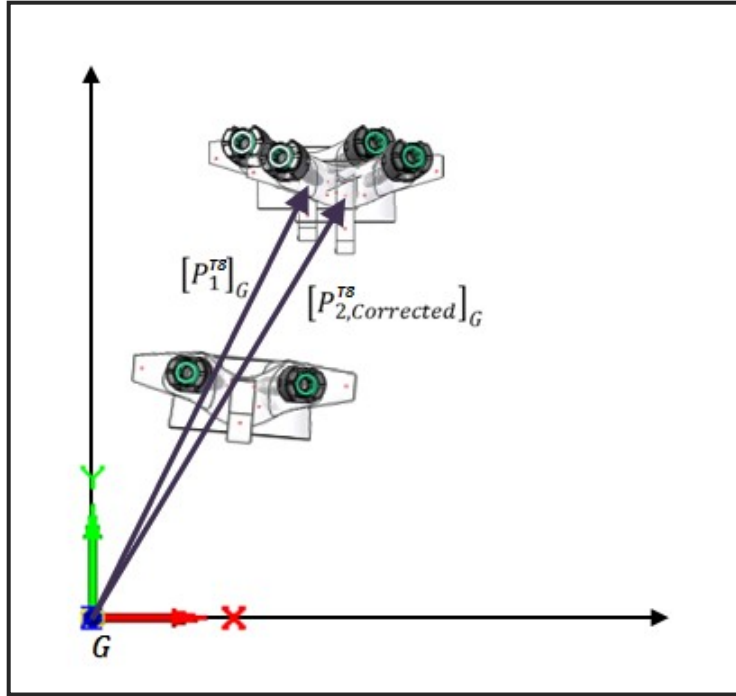
$$[T_{21}^{L1}]_G = [P_2^{L1}]_G [P_1^{L1}]_G^{-1}$$

Equation 3.4



- 2) Apply the time 1-2 transformation to the migratory vertebral marker cluster to bring the time 2 cluster into alignment with time 1.

$$[MM_{2,corrected}^{T8}]_G = [T_{21}^{L1}]_G [MM_2^{T8}]_G \quad \text{Equation 3.5}$$



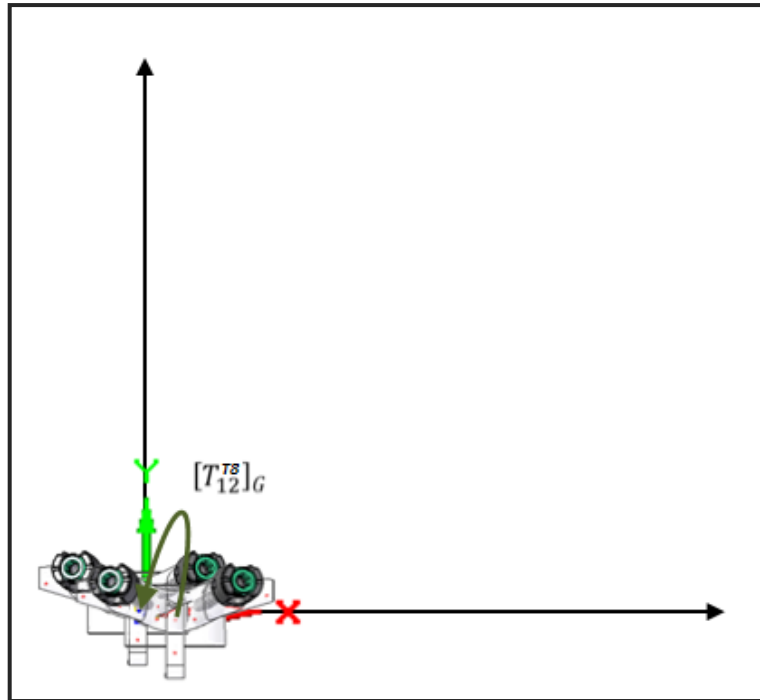
- 3) Translate the centroid of the reference marker cluster and migratory marker clusters to the global origin.

$$[MM_{2,corrected,shifted}^{T8}]_G = [MM_{2,corrected}^{T8}]_G - Centroid_1^{T8} \quad \text{Equation 3.6}$$

$$[MM_{1,shifted}^{T8}]_G = [MM_1^{T8}]_G - Centroid_1^{T8} \quad \text{Equation 3.7}$$

- 4) Determine the transformation of the corrected migratory marker cluster between time 1 and time 2. This transformation is the measured migration with the rotation in the order Y, Z, X.

$$[T_{12}^{T8}]_G = [P_{1,shifted}^{T8}]_G [P_{2,corrected,shifted}^{T8}]_G^{-1} \quad \text{Equation 3.8}$$



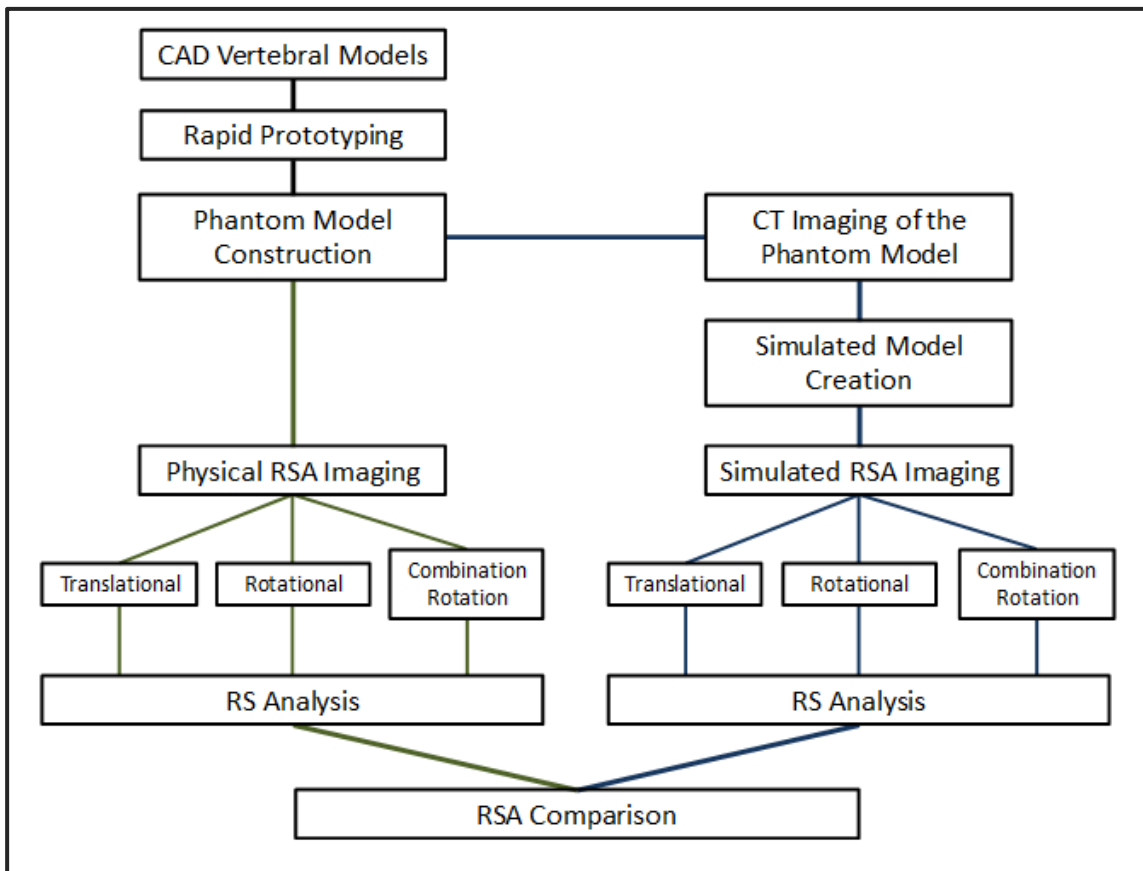
The order used to calculate the rotational displacements of the migratory vertebrae can have a significant impact on the results obtained. In the matrix equations above, the order of rotations is Y, Z, X which is common for this style of calculations.

### 3.2.5 Simulation Precision Validation

To determine the precision validity of the simulated RSA environment a parallel precision study was undertaken. In clinical research situations, RSA system precision is calculated using double exams. These exams are taken at a single time point and are assumed to have no migration associated within them. In phantom model situations, the unaltered model can be imaged several times without having to worry about the adverse



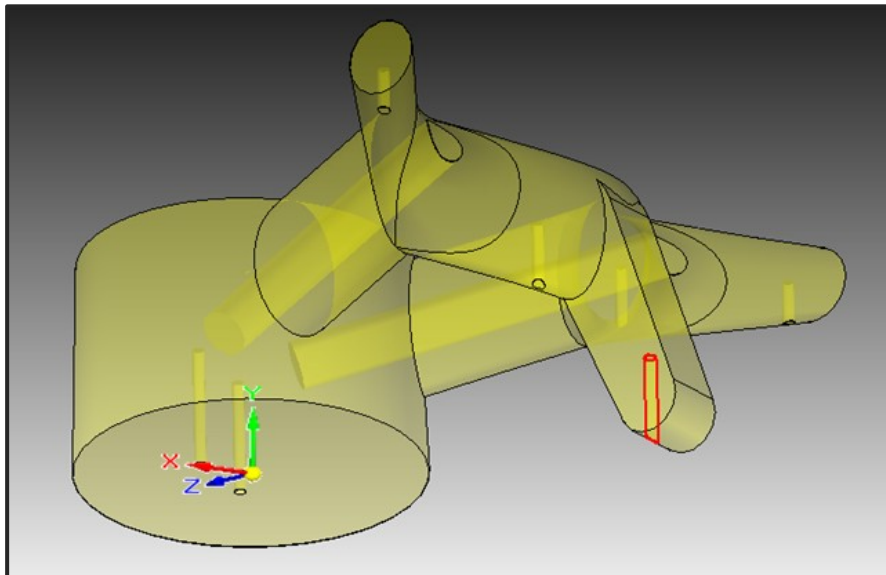
effects of radiation dosages, a limiting factor in clinical research. Protocols for assessing precision using phantom models are well defined in the literature. Madanat et al (2005, 2007), Bragdon et al (2002), Önstén et al (2001), and Allen et al (2004) recommend the repositioning of the phantom model within the RSA environment with no displacement induced within the phantom model [26], [34], [59], [60], [63]. The study was conducted identically on both a phantom and simulated model to compare their respective precisions and assess their congruency. The testing process is summarized in Figure 3.14.



**Figure 3.14: Process flow chart of the parallel simulation precision validation. Green Path - Physical Model Testing, Blue Path - Simulated Model Testing**

### 3.2.5.1 Phantom Model

The phantom model was constructed using the simulated vertebral models previously constructed as described in Section 3.2.1.1. These models were modified to include guide holes for the pedicle screws and for the insertion of the RSA markers. See Figure 3.15 for an example of a modified vertebral model. The holes created for the RSA markers create a marker placement profile identical to that of the simulated marker placement profile as shown in Section 3.2.1.2.3.



**Figure 3.15: Modified T8 vertebral model. Red cylinder indicated the guide hole for the placement of the #2 RSA marker.**

Physical constructs of the three vertebral models (T4, T8 and L1) were created using the Dalhousie University Mechanical Engineering Department's rapid prototyper. This machine creates accurate, three-dimensional plastic replicas of the CAD drawings. These physical models were identical replicas of those used in all computer simulations. The dimensions for these phantom models can be found in Section 3.2.1.1.

Into each of the vertebral models, seven 1mm tantalum RSA markers were implanted into each vertebral model using the marker guide holes shown in Figure 3.15.

The phantom model was assembled using standard spinal fusion pedicle screw implants and instrumentation (DePuy Expedium 5.5mm System; DePuy Spine; Raynham, MA) with the help of Dr. Waleed Kishta, a Pediatric Orthopaedic Fellow at the IWK Health Centre. Six monoaxial pedicle screws and two 5.5mm Cobalt-Chrome fixation rods were used to form the scoliotic and kyphotic curve of the phantom model. The pedicle screws used are listed in Table 3.8.

**Table 3.8: Pedicle screw sizes used in the simulated spinal model**

<b>Vertebra</b>	<b>Screw Length (mm)</b>	<b>Diameter (mm)</b>
<b>T4</b>	25	4.35
<b>T8</b>	40	4.35
<b>L1</b>	40	6.00

The spinal dimensions of the phantom model were modified from the original simulated fusion model to compensate for the limited field of view associated with the physical RSA system. The new phantom model now allows for the phantom to fit within the RSA diagnostic imaging area allowing for the simulation validation to be carried out using the Caudal Origin Style. The nominal dimensions of the physical model are 80% of the full sized simulated model shown in Figure 3.16 and listed in Table 3.9. The use of a scaled model is expected to impact the precision results obtained from the assessment of the two RSA environments. This impact will not be apparent in the simulation validation assessment as both the physical and simulated models are both scaled to 80% of the full size length. No analysis between a scaled and full sized phantom was conducted in this thesis.

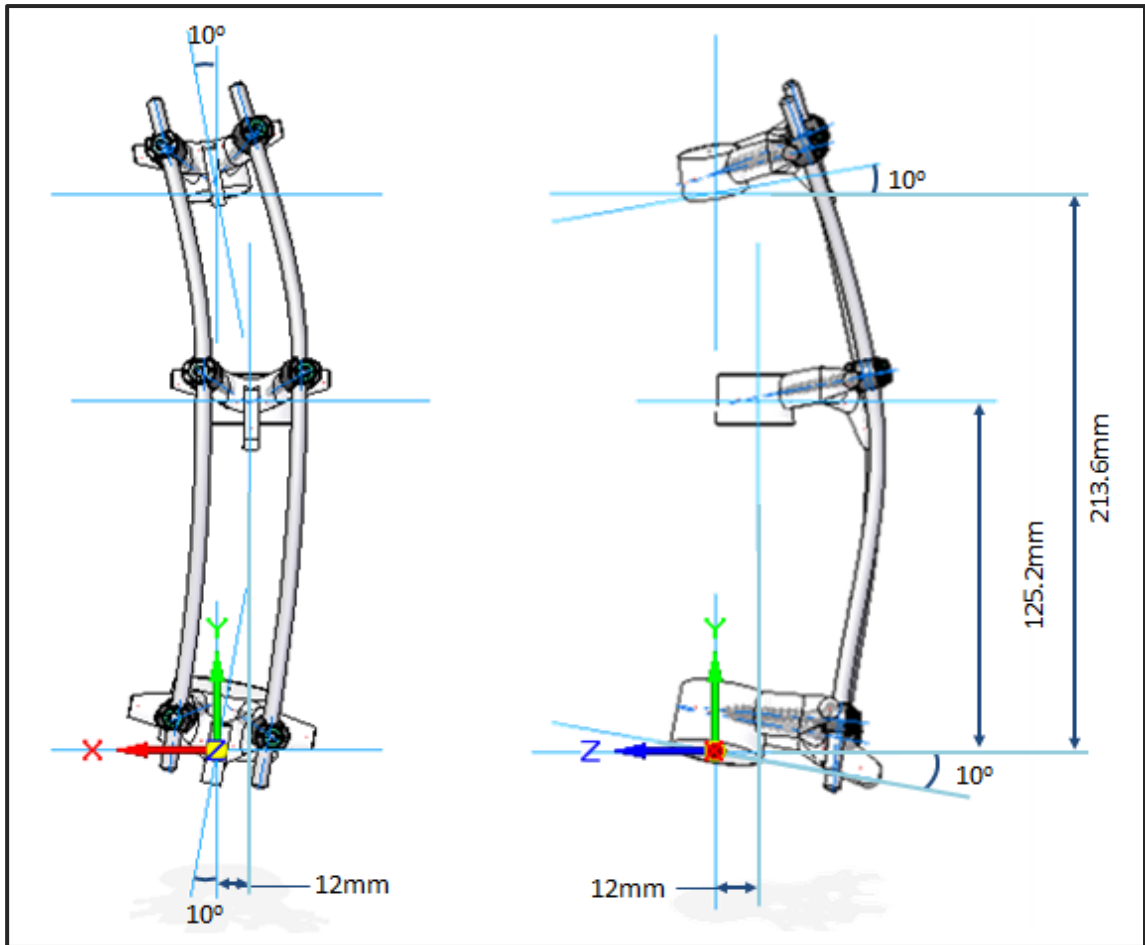
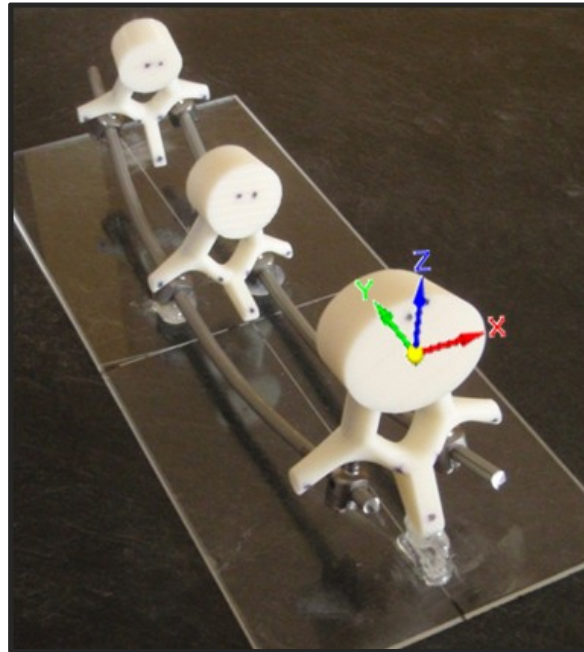


Figure 3.16: Nominal dimensions and Coordinate System of the Phantom Spinal Model.

Table 3.9: Nominal dimensions of the phantom model compared to those of the full-size simulated spinal model.

Locations		Full-Size Simulated Model		Phantom Model	
		Translation (mm)	Rotation (deg)	Translation (mm)	Rotation (deg)
T4	X	0.0	10	0.0	10
	Y	267.0	0	213.6	0
	Z	0.0	-10	0.0	-10
T8	X	-15.0	0	-12.0	0
	Y	156.5	0	152.2	-5
	Z	-15.0	0	-12.0	0
L1	X	0.0	-10	0.0	-10
	Y	0.0	0	0.0	0
	Z	0.0	10	0.0	10

Due to the nature of the surgical techniques, the dimensions of the phantom spine were best approximated at the time of assembly. The completed phantom model mounted to its Plexiglas support backing is shown in Figure 3.17.



**Figure 3.17: Phantom model on its Plexiglas backing. The dots on the vertebral models indicate the locations of the implanted RSA markers. The Spinal Coordinate System is shown.**

To identify the locations of each of the twenty-one implanted RSA markers the assembled phantom model was imaged with a Toshiba Aquilion CT scanner (Toshiba America Medical Systems; Tustin, California). During this CT imaging the phantom model was placed on a level examination surface and aligned so that the Y-axis of the phantom model was approximately in line with the long axis of the CT scanner. A sample image slice of the T8 vertebral model is shown in Figure 3.18. In this image the markers number 3, 6 and 7 can be seen along with the plastic vertebral model, the implanted pedicle screws, the fixation rods, the Plexiglas backing and the top surface of the examination table. The marker location data recorded from this CT scan is shown in Table 3.10.

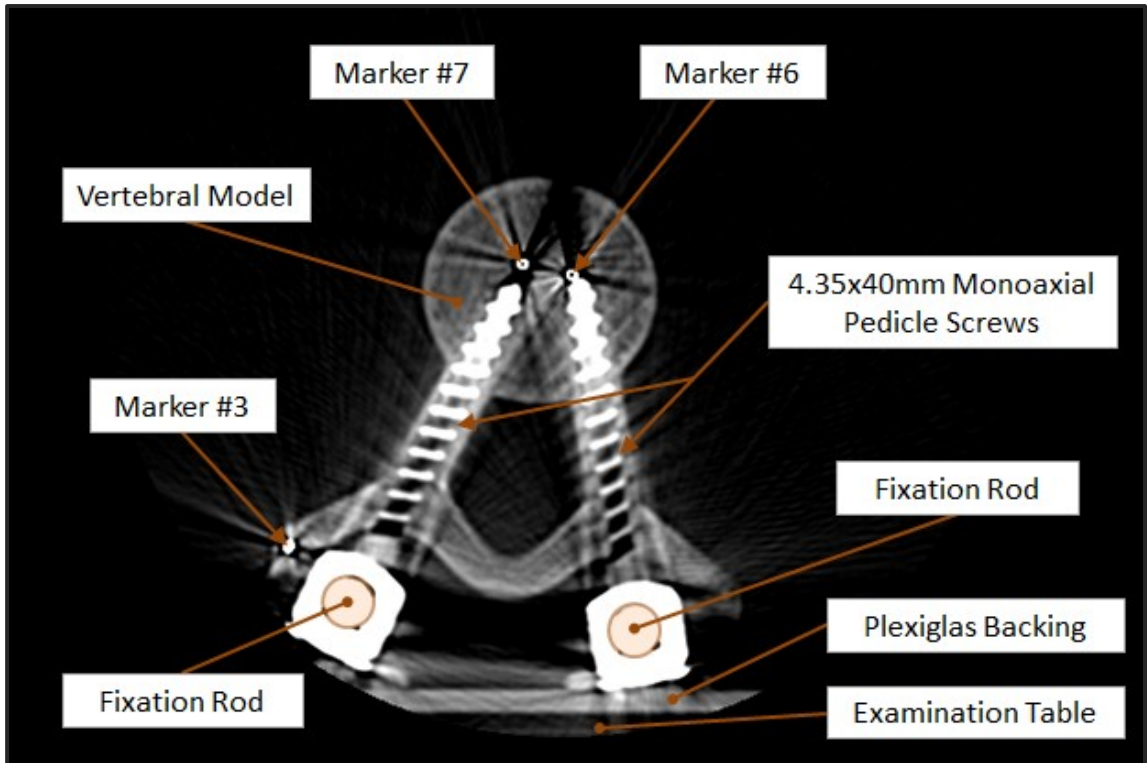
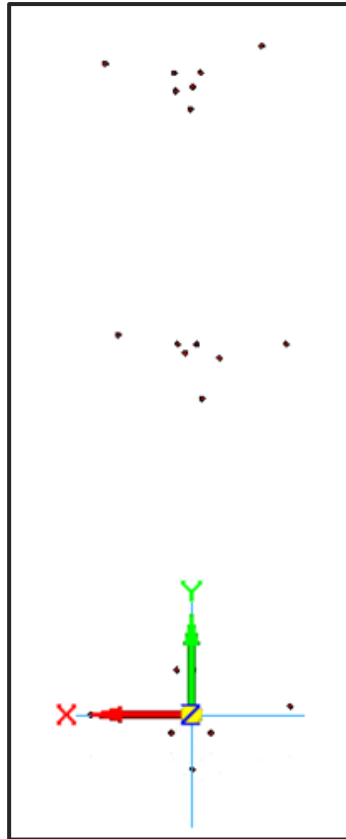


Figure 3.18: A slice from the CT scan performed on the assembled phantom model showing the T8 vertebral model and implanted components. View is from the bottom of the vertebra.

**Table 3.10: Locations of the RSA markers as determined from the assembled phantom CT scan. Locations are described in the Spinal Coordinate System. The L1 marker #2 position was used as the reference point.**

<b>Vertebra</b>	<b>Marker #</b>	<b>Marker Location</b>	<b>X</b>	<b>Y</b>	<b>Z</b>
<b>T4</b>	1	Left Transverse Process	30.07	227.75	-48.67
	2	Spinous Process	1.93	212.75	-60.70
	3	Right Transverse Process	-21.45	233.75	-48.90
	4	Left Lamina	7.37	224.75	-48.90
	5	Right Lamina	-1.48	224.75	-48.90
	6	Left Pedicle Screw Hole	6.69	218.75	-18.25
	7	Right Pedicle Screw Hole	1.25	220.25	-17.57
<b>T8</b>	1	Left Transverse Process	25.76	137.75	-68.19
	2	Spinous Process	-1.93	116.75	-69.10
	3	Right Transverse Process	-29.63	134.75	-61.61
	4	Left Lamina	3.74	131.75	-64.11
	5	Right Lamina	-7.61	130.25	-62.75
	6	Left Pedicle Screw Hole	6.24	134.75	-27.33
	7	Right Pedicle Screw Hole	-0.12	134.75	-25.97
<b>L1</b>	1	Left Transverse Process	34.84	11.75	-45.72
	2	Spinous Process	1.25	-6.25	-55.25
	3	Right Transverse Process	-30.99	14.75	-45.95
	4	Left Lamina	8.06	5.75	-42.54
	5	Right Lamina	-4.88	5.75	-42.54
	6	Left Pedicle Screw Hole	6.47	26.75	8.99
	7	Right Pedicle Screw Hole	1.02	26.75	6.03

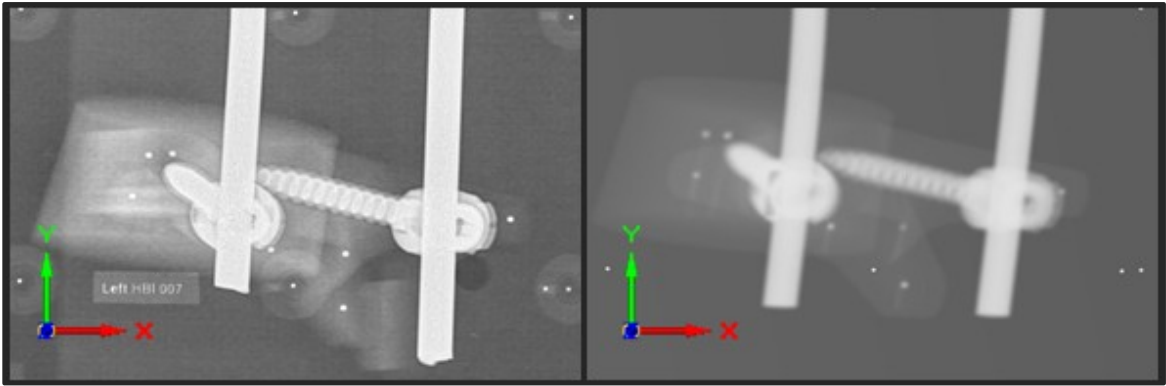
The marker locations recorded from the CT scan were used to develop an identical computer simulation of the marker distribution. The three dimensional marker locations were utilized directly in Solid Edge creating the single, twenty-one marker assembly shown in Figure 3.19.



**Figure 3.19: Simulated Model Marker Distribution. From top to bottom: T4 marker cluster, T8 marker cluster, and L1 marker cluster located at the Spinal Coordinate System origin.**

The position and orientations of the vertebral models and fusion implants were approximated to closely match the orientations of the three marker clusters. The use of an approximated placement of the vertebral models and AIS implants was deemed acceptable since the exact locations of the vertebral models and implants are unimportant in traditional marker based RS assessment past their role in marker occlusion. Assessment of the resultant images shows that marker occlusion between the physical and simulated images are preserved, for an example see Figure 3.20. The physical phantom model was imaged using x-ray energies of 90KV for 10ms.





**Figure 3.20: Comparison of Physical (Left) and Simulated (Right) images of the L1 vertebral models. Marker occlusion and spinal model placement is almost identical between the image pair. The simulated image has been colour inverted to provide comparison with the phantom image.**

For the computer simulation the CAD model of the 4.35x40mm monoaxial pedicle screw implanted into the T8 phantom model vertebrae was unavailable. The 4.35x30mm screw model was used in the computer simulation instead. A test image set was taken to assess the effect of this substitution and it was shown that there were no changes in marker occlusion.

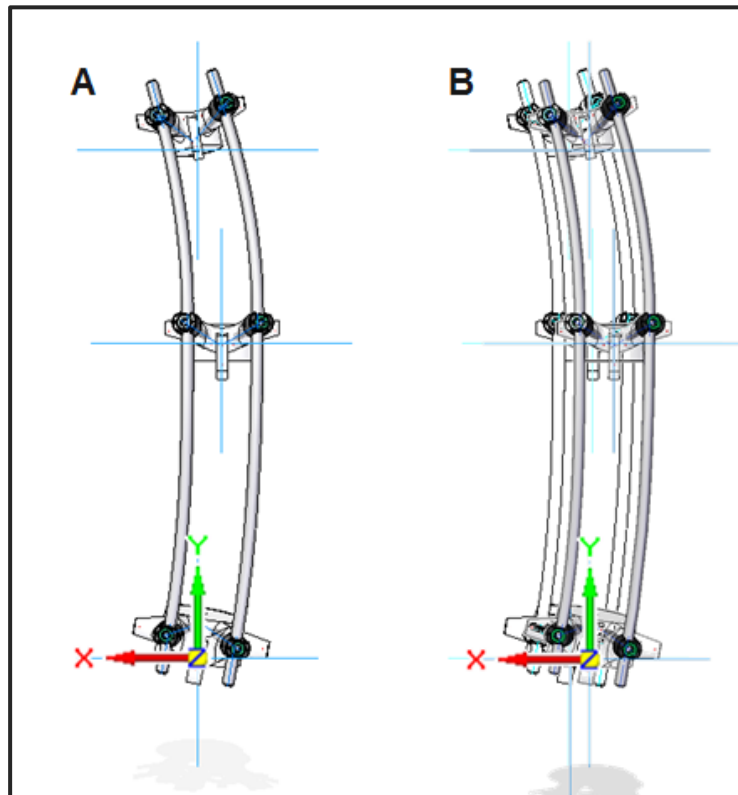
### ***3.2.5.2 Precision Movement Imaging***

To test the system precision and to validate the simulation process, both the physical phantom and simulated model were manipulated in an identical fashion. Both were repositioned as a single rigid unit within the RSA environment with respect to the RSA Coordinate System as defined by the calibration box. No intervertebral movement was induced during all precision imaging. The movements discussed below are described as a single process, applying to both the physical and simulated models except where expressly stated.

The physical model was placed in a supine position on a level examination table at the approximate center of the RSA imaging volume in accordance with the patient placement protocol. The vertical (Y) axis of the model was aligned parallel with the Y-

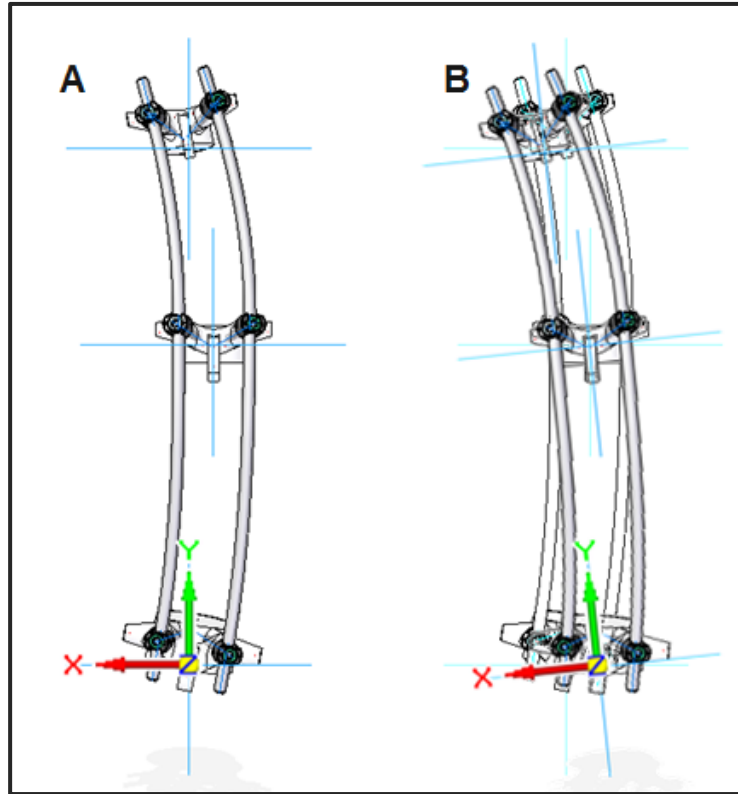
axis of the RSA calibration box. This arrangement aligns the Spinal Coordinate System with the global RSA Coordinate System. After initial placement, a test image was produced to confirm placement and marker clarity. This positioning was used as the “Reference Position”.

To assess the precision of the RSA system and the validity of the simulated environment, sixteen independent migrations were used. The models were moved globally within the RSA environment in three independent movement scenarios. In each case the migration induced was global migration of the spinal model with no intervertebral movement induced. The first of these was that a 10mm translation in all six cardinal directions. An example of this movement is shown in Figure 3.21.



**Figure 3.21: Translational Precision Movement. A) Reference Position, B) Global precision movement of the spine model -10mm along the X axis.**

The second movement scenario was a rotation of the model was  $\pm 6^\circ$  about all three principle global axes. An example of this movement is shown in Figure 3.22.



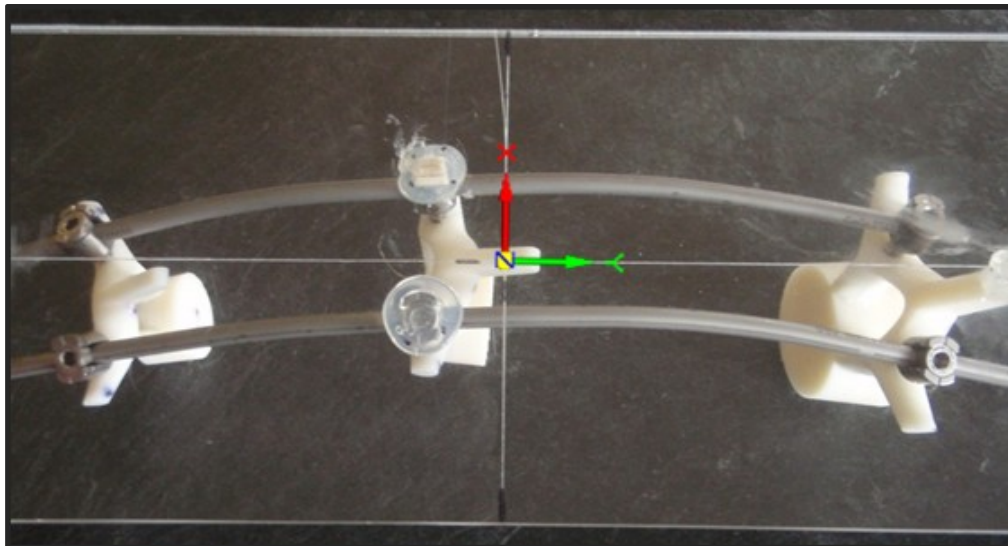
**Figure 3.22: Rotational Precision Movement. A) Reference Position B) Global precision movement of the spine model  $-6^\circ$  about the Z axis.**

The third movement scenario was one simulating a patient undergoing a combination of rotational displacements. In this scenario, the model was rotated about the Y-axis  $\pm 6^\circ$  and then  $\pm 6^\circ$  about the Z-axis. In each of the three scenarios, each examined movement was independent of one another. The model returned to the reference position between each migration scenario. The movements for the three movement scenarios are summarized in Table 3.11.

**Table 3.11: Global movements of the fusion model. Each movement scenario was completed independent of the other two.**

Movement	Translation (mm)	Rotation (deg)	Combination Rotation (deg)
0	Reference	Reference	Reference
1	10 +X	6 +X	6 +Y, 6 +Z
2	10 +Y	6 +Y	6 +Y, 6 -Z
3	10 +Z	6 +Z	6 -Y, 6 +Z
4	10 -X	6 -X	6 -Y, 6 -Z
5	10 -Y	6 -Y	Reference 2
6	10 -Z	6 -Z	
7	Reference 2	Reference 2	

All rotational movements were conducted about a point in the center of the bottom of the Plexiglas backing used to secure the phantom model, Figure 3.23. This point was mirrored in the simulated CAD model as <1.99, 116.75, -82.63>mm in the Spinal Coordinate System. This position of the rotational center was selected to centralize the rotation, keeping the spine centered in the available RSA imaging area. A full definition of this phantom precision rotational coordinate system is described in Appendix B. All Translational movements were along the cardinal axes of the RSA Coordinate System.



**Figure 3.23: Etched phantom precision rotation center.**

At the end of the movements conducted, the phantom model was returned to the zero reference position and another image set was produced, referred to as “Reference 2” in Table 3.11. This second reference image set was not produced for the simulated model due to the precise nature of the simulation process. This second simulated reference image would be identical to that of the first reference image taken. Therefore the “Reference 2” in Table 3.11 for the simulated precision assessment was a repeat of the original reference image for the simulated model assessment.

### ***3.2.5.3 Simulation Precision Validation***

Since no intervertebral movements were introduced in either model during the precision assessment imaging, any intervertebral migrations measured using the RSA calculations are an assessment of the system precision. A total of eighteen image sets were produced for the assessment of the precision for the physical RSA environment, while seventeen were produced for the assessment of the simulated environment. This discrepancy was due to the additional ‘Reference 2’ image set taken during the physical study.

The assessment of the precision was conducted in the same manner as that performed by Madanat et al (2005, 2007), Bragdon et al (2002), Önsten et al (2001), and Allen et al (2004) [26], [34], [59], [60], [63]. When the exams were evaluated using the MB-RSA software, each model repositioning was assessed with respect to the previous model position described in Table 3.11. In this case each repositioning of the models acted as both a migrating scene with respect to the previous model position, and a reference scene with respect to the subsequent model position. For example from Table 3.11, for the translational movement scenario: image set 0 forms the reference scene for

images set 1. Image set 1 then forms the reference scene for image set 2 and so on. This created nineteen data points for the migrations of the T4 and T8 vertebrae for both the physical and simulated models.

Any translational or rotational migrations calculated represent the error within the RSA system. This error is normally based on three main factors: the radiographic positioning and technique, the marker placement, and the migration calculation process which is influenced by the origin style used. Between both the physical phantom and simulated model testing, the marker placement and origin styles were kept constant removing them as sources of error. This left only the radiographic technique as a significant source of error between the real world physical model and its simulated counterpart.

Madanat et al (2005) utilized a simple and effective means of determining system precision shown in Equation 3.9 [60].

$$P = y \times SD \quad \text{Equation 3.9}$$

where  $SD$  is the standard deviation of the migration dataset ( $\Delta X$ ,  $\Delta Y$ ,  $\Delta Z$ ,  $\Delta R_x$ ,  $\Delta R_y$ ,  $\Delta R_z$ ,  $\Delta MTPM$ ) and  $y$  is the 95% confidence interval. For nineteen data points  $y$  is equal to 2.09 as defined from the critical values of a student t-test with nineteen degrees of freedom at an  $\alpha$  of 0.05. The calculations for the precisions can be found in Appendix E, Section E.2.

To compare the precisions of the physical and simulated model, an assessment of their variances was undertaken. Each of the migration datasets ( $\Delta X$ ,  $\Delta Y$ ,  $\Delta Z$ ,  $\Delta R_x$ ,  $\Delta R_y$ ,  $\Delta R_z$ ,  $\Delta MTPM$ ) for both models were tested for equal variance.

The method used to compare the variances is dependent on the distribution of the two assessed datasets. The distribution of each dataset was analyzed using an Anderson-Darling test in Minitab 16. A p-value generated from this test greater than 0.05 indicated that the data was normally distributed. The results of the distribution analysis determined the statistical test used to assess the variance difference. If both compared datasets were normally distributed, an F-Test was used to compare their variance. In dataset pairs where one or both of the sets are non-parametrically distributed the Levene's Test was used. For either of these tests a p-value greater than 0.05 indicated that there is no statistical difference between the two datasets and that the simulated environment mirrored that of the physical RSA system.

### 3.3 Simulation Precision Validation Results

#### 3.3.1 Image Simulation

To assess the settings of the image simulation process, the reference images of both the physical and simulated phantom were assessed. The assessment looked at the image intensities, contrast, SNR and CNR of the two image sets. The image intensities were recorded as 8-bit grey-scale values from 0 to 255 where 0 is black and 255 is white.

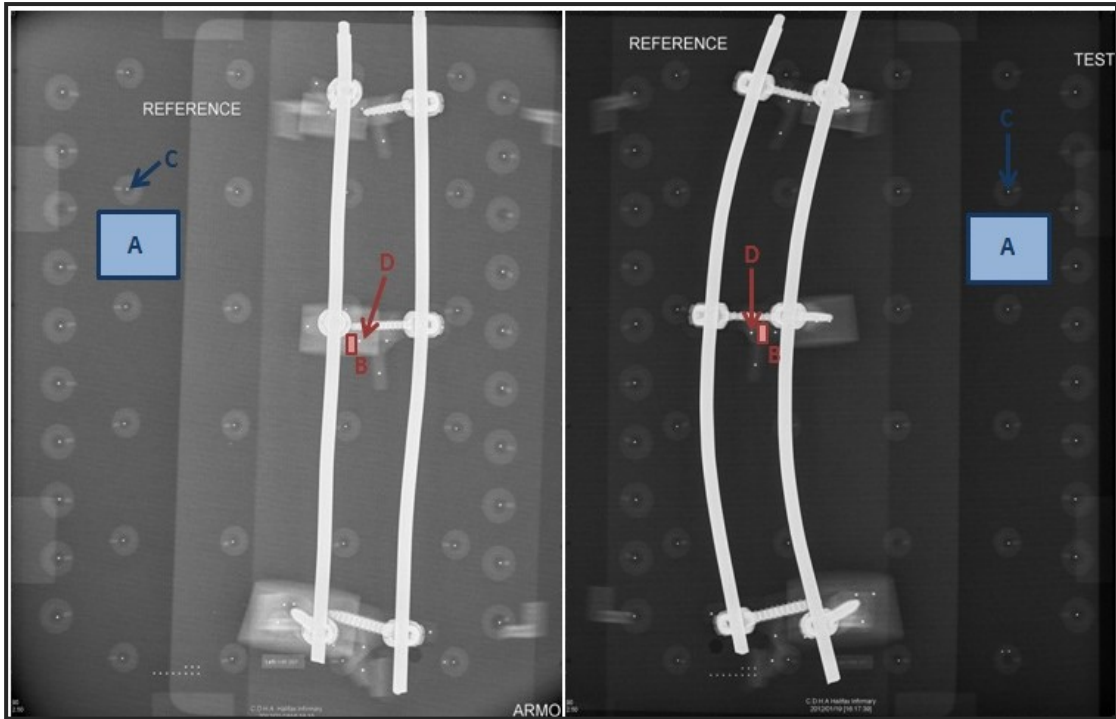
##### 3.3.1.1 Physical Phantom Imaging

The left and right images produced at the Halifax RSA suite produced two images with unique background intensities and were analysed separately. These images, having been created using a physical RSA system displayed image noise. Figure 3.24 shows the Regions of Interest (ROI) used to assess the image properties. The positions of the ROIs for the assessed can be found in Table 3.12.

**Table 3.12: Regions of Interest for the Physical Phantom image assessment.**

		Background Region	Calibration Box Marker	Bone Region	Implanted Bone Marker
<b>Left Image</b>	Start Pixel	300, 750	464, 673	1415, 1223	1393, 1247
	End Pixel	649, 999	469, 677	1466, 1278	1400, 1252
	Dimensions (Pixels)	350x250	6x5	52x56	8x6
<b>Right Image</b>	Start Pixel	1600, 750	1773, 684	757, 1191	743, 1215
	End Pixel	1949, 999	1778, 687	830, 1272	750, 1221
	Dimensions (Pixels)	350x250	6x4	74x82	8x7





**Figure 3.24: Physical Phantom Reference Image Pair with assessed Regions of Interest. Region A: Image Background. Region B: Bone. Marker C: Calibration Box Marker. Marker D: Bone Implanted Marker**

From the assessment of the ROI-A in the images the background noise of the image was calculated as 16.85 for the left image and 10.50 for the right image. The mean signal intensities, marker contrast, SNR and CNRs for the physical phantom images are reported in Table 3.13.

**Table 3.13: Physical Image Properties.**

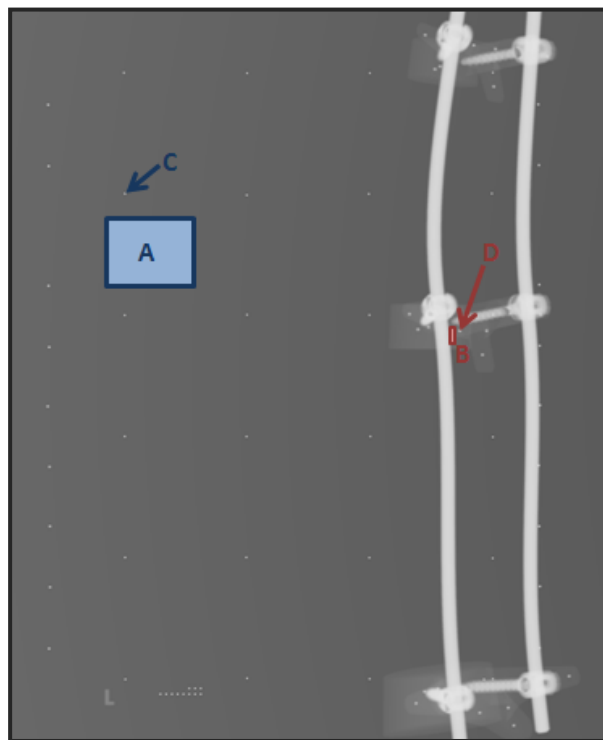
		Left Image	Right Image
<b>Background Noise (<math>\sigma</math>)</b>		16.85	10.50
<b>Mean Signal Strength</b>	Background ROI (A)	98.83	36.92
	Bone ROI (B)	161.96	56.85
	Calibration Box Marker (C)	244.77	212.83
	Bone Marker (D)	246.65	222.50
<b>Contrast</b>	Calibration Box Marker	145.93	175.91
	Bone Marker	84.68	165.65
<b>Noise Ratios</b>	SNR	5.86	3.52
	CNR (Calibration Box)	8.66	16.75
	CNR (Bone)	5.03	15.77

### 3.3.1.2 Simulated Phantom Imaging

The simulated phantom images were assessed likewise. In the case of the simulated images, the left and right image had identical background intensities, therefore only the left image was assessed.

**Table 3.14: Regions of Interest in the Simulate Reference Image**

	Start Pixel	End Pixel	Dimensions
<b>Background</b>	750, 300	999, 649	250x350
<b>Calibration Box Marker</b>	673, 420	677, 424	5x5
<b>Bone Segment In Bone Marker</b>	1167, 1615	1190, 1634	24x20
	1175, 1643	1179, 1647	5x5



**Figure 3.25: Simulated Phantom Left Reference Image with assessed Regions of Interest. Region A: Image Background. Region B: Bone. Marker C: Calibration Box Marker. Marker D: Bone Implanted Marker. The image colour has been inverted to be compared to the physical phantom image pair.**

Due to the perfection of the signal source in the simulated image, the assessment of the ROI-A yielded a result of 0 for the image background noise. The mean signal intensities, marker contrast, SNR and CNRs for the physical phantom images are reported in Table 3.15.

**Table 3.15: Simulated Image Properties**

		Simulated Image
<b>Background Noise (<math>\sigma</math>)</b>		0.0
<b>Mean Signal Strength</b>	Background ROI (A)	100.73
	Bone ROI (B)	114.01
	Calibration Box Marker (C)	219.32
	Bone Marker (D)	194.08
<b>Contrast</b>	Calibration Box Marker	118.59
	Bone Marker	80.07
<b>Noise Ratios</b>	SNR	$\infty$
	CNR (Calibration Box)	$\infty$
	CNR (Bone)	$\infty$

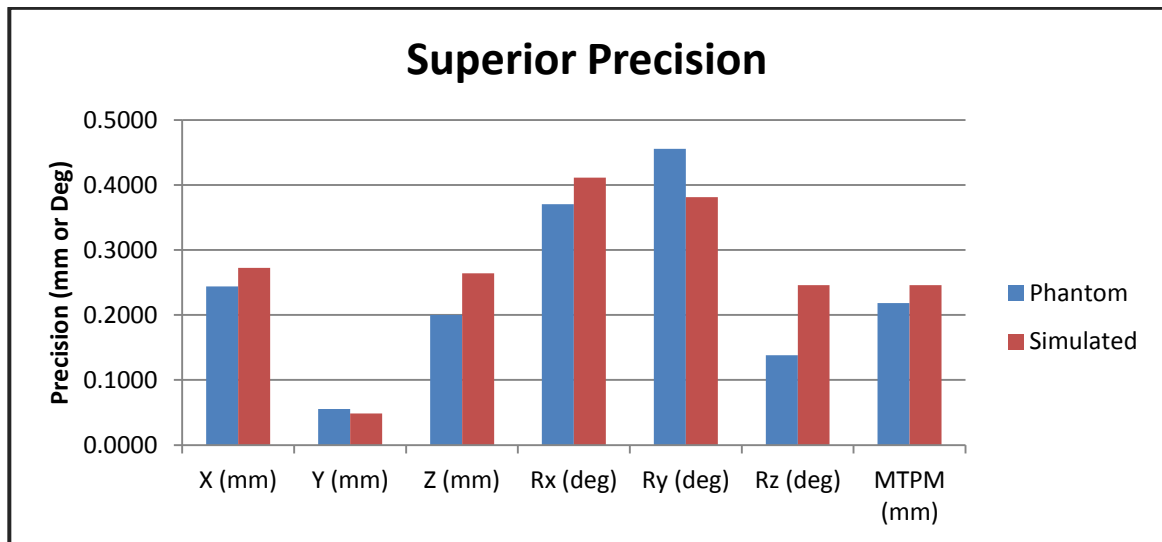
### 3.3.2 Precision Results

To delineate the precision of the T4 measurement and T8 migration measurement the terms superior precision and inferior precision are used. The superior precision pertains to the assessment of the T4 migration in reference to the L1 vertebral marker cluster while the inferior precision pertains to the assessment of the T8 migration, also in reference to the L1 marker cluster. Due to their large size, the data created and the precision calculations are not included here. They are, however, included in this thesis, located in Appendix E, Section E.2.

The resultant superior precision calculated for the phantom and simulated models are shown in Table 3.16 and graphically shown in Figure 3.26.

**Table 3.16: Superior Precisions generated by the Phantom and Simulated model assessments**

	X (mm)	Y (mm)	Z (mm)	Rx (deg)	Ry (deg)	Rz (deg)	MTPM (mm)
<b>Phantom</b>	0.2438	0.0553	0.2001	0.3706	0.4554	0.1382	0.2185
<b>Simulated</b>	0.2725	0.0488	0.2640	0.4112	0.3810	0.2460	0.2461

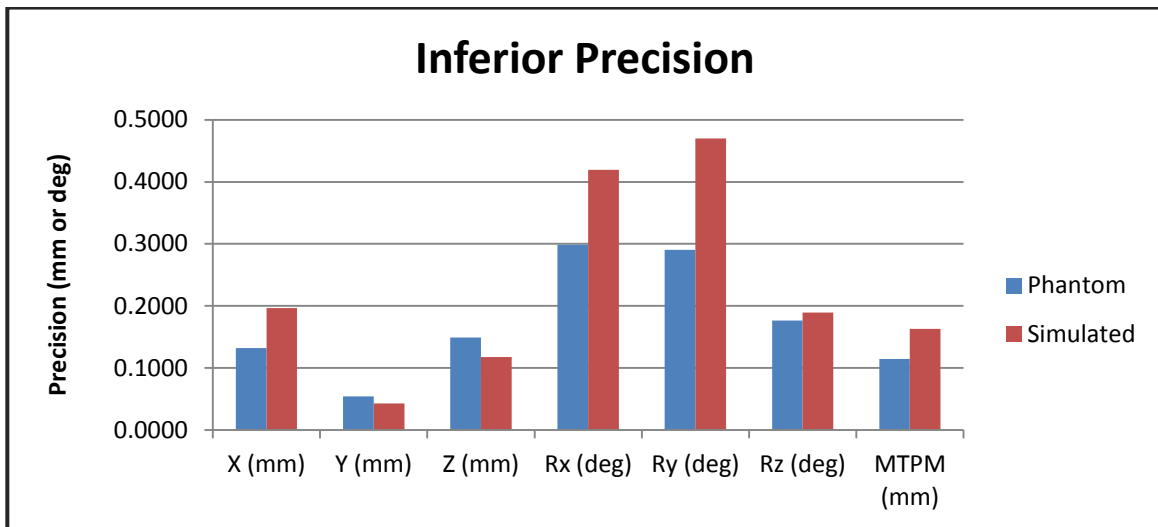


**Figure 3.26: Calculated Superior Precision**

The inferior precisions calculated for the phantom and simulated spinal models are shown in Table 3.17 and graphically shown in Figure 3.27.

**Table 3.17: Inferior Precisions generated by the Phantom and Simulated model assessments**

	X (mm)	Y (mm)	Z (mm)	Rx (deg)	Ry (deg)	Rz (deg)	MTPM (mm)
<b>Phantom</b>	0.1319	0.0544	0.1490	0.2987	0.2902	0.1766	0.1147
<b>Simulated</b>	0.1963	0.0429	0.1175	0.4192	0.4697	0.1892	0.1630



**Figure 3.27: Calculated Inferior Precision.**

### 3.3.3 Precision Comparison

The data from the two spinal models were compared to assess the validity of the simulated RSA environment. Each directional precision was assessed independently for their variance agreement. To do this the distribution of the datasets is required.

#### 3.3.3.1 Dataset Distribution

Each of the twenty-eight datasets (there were seven directions assessed for each migratory vertebra and two migratory vertebrae for each of the two assessed models) was analyzed using an Anderson-Darling test in Minitab 16 to check their distribution. Resultant p-values greater than 0.05 indicated that a dataset was normally distributed. The

results from the assessment of the superior and inferior precision datasets are summarized in Table 3.18. As it can be seen the majority of the data recorded was normally distributed.

**Table 3.18: Distribution of the precision datasets.**

Assessed Direction	Superior Aspect			
	Phantom		Simulated	
	p- value	Normalcy	p- value	Normalcy
<b>X</b>	0.034	Non-Parametric	0.216	Normal
<b>Y</b>	0.078	Normal	0.700	Normal
<b>Z</b>	0.477	Normal	0.608	Normal
<b>Rx</b>	0.714	Normal	0.545	Normal
<b>Ry</b>	0.423	Normal	0.497	Normal
<b>Rz</b>	0.723	Normal	0.008	Non-Parametric
<b>MTPM</b>	<0.005	Non-Parametric	0.893	Normal
Inferior Aspect				
	Phantom		Simulated	
	p- value	Normalcy	p- value	Normalcy
<b>X</b>	0.093	Normal	0.061	Normal
<b>Y</b>	0.959	Normal	0.257	Normal
<b>Z</b>	0.928	Normal	0.522	Normal
<b>Rx</b>	0.806	Normal	0.406	Normal
<b>Ry</b>	0.814	Normal	0.046	Non-Parametric
<b>Rz</b>	0.424	Normal	0.524	Normal
<b>MTPM</b>	<0.005	Non-Parametric	0.285	Normal

### 3.3.3.2 Variance Assessment

An example of the graphical output for a test of equal variance, the analysis of the inferior X rotation is shown in Figure 3.28.

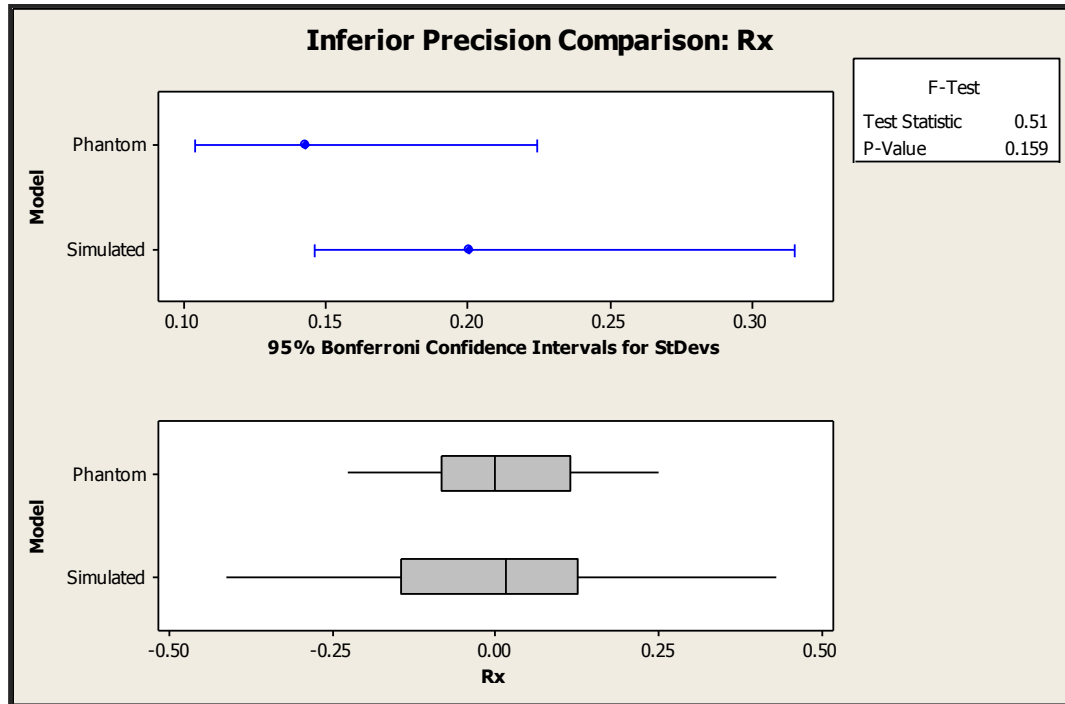


Figure 3.28: Test for equal variance of the Rx direction for the inferior aspect.

In this assessment, both of the two datasets are normally distributed and therefore the F-Test was used. With a p-value of 0.160 this assessment shows that there was no statistical difference between the phantom and simulated models in their X rotational assessment. A full summary of all variance assessment results can be found in Table 3.19.

**Table 3.19: Summary of the results of the assessment of equal variance between the physical and simulated models.**

Assessed Direction	Superior Aspect			Inferior Aspect		
	Statistical Test	p- value	Statistical Difference	Statistical Test	p- value	Statistical Difference
<b>X</b>	Levene's	0.739	No	F-Test	0.100	No
<b>Y</b>	F-Test	0.597	No	F-Test	0.324	No
<b>Z</b>	F-Test	0.250	No	F-Test	0.322	No
<b>Rx</b>	F-Test	0.663	No	F-Test	0.160	No
<b>Ry</b>	F-Test	0.457	No	Levene's	0.211	No
<b>Rz</b>	Levene's	0.297	No	F-Test	0.773	No
<b>MTPM</b>	Levene's	0.431	No	Levene's	0.209	No

From Table 3.19 it can be seen that there is no statistical difference between any of the RSA precision datasets of the physical and simulated models.



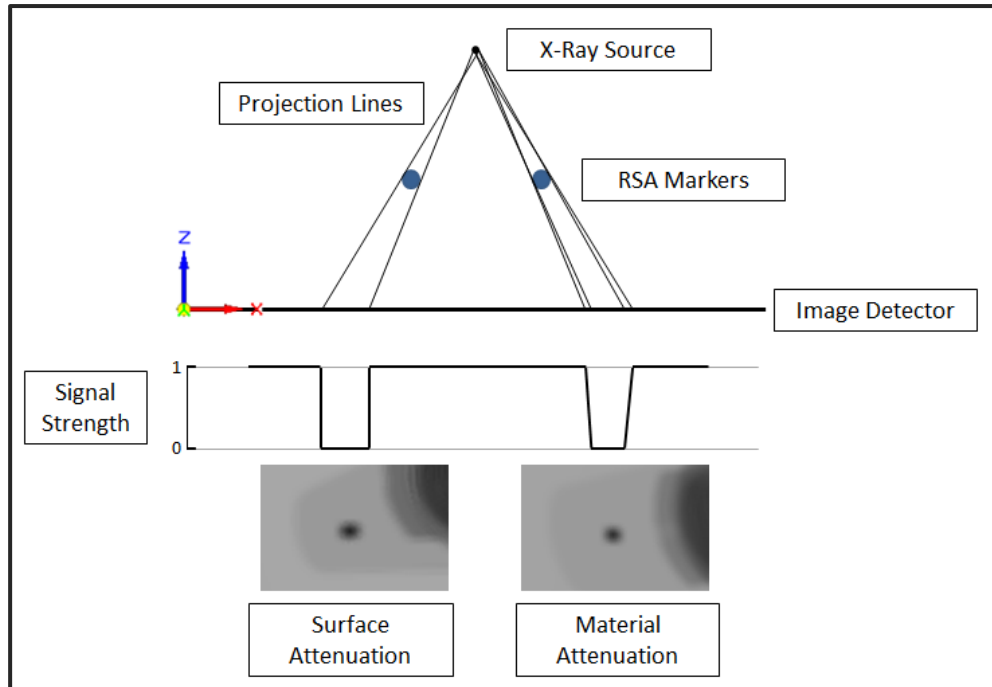
### 3.4 Simulation Precision Validation Discussion

The use of a simulated RSA assessment has been previously used by Madanat et al (2006). They found that in the assessment of distal radius fractures, “...a computer simulation model can be accurately used to replace phantom models in the simulation of RSA studies” [59]. Their use of a computer simulated model and POV-Ray ray-tracing showed “very high correlation” between the simulated movements and the RSA measurement output [59]. This assessment ascertained that a simulated RSA environment provides measurement accuracy comparable to that of physical RSA systems. The article concluded that the use of simulated RSA assessments proved an opportunity for accurate creation of complex movements without the errors associated with the use of micrometers. It was also stated that the use of simulated RSA exams provide a vehicle for the further development of model based RSA. They further concluded that the use of simulated RSA exams can provide fast and cost-effective means for the performing of RSA studies compared to the associated costs of using of physical radiographs and phantoms [59].

The use of a simulated RSA environment has been previously used at this institution by Francis (2009) [27]. He concluded that the simulated environment provided an adequate vehicle for the assessment of the use of RSA in the assessment of the success of spinal fusions. This project used his foundation to further the project goal with the object of assessing the validation of the use of the simulated RSA Environment.

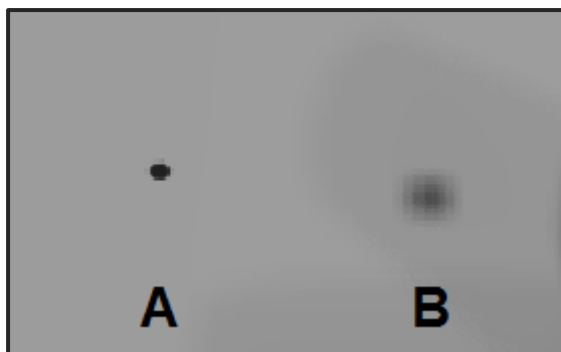
From the foundation work, significant alterations were made to the simulation process to try and create a more realistic x-ray simulation. The impact of these changes on the realism of the simulation remained unknown without a side-by-side comparison study.

One of the most significant impacts of the process improvements was the change in the spatial resolution of the simulated images. The material attenuation method creates a change in the visualization of object edges, enhancing simulation realism. An example of this change is shown in Figure 3.29. With the surface attenuation technique, the photon signal is at either a full and unobstructed strength, or attenuated to a material's contrast strength. However, the material attenuation technique creates a shadow effect where the signal is partially attenuated, like the light grey areas on the right in Figure 3.29. This creates an edge blurring effect. Due to the angle of the x-ray tube to the image detection plate, the shadow effect is not symmetric for the objects. This is standard in RSA exams.



**Figure 3.29: Simulated Photon Attenuation Techniques.** Both markers shown are the #1 marker of the L1 marker cluster and were placed a similar distance from the image detectors during simulated imaging.

The edge blurring created by the material attenuation technique is essentially an application of the edge spread function which causes objects to lose definition, impacting spatial resolution. Due to the intrinsic magnification factor created through the use of the diverging photon rays emitted from the x-ray foci, projections cast by objects in the field of view are enlarged; losing definition at their edges the further they are from the image detectors [56]. This effect is shown in Figure 3.30.



**Figure 3.30: Magnification Blurring. A) Fiducial marker located close to the image detectors showing well defined marker edges. B) Marker #1 located in the T4 vertebra shows much more edge blurring, obscuring the marker edge definition. The image was taken from a section of the left image of the superior spine section's reference exam.**

The further an object is from the image detector, the greater the blurring. This is why the projections of the fiducial markers [Figure 3.30 A] have a much more defined outline than those of the rigid body markers [Figure 3.30 B]. This simple factor, not seen with the surface attenuation technique, adds realism to the simulation previously overlooked. Neither the point spread nor edge spread functions have been defined for the computer simulated RSA set-up.

The first objective of this thesis was to conduct a comparative side-by-side precision assessment of the physical and simulated RSA environments. This comparison found no statistical difference between the any of the recorded precisions of the two environments. The lack of statistical difference validates the use of the simulated RSA process in research performed on the use of RSA in the assessment of multi-level spinal fusion success.

### **3.4.1 Spinal Fusion Precision Comparison**

The precision produced by both the physical and simulated phantom models underperformed those reported in the literature. All precision values reported in other RSA applications were on the order of hundredths to thousandths of a millimetre and tenths to hundredths of a degree. The precision recorded during the simulation validation process was on the order of tenths of a millimetre for translational precision and tenths of a degree for the rotational precision. It was expected that this thesis would cover the most precise modeling situation before adding on additional complexities and sources of error much like the Allen et al (2004) study looked at three levels of RSA modeling (Plexiglas, Sawbones and In Vivo modeling) [63].

The poor precision results presented in this thesis are expected to be due to the large measurement vectors used in the assessment of multilevel spinal fusions. In other applications, like those in the knee, hip and single level spinal fusions, the measurement vectors are limited [1], [2], [26], [28], [34], [59–61], [63]. The reduced length in measurement vectors lowers the error associated with misalignment of the origin marker cluster. In a preliminary experiment conducted after the conclusion of the thesis data collection, simulated single level spinal fusions showed greatly improved precision responses.

### **3.4.2 Limitations**

Although improvements were made over previous simulation work, there remain several limitations within the simulated RSA environment.

#### ***3.4.2.1 Anatomical Information***

The anatomical information used to construct the CAD models used in the RSA simulation was adapted from two publications by Panjabi et al (1991, 1992) [67], [68]. The published measurements were average anatomical measurements taken from healthy adult donor vertebrae. At the standard age at which spinal fusions are often performed for scoliosis patients, the skeleton is matured reaching its adult proportions. Although there is little size discrepancy between the average vertebrae and patient vertebrae, there can be significant individual anatomical variation, especially when examining a patient with scoliosis.

During the conversion from average anatomical measurements to CAD models small anatomical structures were discarded. Examples of discarded structures are the neuroforamen and the facet joints. These structures are not modeled due their meaninglessness in RS assessment or their removal in the surgical setting.

The loss of boney anatomical structures and measurements was not deemed to significantly impact the validity of the use of the vertebral models. RSA does not use the anatomical structures themselves for reference points, therefore the alterations made to create the CAD models of the simulated vertebrae are of little consequence. With the vast difference in the x-ray attenuation properties of the materials, the tantalum markers and ASI implants are clearly recognizable, no matter the anatomical structures simulated.

#### *3.4.2.1.1 Soft Tissue Envelope*

Currently the simulation does not contain a soft tissue envelope. The absence of soft tissue decreases the realism of the simulation as soft tissue interacts with the projected x-rays. The opacity caused by the presence of soft tissue negatively impacts the image clarity and marker visibility, as well as creating tissue induced x-ray scattering which increases image noise characteristics. The presence of a soft tissue envelope would decrease the marker contrast, decreasing the contrast to noise ratio.

The scope of the phantom models produced during this thesis was limited to ‘dry’ phantoms to limit the sources of error. Currently the images produced without a soft tissue envelope are overly accurate and precise, representing the best case scenario for RS assessment of multi-level spinal fusion success. Future work will inevitably involve the addition of a soft tissue envelope as RS assessment of spinal fusions progresses from computer simulation toward clinical application.

#### *3.4.2.2 Model Scaling*

The use of an 80% scale model to conduct the simulation validation objective of this thesis was done to ensure that the model comfortably fits within the available imaging area when utilizing the traditional Caudal Origin Style. The utilization of the scaled phantoms is akin to the selection of a smaller patient or patient with a shorter fusion length to undergo RS assessment. The vertebral models used in the construction of the scaled phantoms are full size representations, having not undergone size reduction. This provides spatially larger marker clusters than would be present in a smaller sized patient.

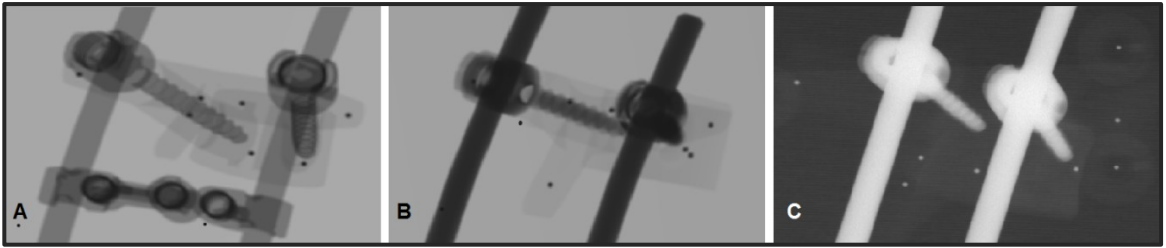
The use of a scaled model has a potential impact on the recorded precision of the RSA system. The precision impact of this scaling was not categorized during the course of this thesis but is expected to have a linear effect. As well the utilization of the spatially larger marker clusters decreases the misalignment in matching the cluster's orientation, improving system precision over the use of marker clusters sized to the anatomical proportions of a smaller patient.

The use of scaling is not expected to have any effect on the conclusions constructed by this thesis as the use of scaled simulated and physical phantom models were segregated from the use of the full sized simulated phantoms. Therefore the compared results between the physical and simulated RSA environment were conducted on identical constructs and are directly comparable.

### ***3.4.2.3 Image Rendering***

The last of the simulation limitations is the material attenuation properties. The coefficients used in the simulations were approximated from images during from a single phantom study. It was not the focus of this thesis to recreate the RSA environment exactly, and as such the approximation of the material attenuation factors was deemed satisfactory. A comparison of the original simulation, the upgraded simulation and an image of a phantom model can be found in Figure 3.31.





**Figure 3.31: A comparison of T4 vertebrae showing the x-ray attenuation techniques. A) Simulated RSA image using the surface attenuation technique. B) Simulated RSA image using the material attenuation technique. C) RSA image of a phantom model of the spine.**

Another limitation is the lack of signal noise present in the images produced. The simulation is “perfect” in that there is no detector noise, signal loss, or other image degradations present in the simulation. Previous work tried to introduce background noise to the images through the use of photo manipulation but this was not done with this simulation procedure. This lack of signal noise is expected to cause the simulation to be overly acute in selecting the RSA markers and allowing for reduced rigid body error and higher marker cluster accuracy. Due to the previously demonstrated acuity in a physical phantom study, the absence of noise is not expected to greatly impact system accuracy and precision but further research should be conducted.

### **3.4.3 Conclusion**

In both qualitative and quantitative measures, the simulated RSA environment accurately emulates the physical RSA environment of the Halifax Infirmar’s RSA Suite. The simulated RSA environment has undergone a parallel comparison with the physical counterpart and has been shown to replicate its performance with no statistically significant differences in the system precisions. The RSA simulation process continues to pass validation assessments and continues to demonstrate adequate validation for the use in research into the use of RSA in multilevel spinal fusion success assessment.

# **Chapter 4 - Thesis Objective #2: Assessment of Novel RSA Origin Styles Used for Spinal Fusion Success Analysis**

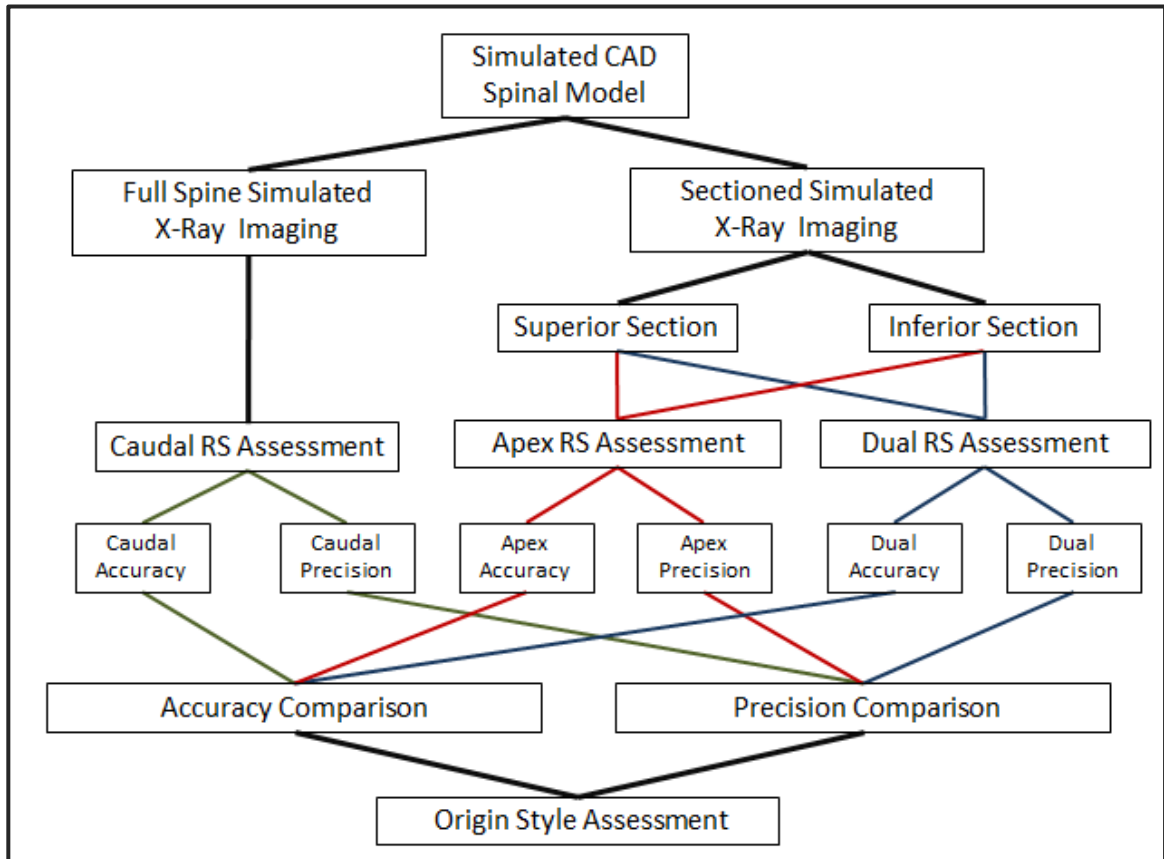
## **4.1 Introduction**

Work by Francis (2009) found physical size limitations effecting the use of the Halifax Infirmary's RSA suite in the assessment of the success of spinal fusions [27]. He found that the length of his average sized phantom model did not adequately fit within the constraints of the diagnostic imaging area. To compensate for this limitation, the simulated environment was adjusted to fit the simulated spinal model. Adjustments to the physical RSA set-up were not feasible so alternative solutions for the spine length were required.

To compensate for the limited imaging length, two new migrational measurement origin styles were created. These two origin styles section the fused spine into two discreet sections imaged in two separate RSA exams. By using two RSA image sets the available imaging area was effectively doubled. The definitions of the novel origin styles, the Apex and Dual Origin Styles, are described in Sections 4.1.1.2 and 4.1.1.3.

The purpose of this second thesis objective is to investigate the implications of the new origin styles on the accuracy and precision of the use of RSA in the assessment of spinal fusion success. The accuracy and precision are dependent on the components of the RSA set-up, including the migration origin style. To be deemed a valid method of assessing the success of spinal fusions, the performance of the new origin styles must

match or exceed the performance of the traditionally used Caudal Origin Style. The Caudal Origin Style represented the benchmark used in this thesis. The process for the testing of the three origin styles is shown in Figure 4.1.



**Figure 4.1: Process flow chart of the testing of the three origin styles. Green Path – Caudal Origin Style, Red Path Apex Origin Style, Blue Path – Dual Origin Style**

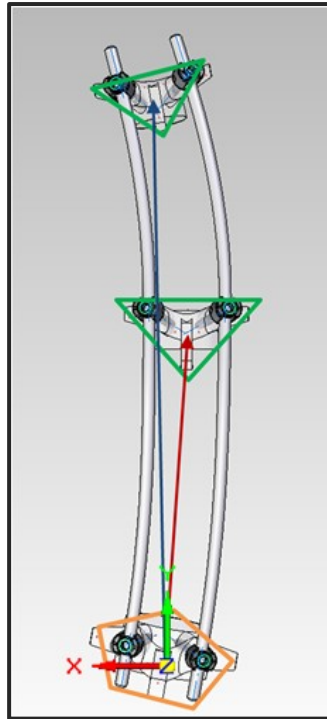
### **4.1.1 RSA Origin Styles**

Three origin styles were examined for their impact on accuracy and precision. The Caudal Origin Style was assessed as a legacy style used in previous project work and throughout the literature. The Apex and Dual Origin Styles, created to compensate for the limited RSA imaging field of view, are novel to this thesis alone.

#### ***4.1.1.1 Caudal Origin Style***

The Caudal Origin Style, simply put, uses the marker cluster at the inferior end of the scoliotic curve as the inter-vertebral migration origin. This origin style was used in previous project work and has been used in the literature, most notably in the study by Pape et al (2002) where the translational Limits of Clinical Significance were defined [1].

In this thesis the Caudal Origin Style compares all movement of the investigated model to the location of the L1 vertebra, Figure 4.2 using a coordinate style defined at the spinal origin. A full definition of the Caudal Coordinate System can be found in Appendix B. This style necessitates that all rigid body marker clusters be fully captured by a single RSA exam image pair.



**Figure 4.2: The Caudal Origin Style and Caudal Coordinate System. The orange pentagon is the migration origin located at the L1 vertebra. The green triangles are the migrating rigid bodies, the T4 and T8 vertebrae. The blue and red arrows are the superior and inferior linear measurement vectors respectively.**

The origin style allows for the single exam assessment of all motion within the fusion, a characteristic not found in the succeeding origin styles. This origin style potentially has the lowest patient radiological dose using only one RSA image set. To achieve proper patient placement allowing for the entire fusion length to be imaged, additional image pairs that may be required. This could negatively impact the low dosage characteristics of this origin style.

Fusion failure localization is achievable using the Caudal Origin Style but this is not as intuitive as the localization found with the other origin styles. Migration of both the T4 and T8 marker clusters must be assessed simultaneously to determine failure localization. To determine if a failure is located in the superior section of the spine, the inferior (T8) migration must be subtracted from the T4 migration. Failure in the inferior

section of the spine is identified by solely assessing the migration of the T8 vertebra with respect to the L1 origin.

In this thesis the simulated patient was placed in a supine position, rather than the prone position used in the previous project analysis [27]. This alteration was done to match current clinical placement positioning, which is more comfortable for the patient. There was no significant difference observed in image quality or RSA applicability between the two patient placement options during preliminary work done for this thesis.

To image the entire spine model during the assessment of the Caudal Origin Style, the origin of the spine model was placed at the point <420, 30, 450>mm in the RSA Coordinate System. The model was aligned so that the Spinal Coordinate System aligned with the RSA Coordinate System. This position was defined as the model's reference position for the Caudal Origin Style.

#### *4.1.1.1.1 Caudal Origin Style Limitations*

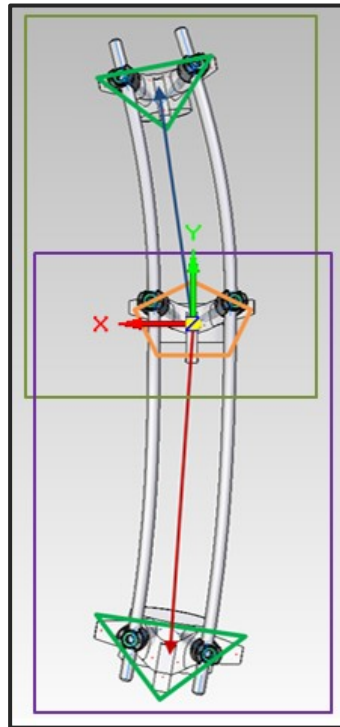
This origin style has limitations which precludes it from use in the local clinical setting. The Caudal Origin Style requires that the full length of the spine fit with the area of the image detectors. The image detectors available at the Halifax Infirmiry severely limit the length of fusion that can be assessed using the caudal origin style. The maximum fusion length that can be assessed is approximately 300mm. This restrictive length would prohibit the use of RSA on a large portion of the patient pool.

The use of the Caudal Origin Style will not be the origin style used during future clinical applications of RS assessment of spinal fusion success at this center. The size limitations are equipment dependent, therefore other equipment may allow for larger

fusion lengths to be assessed using the Caudal Origin Style. The Caudal Origin Style has been previously used by Francis (2009) and in other published literature [1], [2], [27]. Although it will not be used clinically at this center in the future, the Caudal Origin Style has been included in this thesis to provide a benchmark for the new, alternate migration assessment techniques proposed.

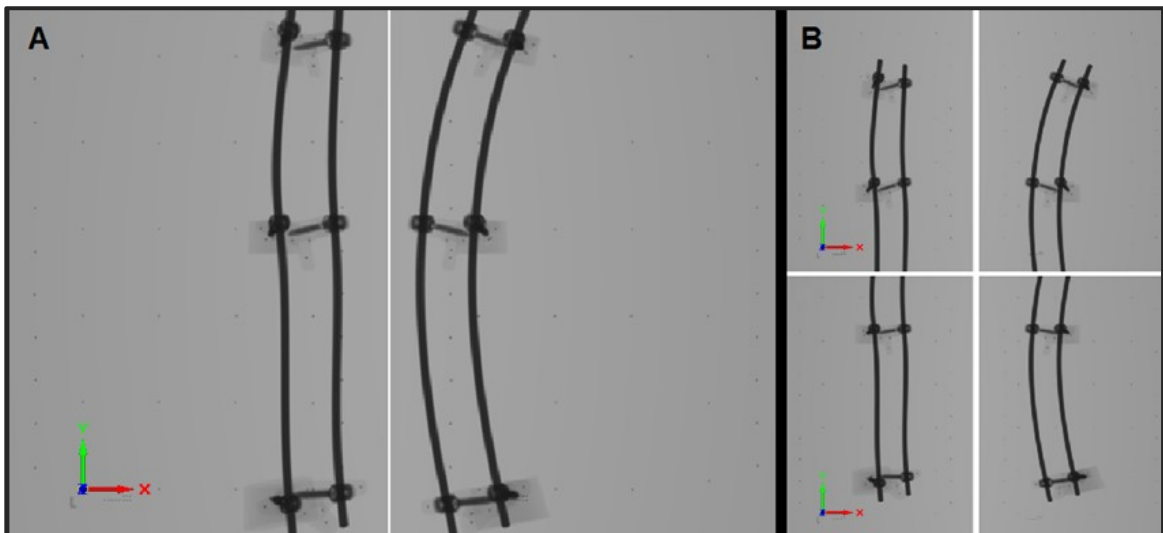
#### **4.1.1.2 Apex Origin Style**

The Apex Origin Style is one that utilizes the vertebra located at the apex of the scoliotic curve as the migration origin, Figure 4.3. A full definition of the Apex Coordinate System used in this origin style can be found in Appendix B.



**Figure 4.3: The Apex Origin Style and associated Apex Coordinate System. The orange pentagon is the migration origin located at the T8 vertebra. The green triangles are the migrating rigid bodies, the T4 and L1 vertebrae. The blue and red arrows are the superior and inferior linear measurement vectors respectively. The green and purple rectangles represent the superior and inferior RSA exam areas respectively.**

Having the migration origin in the center of the fusion allows for the sectioning of the spine into two image sets that are analyzed separately in two separate RSA exams. This sectioning of the spine into two image sets relies on the use of vertebra located at the apex of the scoliotic curve. The T8 vertebra is present in both image sets, which gives both exams a common reference marker cluster. A comparison between the image sets produced from the Caudal and Apex Origin Styles can be seen in Figure 4.4. The positions of the spine origin within the RSA Coordinate system for the two image pairs were:  $\langle 420, -46, 560 \rangle$ mm for the image pair of the superior section of the spine and  $\langle 420, 85, 560 \rangle$ mm for the image pair capturing the inferior section of the spine. As with the Caudal Origin Style, the spine was orientated so that the Spinal Coordinate System aligned with the RSA Coordinate System.



**Figure 4.4: Comparison of the image sets required for the Caudal Origin Style (A) and Apex Origin Style (B). The T8 vertebra is present on both image sets of (B) allowing it to be the migration origin. Each image is has the same dimensions (2208x2688 pixels covering 353x430mm).**

Sectioning the fusion into superior and inferior halves effectively doubles the length of the diagnostic imaging area. This removes the size limitation placed on patients by the Caudal Origin Style. As can be seen in Figure 4.4 (B), the phantom model now fits



comfortably within the diagnostic imaging area. Conversely with the Caudal Origin Style, any global movement in the inferior direction would cause the L1 vertebra to be pushed partially outside the image area, degrading RSA performance. Superior movement in the Caudal Origin Style similarly impacts the visibility of the markers within the T4 vertebra.

The use of the Apex Origin Style allows for the easy localization of fusion failure. A failure in either the superior or the inferior section of the fusion would only appear in the corresponding RSA exam while the other fusion section exam would show no movement. The use of the Apex Origin Style will also reduce the distance between the origin and the T4 vertebral marker cluster, reducing misalignment error and hopefully improving system precision.

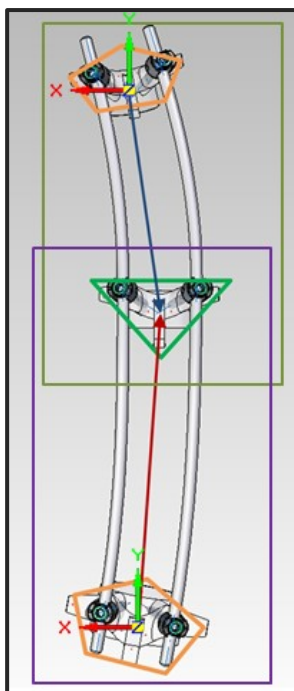
As with most improvements, this new origin style is not without drawbacks. The most significant of these drawbacks is the increased radiological dose experienced by the patient over the caudal benchmark. An increase in the number of image sets increases the effective dose accordingly. Precise patient placement must be achieved to satisfy the requirement that the apex vertebral marker cluster fully appear within both RSA image sets, which leads to the potential use of additional image sets to achieve proper patient placement, further increasing patient effective dose.

With the use of additional RSA exams the use of technician and equipment time is similarly affected. However, this is not a major increase in resource usage and is not a significant concern.

#### ***4.1.1.3 Dual Origin Style***

The Dual Origin Style is the second origin style developed for this thesis. This origin style, like the Apex Origin Style, sections the fusion into a superior and inferior aspect with the apex marker cluster common to both image sets. The Dual Origin Style uses the same superior and inferior RSA image sets as the Apex Origin Style. This means it shares many of the advantages and disadvantages associated with the Apex Origin Style. As with the Apex Origin Style, the use of the Dual Origin Style increases the diagnostically important imaging area as well as increasing patient experienced radiation dose over the Caudal Origin Style benchmark.

The Dual Origin Style differs from the Apex Origin Style by using the marker clusters at both the superior and inferior ends of the fusion as the migration origin (Figure 4.5), instead of using the apex marker cluster. Unlike the other two origin styles, this technique uses two coordinate systems; one for each RSA image pair. The origin for the superior and inferior coordinate system is located at the T4 and L1 vertebral origin respectively. A full definition of these coordinate systems can be found in Appendix B.



**Figure 4.5: The Dual Origin Style and Dual Coordinate Systems. The orange pentagons are the migration origins located at the T4 and L1 vertebrae. The green triangles are the migrating rigid body, the T8 vertebra. The blue and red arrows are the superior and inferior linear measurement vectors respectively. The green and purple rectangles represent the superior and inferior RSA exam areas respectively.**

The migration measurement is inward toward the apex of the curve with the superior and inferior migration measured independently of one another. In this respect, like the Apex Origin Style, the localization of fusion failure is self-evident as displacements in either the superior or the inferior sections of the spine.

Lastly, the use of this origin technique reduces the possibility of the migration origin undergoing rotational displacement. The T4 and L1 vertebrae are unlikely to rotate as they need to maintain alignment with the native spine. The rotation of the T8 (curve apex) vertebra has, in large rotations, led to the occlusion of rigid body RSA markers. The reduction in the visibility of origin markers reduces matching marker pairs which can impact the misalignment error, reducing precision of the Apex Origin Style. The use of the Dual Origin Style alleviates this complication.

## **4.2 Origin Style Assessment Methodology**

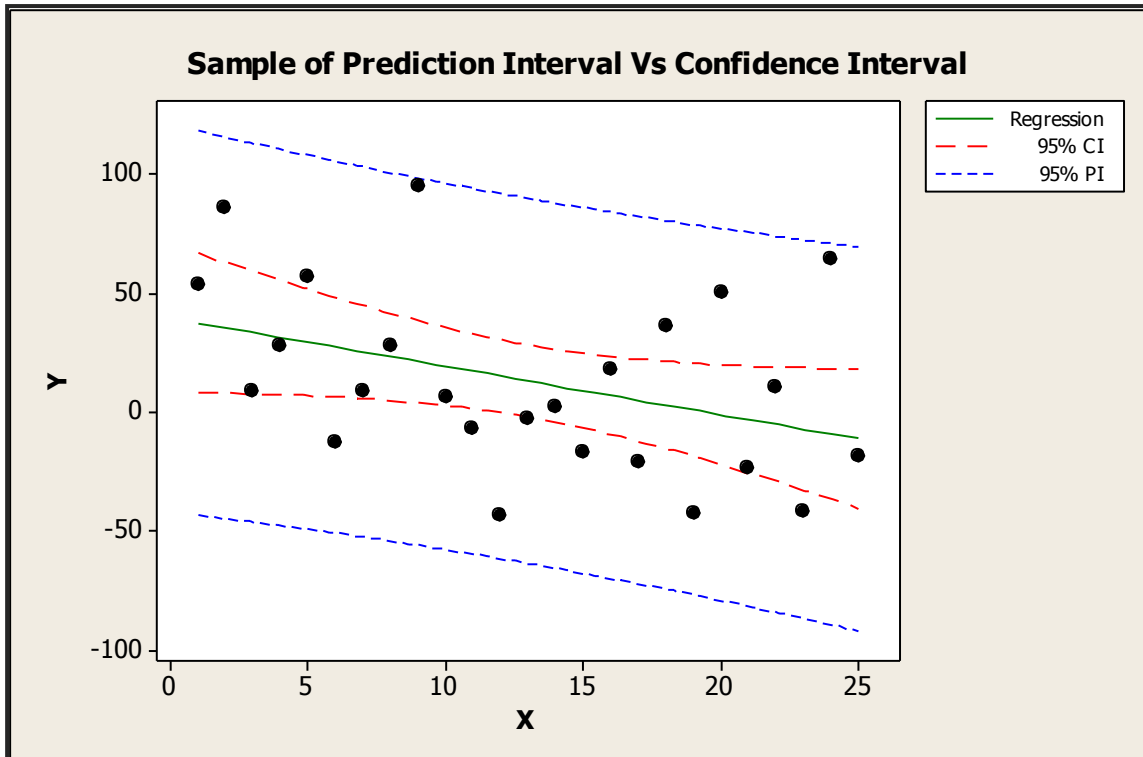
### **4.2.1 Accuracy Assessment**

The validation of the accuracy of the developed origin styles was conducted through manipulations to the simulated phantom model. The T4 and T8 vertebrae were adjusted to create displacements used to assess the translational and rotational accuracy.

#### ***4.2.1.1 Translational Accuracy***

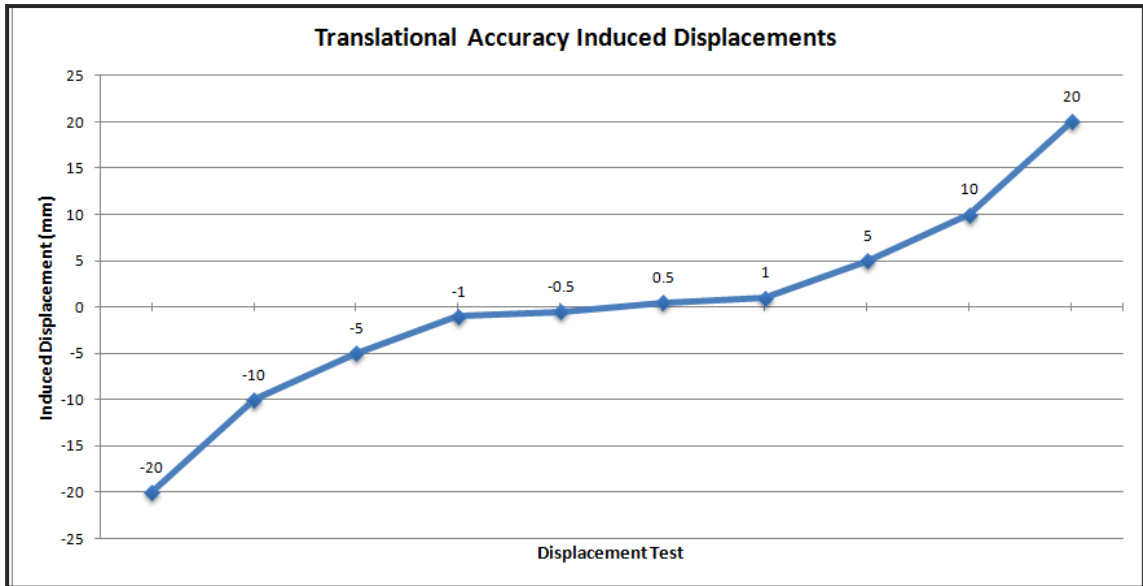
Studies conducted by Madanat et al (2005, 2007), Önsten et al (2001), Wilson (2007), and Laende et al (2009) used a Prediction Interval (PI) method to determine system accuracy from a range of implemented displacements [28], [34], [59–61]. Directional accuracies in these studies were determined to be half the width of the average PI. Prediction Intervals are a statistical method of estimating, within a set confidence, an interval in which future data points will fall.

The Prediction Interval method uses collected data to determine a range in which future values are expected with 95% confidence. The calculation is similar to Confidence Intervals (CI) except that a confidence interval estimates the distribution of a true population. The difference in the determination of the PI and the CI for a set of normally distributed data is graphically shown in Figure 4.6. The accuracy of an RSA system is determined for a direction by taking the  $\frac{1}{2}$  width of the average prediction interval for the assessed direction.



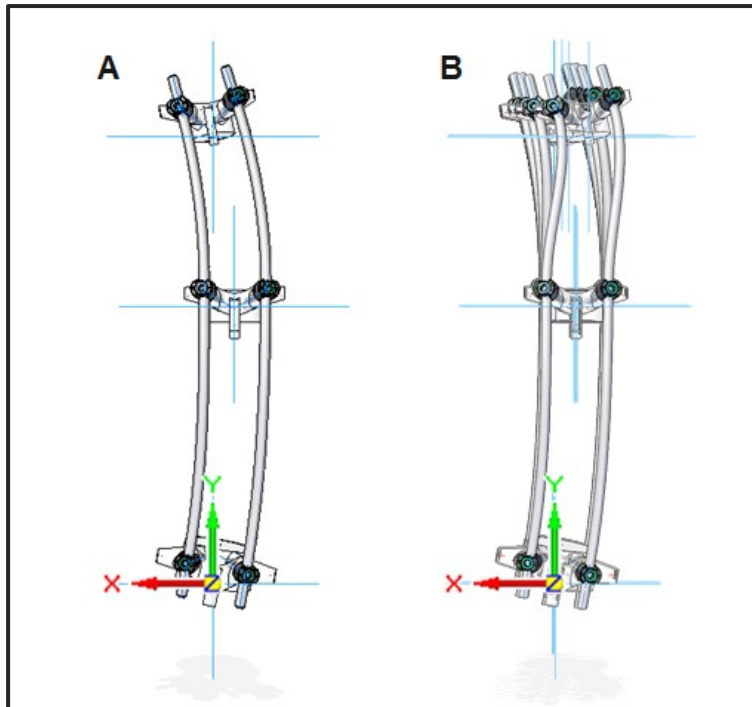
**Figure 4.6: Example showing the 95% Prediction Interval in blue versus 95% Confidence Interval in red. The dataset is a normally distributed set of random variables generated in Microsoft Excel 2007©.**

The translational displacements used to assess accuracy were selected to represent the range of movements found in failed fusions in several RSA studies. In a study of the cervical spine, Lee et al detected motions of 0.35 to 35mm while Johnsson et al observed motions of 0.4 to 10mm in a study focused on the lumbar spine [8], [9]. The protocol used for the assessment of the translational accuracies of the three origin styles is the use of ten displacements covering a range of -20 to 20mm along all three of the principal axes. Each direction was investigated independently from all other movements. Figure 4.7 shows a graphical representation of the implemented displacements.

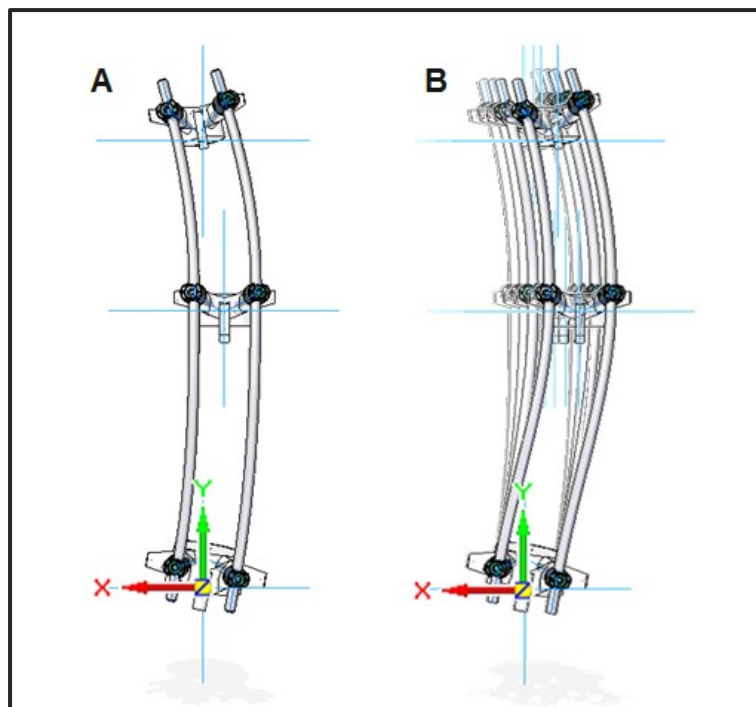


**Figure 4.7: Induced displacements used to assess system translational accuracy.**

To assess translational accuracy, failures of both the superior and inferior sections of the fusion were independently simulated. To simulate a failure in the superior section of the spine, the T4 vertebra was moved in relation to the rest of the spine, Figure 4.8. Simulating a failure in the inferior section of the spine, the T4 and T8 vertebrae were moved, as a solid unit, with respect to the L1 vertebra, Figure 4.9. The induced displacements used for the assessment of the accuracy displacement are summarized in Table 4.1. The repeated translational movements were induced in all three principal directions (X, Y, and Z) of the Spinal Coordinate System. Each migration was independently induced and was measured using the three developed RSA origin styles.



**Figure 4.8: Superior Fusion Failure Translational Accuracy Movement A) Reference Position. B) -X direction migration movements of the T4 vertebral model simulating a superior fusion failure. Migration range from 0.5mm to 20mm.**



**Figure 4.9: Inferior Fusion Failure Translational Accuracy Movement A) Reference Position. B) -X direction migration movements of the T4 and T8 vertebral models simulating an inferior fusion failure. Migration range from 0.5mm to 20mm**

**Table 4.1: Manipulations used to assess translational accuracy of one cardinal direction. Migrations are in relation to the Spinal Coordinate System.**

Migration Scene #	Superior Failure		Inferior Failure	
	T4 migration (mm)	T8 migration (mm)	T4 migration (mm)	T8 migration (mm)
1	20	0	20	20
2	10	0	10	10
3	5	0	5	5
4	1	0	1	1
5	0.5	0	0.5	0.5
6	-0.5	0	-0.5	-0.5
7	-1	0	-1	-1
8	-5	0	-5	-5
9	-10	0	-10	-10
10	-20	0	-20	-20

The thresholds used as the translational Limits of Clinical Significance 0.3, 0.5, and 0.7mm in the transverse (X), vertical (Y), or sagittal (Z) spinal axes, respectively as defined by Pape et al (2002) [1].

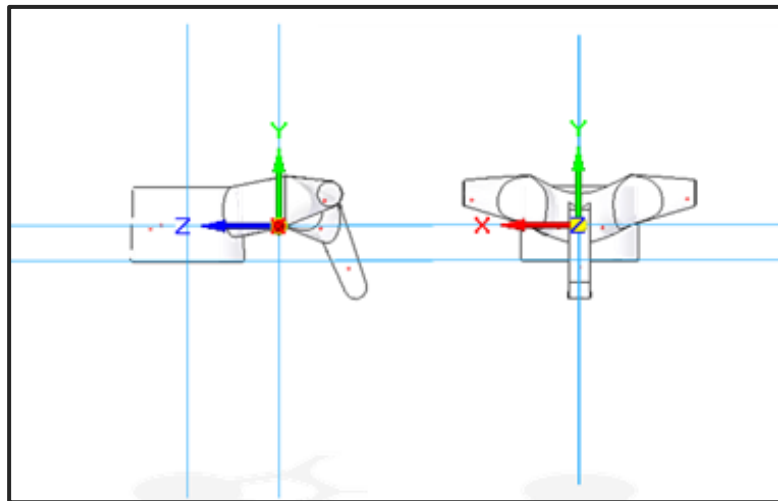
#### **4.2.1.2 Rotational Accuracy**

Rotational accuracy has not been assessed in many RSA studies performed on spinal fusions in the literature and as a result does not have a defined rotational accuracy testing protocol. Johnsson et al (2002) determined that the limit of clinical significance for rotational movements in the spine was 2.0°, 0.5°, and 0.9° about the transverse (X), vertical (Y), or sagittal (Z) spinal axes respectively [2]. Although not in the spine, Madanat et al (2005 and 2007) and Laende et al (2009) used the same PI protocol to assess the rotational accuracy as with the translational accuracy assessment protocol [59–61].

To simulate a rotational failure of the fusion, rotational displacements were induced in the T8 vertebra. The vertebra was rotated around the centroid of the marker



cluster, Figure 4.10. The centroid of the T8 marker cluster is located at the point  $\langle 0.14, 10.07, -25.21 \rangle$  mm in the T8 Vertebral Coordinate System. For a full definition of the rotational coordinate system see Appendix B. The use of the marker cluster centroid as the rotational origin limited the induced displacement to a purely rotational means, as opposed to a rotational and translational displacement pair found when rotating around the T8 Vertebral Coordinate System, whose origin was not located at the marker cluster centroid.

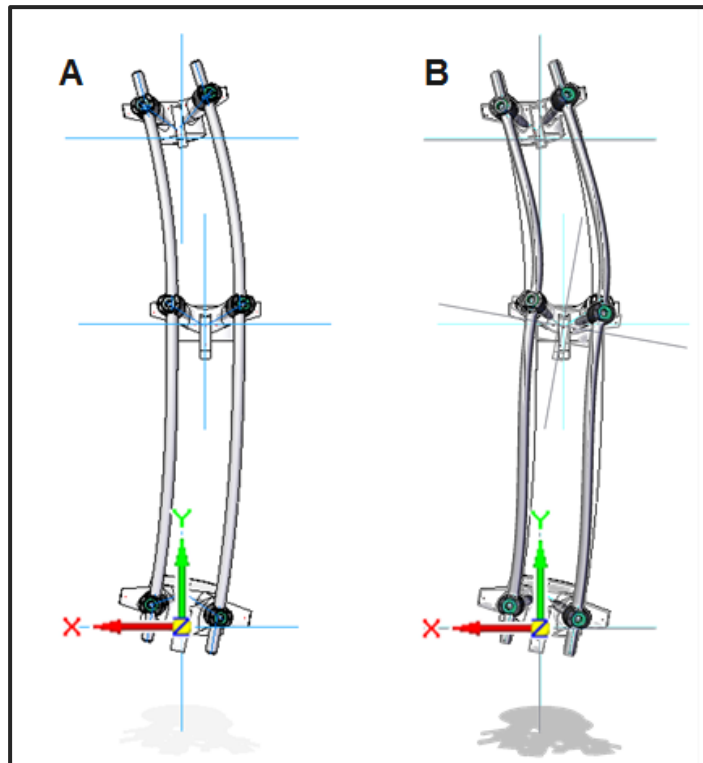


**Figure 4.10: Rotational origin of the T8 vertebra located at the centroid of the marker cluster.**

An example of a  $-10^\circ$  rotation around the Z axis is shown in Figure 4.11 with a summary of the eight displacements that were induced around all three principal axes shown in Table 4.2.

**Table 4.2: Rotations induced during rotational accuracy assessment.**

Migration Scene #	T8 Rotation (deg)
1	10
2	6
3	3
4	1
5	-1
6	-3
7	-6
8	-10



**Figure 4.11: Rotational Accuracy Movement A) Reference Position B) Movement of the T8 vertebral model simulating a 10° rotational failure about the Z axis.**

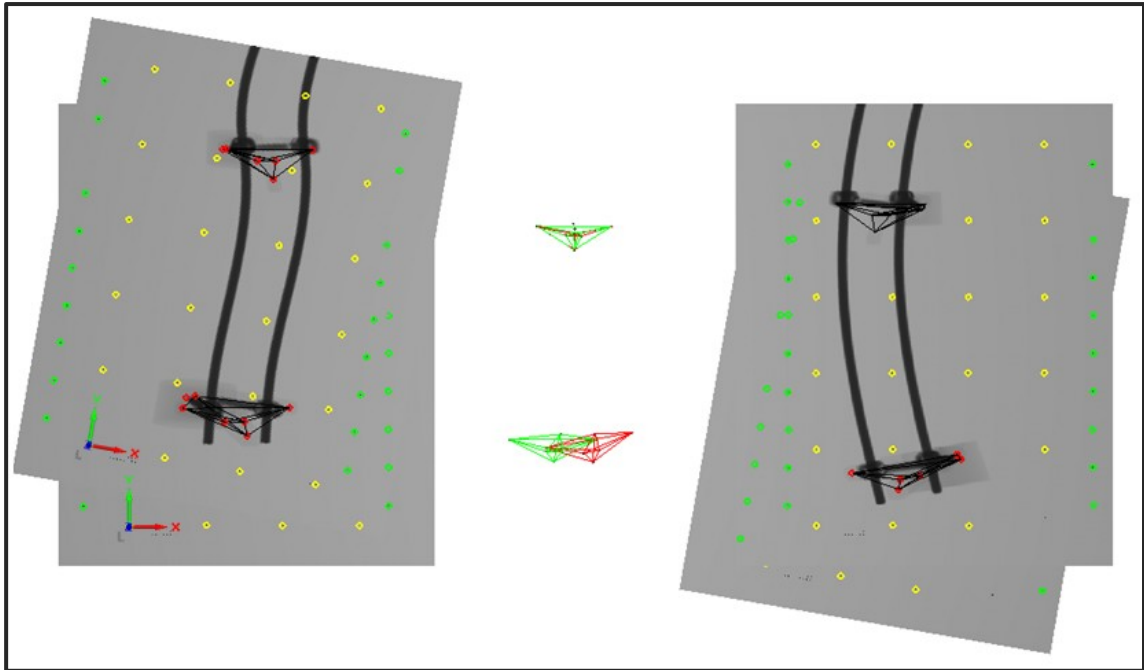
All rotations induced on the T8 vertebrae were conducted independently of one another. Only one rotation about one axis was completed in each case. This eliminated concerns over the order of rotations applied. If a combination rotation is applied to the vertebra, the order of rotation becomes significant, that is an X rotation followed by a Y rotation is different than a Y rotation followed by an X rotation. The measurement of this

rotational displacement also poses sources of error. The measurement of a series of combination rotations can produce a situation of crosstalk between the assessed rotational axes, which can impact the results if the measurement technique follows a different order of rotational assessment than was used to apply the rotations.

The choice to not conduct combination rotation was made to limit the sources of measurement errors and examine the best possible system rotational accuracy scenario.

#### *4.2.1.2.1 Apex Rotation Calculations*

Calculations conducted using the MB-RSA program produced erroneous translational migrations of the T4 and L1 vertebrae when assessing the rotational displacements of the T8 vertebrae using the Apex Origin Style. The MB-RSA software does not create local coordinate systems of the individual marker clusters but assesses all migrations by matching the migration scene with the reference scene and examining the migrations with respect to the global RSA environment. This means that the entire migrating scene was rotated to match the position of the T8 origin in the reference scene, producing a situation where both the T4 and L1 vertebrae have been moved. An example of this scene rotation is shown in Figure 4.12. Local coordinate systems can be created for manufactured implants, such as tibial components of artificial knees, but the process is impractical for patient specific, rigid body marker clusters implanted into the bone.



**Figure 4.12: Alignment of the Migration and Reference scenes in MB-RSA. Red marker clusters are the Reference Scene. Green marker clusters are the migration scene of  $10^\circ$  rotation of the T8 cluster about the Z-axis.**

To use a local coordinate system located at the T8 vertebra, post processing was required. A MatLab program, found in Appendix D Section D.2.3, was used to calculate the rotational displacements for the Apex Origin Style using a local coordinate system. For the T8 vertebral marker cluster, a local coordinate system was defined by the MatLab program. This program used the marker locations originally determined by the MB-RSA software. The core function used in this program was developed by E. Laende and has been reproduced with permission.

This sort of post processing will be required for all clinical RSA exams performed on the spine. The post processing was not necessary during this study because the migration origins were not rotated with the exception of the Apex Origin as discussed above.

#### **4.2.1.3 Accuracy Statistical Assessment**

Each of the simulated models for the translational and rotational fusion failures were used to create a RSA image pair using the image simulation process previously described. These “migrating scenes” for each origin style were compared to the corresponding “reference scene” to generate each data point assessed.

Each origin style, for both translation and rotation, was assessed for its absolute accuracy, confirming that it was measuring the induced displacements to within the acceptable Limits of Clinical Significance. This assessment was accomplished through the application of Bland-Altman (BA) plots. These plots allow for the visual evaluation of datasets, comparing the agreement between the measured values and those of the induced displacement. They were originally developed by Bland and Altman in 1986 and have achieved significant usage within the medical research community [4]. Each origin style was a unique “measurement technique” to compare with the known, induced displacement. Each data point, representing a unique accuracy migration, equate to a separate “patient” as described by the original Bland-Altman paper. This necessitates the use of three individual BA plots for the assessment of the accuracy of each direction (one for each origin style assessed).

Since the analysis contained a reference value for one of the measurement techniques, the expected outcome (the X-axis value of the BA plot) was not an average of the two measurement techniques but the true induced displacement value. The use of this technique over that of an average reference value was discussed by Krouwer et al (2008) [71].

For a measured dataset to agree with the true implemented values, the limits of agreement of the BA plots must fall within the Limits of Clinical Significance. The limits of agreement,  $LA$ , are defined by Equation 4.1, where  $SD$  is the standard deviation. The mean in this equation is in reference to the mean error of the measured dataset. The limits of agreement represent a 95% confidence limit around the mean.

$$LA = Mean \pm 1.96 \times SD \quad \text{Equation 4.1}$$

The results of the BA plots were assessed against the translational and rotational Limits of Clinical Significance as determined by Pape et al (2002) and Johnsson et al (2002) respectively [1], [2]. The Limits of Clinical Significance are summarized in Table 4.3. In graphical analysis, Limits of Clinical Significance have been abbreviated to LoCS.

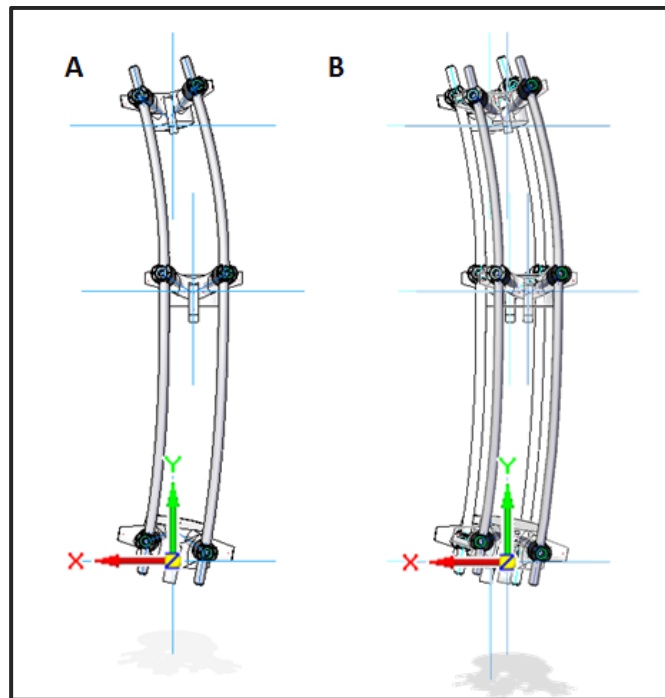
**Table 4.3: Translational and Rotational Limits of Clinical Significance from Pape et al (2002) and Johnsson et al (2002) [1], [2].**

	X	Y	Z
<b>Translational (mm) [1]</b>	0.3000	0.5000	0.7000
<b>Rotational (deg) [2]</b>	2.0000	0.5000	0.9000

## 4.2.2 Precision Assessment Methodology

The methods used to assess the precision of the three origin styles were similar to those used to assess simulation validity, Sections 3.2.5.2 and 3.2.5.3

To test the system precision of the three origin styles, the simulated phantom model was repositioned, as a unit, within the CAD environment with respect to the RSA Coordinate System defined by the calibration box. There was no intervertebral movement induced and as such any migration measured is erroneous and a measure of system precision. Models for all three origin styles underwent two sets of global movement. The first was that the spine model was translated 10mm in all six cardinal directions, an example of this is shown in Figure 4.13. The second movement was that the spine model was rotated  $\pm 10^\circ$  about all three principle global axes, shown in Figure 4.14. The manipulations used to assess system precision are summarized in Table 4.4.



**Figure 4.13: Translational Precision Movement. A) Reference Position, B) Global movement of the spine model -10mm along the X-axis**

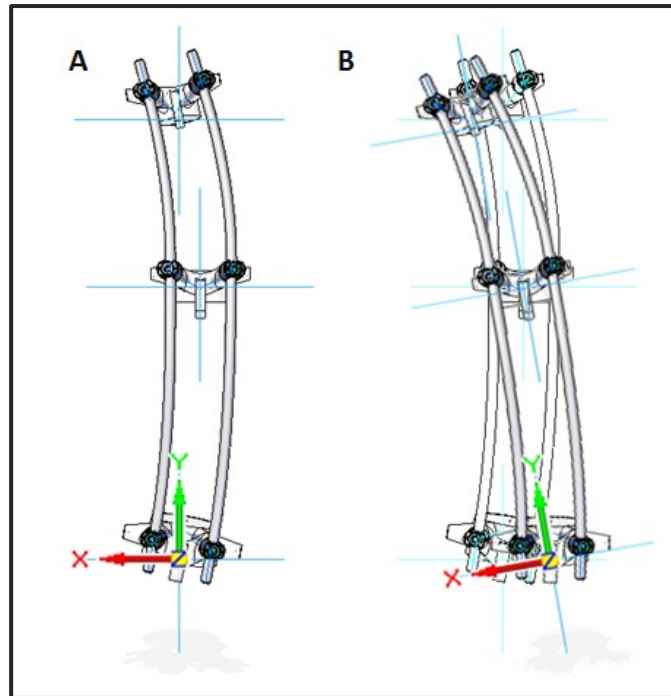


Figure 4.14: Rotational Precision Movement. A) Reference Position, B) Global movement of the spine model  $-10^\circ$  about the Z-axis.

Table 4.4: Global movements used to assess system precision. Each scene was assessed using the previous as the migration reference.

Scene #	Global Translation (mm)	Global Rotation (deg)
0	Reference	Reference
1	10 X	10 X
2	-10 X	-10 X
3	10 Y	10 Y
4	-10 Y	-10 Y
5	10 Z	10 Z
6	-10 Z	-10 Z
7	Reference	Reference

The rotational center for the precision assessment was a point adjacent to the T8 vertebra, half-way along the length of the curve. This point was not the origin of the T8 vertebra, but a point in line with the Y-axis of the spine model defined as  $\langle 0.0, 156.5, 0.0 \rangle$  mm in the Spinal Coordinate System. The full definition of this simulated model rotational coordinate system can be found in Appendix B. The position of the rotational



center was selected to centralize the rotation, keeping the spine centered in the available RSA imaging area.

When the exams were evaluated using the MB-RSA software, each model repositioning was assessed with respect to the previous position. Each repositioning of the phantom model acted as both a migrating scene with respect to the previous position and a reference scene with respect to the subsequent position.

Since there were no intervertebral displacements induced, any translational or rotational migrations calculated represent the error within the RSA system. This error is normally based on three main factors: the radiographic positioning and technique; the marker placement; and the migration calculation process, the latter of which is influenced by the origin style used. Since this is a computer simulated study, the radiographic positioning, technique and marker placement are constants, leaving only the migration calculation as the variable source of system error.

Statistical analysis and comparison of the precision of the three origin styles is identical to that used to assess the validity of the simulated RSA environment.

This statistical analysis once again uses the equation used by Madanat et al (2005) [60], reprinted as Equation 4.2, to assess system precision.

$$P = y \times SD \qquad \text{Equation 4.2}$$

where  $SD$  is the standard deviation of the migration dataset ( $\Delta X$ ,  $\Delta Y$ ,  $\Delta Z$ ,  $\Delta R_x$ ,  $\Delta R_y$ ,  $\Delta R_z$ ,  $\Delta MTPM$ ) and  $y$  is the 95% confidence interval. In this assessment only fourteen data points were created, so  $y$  is equal to 2.14 as defined from the critical values of a student t test with fourteen degrees of freedom at an  $\alpha$  of 0.05. Since precision is an

assessment of the error inherent in the RSA system and origin style, it should be as close to zero as possible.

#### ***4.2.2.1 Precision Statistical Assessment***

To compare the precisions of the three origin styles, an assessment of their variances was undertaken. Each of the seven migration datasets ( $\Delta X$ ,  $\Delta Y$ ,  $\Delta Z$ ,  $\Delta R_x$ ,  $\Delta R_y$ ,  $\Delta R_z$ ,  $\Delta MTPM$ ) for each origin style was tested for equal variance.

The method used to compare the variances is dependent on the distribution of the datasets. Again, the distributions of the datasets for all three origin styles were assessed using the Anderson-Darling test in Minitab 16. If one or more of the dataset groups were non-parametrically distributed then the Levene's test was used to compare the three variances. If all datasets were normally distributed, the Bartlett's test was used. In both tests a p-value above 0.05 indicated no statistical differences. If a significant difference was found, a second equal variance test was performed between the datasets of the Apex and Dual Origin Styles to determine if either of them was displaying a significant difference from the other.

## 4.3 Origin Style Assessment Results

### 4.3.1 Accuracy Assessment Results

For the assessment of the RSA system accuracy, migration was generated by comparing the simulated RSA exams of the Reference Scene and the various Migrating Scenes. This was done to assess both the translational and rotational accuracies.

#### 4.3.1.1 Translational Accuracy

To assess translational accuracy, failure of both the superior and inferior sections of the fusion was simulated with the T4 and T8 vertebrae moved in all principle directions with respect to the L1 vertebra. The data collected for each principle direction and for each origin style was separated into a superior and inferior set. The sets are defined in Table 4.5.

Table 4.5: Superior and inferior migration sets used in the three origin styles.

Origin Style	Superior Set		Inferior Set	
	Migrating Vertebra	Origin Vertebra	Migrating Vertebra	Origin Vertebra
Caudal	T4	L1	T8	L1
Apex	T4	T8	L1	T8
Dual	T8	T4	T8	L1

Data was not collected for migration sets that were not undergoing induced migration. For example, when using the Apex Origin Style, the superior dataset was not measured when an inferior fusion failure was simulated. The practice of not recording and assessing the non-migratory data was developed to avoid repeatedly assessing perfect zero movement data, which would skew results.

The migration data recorded for each principal direction was collected into a format as shown in Table 4.6. Due to the large quantity of data, it cannot all be included in the body of this report. All data analyzed for the creation of the conclusions of this thesis can be found in the appendices. The collected migration data for the accuracy assessment of the three origin styles is collected in Appendix E, Section E.3.

**Table 4.6: Migration data recorded for the Superior aspect of the Caudal Origin Style undergoing a simulated failure of the superior section of the spine. Simulated failure is in the X direction.**

Displacements	X (mm)	Y (mm)	Z (mm)	Rx (deg)	Ry (deg)	Rz (deg)	MTPM (mm)
<b>0.5</b>	0.4925	-0.0197	0.2016	0.0442	-0.0051	0.0182	0.5697
	-0.5210	0.0026	0.0480	0.0155	-0.0218	0.0281	0.5419
<b>1</b>	0.9803	-0.0005	0.1183	0.0448	-0.0086	0.0002	1.0094
	-1.0417	-0.0144	0.2770	0.0625	-0.0467	0.0355	1.1384
<b>5</b>	5.0276	-0.0056	0.0426	0.0525	0.0798	0.0184	5.1832
	-4.9921	0.0025	0.0303	0.0121	0.0061	-0.0015	4.9996
<b>10</b>	10.0019	0.0152	0.0845	0.0706	0.1133	0.0109	10.1155
	-9.9839	-0.0081	0.0990	0.0229	0.0275	0.0059	10.0120
<b>20</b>	20.0235	-0.0143	0.1165	0.0881	0.0472	0.0225	20.1579
	-20.0596	-0.0159	0.1554	0.0506	-0.0243	0.0323	20.0848

Prediction interval assessment was used to calculate the accuracy of the simulated RSA origin styles. All prediction intervals were calculated using Minitab 16. The accuracy of an RSA system is determined for a direction by taking the  $\frac{1}{2}$  width of the average prediction interval for the assessed direction. A calculation of the accuracy produced by the Caudal Origin Style for the X direction is shown in Table 4.7.

**Table 4.7: Accuracy in the X Direction calculated for the Caudal Origin Style. Error in the X direction is  $\pm 0.0444\text{mm}$ .**

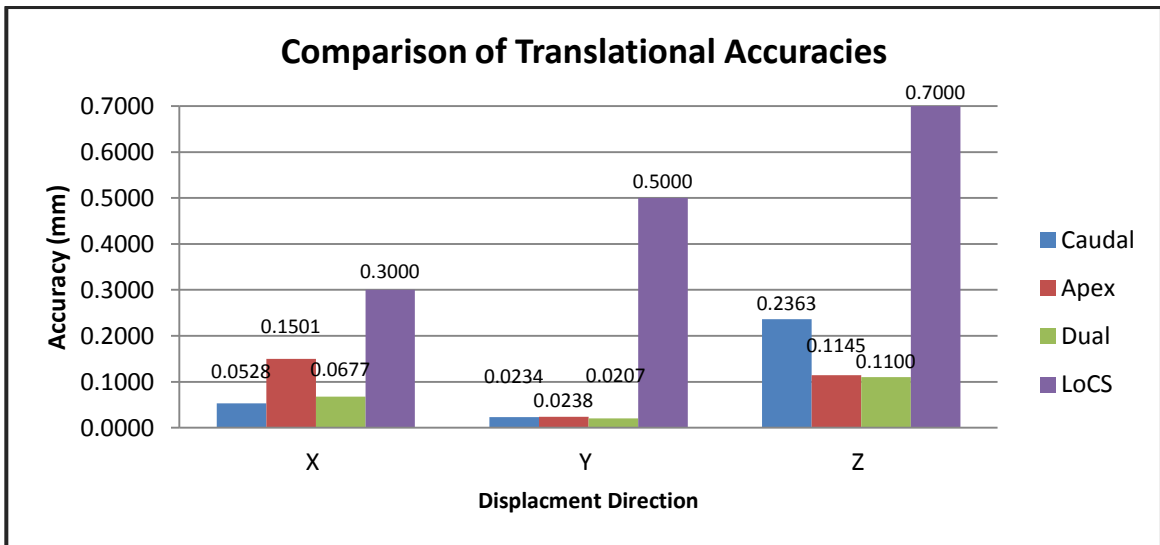
Failure Examined	Data		Prediction Interval				Accuracy
	Displacement (mm)	Measured (mm)	Lower Limit	Upper Limit	Width	Average Width (mm)	Half Width (mm)
Superior (T4)	0.5000	0.4925	0.4348	0.5522	0.1174	<b>0.1057</b>	<b>0.0528</b>
	-0.5000	-0.5210	-0.5667	-0.4493	0.1174		
	1.0000	0.9803	0.9356	1.0530	0.1174		
	-1.0000	-1.0417	-1.0675	-0.9501	0.1174		
	5.0000	5.0276	4.9412	5.0599	0.1187		
	-5.0000	-4.9921	-5.0744	-4.9557	0.1187		
	10.0000	10.0019	9.9472	10.0696	0.1224		
	-10.0000	-9.9839	-10.0841	-9.9617	0.1224		
	20.0000	20.0235	19.9560	20.0921	0.1362		
	-20.0000	-20.0596	-20.1066	-19.9705	0.1362		
Superior (T8)	0.5000	0.4814	0.4177	0.5298	0.1121		
	-0.5000	-0.5233	-0.5847	-0.4726	0.1121		
	1.0000	0.9771	0.9189	1.0310	0.1121		
	-1.0000	-1.0577	-1.0860	-0.9738	0.1121		
	5.0000	5.0022	4.9279	5.0412	0.1133		
	-5.0000	-5.0565	-5.0961	-4.9829	0.1133		
	10.0000	9.9811	9.9382	10.0550	0.1168		
	-10.0000	-10.0048	-10.1099	-9.9931	0.1168		
	20.0000	20.0214	19.9556	20.0856	0.1300		
	-20.0000	-20.0957	-20.1406	-20.0106	0.1300		
Inferior (T4)	0.5000	0.4884	0.4542	0.5288	0.0746		
	-0.5000	-0.5005	-0.5467	-0.4721	0.0746		
	1.0000	0.9909	0.9546	1.0292	0.0746		
	-1.0000	-1.0206	-1.0472	-0.9726	0.0746		
	5.0000	5.0040	4.9578	5.0331	0.0754		
	-5.0000	-5.0072	-5.0511	-4.9757	0.0754		
	10.0000	9.9829	9.9610	10.0387	0.0777		
	-10.0000	-9.9889	-10.0567	-9.9789	0.0777		
	20.0000	20.0094	19.9655	20.0519	0.0865		
	-20.0000	-20.0481	-20.0699	-19.9834	0.0865		

Using this prediction interval method, the data for each origin style was assessed for accuracy in the three translational degrees of freedom. The remainder of these calculations can be found in Appendix E, Section E.4. The results of the accuracy calculations are displayed in Table 4.8.

**Table 4.8: Translational accuracies of the three principle directions of the three origin styles compared to the Limits of Clinical Significance. Accuracies are in mm.**

Origin Style	Principle Direction		
	X	Y	Z
Limits of Clinical Significance	0.3000	0.5000	0.7000
Caudal Technique	0.0528	0.0234	0.2363
Apex Technique	0.1501	0.0238	0.1145
Dual Technique	0.0677	0.0207	0.1100

From Table 4.8 it can be seen that all calculated RSA system translational accuracies come in under the thresholds set by the Limits of Clinical Significance. Figure 4.15 displays a comparison of the three origin styles for each translational direction.



**Figure 4.15: Comparison of the translational accuracies of the three origin techniques compared to the Limits of Clinical Significance.**

#### **4.3.1.2 Rotational Accuracy**

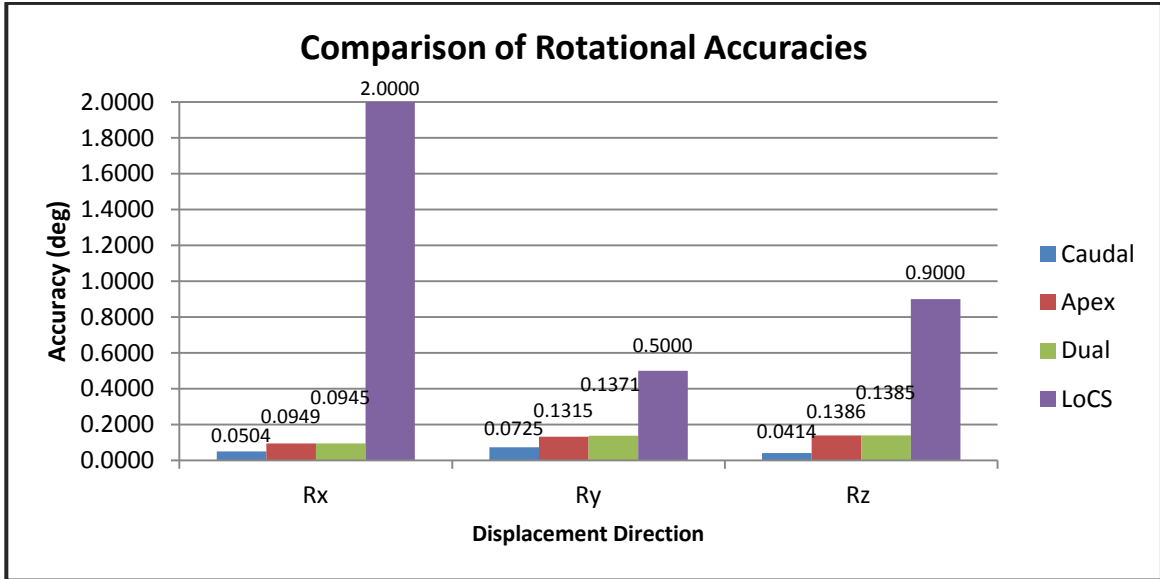
For the assessment of the rotational accuracy, the T8 vertebra was repeatedly rotated about the centroid of the T8 marker cluster, independently of the other vertebrae. The vertebra was rotated to various angles to garner a large enough population size to determine the accuracies of the various origin styles. Rotations were induced around all three principal axes. The rotational measurements were assessed in the identical manner to those of the translational accuracy assessments.

In the current clinical environment, variability of  $5^{\circ}$  has been defined as acceptable when measuring the deformity of the spine on standard bi-planar x-rays.[20] The use of RSA is expected to be more accurate than this current diagnostic tool, providing significantly improved diagnostic information. Johnsson et al have defined the Rotational Limits of Clinical Significance as  $2.0^{\circ}$ ,  $0.5^{\circ}$  and  $0.9^{\circ}$  about the transverse (X), vertical (Y), or sagittal (Z) spinal axes respectively.

To calculate the rotational accuracies for the three origin styles, prediction intervals were once again used. These calculations, found in Appendix E, Section E.4, resulted in the rotational accuracies presented in Table 4.9 with a graphical comparison on the three origin styles is shown in Figure 4.16.

**Table 4.9: Calculated rotational accuracies of the three origin styles. All accuracies are in degrees.**

Origin Style	Principle Direction		
	X	Y	Z
Limits of Clinical Significance	2.0000	0.5000	0.9000
Caudal Technique	0.0504	0.0725	0.0414
Apex Technique	0.0949	0.1315	0.1386
Dual Technique	0.0945	0.1371	0.1385



**Figure 4.16: Comparison of the rotational accuracies of the three origin techniques.**

The differences between the three origin styles for rotational accuracy assessment are negligible when compared to the Limits of Clinical Significance. Removing the overwhelming columns representing the Limits of Clinical Significance Figure 4.16 becomes Figure 4.17. Here it is still shown that the variance between the three origin styles is still minor.



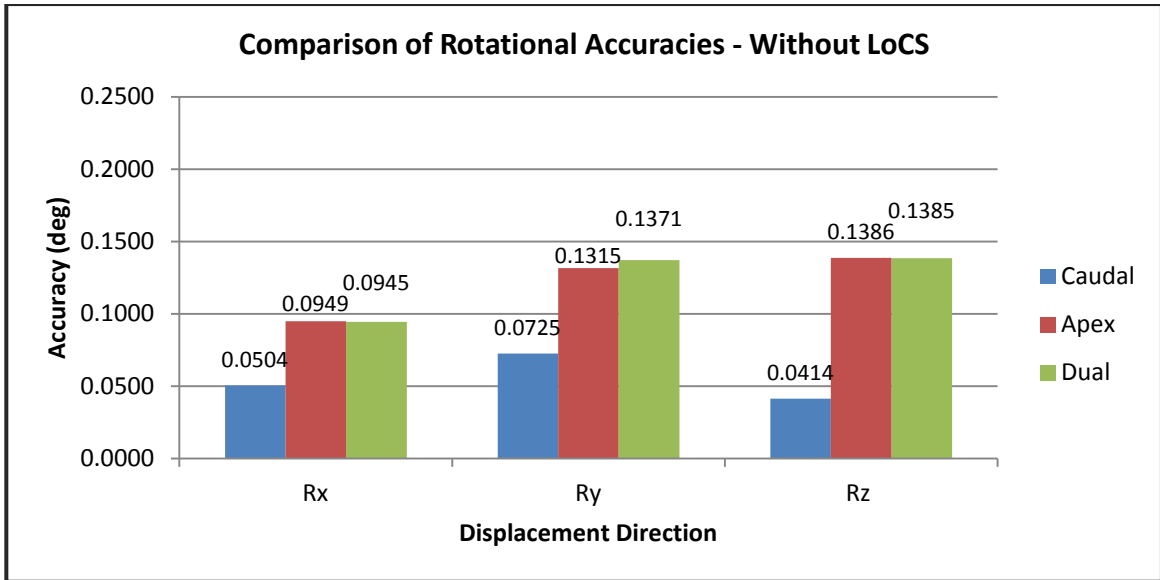


Figure 4.17: Comparison of the rotational accuracies of the three origin styles without the Limits of Clinical Significance indicators.

#### 4.3.1.3 Migrational Measurement Assessment

The measured movement was assessed to determine if the three origin styles were adequately registering the migrations induced in the simulated model. This was accomplished through the application of Bland-Altman (BA) plots. Due to the high number of BA plots analyzed, only a sample is provided here for assessment. All BA plots and their analysis can be found in Appendix F, Section F.2.

The following graphs, Figure 4.18, Figure 4.19, and Figure 4.20, are the BA plots created to examine the ability of the three origin styles to accurately measure the displacement induced within the simulated phantom model. The limits of agreement (ULA – Upper Limit of Agreement, LLA – Lower Limit of Agreement) are represented by the two red lines. All displacements in the three figures are in the X direction.

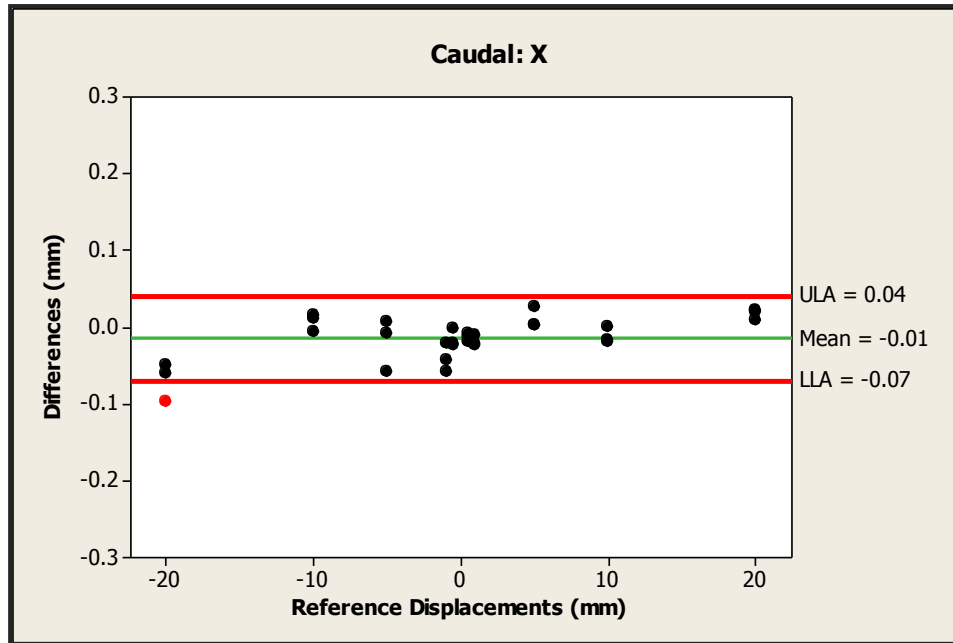


Figure 4.18: Bland-Altman plot showing the accuracy of the Caudal Origin Technique in the X direction. Green Line: Mean, -0.01. Red Lines: Upper and Lower Limits of Agreement, 0.04 and -0.07 respectively. These limits contain the limits of 95% of data. Black data points: Values falling within the limits of agreement. Red data point: Value falling outside the limit of agreement. Limits of Clinical Significance are shown as the maximum and minimum of the ordinate axis.

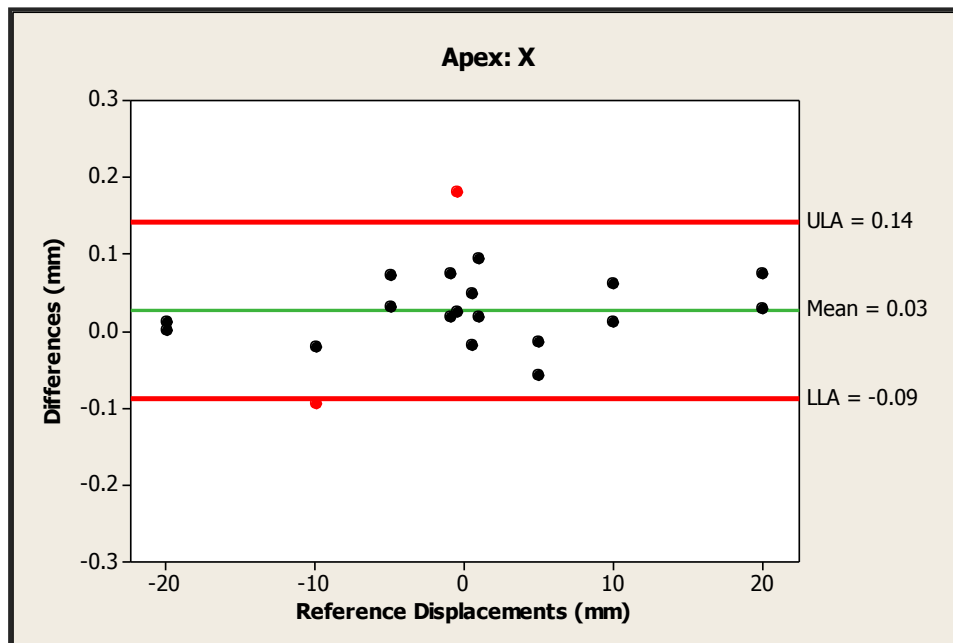
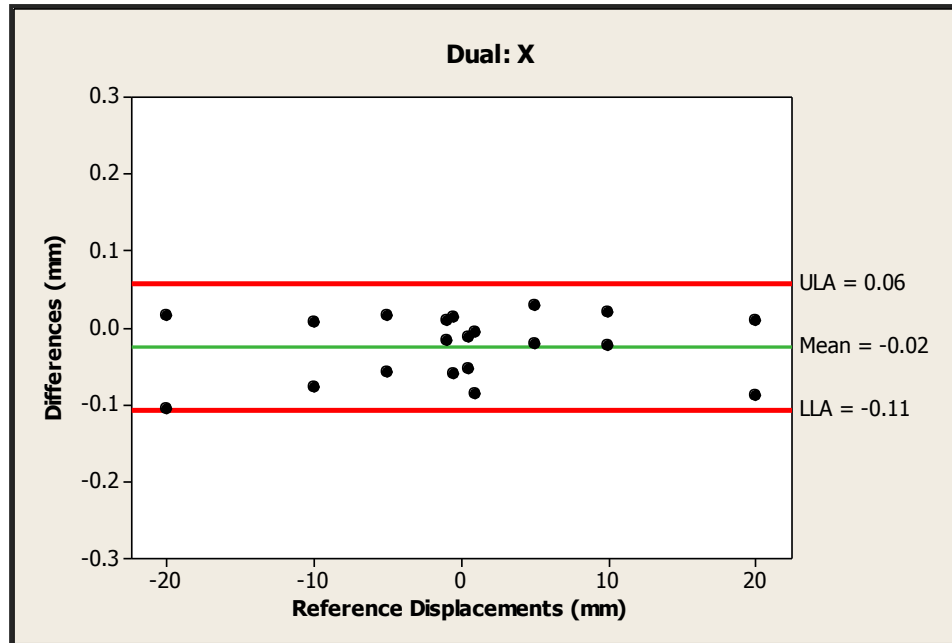


Figure 4.19: Bland-Altman plot showing the accuracy of the Apex Origin Technique in the X direction. Green Line: Mean, 0.03. Red Lines: Upper and Lower Limits of Agreement, 0.14 and -0.09 respectively. These limits contain the limits of 95% of data. Black data points: Values falling within the limits of agreement. Red data point: Value falling outside the limit of agreement. Limits of Clinical Significance are shown as the maximum and minimum of the ordinate axis.



**Figure 4.20: Bland-Altman plot showing the accuracy of the Dual Origin Technique in the X direction. Green Line: Mean, -0.02. Red Lines: Upper and Lower Limits of Agreement, 0.06 and -0.11 respectively. These limits contain the limits of 95% of data. Black data points: Values falling within the limits of agreement. Red data points: Value falling outside the limit of agreement. Limits of Clinical Significance are shown as the maximum and minimum of the ordinate axis.**

For a measurement to agree with the true value on a Bland-Altman plot, the limits of agreement must remain within the Limits of Clinical Significance [61]. For all BA plots presented in this thesis, the limits of the ordinate axis represent the Limits of Clinical Significance; in this sample case 0.300mm as determined by Pape et al (2002) [1]. Figure 4.18, Figure 4.19, and Figure 4.20 all show that each of the three origin styles adequately measured the displacement induced in the simulated model. Therefore there is no significant difference between the measured and true migration values. This is also true for both the Y and Z translational migration and all rotational accuracies. These results are shown in the compressed BA plots, Figure 4.21 and Figure 4.22. These compressed plots show only the Upper and Lower Limits of Agreement (ULA and LLA respectively) for agreement comparison purposes.

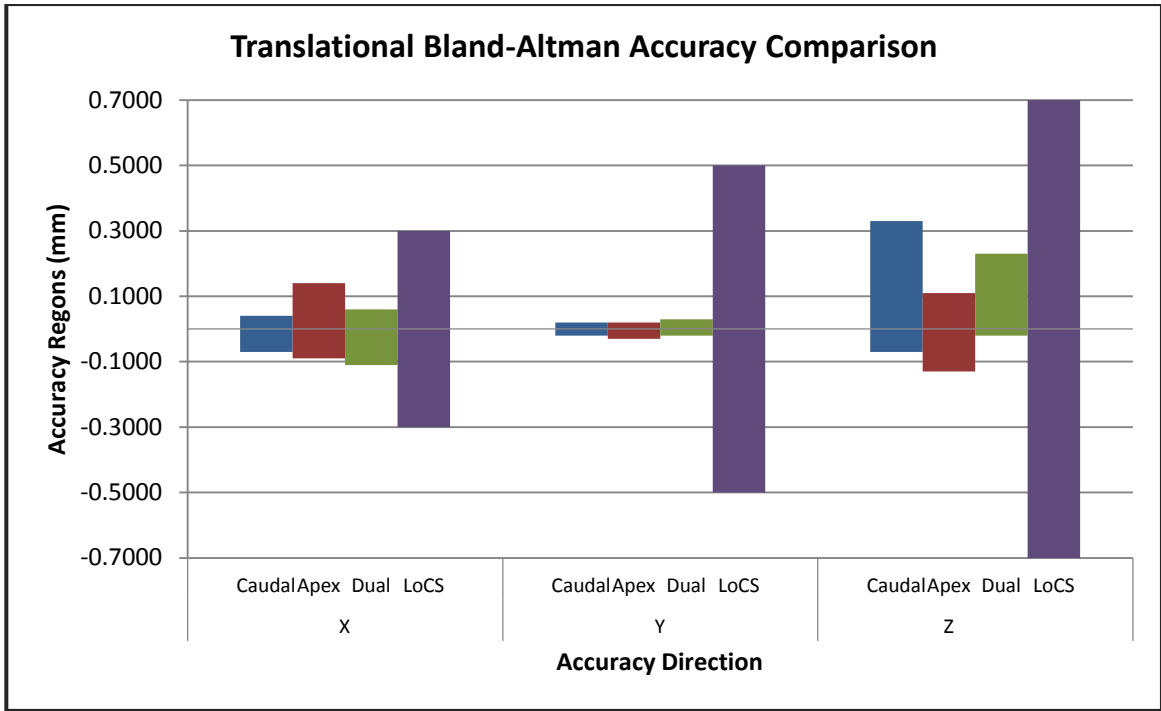


Figure 4.21: Comparison of the Translational Accuracy Bland-Altman plots Limits of Agreement.

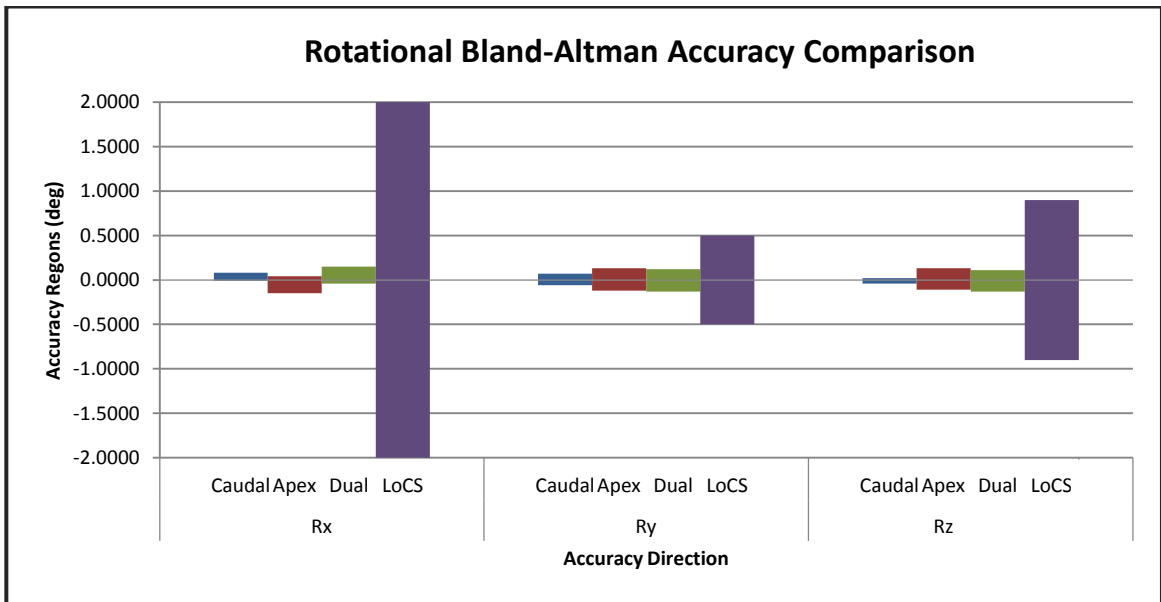


Figure 4.22: Comparison of the Rotational Accuracy Bland-Altman plots Limits of Agreement.

Figures showing the full BA plots with mean and ULA/LLA data are included in Appendix F, Section F.2.

None of the BA plots showed average errors of zero for the three origin styles. This represents a bias of these measurement techniques. The associated bias of the three origin styles are shown in Table 4.10.

**Table 4.10: Measurement Bias of the three origin styles.**

	X (mm)	Y (mm)	Z (mm)	Rx (deg)	Ry (deg)	Rz (deg)
<b>Caudal</b>	-0.0146	-0.0022	0.1289	0.0332	0.0031	-0.0120
<b>Apex</b>	0.0275	0.0027	-0.0095	-0.0537	0.0065	0.0110
<b>Dual</b>	-0.0241	0.0024	0.1024	0.0544	-0.0051	-0.0119

The significant portion of these biases correspond to minor errors which, when compared to their associated Limits of Clinical Significance do not pose a significant concern. As shown in Table 4.11, only two of the eighteen biases exhibit errors which are more than 10% of their Limit of Clinical Significance.

**Table 4.11: Bias Error Percentage of respective Limit of Clinical Significance**

	X (mm)	Y (mm)	Z (mm)	Rx (deg)	Ry (deg)	Rz (deg)
<b>Caudal</b>	-4.86%	-0.43%	18.42%	1.66%	0.62%	-1.33%
<b>Apex</b>	9.16%	0.54%	-1.36%	-2.69%	1.29%	1.23%
<b>Dual</b>	-8.02%	0.49%	14.62%	2.72%	-1.01%	-1.32%

Although these two cases exhibit large percentage bias errors, their respective limits of agreement are well within the 0.7mm Limit of Clinical Significance for the Z translational migration. All biases recorded in this study fall well within the acceptable limits for measurement error in a full fused spine section.

### 4.3.2 Precision Assessment Results

During the assessment of system precision, each Scene was compared to the previous Scene, resulting in the generation of seven samples for each of the two global displacement types, totalling fourteen data points used for the assessment of the precision of the RSA system. Two of the Z rotation precision exams for the Caudal Origin Style caused the L1 vertebra to be located outside of the available imaging area, excluding these exams from use in the caudal precision assessment. Therefore only twelve data points are used in the caudal precision assessment.

Each model was assessed for both superior and inferior precision. The superior precision aspect is a precision assessment of the migration analysis capturing the T4 vertebra. The inferior precision aspect is the precision assessment of the migration analysis capturing the L1 vertebra. The vertebrae compared in the assessment of the separate aspects for each origin technique is expressed in Table 4.12.

**Table 4.12: Migrating and origin vertebrae of the two aspects of precision for each origin style.**

Origin Style	Superior		Inferior	
	Migrating Vertebra	Origin Vertebra	Migrating Vertebra	Origin Vertebra
<b>Caudal</b>	T4	L1	T8	L1
<b>Apex</b>	T4	T8	L1	T8
<b>Dual</b>	T8	T4	T8	L1

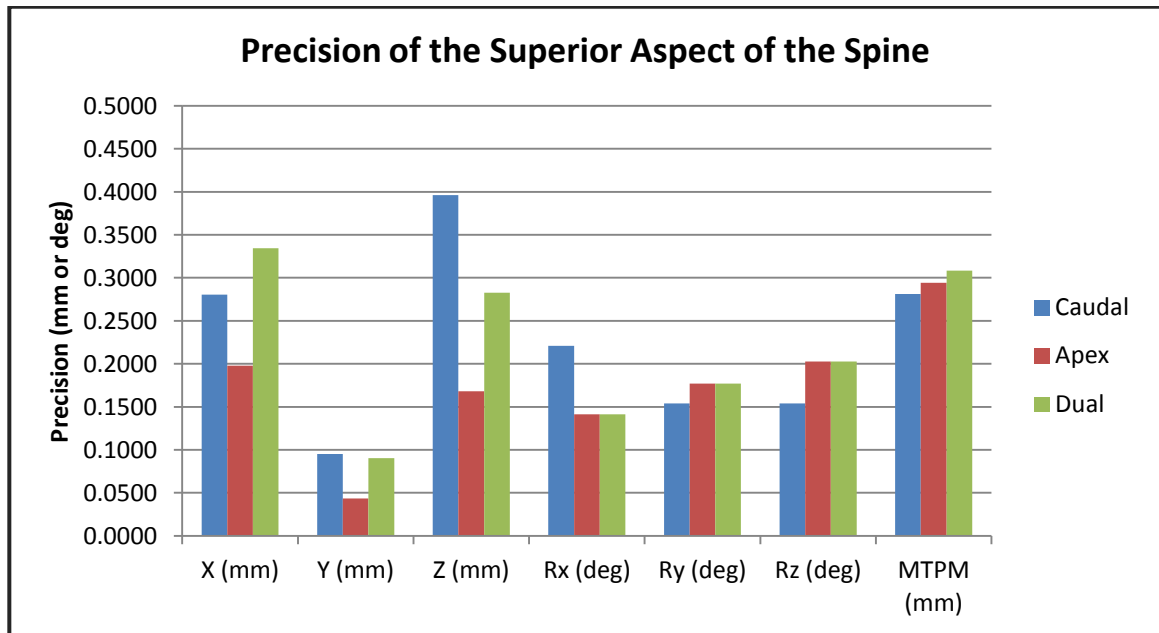
The unprocessed migration data for the fourteen precision exams can be found in Appendix E, Section E.5.

### 4.3.2.1 Precision Calculation

For a set of fourteen sample points, as collected in this project,  $y$  is equal to 2.14. For twelve data points, this value is increased to 2.18. For both spine section aspect and all three origin styles, precision was calculated for the translational and rotational migrations as well as for the Maximum Total Point Motion (MTPM). The calculation results for the superior aspect is shown in Table 4.13 and displayed graphically in Figure 4.23.

**Table 4.13: Precision data for the Superior Aspect.**

	X (mm)	Y (mm)	Z (mm)	Rx (deg)	Ry (deg)	Rz (deg)	MTPM (mm)
<b>Caudal</b>	0.2804	0.0950	0.3963	0.2208	0.1539	0.1539	0.2813
<b>Apex</b>	0.1979	0.0434	0.1681	0.1414	0.1770	0.2028	0.2944
<b>Dual</b>	0.3344	0.0905	0.2828	0.1414	0.1771	0.2027	0.3083



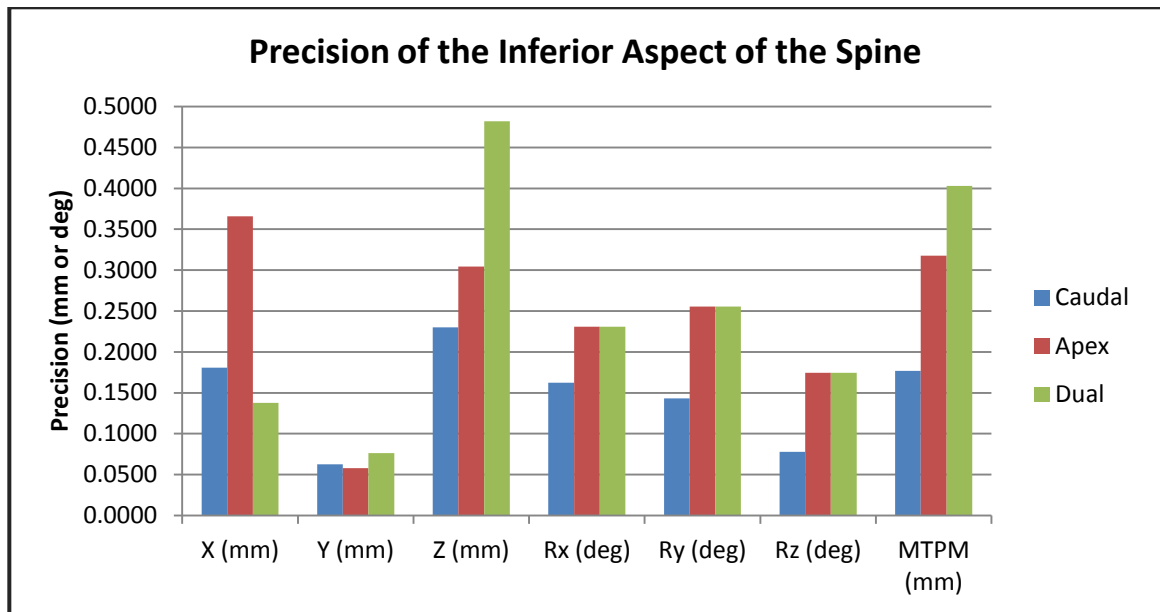
**Figure 4.23: Graphical display of the precision of the superior aspect of the three origin styles.**

For further assessment of the precisions of the superior aspect of the spine, variance comparisons were undertaken. The outcomes to these tests are laid out in Section 4.3.2.2.2.

The calculation results for the inferior aspect is shown in Table 4.14 and displayed graphically in Figure 4.24.

**Table 4.14: Precision Outcomes for the Inferior Aspect.**

	X (mm)	Y (mm)	Z (mm)	Rx (deg)	Ry (deg)	Rz (deg)	MTPM (mm)
<b>Caudal</b>	0.1807	0.0625	0.2300	0.1622	0.1430	0.0778	0.1767
<b>Apex</b>	0.3657	0.0577	0.3043	0.2307	0.2554	0.1744	0.3177
<b>Dual</b>	0.1378	0.0762	0.4819	0.2307	0.2554	0.1744	0.4029



**Figure 4.24: Graphical display of the precision of the inferior aspect for the three origin styles**

Results from the comparisons of directional variances are reported in Section 4.3.2.2.2.



### 4.3.2.2 Precision Comparison

For evaluation of the precision for the different origin styles, each direction was independently compared. Precision is a measure of the variance of the measurements and as such the comparisons of the precisions were done by assessing the variance present in the datasets. The first step to this process is the determining the distribution of the datasets.

#### 4.3.2.2.1 Dataset Distribution

Each of the forty-two datasets were analyzed using an Anderson-Darling test to check for a normal distribution with p-values greater than 0.050 indicating a normal distribution. Figure 4.25 shows an example of the results of a normally distributed dataset subjected to this test.

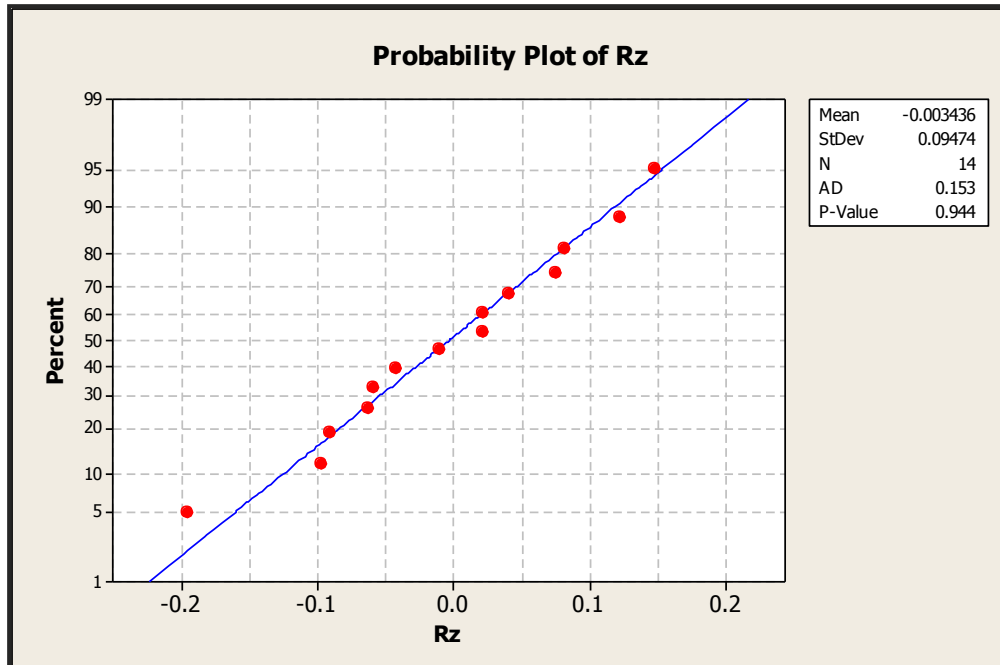


Figure 4.25: Probability Plot for the precision results of the superior aspect of the Apex Origin Style.  $p > 0.050$  indicates normal distribution.

Figure 4.26 shows an example of the results of a non-parametric distributed dataset subjected to the Anderson-Darling test.

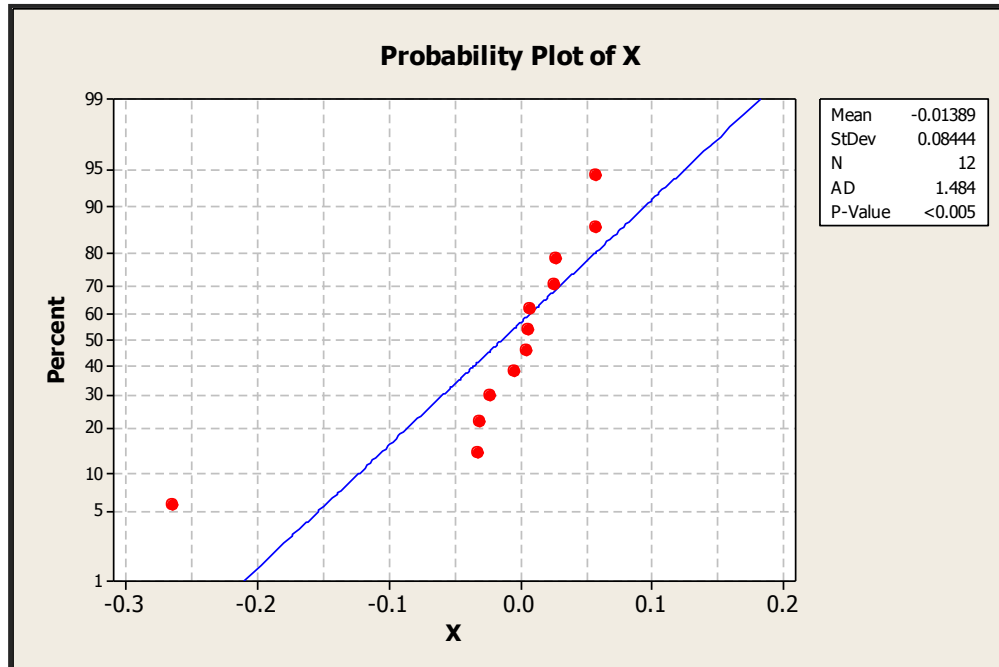


Figure 4.26: Probability Plot for the precision results of the inferior aspect of the Caudal Origin Style.  $p < 0.050$  indicates non-parametric distribution.

Due to the large number of probability plots, they could not be displayed here in the body of this thesis with the remainder of the plots located in Appendix F, Section F.3.1. A summary of the results of distribution assessment are displayed in Table 4.15 and Table 4.16.

**Table 4.15: Assessment of the normalcy of the superior precision datasets for each principal direction. p-value > 0.050 is an indicator of a normal distribution.**

Assessed Direction	Origin Style					
	Caudal		Apex		Dual	
	p-value	Distribution	p-value	Distribution	p-value	Distribution
<b>X</b>	0.014	Non-Parametric	0.589	Normal	0.932	Normal
<b>Y</b>	0.700	Normal	0.117	Normal	0.790	Normal
<b>Z</b>	0.906	Normal	0.486	Normal	0.772	Normal
<b>Rx</b>	0.332	Normal	0.596	Normal	0.602	Normal
<b>Ry</b>	0.027	Non-Parametric	0.785	Normal	0.778	Normal
<b>Rz</b>	0.483	Normal	0.944	Normal	0.944	Normal
<b>MTPM</b>	0.699	Normal	0.473	Normal	0.418	Normal

**Table 4.16: Assessment of the normalcy of the inferior precision datasets for each principal direction. p-value > 0.050 is an indicator of a normal distribution.**

Assessed Direction	Origin Style					
	Caudal		Apex		Dual	
	p-value	Distribution	p-value	Distribution	p-value	Distribution
<b>X</b>	<0.005	Non-Parametric	0.142	Normal	0.943	Normal
<b>Y</b>	0.367	Normal	0.430	Normal	0.014	Non-Parametric
<b>Z</b>	0.761	Normal	0.008	Non-Parametric	0.525	Normal
<b>Rx</b>	0.124	Normal	0.816	Normal	0.820	Normal
<b>Ry</b>	0.097	Normal	0.772	Normal	0.771	Normal
<b>Rz</b>	0.523	Normal	0.299	Normal	0.290	Normal
<b>MTPM</b>	0.278	Normal	<0.005	Non-Parametric	0.013	Normal

The necessity to determine whether a dataset is normally distributed or not is that distribution determines the statistical test required to compare the variances. For a set to be compared using parametric analysis, all three datasets must have normal distribution. In this case, the Bartlett test is utilized. If any or all the datasets are non-parametric, a Levene's test is used to assess the statistical differences.

#### 4.3.2.2.2 Variance Comparison

In order to statistically assess the differences between the three origin styles, an assessment of the variances of the precision data was assessed for each of the fourteen precision conditions. Figure 4.27 is an example of one of these variance tests.

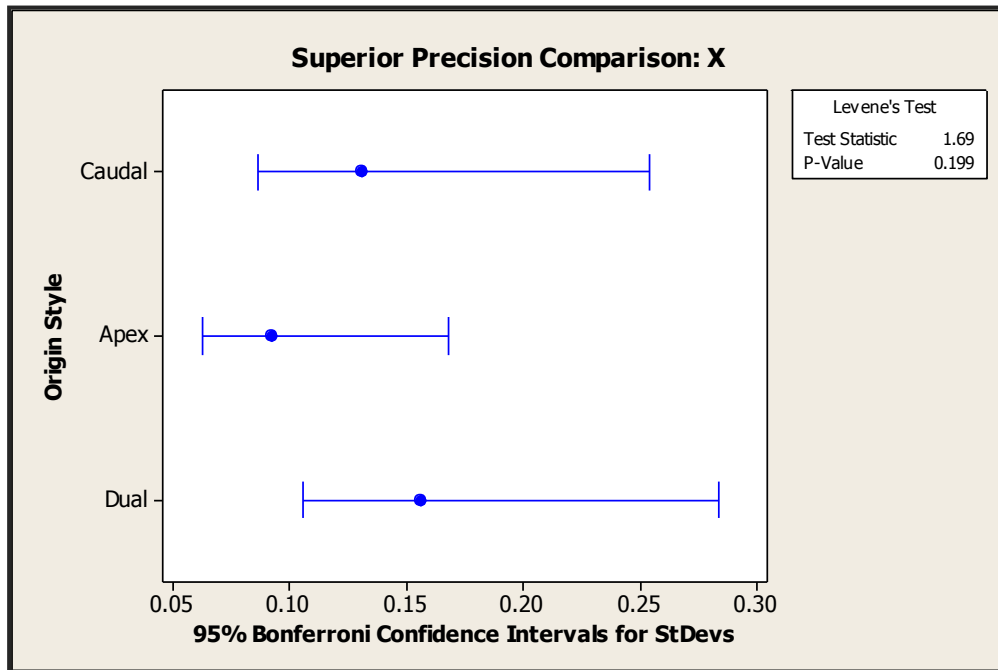


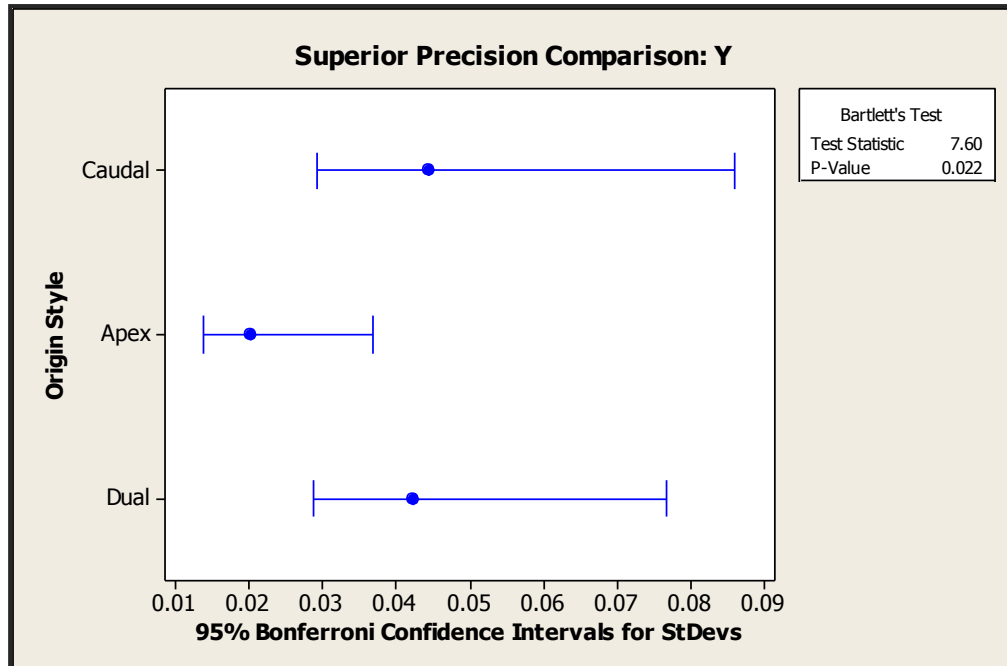
Figure 4.27: Example of one of the ten variance comparisons with no statistical difference. Not all datasets were normally distributed, so the Levene's Test is used. With a p-value of greater than 0.050, no significant statistical difference between the three methods was indicated.

In this plot of the precision variance for X direction of the superior aspect, not all data is normally distributed so the Levene's test was used. The reported p-value of the test is 0.199, above the 0.050 threshold showing that there are no statistical differences between the variances of all three origin styles. This is the standard outcome, occurring in ten of the fourteen conditions tested. A summary of the outcomes can be found in Table 4.17.

**Table 4.17: Summary of the statistical outcome of the precision comparison tests.**

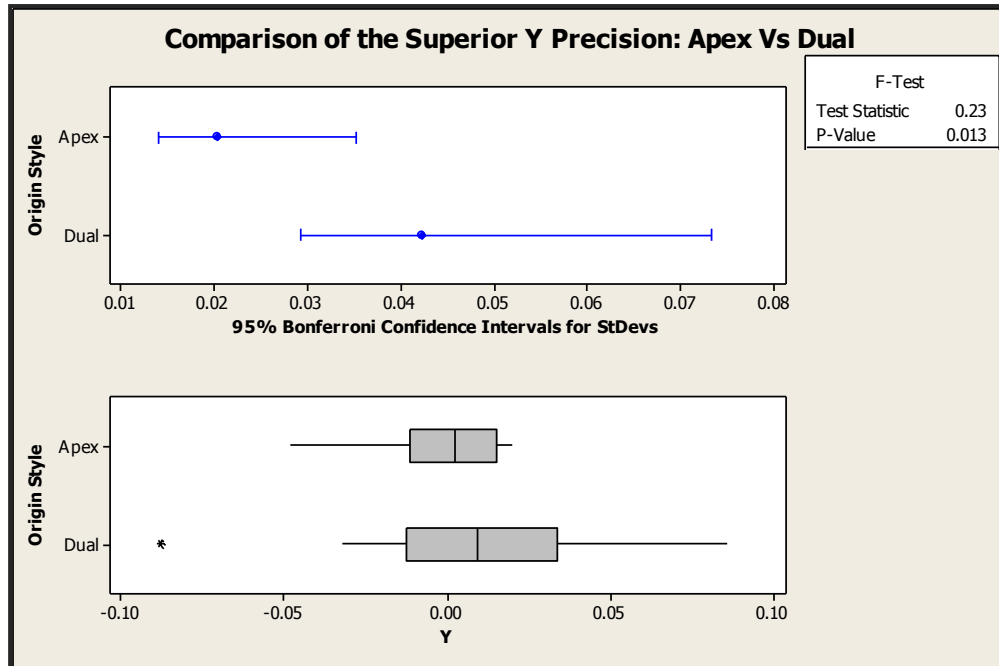
Assessed Direction	Superior Aspect			Inferior Aspect		
	Statistical Test	p-value	Statistical Difference	Statistical Test	p-value	Statistical Difference
<b>X</b>	Levene's	0.199	No	Levene's	0.005	Yes
<b>Y</b>	Bartlett's	0.022	Yes	Levene's	0.903	No
<b>Z</b>	Bartlett's	0.019	Yes	Levene's	0.168	No
<b>Rx</b>	Bartlett's	0.197	No	Bartlett's	0.248	No
<b>Ry</b>	Levene's	0.977	No	Bartlett's	0.001	Yes
<b>Rz</b>	Bartlett's	0.594	No	Bartlett's	0.291	No
<b>MTPM</b>	Bartlett's	0.953	No	Levene's	0.247	No

Four of the variance test conditions showed that there was a statistical difference between the three origin styles. Two conditions were all part of the superior aspect of the precision assessment, directions Y and Z, and two were part of the inferior aspect, directions X and Ry. The plots of these four conditions are shown in Figure 4.28, Figure 4.30, Figure 4.31, and Figure 4.33.



**Figure 4.28: Variance comparison showing statistical difference present in the Y direction for the superior aspect of the spine precision. All datasets were shown to be normally distributed; therefore the p-value reported by the Bartlett test was used. A value of 0.022 shows a significant difference in the variance between the caudal and dual origin precision datasets.**

The results shown in Figure 4.28 indicate that there is a difference between the Apex Origin Style and the other two. This difference is further explored in Figure 4.29, which examines the relationship solely between the Apex and Dual Origin Styles.



**Figure 4.29: Comparison of the Superior Y Precision of the Apex and Dual Origin Styles. Since both datasets are normally distributed, the F-test is used. This test indicates that there is a statistical difference between the Apex and Dual Origin Styles for the precision in the Y direction.**

This test shows that there is a statistical difference between the two origin styles with the Apex Origin Style demonstrating the least variance of the pair. There was no statistical difference between the Caudal and Dual Origin Styles.

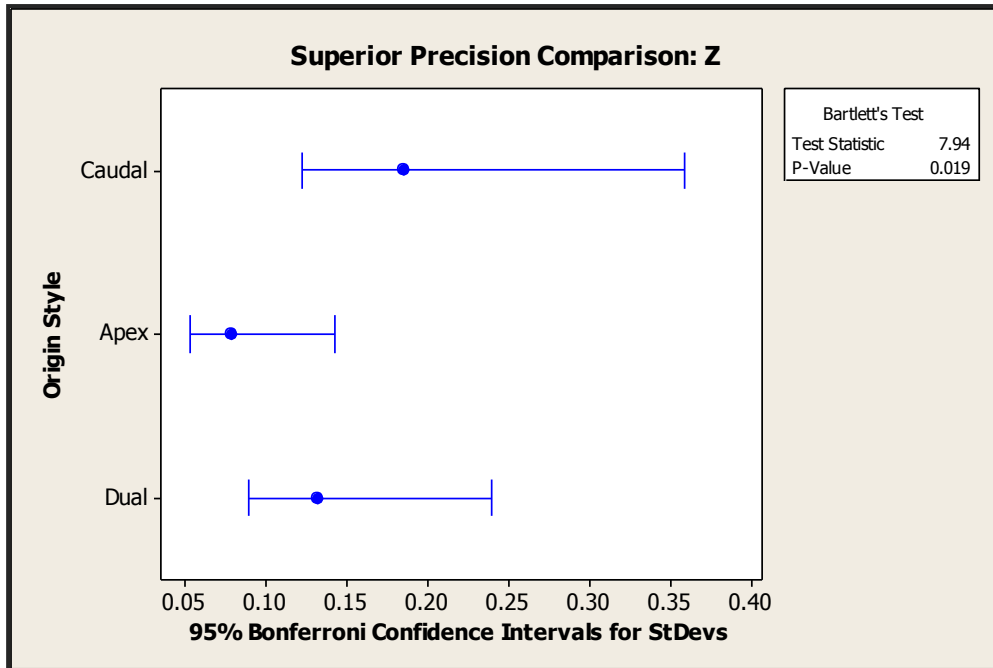
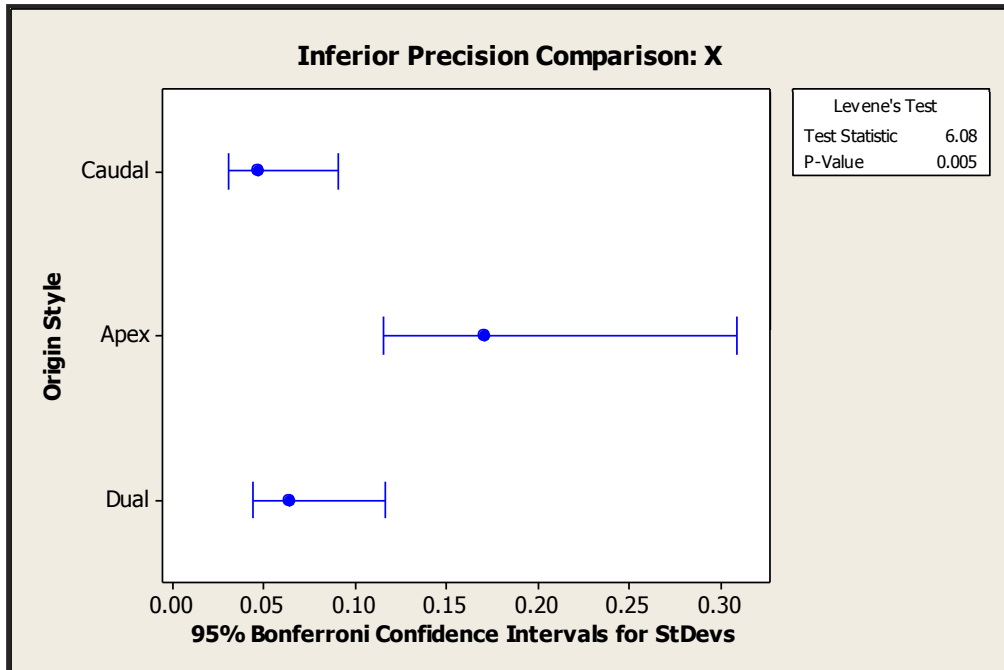


Figure 4.30: Variance comparison showing statistical difference present in the Z direction for the superior aspect of the spine precision. All datasets were shown to be normally distributed; therefore the Bartlett test reported p-value was used. A value of 0.019 shows a significant difference in the variance between datasets.

Figure 4.30 shows that there is a statistical difference between the Caudal and Apex Origin Styles in the Z direction of the superior aspect of the spine. However, further analysis did not demonstrate a statistical difference between the Apex and Dual Origin Styles.





**Figure 4.31: Variance comparison showing statistical difference present in the X direction for the superior aspect of the spine precision. All datasets were not normally distributed; therefore the Levene's test reported p-value was used. A value of 0.005 shows a significant difference in the variance between datasets.**

Figure 4.31 shows that there is a statistical difference between the three origin styles. Further analysis did demonstrate a difference between the Apex and Dual Origin Styles with the Dual Origin Style demonstrating less variance than the Apex counterpart, Figure 4.32.

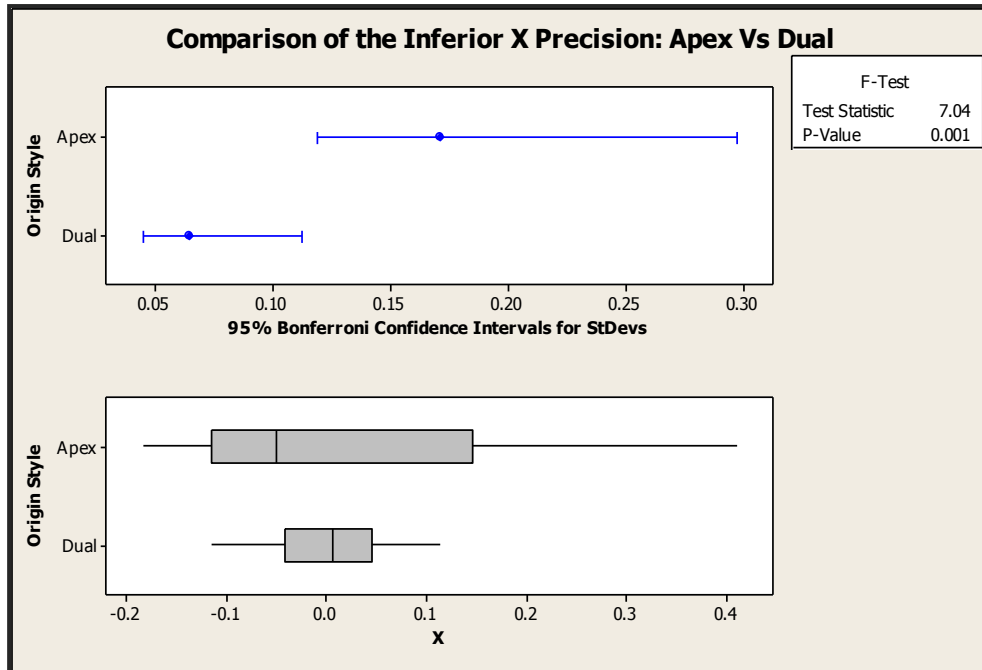


Figure 4.32: Comparison of the Inferior X Precision of the Apex and Dual Origin Styles. Since both datasets are normally distributed, the F-test was used. This test indicates that there was a statistical difference between the Apex and Dual Origin Styles for the precision in the Y direction.

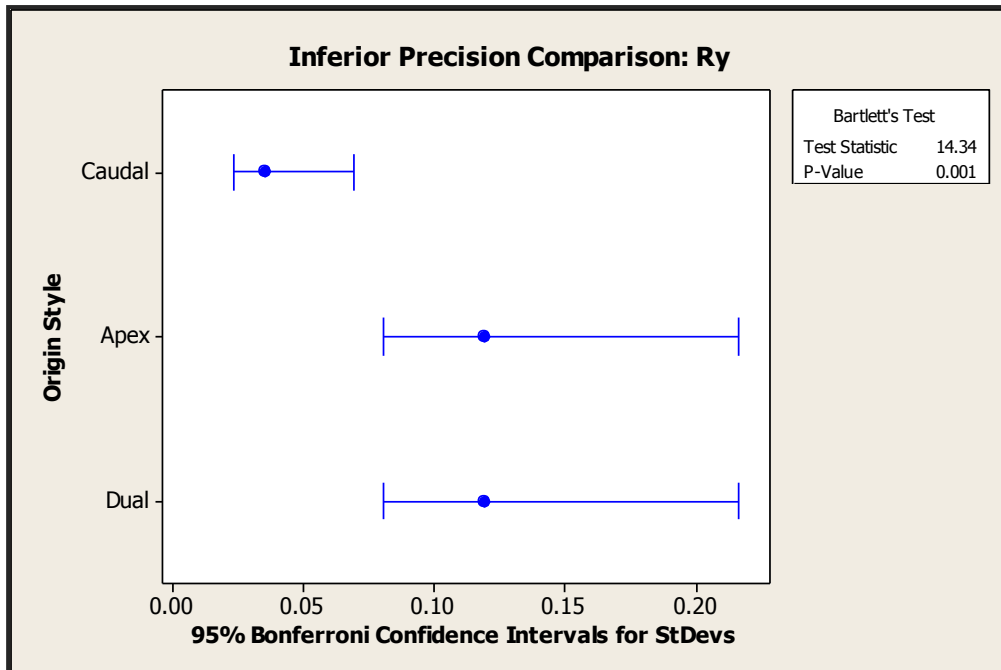
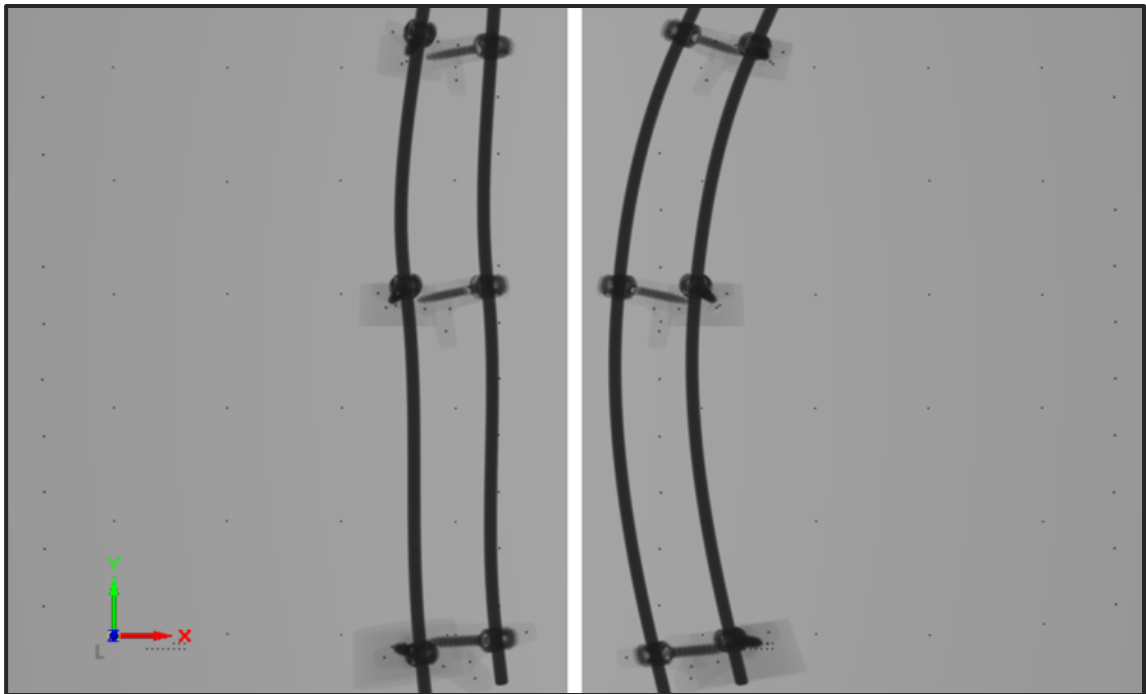


Figure 4.33: Variance comparison showing statistical difference present in the Ry direction for the superior aspect of the spine precision. All datasets were shown to be normally distributed; therefore the Bartlett test reported p-value was used. A value of 0.004 shows a significant difference in the variance between datasets.

Figure 4.33 shows that there is a statistical difference between the Caudal Origin Style and novel origin styles. Further analysis demonstrated no difference between the Apex and Dual Origin Styles. In fact, there were no differences between the variances of the Apex and Dual Origin Styles with respect to any of their rotational precisions. All additional variance comparison graphs can be found in Appendix F, Section F.3.2.

## 4.4 Origin Style Assessment Discussion

This thesis objective set out to examine the impact of RSA origin style on the accuracy and precision associated with the assessment of success of spinal fusions performed for the treatment of Adolescent Idiopathic Scoliosis. The three origin styles examined were the established Caudal Origin Style and two new origin styles: the Apex Origin Style and the Dual Origin Style. Due to physical constraints at the Halifax Infirmary RSA suite the use of the Caudal Origin Style cannot be carried into clinical usage due to the limited imaging area, Figure 4.34. The phantom model, even when optimally placed, barely fits within the imaging area.



**Figure 4.34: X-ray images comprising the reference exam for the Caudal Origin Style. As shown the length of the image barely contains the phantom model length.**

The new origin styles remove the size limitation by using two exams in conjunction to capture intervertebral migration. Both new origin styles use the same image sets, an example of which can be seen in Figure 4.35. For this phantom model the

common vertebra found in both image pairs is the T8 vertebra located at the apex of the simulated scoliotic curve.

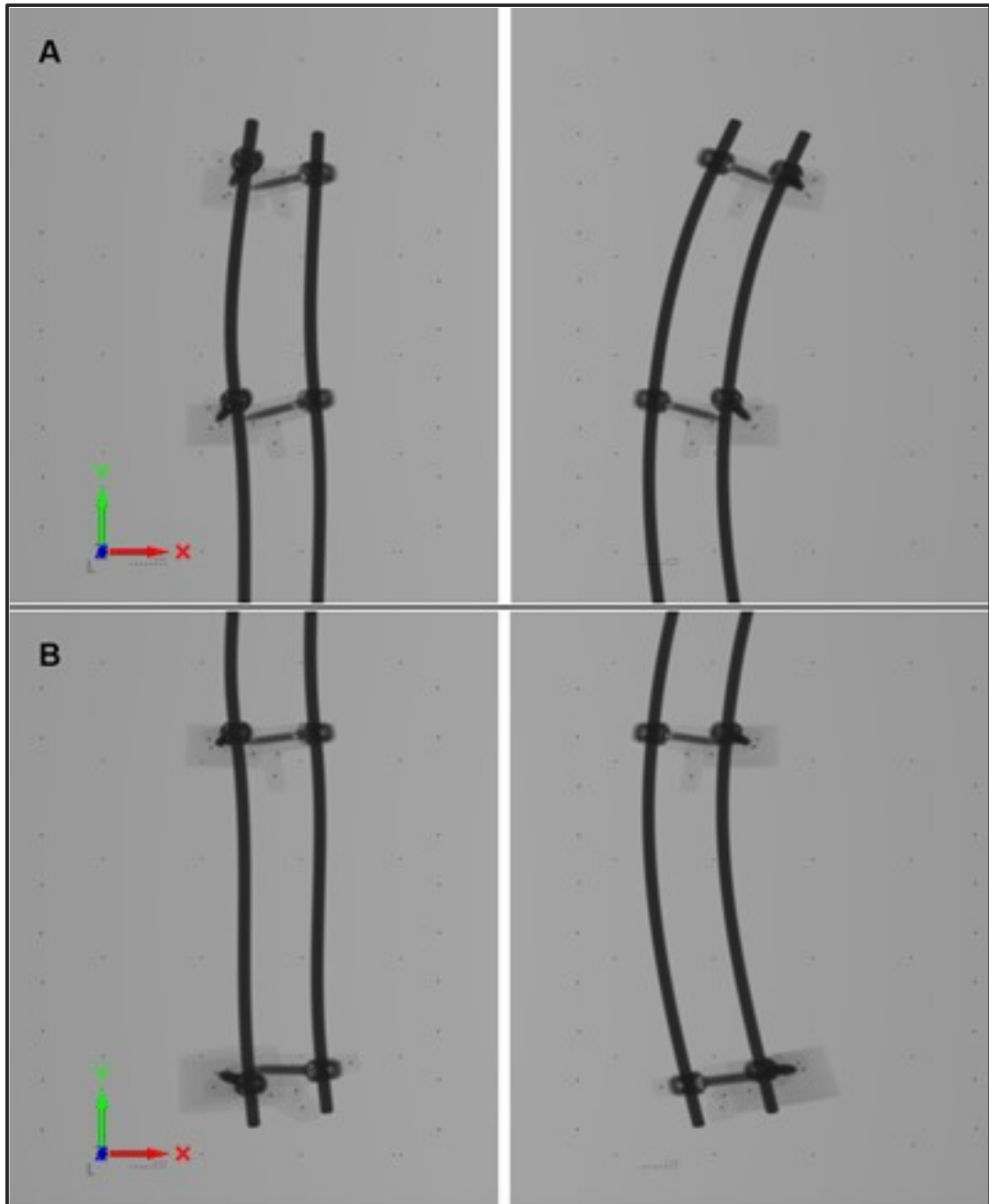
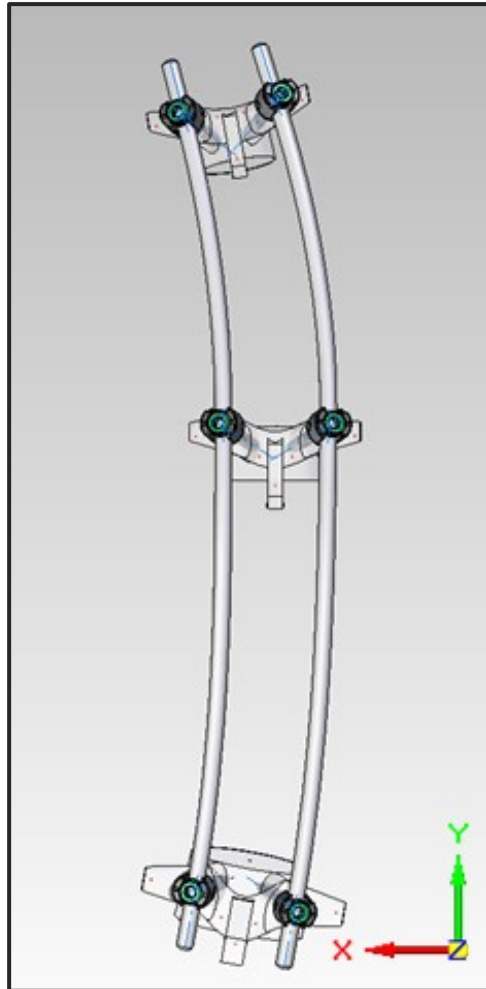


Figure 4.35: X-ray image sets comprising the reference exams for the Apex and Dual Origin Styles. A) Image pair of the superior section of the spine containing the T4 and T8 vertebrae. B) Image pair of the inferior section of the spine containing the T8 and L1 vertebrae.

The assessment of the impact of origin style was accomplished by analyzing the results of simulated RSA exams performed on a computer simulated phantom model of a right thoracic curve surgically corrected to 20°. Figure 4.36 shows the fully assembled computer simulation of the spine.



**Figure 4.36: A posterior-anterior view of the simulated spine assembly showing the residual 20° right main thoracic curve.**

#### 4.4.1 Origin Style Assessment

Traditionally, migration assessment has been performed using a Caudal Origin Technique where the vertebra at the inferior end of the curve is used as the migration origin. This technique was not feasible at our institution, requiring the need for alternate origin techniques. The new techniques introduced were the Apex and Dual Origin Styles. With the Apex Origin Style, the apex vertebra of the scoliotic curve was used as migration origin. In the Dual Origin Style the superior and inferior vertebrae are used as a pair of migration origins. A summary of the three origin styles can be seen in Figure 4.37.

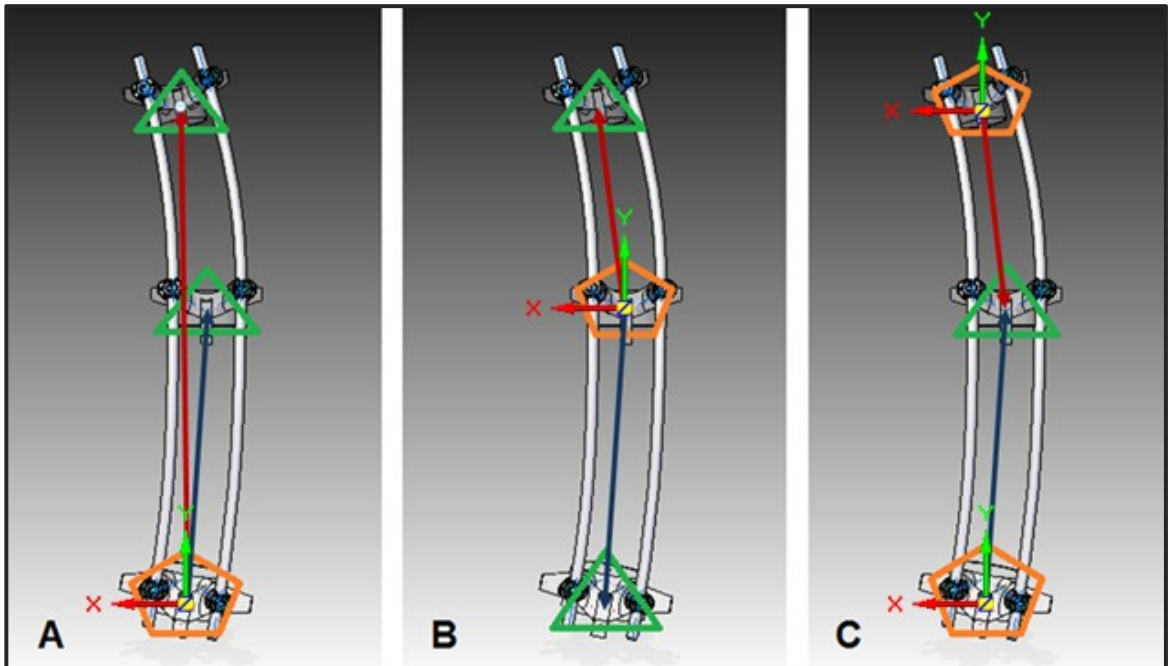


Figure 4.37: Comparison of the three examined origin styles where the pentagons indicate the migration origin vertebrae and triangles the migrating vertebrae. A) Caudal Origin Style. B) Apex Origin Style. C) Dual Origin Style.

#### **4.4.1.1 Translational Accuracy**

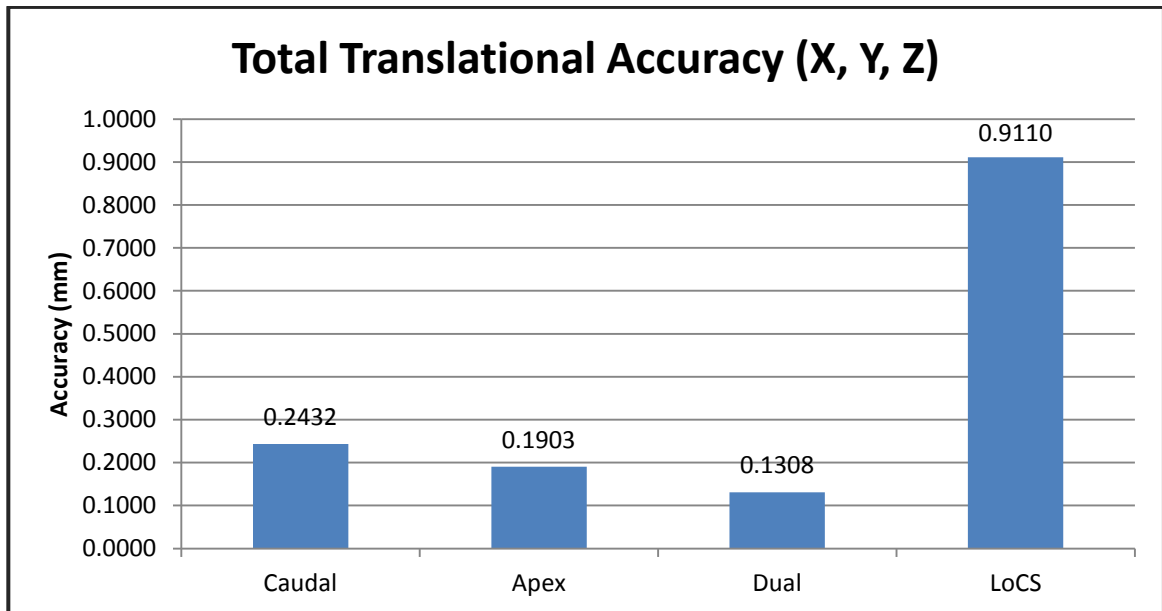
The system accuracy for all six degrees of freedom was assessed with very promising results, shown in Table 4.8 for translational and Table 4.9 for rotational accuracies. All origin styles, in all directions, demonstrated high accuracies, measuring the induced displacements within the Limits of Clinical Significance. Although the origin styles all fell within the Limits of Clinical Significance, the more accurate the system, the higher its diagnostic value will be.

There is no significant difference between the three origin styles with respect to the measurement of true translational migration. Both the Apex and Dual Origin Styles consistently maintain high accuracies in all three cardinal directions. Neither of the two novel origin styles have any directional accuracy worse than 0.1750mm. The Caudal Origin Style, while maintaining the required accuracy below the level of clinical significance, does not perform as well as the new styles with respect to the Z migrational accuracy. In all three origin styles the Z translational accuracy produced the highest results. This is due to the out of plane nature of the measurement. Off-planer RSA systems consistently produce lower accuracies in the out of plane direction. As this is a known limitation patient orientation can be adjusted so that the direction requiring the least accuracy is aligned so that it is out of the image plane. In the case of spinal fusion this direction is along the patient's PA axis.

Figure 4.38 shows an assessment of the total translational accuracy for the three origin styles. This data was created by a vector addition of the X, Y, and Z directional accuracies produced by the origin styles. The Apex and Dual Origin Styles both show improvement over the conventional Caudal Origin Style. The accuracy improvement is



ultimately dwarfed by the accuracy level of all origin styles compared to the total limit of clinical significance.



**Figure 4.38: Vector addition of the translational accuracies for the three origin styles compared with the total vector for the translational Limits of Clinical Significance.**

The improvement in translational accuracy is mostly due to the fact that the Z displacement accuracy in the Caudal Origin Style is worse than displayed in the other two origin styles. This discrepancy is due to the large distance between the migration origin located at the L1 and the T4 vertebra and when measuring the displacement of the T4 vertebra. When the origin to migration vertebra distance is lessened, using the T8 vertebra as a means to measure displacement in the superior section of the spine (as with the Apex and Dual Origin Styles), the accuracy of the measurement improves. This improvement is an example of the change in the factors that influence the misalignment error.

#### **4.4.1.2 Rotational Accuracy**

The use of standard bi-planar x-rays are subject to a  $5^{\circ}$  variability in the assessment of vertebral rotation [20]. The assessment of the rotational accuracies of the three origin styles found over tenfold improvement over the current clinically available diagnostic information.

The Caudal Origin Style demonstrates consistently higher rotational accuracies than the Apex or Dual Origin Styles. The cause for this increased rotational accuracy is unknown but due to the extremely high rotational accuracies recorded for all three origin styles the variations between rotational accuracies are not significant. All origin styles are more than adequate at measuring rotational displacement, producing accuracies under  $0.2000^{\circ}$ .

Interestingly the limits of agreement for the rotational accuracies of the Apex and Dual Origin Style are the inverse of one another. For example, in the rotational X direction, the Apex Upper Limit of Agreement is  $0.04^{\circ}$  while the Lower Limit of Agreement is  $-0.15^{\circ}$  with a mean of  $-0.05^{\circ}$ . The Dual Origin Style on the other hand shows a ULA of  $0.15^{\circ}$ , an LLA of  $-0.04^{\circ}$  and a mean of  $0.05^{\circ}$ . This inverse of the BA plots is due to the negative correlation in the measurements. A positive rotation measured using the Apex Origin Style is measured as a negative rotation in the using the Dual Origin style. This is due to the opposite nature of the origin-migration vertebrae for each measurement. Since the graphs are identically inverted this is a good indicator of the repeatability of the measurement. The errors recorded from both measurement directions are not different enough to change the results of the BA plots.

The differences between the accuracies of the three origin styles in their assessment of rotational migration are inconsequential compared to the associated Limits of Clinical Significance. The choice of any origin style would suitably provide rotational measurements of the vertebral rotation.

#### **4.4.1.3 Precision**

The results of the precision assessment show that RSA precision underperforms other RSA precisions reported in the literature [26], [30], [34], [60], [63]. The precision results can be found in Table 4.13 for the superior aspect and Table 4.14 for the inferior aspect, both of which are found in Section 4.3.2.1. This decrease in system precision is due to the relationship of the misalignment error and the large vector lengths used in the calculation of migration within the spinal fusion [27]. Other RSA studies of spinal fusions have focused on measuring migration in single level fusions or arthroplasty implant migration [1], [32], [37], [43], [46], [47], [49], [60]. In these cases the vector lengths between the migratory and origin components were a fraction of the distances examined in this thesis, producing much more precise measurement pairs.

There were four statistically significant differences found when the variations of the origin style precisions were assessed. Two of the cases just showed statistically significant differences between the Caudal Origin Style and the novel origin styles. The two remaining cases showed statistically significant differences between the Apex and Dual Origin Styles. In both cases where the Apex and Dual Origin Styles were statistically different, the origin style that used a larger marker cluster as the migration origin demonstrated a higher precision. That is, the Dual Origin Style had less variance

when assessing inferior X precision and the Apex Origin Style showed less variance when assessing the superior Y precision.

The precision measurements of the three origin techniques show that much of the precision is not statistically different between the three origin styles. The precision assessment alone was unable to determine a “best” technique for clinical application.

Of the precision results recorded during this thesis objective, eight of the forty-two had translational precisions greater than 0.3000mm. Two of these were recorded for the X directional precision, which is larger than the acceptable level of clinical significance. This indicates that the current origin styles and marker implantation protocol create migration measurement vectors (the distance between the centroids of the reference and migratory marker clusters) that are too large to provide the necessary level of system precision. The reduction of these measurement vectors can reduce the misalignment error associated with RSA migrational measurement and improve system precision [27]. In all other applications of RSA the measurement vectors are very small, existing between adjacent vertebrae, bone fracture elements or arthroplasty implants and the surrounding bone [1], [26], [28], [34], [50], [59–61], [63]. These small distances create a higher system precision which was not demonstrated in this study.

The advantages of vector reduction are shown in the comparison of the Caudal Origin Style precision results with those of the simulated model from Thesis Objective #1. In both the superior and inferior aspects of the spine the 80% scale simulated model of the spine used in Thesis Objective #1 demonstrated higher precision in the Y and Z directions. An improvement in the X direction was only demonstrated in the superior

aspect of the spine. The Z direction showed most significant change with each precision improving by over 0.1mm. It is expected that the creation of a simulated model that would assess the migration of adjacent vertebrae would produce precision values congruent with those published in single level fusion studies. Future work should be conducted to assess methods to reduce the length of the measurement vectors and mitigate the low system precision.

#### **4.4.2 Origin Style Selection**

This thesis objective was to assess the effect of the origin style on the accuracy and precision of the RSA assessment for determination of the success of spinal fusions performed during scoliosis treatment and determine which of the two novel origin styles should be used for future clinical research and diagnostic assessment. The three origin styles assessed were the Caudal Origin Style, the Apex Origin style, and the Dual Origin Style. Each of the origin styles were compared to a set of primary and secondary characteristics. These characteristics were a measure to determine their clinical applicability and ultimately select the most ideal origin style candidate to advance into further research.

Due to the physical limitations of the RSA setup, the future use of the Caudal Origin Style at this institution is not possible. It was used as a benchmark to which the other two origin styles were assessed. The primary comparison characteristics were the assessment of the accuracy and precision of the origin styles. All three of the origin styles maintained accuracies below the Limits of Clinical Significance.

The Apex and Dual Origin Styles outperformed the caudal benchmark with respect to overall translational accuracy. The Caudal Origin Style, due to its measure of the T4 vertebra in reference to the L1 origin, performed poorly in the Z-direction while the other two showed improvement over this benchmark.

In the rotational accuracy, the Apex and Dual Origin Styles were nearly identical in their outcomes, displaying identical accuracies to the nearest  $0.01^\circ$ . These results were slightly worse than the corresponding Caudal Origin Style results, but still over an order of magnitude better than what is currently available by bi-planar x-rays [20].

The assessment of the precision produced variable results. In the superior aspect of the spine, the Apex Origin Style produced translational precision that was consistently better than the other two origin styles. The inferior aspect of the spine showed no clear indicator of a “best” origin style. In both aspects, the Apex and Dual Origin Styles had identical rotational precisions. The assessment of the precision did not clearly indicate a “best” selection between the Apex and Dual Origin Styles for future clinical application. In fact, the precision may suggest the usage of a hybrid origin style where the spine is sectioned into a superior and inferior section but the caudal rigid body marker cluster in both image sets be used as the migration origin.

Along with the quantitative results, the three origin styles also underwent a more subjective assessment. Expected patient radiological dose, diagnostic imaging area, and the industrial expense of performing the RSA exam were assessed to logistically determine the best origin style to proceed toward clinical application.

All Origin styles performed similarly in their ease of use for migration analysis with the Apex and Dual Origin Styles requiring slightly more RSA technician time for assessment.

#### **4.4.2.1 Patient Radiological Risk**

The Apex and Dual Origin Styles provide the potential for almost doubling the available imaging area with the drawback of increased patient radiological dose. To assess the different dose characteristics of the two imaging techniques, an estimate of the effective dose given to an average patient was created.

For this assessment the full spine image was assumed to cover the length from the T4 to L1 vertebrae with the effective dose calculated for all organs anterior to this region. For the multi-image exams the patient effective dose was calculated for two regions: T1 to T10 for the superior image area and from T6 to L2 for the inferior image area. These regions cover much of the central torso, containing several major organs. The organs affected by each imaging area and their associated tissue weighting factor can be found in Table 4.18. It was assumed that the x-ray energies used to produce the full spine, superior and inferior images were identical ( $X$  remains constant).

**Table 4.18: Effective Dose Tissue Weighting Factors. “Remaining Tissue” indicates that this organ makes up part of the Remaining Tissue Weighting Factor. The weighting factors were originally published in IRCP report 103 (2007) and were republished in The Essential Physics of Medical Imaging (3<sup>rd</sup> Edition) (2012) [54]**

Organ	Weighting Factor (Wt)		
	Full Spine Image Area	Superior Image Area	Inferior Image Area
<b>Thyroid</b>	Not in Image Area	0.04	Not in Image Area
<b>Lungs</b>	0.12	0.12	0.12
<b>Heart</b>	Remaining Tissue	Remaining Tissue	Remaining Tissue
<b>Breasts</b>	0.12	0.12	0.12
<b>Esophagus</b>	0.04	0.04	0.04
<b>Stomach</b>	0.12	0.12	0.12
<b>Small Intestine</b>	Not in Image Area	Not in Image Area	Remaining Tissue
<b>Colon</b>	0.12	Not in Image Area	0.12
<b>Liver</b>	0.04	0.04	0.04
<b>Gall Bladder</b>	Remaining Tissue	Not in Image Area	Remaining Tissue
<b>Pancreas</b>	Remaining Tissue	Not in Image Area	Remaining Tissue
<b>Adrenal Glands</b>	Remaining Tissue	Not in Image Area	Remaining Tissue
<b>Kidneys</b>	Remaining Tissue	Not in Image Area	Remaining Tissue
<b>Lymph Nodes</b>	Remaining Tissue	Remaining Tissue	Remaining Tissue
<b>Spleen</b>	Remaining Tissue	Remaining Tissue	Remaining Tissue
<b>Muscles</b>	Remaining Tissue	Remaining Tissue	Remaining Tissue
<b>Ribs and Vertebrae</b>	0.01	0.01	0.01
<b>Red Bone Marrow</b>	0.12	0.12	0.12
<b>Skin</b>	0.01	0.01	0.01
<b>Remaining Tissues</b>	0.12	0.12	0.12
<b>Image Area Total</b>	0.82	0.74	0.82
<b>Origin Style Total</b>	<b>1.64</b>	<b>3.12</b>	

The use of the Apex or Dual Origin Styles causes the patient to experience an effective dose of 1.9 times as much as if they were subjected to a single image pair during the Caudal Origin Style.



From the assessment of both the quantitative and qualitative characteristics, this thesis has concluded that the use of either the Apex or Dual Origin Styles are equally applicable for further research and potential diagnostic implementation.

#### **4.4.3 Limitations**

Several assumptions and simplifications were made to assess of the various origin styles. These alterations induced several known limitations to the scope of the thesis work. The limitations, although impacting the project scope, should not negatively impact the validity of the conclusions made.

The conclusions drawn from this thesis are only applicable for the assessment of scoliotic curves of the 1AN Lenke classification of comparable size and severity [3]. The complex nature of the three-dimensional deformity and correction of scoliosis provides a lot of inter-patient variability that could severely impact the accuracy and precision results reported in this thesis.

The length of the fusions required varies among the patient population, easily changing the distances between the marked vertebrae. With larger distances, the misalignment issue would have a greater impact on system precision [27]. A smaller fusion would bring the marked vertebrae closer together improving system precision.

This thesis only assessed a single curve structure. The compound curve deformity may require additionally marked vertebrae to adequately assess the migrations within the spinal fusion, adding to vertebral marking and migration assessment complexity.

With these variations in curve structure and spine size, marker occlusion becomes a significant issue. Even within single curve structures, small alterations of vertebral

orientation or implant positioning could greatly impact the marker occlusion problem, decreasing marker visibility. The creation of patient or curve classification specific marker placement protocols should be assessed to create RSA marker systems that are adequate at assessing intervertebral migration.

#### **4.4.4 Conclusion**

The results from this objective found that the use of any of the three origin styles tested was successful at accurately measuring the migration induced in the simulated spinal model. With no significant differences between the two origin styles the use of either the Apex or Dual Origin Style are equally applicable for future clinical research and potential diagnostic implantation. Steps should be taken to decrease the length of the inter-cluster measurement vectors to increase system precision.

# Chapter 5 - Discussion

## 5.1 Thesis Impact

The research conducted for the basis of this thesis has the potential for a significant impact on the Radiostereometric Analysis (RSA) body of research.

### 5.1.1 RSA Research

This thesis has validated precision component of a simulation RSA environment which can be used to create x-ray images used in RS analysis. The expanded use of the simulation process could have a significant impact on RSA research for all RSA applications. The use of simulated x-ray images provides economical, ethical and a superior method of assessing RSA performance.

Simulated RSA studies can be performed without specialist personnel or equipment, requiring less time and resources to conduct than the use of physical radiographs. Radiographic imaging equipment is not tied up for research with simulated x-rays, allowing it to maintain its clinical diagnostic assessment duties. With the exception of the phantom model study, the entirety of the research performed during this project has been performed independently on a commercially available notebook computer. After the initial vertebral model construction, each RSA image pair took approximately 25 minutes to complete, during periods of peak image simulation periods. Images were rendered automatically outside of work hours, allowing for over 50 individual images to be created per day during peak periods. Along with being inexpensive, simulated RSA exams have no possibility of radiological exposure to

personnel or patients. Therefore, large in-depth studies can be conducted with zero risk to equipment, personnel, or subjects.

A simulated model provides a superior method for assessing RSA system accuracy. Displacements induced in physical phantom models have error associated with them proportional to the methods used to implement the motion. Micrometers are commonly used to induce displacement in phantom models. The highly accurate nature of RSA creates a situation where the migration inducing and measuring techniques have similar accuracies so that the use of RSA may just be recording the error associated with the induced displacement. The simulation process eliminates this source of error. The displacements induced in the simulated phantom models are “perfect” with no error associated with the measurement. When subsequently measured with RSA software, all errors recorded are inherent to the RSA process alone.

The use of simulated RSA studies also allows for the implementation of complex movements that would be impractical or impossible to simulate with traditional phantom models. Although complex movements were not used during this study, the addition of vertebral rotation to a translational migration would not create any additional complications. To perform the same action on a traditional phantom would require the addition of another micrometer as well as increased marker obstruction concern [59]. For this reason, this thesis agrees with the sentiments expressed by Madanat et al (2007) that the use of simulated RSA research makes the assessment of complex moments possible [59].

### **5.1.2 Spinal Fusion Assessment**

Along with validation of the simulation process, the use of RSA in the assessment of spinal fusion success was also analyzed. This study concludes that either the Apex or the Dual Origin Styles are equally valuable for future clinical research and implementation. RSA provides a unique opportunity to acquire highly accurate migrational measurement data at the initial postoperative assessment level. Patients can undergo RSA assessment similar to the current standard radiological assessment regime, receiving a lower effective radiological dose while increasing the output of diagnostically useful migration information. This increase in highly accurate measurements will provide faster clinical response and reduce the use of CT scans on questionable pseudoarthrosis.

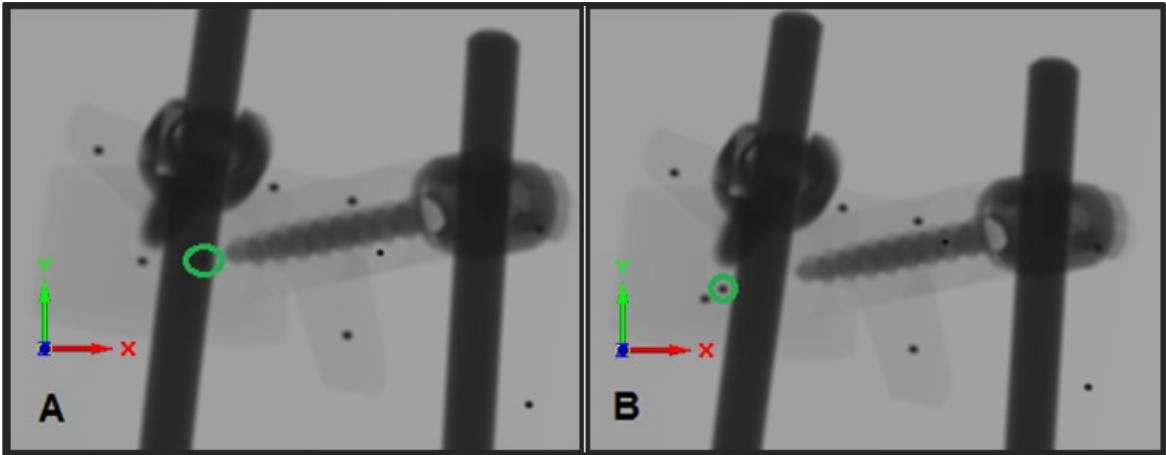
Results of the translational movements of the model spines indicate that the length between the marker clusters is creating a situation of poor precision. As stated by Francis (2009), as the length of measurement vectors increase the effects of the misalignment error increase [27]. During the research completed for this thesis, the use of three marked vertebrae to measure the intervertebral displacements resulted in low precision due to misalignment error. Investigation into the reduction of this effect should be conducted.

It is of this researcher's opinion that research into the use of RSA in the assessment of spinal fusion success should continue toward the point of clinical application.

### **5.1.2.1 Marker Placement**

During the course of this project a marker placement protocol adapted from the previous project work conducted by Francis (2009) was used [27]. As such the placement protocol was expected to maintain the same level of marker dispersion in the vertebrae and marker visibility in the normal, reference position (the “Reference Scene”). The marker placement protocol was also expected to undergo all migrations (the “Migrating Scenes”) associated with the accuracy and precision testing without significant detriment to marker visibility.

As mentioned previously, the markers were placed in the bone, mimicking the level of placement accuracy available to a surgeon during surgery. This intentional inaccuracy provided optimization opportunities with the marker placement protocol. This was done first by placing the markers, then simulating an image set and examining the marker visibility. If a marker was obscured then it was moved to a different location. In one example, marker #6 in the T4 vertebra was moved deeper into the vertebral body, near the anterior edge of the vertebra, from its original position, close to the right screw tip. This allowed the marker to become visible to the left of the fixation rod as shown in Figure 5.1. This kind of optimization would not be available post-operatively if a marker is found to be occluded. Using pre-operative computer simulation, a similar trial-and-error approach could be undertaken on a case-by-case basis to provide surgeons locations for safe, visible positions to implant the markers.



**Figure 5.1: T4 Vertebra with marker movement A) Marker #6 occluded by fixation rod B) Marker moved anteriorly to allow for visibility.**

The placement optimization resulted in very high visibility of the seven implanted markers in each vertebra. In both the T4 and T8 models, all seven markers were visible during reference conditions. The screw placement and global position of the L1 vertebrae occluded L1 marker #7 from view. Although this occlusion was not able to be corrected, work done by Madanat et al (2005) found that the minimum number of markers required to adequately define the position of a marker cluster with high accuracy is four visible markers [60].

During all translational accuracy and precision exams, all markers visible in the reference scene remained visible. Unfortunately, during rotational accuracy and precision movements, not all markers were visible. In a few of the assessments for the rotational precision of Caudal Origin Style the number of visible markers in a rigid body fell to four, however, this is still within the acceptable threshold for rigid body positioning. In a clinical setting, in these cases, the patient would have to be repositioned for better visibility and the x-rays would have to be recaptured.

With the high visibility of the markers and the wide spread of the markers inside the vertebra, the condition numbers of the three vertebral marker clusters were well below the threshold of 100. The condition numbers recorded from the reference image sets were: T4: 18.5, T8: 19.7, and L1: 19.8. In all but four extreme cases, the condition number of all marker models remained under 45.

Some of the extreme movements induced in the simulated model caused the marker clusters to extend out of the range of the imaging area when using the Caudal Origin Style. A total of eight exams were afflicted, three for the accuracy assessment and five for the precision assessment. The three accuracy assessment exams affected were both the superior and inferior +20mm Y failure, where the T4 vertebral cluster was partially outside the imaging area, and the -20mm X failure where one of the matched markers of the T8 vertebra was not accessible. With the +20mm Y failure movements, only three markers of the T4 marker cluster remained matched. While this is below the four marker threshold, the good condition number of 34.4 indicated that it was acceptable to proceed with the use of these exams as part of the accuracy assessment.

The loss of markers outside the imaging area was most profound with the movements induced for the assessment of system precision. Of the five exams affected, four were used for rotational precision assessment. The translational precision exam with negative Y movement exhibited the loss of one marker of the L1 vertebra outside the imaging area. The rotational precision exams were the most affected by the limited imaging area. Rotations around both the X and Z axes caused the L1 vertebra to be positioned partially outside the imaging area. With the X rotation, four L1 markers remained in the image set while Z and -X rotations saw three L1 markers still matched.



Unfortunately, only two of the markers matched in the Z rotated precision assessment were also matched in the preceding and subsequent exams, the Y and -X rotations respectively. This precludes the precision Z rotation exam from being used in the assessment of system precision.

The -Z rotation caused the L1 vertebra to be extended so far outside the imaging area that only two matched markers remained in the image. This is not enough for a determination of the migration origin so this exam was also removed from precision assessment.

All other thresholds required for an adequate marker placement protocol were upheld.

## **5.2 Limitations**

With all research, especially phantom studies, limitations on research outcomes are imposed. The following limitations limit the scope of the presented results and do not negatively impact the conclusions made. The results of this study are only applicable to main thoracic scoliotic curves corrected to  $20^{\circ}$  which correspond to a 1AN Lenke curve classification. Different deformity structures can be created using the simulation process but will result in different intervertebral distances, vertebral marking requirements, and marker occlusion. These curve variations should be assessed before clinical implantation of RSA as a method to assess spinal fusion success.

### **5.2.1 Simulation Limitations**

As stated previously, the image simulation procedure is limited in its photorealism. The most significant of the realism inaccuracies is the absence of image noise and the accuracy of material contrast. The material attenuation coefficients used to create the image contrast were created as a best match scenario to a radiograph taken at the Halifax Infirmary RSA suite in 2010 of a phantom spinal fusion model. Therefore the coefficients used do not correlate precisely to actual anatomical material absorption characteristics. This approximation was found to create adequate image contrast and was deemed acceptable.

The second photorealism inaccuracy was the absence of image noise. The signal-to-noise ratio of the simulated images approached infinity. This allows the simulated images to have higher spatial resolution than a physical x-ray. Previous work tried to compensate for this by adding in a background taken from a blank section of a physical x-

ray as well as adding a gaussian noise blur [27]. These measures were implemented as a best-match scenario to physical x-rays. They were deemed as unnecessary as the physical RSA system could provide spatial resolution to distinguish two touching markers. With this resolution present in a physical RSA system, the absence of image noise in the simulated system would provide little advantage.

## **5.3 Future Work**

Due to the limitations of the RSA simulation, several research avenues exist for future research. To fully validate the RSA simulation, all avenues may require exploration to advance the simulation and to bring the assessment of spinal fusion success using RSA to the level of clinical applicability.

### **5.3.1 Image Simulation Improvements**

Testing should be performed to quantify the x-ray attenuation factors of the various materials encountered during an RSA exam. The current simulated attenuation factors were set to mimic the factors found in a single phantom study. These factors were sufficient enough to differentiate the various materials present in the simulated environment but are not photorealistic. Future studies conducted on the effects of tissue simulants and implant materials would allow for quantification of attenuation characteristics at various x-ray energies and durations. The quantification would create better attenuation coefficients for the simulation process and the ability to vary the simulated x-ray strength administered during the exam.

Along with the quantification of material attenuation properties signal noise could also be quantified and incorporated into the simulation process. The addition of noise should be conducted after an assessment of physical system noise has been undertaken. The noise added to the simulated environment should be correlated with that of the physical environment to ensure that it possesses not only similar amplitude but also the same characteristics in pattern and in the frequency domain. By undertaking this vital step, the noise in the simulation will generate an identical impact on the rendered image

as its real world counterpart. Therefore the image realism can be maintained while additionally allowing for the simulation of image improvement scenarios without having to progress to physical phantoms and clinical equipment.

The improvement of the simulation process would be a great advancement for the research conducted in x-ray and RSA imaging. The use of these simulations could eventually trickle back to the clinical environment allowing for technicians to assess x-ray energy setups for individual patients before subjecting the patients to any extraneous radiological dosage.

### **5.3.2 Complete Simulation Validation**

This thesis completed one of three aspects for complete simulation validation. A precision validation study confirmed that the simulated environment reproduces the same level of systemic errors as the physical RSA environment. Previous work by Madanat et al (2007) and Francis (2009) concluded that the simulation produces accurate simulations of real world counterparts [27], [59].

What remains is the assessment of the system responsiveness. To complete this assay, this researcher recommends the implementation of a parallel measurement accuracy assessment. In this study a phantom model containing migrational staging could be assessed using the physical RSA environment while a simulated phantom undergoes identical intervertebral migrations. The results from the two parallel streams should then be assessed to confirm that the results from the simulated environment reflect those of the physical RSA system.

### **5.3.3 Patient Specific Anatomical Information**

Using this research as a foundation, future research should focus on the creation of patient specific simulations. The use of simulated phantom models leads to the simple, efficient and cost effective means of altering the shape of examined spinal deformities. Utilizing a complete spine model and a full complement of correction implants, a wide range of corrections could be simulated and their RSA applicability examined. This would be a vehicle for the creation of patient specific marker placement protocols, selection of surgical implants, and possible assistance in surgical planning processes. The use of patient specific anatomical information would ensure that each simulation would be tailored to the individual surgical case. Utilizing this information marker placement protocols could be customized so that all implanted markers would be visible post-operatively.

Another benefit to the use of patient specific simulations is the reduction in surgical overhead. Using a simulation based pre-operative planning processes, the required implant hardware could be selected and ordered on a case-by-case basis which would eliminate the necessity for each hospital to order and maintain a full set of implant pedicle screw and fixation rod options.

To create patient specific spinal models, several methods were examined during initial project research. The easiest of these methods is the creation of three dimensional models from pre-operative CT scans. However these scans would subject patients to high doses of radiation eliminating the radiological advantage of using RSA. The use of pre-operative CT scans should be avoided for the sole use of model construction, but they

remain a viable source of anatomical information for those already undergoing the scans for other clinical reasons.

The second option for the acquisition of patient anatomical information is taking measurements from traditional bi-planer x-rays. These are part of the standard pre-surgical work-up and could provide adequate accuracy for gross placement of the modeled vertebrae. However, the use of bi-planer x-rays would not be adequate for the precise modeling of individual vertebral structures [72], [73].

The final and most intriguing method would be the use of Magnetic Resonance Imaging (MRI) to develop the simulated models. There were several articles found in the literature discussing the creation of models of the lumbar spine, however, it was outside the scope of this project to develop a method of acquiring anatomical information of the vertebral structures of the thoracic and lumbar spine at the IWK Health Centre [74], [75]. The use of MR imaging remains intriguing due to the safety factor associated with the method. MR imaging is non-destructive and does not subject the patient to any radiological risk.

All of these methods remain as options for further research in creating precise, patient specific anatomical models of the spine for use in later simulations.

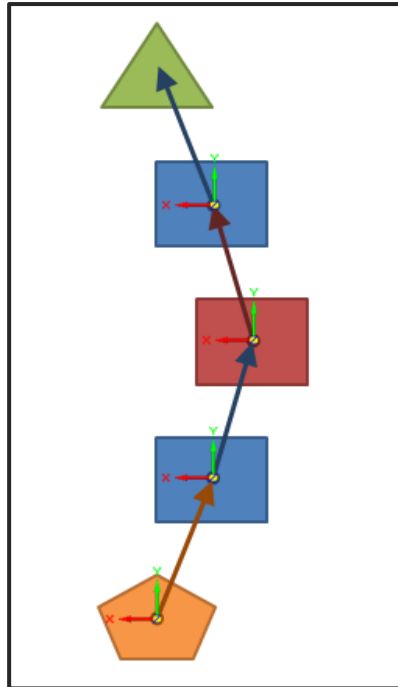
### **5.3.4 Vertebral Marking Protocols**

Current work used a placement protocol where three vertebrae are marked to determine the intervertebral migration. The superior and inferior ends of the curve as well as the curve apex were marked. This was seen as the minimum number of levels which would adequately report fusion movement. Therefore, it provided a balance between acquiring spatial information and patient safety.

This study has found that the system precision currently precludes the use of RSA to evaluate spinal fusion success. Future research should focus on the mitigation of this precision effect by limiting the distance between the marked vertebrae. This will require the use of additional marked vertebrae. This researcher suggests that moving to a system where four or five vertebrae are marked would limit the inter-cluster distances so that the required system precision is achieved.

Along with the additional marking of vertebrae, a hybrid origin style should be assessed. This new origin style should combine the use of a spatially larger origin marker cluster, the segmental analysis of the Apex and Dual Origin Styles, and the standard migrational orientation of the Caudal Origin Style. This technique would be a Sectional Origin Style. Here each marked vertebrae would act as both a migrational vertebrae for the adjacent inferior marker cluster and a migration origin for the adjacent superior marker cluster. An example of this proposed Sectional Origin Style is shown in Figure 5.2.





**Figure 5.2: Sectional Origin Style. Orange Pentagon: Inferior Vertebra, Red Square: Apex Vertebra, Green Triangle: Superior Vertebra, Blue Squares: Intermediate Marked Vertebrae. Arrow colour corresponds with measurement origin vertebrae. Coordinate systems of origin vertebrae shown.**

In addition to the investigation of the increase of marked vertebrae, an investigation in marker redundancy should be undertaken. The current marking protocol was developed by Francis (2009) and contains 7 markers per vertebra [27]. It was not in the scope of this thesis to assess the marking protocol past the adjustment to the use of anatomical landmarks in marker placement. Valstar et al (2005) recommend the use of 6-9 well placed markers in a rigid body to compensate for marker occlusion and marker loosening [5]. Using the impact on CN as a guide for marker importance, the markers which are expected to create the lowest CN are the markers in the Transverse Processes, the Spinous Process and the markers down the pedicle screw holes in the vertebral body. The least important markers are those in the lamina in that they would have the least effect on marker cluster distribution and potentially the least impact on CN. This researcher does not recommend reducing the number of markers in the vertebrae below five markers.

## 5.4 Summary and Conclusion

This thesis used simulated Radiostereometric Analysis (RSA) exams for research for its use in spinal fusions and assessed the impact of the RSA origin style on the system accuracy and precision. This research was conducted on a spinal fusion conducted on a simulated ten segment 20° right thoracic scoliotic curve extending from the T4 to L1 vertebrae. A parallel precision assessment study was undertaken to validate the systemic errors present within the simulated RSA environment as part of a continual validation of the simulated RSA exams.

Several advances were made to the simulation process to make it more realistic. The most significant of these advances was the use of material attenuation factors to create the required radio-opacity of the simulated materials. This is an upgrade from the surface attenuation method used in previous simulations. These advancements were put to the test in a parallel phantom/simulated model validation study. This study concluded that the simulated RSA environment replicates the physical system present at the Halifax Infirmary and that the simulated RSA environment has been validated for use in RSA research.

The work completed in this thesis found that all origin styles examined performed adequately, producing measurements that were accurate within the Limits of Clinical Significance. No statistically significant data was produced in the assessment of the two introduced and novel origin styles with both measuring the induced migrations within the respective Limits of Clinical Significance. The system precision was ineffective to produce a definite ruling on the “best” origin style with all of them producing similar

precision results. These precision results currently preclude the use of RSA in the assessment of spinal fusions. Future research into alternative curve marking protocols and origin styles should improve system precision to adequate levels.

In conclusion this thesis has shown that RSA should continue to be pursued as a future method for use clinically in the assessment of spinal fusion, replacing the current use of bi-planar x-rays. Furthermore, this thesis has also created and assessed two new measurement styles, enabling RSA measurement to be used on patients whose spines are too long to fit within the diagnostic area of the current RSA equipment. Patient or curve classification specific simulations should be undertaken to develop new vertebral marking protocols, leading the way for clinical application of RSA in spinal fusion success assessment.

## Bibliography

- [1] D. Pape et al., "Lumbosacral stability of consolidated anteroposterior fusion after instrumentation removal determined by roentgen stereophotogrammetric analysis and direct surgical exploration," *Spine*, vol. 27, no. 3, pp. 269-74, Feb. 2002.
- [2] R. Johnsson, B. Strömqvist, and P. Aspenberg, "Randomized radiostereometric study comparing osteogenic protein-1 (BMP-7) and autograft bone in human noninstrumented posterolateral lumbar fusion: 2002 Volvo Award in clinical studies.," *Spine*, vol. 27, no. 23, pp. 2654-61, Dec. 2002.
- [3] L. G. Lenke et al., "Adolescent idiopathic scoliosis: a new classification to determine extent of spinal arthrodesis.," *The Journal of bone and joint surgery. American volume*, vol. 83-A, no. 8, pp. 1169-81, Aug. 2001.
- [4] J. M. Bland and D. G. Altman, "Statistical methods for assessing agreement between two methods of clinical measurement.," *Lancet*, vol. 1, no. 8476, pp. 307-10, Feb. 1986.
- [5] E. R. Valstar, R. Gill, L. Ryd, G. Flivik, N. Börlin, and J. Kärrholm, "Guidelines for standardization of radiostereometry (RSA) of implants.," *Acta orthopaedica*, vol. 76, no. 4, pp. 563-72, Aug. 2005.
- [6] S. Strandring and H. Gray, *Gray's Anatomy: the Anatomical Basis of Clinical Practice*, 40th, Anni. Churchill Livingstone/Elsevier, 2008, p. 1551.
- [7] A. P. Schnuerer, *Basic Anatomy and Pathology of the Spine*, Second. Medtronic Sofamor Danek, 2003, p. 168.
- [8] R. L. Drake, W. Vogl, A. W. M. Mitchell, and H. Gray, *Gray's Anatomy for Students*, 2nd ed. Churchill Livingstone/Elsevier, 2009, p. 1103.
- [9] W. A. N. Dorland, *Dorland's Pocket Medical Dictionary*, 28th ed. Philadelphia: Elsevier Saunders, 2009.
- [10] J. A. Herring, *Tachdjian's Pediatric Orthopaedics, vols 1-3*, 3rd ed., vol. 288, no. 6. W.B. Saunders Company, 2001, p. 2950.
- [11] W. W. Lovell, R. B. Winter, R. T. Morrissy, and S. L. Weinstein, *Lovell and Winter's pediatric orthopaedics*, Fifth., vol. 1. Philadelphia: Lippincott Williams & Wilkins, 2001, p. 1600.
- [12] S. L. Weinstein, *The Pediatric Spine: Principles and Practice*, 1st ed., vol. 1. New York: Raven Press Ltd., 1994, p. 1959.

- [13] L. A. Karol, "Effectiveness of bracing in male patients with idiopathic scoliosis," *Spine*, vol. 26, no. 18, pp. 2001-2005, Sep. 2001.
- [14] D. E. Katz, B. S. Richards, R. H. Browne, and J. A. Herring, "A comparison between the Boston brace and the Charleston bending brace in adolescent idiopathic scoliosis," *Spine*, vol. 22, no. 12, pp. 1302-1312, Jun. 1997.
- [15] A. S. Hilibrand and T. S. Dina, "The use of diagnostic imaging to assess spinal arthrodesis," *The Orthopedic clinics of North America*, vol. 29, no. 4, p. 591, 1998.
- [16] E. R. G. Santos, D. G. Goss, R. K. Morcom, and R. D. Fraser, "Radiologic assessment of interbody fusion using carbon fiber cages," *Spine*, vol. 28, no. 10, pp. 997-1001, May 2003.
- [17] P. Lang, N. Chafetz, H. K. Genant, and J. M. Morris, "Lumbar spinal fusion. Assessment of functional stability with magnetic resonance imaging," *Spine*, vol. 15, no. 6, pp. 581-588, Jun. 1990.
- [18] L. K. Cannada, S. C. Scherping, J. U. Yoo, P. K. Jones, and S. E. Emery, "Pseudoarthrosis of the cervical spine: a comparison of radiographic diagnostic measures," *Spine*, vol. 28, no. 1, pp. 46-51, Jan. 2003.
- [19] W. Frobin, P. Brinckmann, G. Leivseth, M. Biggemann, and O. Reikerås, "Precision measurement of segmental motion from flexion-extension radiographs of the lumbar spine," *Clinical biomechanics (Bristol, Avon)*, vol. 11, no. 8, pp. 457-465, Dec. 1996.
- [20] G. C. Lam, D. L. Hill, L. H. Le, J. V. Raso, and E. H. Lou, "Vertebral rotation measurement: a summary and comparison of common radiographic and CT methods," *Scoliosis*, vol. 3, p. 16, Jan. 2008.
- [21] W. Huda, J. V. Atherton, D. E. Ware, and W. A. Cumming, "An approach for the estimation of effective radiation dose at CT in pediatric patients," *Radiology*, vol. 203, no. 2, pp. 417-22, May 1997.
- [22] A. E. Brodsky, E. S. Kovalsky, and M. A. Khalil, "Correlation of radiologic assessment of lumbar spine fusions with surgical exploration," *Spine*, vol. 16, no. 6S, p. S261, 1991.
- [23] G. Selvik, "Roentgen stereophotogrammetric analysis," *Acta radiologica (Stockholm, Sweden : 1987)*, vol. 31, no. 2, pp. 113-26, Mar. 1990.
- [24] G. Selvik, "Roentgen stereophotogrammetry. A method for the study of the kinematics of the skeletal system," *Acta orthopaedica Scandinavica. Supplementum*, vol. 232, pp. 1-51, Jan. 1989.

- [25] J. Kärrholm, "Roentgen stereophotogrammetry. Review of orthopedic applications.," *Acta orthopaedica Scandinavica*, vol. 60, no. 4, pp. 491-503, Aug. 1989.
- [26] C. R. Bragdon et al., "Experimental assessment of precision and accuracy of radiostereometric analysis for the determination of polyethylene wear in a total hip replacement model," *Journal of Orthopaedic Research*, vol. 20, no. 4, pp. 688–695, 2002.
- [27] A. Francis, "Simulation of a Standardized Bead Placement Protocol for Radiostereometric Analysis of Thoracic Spinal Fusion," Dalhousie University, 2009.
- [28] D. Wilson, "Radiostereometric Analysis of Migration and Inducible Displacement of a Novel Porous Biomaterial used in Total Knee Arthroplasty," Dalhousie University, 2007.
- [29] E. Laende, "Radiostereometric analysis of migration and inducible displacement for the evaluation of total knee replacement fixation," Dalhousie University, 2006.
- [30] L. Ryd, "Micromotion in knee arthroplasty," *Acta Orthopaedica*, vol. 57, no. s220, pp. 3-80, Jan. 1986.
- [31] J. W. Fong, "Model-Based Radiostereometric Analysis of an Uncemented Mobile-Bearing Total Ankle Arthroplasty System," Dalhousie University, 2010.
- [32] L. Ryd, A. Lindstrand, R. Rosenquist, and G. Selvik, "Tibial component fixation in knee arthroplasty," *Clinical orthopaedics and related research*, vol. 213, p. 141, 1986.
- [33] L. Ryd et al., "Roentgen stereophotogrammetric analysis as a predictor of mechanical loosening of knee prostheses.," *The Journal of bone and joint surgery. British volume*, vol. 77, no. 3, pp. 377-83, May 1995.
- [34] I. Onsten, A. Berzins, S. Shott, and D. R. Sumner, "Accuracy and precision of radiostereometric analysis in the measurement of THR femoral component translations: human and canine in vitro models," *Journal of Orthopaedic Research*, vol. 19, no. 6, pp. 1162-1167, Nov. 2001.
- [35] P. Axelsson, R. Johnsson, and B. Strömquist, "Effect of lumbar orthosis on intervertebral mobility. A roentgen stereophotogrammetric analysis.," *Spine*, vol. 17, no. 6, pp. 678-81, Jun. 1992.

- [36] R. Johnsson, B. Strömquist, P. Axelsson, and G. Selvik, "Influence of spinal immobilization on consolidation of posterolateral lumbosacral fusion. A roentgen stereophotogrammetric and radiographic analysis.," *Spine*, vol. 17, no. 1, pp. 16-21, Jan. 1992.
- [37] P. Axelsson and B. S. Karlsson, "Intervertebral mobility in the progressive degenerative process. A radiostereometric analysis," *European Spine Journal*, vol. 13, no. 6, pp. 567-572, Oct. 2004.
- [38] T. H. Olsson, G. Selvik, and S. Willner, "Kinematic analysis of spinal fusions.," *Investigative radiology*, vol. 11, no. 3, pp. 202-209, 1976.
- [39] G. Gunnarsson, P. Axelsson, R. Johnsson, and B. Strömquist, "A method to evaluate the in vivo behaviour of lumbar spine implants.," *European spine journal : official publication of the European Spine Society, the European Spinal Deformity Society, and the European Section of the Cervical Spine Research Society*, vol. 9, no. 3, pp. 230-234, Jun. 2000.
- [40] P. Axelsson and B. S. Karlsson, "Standardized provocation of lumbar spine mobility: three methods compared by radiostereometric analysis," *Spine*, vol. 30, no. 7, pp. 792-7, Apr. 2005.
- [41] K. Greene-Donnelly, K. Ogden, N. Ordway, M. Roskopf, and J. Calabrese, "SUGG-I-60: Effective Dose to Patients Undergoing Radiostereometric Analysis of the Lumbar Spine," *Medical Physics*, vol. 35, no. 6, p. 2656, 2008.
- [42] R. Johnsson, P. Axelsson, and B. Strömquist, "Posterolateral lumbar fusion using facet joint fixation with biodegradable rods: a pilot study.," *European spine journal : official publication of the European Spine Society, the European Spinal Deformity Society, and the European Section of the Cervical Spine Research Society*, vol. 6, no. 2, pp. 144-148, Jan. 1997.
- [43] R. Johnsson, G. Selvik, B. Strömquist, and G. Sundén, "Mobility of the lower lumbar spine after posterolateral fusion determined by roentgen stereophotogrammetric analysis.," *Spine*, vol. 15, no. 5, pp. 347-50, May 1990.
- [44] G. Leivseth, P. Brinckmann, W. Frobin, R. Johnsson, and B. Strömquist, "Assessment of sagittal plane segmental motion in the lumbar spine: a comparison between distortion-compensated and stereophotogrammetric roentgen analysis," *Spine*, vol. 23, no. 23, p. 2648, 1998.
- [45] B. Zoëga, J. Kärrholm, and B. Lind, "Mobility provocation radiostereometry in anterior cervical spine fusions.," *European spine journal*, vol. 12, no. 6, pp. 631-6, Dec. 2003.

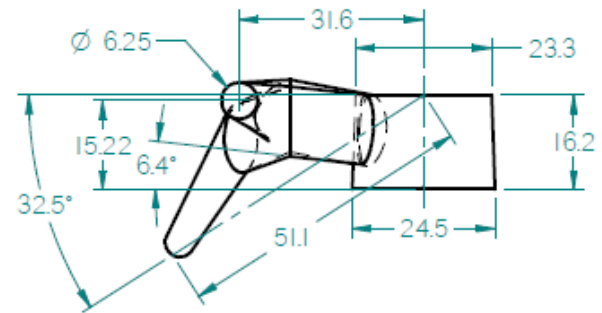
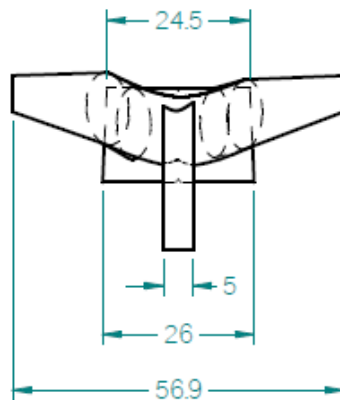
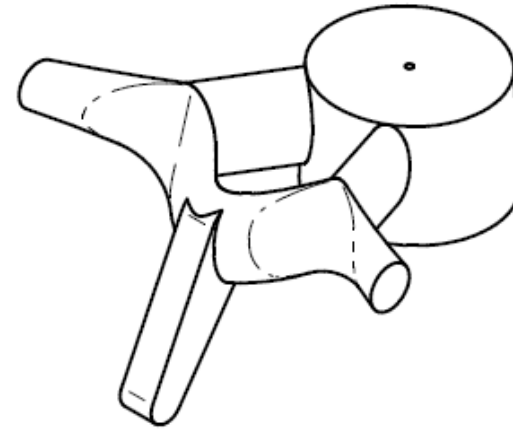
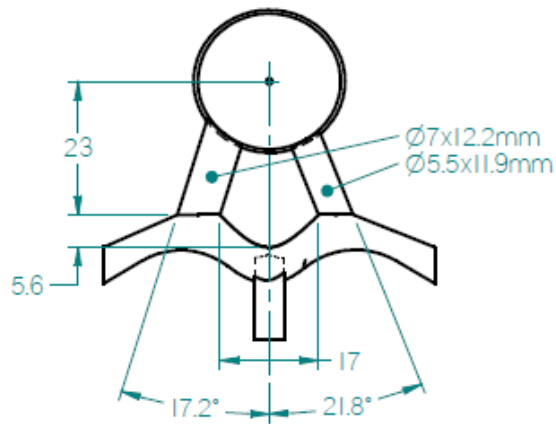
- [46] P. Axelsson, R. Johnsson, and B. Strömqvist, "Mechanics of the External Fixation Test in the Lumbar Spine : A Roentgen stereogrammetric analysis," *Imaging*, vol. 21, no. 3, pp. 330-333, 1996.
- [47] R. Johnsson, P. Axelsson, G. Gunnarsson, and B. Strömqvist, "Stability of lumbar fusion with transpedicular fixation determined by roentgen stereophotogrammetric analysis.," *Spine*, vol. 24, no. 7, pp. 687-690, Apr. 1999.
- [48] S. Lee, K. G. Harris, V. K. Goel, and C. R. Clark, "Spinal motion after cervical fusion. In vivo assessment with roentgen stereophotogrammetry.," *Spine*, vol. 19, no. 20, pp. 2336-42, Oct. 1994.
- [49] G. Leivseth, F. Kolstad, O. P. Nygaard, B. Zoëga, W. Frobin, and P. Brinckmann, "Comparing precision of distortion-compensated and stereophotogrammetric Roentgen analysis when monitoring fusion in the cervical spine," *European spine journal*, vol. 15, no. 6, pp. 774-779, Jun. 2006.
- [50] D. Pape, F. Adam, E. Fritsch, K. Müller, and D. Kohn, "Primary lumbosacral stability after open posterior and endoscopic anterior fusion with interbody implants: a roentgen stereophotogrammetric analysis," *Spine*, vol. 25, no. 19, pp. 2514-2518, Oct. 2000.
- [51] G. Selvik, P. Alberius, and A. S. Aronson, "A roentgen stereophotogrammetric system. Construction, calibration and technical accuracy.," *Acta radiologica: diagnosis*, vol. 24, no. 4, pp. 343-52, Jan. 1983.
- [52] B. L. Kaptein, E. R. Valstar, B. C. Stoel, P. M. Rozing, and J. H. C. Reiber, "A new type of model-based Roentgen stereophotogrammetric analysis for solving the occluded marker problem.," *Journal of biomechanics*, vol. 38, no. 11, pp. 2330-4, Nov. 2005.
- [53] L. Ryd, X. Yuan, and H. Löfgren, "Methods for determining the accuracy of radiostereometric analysis (RSA)," *Acta orthopaedica Scandinavica*, vol. 71, no. 4, pp. 403-8, Aug. 2000.
- [54] Jerrold T. Bushberg, J. A. Seibert, E. M. Leidholdt Jr., and J. M. Boone, *The Essential Physics of Medical Imaging*, 3rd ed. Philadelphia: Lippincott Williams & Wilkins, 2012.
- [55] C. Guy and D. Ffytche, *An Introduction to the Principles of Medical Imaging*. London: Imperial Collage Press, 2005, p. 374.
- [56] J. T. Bushberg, J. A. Seibert, E. M. Leidholdt Jr., and J. M. Boone, *The Essential Physics of Medical Imaging*, 2nd ed. Lippincott Williams & Wilkins, 2001, p. 933.
- [57] Medis specials bv., "Model-based RSA 3.2 Software User Manual." p. 80, 2008.



- [58] “Merriam-Webster Online Dictionary.” [Online]. Available: <http://www.merriam-webster.com/dictionary/accuracy>. [Accessed: 04-Mar-2012].
- [59] R. Madanat, N. Moritz, and H. T. Aro, “Three-dimensional computer simulation of radiostereometric analysis (RSA) in distal radius fractures.,” *Journal of biomechanics*, vol. 40, no. 8, pp. 1855-61, Jan. 2007.
- [60] R. Madanat, T. J. Mäkinen, N. Moritz, K. T. Mattila, and H. T. Aro, “Accuracy and precision of radiostereometric analysis in the measurement of three-dimensional micromotion in a fracture model of the distal radius,” *Journal of orthopaedic research*, vol. 23, no. 2, pp. 481-488, Mar. 2005.
- [61] E. K. Laende, K. J. Deluzio, A. W. Hennigar, and M. J. Dunbar, “Implementation and validation of an implant-based coordinate system for RSA migration calculation.,” *Journal of biomechanics*, vol. 42, no. 14, pp. 2387-93, Oct. 2009.
- [62] T. J. Mäkinen, J. K. Koort, K. T. Mattila, and H. T. Aro, “Precision measurements of the RSA method using a phantom model of hip prosthesis.,” *Journal of biomechanics*, vol. 37, no. 4, pp. 487-493, Apr. 2004.
- [63] M. J. Allen, S. M. Hartmann, J. M. Sacks, J. Calabrese, and P. R. Brown, “Technical feasibility and precision of radiostereometric analysis as an outcome measure in canine cemented total hip replacement,” *Journal of orthopaedic science*, vol. 9, no. 1, pp. 66-75, Jan. 2004.
- [64] P. Axelsson, R. Johnsson, and B. Strömquist, “Adjacent segment hypermobility after lumbar spine fusion: no association with progressive degeneration of the segment 5 years after surgery,” *Acta orthopaedica*, vol. 78, no. 6, pp. 834-839, Dec. 2007.
- [65] I. Söderkvist and P.-Å. Wedin, “Determining the movements of the skeleton using well-configured markers.,” *Journal of biomechanics*, vol. 26, no. 12, pp. 1473-7, Dec. 1993.
- [66] D. P. Breglia, “Generation of a 3-D Parametric Solid Model of the Human Spine Using Anthropomorphic Parameters,” Ohio University, 2006.
- [67] M. M. Panjabi et al., “Thoracic human vertebrae. Quantitative three-dimensional anatomy.,” *Spine*, vol. 16, no. 8, pp. 888-901, Aug. 1991.
- [68] M. M. Panjabi et al., “Human lumbar vertebrae. Quantitative three-dimensional anatomy.,” *Spine*, vol. 17, no. 3, pp. 299-306, Mar. 1992.
- [69] Canon, “Digital Radiography: CXDI-50C User ’ s Manual,” *Group*. p. 36, 2008.

- [70] B. L. Kaptein, E. R. Valstar, B. C. Stoel, P. M. Rozing, and J. H. C. Reiber, "Evaluation of three pose estimation algorithms for model-based roentgen stereophotogrammetric analysis.," *Proceedings of the Institution of Mechanical Engineers. Part H, Journal of engineering in medicine*, vol. 218, no. 4, pp. 231-8, Jan. 2004.
- [71] J. S. Krouwer, "Why Bland-Altman plots should use X, not  $(Y+X)/2$  when X is a reference method.," *Statistics in medicine*, vol. 27, no. 5, pp. 778-80, Feb. 2008.
- [72] R. Dumas et al., "A semi-automated method using interpolation and optimisation for the 3D reconstruction of the spine from bi-planar radiography: a precision and accuracy study," *Medical & biological engineering & computing*, vol. 46, no. 1, pp. 85-92, Jan. 2008.
- [73] L. Humbert, J. A. de Guise, B. Aubert, B. Godbout, and W. Skalli, "3D reconstruction of the spine from biplanar X-rays using parametric models based on transversal and longitudinal inferences.," *Medical engineering & physics*, vol. 31, no. 6, pp. 681-687, Jul. 2009.
- [74] C. L. Hoad, a L. Martel, R. Kerslake, and M. Grevitt, "A 3D MRI sequence for computer assisted surgery of the lumbar spine.," *Physics in medicine and biology*, vol. 46, no. 8, pp. N213-20, Aug. 2001.
- [75] C. L. Hoad and A. L. Martel, "Segmentation of MR images for computer-assisted surgery of the lumbar spine.," *Physics in medicine and biology*, vol. 47, no. 19, pp. 3503-17, Oct. 2002.

## **Appendix A - CAD Drawings**



DALHOUSIE BIOMEDICAL  
ENGINEERING

TITLE: T4 Vertebra

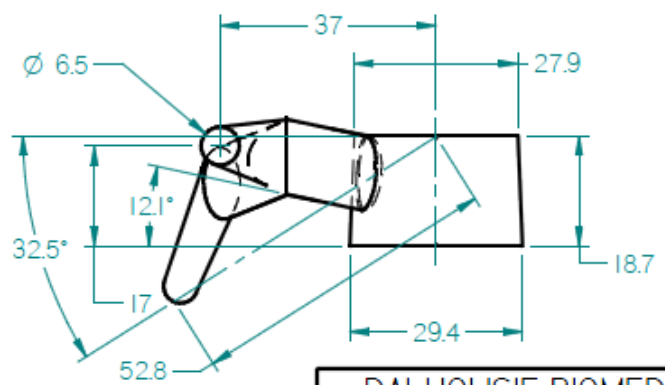
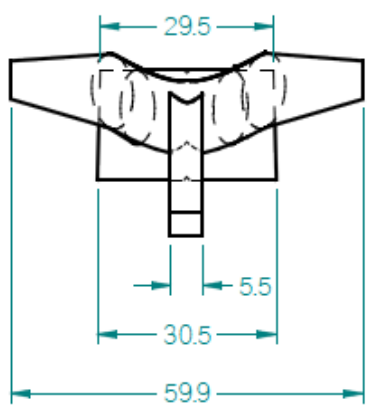
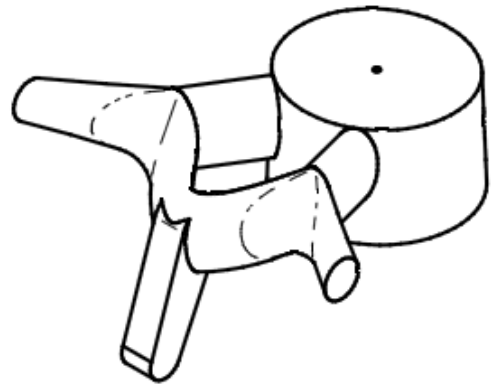
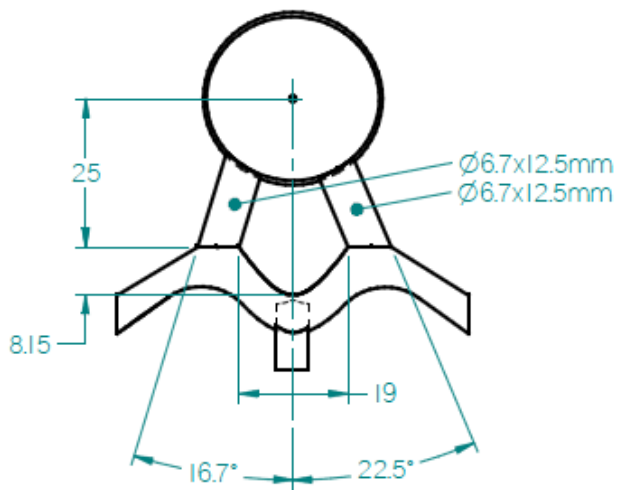
SIZE A DRAWN BY: Alan Spurway REV 1

DATE: 03/25/2011

SCALE: 1:1 SHEET 1 OF 1

UNLESS OTHERWISE SPECIFIED  
DIMENSIONS ARE IN MILLIMETERS

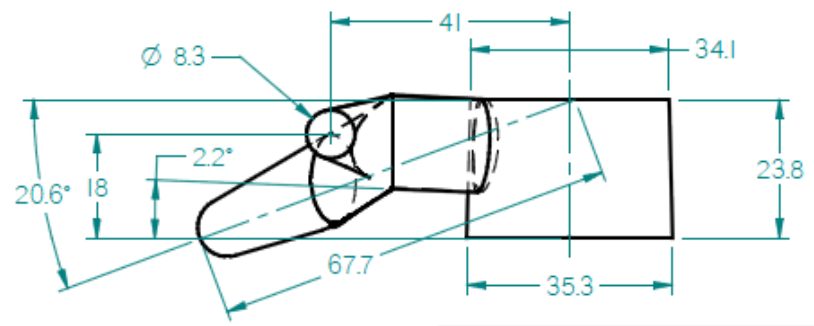
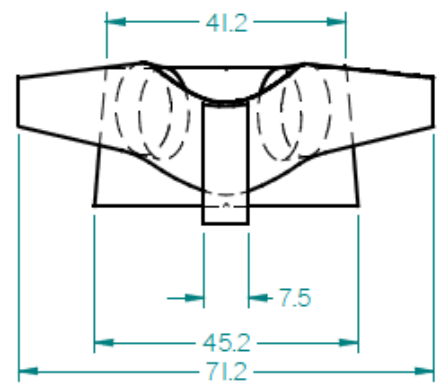
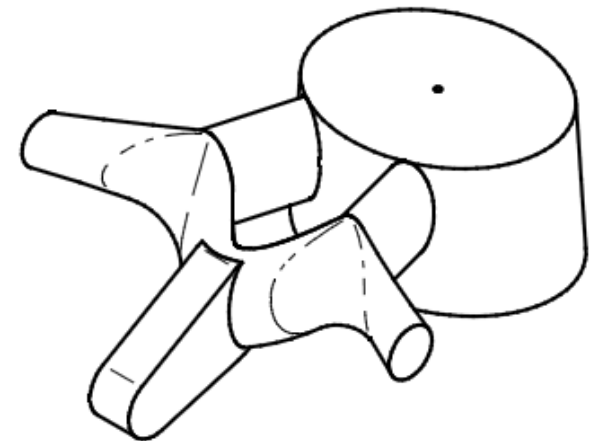
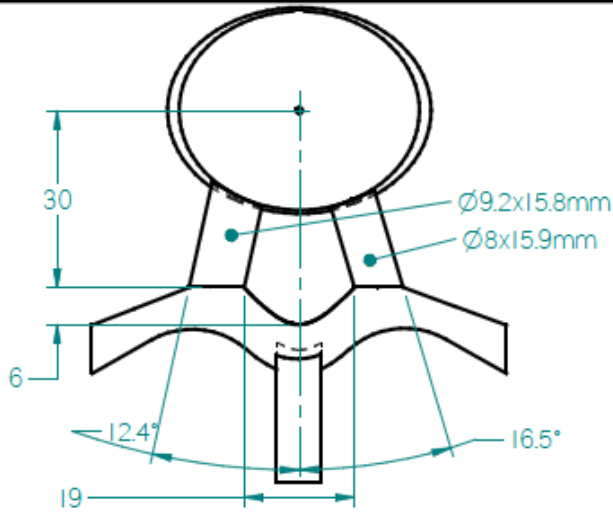
SOLID EDGE ACADEMIC CO.



DALHOUSIE BIOMEDICAL ENGINEERING		
TITLE: <b>T8 Vertebra</b>		
SIZE A	DRAWN BY: Alan Spurway	REV 1
DATE: 03/25/2011		
SCALE: 1:1		SHEET 1 OF 1

UNLESS OTHERWISE SPECIFIED  
DIMENSIONS ARE IN MILLIMETERS

SOLID EDGE ACADEMIC CO.



DALHOUSIE BIOMEDICAL ENGINEERING		
TITLE: LI Vertebra		
SIZE A	DRAWN BY: Alan Spurway	REV 1
DATE: 03/24/2011		
SCALE: 1:1		SHEET 1 OF 1

UNLESS OTHERWISE SPECIFIED  
DIMENSIONS ARE IN MILLIMETERS

SOLID EDGE ACADEMIC CO

# Appendix B - Thesis Coordinate Systems

Throughout this thesis there have been eight distinct coordinate systems used. These systems, along with several specialized systems, are defined in this appendix.

## B.1 Vertebral Coordinate Systems

Each vertebral model has its own, distinct coordinate system that was used for model construction, rigid body marker placement and for model placement in the larger spinal model. The origin for each coordinate system is the center of the inferior end plate of the vertebral body. For each vertebra the three axes are orientated so that the positive X-axis is left, positive Y-axis is superior and the positive Z-axis is anterior. The three coordinate systems are shown in Figure B.1.

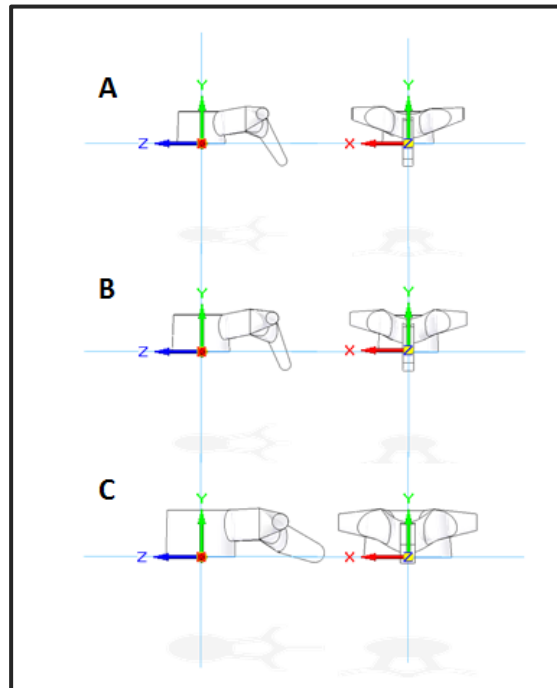


Figure B.1: Vertebral Coordinate Systems. A) T4 Coordinate System, B) T8 Coordinate System, C) L1 Coordinate System

## B.2 T8 Rotational Coordinate System

To create accuracy migrations that produce only rotational migrations in MB-RSA the origin of the migration origin for the T8 vertebral model had to be translated to the centroid of the marker cluster. The centroid of the T8 marker cluster is located at  $\langle 0.14, 10.07, -25.21 \rangle$  mm in the T8 Vertebral Coordinate System. The orientation of the T8 Rotational Coordinate System is in line with the spinal coordinate system with: X - Left, Y - Superior, Z - Anterior of the patient. The T8 Rotational Coordinate System is shown in Figure B.2.

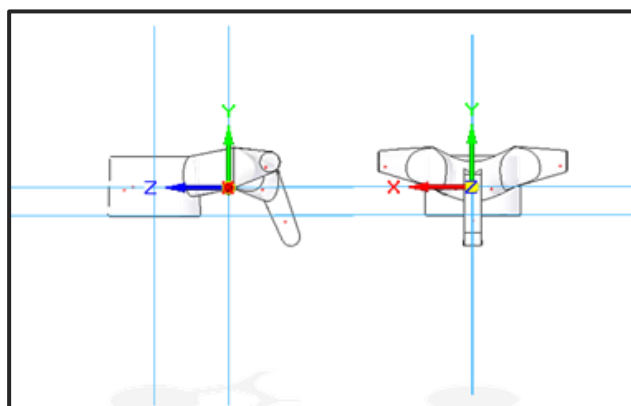


Figure B.2: T8 Rotational Coordinate System.



### B.3 Spinal Coordinate System

The Spinal Coordinate System pertains to the coordinate system of the full simulated spine model. It describes the placement of the three vertebral models and is used to define the migrations associated with the accuracy assessment present in this thesis. The position of the Spinal Coordinate System origin and axis alignment is shown in Figure B.3. The axes are orientated so that the X-axis is positive to the left, the Y-axis is positive in the superior direction and the Z-axis is positive anteriorly. The origin of this coordinate system was located as the origin of the L1 Vertebral Coordinate System.

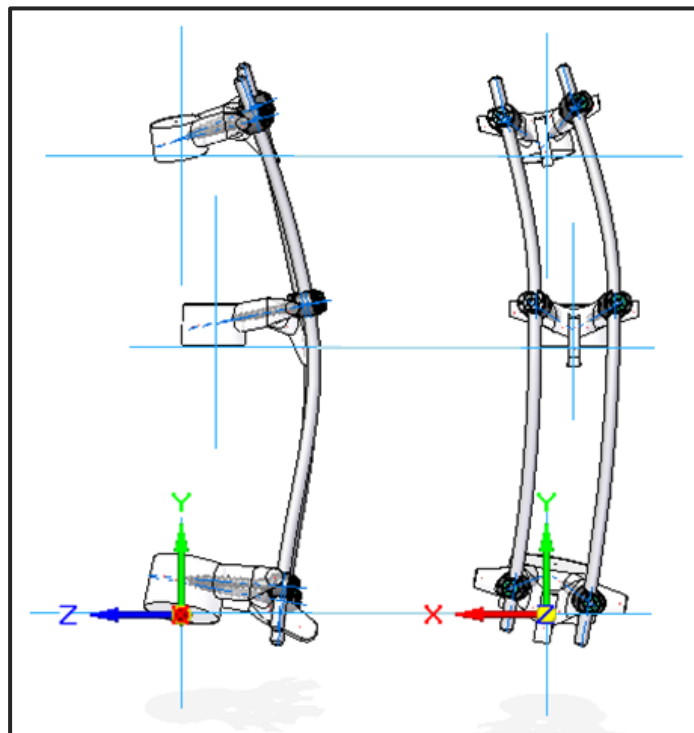


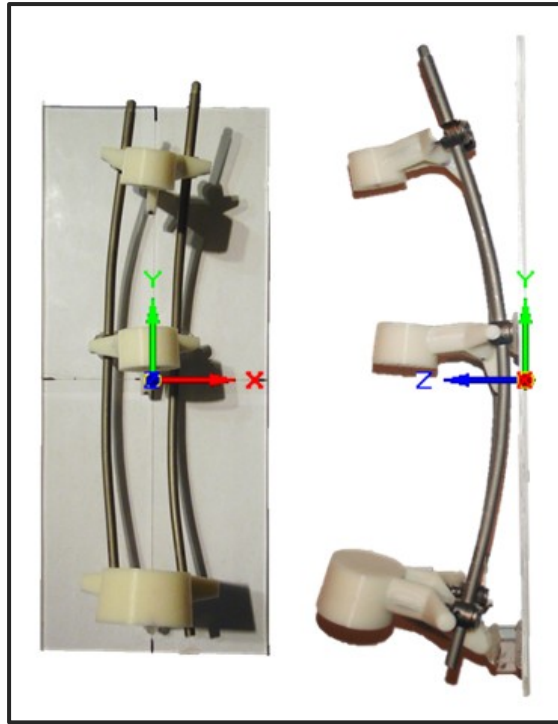
Figure B.3: Spinal Coordinate System

### **B.3.1 Precision Movement Coordinate Systems**

The rotations used during precision assessments required a centralized rotation origin to keep the marker clusters of the superior and inferior vertebral models within the RSA diagnostic imaging volume. Without these translated coordinate systems the spine model would move outside of the image, making migration analysis impossible.

#### ***B.3.1.1 Phantom Model Precision Coordinate System***

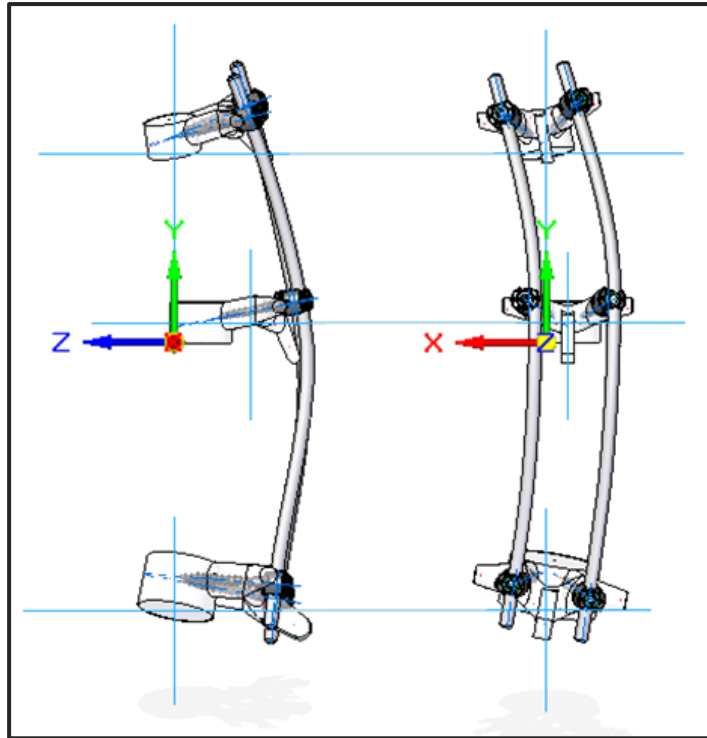
The phantom model precision coordinate system was defined to provide an easily identifiable reference for translations and rotations undertaken during the phantom model precision assessment. The location of the coordinate system origin was also designed to keep the phantom model centered within the RSA diagnostic imaging area during the 6° precision rotations. This coordinate system has the same orientation as that of the Spinal Coordinate System with the X-axis pointing left, the Y-axis pointing superiorly and the Z-axis pointing anteriorly. The location of the translated coordinate system origin was nominally defined as <1.99, 116.75, -82.63>mm in the Spinal Coordinate System. The translated coordinate system origin is shown in Figure B.4. This coordinate system was used for the all rotational movements of the simulation validation procedure.



**Figure B.4: Location of the translated origin used for the rotational precision assessment of the phantom spinal model.**

### ***B.3.1.2 Simulated Model Precision Coordinate System***

The simulated model precision coordinate system was defined to keep the spinal model centered within the RSA diagnostic imaging area during the 10° rotations undertaken to assess the rotational accuracy of the three origin styles. This coordinate system has the same orientation as that of the Spinal Coordinate System with the X-axis pointing left, the Y-axis pointing superiorly and the Z-axis pointing anteriorly. The location of the translated coordinate system origin was defined as  $\langle 0.0, 156.5, 0.0 \rangle$  mm in the Spinal Coordinate System. The translated coordinate system origin is shown in Figure B.5.



**Figure B.5: Location of the translated origin used for the rotational precision assessment of the simulated spinal model.**

#### **B.4 RSA Origin Style Coordinate Systems**

The measurement of the intervertebral manipulations of the spine was conducted using three distinct coordinate systems passed on the origin style used. These coordinate systems were defined by the MB-RSA software and patient orientation. With the patient placed so that the Spinal Coordinate System native to the spine model aligns with the global RSA Coordinate System the subsequent origin style coordinate systems are also aligned with the Spinal Coordinate System. The locations of the origins to these coordinate systems are located at the centroid of their respective marker clusters.

### B.4.1 Caudal Coordinate System

The Caudal Coordinate System was used to define intervertebral migrations when using the Caudal Origin Style. This coordinate system has a single origin located at the centroid of the L1 migration origin marker cluster. The orientation of the Caudal Coordinate System aligns with that of the Spinal Coordinate System with the X-axis pointing left, the Y-axis pointing in a superior direction and the Z-axis pointing anteriorly as shown in Figure B.6. Since this coordinate system and associated origin style both use the L1 vertebra as the migration origin all recorded measurements match the migrations induced using the Spinal Coordinate System.

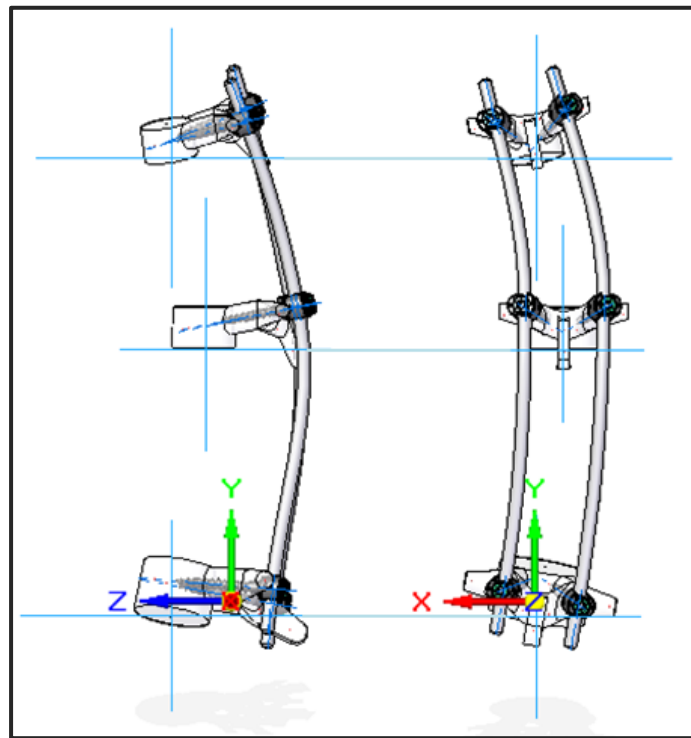
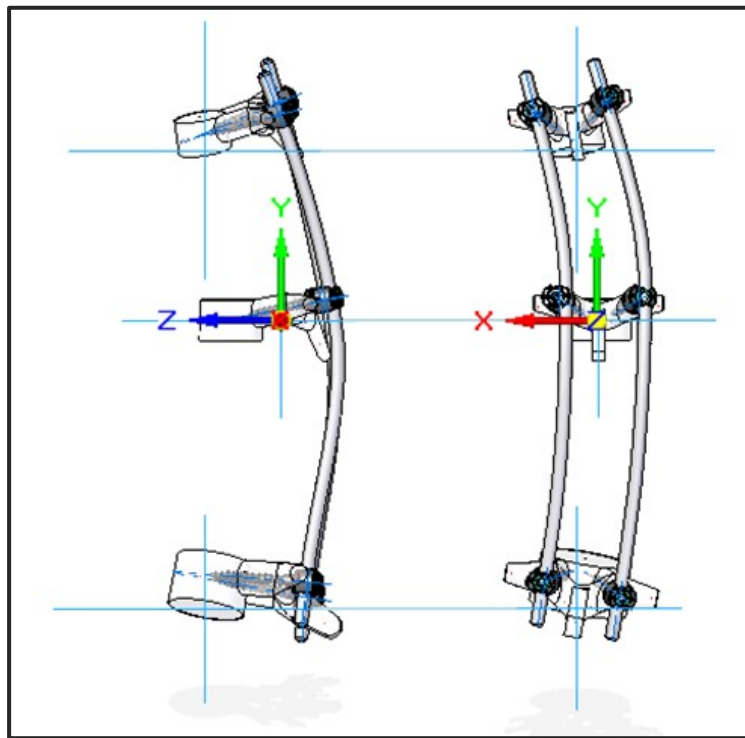


Figure B.6: The Caudal Coordinate System. The origin of this coordinate system is located at the centroid of the L1 marker cluster.

## B.4.2 Apex Coordinate System

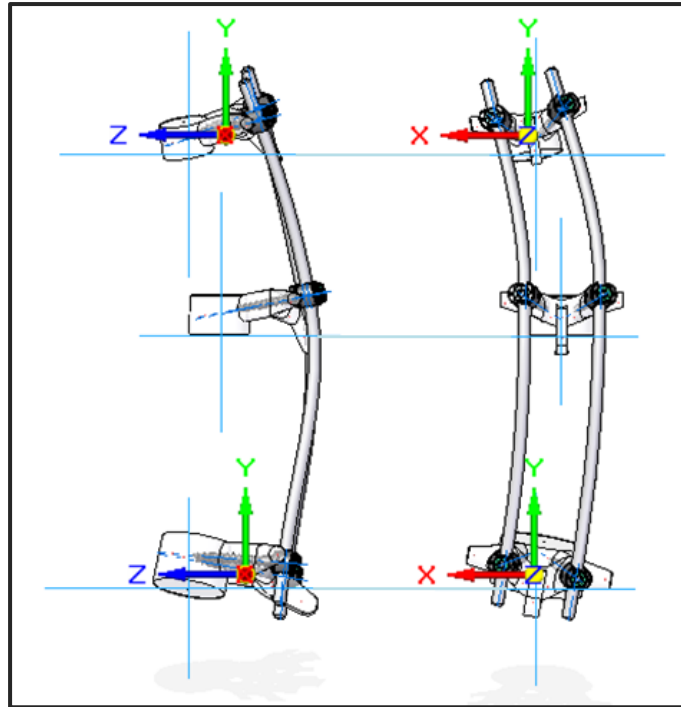
The Apex Coordinate System was used to define intervertebral migrations when using the Apex Origin Style. This coordinate system has a single origin located at the centroid of the T8 migration origin marker cluster. The orientation of the Apex Coordinate System aligns with that of the Spinal Coordinate System with the X-axis pointing left, the Y-axis pointing in a superior direction and the Z-axis pointing anteriorly as shown in Figure B.7. Due to the inversion of the migratory and origin vertebra the measurement of the migration of the L1 vertebra with respect to the T8 vertebra will be subsequently inverted from the induced migrations of the T8 vertebra.



**Figure B.7: Apex Coordinate System. The origin of this coordinate system is located at the centroid of the T8 marker cluster.**

### **B.4.3 Dual Coordinate System**

The Dual Coordinate System was used to define intervertebral migrations when using the Dual Origin Style. Unlike the other two origin styles, this coordinate system contains two sub-coordinate systems: the superior and inferior coordinate systems. This is due to the use of two migration origins. The origin for each sub-coordinate system is located at the centroid of the marker clusters that make up the two migration origins. The superior origin is located at the centroid of the T4 vertebra while the inferior origin is located at the centroid of the L1 vertebra. The alignments of the two coordinate systems both parallel the directions of the Spinal Coordinate System where the X-axis is left, the Y-axis is superior and the Z-axis is anterior as shown in Figure B.8. The superior coordinate system, due to the reversal of the migratory and origin vertebrae will record the migrations of the T8 vertebra opposite than what was inputted using the Spinal Coordinate System.



**Figure B.8: The Superior and Inferior Coordinate Systems which make up the Dual Coordinate System.**

## **B.5 RSA Coordinate System**

The RSA Coordinate System is the global coordinate system defining the overall diagnostic area. The coordinate system is defined by the calibration box native to the Halifax RSA Suite and the MB-RSA software. The origin of this coordinate system is the lower left marker of the fiducial plane with the fiducial plane forming the X-Y plane of the system. The Z axis protrudes out of the image plane, creating the RSA diagnostic space. The RSA Coordinate System is shown in both Figure B.9 and Figure B.10. The RSA Coordinate System is used to locate the x-ray sources and rigid body markers implanted into the spine model. These locations are used to calculate intervertebral migrations.



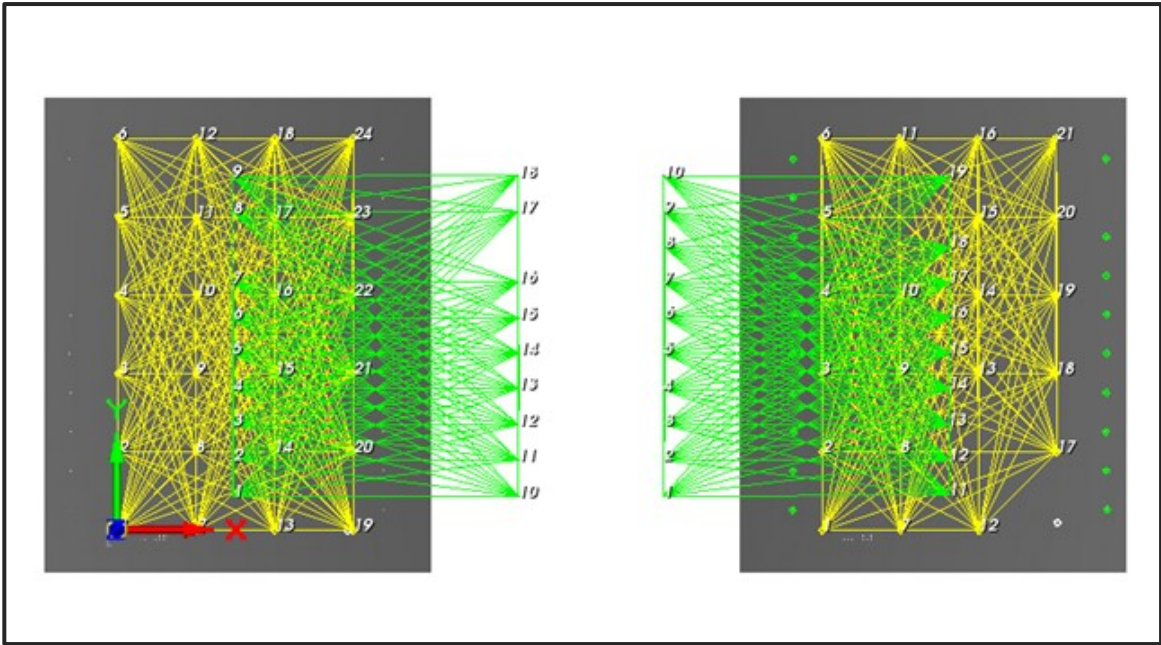


Figure B.9: Front view of the RSA Coordinate System. The yellow grids indicate the positions of the markers in the fiducial plane while the green grids show the positions of the markers in the control plane. The green circles on the image are the projected positions of the control markers. The images are blank simulations of the calibration box with the colours inverted.

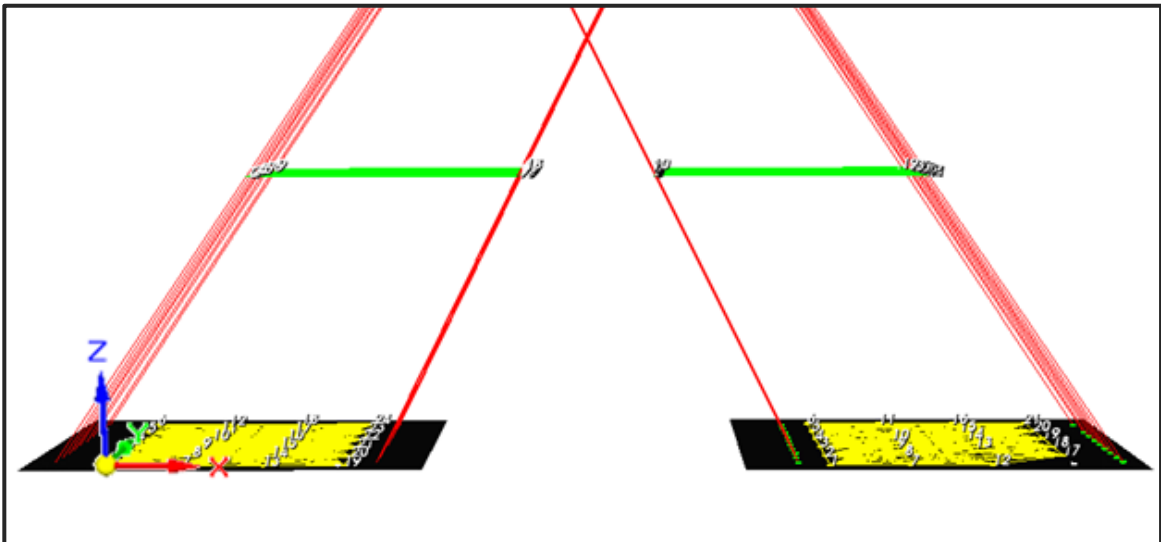


Figure B.10: Bottom view of the RSA Coordinate System. The black planes are the images with the yellow fiducial markers shown. The green planes are the locations of the control markers with the red lines showing the projection lines of the control markers running from the x-ray sources to the images. The images are blank simulations of the calibration box with the colours inverted.

# Appendix C - Simulation Process

## C.1 Programs Used:

SolidEdge with Synchronous Technology 2 (Siemens, Germany)

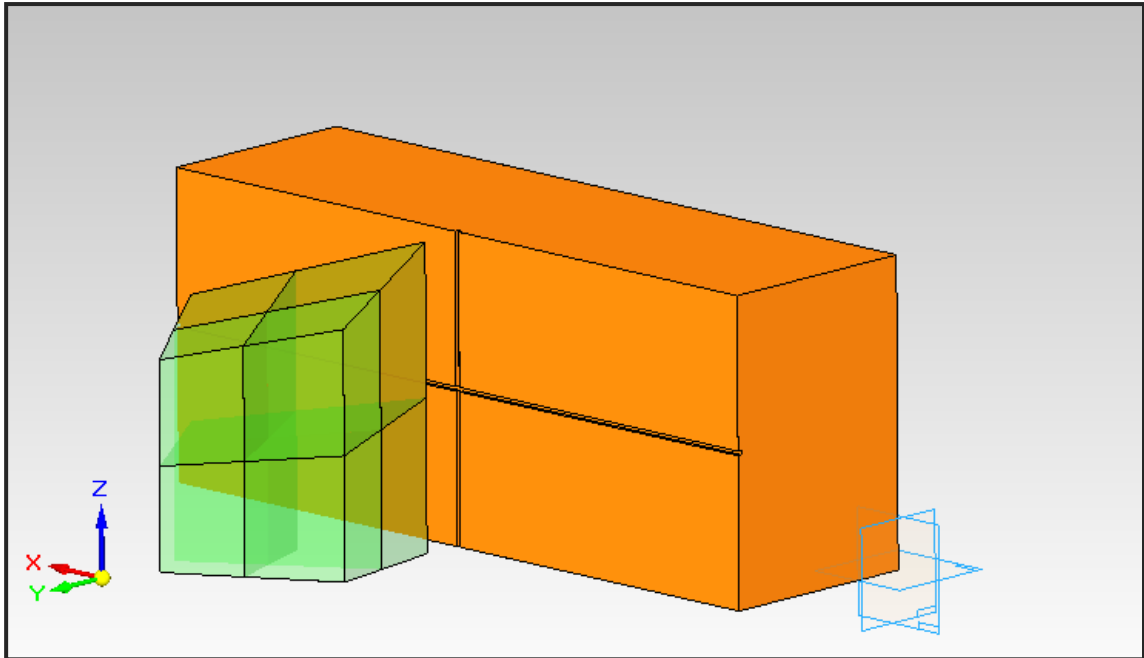
Rhinoceros - Service Release 8 (McNeel North America, USA)

POV-Ray 3.7 (Beta Release) (Persistence of Vision Raytracer Pty. Ltd.)

## C.2 RSA Setup

\* Note: coordinate systems shown in the following images are the coordinate systems used in the Solid Edge software, not the anatomically defined systems described in Appendix B.

**SolidEdge** – Construct a calibration box stand-in for the CAD environment using dimensions specified for the RSA system to be simulated. Ensure that the calibration box is oriented so that the bottom right corner is located at the CAD environment origin as shown in Figure C.1. The Z axis should point up and the Y should point toward the front of the calibration box. This alignment is due to the left hand coordinate system used by POV-Ray. The green area shown in Figure C.1 is the volume that will appear on both image plates.



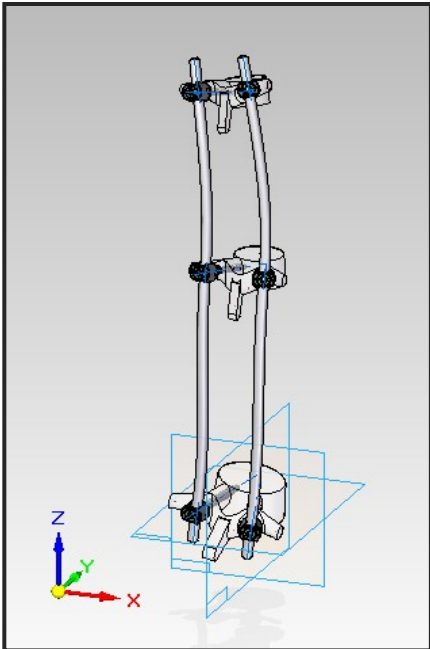
**Figure C.1: Calibration box (orange) and imaging area (green) in the CAD environment.**

**POV-Ray** – Construct a simulated calibration box using the marker locations and size as specified by the layout in the physical calibration box. The X coordinate of each marker must be of the must be entered as:

$$x_{POV} = L_{nom} - x_{CB} \quad \text{Equation C.1}$$

where  $x_{POV}$  is the x coordinate in POV-Ray,  $x_{CB}$  is the x coordinate in the calibration box and  $L_{nom}$  is the nominal length of the calibration box in the x-direction. Both the Y and Z coordinates stay the same. This process allows for the matching of the CAD and RSA right hand coordinate system with the left hand system used by POV-Ray.

### C.3 Model Construction and Placement



**Figure C.2: Image of the fully assembled spine model.**

Build all required models in Solid Edge. For the spine simulations this consisted of 38 separate models: 3 vertebrae, 6 pedicle screws, 6 set screws, 2 fixation rods, and 21 implanted tantalum markers. Assemble all components into a single assembly. The origin of this assembly should be in a desirable location for later placement in the RSA environment (planes shown in Figure C.2).

## C.4 Placement in the RSA Environment

In the CAD RSA environment, place three orthogonal reference planes in the desired location of the model origin [Figure C.3].

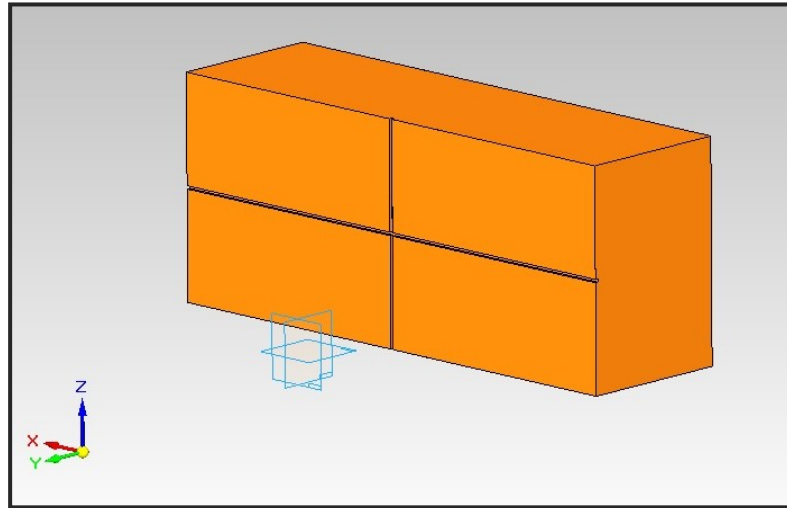


Figure C.3: Planes used to locate model to be imaged.

Import simulated model and mate model origin planes with placement planes, example shown in Figure C.4.

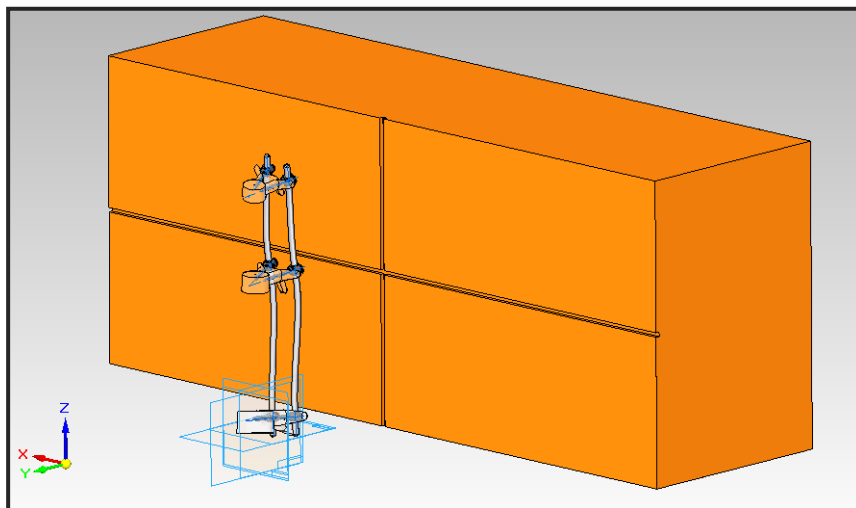


Figure C.4: Simulated model located within RSA environment.

## C.5 File Conversion

Before saving the Solid Edge assembly file, delete all parts you do not wish to render. This is generally the calibration box and imaging area. Save the assembly file as a STEP Document (.stp or .step file extension). Open the .stp file in Rhinoceros SR8 and save the file as a .pov file in a separate *empty folder*. Use a single letter as a filename. Throughout this project “A.pov” was used. When asked, select the “Create separate .INC file for each object” option. A separate file will be created for each component of the simulated model (each Solid Edge part). When prompted, slide the indicator to the “more polygons” setting so that the largest number of polygons will be used to create the components.

## C.6 POV-Ray Processing

Open the .pov file in POV-Ray and replace the following:

```
// POV-Ray file generated from Rhinoceros.

camera {
  perspective
  location <784.987, 593.639, -199.165>
  right <1.15471, 1.19804e-17, 0.666652>
  up <-0.249996, 0.866024, 0.433018>
  direction <-0.433002, -0.500003, 0.750004>
  angle 35.9886
  /*
  // to get an image that's the same as the viewport in Rhino,
  // uncomment this section and render with command line options (alt+c):
  // +w348 +h327
  right <603.198, 6.25835e-15, 348.246>
  up <-163.642, 566.88, 283.444>
  direction <-0.433002, -0.500003, 0.750004>
  */
  look_at <424.516, 177.392, 425.206>
}

background { color rgb <0.627451, 0.627451, 0.627451> }
global_settings { ambient_light color rgb <0, 0, 0> }

// default light
light_source { <300513, 346699, -519358> color rgb <1,1,1> }
```

With:

```
#version 3.6;
global_settings {max_trace_level 256}

#include "colors.inc"
#include "RSAMaterials2.inc"

//Calibration Box
#include "CalBox.inc"

//Camera Locatoins
background {color Black}
camera {
  perspective
  // location <100, 175, 633> // Right Image
  // look_at <100, 175, -20> // Right Image
  location <745, 175, 633> // Left Image
  look_at <745, 175, -20> // Left Image
  right <.814,0,0>
  up <0,1,0>
  angle 30
}
```

```

// X-Ray Tubes

light_source {
// <1024, 175, 1580> // Right Image
  <-179, 175, 1580> // Left Image
  color <1,1,1>
// area_light <2.6, 0, -1.5>, <0, 3, 0>, 5, 5 // Right Image
  area_light <-2.6, 0, -1.5>, <0, 3, 0>, 5, 5 // Left Image
  adaptive 1
}

// X-Ray Plates

//Left Image Plate
box {
  <-75,-41,-20>
  <275,391,-21>
  pigment {color <1,1,1>}
}

//Right Image Plate
box {
  <570,-41,-20>
  <920,391,-21>
  pigment {color <1,1,1>}
}

```

This code recreates the RSA environment with the x-ray foci located 1.6m above the detectors at an angle of 30°.

Each object code needs to be converted from:

```

// (#2911) Right Rod (Object1)
#declare Object1Material = material {
texture {
  pigment { color rgbf <1, 1, 1, 0> }
  finish { ambient 1 diffuse 1 }
}
}
#declare Object1 = object {
  #include "A.inc"
}
object { Object1 material { Object1Material }}

```

To:

```

// (#3169) Right Rod (Object1)

#declare Object1 = object {
  #include "A1.inc"
}
object { Object1 material { CoCr }no_image}

```



When converting the object code to the required format, the object materials are specified. The materials and their call functions are:

<b>Material</b>	<b>Call Function</b>
<b>Bone</b>	Bone
<b>Cobalt-Chrome</b>	CoCr
<b>Titanium</b>	Ti
<b>Tantalum</b>	Tant

To produce a left and right image the file will have to be rendered twice. Once with the “//Right Image” tagged lines activated and once with the “//Left Image” tagged lines.

## **C.7 RS Assessment**

Process the image pair as with any other RSA exam making sure to check the “Black on White” box when detecting markers on the calibration tab.

# Appendix D - Programming Code

## D.1 POV-Ray Code

The POV-Ray code shown here is for the left image of the image pair. For the right image the lines tagged “//Right Image” need to be activated while the “//Left Image” tagged lines, deactivated. The calibration box coding contains proprietary information on marker placement and is not included in this thesis.

### D.1.1 RSA Image Code

```
#version 3.6;
global_settings {max_trace_level 256}

#include "colors.inc"
#include "RSAMaterials2.inc"

//Calibration Box
#include "CalBox.inc"

//Camera Locatoins
background {color Black}
camera {
  perspective
  // location <100, 175, 633>      // Right Image
  // look_at <100, 175, -20>      // Right Image
  location <745, 175, 633>      // Left Image
  look_at <745, 175, -20>      // Left Image
  right <.814,0,0>
  up <0,1,0>
  angle 30
}

// X-Ray Tubes

light_source {
  // <1024, 175, 1580>           // Right Image
  <-179, 175, 1580>           // Left Image
  color <1,1,1>
  // area_light <2.6, 0, -1.5>, <0, 3, 0>, 5, 5 // Right Image
  area_light <-2.6, 0, -1.5>, <0, 3, 0>, 5, 5 // Left Image
  adaptive 1
}
```

```

// X-Ray Plates

//Left Image Plate
box {
  <-75,-41,-20>
  <275,391,-21>
  pigment {color <1,1,1>}
}

//Right Image Plate
box {
  <570,-41,-20>
  <920,391,-21>
  pigment {color <1,1,1>}
}

//Phantom Model

// (#3169) Right Rod (Object1)

#declare Object1 = object {
  #include "A1.inc"
}
object { Object1 material { CoCr }no_image}

// (#3172) Left Rod (Object2)

#declare Object2 = object {
  #include "A2.inc"
}
object { Object2 material { CoCr }no_image}

// (#3160) T4 Vertebrae (Object3)

#declare Object3 = object {
  #include "A3.inc"
}
object { Object3 material { Bone }no_image}

// (#3250) 5.00x30 Monoaxial Screw (Object4)

#declare Object4 = object {
  #include "A4.inc"
}
object { Object4 material { Ti }no_image}

// (#3253) 5.00x30-Monoaxial-Screw-SET (Object5)

#declare Object5 = object {
  #include "A5.inc"
}
object { Object5 material { Ti }no_image}

```

```

// (#3250) 5.00x30 Monoaxial Screw (Object6)

#declare Object6 = object {
  #include "A6.inc"
}
object { Object6 material { Ti }no_image}

// (#3253) 5.00x30-Monoaxial-Screw-SET (Object7)

#declare Object7 = object {
  #include "A7.inc"
}
object { Object7 material { Ti }no_image}

// (#3247) Tantalum Bead (Object8)

#declare Object8 = object {
  #include "A8.inc"
}
object { Object8 material { Tant }no_image}

// (#3247) Tantalum Bead (Object9)

#declare Object9 = object {
  #include "A9.inc"
}
object { Object9 material { Tant }no_image}

// (#3247) Tantalum Bead (Object10)

#declare Object10 = object {
  #include "A10.inc"
}
object { Object10 material { Tant }no_image}

// (#3247) Tantalum Bead (Object11)

#declare Object11 = object {
  #include "A11.inc"
}
object { Object11 material { Tant }no_image}

// (#3247) Tantalum Bead (Object12)

#declare Object12 = object {
  #include "A12.inc"
}
object { Object12 material { Tant }no_image}

// (#3247) Tantalum Bead (Object13)

#declare Object13 = object {
  #include "A13.inc"
}
object { Object13 material { Tant }no_image}

```

```

// (#3247) Tantalum Bead (Object14)

#declare Object14 = object {
  #include "A14.inc"
}
object { Object14 material { Tant }no_image}

// (#3265) T8 Vertebrae (Object15)

#declare Object15 = object {
  #include "A15.inc"
}
object { Object15 material { Bone }no_image}

// (#3241) 5.00x35 Monoaxial Screw (Object16)

#declare Object16 = object {
  #include "A16.inc"
}
object { Object16 material { Ti }no_image}

// (#3244) 5.00x35-Monoaxial-Screw-SET (Object17)

#declare Object17 = object {
  #include "A17.inc"
}
object { Object17 material { Ti }no_image}

// (#3241) 5.00x35 Monoaxial Screw (Object18)

#declare Object18 = object {
  #include "A18.inc"
}
object { Object18 material { Ti }no_image}

// (#3244) 5.00x35-Monoaxial-Screw-SET (Object19)

#declare Object19 = object {
  #include "A19.inc"
}
object { Object19 material { Ti }no_image}

// (#3247) Tantalum Bead (Object20)

#declare Object20 = object {
  #include "A20.inc"
}
object { Object20 material { Tant }no_image}

```

```

// (#3247) Tantalum Bead (Object21)

#declare Object21 = object {
  #include "A21.inc"
}
object { Object21 material { Tant }no_image}

// (#3247) Tantalum Bead (Object22)

#declare Object22 = object {
  #include "A22.inc"
}
object { Object22 material { Tant }no_image}

// (#3247) Tantalum Bead (Object23)

#declare Object23 = object {
  #include "A23.inc"
}
object { Object23 material { Tant }no_image}

// (#3247) Tantalum Bead (Object24)

#declare Object24 = object {
  #include "A24.inc"
}
object { Object24 material { Tant }no_image}

// (#3247) Tantalum Bead (Object25)

#declare Object25 = object {
  #include "A25.inc"
}
object { Object25 material { Tant }no_image}

// (#3247) Tantalum Bead (Object26)

#declare Object26 = object {
  #include "A26.inc"
}
object { Object26 material { Tant }no_image}

// (#3268) L1 Vertebrae (Object27)

#declare Object27 = object {
  #include "A27.inc"
}
object { Object27 material { Bone }no_image}

// (#3256) 6.00x40 Monoaxial Screw (Object28)

#declare Object28 = object {

```

```

#include "A28.inc"
}
object { Object28 material { Ti }no_image}

// (#3259) 6.00x40-Monoaxial-Screw-SET (Object29)

#declare Object29 = object {
#include "A29.inc"
}
object { Object29 material { Ti }no_image}

// (#3256) 6.00x40 Monoaxial Screw (Object30)

#declare Object30 = object {
#include "A30.inc"
}
object { Object30 material { Ti }no_image}

// (#3259) 6.00x40-Monoaxial-Screw-SET (Object31)

#declare Object31 = object {
#include "A31.inc"
}
object { Object31 material { Ti }no_image}

// (#3247) Tantalum Bead (Object32)

#declare Object32 = object {
#include "A32.inc"
}
object { Object32 material { Tant }no_image}

// (#3247) Tantalum Bead (Object33)

#declare Object33 = object {
#include "A33.inc"
}
object { Object33 material { Tant }no_image}

// (#3247) Tantalum Bead (Object34)

#declare Object34 = object {
#include "A34.inc"
}
object { Object34 material { Tant }no_image}

// (#3247) Tantalum Bead (Object35)

#declare Object35 = object {
#include "A35.inc"
}
object { Object35 material { Tant }no_image}

// (#3247) Tantalum Bead (Object36)

```

```
#declare Object36 = object {
  #include "A36.inc"
}
object { Object36 material { Tant }no_image}

// (#3247) Tantalum Bead (Object37)

#declare Object37 = object {
  #include "A37.inc"
}
object { Object37 material { Tant }no_image}

// (#3247) Tantalum Bead (Object38)

#declare Object38 = object {
  #include "A38.inc"
}
object { Object38 material { Tant }no_image}

//END
```



## D.1.2 Material Attenuation Properties

The material attenuation values shown here were developed as “best match” conditions based on real x-rays taken of a phantom model. As it was beyond the scope of this project to create real world attenuation conditions, future work is required to refine the material attenuation properties to produce photo-real image contrast.

```
// ##### RSA Material Attenuation #####  
  
#version 3.6;  
  
//Bone  
#declare Bone=material{  
    texture { pigment { color rgbt < 0, 0, 0, .97>} }  
    interior { fade_distance 100  
                fade_power 2 }  
}  
  
// Tantalum  
#declare Tant=material{  
    texture { pigment { color rgbt < 0, 0, 0, 1>} }  
    interior { fade_distance .21  
                fade_power 2 }  
}  
  
//Titanium  
#declare Ti=material{  
    texture { pigment { color rgbt < 0, 0, 0, .9>} }  
    interior { fade_distance 4.2  
                fade_power 2 }  
}  
  
//Cobalt Chrome  
#declare CoCr=material{  
    texture { pigment { color rgbt < 0, 0, 0, .75>} }  
    interior { fade_distance 2.7  
                fade_power 2 }  
}  
  
//END
```

## D.2 MatLab Code

### D.2.1 RSA Calculations – Global Reference Frame

#### D.2.1.1 Translational

This code uses the matrix calculations in Section ### to report the migrations of the T8 vertebra. This example utilized the inferior image pair of an inferior fusion failure of 5mm in the X direction. At the end of the program the results are given as well as the error between this method and the MB-RSA calculated results.

```
clc
clear
%% Global Coord Sys
Xg = [1,0,0];
Yg = [0,1,0];
Zg = [0,0,1];

%% Raw Marker Data

%MB-RSA Calculated Values
MBRSA = [5.0297 -0.0009 0.0055 -0.0064 0.0536 -0.0378];

%L1 at Time 0
L1o = [385.616 89.727 516.525
       421.117 78.7006 504.620
       450.592 101.353 516.513
       413.967 85.9599 519.021
       426.023 88.136 519.045
       422.252 101.941 567.842];

CentL1o = sum(L1o)./6;

%L1 at Time 1
L1i = [385.616 89.727 516.525
       421.118 78.7006 504.620
       450.592 101.353 516.513
       413.967 85.9598 519.020
       426.024 88.1359 519.044
       422.200 101.960 567.887];

CentL1i = sum(L1i)./6;

%T8 at Time 0
T8o = [379.040 257.003 509.614
       407.032 239.469 503.434
       435.009 256.787 509.662
       401.046 249.726 510.637
       412.546 249.730 510.581
       406.956 249.585 554.651
```

```

409.744 250.621 551.856];

CentT8o = sum(T8o)./7;

%T8 at Time 1
T8i = [384.024 257.016 509.592
        412.043 239.477 503.432
        440.027 256.758 509.626
        406.037 249.724 510.638
        417.548 249.732 510.577
        411.959 249.581 554.652
        414.788 250.640 551.874];

CentT8i = sum(T8i)./7;

%% Pose Matrix Calculations
%L1 at Time 0
xL1o = [L1o(3,:)-L1o(1,:)];
ztempL1o = [L1o(6,:)-L1o(1,:)];
yL1o = cross(xL1o,ztempL1o);
zL1o = cross(yL1o,xL1o);

XL1o = xL1o/norm(xL1o);
YL1o = yL1o/norm(yL1o);
ZL1o = zL1o/norm(zL1o);

PL1o = [dot(XL1o,Xg) dot(YL1o,Xg) dot(ZL1o,Xg)
        dot(XL1o,Yg) dot(YL1o,Yg) dot(ZL1o,Yg)
        dot(XL1o,Zg) dot(YL1o,Zg) dot(ZL1o,Zg)];

%L1 at Time 1
xL1i = [L1i(3,:)-L1i(1,:)];
ztempL1i = [L1i(6,:)-L1i(1,:)];
yL1i = cross(xL1i,ztempL1i);
zL1i = cross(yL1i,xL1i);

XL1i = xL1i/norm(xL1i);
YL1i = yL1i/norm(yL1i);
ZL1i = zL1i/norm(zL1i);

PL1i = [dot(XL1i,Xg) dot(YL1i,Xg) dot(ZL1i,Xg)
        dot(XL1i,Yg) dot(YL1i,Yg) dot(ZL1i,Yg)
        dot(XL1i,Zg) dot(YL1i,Zg) dot(ZL1i,Zg)];

%T8 at Time 0
xT8o = [T8o(3,:)-T8o(1,:)];
ztempT8o = [T8o(6,:)-T8o(1,:)];
yT8o = cross(xT8o,ztempT8o);
zT8o = cross(yT8o,xT8o);

XT8o = xT8o/norm(xT8o);
YT8o = yT8o/norm(yT8o);
ZT8o = zT8o/norm(zT8o);

PT8o = [dot(XT8o,Xg) dot(YT8o,Xg) dot(ZT8o,Xg)
        dot(XT8o,Yg) dot(YT8o,Yg) dot(ZT8o,Yg)
        dot(XT8o,Zg) dot(YT8o,Zg) dot(ZT8o,Zg)];

%T8 at Time 1
xT8i = [T8i(3,:)-T8i(1,:)];
ztempT8i = [T8i(6,:)-T8i(1,:)];
yT8i = cross(xT8i,ztempT8i);

```

```

zT8i      = cross(yT8i,xT8i);

XT8i = xT8i/norm(xT8i);
YT8i = yT8i/norm(yT8i);
ZT8i = zT8i/norm(zT8i);

PT8i = [dot(XT8i,Xg) dot(YT8i,Xg) dot(ZT8i,Xg)
         dot(XT8i,Yg) dot(YT8i,Yg) dot(ZT8i,Yg)
         dot(XT8i,Zg) dot(YT8i,Zg) dot(ZT8i,Zg)];

%% RSA Calculations

%Step 1
TL1 = PL1i*PL1o';

%Step 2
T8icor = [[TL1*[T8i(1,:)]]'
          [TL1*[T8i(2,:)]]'
          [TL1*[T8i(3,:)]]'
          [TL1*[T8i(4,:)]]'
          [TL1*[T8i(5,:)]]'
          [TL1*[T8i(6,:)]]'
          [TL1*[T8i(7,:)]]'];

%Step 3
T8oshift = [T8o(1,.)-CentT8o
            T8o(2,.)-CentT8o
            T8o(3,.)-CentT8o
            T8o(4,.)-CentT8o
            T8o(5,.)-CentT8o
            T8o(6,.)-CentT8o
            T8o(7,.)-CentT8o];

T8icorshift = [T8icor(1,.)-CentT8o
               T8icor(2,.)-CentT8o
               T8icor(3,.)-CentT8o
               T8icor(4,.)-CentT8o
               T8icor(5,.)-CentT8o
               T8icor(6,.)-CentT8o
               T8icor(7,.)-CentT8o];

%Step 4
%T8oshift
xT8oshift      = [T8oshift(3,.)-T8oshift(1,.)];
ztempT8oshift = [T8oshift(6,.)-T8oshift(1,.)];
yT8oshift      = cross(xT8oshift,ztempT8oshift);
zT8oshift      = cross(yT8oshift,xT8oshift);

XT8oshift = xT8oshift/norm(xT8oshift);
YT8oshift = yT8oshift/norm(yT8oshift);
ZT8oshift = zT8oshift/norm(zT8oshift);

CentT8oshift = sum(T8oshift)./7;

PT8oshift = [dot(XT8oshift,Xg) dot(YT8oshift,Xg) dot(ZT8oshift,Xg)
             dot(XT8oshift,Yg) dot(YT8oshift,Yg) dot(ZT8oshift,Yg)
             dot(XT8oshift,Zg) dot(YT8oshift,Zg) dot(ZT8oshift,Zg)];

%T8icorshift
xT8icorshift      = [T8icorshift(3,.)-T8icorshift(1,.)];
ztempT8icorshift = [T8icorshift(6,.)-T8icorshift(1,.)];
yT8icorshift      = cross(xT8icorshift,ztempT8icorshift);

```

```

zT8icorshift      = cross(yT8icorshift,xT8icorshift);

XT8icorshift = xT8icorshift/norm(xT8icorshift);
YT8icorshift = yT8icorshift/norm(yT8icorshift);
ZT8icorshift = zT8icorshift/norm(zT8icorshift);

CentT8icorshift = sum(T8icorshift)./7;

PT8icorshift=[dot(XT8icorshift,Xg) dot(YT8icorshift,Xg) dot(ZT8icorshift,Xg)
              dot(XT8icorshift,Yg) dot(YT8icorshift,Yg) dot(ZT8icorshift,Yg)
              dot(XT8icorshift,Zg) dot(YT8icorshift,Zg) dot(ZT8icorshift,Zg)];

TT8io = PT8icorshift*PT8oshift';

%% Results
TransMig = CentT8icorshift-CentT8oshift;

beta = asin(TT8io(3,1));
alpha = asin(((TT8io(3,2))/(cos(beta))));
gamma = asin(((TT8io(2,1))/(cos(beta))));

Rotation = [alpha*(180/pi),beta*(180/pi),gamma*(180/pi)];

Results = [TransMig,Rotation]

>Error from MB-RSA Calculated
Error = Results-MBRSA

```

## Results:

	X (mm)	Y (mm)	Z (mm)	Rx (deg)	Ry (deg)	Rz (deg)
Results	4.9669	0.2280	-0.0832	-0.0358	-0.0099	-0.0428
Error	-0.0628	0.2289	-0.0887	-0.0294	-0.0635	-0.0050

### **D.2.1.2 Rotational**

The code in this section uses the matrix calculations in Section ### to report the migrations of the T8 vertebra. This example utilized the inferior image pair assessing the results of a rotational fusion failure of  $6^\circ$  about the X axis. At the end of the program the results are given as well as the error between this method and the MB-RSA calculated results.

```
clc
clear
%% Global Coord Sys
Xg = [1,0,0];
Yg = [0,1,0];
Zg = [0,0,1];

%% Raw Marker Data

%MB-RSA Calculated Values
MBRSA = [0.0206 -0.0208 0.0288 6.0296 0.0222 -0.0297];

%L1 at Time 0
L1o = [385.616 89.727 516.525
       421.117 78.7006 504.620
       450.592 101.353 516.513
       413.967 85.9599 519.021
       426.023 88.136 519.045
       422.252 101.941 567.842];

CentL1o = sum(L1o)./6;

%L1 at Time 1
L1i = [385.611 89.7258 516.535
       421.113 78.6992 504.628
       450.588 101.352 516.519
       413.962 85.9585 519.03
       426.019 88.1346 519.053
       422.208 101.96 567.873];

CentL1i = sum(L1i)./6;

%T8 at Time 0
T8o = [379.040 257.003 509.614
       407.032 239.469 503.434
       435.009 256.787 509.662
       401.046 249.726 510.637
       412.546 249.730 510.581
       406.956 249.585 554.651
       409.744 250.621 551.856];

CentT8o = sum(T8o)./7;

%T8 at Time 1
T8i = [378.993 258.186 510.289
```

```

407.05 241.41 502.402
435.022 257.927 510.343
401.039 250.885 510.639
412.536 250.888 510.593
406.946 246.09 554.428
409.781 247.393 551.688];

CentT8i = sum(T8i)./7;

%% Pose Matrix Calculations
%L1 at Time 0
xL1o = [L1o(3,:)-L1o(1,:)];
ztempL1o = [L1o(6,:)-L1o(1,:)];
yL1o = cross(xL1o,ztempL1o);
zL1o = cross(yL1o,xL1o);

XL1o = xL1o/norm(xL1o);
YL1o = yL1o/norm(yL1o);
ZL1o = zL1o/norm(zL1o);

PL1o = [dot(XL1o,Xg) dot(YL1o,Xg) dot(ZL1o,Xg)
dot(XL1o,Yg) dot(YL1o,Yg) dot(ZL1o,Yg)
dot(XL1o,Zg) dot(YL1o,Zg) dot(ZL1o,Zg)];

%L1 at Time 1
xL1i = [L1i(3,:)-L1i(1,:)];
ztempL1i = [L1i(6,:)-L1i(1,:)];
yL1i = cross(xL1i,ztempL1i);
zL1i = cross(yL1i,xL1i);

XL1i = xL1i/norm(xL1i);
YL1i = yL1i/norm(yL1i);
ZL1i = zL1i/norm(zL1i);

PL1i = [dot(XL1i,Xg) dot(YL1i,Xg) dot(ZL1i,Xg)
dot(XL1i,Yg) dot(YL1i,Yg) dot(ZL1i,Yg)
dot(XL1i,Zg) dot(YL1i,Zg) dot(ZL1i,Zg)];

%T8 at Time 0
xT8o = [T8o(3,:)-T8o(1,:)];
ztempT8o = [T8o(6,:)-T8o(1,:)];
yT8o = cross(xT8o,ztempT8o);
zT8o = cross(yT8o,xT8o);

XT8o = xT8o/norm(xT8o);
YT8o = yT8o/norm(yT8o);
ZT8o = zT8o/norm(zT8o);

PT8o = [dot(XT8o,Xg) dot(YT8o,Xg) dot(ZT8o,Xg)
dot(XT8o,Yg) dot(YT8o,Yg) dot(ZT8o,Yg)
dot(XT8o,Zg) dot(YT8o,Zg) dot(ZT8o,Zg)];

%T8 at Time 1
xT8i = [T8i(3,:)-T8i(1,:)];
ztempT8i = [T8i(6,:)-T8i(1,:)];
yT8i = cross(xT8i,ztempT8i);
zT8i = cross(yT8i,xT8i);

XT8i = xT8i/norm(xT8i);
YT8i = yT8i/norm(yT8i);
ZT8i = zT8i/norm(zT8i);

```

```

PT8i = [dot(XT8i,Xg) dot(YT8i,Xg) dot(ZT8i,Xg)
        dot(XT8i,Yg) dot(YT8i,Yg) dot(ZT8i,Yg)
        dot(XT8i,Zg) dot(YT8i,Zg) dot(ZT8i,Zg)];

%% RSA Calculations

% Step 1
TL1 = PL1i*PL1o';

%Step 2
T8icor = [[TL1*[T8i(1,:)]]'
          [TL1*[T8i(2,:)]]'
          [TL1*[T8i(3,:)]]'
          [TL1*[T8i(4,:)]]'
          [TL1*[T8i(5,:)]]'
          [TL1*[T8i(6,:)]]'
          [TL1*[T8i(7,:)]]'];

%Step 3
T8oshift = [T8o(1,)-CentT8o
            T8o(2,)-CentT8o
            T8o(3,)-CentT8o
            T8o(4,)-CentT8o
            T8o(5,)-CentT8o
            T8o(6,)-CentT8o
            T8o(7,)-CentT8o];

T8icorshift = [T8icor(1,)-CentT8o
               T8icor(2,)-CentT8o
               T8icor(3,)-CentT8o
               T8icor(4,)-CentT8o
               T8icor(5,)-CentT8o
               T8icor(6,)-CentT8o
               T8icor(7,)-CentT8o];

%Step 4
%T8oshift
xT8oshift = [T8oshift(3,)-T8oshift(1,)];
ztempT8oshift = [T8oshift(6,)-T8oshift(1,)];
yT8oshift = cross(xT8oshift,ztempT8oshift);
zT8oshift = cross(yT8oshift,xT8oshift);

XT8oshift = xT8oshift/norm(xT8oshift);
YT8oshift = yT8oshift/norm(yT8oshift);
ZT8oshift = zT8oshift/norm(zT8oshift);

CentT8oshift = sum(T8oshift)./7;

PT8oshift = [dot(XT8oshift,Xg) dot(YT8oshift,Xg) dot(ZT8oshift,Xg)
             dot(XT8oshift,Yg) dot(YT8oshift,Yg) dot(ZT8oshift,Yg)
             dot(XT8oshift,Zg) dot(YT8oshift,Zg) dot(ZT8oshift,Zg)];

%T8icorshift
xT8icorshift = [T8icorshift(3,)-T8icorshift(1,)];
ztempT8icorshift = [T8icorshift(6,)-T8icorshift(1,)];
yT8icorshift = cross(xT8icorshift,ztempT8icorshift);
zT8icorshift = cross(yT8icorshift,xT8icorshift);

XT8icorshift = xT8icorshift/norm(xT8icorshift);
YT8icorshift = yT8icorshift/norm(yT8icorshift);
ZT8icorshift = zT8icorshift/norm(zT8icorshift);

```



```

CentT8icorshift = sum(T8icorshift)./7;

PT8icorshift =[dot(XT8icorshift,Xg) dot(YT8icorshift,Xg) dot(ZT8icorshift,Xg)
               dot(XT8icorshift,Yg) dot(YT8icorshift,Yg) dot(ZT8icorshift,Yg)
               dot(XT8icorshift,Zg) dot(YT8icorshift,Zg) dot(ZT8icorshift,Zg)];

TT8io = PT8icorshift*PT8oshift';

%% Results
TransMig = CentT8icorshift-CentT8oshift;

beta = asin(TT8io(3,1));
alpha = asin(((TT8io(3,2))/(cos(beta))));
gamma = asin(((TT8io(2,1))/(cos(beta))));

Rotation = [alpha*(180/pi),beta*(180/pi),gamma*(180/pi)];

Results = [TransMig,Rotation]

>Error from MB-RSA Calculated
Error = Results-MBRSA

```

### Results:

	X (mm)	Y (mm)	Z (mm)	Rx (deg)	Ry (deg)	Rz (deg)
Results	-0.0127	0.2246	-0.1160	5.9265	0.0306	-0.0398
Error	-0.0333	0.2454	-0.1448	-0.1031	0.0084	-0.0101

## D.2.2 Apex Rotation Calculation

The following code was used to calculate the rotational displacements in the apex origin style. Section 0 was adapted from a similar program written by E. Laende to utilize the marker cluster locations specific to the Apex rotational migration calculations. The LocalMigration Function was written by E. Laende and published here with permission.

```
% Apex Rotation Calculations
clc;
clear;

%General Input
button = 'Yes';

%% Top
%Input
load TopRotation;
T_pop1 = [1, 0, 0, 407.355
          0, 1, 0, 119.403
          0, 0, 1, 521.471
          0, 0, 0, 1    ];

%Top Calcs

Origin0      = O0;
Mig0         = M0;
TopMigrations = [0,0,0,0,0,0,0];

for count=1:24;

    eval(['MigOrigin  = O' num2str(count) ';'])
    eval(['MigMig     = M' num2str(count) ';'])

    [MigrLocal_matrix, RedoZYX, localMTPM, pm, tpm, Pros_local0, Pros_local1] =
    LocalMigration(Origin0,MigOrigin,Mig0,MigMig,T_pop1,button);

    TopMigrations(count,:) =
    [MigrLocal_matrix(1,1),MigrLocal_matrix(1,2),MigrLocal_matrix(1,3),RedoZYX(1,1),
    RedoZYX(1,2),RedoZYX(1,3),localMTPM];
end

% Corrections for Missing Origin Markers (for Top only)

% 14th Exam
[MigrLocal_matrix,RedoZYX, localMTPM, pm, tpm, Pros_local0, Pros_local1] =
LocalMigration(O0(1:6,:),O14(1:6,:),Mig0,M14,T_pop1,button);

TopMigrations(14,:) =
[MigrLocal_matrix(1,1),MigrLocal_matrix(1,2),MigrLocal_matrix(1,3),RedoZYX(1,1),
RedoZYX(1,2),RedoZYX(1,3),localMTPM];

% 22nd Exam
[MigrLocal_matrix,RedoZYX, localMTPM, pm, tpm, Pros_local0, Pros_local1] =
LocalMigration(O0(1:6,:),O22(1:6,:),Mig0,M19,T_pop1,button);
```

```

TopMigrations(22,:) =
[MigrLocal_matrix(1,1),MigrLocal_matrix(1,2),MigrLocal_matrix(1,3),RedoZYX(1,1),
RedoZYX(1,2),RedoZYX(1,3),localMTPM];

% 23rd Exam
O0StarB = [O0(1:2,:);O0(4:7,:)];
O23Star = [O23(1:2,:);O23(4:7,:)];

[MigrLocal_matrix,RedoZYX, localMTPM, pm, tpm, Pros_local0, Pros_local1] =
LocalMigration(O0StarB,O23Star,Mig0,M23,T_pop1,button);

TopMigrations(23,:) =
[MigrLocal_matrix(1,1),MigrLocal_matrix(1,2),MigrLocal_matrix(1,3),RedoZYX(1,1),
RedoZYX(1,2),RedoZYX(1,3),localMTPM];

%% Bottom
%Input
load BotRotation;
T_pop2 = [1, 0, 0, 407.339
          0, 1, 0, 250.417
          0, 0, 1, 521.491
          0, 0, 0, 1    ];

%Bottom Calcs

BotOrigin0 = BO0;
BotMig0 = BM0;
BotMigrations = [0,0,0,0,0,0,0];

for count=1:24;

    eval(['BotMigOrigin = BO' num2str(count) ';' ])
    eval(['BotMigMig = BM' num2str(count) ';' ])

    [MigrLocal_matrix,RedoZYX, localMTPM, pm, tpm, Pros_local0, Pros_local1] =
LocalMigration(BotOrigin0,BotMigOrigin,BotMig0,BotMigMig,T_pop2,button);

    BotMigrations(count,:) =
[MigrLocal_matrix(1,1),MigrLocal_matrix(1,2),MigrLocal_matrix(1,3),RedoZYX(1,1),
RedoZYX(1,2),RedoZYX(1,3),localMTPM];
end

% Corrections for Missing Origin Markers (for Bot only)

% 10th Exam
[MigrLocal_matrix,RedoZYX, localMTPM, pm, tpm, Pros_local0, Pros_local1] =
LocalMigration(BO0(1:6,:),BO10(1:6,:),BotMig0,BM10,T_pop2,button);

BotMigrations(10,:) =
[MigrLocal_matrix(1,1),MigrLocal_matrix(1,2),MigrLocal_matrix(1,3),RedoZYX(1,1),
RedoZYX(1,2),RedoZYX(1,3),localMTPM];

% 14th Exam
[MigrLocal_matrix,RedoZYX, localMTPM, pm, tpm, Pros_local0, Pros_local1] =
LocalMigration(BO0(2:6,:),BO14(2:6,:),BotMig0,BM10,T_pop2,button);

BotMigrations(14,:) =
[MigrLocal_matrix(1,1),MigrLocal_matrix(1,2),MigrLocal_matrix(1,3),RedoZYX(1,1),
RedoZYX(1,2),RedoZYX(1,3),localMTPM];
% 15, 16 Exams
for count=15:16;

    eval(['BotMigOrigin = BO' num2str(count) '(1:6,);'])

```

```

eval(['BotMigMig      = BM' num2str(count) ';''])

[MigrLocal_matrix,RedoZYX, localMTPM, pm, tpm, Pros_local0, Pros_local1] =
LocalMigration(BotOrigin0(1:6,:),BotMigOrigin,BotMig0,BotMigMig,T_pop2,button);

BotMigrations(count,:) =
[MigrLocal_matrix(1,1),MigrLocal_matrix(1,2),MigrLocal_matrix(1,3),RedoZYX(1,1),
RedoZYX(1,2),RedoZYX(1,3),localMTPM];
end

% 21,22 Exams
for count=21:22;

eval(['BotMigOrigin  = BO' num2str(count) '(1:6,);'])
eval(['BotMigMig     = BM' num2str(count) ';''])

[MigrLocal_matrix,RedoZYX, localMTPM, pm, tpm, Pros_local0, Pros_local1] =
LocalMigration(BotOrigin0(1:6,:),BotMigOrigin,BotMig0,BotMigMig,T_pop2,button);

BotMigrations(count,:) =
[MigrLocal_matrix(1,1),MigrLocal_matrix(1,2),MigrLocal_matrix(1,3),RedoZYX(1,1),
RedoZYX(1,2),RedoZYX(1,3),localMTPM];
end

% 23th Exam
BO0Star = [BO0(1:2,:);BO0(4:7,:)];
BO23Star = [BO23(1:2,:);BO23(4:7,:)];

[MigrLocal_matrix,RedoZYX, localMTPM, pm, tpm, Pros_local0, Pros_local1] =
LocalMigration(BO0Star,BO23Star,BotMig0,BM23,T_pop2,button);

BotMigrations(23,:) =
[MigrLocal_matrix(1,1),MigrLocal_matrix(1,2),MigrLocal_matrix(1,3),RedoZYX(1,1),
RedoZYX(1,2),RedoZYX(1,3),localMTPM];

```

## D.2.3 LocalMigration Function

The LocalMigration Function was developed by Elise Laende and is reproduced here with permission.

```
function [MigrLocal_matrix,RedoZYX, localMTPM, pm, tpm, Pros_local0,
Pros_local1] = LocalMigration(TibMatrix0,TibMatrix1,ProsMatrix0,
ProsMatrix1,T_pop,button)
%LocalMigration.m

%Version 4 Updated 18 Jul 2007 by E Laende

%Calculates migration results in the local coordinate system.

%Revision History
%Ver 1. 15 Jun 2005. Created.
%Ver 2. 19 Apr 2006. Added plot option for single analysis
%Ver 3. 15 Jul 2006. Corrected pm (now 1-0)
%Ver 4. 18 Jul 2007. Corrected ZYX - now the axes are correct so ZYX
%no longer necessary (ZYX is now the same as XYZ so no need to
%change results matrix)

%Inputs:
%TibMatrix0: n x 3 matrix of the post-op tibial bead locations in the
%global coordinate system
%[x1 y1 z1
%x2 y2 z2
%...
%xn yn zn]
%TibMatrix1: n x 3 matrix of the follow-up exam tibial bead locations in the
%global coordinate system
%ProsMatrix0: n x 3 matrix of the post-op prosthesis bead locations in the
%global coordinate system
%ProsMatrix1: n x 3 matrix of the follow-up exam prosthesis bead locations
in the
%global coordinate system
%T_pop: 4 x 4 transformation matrix from global to local coordinate
%systems:
%T-pop=[ x
% R Y
% z
% 0 0 0 1]
%button: 'Yes' for batch processing or 'No' single subject analysis

%Outputs:
%MigrLocal_matrix: 1x6 matrix [xtrans ytrans ztrans xrot yrot zrot].
%Note these results are in the box coordinate system. Corrections
%for L/R leg & incorrect orientation of ap & ml axes (for biplanar)
%are made in CorrectForConventionsLM.m before being output to the
%MasterResults matrix
%RedoZYX: 1x3 matrix: [xrot yrot zrot]. Recalculates the rotations
%using the correct order of rotations with ml rot calculated first.
%Note these results are in the box coordinate system. Corrections
%for L/R leg & incorrect orientation of ap & ml axes (for biplanar)
%are made in CorrectForConventionsLM.m before being output to the
%MasterResults matrix
%localMTPM: maximum total point motion. Will be the same value as
%calculated in the conventional method with the stem tip centre
%included as an implant marker (independent of coordinate system)
```

```

    %pm: "point motion" n x 3 matrix of migration of each implant marker in
        %3 directions:
        % [x1 x2 ...xn
        % y1 y2 ...yn
        % z1 z2 ...zn]
        %Note: these results are in the box coordinate system.
    %tmp: "total point motion" 1 x n matrix of the vector length of the
        %migration of each implant marker
    %Pros_local0: 4 x n matrix of the location of each implant marker in
        %post-op exam. Used by FictiveMigration.m. Note: 4th row is a row of 1s
(place holders for matrix
    %multiplication). Note that one marker is the stem tip centre so the
    %coordinates are [0;0;0]
    %Pros_local1: 4 x n matrix of the location of each implant marker in
        %the follow-up exam. Used by FictiveMigration.m. Note: 4th row is a row
of 1s (place holders for matrix
    %multiplication).

%Calls the following functions:
    %RBT_rsa.m
    %cardan.m

    %Called by:
        %TheGuts.m
%-----
%3 x n matrices
ProsMarkers0=ProsMatrix0';
ProsMarkers1=ProsMatrix1';
%matrices now in form   x1  x2  ...xn
%                       y1  y2  ...yn
%                       z1  z2  ...zn
%includes stem tip centre as a pros marker

%transformation between reference and follow up exams (aligning exams based
%on tibia beads)
direct_disp_1to0=RBT_rsa(TibMatrix0', TibMatrix1');
TibMarkers0=TibMatrix0';
TibMarkers1=TibMatrix1';
ntib=size(TibMarkers1,2);
TibMarkers1_corrected_sqr = direct_disp_1to0*[TibMarkers1;ones(1,ntib)];
TibMarkers1_corrected=TibMarkers1_corrected_sqr(1:3,:);

npros=size(ProsMarkers0,2); %number of prosthesis markers

%Apply the global transformation to the prosthesis markers at time 1 to
%correct for positioning within calibration box (i.e. align with time 0)
ProsMarkers1_corrected_sqr = direct_disp_1to0*[ProsMarkers1;ones(1,npros)];
ProsMarkers1_corrected=ProsMarkers1_corrected_sqr(1:3,:);

%transforming prosthesis beads into local coordinate system
Pros_local1=inv(T_pop)*ProsMarkers1_corrected_sqr;
Pros_local0=inv(T_pop)*[ProsMarkers0;ones(1,npros)];

%point motion of each prosthesis bead
for l=1:npros;
    pm(1:3,l)=Pros_local1(1:3,l)-Pros_local0(1:3,l);
    tpm(1,l)=norm(pm(:,l));
end
localMTPM=max(tpm); %maximum total point motion

MigrLocal=RBT_rsa(Pros_local1(1:3,:),Pros_local0(1:3,:));
%norm(MigrLocal(1:3,4));

```

```

x=MigrLocal(1,4);
y=MigrLocal(2,4);
z=MigrLocal(3,4);

[phi1, phi2, phi3] = cardan(MigrLocal,'body3_123');
angle_x = phi1*180/pi;
angle_y = phi2*180/pi;
angle_z = phi3*180/pi;

MigrLocal_matrix=[x y z angle_x angle_y angle_z];

%Axes correct (x & z no longer reversed) so ZYX calculation of rotations
%not necessary - now the correct order of rotations is the same as the
%original calculations. Left in so results matrix doesn't need to be
%adjusted.
[check1 check2 check3]= cardan(MigrLocal,'body3_123');

check_x = check1*180/pi;
check_y = check2*180/pi;
check_z = check3*180/pi;
RedoZYX=[check_x check_y check_z];
%
% %Checking for fictive markers:
% NoCentre=[Pros_local0(1:3,1)';Pros_local0(1:3,3)';Pros_local0(1:3,4)']
% PEcentroid=mean(NoCentre) % [x y z]

%Plot to check calculations
% if strcmp(button,'Yes')==1;
%     %do not plot

if strcmp(button,'No')==1;
    figure,
    plot3(TibMarkers0(1,:),TibMarkers0(2,:),TibMarkers0(3:),'r');
    hold on,plot3(TibMarkers1(1,:),TibMarkers1(2,:),TibMarkers1(3:),'b');
    hold
on,plot3(TibMarkers1_corrected(1,:),TibMarkers1_corrected(2,:),TibMarkers1_corre
cted(3:),'ob');
    hold on, plot3(ProsMarkers0(1,:),ProsMarkers0(2,:),ProsMarkers0(3:),'*c');
    hold
on,plot3(ProsMarkers1_corrected(1,:),ProsMarkers1_corrected(2,:),ProsMarkers1_co
rrected(3:),'om');
    hold on,plot3(Pros_local0(1,:),Pros_local0(2,:),Pros_local0(3:),'c');
    hold on,plot3(Pros_local1(1,:),Pros_local1(2,:),Pros_local1(3:),'m');
    xlabel('x');
    ylabel('y');
    zlabel('z');
    legend('tib0','tib1','tib1_corrected','pros0','pros1_corrected','pros0
local','pros1 local');

    view(2);
end

```

# **Appendix E - Tabulated Data**

## **E.1 Simulation Precision Validation Data**

The raw data for the precision exams collected from MB-RSA are displayed in the tables beyond. This raw data was used to calculate the directional precision using the standard deviation multiplied by the 95% confidence limit. These calculations are found within Section E.2.



### E.1.1 Phantom Model: Translation

----- Migration Results -----

Reference Axis: Automatic

=====

Available scenes:

-----

- PhantomX0M0R --- X-number: 0 --- Reference Position
- PhantomX11M0R --- X-number: 11 --- +X Translation
- PhantomX12M0R --- X-number: 12 --- +Y Translation
- PhantomX13M0R --- X-number: 13 --- +Z Translation
- PhantomX14M0R --- X-number: 14 --- -X Translation
- PhantomX15M0R --- X-number: 15 --- -Y Translation
- PhantomX16M0R --- X-number: 16 --- -Z Translation
- PhantomX00M0R --- X-number: 00 --- Reference Position 2

-----

Xref	Xmig	X	Y	Z	Rx	Ry	Rz	#Matched Markers	#Matched Reference Markers	Rigid Body Error	Rigid Body Error Reference	Condition Number	Condition Number Reference Model	Maximum Total Point Motion
Model: T4														
0	11	-0.0959	0.0047	-0.0994	-0.1921	0.1246	0.1316	4	7	0.0584	0.0246	29.8	17.0	0.2006
11	12	0.0919	-0.0142	0.0010	0.3134	0.0404	-0.0137	4	7	0.0478	0.0368	29.9	17.0	0.1852
12	13	-0.0495	-0.0076	-0.0076	-0.0389	-0.1682	0.0249	5	7	0.0516	0.0358	29.6	17.1	0.1736
13	14	-0.1073	-0.0069	0.0233	-0.0371	-0.1174	0.0025	5	7	0.0437	0.0306	29.6	17.0	0.1819
14	15	0.2001	0.0039	0.0940	-0.2776	0.2825	-0.1079	5	7	0.1116	0.0472	29.5	17.1	0.3738
15	16	0.0013	0.0078	-0.1109	0.2959	-0.1338	0.0222	5	7	0.0797	0.0407	29.5	16.9	0.1822
16	00	-0.1103	0.0059	-0.0207	-0.0881	0.3406	0.0932	5	7	0.0718	0.0269	29.7	17.0	0.1970
Model: T8														
0	11	-0.0695	-0.0016	-0.0228	-0.0753	-0.1150	0.1038	5	7	0.0342	0.0246	27.0	17.0	0.1520
11	12	0.0464	0.0119	-0.0657	-0.0821	0.2288	-0.0056	5	7	0.0575	0.0368	27.3	17.0	0.1725
12	13	-0.0430	-0.0473	-0.0229	-0.2250	-0.1479	0.0923	5	7	0.0541	0.0358	27.0	17.1	0.2254
13	14	-0.0489	0.0145	0.0097	0.1422	0.1446	0.0334	5	7	0.0352	0.0306	26.9	17.0	0.1160
14	15	0.1131	0.0259	0.1476	0.2422	-0.1413	-0.1126	5	7	0.0233	0.0472	26.8	17.1	0.3018
15	16	-0.0076	-0.0246	-0.1430	-0.1811	-0.0316	0.0382	5	7	0.0504	0.0407	27.1	16.9	0.2149
16	00	-0.0557	0.0306	0.0422	0.1102	0.0293	-0.0472	5	7	0.0362	0.0269	27.2	17.0	0.1257

## E.1.2 Phantom Model: Rotation

----- Migration Results -----

Reference Axis: Automatic

=====

Available scenes:

-----

PhantomX0M0R --- X-number: 0 --- Reference Position  
 PhantomX21M0R --- X-number: 21 --- +X Rotation  
 PhantomX22M0R --- X-number: 22 --- +Y Rotation  
 PhantomX23M0R --- X-number: 23 --- +Z Rotation  
 PhantomX24M0R --- X-number: 24 --- -X Rotation  
 PhantomX25M0R --- X-number: 25 --- -Y Rotation  
 PhantomX26M0R --- X-number: 26 --- -Z Rotation  
 PhantomX00M0R --- X-number: 00 --- Reference Position 2

-----

Xref	Xmig	X	Y	Z	Rx	Ry	Rz	#Matched Markers	#Matched Reference Markers	Rigid Body Error	Rigid Body Error Reference	Condition Number	Condition Number Reference Model	Maximum Total Point Motion
-----														
Model: T4														
0	21	-0.0419	0.0028	-0.1568	-0.1478	0.1946	0.1006	5	6	0.0491	0.0504	29.6	19.0	0.2931
21	22	-0.0352	-0.0654	0.2452	0.1499	-0.4426	-0.0420	4	6	0.0811	0.0370	54.4	19.2	0.4663
22	23	0.0005	0.0471	-0.1789	-0.1704	0.1772	0.0060	4	6	0.0348	0.0389	50.6	19.1	0.2746
23	24	-0.0040	-0.0475	-0.0031	0.1193	0.1932	0.0321	5	7	0.0680	0.0280	30.1	16.6	0.1274
24	25	-0.0860	0.0311	0.0661	0.2073	-0.1507	-0.0379	5	7	0.0505	0.0259	29.7	16.7	0.2212
25	26	0.1784	-0.0045	-0.0509	-0.2825	0.4578	0.0068	5	7	0.1256	0.0452	31.0	16.5	0.4829
26	00	-0.0869	0.0295	0.0104	-0.0407	-0.1112	0.0405	5	7	0.0278	0.0519	28.9	17.5	0.1375
-----														
Model: T8														
0	21	-0.0504	0.0131	-0.1080	-0.2124	0.0444	0.1574	4	6	0.0193	0.0504	42.2	19.0	0.1837
21	22	-0.0061	-0.0181	0.0786	-0.0067	0.0873	-0.0080	5	6	0.0748	0.0370	30.8	19.2	0.1618
22	23	-0.0034	-0.0116	-0.0963	0.0346	-0.0111	-0.0624	5	6	0.0386	0.0389	31.8	19.1	0.1532
23	24	0.0157	-0.0092	0.0138	0.1171	0.0511	0.0489	4	7	0.0261	0.0280	41.7	16.6	0.1109
24	25	-0.0210	0.0566	0.0884	0.2524	0.2801	-0.0152	5	7	0.0725	0.0259	26.8	16.7	0.3024
25	26	0.0630	-0.0265	-0.0135	0.0103	-0.1812	-0.0237	5	7	0.0442	0.0452	28.7	16.5	0.1545
26	00	-0.0498	0.0223	0.0139	0.1267	-0.1597	-0.0596	5	7	0.0257	0.0519	26.6	17.5	0.1328

### E.1.3 Phantom Model: Combination Rotations

----- Migration Results -----

Reference Axis: Automatic

=====

Available scenes:

-----

- PhantomX0M0R --- X-number: 0 --- Reference Position
- PhantomX31M0R --- X-number: 31 --- +Y and +Z Rotation
- PhantomX32M0R --- X-number: 32 --- +Y and -Z Rotation
- PhantomX33M0R --- X-number: 33 --- -Y and +Z Rotation
- PhantomX34M0R --- X-number: 34 --- -Y and -Z Rotation
- PhantomX00M0R --- X-number: 00 --- Reference Position 2

-----

Xref	Xmig	X	Y	Z	Rx	Ry	Rz	#Matched Markers	#Matched Reference Markers	Rigid Body Error	Rigid Body Error Reference	Condition Number	Condition Number Reference Model	Maximum Total Point Motion
-----														
Model: T4														
0	31	-0.1188	-0.0008	-0.0603	0.0861	-0.1392	0.0232	4	6	0.0464	0.0268	54.0	19.0	0.1689
31	32	0.2238	0.0135	0.0548	-0.0012	0.0183	-0.1154	5	6	0.0789	0.0380	33.6	18.8	0.2986
32	33	-0.1889	0.0318	0.0519	-0.0144	0.0025	0.0798	5	6	0.0853	0.0640	32.5	19.4	0.2805
33	34	0.0826	0.0124	-0.0156	0.1889	0.1599	-0.0452	4	7	0.0606	0.0586	39.8	16.1	0.1534
34	00	-0.0869	0.0205	-0.0415	-0.0164	-0.0999	0.0734	4	7	0.0376	0.0472	39.2	16.9	0.1633
-----														
Model: T8														
0	31	-0.0858	-0.0031	-0.0638	-0.1601	0.0049	0.2068	4	6	0.0374	0.0268	42.2	19.0	0.1552
31	32	0.1168	0.0471	0.0189	-0.0590	0.0066	-0.0850	5	6	0.0427	0.0380	31.5	18.8	0.1588
32	33	-0.0833	0.0201	0.0353	0.0000	-0.0393	0.0501	5	6	0.0716	0.0640	28.9	19.4	0.1353
33	34	0.0579	0.0028	-0.0424	-0.0653	0.0991	-0.0183	4	7	0.0256	0.0586	44.5	16.1	0.1280
34	00	-0.0729	0.0208	-0.0008	0.0869	-0.2382	-0.0767	5	7	0.0440	0.0472	28.1	16.9	0.1648

## E.1.4 Simulated Model: Translation

----- Migration Results -----

Reference Axis: Automatic

=====

Available scenes:

-----

SimulationX0MOR --- X-number: 0 --- Reference Position  
 SimulationX11MOR --- X-number: 11 --- +X Translation  
 SimulationX12MOR --- X-number: 12 --- +Y Translation  
 SimulationX13MOR --- X-number: 13 --- +Z Translation  
 SimulationX14MOR --- X-number: 14 --- -X Translation  
 SimulationX15MOR --- X-number: 15 --- -Y Translation  
 SimulationX16MOR --- X-number: 16 --- -Z Translation

-----

Xref	Xmig	X	Y	Z	Rx	Ry	Rz	#Matched Markers	#Matched Reference Markers	Rigid Body Error	Rigid Body Error Reference	Condition Number	Condition Number Reference Model	Maximum Total Point Motion
-----														
Model: T4														
0	11	-0.0491	0.0117	0.0952	0.0319	-0.0367	-0.0132	5	7	0.0150	0.0725	30.1	16.9	0.1632
11	12	0.1124	0.0100	-0.0357	-0.0360	0.1129	-0.0397	5	7	0.0374	0.0496	30.3	16.9	0.1559
12	13	0.0416	-0.0301	-0.0456	-0.1366	-0.0891	-0.0127	5	7	0.0252	0.0545	30.1	17.0	0.1416
13	14	-0.0352	0.0011	-0.0052	0.0740	-0.0480	-0.0574	5	7	0.0405	0.0735	30.0	17.0	0.0791
14	15	-0.0426	0.0200	-0.0054	0.1657	0.1601	0.0634	5	7	0.0500	0.0847	30.0	17.0	0.1311
15	16	-0.1226	-0.0042	0.0529	-0.1410	0.0619	0.0542	5	7	0.0829	0.0257	30.2	16.9	0.2870
16	0	0.0951	-0.0087	-0.0562	0.0414	-0.1606	0.0059	5	7	0.0991	0.0453	30.2	16.9	0.2725
-----														
Model: T8														
0	11	-0.0416	0.0089	0.0003	-0.4128	-0.1114	0.0448	5	7	0.0669	0.0725	27.3	16.9	0.1974
11	12	0.0934	0.0136	-0.0076	0.0331	0.0934	-0.0362	5	7	0.0249	0.0496	27.5	16.9	0.1515
12	13	0.0227	-0.0329	-0.0266	0.1283	0.0137	-0.0417	5	7	0.0196	0.0545	27.3	17.0	0.0631
13	14	-0.0156	-0.0012	0.0344	0.4323	0.1770	0.0576	5	7	0.0492	0.0735	27.1	17.0	0.2425
14	15	-0.0428	0.0118	-0.0046	-0.0775	-0.1656	0.0320	5	7	0.0425	0.0847	27.1	17.0	0.1294
15	16	-0.0648	0.0139	-0.0003	-0.2766	-0.0367	-0.0377	5	7	0.0515	0.0257	27.4	16.9	0.1415
16	0	0.0485	-0.0142	0.0044	0.1747	0.0293	-0.0216	5	7	0.0270	0.0453	27.5	16.9	0.0806

## E.1.5 Simulated Model: Rotation

----- Migration Results -----

Reference Axis: Automatic

Available scenes:

-----  
 SimulationX0M0R --- X-number: 0 --- Reference Position  
 SimulationX21M0R --- X-number: 21 --- +X Rotation  
 SimulationX22M0R --- X-number: 22 --- +Y Rotation  
 SimulationX23M0R --- X-number: 23 --- +Z Rotation  
 SimulationX24M0R --- X-number: 24 --- -X Rotation  
 SimulationX25M0R --- X-number: 25 --- -Y Rotation  
 SimulationX26M0R --- X-number: 26 --- -Z Rotation  
 -----

Xref	Xmig	X	Y	Z	Rx	Ry	Rz	#Matched Markers	#Matched Reference Markers	Rigid Body Error	Rigid Body Error Reference	Condition Number	Condition Number Reference Model	Maximum Total Point Motion
-----														
Model: T4														
0	21	0.1201	-0.0150	0.1350	-0.0919	-0.0106	-0.0556	5	6	0.1261	0.0539	30.1	18.9	0.3653
21	22	0.1125	0.0300	-0.0653	-0.1740	-0.2689	-0.1185	4	6	0.1139	0.0762	55.0	19.1	0.3169
22	23	-0.0672	-0.0195	0.0950	0.1321	0.2484	-0.0282	4	7	0.0614	0.0963	51.0	17.4	0.2090
23	24	-0.0782	-0.0149	-0.1537	0.1273	0.0612	0.0497	5	7	0.0540	0.0753	30.6	16.5	0.2283
24	25	-0.1012	0.0131	-0.0691	-0.3526	-0.1185	0.0500	5	7	0.1103	0.1274	30.1	16.6	0.2652
25	26	-0.0722	0.0265	0.2958	0.4590	0.1509	0.0515	5	7	0.1636	0.0880	31.5	16.5	0.5103
26	0	0.0472	-0.0375	-0.2425	-0.1615	-0.0546	0.0260	5	7	0.1418	0.0644	29.6	17.3	0.4189
-----														
Model: T8														
0	21	0.1022	-0.0086	0.0890	0.0180	-0.1104	0.0176	4	6	0.0463	0.0539	41.8	18.9	0.1870
21	22	0.0885	0.0102	-0.0599	0.1529	0.4747	-0.1109	4	6	0.0657	0.0762	43.2	19.1	0.3160
22	23	-0.0431	0.0204	0.0032	-0.1576	-0.2926	0.1791	4	7	0.0221	0.0963	39.5	17.4	0.1600
23	24	-0.0741	0.0102	-0.0513	-0.1450	-0.1477	0.0483	4	7	0.0809	0.0753	41.3	16.5	0.1494
24	25	-0.0529	-0.0205	-0.0263	0.0041	0.3762	-0.1123	4	7	0.1143	0.1274	40.6	16.6	0.1975
25	26	-0.0446	0.0391	0.1318	0.2022	-0.1967	0.1092	4	7	0.0550	0.0880	44.1	16.5	0.2761
26	0	-0.0106	-0.0058	-0.0983	-0.0298	-0.1071	-0.2350	5	7	0.0716	0.0644	26.9	17.3	0.2455

## E.1.6 Simulated Model: Combination Rotations

----- Migration Results -----

Reference Axis: Automatic

=====

Available scenes:

-----

SimulationX0M0R --- X-number: 0 --- Reference Position  
 SimulationX31M0R --- X-number: 31 --- +Y and +Z Rotation  
 SimulationX32M0R --- X-number: 32 --- +Y and -Z Rotation  
 SimulationX33M0R --- X-number: 33 --- -Y and +Z Rotation  
 SimulationX34M0R --- X-number: 34 --- -Y and -Z Rotation

-----

Xref	Xmig	X	Y	Z	Rx	Ry	Rz	#Matched Markers	#Matched Reference Markers	Rigid Body Error	Rigid Body Error Reference	Condition Number	Condition Number Reference Model	Maximum Total Point Motion
-----														
Model: T4														
0	31	-0.0343	-0.0034	0.0682	-0.3777	-0.1386	-0.0654	5	7	0.1161	0.0653	30.1	16.9	0.3778
31	32	0.0161	-0.0030	-0.0272	0.0577	0.2296	0.1782	5	7	0.0731	0.0726	32.1	16.1	0.1811
32	33	0.1367	-0.0162	-0.0049	-0.1437	-0.5077	-0.4008	4	7	0.0697	0.0930	57.2	16.8	0.2413
33	34	0.2310	0.0119	0.1454	0.0148	-0.0250	-0.0206	5	6	0.0506	0.0910	33.6	18.7	0.3207
34	0	-0.3651	0.0615	-0.1895	-0.2222	0.1249	0.1269	4	6	0.1069	0.0877	50.5	19.3	0.4516
-----														
Model: T8														
0	31	0.0394	0.0102	-0.0304	-0.0012	0.3588	-0.0091	4	7	0.0636	0.0653	41.8	16.9	0.1941
31	32	-0.0351	-0.0201	0.0395	0.0447	-0.1245	-0.0117	4	7	0.0427	0.0726	43.7	16.1	0.1279
32	33	0.1242	-0.0373	0.0166	0.0745	-0.1716	-0.0457	4	7	0.0319	0.0930	44.4	16.8	0.1950
33	34	0.1234	0.0316	0.0725	0.0033	-0.0377	-0.0835	4	6	0.0427	0.0910	53.5	18.7	0.1848
34	0	-0.2747	0.0155	-0.0709	-0.3450	-0.3473	0.0496	4	6	0.0418	0.0877	39.7	19.3	0.3853

## E.2 Precision Validation Calculations

### E.2.1 Phantom Model Precision

Superior Precision	X	Y	Z	Rx	Ry	Rz	MTPM
Translation	-0.0959	0.0047	-0.0994	-0.1921	0.1246	0.1316	0.2006
	0.0919	-0.0142	0.0010	0.3134	0.0404	-0.0137	0.1852
	-0.0495	-0.0076	-0.0076	-0.0389	-0.1682	0.0249	0.1736
	-0.1073	-0.0069	0.0233	-0.0371	-0.1174	0.0025	0.1819
	0.2001	0.0039	0.0940	-0.2776	0.2825	-0.1079	0.3738
	0.0013	0.0078	-0.1109	0.2959	-0.1338	0.0222	0.1822
	-0.1103	0.0059	-0.0207	-0.0881	0.3406	0.0932	0.1970
Rotation	-0.0419	0.0028	-0.1568	-0.1478	0.1946	0.1006	0.2931
	-0.0352	-0.0654	0.2452	0.1499	-0.4426	-0.0420	0.4663
	0.0005	0.0471	-0.1789	-0.1704	0.1772	0.0060	0.2746
	-0.0040	-0.0475	-0.0031	0.1193	0.1932	0.0321	0.1274
	-0.0860	0.0311	0.0661	0.2073	-0.1507	-0.0379	0.2212
	0.1784	-0.0045	-0.0509	-0.2825	0.4578	0.0068	0.4829
	-0.0869	0.0295	0.0104	-0.0407	-0.1112	0.0405	0.1375
Combination Rotation	-0.1188	-0.0008	-0.0603	0.0861	-0.1392	0.0232	0.1689
	0.2238	0.0135	0.0548	-0.0012	0.0183	-0.1154	0.2986
	-0.1889	0.0318	0.0519	-0.0144	0.0025	0.0798	0.2805
	0.0826	0.0124	-0.0156	0.1889	0.1599	-0.0452	0.1534
	-0.0869	0.0205	-0.0415	-0.0164	-0.0999	0.0734	0.1633
Standard Deviation	0.1167	0.0265	0.0958	0.1773	0.2179	0.0661	0.1045
Precision	<b>0.2438</b>	<b>0.0553</b>	<b>0.2001</b>	<b>0.3706</b>	<b>0.4554</b>	<b>0.1382</b>	<b>0.2185</b>

<b>Inferior Precision</b>	X	Y	Z	Rx	Ry	Rz	MTPM
Translation	-0.0695	-0.0016	-0.0228	-0.0753	-0.1150	0.1038	0.1520
	0.0464	0.0119	-0.0657	-0.0821	0.2288	-0.0056	0.1725
	-0.0430	-0.0473	-0.0229	-0.2250	-0.1479	0.0923	0.2254
	-0.0489	0.0145	0.0097	0.1422	0.1446	0.0334	0.1160
	0.1131	0.0259	0.1476	0.2422	-0.1413	-0.1126	0.3018
	-0.0076	-0.0246	-0.1430	-0.1811	-0.0316	0.0382	0.2149
	-0.0557	0.0306	0.0422	0.1102	0.0293	-0.0472	0.1257
Rotation	-0.0504	0.0131	-0.1080	-0.2124	0.0444	0.1574	0.1837
	-0.0061	-0.0181	0.0786	-0.0067	0.0873	-0.0080	0.1618
	-0.0034	-0.0116	-0.0963	0.0346	-0.0111	-0.0624	0.1532
	0.0157	-0.0092	0.0138	0.1171	0.0511	0.0489	0.1109
	-0.0210	0.0566	0.0884	0.2524	0.2801	-0.0152	0.3024
	0.0630	-0.0265	-0.0135	0.0103	-0.1812	-0.0237	0.1545
	-0.0498	0.0223	0.0139	0.1267	-0.1597	-0.0596	0.1328
Combination Rotation	-0.0858	-0.0031	-0.0638	-0.1601	0.0049	0.2068	0.1552
	0.1168	0.0471	0.0189	-0.0590	0.0066	-0.0850	0.1588
	-0.0833	0.0201	0.0353	0.0000	-0.0393	0.0501	0.1353
	0.0579	0.0028	-0.0424	-0.0653	0.0991	-0.0183	0.1280
	-0.0729	0.0208	-0.0008	0.0869	-0.2382	-0.0767	0.1648
Standard Deviation	0.0631	0.0260	0.0713	0.1429	0.1389	0.0845	0.0549
Precision	<b>0.1319</b>	<b>0.0544</b>	<b>0.1490</b>	<b>0.2987</b>	<b>0.2902</b>	<b>0.1766</b>	<b>0.1147</b>



## E.2.2 Simulation Model Precision

<b>Superior Precision</b>	X	Y	Z	Rx	Ry	Rz	MTPM
Translation	-0.0491	0.0117	0.0952	0.0319	-0.0367	-0.0132	0.1632
	0.1124	0.0100	-0.0357	-0.0360	0.1129	-0.0397	0.1559
	0.0416	-0.0301	-0.0456	-0.1366	-0.0891	-0.0127	0.1416
	-0.0352	0.0011	-0.0052	0.0740	-0.0480	-0.0574	0.0791
	-0.0426	0.0200	-0.0054	0.1657	0.1601	0.0634	0.1311
	-0.1226	-0.0042	0.0529	-0.1410	0.0619	0.0542	0.2870
	0.0951	-0.0087	-0.0562	0.0414	-0.1606	0.0059	0.2725
Rotation	0.1201	-0.0150	0.1350	-0.0919	-0.0106	-0.0556	0.3653
	0.1125	0.0300	-0.0653	-0.1740	-0.2689	-0.1185	0.3169
	-0.0672	-0.0195	0.0950	0.1321	0.2484	-0.0282	0.2090
	-0.0782	-0.0149	-0.1537	0.1273	0.0612	0.0497	0.2283
	-0.1012	0.0131	-0.0691	-0.3526	-0.1185	0.0500	0.2652
	-0.0722	0.0265	0.2958	0.4590	0.1509	0.0515	0.5103
	0.0472	-0.0375	-0.2425	-0.1615	-0.0546	0.0260	0.4189
Combination Rotation	-0.0343	-0.0034	0.0682	-0.3777	-0.1386	-0.0654	0.3778
	0.0161	-0.0030	-0.0272	0.0577	0.2296	0.1782	0.1811
	0.1367	-0.0162	-0.0049	-0.1437	-0.5077	-0.4008	0.2413
	0.2310	0.0119	0.1454	0.0148	-0.0250	-0.0206	0.3207
	-0.3651	0.0615	-0.1895	-0.2222	0.1249	0.1269	0.4516
Standard Deviation	0.1304	0.0233	0.1263	0.1968	0.1823	0.1177	0.1177
Precision	<b>0.2725</b>	<b>0.0488</b>	<b>0.2640</b>	<b>0.4112</b>	<b>0.3810</b>	<b>0.2460</b>	<b>0.2461</b>

<b>Inferior Precision</b>	X	Y	Z	Rx	Ry	Rz	MTPM
Translation	-0.0416	0.0089	0.0003	-0.4128	-0.1114	0.0448	0.1974
	0.0934	0.0136	-0.0076	0.0331	0.0934	-0.0362	0.1515
	0.0227	-0.0329	-0.0266	0.1283	0.0137	-0.0417	0.0631
	-0.0156	-0.0012	0.0344	0.4323	0.1770	0.0576	0.2425
	-0.0428	0.0118	-0.0046	-0.0775	-0.1656	0.0320	0.1294
	-0.0648	0.0139	-0.0003	-0.2766	-0.0367	-0.0377	0.1415
	0.0485	-0.0142	0.0044	0.1747	0.0293	-0.0216	0.0806
Rotation	0.1022	-0.0086	0.0890	0.0180	-0.1104	0.0176	0.1870
	0.0885	0.0102	-0.0599	0.1529	0.4747	-0.1109	0.3160
	-0.0431	0.0204	0.0032	-0.1576	-0.2926	0.1791	0.1600
	-0.0741	0.0102	-0.0513	-0.1450	-0.1477	0.0483	0.1494
	-0.0529	-0.0205	-0.0263	0.0041	0.3762	-0.1123	0.1975
	-0.0446	0.0391	0.1318	0.2022	-0.1967	0.1092	0.2761
	-0.0106	-0.0058	-0.0983	-0.0298	-0.1071	-0.2350	0.2455
Combination Rotation	0.0394	0.0102	-0.0304	-0.0012	0.3588	-0.0091	0.1941
	-0.0351	-0.0201	0.0395	0.0447	-0.1245	-0.0117	0.1279
	0.1242	-0.0373	0.0166	0.0745	-0.1716	-0.0457	0.1950
	0.1234	0.0316	0.0725	0.0033	-0.0377	-0.0835	0.1848
	-0.2747	0.0155	-0.0709	-0.3450	-0.3473	0.0496	0.3853
Standard Deviation	0.0939	0.0205	0.0562	0.2006	0.2247	0.0905	0.0780
Precision	<b>0.1963</b>	<b>0.0429</b>	<b>0.1175</b>	<b>0.4192</b>	<b>0.4697</b>	<b>0.1892</b>	<b>0.1630</b>

### **E.3 Accuracy Data**

This is the raw output for the accuracy assessment exams as created by MB-RSA and imported into excel. This data was then used to calculate the prediction intervals using Minitab 16. The accuracy was calculated as half the width of the average prediction interval for each direction assessed as shown in Section E.4.

### E.3.1 Caudal Superior: 0.5mm

----- Migration Results -----

Reference Axis: Automatic

=====

Available scenes:

-----

CaudalX0M0R --- X-number: 0 --- Follow-up: Postoperative  
 C S 05X1M0R --- X-number: 1 --- Follow-up: Postoperative  
 C S 05X2M0R --- X-number: 2 --- Follow-up: Postoperative  
 C S 05X3M0R --- X-number: 3 --- Follow-up: Postoperative  
 C S 05X4M0R --- X-number: 4 --- Follow-up: Postoperative  
 C S 05X5M0R --- X-number: 5 --- Follow-up: Postoperative  
 C S 05X6M0R --- X-number: 6 --- Follow-up: Postoperative

-----

Xref	Xmig	X	Y	Z	Rx	Ry	Rz	#Matched Markers	#Matched Reference Markers	Rigid Body Error	Rigid Body Error Reference	Condition Number	Condition Number Reference Model	Maximum Total Point Motion
-----														
Model: T4														
Reference: CaudalX0M0R --- L1														
0	1	0.4925	-0.0197	0.2016	0.0442	-0.0051	0.0182	7	6	0.0268	0.0065	18.5	19.8	0.5697
0	2	-0.0202	0.4983	0.1618	0.0574	-0.0271	0.0256	7	6	0.0221	0.0064	18.5	19.8	0.5632
0	3	-0.0059	-0.0122	0.6843	0.0564	-0.0217	0.0319	7	6	0.0300	0.0120	18.5	19.8	0.7311
0	4	-0.5210	0.0026	0.0480	0.0155	-0.0218	0.0281	7	6	0.0268	0.0091	18.5	19.8	0.5419
0	5	-0.0104	-0.4976	0.0704	0.0387	-0.0178	0.0278	7	6	0.0208	0.0092	18.5	19.8	0.5232
0	6	-0.0022	0.0100	-0.4760	0.0338	-0.0040	0.0258	7	6	0.0357	0.0023	18.5	19.8	0.5243
-----														
Model: T8														
Reference: CaudalX0M0R --- L1														
0	1	-0.0105	0.0070	0.1107	0.0624	-0.0169	0.0016	7	6	0.0150	0.0065	19.7	19.8	0.1577
0	2	-0.0137	0.0021	0.0717	0.0252	-0.0218	-0.0051	7	6	0.0261	0.0064	19.7	19.8	0.0853
0	3	-0.0010	-0.0058	0.0775	0.0224	0.0090	0.0080	7	6	0.0272	0.0120	19.7	19.8	0.0927
0	4	-0.0110	0.0017	0.0133	-0.0001	-0.0122	-0.016	7	6	0.0164	0.0091	19.7	19.8	0.0284
0	5	-0.0031	-0.0007	0.0215	-0.0001	0.0021	0.0234	7	6	0.0215	0.0092	19.7	19.8	0.0329
0	6	-0.0047	0.0036	-0.0155	-0.0116	-0.0108	0.0057	7	6	0.0365	0.0023	19.7	19.8	0.0831

### E.3.2 Caudal Superior: 1mm

----- Migration Results -----

Reference Axis: Automatic

=====

Available scenes:

-----

CaudalX0M0R --- X-number: 0 --- Follow-up: Postoperative  
 C S 1X1M0R --- X-number: 1 --- Follow-up: Postoperative  
 C S 1X2M0R --- X-number: 2 --- Follow-up: Postoperative  
 C S 1X3M0R --- X-number: 3 --- Follow-up: Postoperative  
 C S 1X4M0R --- X-number: 4 --- Follow-up: Postoperative  
 C S 1X5M0R --- X-number: 5 --- Follow-up: Postoperative  
 C S 1X6M0R --- X-number: 6 --- Follow-up: Postoperative

-----

Xref	Xmig	X	Y	Z	Rx	Ry	Rz	#Matched Markers	#Matched Reference Markers	Rigid Body Error	Rigid Body Error Reference	Condition Number	Condition Number Reference Model	Maximum Total Point Motion
-----														
Model: T4														
Reference: CaudalX0M0R --- L1														
0	1	0.9803	-0.0005	0.1183	0.0448	-0.0086	0.0002	7	6	0.0224	0.0146	18.5	19.8	1.0094
0	2	-0.0102	1.0062	0.0365	0.0337	0.0029	0.0362	7	6	0.0201	0.0033	18.5	19.8	1.0461
0	3	-0.0157	-0.0092	1.1696	0.0438	0.0015	0.0169	7	6	0.0200	0.0070	18.5	19.8	1.2056
0	4	-1.0417	-0.0144	0.2770	0.0625	-0.0467	0.0355	7	6	0.0369	0.0270	18.5	19.8	1.1384
0	5	-0.0154	-0.989	0.0827	0.0361	-0.0185	0.0275	7	6	0.0188	0.0041	18.5	19.8	1.0078
0	6	-0.013	0.0154	-1.0138	0.0158	-0.0220	0.0197	7	6	0.0254	0.0039	18.5	19.8	1.0493
-----														
Model: T8														
Reference: CaudalX0M0R --- L1														
0	1	-0.0107	-0.0005	0.0551	0.0073	-0.0020	-0.0262	7	6	0.0238	0.0146	19.7	19.8	0.0706
0	2	-0.0036	0.0040	0.0160	0.0102	0.0053	-0.0136	7	6	0.0143	0.0033	19.7	19.8	0.0414
0	3	-0.0082	-0.0044	0.0912	0.0232	-0.0004	-0.0469	7	6	0.0173	0.0070	19.7	19.8	0.1028
0	4	-0.0144	-0.0136	0.1525	0.0384	-0.0075	0.0037	7	6	0.0159	0.0270	19.7	19.8	0.1747
0	5	-0.0078	0.0002	0.0326	0.0067	-0.0068	0.0254	7	6	0.0071	0.0041	19.7	19.8	0.0385
0	6	-0.0067	0.0085	-0.0227	-0.0072	-0.0047	0.0103	7	6	0.0144	0.0039	19.7	19.8	0.0474

### E.3.3 Caudal Superior: 5mm

----- Migration Results -----

Reference Axis: Automatic

=====

Available scenes:

-----

- CaudalX0M0R --- X-number: 0 --- Follow-up: Postoperative
- C S 5X1M0R --- X-number: 1 --- Follow-up: Postoperative
- C S 5X2M0R --- X-number: 2 --- Follow-up: Postoperative
- C S 5X3M0R --- X-number: 3 --- Follow-up: Postoperative
- C S 5X4M0R --- X-number: 4 --- Follow-up: Postoperative
- C S 5X5M0R --- X-number: 5 --- Follow-up: Postoperative
- C S 5X6M0R --- X-number: 6 --- Follow-up: Postoperative

-----

Xref	Xmig	X	Y	Z	Rx	Ry	Rz	#Matched Markers	#Matched Reference Markers	Rigid Body Error	Rigid Body Error Reference	Condition Number	Condition Number Reference Model	Maximum Total Point Motion
-----														
Model: T4														
Reference: CaudalX0M0R --- L1														
0	1	5.0276	-0.0056	0.0426	0.0525	0.0798	0.0184	7	6	0.1617	0.0165	18.5	19.8	5.1832
0	2	0.0063	4.9920	0.1007	0.0664	-0.0207	0.0159	7	6	0.0402	0.0250	18.5	19.8	5.0161
0	3	-0.0243	-0.0283	5.3431	0.0736	-0.0115	0.0122	7	6	0.0175	0.0184	18.5	19.8	5.3606
0	4	-4.9921	0.0025	0.0303	0.0121	0.0061	-0.0015	7	6	0.0166	0.0150	18.5	19.8	4.9996
0	5	-0.0358	-5.0194	0.3036	0.0730	-0.0277	0.0376	7	6	0.0200	0.0180	18.5	19.8	5.0698
0	6	-0.0042	-0.0036	-4.8776	0.0415	-0.0300	0.0419	7	6	0.0382	0.0038	18.5	19.8	4.9215
-----														
Model: T8														
Reference: CaudalX0M0R --- L1														
0	1	-0.0014	-0.0050	0.0392	0.0068	-0.0014	-0.0171	7	6	0.0202	0.0165	19.7	19.8	0.0502
0	2	0.0013	-0.0115	0.0365	0.0048	-0.0007	0.0256	7	6	0.0163	0.0250	19.7	19.8	0.0490
0	3	-0.0080	-0.0106	0.1861	0.0576	0.0078	-0.0068	7	6	0.0247	0.0184	19.7	19.8	0.2148
0	4	0.0043	0.0031	-0.0046	-0.0089	0.0056	-0.0299	7	6	0.0407	0.0150	19.7	19.8	0.0773
0	5	-0.0172	-0.0007	0.1652	0.0551	-0.0060	-0.0045	7	6	0.0202	0.0180	19.7	19.8	0.1798
0	6	0.0033	-0.0034	0.0604	0.0185	0.0029	-0.0053	7	6	0.0190	0.0038	19.7	19.8	0.0688

### E.3.4 Caudal Superior: 10mm

----- Migration Results -----

Reference Axis: Automatic

=====

Available scenes:

-----

- CaudalX0M0R --- X-number: 0 --- Follow-up: Postoperative
- C S 10X1M0R --- X-number: 1 --- Follow-up: Postoperative
- C S 10X2M0R --- X-number: 2 --- Follow-up: Postoperative
- C S 10X3M0R --- X-number: 3 --- Follow-up: Postoperative
- C S 10X4M0R --- X-number: 4 --- Follow-up: Postoperative
- C S 10X5M0R --- X-number: 5 --- Follow-up: Postoperative
- C S 10X6M0R --- X-number: 6 --- Follow-up: Postoperative

-----

Xref	Xmig	X	Y	Z	Rx	Ry	Rz	#Matched Markers	#Matched Reference Markers	Rigid Body Error	Rigid Body Error Reference	Condition Number	Condition Number Reference Model	Maximum Total Point Motion
-----														
Model: T4														
Reference: CaudalX0M0R --- L1														
0	1	10.0019	0.0152	0.0845	0.0706	0.1133	0.0109	7	6	0.1525	0.0176	18.5	19.8	10.1155
0	2	-0.0315	10.0134	0.0164	0.0105	-0.0430	0.0418	7	6	0.0216	0.0117	18.5	19.8	10.0264
0	3	-0.0388	0.0050	10.1872	0.0620	-0.0690	0.0445	7	6	0.0605	0.0234	18.5	19.8	10.2793
0	4	-9.9839	-0.0081	0.0990	0.0229	0.0275	0.0059	7	6	0.0348	0.0332	18.5	19.8	10.0120
0	5	-0.0184	-9.9639	0.0143	0.0457	-0.0086	0.0028	7	6	0.0226	0.0177	18.5	19.8	9.9861
0	6	0.0023	-0.0214	-9.7871	0.0630	-0.0284	0.0555	7	6	0.0256	0.0122	18.5	19.8	9.8336
-----														
Model: T8														
Reference: CaudalX0M0R --- L1														
0	1	-0.0112	-0.0014	0.0631	0.0177	0.0089	-0.0221	7	6	0.0279	0.0176	19.7	19.8	0.1152
0	2	-0.0147	0.0027	-0.0170	0.0208	-0.0127	-0.0364	7	6	0.0160	0.0117	19.7	19.8	0.0457
0	3	-0.0242	0.0034	0.0959	0.0185	-0.0259	-0.0132	7	6	0.0305	0.0234	19.7	19.8	0.1554
0	4	0.0032	-0.0024	0.0479	0.0333	-0.0043	-0.0264	7	6	0.0231	0.0332	19.7	19.8	0.0834
0	5	-0.0068	0.0112	-0.0092	-0.0004	-0.0017	-0.0346	7	6	0.0145	0.0177	19.7	19.8	0.0467
0	6	-0.0026	-0.0154	0.1084	0.0395	-0.0116	0.0067	7	6	0.0242	0.0122	19.7	19.8	0.1353

### E.3.5 Caudal Superior: 20mm

----- Migration Results -----

Reference Axis: Automatic

=====

Available scenes:

-----

- CaudalX0M0R --- X-number: 0 --- Follow-up: Postoperative
- C S 20X1M0R --- X-number: 1 --- Follow-up: Postoperative
- C S 20X2M0R --- X-number: 2 --- Follow-up: Postoperative
- C S 20X3M0R --- X-number: 3 --- Follow-up: Postoperative
- C S 20X4M0R --- X-number: 4 --- Follow-up: Postoperative
- C S 20X5M0R --- X-number: 5 --- Follow-up: Postoperative
- C S 20X6M0R --- X-number: 6 --- Follow-up: Postoperative

-----

Xref	Xmig	X	Y	Z	Rx	Ry	Rz	#Matched Markers	#Matched Reference Markers	Rigid Body Error	Rigid Body Error Reference	Condition Number	Condition Number Reference Model	Maximum Total Point Motion
-----														
Model: T4														
Reference: CaudalX0M0R --- L1														
0	1	20.0235	-0.0143	0.1165	0.0881	0.0472	0.0225	7	6	0.1471	0.0099	18.5	19.8	20.1579
0	2	-0.0391	19.9844	0.1162	0.0430	-0.0063	0.3203	3	6	0.0148	0.0240	34.4	19.8	19.9992
0	3	-0.0377	-0.0211	20.1803	0.0568	-0.0673	0.0413	7	6	0.0501	0.0237	18.5	19.8	20.2652
0	4	-20.0596	-0.0159	0.1554	0.0506	-0.0243	0.0323	7	6	0.0318	0.0421	18.5	19.8	20.0848
0	5	-0.0173	-20.004	0.1911	0.0621	-0.0156	0.0426	7	6	0.0154	0.0078	18.5	19.8	20.0526
0	6	-0.0098	0.0211	-19.8533	0.0608	-0.0058	0.0657	7	6	0.1258	0.0313	18.5	19.8	20.0629
-----														
Model: T8														
Reference: CaudalX0M0R --- L1														
0	1	0.0010	-0.0123	0.0802	0.0231	0.0094	-0.0115	6	6	0.0120	0.0099	19.8	19.8	0.0930
0	2	-0.0144	-0.0043	0.0552	0.0143	-0.0008	-0.0126	7	6	0.0245	0.0240	19.7	19.8	0.0735
0	3	-0.0100	-0.0016	0.0819	0.0279	0.0042	-0.0350	7	6	0.0248	0.0237	19.7	19.8	0.1081
0	4	-0.0290	-0.0067	0.0878	0.0272	-0.0196	-0.0096	7	6	0.0178	0.0421	19.7	19.8	0.1116
0	5	-0.0042	-0.0121	0.1105	0.0210	0.0106	0.0141	7	6	0.0220	0.0078	19.7	19.8	0.1446
0	6	-0.0083	-0.0025	0.0856	0.0193	0.0041	0.0010	7	6	0.0323	0.0313	19.7	19.8	0.1106



### E.3.6 Caudal Inferior: 0.5mm

----- Migration Results -----

Reference Axis: Automatic

=====

Available scenes:

-----

- CaudalX0M0R --- X-number: 0 --- Follow-up: Postoperative
- C I 05X1M0R --- X-number: 1 --- Follow-up: Postoperative
- C I 05X2M0R --- X-number: 2 --- Follow-up: Postoperative
- C I 05X3M0R --- X-number: 3 --- Follow-up: Postoperative
- C I 05X4M0R --- X-number: 4 --- Follow-up: Postoperative
- C I 05X5M0R --- X-number: 5 --- Follow-up: Postoperative
- C I 05X6M0R --- X-number: 6 --- Follow-up: Postoperative

-----

Xref	Xmig	X	Y	Z	Rx	Ry	Rz	#Matched Markers	#Matched Reference Markers	Rigid Body Error	Rigid Body Error Reference	Condition Number	Condition Number Reference Model	Maximum Total Point Motion
-----														
Model: T4														
Reference: CaudalX0M0R --- L1														
0	1	0.4814	-0.0079	0.2330	0.0426	-0.0066	0.0082	7	6	0.0200	0.0132	18.5	19.8	0.5539
0	2	-0.0241	0.4883	0.1958	0.0630	-0.0174	0.0348	7	6	0.0142	0.0072	18.5	19.8	0.5634
0	3	-0.0112	-0.0100	0.7189	0.0601	-0.0029	0.0220	7	6	0.0381	0.0138	18.5	19.8	0.7629
0	4	-0.5233	-0.0176	0.1902	0.0446	-0.0280	0.0290	7	6	0.0270	0.0441	18.5	19.8	0.5888
0	5	-0.0223	-0.4976	0.0513	0.0264	-0.0362	0.0294	7	6	0.0139	0.0092	18.5	19.8	0.5216
0	6	-0.0121	0.0208	-0.5006	0.0290	0.0008	0.0183	7	6	0.0308	0.0070	18.5	19.8	0.5405
-----														
Model: T8														
Reference: CaudalX0M0R --- L1														
0	1	0.4884	0.0012	0.1296	0.0334	0.0050	0.0054	7	6	0.0184	0.0132	19.7	19.8	0.5213
0	2	-0.0081	0.4919	0.0909	0.0212	0.0058	-0.0278	7	6	0.0295	0.0072	19.7	19.8	0.5321
0	3	-0.0069	-0.0055	0.6095	0.0352	0.0029	-0.0275	7	6	0.0337	0.0138	19.7	19.8	0.6460
0	4	-0.5005	-0.0074	0.1010	0.0165	0.0018	-0.0294	7	6	0.0360	0.0441	19.7	19.8	0.5348
0	5	-0.0055	-0.5076	0.0148	-0.0119	0.0035	-0.0259	7	6	0.0235	0.0092	19.7	19.8	0.5281
0	6	0.0018	0.0071	-0.5137	-0.0061	0.0028	-0.0068	7	6	0.0262	0.0070	19.7	19.8	0.5541

### E.3.7 Caudal Inferior: 1mm

----- Migration Results -----

Reference Axis: Automatic

=====

Available scenes:

-----

- CaudalX0M0R --- X-number: 0 --- Follow-up: Postoperative
- C I 1X1M0R --- X-number: 1 --- Follow-up: Postoperative
- C I 1X2M0R --- X-number: 2 --- Follow-up: Postoperative
- C I 1X3M0R --- X-number: 3 --- Follow-up: Postoperative
- C I 1X4M0R --- X-number: 4 --- Follow-up: Postoperative
- C I 1X5M0R --- X-number: 5 --- Follow-up: Postoperative
- C I 1X6M0R --- X-number: 6 --- Follow-up: Postoperative

-----

Xref	Xmig	X	Y	Z	Rx	Ry	Rz	#Matched Markers	#Matched Reference Markers	Rigid Body Error	Rigid Body Error Reference	Condition Number	Condition Number Reference Model	Maximum Total Point Motion
-----														
Model: T4														
Reference: CaudalX0M0R --- L1														
0	1	0.9771	0.0144	0.0630	0.0435	-0.0207	0.0236	7	6	0.0218	0.0308	18.5	19.8	1.0009
0	2	-0.0168	0.9881	0.2110	0.0649	-0.0038	0.0158	7	6	0.0139	0.0077	18.5	19.8	1.0347
0	3	-0.0370	-0.0156	1.1599	0.0483	-0.0164	0.0266	7	6	0.0227	0.0037	18.5	19.8	1.2011
0	4	-1.0577	-0.0047	0.0990	0.0203	-0.0255	0.0202	7	6	0.0262	0.0497	18.5	19.8	1.0882
0	5	-0.0040	-1.0189	0.2377	0.0637	0.0138	0.0058	7	6	0.0218	0.0079	18.5	19.8	1.0764
0	6	-0.0158	-0.0055	-0.7756	0.0590	-0.0079	-0.0083	7	6	0.0232	0.0217	18.5	19.8	0.8091
-----														
Model: T8														
Reference: CaudalX0M0R --- L1														
0	1	0.9909	0.0135	0.0344	0.0126	-0.0082	-0.0086	7	6	0.0134	0.0308	19.7	19.8	1.0080
0	2	-0.0063	0.9974	0.1011	0.0337	0.0108	-0.0367	7	6	0.0372	0.0077	19.7	19.8	1.0306
0	3	-0.0131	-0.0084	1.0845	0.0289	0.0010	-0.0155	7	6	0.0209	0.0037	19.7	19.8	1.1114
0	4	-1.0206	-0.0077	0.0579	0.0192	-0.0253	0.0019	7	6	0.0170	0.0497	19.7	19.8	1.0531
0	5	-0.0031	-1.0087	0.1164	0.0411	0.0011	-0.0400	7	6	0.0338	0.0079	19.7	19.8	1.0493
0	6	-0.0048	0.0008	-0.8680	0.0479	-0.0127	-0.0120	7	6	0.0173	0.0217	19.7	19.8	0.8908

### E.3.8 Caudal Inferior: 5mm

----- Migration Results -----

Reference Axis: Automatic

=====

Available scenes:

-----

- CaudalX0M0R --- X-number: 0 --- Follow-up: Postoperative
- C I 5X1M0R --- X-number: 1 --- Follow-up: Postoperative
- C I 5X2M0R --- X-number: 2 --- Follow-up: Postoperative
- C I 5X3M0R --- X-number: 3 --- Follow-up: Postoperative
- C I 5X4M0R --- X-number: 4 --- Follow-up: Postoperative
- C I 5X5M0R --- X-number: 5 --- Follow-up: Postoperative
- C I 5X6M0R --- X-number: 6 --- Follow-up: Postoperative

-----

Xref	Xmig	X	Y	Z	Rx	Ry	Rz	#Matched Markers	#Matched Reference Markers	Rigid Body Error	Rigid Body Error Reference	Condition Number	Condition Number Reference Model	Maximum Total Point Motion
-----														
Model: T4														
Reference: CaudalX0M0R --- L1														
0	1	5.0022	0.0105	0.1040	0.0336	0.0081	0.0085	7	6	0.0206	0.0089	18.5	19.8	5.0281
0	2	-0.0319	4.9978	0.2191	0.0738	-0.0509	0.0209	7	6	0.0352	0.0212	18.5	19.8	5.0346
0	3	-0.0167	-0.0604	5.3170	0.0604	0.0065	0.0061	7	6	0.0210	0.0151	18.5	19.8	5.3362
0	4	-5.0565	-0.0076	0.2210	0.0592	-0.0378	0.0175	7	6	0.0231	0.0368	18.5	19.8	5.0780
0	5	-0.0118	-4.9983	0.0372	0.0226	-0.0235	0.0356	7	6	0.0192	0.0236	18.5	19.8	5.0164
0	6	-0.0007	0.0501	-4.9900	0.0051	0.0125	0.0184	7	6	0.0323	0.0058	18.5	19.8	5.0359
-----														
Model: T8														
Reference: CaudalX0M0R --- L1														
0	1	5.0040	0.0091	0.0647	0.0328	0.0104	0.0009	7	6	0.0213	0.0089	19.7	19.8	5.0199
0	2	-0.0036	5.0017	0.1111	0.0284	-0.0161	-0.0061	7	6	0.0238	0.0212	19.7	19.8	5.0207
0	3	-0.0155	-0.0330	5.1620	0.0450	0.0051	-0.0089	7	6	0.0347	0.0151	19.7	19.8	5.1994
0	4	-5.0072	-0.0022	0.1256	0.0209	0.0071	-0.0139	7	6	0.0371	0.0368	19.7	19.8	5.0385
0	5	0.0002	-5.0029	0.0106	-0.0100	-0.0019	-0.0232	7	6	0.0194	0.0236	19.7	19.8	5.0255
0	6	0.0017	0.0162	-4.9889	0.0103	0.0085	0.0028	7	6	0.0255	0.0058	19.7	19.8	5.0159

### E.3.9 Caudal Inferior: 10mm

----- Migration Results -----

Reference Axis: Automatic

=====

Available scenes:

-----

- CaudalX0M0R --- X-number: 0 --- Follow-up: Postoperative
- C I 10X1M0R --- X-number: 1 --- Follow-up: Postoperative
- C I 10X2M0R --- X-number: 2 --- Follow-up: Postoperative
- C I 10X3M0R --- X-number: 3 --- Follow-up: Postoperative
- C I 10X4M0R --- X-number: 4 --- Follow-up: Postoperative
- C I 10X5M0R --- X-number: 5 --- Follow-up: Postoperative
- C I 10X6M0R --- X-number: 6 --- Follow-up: Postoperative

-----

Xref	Xmig	X	Y	Z	Rx	Ry	Rz	#Matched Markers	#Matched Reference Markers	Rigid Body Error	Rigid Body Error Reference	Condition Number	Condition Number Reference Model	Maximum Total Point Motion
-----														
Model: T4														
Reference: CaudalX0M0R --- L1														
0	1	9.9811	0.0148	-0.0664	0.0502	-0.0069	0.0109	7	6	0.0542	0.0234	18.5	19.8	10.0070
0	2	-0.0117	9.9884	0.1782	0.0317	-0.0132	0.0435	7	6	0.0220	0.0166	18.5	19.8	10.0200
0	3	0.0231	-0.0118	10.0430	0.0306	0.0170	-0.0348	7	6	0.0359	0.0289	18.5	19.8	10.0820
0	4	-10.0048	-0.0076	0.0724	0.0214	0.0029	-0.0168	7	6	0.0286	0.0134	18.5	19.8	10.0303
0	5	-0.0487	-9.9917	0.2292	0.0814	-0.0293	0.0387	7	6	0.0215	0.0142	18.5	19.8	10.0415
0	6	-0.0509	-0.0089	-9.7468	0.0850	-0.0470	0.0134	7	6	0.0403	0.0490	18.5	19.8	9.8065
-----														
Model: T8														
Reference: CaudalX0M0R --- L1														
0	1	9.9829	-0.0008	-0.0227	-0.0114	-0.0331	-0.0259	7	6	0.0243	0.0307	19.3	19.8	10.0043
0	2	-0.0112	9.9966	0.1082	0.0458	-0.0185	0.0156	7	6	0.0277	0.0223	19.3	19.8	10.0374
0	3	0.0174	-0.0034	10.0013	0.0204	0.0218	-0.0273	7	6	0.0297	0.0273	19.3	19.8	10.1469
0	4	-9.9889	-0.0037	0.0368	0.0318	0.0086	-0.0005	7	6	0.0412	0.0233	19.3	19.8	10.0583
0	5	-0.0104	-10.0047	0.1427	0.0503	0.0246	-0.0314	7	6	0.0164	0.0123	19.3	19.8	10.0389
0	6	-0.0386	-0.0072	-9.8783	0.0449	-0.0440	-0.0131	7	6	0.0231	0.0330	19.3	19.8	9.8462

### E.3.10 Caudal Inferior: 20mm

----- Migration Results -----

Reference Axis: Automatic

=====

Available scenes:

-----

- CaudalX0M0R --- X-number: 0 --- Follow-up: Postoperative
- C I 20X1M0R --- X-number: 1 --- Follow-up: Postoperative
- C I 20X2M0R --- X-number: 2 --- Follow-up: Postoperative
- C I 20X3M0R --- X-number: 3 --- Follow-up: Postoperative
- C I 20X4M0R --- X-number: 4 --- Follow-up: Postoperative
- C I 20X5M0R --- X-number: 5 --- Follow-up: Postoperative
- C I 20X6M0R --- X-number: 6 --- Follow-up: Postoperative

-----

Xref	Xmig	X	Y	Z	Rx	Ry	Rz	#Matched Markers	#Matched Reference Markers	Rigid Body Error	Rigid Body Error Reference	Condition Number	Condition Number Reference Model	Maximum Total Point Motion
-----														
Model: T4														
Reference: CaudalX0M0R --- L1														
0	1	20.0214	-0.0009	0.1092	0.0631	0.0030	0.0371	7	6	0.0912	0.0047	18.5	19.8	20.0918
0	2	-0.0464	19.9808	0.1233	0.0484	-0.0075	0.3263	3	6	0.0143	0.0184	34.4	19.8	19.9986
0	3	0.0099	0.0091	20.031	0.0319	-0.0381	0.0431	7	6	0.0484	0.0170	18.5	19.8	20.1022
0	4	-20.0957	0.0154	0.1321	0.0353	-0.0087	-0.0019	7	6	0.0287	0.0494	18.5	19.8	20.1244
0	5	-0.0286	-19.9884	0.1451	0.0518	-0.0311	0.0436	7	6	0.0160	0.0244	18.5	19.8	20.0325
0	6	-0.0072	0.0024	-19.7200	0.0915	-0.0251	0.0239	7	6	0.0231	0.0208	18.5	19.8	19.7498
-----														
Model: T8														
Reference: CaudalX0M0R --- L1														
0	1	20.0094	-0.0066	0.0620	0.0122	0.0104	-0.0139	7	6	0.0347	0.0047	19.7	19.8	20.0442
0	2	-0.0170	20.0036	0.0807	0.0339	-0.0032	-0.0246	7	6	0.0188	0.0184	19.7	19.8	20.0377
0	3	0.0194	0.0004	19.999	0.0010	0.0409	-0.0352	7	6	0.0336	0.0170	19.7	19.8	20.0508
0	4	-20.0481	0.0030	0.0986	0.0154	-0.0140	0.0043	6	6	0.0150	0.0494	21.6	19.8	20.0675
0	5	-0.0024	-20.001	0.0563	0.0136	0.0061	-0.0302	7	6	0.0402	0.0244	19.7	19.8	20.0266
0	6	0.0099	0.0138	-19.8335	0.0682	-0.0035	-0.0042	7	6	0.0214	0.0208	19.7	19.8	19.8500

### E.3.11 Caudal Rotation: 1°

----- Migration Results -----

Reference Axis: Automatic

=====

Available scenes:

-----

- CaudalX0M0R --- X-number: 0 --- Follow-up: Postoperative
- C R 1X1M0R --- X-number: 1 --- Follow-up: Postoperative
- C R 1X2M0R --- X-number: 2 --- Follow-up: Postoperative
- C R 1X3M0R --- X-number: 3 --- Follow-up: Postoperative
- C R 1X4M0R --- X-number: 4 --- Follow-up: Postoperative
- C R 1X5M0R --- X-number: 5 --- Follow-up: Postoperative
- C R 1X6M0R --- X-number: 6 --- Follow-up: Postoperative

-----

Xref	Xmig	X	Y	Z	Rx	Ry	Rz	#Matched Markers	#Matched Reference Markers	Rigid Body Error	Rigid Body Error Reference	Condition Number	Condition Number Reference Model	Maximum Total Point Motion
-----														
Model: T4														
Reference: CaudalX0M0R --- L1														
0	1	-0.0333	0.0054	0.1302	0.0396	-0.0071	0.0205	7	6	0.0262	0.0268	18.5	19.8	0.1786
0	2	-0.0411	-0.0061	0.1754	0.0424	-0.0429	0.0324	7	6	0.0161	0.0313	18.5	19.8	0.2319
0	3	-0.0329	-0.0154	0.2730	0.0650	-0.0273	0.0303	7	6	0.0103	0.0173	18.5	19.8	0.3080
0	4	-0.0275	-0.0407	0.3257	0.0743	-0.0272	0.0321	7	6	0.0170	0.0124	18.5	19.8	0.3729
0	5	-0.0047	0.0171	0.0327	0.0168	0.0114	0.0012	7	6	0.0128	0.0184	18.5	19.8	0.0653
0	6	-0.0124	-0.0231	0.3106	0.0694	-0.0094	0.0219	7	6	0.0034	0.0231	18.5	19.8	0.3213
-----														
Model: T8														
Reference: CaudalX0M0R --- L1														
0	1	-0.0084	0.0007	0.0604	1.0229	-0.0059	-0.0248	7	6	0.0240	0.0268	19.7	19.8	0.5853
0	2	-0.0139	-0.0103	0.1008	0.0351	0.9896	0.0078	7	6	0.0118	0.0313	19.7	19.8	0.6349
0	3	-0.0078	-0.0127	0.1494	0.0421	0.0050	1.0090	7	6	0.0279	0.0173	19.7	19.8	0.5534
0	4	-0.0137	-0.0158	0.1830	-0.9431	-0.0151	-0.0251	7	6	0.0111	0.0124	19.7	19.8	0.5612
0	5	0.0047	0.0133	0.0262	0.0015	-0.9950	0.0003	7	6	0.0097	0.0184	19.7	19.8	0.5758
0	6	0.0013	-0.0103	0.1862	0.0803	-0.0042	-1.0087	7	6	0.0158	0.0231	19.7	19.8	0.5673

### E.3.12 Caudal Rotation: 3°

----- Migration Results -----

Reference Axis: Automatic

=====

Available scenes:

-----

- CaudalX0M0R --- X-number: 0 --- Follow-up: Postoperative
- C R 3X1M0R --- X-number: 1 --- Follow-up: Postoperative
- C R 3X2M0R --- X-number: 2 --- Follow-up: Postoperative
- C R 3X3M0R --- X-number: 3 --- Follow-up: Postoperative
- C R 3X4M0R --- X-number: 4 --- Follow-up: Postoperative
- C R 3X5M0R --- X-number: 5 --- Follow-up: Postoperative
- C R 3X6M0R --- X-number: 6 --- Follow-up: Postoperative

-----

Xref	Xmig	X	Y	Z	Rx	Ry	Rz	#Matched Markers	#Matched Reference Markers	Rigid Body Error	Rigid Body Error Reference	Condition Number	Condition Number Reference Model	Maximum Total Point Motion
-----														
Model: T4														
Reference: CaudalX0M0R --- L1														
0	1	-0.0170	0.0150	0.0324	0.0192	0.0026	-0.0043	7	6	0.0135	0.0065	18.5	19.8	0.0644
0	2	-0.0109	0.0037	0.2080	0.0536	-0.0066	0.0162	7	6	0.0192	0.0315	18.5	19.8	0.2497
0	3	-0.0127	0.0634	0.1064	0.0251	0.0115	0.0020	7	6	0.0229	0.0280	18.5	19.8	0.1617
0	4	-0.0306	-0.0138	0.3659	0.0856	-0.0325	0.0298	7	6	0.0164	0.0366	18.5	19.8	0.4135
0	5	-0.0052	-0.0211	0.4238	0.0864	-0.0084	0.0076	7	6	0.0041	0.0179	18.5	19.8	0.4394
0	6	-0.0010	-0.0459	0.5564	0.1316	0.0213	0.0010	7	6	0.0217	0.0191	18.5	19.8	0.6234
-----														
Model: T8														
Reference: CaudalX0M0R --- L1														
0	1	-0.0012	0.0052	0.0213	3.0136	-0.0033	-0.0098	7	6	0.0098	0.0065	19.7	19.8	1.7276
0	2	0.0034	0.0117	0.1301	0.0265	-2.9943	-0.0112	7	6	0.0290	0.0315	19.7	19.8	1.7397
0	3	0.0024	0.0413	0.0698	0.0096	-0.0037	2.9892	7	6	0.0218	0.0280	19.7	19.8	1.5388
0	4	-0.0119	0.0079	0.2308	-2.9579	-0.0444	0.0022	7	6	0.0338	0.0366	19.7	19.8	1.7369
0	5	0.0052	-0.0001	0.2573	0.0950	3.0038	-0.0226	7	6	0.0306	0.0179	19.7	19.8	1.8406
0	6	0.0028	-0.0191	0.3198	0.1158	0.0013	-3.0443	7	6	0.0186	0.0191	19.7	19.8	1.5752

### E.3.13 Caudal Rotation: 6°

----- Migration Results -----

Reference Axis: Automatic

=====

Available scenes:

-----

CaudalX0M0R --- X-number: 0 --- Follow-up: Postoperative  
 C R 6X1M0R --- X-number: 1 --- Follow-up: Postoperative  
 C R 6X2M0R --- X-number: 2 --- Follow-up: Postoperative  
 C R 6X3M0R --- X-number: 3 --- Follow-up: Postoperative  
 C R 6X4M0R --- X-number: 4 --- Follow-up: Postoperative  
 C R 6X5M0R --- X-number: 5 --- Follow-up: Postoperative  
 C R 6X6M0R --- X-number: 6 --- Follow-up: Postoperative

-----

Xref	Xmig	X	Y	Z	Rx	Ry	Rz	#Matched Markers	#Matched Reference Markers	Rigid Body Error	Rigid Body Error Reference	Condition Number	Condition Number Reference Model	Maximum Total Point Motion
-----														
Model: T4														
Reference: CaudalX0M0R --- L1														
0	1	-0.0173	-0.0099	0.2219	0.0461	-0.0113	0.0088	7	6	0.0189	0.0199	18.5	19.8	0.2562
0	2	-0.0272	-0.0030	0.0986	0.0152	-0.0002	-0.0094	7	6	0.0175	0.0203	18.5	19.8	0.1232
0	3	0.0062	-0.0166	0.3737	0.0828	0.0265	-0.0157	7	6	0.0262	0.0124	18.5	19.8	0.4445
0	4	-0.0415	-0.0226	0.2695	0.0585	-0.0319	0.0260	7	6	0.0214	0.0324	18.5	19.8	0.3135
0	5	-0.0029	-0.0360	0.4104	0.0829	0.0107	0.0145	7	6	0.0242	0.0109	18.5	19.8	0.4616
0	6	-0.0057	-0.0342	0.3364	0.0744	-0.0214	0.0223	7	6	0.0213	0.0137	18.5	19.8	0.3716
-----														
Model: T8														
Reference: CaudalX0M0R --- L1														
0	1	0.0077	0.0040	0.1366	6.0519	0.0311	-0.0545	7	6	0.0429	0.0199	19.7	19.8	3.4800
0	2	-0.5303	0.0179	0.1293	0.0311	6.0738	-0.0073	6	6	0.0840	0.0203	22.0	19.8	3.5713
0	3	-0.0018	0.0010	0.2340	0.0175	-0.0308	6.0028	7	6	0.0466	0.0124	19.7	19.8	3.0556
0	4	-0.0049	-0.5317	0.1797	-5.9859	-0.0011	-0.0198	6	6	0.0129	0.0324	22.0	19.8	3.4607
0	5	-0.0068	-0.0067	0.2155	0.0624	-6.0375	-0.0078	7	6	0.0485	0.0109	19.7	19.8	3.5246
0	6	0.0269	-0.0156	0.1830	0.0980	0.0055	-6.0167	6	6	0.0185	0.0137	23.3	19.8	3.0761



### E.3.14 Caudal Rotation: 10°

----- Migration Results -----

Reference Axis: Automatic

=====

Available scenes:

-----

- CaudalX0M0R --- X-number: 0 --- Follow-up: Postoperative
- C R 10X1M0R --- X-number: 1 --- Follow-up: Postoperative
- C R 10X2M0R --- X-number: 2 --- Follow-up: Postoperative
- C R 10X3M0R --- X-number: 3 --- Follow-up: Postoperative
- C R 10X4M0R --- X-number: 4 --- Follow-up: Postoperative
- C R 10X5M0R --- X-number: 5 --- Follow-up: Postoperative
- C R 10X6M0R --- X-number: 6 --- Follow-up: Postoperative

-----

Xref	Xmig	X	Y	Z	Rx	Ry	Rz	#Matched Markers	#Matched Reference Markers	Rigid Body Error	Rigid Body Error Reference	Condition Number	Condition Number Reference Model	Maximum Total Point Motion
-----														
Model: T4														
Reference: CaudalX0M0R --- L1														
0	1	-0.0299	0.0164	0.2356	0.0623	-0.0218	0.0265	7	6	0.0262	0.0205	18.5	19.8	0.2792
0	2	-0.0377	-0.0497	0.3867	0.0861	-0.0237	0.0291	7	6	0.0269	0.0249	18.5	19.8	0.4312
0	3	0.0029	-0.0381	0.3059	0.0713	0.0072	0.0043	7	6	0.0270	0.0174	18.5	19.8	0.3524
0	4	-0.0206	-0.0229	0.2421	0.0467	-0.0309	0.0250	7	6	0.0229	0.0265	18.5	19.8	0.2796
0	5	-0.0444	0.0082	0.1542	0.0350	-0.0351	0.0241	7	6	0.0200	0.0306	18.5	19.8	0.2014
0	6	-0.0154	-0.0068	0.0980	0.0253	-0.0251	0.0246	7	6	0.0207	0.0206	18.5	19.8	0.1361
-----														
Model: T8														
Reference: CaudalX0M0R --- L1														
0	1	-0.0047	-0.0061	0.1444	10.0662	0.0105	-0.0497	7	6	0.0253	0.0205	19.7	19.8	5.7999
0	2	-0.9632	-0.0256	0.3214	0.1559	10.0106	-0.0162	6	6	0.0354	0.0249	23.3	19.8	5.6302
0	3	0.0123	-0.0809	0.1717	0.0512	0.0100	9.9927	6	6	0.0207	0.0174	22.0	19.8	5.0786
0	4	0.0013	-0.9031	0.1722	-10.002	-0.0207	-0.0165	6	6	0.0768	0.0265	22.0	19.8	5.7419
0	5	-0.2795	-0.0051	-0.7482	0.0199	-10.0263	0.0553	6	6	0.0516	0.0306	24.8	19.8	5.7560
0	6	0.0054	0.0008	0.0381	0.0198	-0.0037	-10.0196	7	6	0.0239	0.0206	19.7	19.8	5.0775

### E.3.15 Apex Superior: 0.5mm

----- Migration Results -----

Reference Axis: Automatic

=====

Available scenes:

-----

- TopX0M0R --- X-number: 0 --- Follow-up: Postoperative
- T S 05X1M0R --- X-number: 1 --- Follow-up: Postoperative
- T S 05X2M0R --- X-number: 2 --- Follow-up: Postoperative
- T S 05X3M0R --- X-number: 3 --- Follow-up: Postoperative
- T S 05X4M0R --- X-number: 4 --- Follow-up: Postoperative
- T S 05X5M0R --- X-number: 5 --- Follow-up: Postoperative
- T S 05X6M0R --- X-number: 6 --- Follow-up: Postoperative

-----

Xref	Xmig	X	Y	Z	Rx	Ry	Rz	#Matched Markers	#Matched Reference Markers	Rigid Body Error	Rigid Body Error Reference	Condition Number	Condition Number Reference Model	Maximum Total Point Motion
-----														
Model: T4														
Reference: TopX0M0R --- T8														
0	1	0.5481	-0.0050	-0.0771	-0.0320	-0.0002	0.0057	7	7	0.0588	0.0237	19.8	20.9	0.5893
0	2	0.0862	0.4826	-0.0336	-0.0272	0.0001	-0.0655	7	7	0.0407	0.0328	19.8	20.9	0.5290
0	3	0.0049	-0.0168	0.3915	-0.0626	-0.0130	0.0285	7	7	0.0379	0.0229	19.8	20.9	0.4318
0	4	-0.4761	-0.0031	-0.0706	-0.0295	-0.0070	0.0135	7	7	0.0224	0.0235	19.8	20.9	0.4901
0	5	-0.1019	-0.4914	-0.0452	0.0018	0.0006	0.0854	7	7	0.0475	0.0235	19.8	20.9	0.5586
0	6	-0.0066	-0.0014	-0.5483	0.0156	0.0250	-0.0339	7	7	0.0394	0.0224	19.8	20.9	0.6097

### E.3.16 Apex Superior: 1mm

----- Migration Results -----

Reference Axis: Automatic

=====

Available scenes:

-----

- TopX0M0R --- X-number: 0 --- Follow-up: Postoperative
- T S 1X1M0R --- X-number: 1 --- Follow-up: Postoperative
- T S 1X2M0R --- X-number: 2 --- Follow-up: Postoperative
- T S 1X3M0R --- X-number: 3 --- Follow-up: Postoperative
- T S 1X4M0R --- X-number: 4 --- Follow-up: Postoperative
- T S 1X5M0R --- X-number: 5 --- Follow-up: Postoperative
- T S 1X6M0R --- X-number: 6 --- Follow-up: Postoperative

-----

Xref	Xmig	X	Y	Z	Rx	Ry	Rz	#Matched Markers	#Matched Reference Markers	Rigid Body Error	Rigid Body Error Reference	Condition Number	Condition Number Reference Model	Maximum Total Point Motion
-----														
Model: T4														
Reference: TopX0M0R --- T8														
0	1	1.0937	-0.0333	0.0193	-0.0025	-0.0090	-0.0405	7	7	0.0325	0.0248	19.8	20.9	1.1118
0	2	-0.0619	0.9991	-0.0179	-0.0107	-0.0150	0.0428	7	7	0.0437	0.0245	19.8	20.9	1.0312
0	3	0.0371	-0.0047	0.9519	0.0236	-0.0560	0.0081	7	7	0.0885	0.0235	19.8	20.9	1.1327
0	4	-0.9808	-0.0073	-0.0759	-0.0267	-0.0060	0.0327	7	7	0.0693	0.0235	19.8	20.9	1.0440
0	5	-0.0495	-0.9961	-0.0235	0.0082	-0.0420	0.0714	7	7	0.0260	0.0253	19.8	20.9	1.0320
0	6	-0.0946	-0.0047	-0.9953	0.0274	-0.0320	0.0420	7	7	0.0357	0.0393	19.8	20.9	1.0574

### E.3.17 Apex Superior: 5mm

----- Migration Results -----

Reference Axis: Automatic

=====

Available scenes:

-----

- TopX0M0R --- X-number: 0 --- Follow-up: Postoperative
- T S 5X1M0R --- X-number: 1 --- Follow-up: Postoperative
- T S 5X2M0R --- X-number: 2 --- Follow-up: Postoperative
- T S 5X3M0R --- X-number: 3 --- Follow-up: Postoperative
- T S 5X4M0R --- X-number: 4 --- Follow-up: Postoperative
- T S 5X5M0R --- X-number: 5 --- Follow-up: Postoperative
- T S 5X6M0R --- X-number: 6 --- Follow-up: Postoperative

-----

Xref	Xmig	X	Y	Z	Rx	Ry	Rz	#Matched Markers	#Matched Reference Markers	Rigid Body Error	Rigid Body Error Reference	Condition Number	Condition Number Reference Model	Maximum Total Point Motion
Model: T4														
Reference: TopX0M0R --- T8														
0	1	4.9426	0.0165	-0.0463	0.0027	-0.0210	0.0546	7	7	0.0612	0.0253	19.8	20.9	5.0044
0	2	0.0179	4.9853	-0.0723	-0.0091	-0.0140	0.0076	7	7	0.0309	0.0337	19.8	20.9	5.0063
0	3	0.0107	-0.0029	4.9133	-0.0176	0.0240	0.0433	7	7	0.0991	0.0235	19.8	20.9	5.0106
0	4	-4.9686	-0.0139	-0.0415	0.0028	-0.0170	-0.0089	7	7	0.0641	0.0234	19.8	20.9	4.9935
0	5	0.0193	-5.0086	-0.0709	-0.0027	-0.0001	0.0103	7	7	0.0441	0.0235	19.8	20.9	5.0396
0	6	0.0340	-0.0212	-5.0707	-0.0060	0.0146	0.0104	7	7	0.0382	0.0235	19.8	20.9	5.1207

### E.3.18 Apex Superior: 10mm

----- Migration Results -----

Reference Axis: Automatic

=====

Available scenes:

-----

- TopX0M0R --- X-number: 0 --- Follow-up: Postoperative
- T S 10X1M0R --- X-number: 1 --- Follow-up: Postoperative
- T S 10X2M0R --- X-number: 2 --- Follow-up: Postoperative
- T S 10X3M0R --- X-number: 3 --- Follow-up: Postoperative
- T S 10X4M0R --- X-number: 4 --- Follow-up: Postoperative
- T S 10X5M0R --- X-number: 5 --- Follow-up: Postoperative
- T S 10X6M0R --- X-number: 6 --- Follow-up: Postoperative

-----

Xref	Xmig	X	Y	Z	Rx	Ry	Rz	#Matched Markers	#Matched Reference Markers	Rigid Body Error	Rigid Body Error Reference	Condition Number	Condition Number Reference Model	Maximum Total Point Motion
Model: T4														
Reference: TopX0M0R --- T8														
0	1	10.0617	0.0005	-0.0684	0.0153	0.0029	0.0081	7	7	0.0583	0.0230	19.8	20.9	10.1266
0	2	-0.0848	9.9959	0.0298	0.0165	-0.0338	0.0269	7	7	0.0359	0.0303	19.8	20.9	10.0322
0	3	0.0115	-0.0074	10.0433	0.0660	-0.0409	0.0082	7	7	0.0467	0.0292	19.8	20.9	10.0945
0	4	-10.0206	0.0100	-0.0644	0.0069	0.0032	0.0000	7	7	0.0611	0.0262	19.8	20.9	10.0452
0	5	0.0068	-10.0049	-0.0323	-0.0384	-0.0214	0.0453	7	7	0.0427	0.0258	19.8	20.9	10.0491
0	6	0.0889	-0.0069	-10.053	-0.0085	0.0088	-0.0230	7	7	0.0654	0.0253	19.8	20.9	10.1951

### E.3.19 Apex Superior: 20mm

----- Migration Results -----

Reference Axis: Automatic

=====

Available scenes:

-----

- TopX0M0R --- X-number: 0 --- Follow-up: Postoperative
- T S 20X1M0R --- X-number: 1 --- Follow-up: Postoperative
- T S 20X2M0R --- X-number: 2 --- Follow-up: Postoperative
- T S 20X3M0R --- X-number: 3 --- Follow-up: Postoperative
- T S 20X4M0R --- X-number: 4 --- Follow-up: Postoperative
- T S 20X5M0R --- X-number: 5 --- Follow-up: Postoperative
- T S 20X6M0R --- X-number: 6 --- Follow-up: Postoperative

-----

Xref	Xmig	X	Y	Z	Rx	Ry	Rz	#Matched Markers	#Matched Reference Markers	Rigid Body Error	Rigid Body Error Reference	Condition Number	Condition Number Reference Model	Maximum Total Point Motion
-----														
Model: T4														
Reference: TopX0M0R --- T8														
0	1	20.0293	-0.0089	-0.0500	0.0097	-0.0540	0.0288	7	7	0.0662	0.0231	19.8	20.9	20.0898
0	2	0.1158	20.0047	-0.0345	0.0273	-0.0440	0.0112	7	7	0.0570	0.0208	19.8	20.9	20.0852
0	3	0.0138	-0.0031	19.9065	-0.0299	-0.0110	0.0551	7	7	0.0304	0.0237	19.8	20.9	19.9668
0	4	-19.9879	-0.0111	-0.1093	-0.0525	0.0150	0.0403	7	7	0.0499	0.0236	19.8	20.9	20.0480
0	5	0.0135	-20.0114	-0.0670	-0.0157	-0.0080	-0.0058	7	7	0.0386	0.0239	19.8	20.9	20.0417
0	6	0.1003	-0.0246	-20.0465	0.0050	0.0104	-0.0438	7	7	0.0577	0.0223	19.8	20.9	20.1187

### E.3.20 Apex Inferior: 0.5mm

----- Migration Results -----

Reference Axis: Automatic

=====

Available scenes:

-----

- BottomX0M0R --- X-number: 0 --- Follow-up: Postoperative
- B I 05X1M0R --- X-number: 1 --- Follow-up: Postoperative
- B I 05X2M0R --- X-number: 2 --- Follow-up: Postoperative
- B I 05X3M0R --- X-number: 3 --- Follow-up: Postoperative
- B I 05X4M0R --- X-number: 4 --- Follow-up: Postoperative
- B I 05X5M0R --- X-number: 5 --- Follow-up: Postoperative
- B I 05X6M0R --- X-number: 6 --- Follow-up: Postoperative

-----

Xref	Xmig	X	Y	Z	Rx	Ry	Rz	#Matched Markers	#Matched Reference Markers	Rigid Body Error	Rigid Body Error Reference	Condition Number	Condition Number Reference Model	Maximum Total Point Motion
-----														
Model: L1														
Reference: BottomX0M0R --- T8														
0	1	-0.3202	0.0180	-0.1410	0.0585	0.0531	0.0593	6	7	0.0046	0.0448	20.2	20.0	0.3782
0	2	-0.0004	-0.5019	-0.0072	-0.0130	-0.0080	0.0016	6	7	0.0100	0.0265	20.2	20.0	0.5039
0	3	0.0109	0.0254	-0.4686	-0.0800	-0.0320	0.0105	6	7	0.0108	0.0244	20.2	20.0	0.4808
0	4	0.4822	0.0025	-0.0258	-0.0312	-0.0140	-0.0014	6	7	0.0186	0.0339	20.2	20.0	0.4896
0	5	0.0061	0.5101	-0.0817	-0.0080	0.0015	0.0033	6	7	0.0069	0.0208	20.2	20.0	0.5262
0	6	-0.2275	-0.0037	0.5599	-0.0770	0.0337	-0.0841	6	7	0.0160	0.0273	20.2	20.0	0.6357

### E.3.21 Apex Inferior: 1mm

----- Migration Results -----

Reference Axis: Automatic

=====

Available scenes:

-----

- BottomX0M0R --- X-number: 0 --- Follow-up: Postoperative
- B I 1X1M0R --- X-number: 1 --- Follow-up: Postoperative
- B I 1X2M0R --- X-number: 2 --- Follow-up: Postoperative
- B I 1X3M0R --- X-number: 3 --- Follow-up: Postoperative
- B I 1X4M0R --- X-number: 4 --- Follow-up: Postoperative
- B I 1X5M0R --- X-number: 5 --- Follow-up: Postoperative
- B I 1X6M0R --- X-number: 6 --- Follow-up: Postoperative

-----

Xref	Xmig	X	Y	Z	Rx	Ry	Rz	#Matched Markers	#Matched Reference Markers	Rigid Body Error	Rigid Body Error Reference	Condition Number	Condition Number Reference Model	Maximum Total Point Motion
Model: L1														
Reference: BottomX0M0R --- T8														
0	1	-0.9248	0.0209	-0.0165	-0.0623	0.0446	0.0241	6	7	0.0092	0.0551	20.2	20.0	0.9374
0	2	-0.0213	-0.9931	-0.0105	-0.0286	0.0228	-0.0099	6	7	0.0192	0.0331	20.2	20.0	1.0024
0	3	0.0422	0.0169	-0.9698	-0.0751	0.0019	0.0155	6	7	0.0144	0.0243	20.2	20.0	1.0113
0	4	1.0194	0.0084	-0.0237	-0.0307	0.0131	0.0099	6	7	0.0065	0.0318	20.2	20.0	1.0239
0	5	-0.0509	0.9951	0.1007	-0.0537	0.0225	-0.0187	6	7	0.0048	0.0288	20.2	20.0	1.0408
0	6	0.0250	0.0287	1.0540	-0.0867	-0.0100	0.0149	6	7	0.0107	0.0428	20.2	20.0	1.0613



### E.3.22 Apex Inferior: 5mm

----- Migration Results -----

Reference Axis: Automatic

=====

Available scenes:

-----

- BottomX0M0R --- X-number: 0 --- Follow-up: Postoperative
- B I 5X1M0R --- X-number: 1 --- Follow-up: Postoperative
- B I 5X2M0R --- X-number: 2 --- Follow-up: Postoperative
- B I 5X3M0R --- X-number: 3 --- Follow-up: Postoperative
- B I 5X4M0R --- X-number: 4 --- Follow-up: Postoperative
- B I 5X5M0R --- X-number: 5 --- Follow-up: Postoperative
- B I 5X6M0R --- X-number: 6 --- Follow-up: Postoperative

-----

Xref	Xmig	X	Y	Z	Rx	Ry	Rz	#Matched Markers	#Matched Reference Markers	Rigid Body Error	Rigid Body Error Reference	Condition Number	Condition Number Reference Model	Maximum Total Point Motion
-----														
Model: L1														
Reference: BottomX0M0R --- T8														
0	1	-4.9268	0.0057	-0.0163	0.0065	-0.0540	0.0378	6	7	0.0270	0.0407	20.2	20.0	4.9952
0	2	-0.0702	-4.9853	0.0533	-0.0712	-0.0160	-0.021	6	7	0.0092	0.0297	20.2	20.0	5.0107
0	3	0.1073	0.0247	-4.9782	-0.0338	0.0312	0.0415	6	7	0.0064	0.0449	20.2	20.0	5.0080
0	4	4.9868	0.0083	-0.0661	-0.0497	-0.0210	0.0012	6	7	0.0149	0.0299	20.2	20.0	4.9932
0	5	-0.0034	5.0031	-0.0157	-0.0268	-0.0070	0.0067	6	7	0.0247	0.0439	20.2	20.0	5.0341
0	6	-0.0979	0.0145	5.0579	-0.0836	-0.0070	-0.0305	6	7	0.0138	0.0424	20.2	20.0	5.0693

### E.3.23 Apex Inferior: 10mm

----- Migration Results -----

Reference Axis: Automatic

=====

Available scenes:

-----

- BottomX0M0R --- X-number: 0 --- Follow-up: Postoperative
- B I 10X1M0R --- X-number: 1 --- Follow-up: Postoperative
- B I 10X2M0R --- X-number: 2 --- Follow-up: Postoperative
- B I 10X3M0R --- X-number: 3 --- Follow-up: Postoperative
- B I 10X4M0R --- X-number: 4 --- Follow-up: Postoperative
- B I 10X5M0R --- X-number: 5 --- Follow-up: Postoperative
- B I 10X6M0R --- X-number: 6 --- Follow-up: Postoperative

-----

Xref	Xmig	X	Y	Z	Rx	Ry	Rz	#Matched Markers	#Matched Reference Markers	Rigid Body Error	Rigid Body Error Reference	Condition Number	Condition Number Reference Model	Maximum Total Point Motion
-----														
Model: L1														
Reference: BottomX0M0R --- T8														
0	1	-10.0948	0.0006	0.0722	-0.0745	0.0014	-0.0423	6	7	0.0229	0.0339	20.2	20	10.1261
0	2	0.1132	-9.9891	-0.1226	-0.0146	-0.0069	0.0346	6	7	0.0082	0.0628	20.2	20	10.0158
0	3	-0.0265	-0.0023	-10.0040	-0.0288	0.0013	-0.0107	6	7	0.0093	0.0385	20.2	20	10.0143
0	4	10.0113	0.0141	0.0543	-0.0522	-0.0068	0.0066	6	7	0.0061	0.0494	20.2	20	10.0152
0	5	-0.0221	10.0275	0.1554	-0.1558	0.0150	-0.0089	6	7	0.0254	0.0705	20.2	20	10.1611
0	6	-0.0139	0.0019	10.0618	-0.0570	0.0020	-0.0150	6	7	0.0274	0.0390	20.2	20	10.1044

### E.3.24 Apex Inferior: 20mm

----- Migration Results -----

Reference Axis: Automatic

=====

Available scenes:

-----

- BottomX0M0R --- X-number: 0 --- Follow-up: Postoperative
- B I 20X1M0R --- X-number: 1 --- Follow-up: Postoperative
- B I 20X2M0R --- X-number: 2 --- Follow-up: Postoperative
- B I 20X3M0R --- X-number: 3 --- Follow-up: Postoperative
- B I 20X4M0R --- X-number: 4 --- Follow-up: Postoperative
- B I 20X5M0R --- X-number: 5 --- Follow-up: Postoperative
- B I 20X6M0R --- X-number: 6 --- Follow-up: Postoperative

-----

Xref	Xmig	X	Y	Z	Rx	Ry	Rz	#Matched Markers	#Matched Reference Markers	Rigid Body Error	Rigid Body Error Reference	Condition Number	Condition Number Reference Model	Maximum Total Point Motion
-----														
Model: L1														
Reference: BottomX0M0R --- T8														
0	1	-19.9985	0.0128	0.0811	-0.0851	0.0129	0.0036	6	7	0.0110	0.0409	20.2	20.0	20.0048
0	2	0.1417	-19.9824	-0.1734	-0.0074	-0.0060	0.0475	6	7	0.0099	0.0183	20.2	20.0	20.0136
0	3	-0.0906	-0.0011	-19.9130	-0.0911	-0.0260	-0.0253	6	7	0.0193	0.0520	20.2	20.0	19.9193
0	4	20.0738	0.0365	-0.0135	-0.0536	-0.0260	0.0327	6	7	0.0208	0.0261	20.2	20.0	20.0866
0	5	-0.0546	20.0149	0.0965	-0.0897	-0.0370	-0.0126	6	7	0.0304	0.0376	20.2	20.0	20.0990
0	6	0.0747	0.0079	19.9173	-0.0377	-0.0060	0.0304	6	7	0.0131	0.0351	20.2	20.0	19.9267

### E.3.25 Apex Rotation Superior: 1°

----- Migration Results -----

Reference Axis: Automatic

=====

Available scenes:

-----

- TopX0M0R --- X-number: 0 --- Follow-up: Postoperative
- T R 1X1M0R --- X-number: 1 --- Follow-up: Postoperative
- T R 1X2M0R --- X-number: 2 --- Follow-up: Postoperative
- T R 1X3M0R --- X-number: 3 --- Follow-up: Postoperative
- T R 1X4M0R --- X-number: 4 --- Follow-up: Postoperative
- T R 1X5M0R --- X-number: 5 --- Follow-up: Postoperative
- T R 1X6M0R --- X-number: 6 --- Follow-up: Postoperative

-----

Xref	Xmig	X	Y	Z	Rx	Ry	Rz	#Matched Markers	#Matched Reference Markers	Rigid Body Error	Rigid Body Error Reference	Condition Number	Condition Number Reference Model	Maximum Total Point Motion
-----														
Model: T4														
Reference: TopX0M0R --- T8														
0	1	0.0388	-0.0191	0.0102	-1.0193	-0.0330	0.0462	7	7	0.0280	0.0319	19.8	20.9	2.2510
0	2	0.0875	-0.0300	0.0116	-0.0396	-0.9830	-0.0257	7	7	0.0395	0.0281	19.8	20.9	0.7542
0	3	-0.0593	-0.0092	0.0237	-0.0201	-0.0130	-1.0203	7	7	0.0404	0.0365	19.8	20.9	2.1602
0	4	0.0126	-0.0212	0.0451	0.9722	0.0149	0.0318	7	7	0.0524	0.0334	19.8	20.9	2.1546
0	5	0.0058	-0.0105	-0.0094	-0.0561	1.0357	-0.0394	7	7	0.0617	0.0276	19.8	20.9	1.0446
0	6	0.0413	-0.0302	0.0172	-0.0396	-0.0110	1.0229	7	7	0.0586	0.0307	19.8	20.9	2.1884

### E.3.26 Apex Rotation Inferior: 1°

----- Migration Results -----

Reference Axis: Automatic

=====

Available scenes:

-----

- BottomX0M0R --- X-number: 0 --- Follow-up: Postoperative
- B R 1X1M0R --- X-number: 1 --- Follow-up: Postoperative
- B R 1X2M0R --- X-number: 2 --- Follow-up: Postoperative
- B R 1X3M0R --- X-number: 3 --- Follow-up: Postoperative
- B R 1X4M0R --- X-number: 4 --- Follow-up: Postoperative
- B R 1X5M0R --- X-number: 5 --- Follow-up: Postoperative
- B R 1X6M0R --- X-number: 6 --- Follow-up: Postoperative

-----

Xref	Xmig	X	Y	Z	Rx	Ry	Rz	#Matched Markers	#Matched Reference Markers	Rigid Body Error	Rigid Body Error Reference	Condition Number	Condition Number Reference Model	Maximum Total Point Motion
-----														
Model: L1														
Reference: BottomX0M0R --- T8														
0	1	-0.0177	0.0181	-0.2616	-1.1569	-0.0400	-0.0139	6	7	0.0083	0.0484	20.2	20.0	3.2114
0	2	0.0095	0.0226	-0.1444	-0.0775	-1.0010	-0.0186	6	7	0.0294	0.0338	20.2	20.0	0.8872
0	3	-0.0092	0.0196	-0.1545	-0.0781	-0.0150	-0.9408	6	7	0.0041	0.0378	20.2	20.0	2.8346
0	4	-0.0198	0.0165	-0.1682	0.9366	-0.0190	0.0604	6	7	0.0213	0.0324	20.2	20.0	3.0091
0	5	-0.0154	0.0120	-0.2521	-0.0830	0.9893	-0.0083	6	7	0.0083	0.0445	20.2	20.0	0.8182
0	6	-0.0173	0.0084	-0.2283	-0.0683	-0.0380	0.9608	6	7	0.0240	0.0400	20.2	20.0	2.8788

### E.3.27 Apex Rotation Superior: 3°

----- Migration Results -----

Reference Axis: Automatic

=====

Available scenes:

-----

TopX0M0R --- X-number: 0 --- Follow-up: Postoperative  
 T R 3X1M0R --- X-number: 1 --- Follow-up: Postoperative  
 T R 3X2M0R --- X-number: 2 --- Follow-up: Postoperative  
 T R 3X3M0R --- X-number: 3 --- Follow-up: Postoperative  
 T R 3X4M0R --- X-number: 4 --- Follow-up: Postoperative  
 T R 3X5M0R --- X-number: 5 --- Follow-up: Postoperative  
 T R 3X6M0R --- X-number: 6 --- Follow-up: Postoperative

-----

Xref	Xmig	X	Y	Z	Rx	Ry	Rz	#Matched Markers	#Matched Reference Markers	Rigid Body Error	Rigid Body Error Reference	Condition Number	Condition Number Reference Model	Maximum Total Point Motion
-----														
Model: T4														
Reference: TopX0M0R --- T8														
0	1	0.0154	-0.0380	0.0171	-3.0643	-0.0040	0.0044	7	7	0.0627	0.0456	19.8	20.9	6.6797
0	2	0.0061	-0.0130	-0.0171	-0.0068	2.9733	0.0548	7	7	0.0481	0.0513	19.8	20.9	2.6209
0	3	0.0653	-0.0320	0.0076	-0.0448	-0.0250	-2.9504	7	7	0.0443	0.0363	19.8	20.9	6.4816
0	4	-0.0105	-0.0289	0.0261	2.9739	0.0054	-0.0407	7	7	0.0251	0.0376	19.8	20.9	6.4884
0	5	0.0426	-0.0231	0.0249	-0.0410	-2.9910	-0.0218	7	7	0.0604	0.0231	19.8	20.9	2.6280
0	6	0.1222	-0.0327	0.0253	-0.0358	0.0092	2.9887	7	7	0.0584	0.0401	19.8	20.9	6.4027

### E.3.28 Apex Rotation Inferior: 3°

----- Migration Results -----

Reference Axis: Automatic

=====

Available scenes:

-----

- BottomX0M0R --- X-number: 0 --- Follow-up: Postoperative
- B R 3X1M0R --- X-number: 1 --- Follow-up: Postoperative
- B R 3X2M0R --- X-number: 2 --- Follow-up: Postoperative
- B R 3X3M0R --- X-number: 3 --- Follow-up: Postoperative
- B R 3X4M0R --- X-number: 4 --- Follow-up: Postoperative
- B R 3X5M0R --- X-number: 5 --- Follow-up: Postoperative
- B R 3X6M0R --- X-number: 6 --- Follow-up: Postoperative

-----

Xref	Xmig	X	Y	Z	Rx	Ry	Rz	#Matched Markers	#Matched Reference Markers	Rigid Body Error	Rigid Body Error Reference	Condition Number	Condition Number Reference Model	Maximum Total Point Motion
-----														
Model: L1														
Reference: BottomX0M0R --- T8														
0	1	-0.0140	0.0042	-0.1597	-3.0925	-0.0620	-0.0550	6	7	0.0086	0.0504	20.2	20.0	9.1602
0	2	-0.0190	0.0157	-0.1812	-0.0439	2.9917	0.0278	6	7	0.0079	0.0373	20.2	20.0	2.6207
0	3	-0.0378	0.0324	-0.2780	-0.1095	-0.0500	-2.8801	6	7	0.0474	0.0394	20.2	20.0	8.6847
0	4	-0.0243	0.0371	-0.0946	2.9513	-0.1500	0.1371	6	6	0.0112	0.0765	20.2	21.9	8.9658
0	5	-0.0319	0.0047	-0.0505	-0.0238	-3.0960	0.0039	6	7	0.0625	0.0587	20.2	20.0	2.7038
0	6	-0.0100	0.0006	-0.2443	-0.1084	-0.0220	2.8758	6	7	0.0046	0.0545	20.2	20.0	8.6373

### E.3.29 Apex Rotation Superior: 6°

----- Migration Results -----

Reference Axis: Automatic

=====

Available scenes:

-----

- TopX0M0R --- X-number: 0 --- Follow-up: Postoperative
- T R 6X1M0R --- X-number: 1 --- Follow-up: Postoperative
- T R 6X2M0R --- X-number: 2 --- Follow-up: Postoperative
- T R 6X3M0R --- X-number: 3 --- Follow-up: Postoperative
- T R 6X4M0R --- X-number: 4 --- Follow-up: Postoperative
- T R 6X5M0R --- X-number: 5 --- Follow-up: Postoperative
- T R 6X6M0R --- X-number: 6 --- Follow-up: Postoperative

-----

Xref	Xmig	X	Y	Z	Rx	Ry	Rz	#Matched Markers	#Matched Reference Markers	Rigid Body Error	Rigid Body Error Reference	Condition Number	Condition Number Reference Model	Maximum Total Point Motion
-----														
Model: T4														
Reference: TopX0M0R --- T8														
0	1	-0.0221	0.0027	-0.0030	-5.9829	0.0052	0.0427	7	7	0.0613	0.0284	19.8	20.9	12.9746
0	2	0.0396	-0.0113	-0.0572	-0.0397	-5.9900	-0.0615	7	6	0.0373	0.0654	19.8	22.7	5.2681
0	3	-0.0222	-0.0022	-0.0460	-0.0016	-0.0020	-6.0215	7	7	0.0264	0.0448	19.8	20.9	13.0851
0	4	0.0144	-0.0211	0.0044	5.9843	0.0223	-0.0038	7	7	0.0482	0.0441	19.8	20.9	13.0334
0	5	-0.0205	-0.0153	-0.0690	-0.0469	6.1091	-0.0567	7	7	0.0675	0.1407	19.8	20.9	5.6837
0	6	-0.0119	-0.0264	0.0216	-0.0330	0.0288	5.9829	7	7	0.0292	0.0272	19.8	20.9	13.0119



### E.3.30 Apex Rotation Inferior: 6°

----- Migration Results -----

Reference Axis: Automatic

=====

Available scenes:

-----

- BottomX0M0R --- X-number: 0 --- Follow-up: Postoperative
- B R 6X1M0R --- X-number: 1 --- Follow-up: Postoperative
- B R 6X2M0R --- X-number: 2 --- Follow-up: Postoperative
- B R 6X3M0R --- X-number: 3 --- Follow-up: Postoperative
- B R 6X4M0R --- X-number: 4 --- Follow-up: Postoperative
- B R 6X5M0R --- X-number: 5 --- Follow-up: Postoperative
- B R 6X6M0R --- X-number: 6 --- Follow-up: Postoperative

-----

Xref	Xmig	X	Y	Z	Rx	Ry	Rz	#Matched Markers	#Matched Reference Markers	Rigid Body Error	Rigid Body Error Reference	Condition Number	Condition Number Reference Model	Maximum Total Point Motion
-----														
Model: L1														
Reference: BottomX0M0R --- T8														
0	1	-0.0216	0.0175	-0.0315	-6.0302	-0.0250	0.0268	6	7	0.0159	0.0502	20.2	20.0	18.1160
0	2	-0.0008	0.0085	-0.1033	-0.0045	-6.1180	0.1308	6	5	0.0246	0.0710	20.2	26.2	4.8536
0	3	-0.0086	0.0304	-0.1855	-0.0340	0.0001	-5.9309	6	6	0.0229	0.0620	20.2	21.9	17.8341
0	4	-0.0518	0.0713	-0.2443	5.9096	-0.0960	0.0675	6	6	0.0378	0.0427	20.2	21.9	18.0482
0	5	-0.0572	0.0277	-0.2980	-0.1361	5.9683	0.0064	6	7	0.0396	0.0791	20.2	20.0	4.9872
0	6	-0.0127	0.0119	-0.1676	-0.0989	-0.0300	5.9876	6	7	0.0158	0.0658	20.2	20.0	17.9886

### E.3.31 Apex Rotation Superior: 10°

----- Migration Results -----

Reference Axis: Automatic

=====

Available scenes:

-----

- TopX0M0R --- X-number: 0 --- Follow-up: Postoperative
- T R 10X1M0R --- X-number: 1 --- Follow-up: Postoperative
- T R 10X2M0R --- X-number: 2 --- Follow-up: Postoperative
- T R 10X3M0R --- X-number: 3 --- Follow-up: Postoperative
- T R 10X4M0R --- X-number: 4 --- Follow-up: Postoperative
- T R 10X5M0R --- X-number: 5 --- Follow-up: Postoperative
- T R 10X6M0R --- X-number: 6 --- Follow-up: Postoperative

-----

Xref	Xmig	X	Y	Z	Rx	Ry	Rz	#Matched Markers	#Matched Reference Markers	Rigid Body Error	Rigid Body Error Reference	Condition Number	Condition Number Reference Model	Maximum Total Point Motion
-----														
Model: T4														
Reference: TopX0M0R --- T8														
0	1	0.0088	0.0172	0.0087	-9.9811	0.0362	0.0188	7	7	0.1044	0.0481	19.8	20.9	21.6566
0	2	0.0216	-0.0066	-0.0295	0.0113	-9.9799	0.0359	7	7	0.0429	0.1031	19.8	20.9	9.1124
0	3	-0.0007	-0.0273	0.0051	-0.0293	-0.0252	-10.022	7	7	0.0427	0.0609	19.8	20.9	21.7636
0	4	-0.0119	0.0087	-0.0133	9.9711	0.0020	0.0742	7	6	0.0731	0.0513	19.8	22.7	21.6711
0	5	-0.0318	0.0178	0.0033	-0.0322	10.1029	0.0111	7	6	0.0479	0.0601	19.8	28.2	9.1217
0	6	0.0052	-0.0217	0.0179	-0.0340	0.0404	9.9879	7	7	0.0628	0.0358	19.8	20.9	21.7007

### E.3.32 Apex Rotation Inferior: 10°

----- Migration Results -----

Reference Axis: Automatic

=====

Available scenes:

-----

- BottomX0M0R --- X-number: 0 --- Follow-up: Postoperative
- B R 10X1M0R --- X-number: 1 --- Follow-up: Postoperative
- B R 10X2M0R --- X-number: 2 --- Follow-up: Postoperative
- B R 10X3M0R --- X-number: 3 --- Follow-up: Postoperative
- B R 10X4M0R --- X-number: 4 --- Follow-up: Postoperative
- B R 10X5M0R --- X-number: 5 --- Follow-up: Postoperative
- B R 10X6M0R --- X-number: 6 --- Follow-up: Postoperative

-----

Xref	Xmig	X	Y	Z	Rx	Ry	Rz	#Matched Markers	#Matched Reference Markers	Rigid Body Error	Rigid Body Error Reference	Condition Number	Condition Number Reference Model	Maximum Total Point Motion
-----														
Model: L1														
Reference: BottomX0M0R --- T8														
0	1	-0.0190	-0.0108	-0.1963	-10.1030	-0.0200	0.0175	6	7	0.0052	0.0398	20.2	20.0	30.1799
0	2	-0.0016	0.04671	-0.1588	-0.1147	-10.0090	0.0444	6	7	0.0300	0.1471	20.2	20.0	8.4601
0	3	-0.0067	0.04429	-0.2915	-0.1065	0.0112	-9.8970	6	6	0.0395	0.0488	20.2	21.9	29.7324
0	4	-0.0599	0.07876	-0.2741	9.8710	-0.1694	0.0399	6	6	0.0052	0.2043	20.2	21.9	29.9482
0	5	-0.0413	0.02217	-0.1459	-0.1470	10.1016	0.1315	6	6	0.0057	0.1637	20.2	26.0	8.7817
0	6	-0.0083	0.03130	-0.3592	-0.1693	-0.0475	10.0333	6	7	0.0444	0.0528	20.2	20.0	30.1305

### E.3.33 Dual Superior: 0.5mm

----- Migration Results -----

Reference Axis: Automatic

=====

Available scenes:

-----

- TopX0M0R --- X-number: 0 --- Follow-up: Postoperative
- T S 05X1M0R --- X-number: 1 --- Follow-up: Postoperative
- T S 05X2M0R --- X-number: 2 --- Follow-up: Postoperative
- T S 05X3M0R --- X-number: 3 --- Follow-up: Postoperative
- T S 05X4M0R --- X-number: 4 --- Follow-up: Postoperative
- T S 05X5M0R --- X-number: 5 --- Follow-up: Postoperative
- T S 05X6M0R --- X-number: 6 --- Follow-up: Postoperative

-----

Xref	Xmig	X	Y	Z	Rx	Ry	Rz	#Matched Markers	#Matched Reference Markers	Rigid Body Error	Rigid Body Error Reference	Condition Number	Condition Number Reference Model	Maximum Total Point Motion
-----														
Model: T8														
Reference: TopX0M0R --- T4														
0	1	-0.5594	0.0175	0.0138	0.0320	0.0002	-0.0057	7	7	0.0237	0.0588	20.9	19.8	0.5834
0	2	0.0440	-0.4908	-0.0204	0.0272	-0.0001	0.0655	7	7	0.0328	0.0407	20.9	19.8	0.5316
0	3	-0.0657	0.0463	-0.5120	0.0626	0.0124	-0.0286	7	7	0.0229	0.0379	20.9	19.8	0.5372
0	4	0.4470	0.0166	0.0141	0.0295	0.0072	-0.0135	7	7	0.0235	0.0224	20.9	19.8	0.4750
0	5	-0.0662	0.5135	0.0486	-0.0018	-0.0006	-0.0854	7	7	0.0235	0.0475	20.9	19.8	0.5740
0	6	0.0819	-0.0128	0.5724	-0.0155	-0.0250	0.0338	7	7	0.0224	0.0394	20.9	19.8	0.6109

### E.3.34 Dual Superior: 1mm

----- Migration Results -----

Reference Axis: Automatic

=====

Available scenes:

-----

- TopX0M0R --- X-number: 0 --- Follow-up: Postoperative
- T S 1X1M0R --- X-number: 1 --- Follow-up: Postoperative
- T S 1X2M0R --- X-number: 2 --- Follow-up: Postoperative
- T S 1X3M0R --- X-number: 3 --- Follow-up: Postoperative
- T S 1X4M0R --- X-number: 4 --- Follow-up: Postoperative
- T S 1X5M0R --- X-number: 5 --- Follow-up: Postoperative
- T S 1X6M0R --- X-number: 6 --- Follow-up: Postoperative

-----

Xref	Xmig	X	Y	Z	Rx	Ry	Rz	#Matched Markers	#Matched Reference Markers	Rigid Body Error	Rigid Body Error Reference	Condition Number	Condition Number Reference Model	Maximum Total Point Motion
-----														
Model: T8														
Reference: TopX0M0R --- T4														
0	1	-1.0166	0.0226	-0.0217	0.0025	0.0090	0.0405	7	7	0.0248	0.0325	20.9	19.8	1.0405
0	2	-0.0287	-0.9840	0.0005	0.0108	0.0154	-0.0428	7	7	0.0245	0.0437	20.9	19.8	0.9952
0	3	-0.0730	-0.0016	-0.8903	-0.0236	0.0555	-0.0081	7	7	0.0235	0.0885	20.9	19.8	0.9127
0	4	0.9141	0.0246	0.0245	0.0267	0.0060	-0.0327	7	7	0.0235	0.0693	20.9	19.8	0.9439
0	5	-0.1047	1.0123	0.0507	-0.0081	0.0418	-0.0714	7	7	0.0253	0.0260	20.9	19.8	1.0728
0	6	0.0013	0.0069	1.0578	-0.0273	0.0316	-0.0420	7	7	0.0393	0.0357	20.9	19.8	1.1072

### E.3.35 Dual Superior: 5mm

----- Migration Results -----

Reference Axis: Automatic

=====

Available scenes:

-----

- TopX0M0R --- X-number: 0 --- Follow-up: Postoperative
- T S 5X1M0R --- X-number: 1 --- Follow-up: Postoperative
- T S 5X2M0R --- X-number: 2 --- Follow-up: Postoperative
- T S 5X3M0R --- X-number: 3 --- Follow-up: Postoperative
- T S 5X4M0R --- X-number: 4 --- Follow-up: Postoperative
- T S 5X5M0R --- X-number: 5 --- Follow-up: Postoperative
- T S 5X6M0R --- X-number: 6 --- Follow-up: Postoperative

-----

Xref	Xmig	X	Y	Z	Rx	Ry	Rz	#Matched Markers	#Matched Reference Markers	Rigid Body Error	Rigid Body Error Reference	Condition Number	Condition Number Reference Model	Maximum Total Point Motion
-----														
Model: T8														
Reference: TopX0M0R --- T4														
0	1	-5.0578	0.0019	0.0591	-0.0027	0.0209	-0.0546	7	7	0.0253	0.0612	20.9	19.8	5.0865
0	2	-0.0382	-4.9802	0.0571	0.0091	0.0138	-0.0076	7	7	0.0337	0.0309	20.9	19.8	5.0034
0	3	-0.0860	0.0220	-4.9546	0.0176	-0.0240	-0.0433	7	7	0.0235	0.0991	20.9	19.8	4.9700
0	4	4.9803	0.0113	0.0502	-0.0028	0.0174	0.0089	7	7	0.0234	0.0641	20.9	19.8	4.9999
0	5	-0.0388	5.0123	0.0659	0.0027	0.0001	-0.0103	7	7	0.0235	0.0441	20.9	19.8	5.0479
0	6	-0.0509	0.0255	5.0550	0.0060	-0.0150	-0.0104	7	7	0.0235	0.0382	20.9	19.8	5.0878

### E.3.36 Dual Superior: 10mm

----- Migration Results -----

Reference Axis: Automatic

=====

Available scenes:

-----

- TopX0M0R --- X-number: 0 --- Follow-up: Postoperative
- T S 10X1M0R --- X-number: 1 --- Follow-up: Postoperative
- T S 10X2M0R --- X-number: 2 --- Follow-up: Postoperative
- T S 10X3M0R --- X-number: 3 --- Follow-up: Postoperative
- T S 10X4M0R --- X-number: 4 --- Follow-up: Postoperative
- T S 10X5M0R --- X-number: 5 --- Follow-up: Postoperative
- T S 10X6M0R --- X-number: 6 --- Follow-up: Postoperative

-----

Xref	Xmig	X	Y	Z	Rx	Ry	Rz	#Matched Markers	#Matched Reference Markers	Rigid Body Error	Rigid Body Error Reference	Condition Number	Condition Number Reference Model	Maximum Total Point Motion
-----														
Model: T8														
Reference: TopX0M0R --- T4														
0	1	-10.0768	-0.0022	0.0973	-0.0153	-0.0029	-0.0081	7	7	0.0230	0.0583	20.9	19.8	10.0963
0	2	0.0153	-9.9944	0.0146	-0.0165	0.0338	-0.0269	7	7	0.0303	0.0359	20.9	19.8	10.0297
0	3	-0.0488	-0.0244	-9.9018	-0.0660	0.0409	-0.0081	7	7	0.0292	0.0467	20.9	19.8	9.9498
0	4	10.0215	-0.0123	0.0777	-0.0069	-0.0032	0.0000	7	7	0.0262	0.0611	20.9	19.8	10.0444
0	5	-0.0958	10.0301	-0.0313	0.0384	0.0214	-0.0453	7	7	0.0258	0.0427	20.9	19.8	10.0866
0	6	-0.0419	0.0022	10.0338	0.0085	-0.0088	0.0230	7	7	0.0253	0.0654	20.9	19.8	10.0646

### E.3.37 Dual Superior: 20mm

----- Migration Results -----

Reference Axis: Automatic

=====

Available scenes:

-----

- TopX0M0R --- X-number: 0 --- Follow-up: Postoperative
- T S 20X1M0R --- X-number: 1 --- Follow-up: Postoperative
- T S 20X2M0R --- X-number: 2 --- Follow-up: Postoperative
- T S 20X3M0R --- X-number: 3 --- Follow-up: Postoperative
- T S 20X4M0R --- X-number: 4 --- Follow-up: Postoperative
- T S 20X5M0R --- X-number: 5 --- Follow-up: Postoperative
- T S 20X6M0R --- X-number: 6 --- Follow-up: Postoperative

-----

Xref	Xmig	X	Y	Z	Rx	Ry	Rz	#Matched Markers	#Matched Reference Markers	Rigid Body Error	Rigid Body Error Reference	Condition Number	Condition Number Reference Model	Maximum Total Point Motion
-----														
Model: T8														
Reference: TopX0M0R --- T4														
0	1	-20.1047	0.0234	0.1025	-0.0097	0.0539	-0.0288	7	7	0.0231	0.0662	20.9	19.8	20.1378
0	2	-0.1566	-20.0110	0.1097	-0.0273	0.0435	-0.0112	7	7	0.0208	0.0570	20.9	19.8	20.0361
0	3	-0.1302	0.0385	-19.9628	0.0299	0.0106	-0.0551	7	7	0.0237	0.0304	20.9	19.8	19.9787
0	4	19.9133	0.0257	0.0066	0.0525	-0.0150	-0.0403	7	7	0.0236	0.0499	20.9	19.8	19.9452
0	5	-0.0069	20.0152	0.0436	0.0157	0.0083	0.0058	7	7	0.0239	0.0386	20.9	19.8	20.0542
0	6	-0.0138	0.0129	20.0536	-0.0050	-0.0100	0.0438	7	7	0.0223	0.0577	20.9	19.8	20.0950



### E.3.38 Dual Inferior: 0.5mm

----- Migration Results -----

Reference Axis: Automatic

=====

Available scenes:

-----

- BottomX0M0R --- X-number: 0 --- Follow-up: Postoperative
- B I 05X1M0R --- X-number: 1 --- Follow-up: Postoperative
- B I 05X2M0R --- X-number: 2 --- Follow-up: Postoperative
- B I 05X3M0R --- X-number: 3 --- Follow-up: Postoperative
- B I 05X4M0R --- X-number: 4 --- Follow-up: Postoperative
- B I 05X5M0R --- X-number: 5 --- Follow-up: Postoperative
- B I 05X6M0R --- X-number: 6 --- Follow-up: Postoperative

-----

Xref	Xmig	X	Y	Z	Rx	Ry	Rz	#Matched Markers	#Matched Reference Markers	Rigid Body Error	Rigid Body Error Reference	Condition Number	Condition Number Reference Model	Maximum Total Point Motion
-----														
Model: T8														
Reference: BottomX0M0R --- L1														
0	1	0.4876	-0.0078	-0.0331	-0.0586	-0.0530	-0.0594	7	6	0.0448	0.0046	20.0	20.2	0.5126
0	2	0.0047	0.5029	0.0452	0.0130	0.0080	-0.0016	7	6	0.0265	0.0100	20.0	20.2	0.5236
0	3	0.0175	-0.0205	0.6983	0.0801	0.0315	-0.0106	7	6	0.0244	0.0108	20.0	20.2	0.7179
0	4	-0.4867	-0.0015	0.1157	0.0312	0.0140	0.0014	7	6	0.0339	0.0186	20.0	20.2	0.5378
0	5	0.0032	-0.5090	0.1036	0.0080	-0.0020	-0.0033	7	6	0.0208	0.0069	20.0	20.2	0.5302
0	6	-0.0049	-0.0107	-0.3528	0.0771	-0.0340	0.0841	7	6	0.0273	0.0160	20.0	20.2	0.3879

### E.3.39 Dual Inferior: 1mm

----- Migration Results -----

Reference Axis: Automatic

=====

Available scenes:

-----

BottomX0M0R --- X-number: 0 --- Follow-up: Postoperative

B I 1X1M0R --- X-number: 1 --- Follow-up: Postoperative

B I 1X2M0R --- X-number: 2 --- Follow-up: Postoperative

B I 1X3M0R --- X-number: 3 --- Follow-up: Postoperative

B I 1X4M0R --- X-number: 4 --- Follow-up: Postoperative

B I 1X5M0R --- X-number: 5 --- Follow-up: Postoperative

B I 1X6M0R --- X-number: 6 --- Follow-up: Postoperative

-----

Xref	Xmig	X	Y	Z	Rx	Ry	Rz	#Matched Markers	#Matched Reference Markers	Rigid Body Error	Rigid Body Error Reference	Condition Number	Condition Number Reference Model	Maximum Total Point Motion
-----														
Model: T8														
Reference: BottomX0M0R --- L1														
0	1	0.9937	-0.0135	0.1807	0.0622	-0.0450	-0.0241	7	6	0.0551	0.0092	20.0	20.2	1.0353
0	2	-0.0055	0.9921	0.0856	0.0286	-0.0230	0.0099	7	6	0.0331	0.0192	20.0	20.2	1.0115
0	3	0.0009	-0.0117	1.1783	0.0751	-0.0020	-0.0155	7	6	0.0243	0.0144	20.0	20.2	1.1997
0	4	-0.9913	-0.0047	0.1060	0.0307	-0.0130	-0.0099	7	6	0.0318	0.0065	20.0	20.2	1.0169
0	5	0.0002	-0.9969	0.0430	0.0538	-0.0230	0.0187	7	6	0.0288	0.0048	20.0	20.2	1.0533
0	6	0.0159	-0.0204	-0.8105	0.0867	0.0097	-0.0149	7	6	0.0428	0.0107	20.0	20.2	0.8592

### E.3.40 Dual Inferior: 5mm

----- Migration Results -----

Reference Axis: Automatic

=====

Available scenes:

-----

BottomX0M0R --- X-number: 0 --- Follow-up: Postoperative

B I 5X1M0R --- X-number: 1 --- Follow-up: Postoperative

B I 5X2M0R --- X-number: 2 --- Follow-up: Postoperative

B I 5X3M0R --- X-number: 3 --- Follow-up: Postoperative

B I 5X4M0R --- X-number: 4 --- Follow-up: Postoperative

B I 5X5M0R --- X-number: 5 --- Follow-up: Postoperative

B I 5X6M0R --- X-number: 6 --- Follow-up: Postoperative

-----

Xref	Xmig	X	Y	Z	Rx	Ry	Rz	#Matched Markers	#Matched Reference Markers	Rigid Body Error	Rigid Body Error Reference	Condition Number	Condition Number Reference Model	Maximum Total Point Motion
-----														
Model: T8														
Reference: BottomX0M0R --- L1														
0	1	5.0297	-0.0009	0.0055	-0.0064	0.0536	-0.0378	7	6	0.0407	0.0270	20.0	20.2	5.0821
0	2	0.0094	4.9836	0.1544	0.0712	0.0159	0.0209	7	6	0.0297	0.0092	20.0	20.2	5.0239
0	3	0.0069	-0.0171	5.0653	0.0338	-0.031	-0.0415	7	6	0.0449	0.0064	20.0	20.2	5.1142
0	4	-4.9842	-0.0059	0.2107	0.0497	0.0209	-0.0012	7	6	0.0299	0.0149	20.0	20.2	5.0032
0	5	0.0211	-5.0005	0.0896	0.0268	0.0072	-0.0067	7	6	0.0439	0.0247	20.0	20.2	5.0267
0	6	0.0122	-0.0104	-4.8238	0.0836	0.0071	0.0305	7	6	0.0424	0.0138	20.0	20.2	4.8683

### E.3.41 Dual Inferior: 10mm

----- Migration Results -----

Reference Axis: Automatic

=====

Available scenes:

-----

- BottomX0M0R --- X-number: 0 --- Follow-up: Postoperative
- B I 10X1M0R --- X-number: 1 --- Follow-up: Postoperative
- B I 10X2M0R --- X-number: 2 --- Follow-up: Postoperative
- B I 10X3M0R --- X-number: 3 --- Follow-up: Postoperative
- B I 10X4M0R --- X-number: 4 --- Follow-up: Postoperative
- B I 10X5M0R --- X-number: 5 --- Follow-up: Postoperative
- B I 10X6M0R --- X-number: 6 --- Follow-up: Postoperative

-----

Xref	Xmig	X	Y	Z	Rx	Ry	Rz	#Matched Markers	#Matched Reference Markers	Rigid Body Error	Rigid Body Error Reference	Condition Number	Condition Number Reference Model	Maximum Total Point Motion
-----														
Model: T8														
Reference: BottomX0M0R --- L1														
0	1	9.9771	0.0007	0.1351	0.0745	-0.0014	0.0423	7	6	0.0339	0.0229	20	20.2	9.9963
0	2	-0.0112	9.9973	0.1672	0.0146	0.0069	-0.0346	7	6	0.0628	0.0082	20	20.2	10.0355
0	3	-0.0035	-0.0039	10.0836	0.0288	-0.0013	0.0107	7	6	0.0385	0.0093	20	20.2	10.1468
0	4	-9.9933	-0.0093	0.0936	0.0522	0.0068	-0.0066	7	6	0.0494	0.0061	20	20.2	10.0155
0	5	-0.0006	-10.0230	0.2476	0.1558	-0.0150	0.0090	7	6	0.0705	0.0254	20	20.2	10.1048
0	6	-0.0275	0.0072	-9.9036	0.0570	-0.0020	0.0150	7	6	0.0390	0.0274	20	20.2	9.9447

### E.3.42 Dual Inferior: 20mm

----- Migration Results -----

Reference Axis: Automatic

=====

Available scenes:

-----

- BottomX0M0R --- X-number: 0 --- Follow-up: Postoperative
- B I 20X1M0R --- X-number: 1 --- Follow-up: Postoperative
- B I 20X2M0R --- X-number: 2 --- Follow-up: Postoperative
- B I 20X3M0R --- X-number: 3 --- Follow-up: Postoperative
- B I 20X4M0R --- X-number: 4 --- Follow-up: Postoperative
- B I 20X5M0R --- X-number: 5 --- Follow-up: Postoperative
- B I 20X6M0R --- X-number: 6 --- Follow-up: Postoperative

-----

Xref	Xmig	X	Y	Z	Rx	Ry	Rz	#Matched Markers	#Matched Reference Markers	Rigid Body Error	Rigid Body Error Reference	Condition Number	Condition Number Reference Model	Maximum Total Point Motion
-----														
Model: T8														
Reference: BottomX0M0R --- L1														
0	1	20.0089	-0.0097	0.1574	0.0851	-0.0130	-0.0035	7	6	0.0409	0.0110	20.0	20.2	20.0304
0	2	0.0067	19.9932	0.1978	0.0074	0.0059	-0.0475	7	6	0.0183	0.0099	20.0	20.2	20.0199
0	3	0.0282	-0.0324	20.1722	0.0911	0.0261	0.0253	7	6	0.0520	0.0193	20.0	20.2	20.2207
0	4	-19.9838	-0.0157	0.1771	0.0536	0.0254	-0.0327	7	6	0.0261	0.0208	20.0	20.2	19.9999
0	5	0.0225	-20.0138	0.1297	0.0897	0.0365	0.0125	7	6	0.0376	0.0304	20.0	20.2	20.0849
0	6	0.0075	0.0134	-19.8111	0.0377	0.0062	-0.0304	7	6	0.0351	0.0131	20.0	20.2	19.8528

### E.3.43 Dual Rotation Superior: 1°

----- Migration Results -----

Reference Axis: Automatic

=====

Available scenes:

-----

- TopX0M0R --- X-number: 0 --- Follow-up: Postoperative
- T R 1X1M0R --- X-number: 1 --- Follow-up: Postoperative
- T R 1X2M0R --- X-number: 2 --- Follow-up: Postoperative
- T R 1X3M0R --- X-number: 3 --- Follow-up: Postoperative
- T R 1X4M0R --- X-number: 4 --- Follow-up: Postoperative
- T R 1X5M0R --- X-number: 5 --- Follow-up: Postoperative
- T R 1X6M0R --- X-number: 6 --- Follow-up: Postoperative

-----

Xref	Xmig	X	Y	Z	Rx	Ry	Rz	#Matched Markers	#Matched Reference Markers	Rigid Body Error	Rigid Body Error Reference	Condition Number	Condition Number Reference Model	Maximum Total Point Motion
-----														
Model: T8														
Reference: TopX0M0R --- T4														
0	1	-0.0405	0.0195	-0.0102	1.0196	0.0330	-0.0475	7	7	0.0319	0.0280	20.9	19.8	0.5608
0	2	-0.0875	0.0298	-0.0101	0.0384	0.9828	0.0249	7	7	0.0281	0.0395	20.9	19.8	0.5632
0	3	0.0578	0.0103	-0.0227	0.0188	0.0138	1.0198	7	7	0.0365	0.0404	20.9	19.8	0.5273
0	4	-0.0136	0.0207	-0.0456	-0.9725	-0.0140	-0.0319	7	7	0.0334	0.0524	20.9	19.8	0.5864
0	5	-0.0060	0.0107	0.0092	0.0557	-1.0360	0.0399	7	7	0.0276	0.0617	20.9	19.8	0.6094
0	6	-0.0421	0.0313	-0.0184	0.0397	0.0106	-1.0246	7	7	0.0307	0.0586	20.9	19.8	0.5697

### E.3.44 Dual Rotation Inferior: 1°

----- Migration Results -----

Reference Axis: Automatic

=====

Available scenes:

-----

- BottomX0M0R --- X-number: 0 --- Follow-up: Postoperative
- B R 1X1M0R --- X-number: 1 --- Follow-up: Postoperative
- B R 1X2M0R --- X-number: 2 --- Follow-up: Postoperative
- B R 1X3M0R --- X-number: 3 --- Follow-up: Postoperative
- B R 1X4M0R --- X-number: 4 --- Follow-up: Postoperative
- B R 1X5M0R --- X-number: 5 --- Follow-up: Postoperative
- B R 1X6M0R --- X-number: 6 --- Follow-up: Postoperative

-----

Xref	Xmig	X	Y	Z	Rx	Ry	Rz	#Matched Markers	#Matched Reference Markers	Rigid Body Error	Rigid Body Error Reference	Condition Number	Condition Number Reference Model	Maximum Total Point Motion
-----														
Model: T8														
Reference: BottomX0M0R --- L1														
0	1	0.0180	-0.0231	0.2596	1.1562	0.0400	0.0120	7	6	0.0484	0.0083	20.0	20.2	0.7163
0	2	-0.0066	-0.0227	0.1431	0.0767	1.0017	0.0171	7	6	0.0338	0.0294	20.0	20.2	0.6706
0	3	0.0094	-0.0196	0.1545	0.0777	0.0167	0.9409	7	6	0.0378	0.0041	20.0	20.2	0.5143
0	4	0.0195	-0.0139	0.1677	-0.9374	0.0199	-0.0600	7	6	0.0324	0.0213	20.0	20.2	0.5666
0	5	0.0105	-0.0124	0.2530	0.0834	-0.9900	0.0094	7	6	0.0445	0.0083	20.0	20.2	0.7747
0	6	0.0177	-0.0088	0.2267	0.0682	0.0373	-0.9620	7	6	0.0400	0.0240	20.0	20.2	0.5648

### E.3.45 Dual Rotation Superior: 3°

----- Migration Results -----

Reference Axis: Automatic

=====

Available scenes:

-----

- TopX0M0R --- X-number: 0 --- Follow-up: Postoperative
- T R 3X1M0R --- X-number: 1 --- Follow-up: Postoperative
- T R 3X2M0R --- X-number: 2 --- Follow-up: Postoperative
- T R 3X3M0R --- X-number: 3 --- Follow-up: Postoperative
- T R 3X4M0R --- X-number: 4 --- Follow-up: Postoperative
- T R 3X5M0R --- X-number: 5 --- Follow-up: Postoperative
- T R 3X6M0R --- X-number: 6 --- Follow-up: Postoperative

-----

Xref	Xmig	X	Y	Z	Rx	Ry	Rz	#Matched Markers	#Matched Reference Markers	Rigid Body Error	Rigid Body Error Reference	Condition Number	Condition Number Reference Model	Maximum Total Point Motion
-----														
Model: T8														
Reference: TopX0M0R --- T4														
0	1	-0.0161	0.0388	-0.0146	3.0637	0.0046	-0.0044	7	7	0.0456	0.0627	20.9	19.8	1.7399
0	2	-0.0066	0.0128	0.0170	0.0025	-2.9730	-0.0549	7	7	0.0513	0.0481	20.9	19.8	1.7577
0	3	-0.0690	0.0290	-0.0083	0.0437	0.0281	2.9486	7	7	0.0363	0.0443	20.9	19.8	1.5312
0	4	0.0095	0.0281	-0.0277	-2.9744	-0.0070	0.0398	7	7	0.0376	0.0251	20.9	19.8	1.7383
0	5	-0.0463	0.0232	-0.0220	0.0394	2.9911	0.0175	7	7	0.0231	0.0604	20.9	19.8	1.6954
0	6	-0.1213	0.0392	-0.0254	0.0346	-0.0110	-2.9899	7	7	0.0401	0.0584	20.9	19.8	1.5427



### E.3.46 Dual Rotation Inferior: 3°

----- Migration Results -----

Reference Axis: Automatic

=====

Available scenes:

-----

- BottomX0M0R --- X-number: 0 --- Follow-up: Postoperative
- B R 3X1M0R --- X-number: 1 --- Follow-up: Postoperative
- B R 3X2M0R --- X-number: 2 --- Follow-up: Postoperative
- B R 3X3M0R --- X-number: 3 --- Follow-up: Postoperative
- B R 3X4M0R --- X-number: 4 --- Follow-up: Postoperative
- B R 3X5M0R --- X-number: 5 --- Follow-up: Postoperative
- B R 3X6M0R --- X-number: 6 --- Follow-up: Postoperative

-----

Xref	Xmig	X	Y	Z	Rx	Ry	Rz	#Matched Markers	#Matched Reference Markers	Rigid Body Error	Rigid Body Error Reference	Condition Number	Condition Number Reference Model	Maximum Total Point Motion
-----														
Model: T8														
Reference: BottomX0M0R --- L1														
0	1	0.0130	-0.0126	0.1575	3.0910	0.0651	0.0514	7	6	0.0504	0.0086	20.0	20.2	1.7855
0	2	0.0090	-0.0157	0.1814	0.0418	-2.9910	-0.0256	7	6	0.0373	0.0079	20.0	20.2	1.7379
0	3	0.0382	-0.0311	0.2768	0.1061	0.0560	2.8804	7	6	0.0394	0.0474	20.0	20.2	1.5180
0	4	0.0097	-0.2917	0.1053	-2.9510	0.1573	-0.1291	6	6	0.0765	0.0112	21.9	20.2	1.6665
0	5	0.0340	-0.0047	0.0483	0.0241	3.0967	-0.0053	7	6	0.0587	0.0625	20.0	20.2	1.8136
0	6	0.0102	-0.0014	0.2438	0.1089	0.0162	-2.8766	7	6	0.0545	0.0046	20.0	20.2	1.5319

### E.3.47 Dual Rotation Superior: 6°

----- Migration Results -----

Reference Axis: Automatic

=====

Available scenes:

-----

- TopX0M0R --- X-number: 0 --- Follow-up: Postoperative
- T R 6X1M0R --- X-number: 1 --- Follow-up: Postoperative
- T R 6X2M0R --- X-number: 2 --- Follow-up: Postoperative
- T R 6X3M0R --- X-number: 3 --- Follow-up: Postoperative
- T R 6X4M0R --- X-number: 4 --- Follow-up: Postoperative
- T R 6X5M0R --- X-number: 5 --- Follow-up: Postoperative
- T R 6X6M0R --- X-number: 6 --- Follow-up: Postoperative

-----

Xref	Xmig	X	Y	Z	Rx	Ry	Rz	#Matched Markers	#Matched Reference Markers	Rigid Body Error	Rigid Body Error Reference	Condition Number	Condition Number Reference Model	Maximum Total Point Motion
-----														
Model: T8														
Reference: TopX0M0R --- T4														
0	1	0.0197	-0.0025	0.0024	5.9828	-0.0090	-0.0436	7	7	0.0284	0.0613	20.9	19.8	3.4706
0	2	-0.5618	0.0140	0.1314	0.0327	5.9908	0.0555	6	7	0.0654	0.0373	22.7	19.8	3.4597
0	3	0.0205	0.0047	0.0458	0.0010	0.0023	6.0203	7	7	0.0448	0.0264	20.9	19.8	3.0084
0	4	-0.0154	0.0209	-0.0066	-5.9846	-0.0220	0.0012	7	7	0.0441	0.0482	20.9	19.8	3.4867
0	5	0.0117	0.0153	0.0706	0.0528	-6.1090	0.0609	7	7	0.1407	0.0675	20.9	19.8	3.4527
0	6	0.0139	0.0252	-0.0205	0.0290	-0.0320	-5.9840	7	7	0.0272	0.0292	20.9	19.8	3.0723

### E.3.48 Dual Rotation Inferior: 6°

----- Migration Results -----

Reference Axis: Automatic

=====

Available scenes:

-----

- BottomX0M0R --- X-number: 0 --- Follow-up: Postoperative
- B R 6X1M0R --- X-number: 1 --- Follow-up: Postoperative
- B R 6X2M0R --- X-number: 2 --- Follow-up: Postoperative
- B R 6X3M0R --- X-number: 3 --- Follow-up: Postoperative
- B R 6X4M0R --- X-number: 4 --- Follow-up: Postoperative
- B R 6X5M0R --- X-number: 5 --- Follow-up: Postoperative
- B R 6X6M0R --- X-number: 6 --- Follow-up: Postoperative

-----

Xref	Xmig	X	Y	Z	Rx	Ry	Rz	#Matched Markers	#Matched Reference Markers	Rigid Body Error	Rigid Body Error Reference	Condition Number	Condition Number Reference Model	Maximum Total Point Motion
-----														
Model: T8														
Reference: BottomX0M0R --- L1														
0	1	0.0206	-0.0208	0.0288	6.0296	0.0222	-0.0297	7	6	0.0502	0.0159	20.0	20.2	3.5100
0	2	-0.3929	-0.0176	-0.5471	-0.0215	6.1390	-0.1384	5	6	0.0710	0.0246	26.2	20.2	3.5593
0	3	0.0166	-0.0678	0.1852	0.0341	0.0033	5.9310	6	6	0.0620	0.0229	21.9	20.2	3.0675
0	4	0.0431	-0.5663	0.2822	-5.9088	0.1027	-0.0581	6	6	0.0427	0.0378	21.9	20.2	3.3841
0	5	0.0251	-0.0285	0.3027	0.1365	-5.9690	0.0070	7	6	0.0791	0.0396	20.0	20.2	3.5124
0	6	0.0110	-0.0133	0.1649	0.1011	0.0195	-5.9877	7	6	0.0658	0.0158	20.0	20.2	3.0478

### E.3.49 Dual Rotation Superior: 10°

----- Migration Results -----

Reference Axis: Automatic

=====

Available scenes:

-----

- TopX0M0R --- X-number: 0 --- Follow-up: Postoperative
- T R 10X1M0R --- X-number: 1 --- Follow-up: Postoperative
- T R 10X2M0R --- X-number: 2 --- Follow-up: Postoperative
- T R 10X3M0R --- X-number: 3 --- Follow-up: Postoperative
- T R 10X4M0R --- X-number: 4 --- Follow-up: Postoperative
- T R 10X5M0R --- X-number: 5 --- Follow-up: Postoperative
- T R 10X6M0R --- X-number: 6 --- Follow-up: Postoperative

-----

Xref	Xmig	X	Y	Z	Rx	Ry	Rz	#Matched Markers	#Matched Reference Markers	Rigid Body Error	Rigid Body Error Reference	Condition Number	Condition Number Reference Model	Maximum Total Point Motion
-----														
Model: T8														
Reference: TopX0M0R --- T4														
0	1	-0.0086	-0.0154	-0.0111	9.9804	-0.0385	-0.0127	7	7	0.0481	0.1044	20.9	19.8	5.7744
0	2	-0.0166	0.0068	0.0327	-0.0055	9.9796	-0.0348	7	7	0.1031	0.0429	20.9	19.8	5.8205
0	3	-0.0058	0.0273	-0.0055	0.0242	0.0303	10.0201	7	7	0.0609	0.0427	20.9	19.8	5.0389
0	4	0.0297	-0.8873	0.0740	-9.9706	0.0044	-0.0529	6	7	0.0513	0.0731	22.7	19.8	5.7687
0	5	-0.2450	-0.0176	-0.8381	0.0292	-10.103	-0.0083	6	7	0.0601	0.0479	28.2	19.8	5.8576
0	6	-0.0019	0.0228	-0.0183	0.0259	-0.0460	-9.9888	7	7	0.0358	0.0628	20.9	19.8	5.1156

### E.3.50 Dual Rotation Inferior: 10°

----- Migration Results -----

Reference Axis: Automatic

=====

Available scenes:

-----

- BottomX0M0R --- X-number: 0 --- Follow-up: Postoperative
- B R 10X1M0R --- X-number: 1 --- Follow-up: Postoperative
- B R 10X2M0R --- X-number: 2 --- Follow-up: Postoperative
- B R 10X3M0R --- X-number: 3 --- Follow-up: Postoperative
- B R 10X4M0R --- X-number: 4 --- Follow-up: Postoperative
- B R 10X5M0R --- X-number: 5 --- Follow-up: Postoperative
- B R 10X6M0R --- X-number: 6 --- Follow-up: Postoperative

-----

Xref	Xmig	X	Y	Z	Rx	Ry	Rz	#Matched Markers	#Matched Reference Markers	Rigid Body Error	Rigid Body Error Reference	Condition Number	Condition Number Reference Model	Maximum Total Point Motion
-----														
Model: T8														
Reference: BottomX0M0R --- L1														
0	1	0.0179	-0.0236	0.1934	10.1017	0.0167	-0.0212	7	6	0.0398	0.0052	20.0	20.2	5.8419
0	2	0.0290	-0.0470	0.1545	0.1232	10.0098	-0.0658	7	6	0.1471	0.0300	20.0	20.2	5.8937
0	3	0.0249	-0.1019	0.2897	0.1070	0.0074	9.8961	6	6	0.0488	0.0395	21.9	20.2	5.0752
0	4	0.0451	-0.8973	0.3655	-9.8709	0.1737	-0.0102	6	6	0.2043	0.0052	21.9	20.2	5.7059
0	5	-0.2614	-0.0161	-0.6923	0.1258	-10.1020	-0.1078	6	6	0.1637	0.0057	26.0	20.2	5.8316
0	6	0.0018	-0.0332	0.3589	0.1750	0.0175	-10.0340	7	6	0.0528	0.0444	20.0	20.2	5.0853

## E.4 Prediction Interval Accuracy Calculations

### E.4.1 Caudal: X

Failure Examined	Data		Prediction Interval			Average Width	Accuracy Half Width
	Induced Displacement	Measured	Lower Limit	Upper Limit	Width		
Superior (T4)	0.5000	0.4925	0.4348	0.5522	0.1174	0.0528	<b>0.1057</b>
	-0.5000	-0.5210	-0.5667	-0.4493	0.1174		
	1.0000	0.9803	0.9356	1.0530	0.1174		
	-1.0000	-1.0417	-1.0675	-0.9501	0.1174		
	5.0000	5.0276	4.9412	5.0599	0.1187		
	-5.0000	-4.9921	-5.0744	-4.9557	0.1187		
	10.0000	10.0019	9.9472	10.0696	0.1224		
	-10.0000	-9.9839	-10.0841	-9.9617	0.1224		
	20.0000	20.0235	19.9560	20.0921	0.1362		
-20.0000	-20.0596	-20.1066	-19.9705	0.1362			
Inferior (T8)	0.5000	0.4814	0.4177	0.5298	0.1121	0.0528	<b>0.1057</b>
	-0.5000	-0.5233	-0.5847	-0.4726	0.1121		
	1.0000	0.9771	0.9189	1.0310	0.1121		
	-1.0000	-1.0577	-1.0860	-0.9738	0.1121		
	5.0000	5.0022	4.9279	5.0412	0.1133		
	-5.0000	-5.0565	-5.0961	-4.9829	0.1133		
	10.0000	9.9811	9.9382	10.0550	0.1168		
	-10.0000	-10.0048	-10.1099	-9.9931	0.1168		
	20.0000	20.0214	19.9556	20.0856	0.1300		
-20.0000	-20.0957	-20.1406	-20.0106	0.1300			
Inferior (T8)	0.5000	0.4884	0.4542	0.5288	0.0746	0.0528	<b>0.1057</b>
	-0.5000	-0.5005	-0.5467	-0.4721	0.0746		
	1.0000	0.9909	0.9546	1.0292	0.0746		
	-1.0000	-1.0206	-1.0472	-0.9726	0.0746		
	5.0000	5.0040	4.9578	5.0331	0.0754		
	-5.0000	-5.0072	-5.0511	-4.9757	0.0754		
	10.0000	9.9829	9.9610	10.0387	0.0777		
	-10.0000	-9.9889	-10.0567	-9.9789	0.0777		
	20.0000	20.0094	19.9655	20.0519	0.0865		
-20.0000	-20.0481	-20.0699	-19.9834	0.0865			

### E.4.2 Caudal: Y

Failure Examined	Data		Prediction Interval			Average Width	Accuracy Half Width
	Induced Displacement	Measured	Lower Limit	Upper Limit	Width		
Superior (T4)	0.5000	0.4983	0.4622	0.5415	0.0793	0.0468	0.0234
	-0.5000	-0.4976	-0.5374	-0.4581	0.0793		
	1.0000	1.0062	0.9620	1.0413	0.0793		
	-1.0000	-0.9890	-1.0372	-0.9579	0.0793		
	5.0000	4.9920	4.9600	5.0402	0.0802		
	-5.0000	-5.0194	-5.0361	-4.9559	0.0802		
	10.0000	10.0134	9.9568	10.0395	0.0827		
	-10.0000	-9.9639	-10.0354	-9.9527	0.0827		
	20.0000	19.9844	19.9483	20.0403	0.0920		
-20.0000	-20.0040	-20.0362	-19.9442	0.0920			
Inferior (T8)	0.5000	0.4883	0.4767	0.5122	0.0354	0.0468	0.0234
	-0.5000	-0.4976	-0.5225	-0.4870	0.0354		
	1.0000	0.9881	0.9763	1.0118	0.0354		
	-1.0000	-1.0189	-1.0221	-0.9866	0.0354		
	5.0000	4.9978	4.9730	5.0088	0.0358		
	-5.0000	-4.9983	-5.0191	-4.9833	0.0358		
	10.0000	9.9884	9.9685	10.0054	0.0369		
	-10.0000	-9.9917	-10.0157	-9.9788	0.0369		
	20.0000	19.9808	19.9585	19.9995	0.0411		
-20.0000	-19.9884	-20.0098	-19.9688	0.0411			
Inferior (T8)	0.5000	0.4919	0.4868	0.5066	0.0198	0.0468	0.0234
	-0.5000	-0.5076	-0.5133	-0.4935	0.0198		
	1.0000	0.9974	0.9868	1.0067	0.0198		
	-1.0000	-1.0087	-1.0134	-0.9936	0.0198		
	5.0000	5.0017	4.9873	5.0073	0.0200		
	-5.0000	-5.0029	-5.0140	-4.9940	0.0200		
	10.0000	9.9966	9.9876	10.0082	0.0206		
	-10.0000	-10.0047	-10.0150	-9.9943	0.0206		
	20.0000	20.0036	19.9877	20.0107	0.0230		
-20.0000	-20.0010	-20.0174	-19.9944	0.0230			

### E.4.3 Caudal: Z

Failure Examined	Data		Prediction Interval			Average Width	Accuracy Half Width
	Induced Displacement	Measured	Lower Limit	Upper Limit	Width		
Superior (T4)	0.5000	0.6843	0.4068	0.9062	0.4994	0.4725	<b>0.2363</b>
	-0.5000	-0.4760	-0.5949	-0.0955	0.4994		
	1.0000	1.1696	0.9076	1.4071	0.4995		
	-1.0000	-1.0138	-1.0958	-0.5963	0.4995		
	5.0000	5.3431	4.9118	5.4165	0.5047		
	-5.0000	-4.8776	-5.1051	-4.6005	0.5047		
	10.0000	10.1872	9.9124	10.4328	0.5204		
	-10.0000	-9.7871	-10.1215	-9.6010	0.5204		
	20.0000	20.1803	19.8999	20.4791	0.5792		
-20.0000	-19.8533	-20.1678	-19.5886	0.5792			
Inferior (T8)	0.5000	0.7189	0.3742	0.9279	0.5537	0.4725	<b>0.2363</b>
	-0.5000	-0.5006	-0.6206	-0.0668	0.5537		
	1.0000	1.1599	0.8715	1.4254	0.5539		
	-1.0000	-0.7756	-1.1180	-0.5641	0.5539		
	5.0000	5.3170	4.8477	5.4074	0.5596		
	-5.0000	-4.9900	-5.1000	-4.5404	0.5596		
	10.0000	10.0430	9.8129	10.3900	0.5771		
	-10.0000	-9.7468	-10.0826	-9.5055	0.5771		
	20.0000	20.0310	19.7280	20.3703	0.6422		
-20.0000	-19.7200	-20.0629	-19.4207	0.6422			
Inferior (T8)	0.5000	0.6095	0.4223	0.7289	0.3066	0.4725	<b>0.2363</b>
	-0.5000	-0.5137	-0.5741	-0.2675	0.3066		
	1.0000	1.0845	0.9204	1.2272	0.3067		
	-1.0000	-0.8680	-1.0724	-0.7657	0.3067		
	5.0000	5.1620	4.9045	5.2143	0.3099		
	-5.0000	-4.9889	-5.0596	-4.7497	0.3099		
	10.0000	10.0013	9.8816	10.2012	0.3196		
	-10.0000	-9.8783	-10.0464	-9.7269	0.3196		
	20.0000	19.9990	19.8276	20.1833	0.3556		
-20.0000	-19.8335	-20.0285	-19.6729	0.3556			



#### E.4.4 Caudal: Rx

Failure Examined	Data		Prediction Interval			Average Width	Accuracy Half Width
	Induced Displacement	Measured	Lower Limit	Upper Limit	Width		
Inferior (T8)	1.0000	1.0229	0.9880	1.0838	0.0959	0.1008	<b>0.0504</b>
	-1.0000	-0.9431	-1.0174	-0.9216	0.0959		
	3.0000	3.0136	2.9928	3.0898	0.0970		
	-3.0000	-2.9579	-3.0234	-2.9264	0.0970		
	6.0000	6.0519	5.9990	6.0998	0.1008		
	-6.0000	-5.9859	-6.0334	-5.9326	0.1008		
	10.0000	10.0662	10.0056	10.1149	0.1093		
	-10.0000	-10.0020	-10.0485	-9.9392	0.1093		

#### E.4.5 Caudal: Ry

Failure Examined	Data		Prediction Interval			Average Width	Accuracy Half Width
	Induced Displacement	Measured	Lower Limit	Upper Limit	Width		
Inferior (T8)	1.0000	0.9896	0.9376	1.0756	0.1380	0.1450	<b>0.0725</b>
	-1.0000	-0.9950	-1.0694	-0.9314	0.1380		
	-3.0000	3.0038	2.9437	3.0834	0.1397		
	3.0000	-2.9943	-3.0772	-2.9375	0.1397		
	6.0000	6.0738	5.9514	6.0965	0.1451		
	-6.0000	-6.0375	-6.0904	-5.9452	0.1451		
	10.0000	10.0106	9.9592	10.1166	0.1574		
	-10.0000	-10.0263	-10.1104	-9.9530	0.1574		

#### E.4.6 Caudal: Rz

Failure Examined	Data		Prediction Interval			Average Width	Accuracy Half Width
	Induced Displacement	Measured	Lower Limit	Upper Limit	Width		
Inferior (T8)	1.0000	1.0090	0.9499	1.0287	0.0788	0.0828	<b>0.0414</b>
	-1.0000	-1.0087	-1.0526	-0.9738	0.0788		
	3.0000	2.9892	2.9519	3.0316	0.0797		
	-3.0000	-3.0443	-3.0555	-2.9758	0.0797		
	6.0000	6.0028	5.9540	6.0368	0.0829		
	-6.0000	-6.0167	-6.0607	-5.9779	0.0829		
	10.0000	9.9927	9.9554	10.0452	0.0898		
	-10.0000	-10.0196	-10.0691	-9.9793	0.0898		

### E.4.7 Apex: X

Failure Examined	Data		Prediction Interval			Average Width	Accuracy Half Width
	Induced Displacement	Measured	Lower Limit	Upper Limit	Width		
Superior (T4)	0.5000	0.5481	0.4194	0.6296	0.2102	0.3003	<b>0.1501</b>
	-0.5000	-0.4761	-0.5813	-0.3712	0.2102		
	1.0000	1.0937	0.9198	1.1300	0.2102		
	-1.0000	-0.9808	-1.0817	-0.8715	0.2102		
	5.0000	4.9426	4.9218	5.1342	0.2124		
	-5.0000	-4.9686	-5.0859	-4.8735	0.2124		
	10.0000	10.0617	9.9223	10.1414	0.2190		
	-10.0000	-10.0206	-10.0931	-9.8740	0.2190		
	20.0000	20.0293	19.9176	20.1614	0.2438		
-20.0000	-19.9879	-20.1131	-19.8694	0.2438			
Inferior (L1)	-0.5000	-0.3202	-0.6530	-0.2871	0.3659	0.3003	<b>0.1501</b>
	0.5000	0.4822	0.3488	0.7147	0.3659		
	-1.0000	-0.9248	-1.1540	-0.7880	0.3660		
	1.0000	1.0194	0.8497	1.2157	0.3660		
	-5.0000	-4.9268	-5.1632	-4.7934	0.3698		
	5.0000	4.9868	4.8551	5.2248	0.3698		
	-10.0000	-10.0948	-10.1781	-9.7968	0.3813		
	10.0000	10.0113	9.8584	10.2397	0.3813		
	-20.0000	-19.9985	-20.2178	-19.7935	0.4243		
20.0000	20.0738	19.8552	20.2795	0.4243			

### E.4.8 Apex: Y

Failure Examined	Data		Prediction Interval			Average Width	Accuracy Half Width
	Induced Displacement	Measured	Lower Limit	Upper Limit	Width		
Superior (T4)	0.5000	0.4826	0.4747	0.5166	0.0419	0.0475	<b>0.0238</b>
	-0.5000	-0.4914	-0.5256	-0.4837	0.0419		
	1.0000	0.9991	0.9748	1.0167	0.0419		
	-1.0000	-0.9961	-1.0257	-0.9838	0.0419		
	5.0000	4.9853	4.9757	5.0180	0.0423		
	-5.0000	-5.0086	-5.0270	-4.9847	0.0423		
	10.0000	9.9959	9.9764	10.0200	0.0436		
	-10.0000	-10.0049	-10.0290	-9.9853	0.0436		
	20.0000	20.0047	19.9766	20.0252	0.0486		
-20.0000	-20.0114	-20.0341	-19.9855	0.0486			
Inferior (L1)	-0.5019	-0.5019	-0.5148	-0.4655	0.0493	0.0475	<b>0.0238</b>
	0.5101	0.5101	0.4853	0.5345	0.0493		
	-1.0000	-0.9931	-1.0148	-0.9655	0.0493		
	1.0000	0.9951	0.9853	1.0346	0.0493		
	-5.0000	-4.9853	-5.0152	-4.9654	0.0498		
	5.0000	5.0031	4.9852	5.0350	0.0498		
	-10.0000	-9.9891	-10.0162	-9.9649	0.0513		
	10.0000	10.0275	9.9847	10.0360	0.0513		
	-20.0000	-19.9824	-20.0196	-19.9625	0.0571		
20.0000	20.0149	19.9822	20.0394	0.0571			

### E.4.9 Apex: Z

Failure Examined	Data		Prediction Interval			Average Width	Accuracy Half Width
	Induced Displacement	Measured	Lower Limit	Upper Limit	Width		
Superior (T4)	0.5000	0.3915	0.3320	0.5664	0.2345	0.2290	<b>0.1145</b>
	-0.5000	-0.5483	-0.6679	-0.4334	0.2345		
	1.0000	0.9519	0.8319	1.0664	0.2345		
	-1.0000	-0.9953	-1.1679	-0.9333	0.2345		
	5.0000	4.9133	4.8301	5.0671	0.2369		
	-5.0000	-5.0707	-5.1685	-4.9316	0.2369		
	10.0000	10.0433	9.8258	10.0701	0.2443		
	-10.0000	-10.0530	-10.1716	-9.9272	0.2443		
	20.0000	19.9065	19.8106	20.0826	0.2719		
-20.0000	-20.0465	-20.1840	-19.9121	0.2719			
Inferior (L1)	-0.5000	-0.4686	-0.5695	-0.3646	0.2049	0.2290	<b>0.1145</b>
	0.5000	0.5599	0.4281	0.6330	0.2049		
	-1.0000	-0.9698	-1.0683	-0.8634	0.2049		
	1.0000	1.0540	0.9269	1.1318	0.2049		
	-5.0000	-4.9782	-5.0598	-4.8527	0.2071		
	5.0000	5.0579	4.9163	5.1233	0.2071		
	-10.0000	-10.0037	-10.0511	-9.8375	0.2135		
	10.0000	10.0618	9.9011	10.1146	0.2135		
	-20.0000	-19.9130	-20.0392	-19.8015	0.2376		
20.0000	19.9173	19.8651	20.1027	0.2376			

### E.4.10 Apex: Rx

Failure Examined	Data		Prediction Interval			Average Width	Accuracy Half Width
	Induced Displacement	Measured	Lower Limit	Upper Limit	Width		
Superior (T4)	-1.0000	-1.0193	-1.0827	-0.9499	0.1327	0.1899	<b>0.0949</b>
	1.0000	0.9722	0.9134	1.0462	0.1327		
	-3.0000	-3.0643	-3.0796	-2.9452	0.1344		
	3.0000	2.9739	2.9087	3.0431	0.1344		
	-6.0000	-5.9829	-6.0764	-5.9368	0.1396		
	6.0000	5.9843	5.9002	6.0398	0.1396		
	-10.0000	-9.9811	-10.0745	-9.9231	0.1514		
10.0000	9.9711	9.8865	10.0379	0.1514			
Inferior (L1)	-1.0000	-1.1569	-1.2021	-0.9736	0.2286	0.1899	<b>0.0949</b>
	1.0000	0.9366	0.7951	1.0237	0.2286		
	-3.0000	-3.0925	-3.2008	-2.9695	0.2313		
	3.0000	2.9513	2.7910	3.0223	0.2313		
	-6.0000	-6.0302	-6.2012	-5.9608	0.2404		
	6.0000	5.9096	5.7824	6.0228	0.2404		
	-10.0000	-10.1027	-10.2059	-9.9452	0.2606		
10.0000	9.8710	9.7668	10.0274	0.2606			

### E.4.11 Apex: Ry

Failure Examined	Data		Prediction Interval			Average Width	Accuracy Half Width
	Induced Displacement	Measured	Lower Limit	Upper Limit	Width		
Superior (T4)	-1.0000	-0.9826	-1.0741	-0.8656	0.2085	0.2631	<b>0.1315</b>
	1.0000	1.0357	0.9350	1.1435	0.2085		
	3.0000	2.9733	2.9429	3.1539	0.2111		
	-3.0000	-2.9910	-3.0845	-2.8735	0.2111		
	-6.0000	-5.9899	-6.1024	-5.8830	0.2193		
	6.0000	6.1091	5.9524	6.1718	0.2193		
	-10.0000	-9.9799	-10.1299	-9.8921	0.2378		
	10.0000	10.1029	9.9615	10.1993	0.2378		
Inferior (L1)	-1.0000	-1.0015	-1.1743	-0.8822	0.2921		
	1.0000	0.9893	0.8386	1.1307	0.2921		
	3.0000	2.9917	2.8497	3.1453	0.2956		
	-3.0000	-3.0962	-3.1889	-2.8934	0.2956		
	-6.0000	-6.1184	-6.2141	-5.9069	0.3072		
	6.0000	5.9683	5.8633	6.1705	0.3072		
	-10.0000	-10.0092	-10.2528	-9.9198	0.3331		
	10.0000	10.1016	9.8762	10.2092	0.3331		

### E.4.12 Apex: Rz

Failure Examined	Data		Prediction Interval			Average Width	Accuracy Half Width
	Induced Displacement	Measured	Lower Limit	Upper Limit	Width		
Superior (T4)	-1.0000	-1.0203	-1.0774	-0.9305	0.1469	0.2771	<b>0.1386</b>
	1.0000	1.0229	0.9225	1.0694	0.1469		
	-3.0000	-2.9504	-3.0782	-2.9296	0.1486		
	3.0000	2.9887	2.9215	3.0702	0.1486		
	-6.0000	-6.0215	-6.0810	-5.9265	0.1545		
	6.0000	5.9829	5.9185	6.0730	0.1545		
	-10.0000	-10.0222	-10.0873	-9.9199	0.1675		
	10.0000	9.9879	9.9118	10.0793	0.1675		
Inferior (L1)	-1.0000	-0.9408	-1.1572	-0.7768	0.3804		
	1.0000	0.9608	0.8290	1.2094	0.3804		
	-3.0000	-2.8801	-3.1457	-2.7607	0.3850		
	3.0000	2.8758	2.8129	3.1979	0.3850		
	-6.0000	-5.9309	-6.1325	-5.7324	0.4001		
	6.0000	5.9876	5.7846	6.1847	0.4001		
	-10.0000	-9.8970	-10.1217	-9.6879	0.4338		
	10.0000	10.0333	9.7401	10.1739	0.4338		

### E.4.13 Dual: X

Failure Examined	Data		Prediction Interval			Average Width	Accuracy Half Width
	Induced Displacement	Measured	Lower Limit	Upper Limit	Width		
Superior (T8)	-0.5000	-0.5594	-0.6461	-0.4631	0.1830	0.1353	<b>0.0677</b>
	0.5000	0.4470	0.3553	0.5383	0.1830		
	-1.0000	-1.0166	-1.1468	-0.9638	0.1831		
	1.0000	0.9141	0.8559	1.0390	0.1831		
	-5.0000	-5.0578	-5.1534	-4.9684	0.1850		
	5.0000	4.9803	4.8606	5.0455	0.1850		
	-10.0000	-10.0768	-10.1632	-9.9725	0.1907		
	10.0000	10.0215	9.8647	10.0554	0.1907		
	-20.0000	-20.1047	-20.1879	-19.9757	0.2123		
20.0000	19.9133	19.8678	20.0801	0.2123			
Inferior (T8)	0.5000	0.4876	0.46730152	0.543858101	0.0766	0.1353	<b>0.0677</b>
	-0.5000	-0.4867	-0.5323181	-0.45576152	0.0766		
	1.0000	0.9937	0.96709894	1.043680305	0.0766		
	-1.0000	-0.9913	-1.0321403	-0.95555894	0.0766		
	5.0000	5.0297	4.96518291	5.04255329	0.0774		
	-5.0000	-4.9842	-5.0310133	-4.95364291	0.0774		
	10.0000	9.9771	9.96207332	10.04185908	0.0798		
	-10.0000	-9.9933	-10.030319	-9.95053332	0.0798		
	20.0000	20.0089	19.9537661	20.04255874	0.0888		
-20.0000	-19.9838	-20.031019	-19.9422261	0.0888			

### E.4.14 Dual: Y

Failure Examined	Data		Prediction Interval			Average Width	Accuracy Half Width
	Induced Displacement	Measured	Lower Limit	Upper Limit	Width		
Superior (T8)	-0.5000	-0.4908	-0.5069	-0.4692	0.0378	0.0414	<b>0.0207</b>
	0.5000	0.5135	0.4938	0.5315	0.0378		
	-1.0000	-0.9840	-1.0073	-0.9695	0.0378		
	1.0000	1.0123	0.9941	1.0319	0.0378		
	-5.0000	-4.9802	-5.0103	-4.9721	0.0382		
	5.0000	5.0123	4.9967	5.0349	0.0382		
	-10.0000	-9.9944	-10.0143	-9.9750	0.0394		
	10.0000	10.0301	9.9996	10.0389	0.0394		
	-20.0000	-20.0110	-20.0235	-19.9797	0.0438		
20.0000	20.0152	20.0043	20.0481	0.0438			
Inferior (T8)	0.5000	0.5029	0.47192176	0.513503797	0.0416	0.0414	<b>0.0207</b>
	-0.5000	-0.5090	-0.5283238	-0.48674176	0.0416		
	1.0000	0.9921	0.97203781	1.013633308	0.0416		
	-1.0000	-0.9969	-1.0284533	-0.98685781	0.0416		
	5.0000	4.9836	4.97280576	5.014829818	0.0420		
	-5.0000	-5.0005	-5.0296498	-4.98762576	0.0420		
	10.0000	9.9973	9.97337759	10.01671357	0.0433		
	-10.0000	-10.0230	-10.031534	-9.98819759	0.0433		
	20.0000	19.9932	19.9733871	20.02161522	0.0482		
-20.0000	-20.0138	-20.036435	-19.9882071	0.0482			

### E.4.15 Dual: Z

Failure Examined	Data		Prediction Interval			Average Width	Accuracy Half Width
	Induced Displacement	Measured	Lower Limit	Upper Limit	Width		
Superior (T8)	-0.5000	-0.5120	-0.5322	-0.3574	0.1748	0.2200	<b>0.1100</b>
	0.5000	0.5724	0.4676	0.6424	0.1748		
	-1.0000	-0.8903	-1.0321	-0.8572	0.1749		
	1.0000	1.0578	0.9674	1.1423	0.1749		
	-5.0000	-4.9546	-5.0319	-4.8552	0.1767		
	5.0000	5.0550	4.9655	5.1421	0.1767		
	-10.0000	-9.9018	-10.0333	-9.8512	0.1822		
	10.0000	10.0338	9.9614	10.1436	0.1822		
	-20.0000	-19.9628	-20.0410	-19.8382	0.2027		
20.0000	20.0536	19.9485	20.1512	0.2027			
Inferior (T8)	0.5000	0.6983	0.5255	0.7727	0.2472	0.2200	<b>0.1100</b>
	-0.5000	-0.3528	-0.4735	-0.2263	0.2472		
	1.0000	1.1783	1.0250	1.2723	0.2473		
	-1.0000	-0.8105	-0.9731	-0.7258	0.2473		
	5.0000	5.0653	5.0199	5.2698	0.2499		
	-5.0000	-4.8238	-4.9706	-4.7207	0.2499		
	10.0000	10.0836	10.0112	10.2689	0.2577		
	-10.0000	-9.9036	-9.9697	-9.7121	0.2577		
	20.0000	20.1722	19.9872	20.2739	0.2867		
-20.0000	-19.8111	-19.9747	-19.6880	0.2867			

### E.4.16 Dual: Rx

Failure Examined	Data		Prediction Interval			Average Width	Accuracy Half Width
	Induced Displacement	Measured	Lower Limit	Upper Limit	Width		
Superior (T8)	1.0000	1.0196	0.9500	1.0822	0.1322	0.1891	<b>0.0945</b>
	-1.0000	-0.9725	-1.0461	-0.9139	0.1322		
	3.0000	3.0637	2.9452	3.0790	0.1338		
	-3.0000	-2.9744	-3.0429	-2.9091	0.1338		
	6.0000	5.9828	5.9366	6.0757	0.1390		
	-6.0000	-5.9846	-6.0396	-5.9005	0.1390		
	10.0000	9.9804	9.9228	10.0736	0.1507		
	-10.0000	-9.9706	-10.0375	-9.8867	0.1507		
Inferior (T8)	1.0000	1.1562	0.9735	1.2012	0.2276	0.1891	<b>0.0945</b>
	-1.0000	-0.9374	-1.0236	-0.7959	0.2276		
	3.0000	3.0910	2.9693	3.1996	0.2304		
	-3.0000	-2.9510	-3.0220	-2.7917	0.2304		
	6.0000	6.0296	5.9604	6.1998	0.2394		
	-6.0000	-5.9088	-6.0222	-5.7828	0.2394		
	10.0000	10.1017	9.9445	10.2041	0.2596		
-10.0000	-9.8709	-10.0265	-9.7669	0.2596			

### E.4.17 Dual: Ry

Failure Examined	Data		Prediction Interval			Average Width	Accuracy Half Width
	Induced Displacement	Measured	Lower Limit	Upper Limit	Width		
Superior (T8)	1.0000	0.9828	0.8653	1.0747	0.2094	0.2741	<b>0.1371</b>
	-1.0000	-1.0358	-1.1439	-0.9345	0.2094		
	-3.0000	-2.9730	-3.1543	-2.9424	0.2119		
	3.0000	2.9911	2.8732	3.0851	0.2119		
	6.0000	5.9908	5.8828	6.1030	0.2202		
	-6.0000	-6.1093	-6.1722	-5.9519	0.2202		
	10.0000	9.9796	9.8918	10.1306	0.2388		
	-10.0000	-10.1029	-10.1997	-9.9610	0.2388		
Inferior (T8)	1.0000	1.0017	0.8753	1.1875	0.3122	0.2770	<b>0.1385</b>
	-1.0000	-0.9895	-1.1386	-0.8263	0.3122		
	-3.0000	-2.9912	-3.1543	-2.8383	0.3160		
	3.0000	3.0967	2.8872	3.2032	0.3160		
	6.0000	6.1390	5.9018	6.2302	0.3284		
	-6.0000	-5.9685	-6.1813	-5.8529	0.3284		
	10.0000	10.0098	9.9156	10.2717	0.3560		
	-10.0000	-10.1023	-10.2228	-9.8667	0.3560		

### E.4.18 Dual: Rz

Failure Examined	Data		Prediction Interval			Average Width	Accuracy Half Width
	Induced Displacement	Measured	Lower Limit	Upper Limit	Width		
Superior (T8)	1.0000	1.0198	0.9285	1.0767	0.1482	0.2770	<b>0.1385</b>
	-1.0000	-1.0246	-1.0713	-0.9231	0.1482		
	3.0000	2.9486	2.9274	3.0774	0.1500		
	-3.0000	-2.9899	-3.0721	-2.9220	0.1500		
	6.0000	6.0203	5.9242	6.0801	0.1559		
	-6.0000	-5.9840	-6.0747	-5.9188	0.1559		
	10.0000	10.0201	9.9173	10.0863	0.1690		
	-10.0000	-9.9888	-10.0810	-9.9119	0.1690		
Inferior (T8)	1.0000	0.9409	0.7772	1.1560	0.3788	0.2770	<b>0.1385</b>
	-1.0000	-0.9620	-1.2090	-0.8302	0.3788		
	3.0000	2.8804	2.7611	3.1445	0.3834		
	-3.0000	-2.8766	-3.1975	-2.8141	0.3834		
	6.0000	5.9310	5.7329	6.1314	0.3984		
	-6.0000	-5.9877	-6.1844	-5.7859	0.3984		
	10.0000	9.8961	9.6886	10.1206	0.4320		
	-10.0000	-10.0341	-10.1736	-9.7416	0.4320		

## **E.5 Precision Data**

The raw data for the precision exams collected from MB-RSA are displayed in the tables beyond. This raw data was used to calculate the directional precision using the standard deviation multiplied by the 95% confidence limit. These calculations are found within Section E.6.



## E.5.1 Caudal: Translation

----- Migration Results -----

Reference Axis: Automatic

=====

Available scenes:

-----

CREFX0M0R --- X-number: 0 --- Follow-up: Postoperative  
 C P TX2M0R --- X-number: 2 --- Follow-up: Postoperative  
 C P TX3M0R --- X-number: 3 --- Follow-up: Postoperative  
 C P TX4M0R --- X-number: 4 --- Follow-up: Postoperative  
 C P TX5M0R --- X-number: 5 --- Follow-up: Postoperative  
 C P TX6M0R --- X-number: 6 --- Follow-up: Postoperative  
 C P TX1M0R --- X-number: 1 --- Follow-up: Postoperative

Xref	Xmig	X	Y	Z	Rx	Ry	Rz	#Matched Markers	#Matched Reference Markers	Rigid Body Error	Rigid Body Error Reference	Condition Number	Condition Number Reference Model	Maximum Total Point Motion
-----														
Model: T4														
Reference: L1														
0	1	-0.0194	-0.0210	0.0611	0.0039	-0.0416	0.0627	7	6	0.0523	0.0407	18.5	19.8	0.1764
1	2	-0.0242	0.0333	0.0745	0.0460	0.0136	0.0111	7	6	0.0406	0.0420	18.5	19.8	0.1405
2	3	0.0368	-0.0218	-0.1871	-0.0514	0.0144	-0.0081	7	6	0.0492	0.0275	18.5	19.9	0.2458
3	4	0.0006	-0.0419	0.3005	0.0668	-0.0133	-0.0159	7	6	0.0536	0.0111	18.5	19.8	0.3797
4	5	-0.0667	0.0939	-0.3500	-0.0573	-0.0515	0.0469	7	5	0.0376	0.0504	18.5	21.6	0.4062
5	6	0.0677	-0.0832	0.1202	-0.0185	0.0366	-0.0207	7	5	0.0423	0.0426	18.6	21.6	0.1953
6	0	0.0142	0.0417	-0.0720	-0.0016	0.0411	-0.0781	7	6	0.0369	0.0182	18.6	19.8	0.1190
-----														
Model: T8														
Reference: L1														
0	1	0.0067	-0.0082	0.0496	0.0274	0.0125	-0.0324	7	6	0.0640	0.0407	19.3	19.8	0.1758
1	2	-0.0229	0.0287	0.0243	-0.0006	-0.0054	0.0009	7	6	0.0312	0.0420	19.4	19.8	0.0701
2	3	0.0259	-0.0131	-0.0829	-0.0273	-0.0113	0.0061	7	6	0.0298	0.0275	19.3	19.9	0.1321
3	4	-0.0049	-0.0123	0.1653	0.0747	0.0061	0.0063	7	6	0.0199	0.0111	19.3	19.8	0.1992
4	5	-0.0318	0.0189	-0.2072	-0.0862	-0.0303	-0.0131	7	5	0.0132	0.0504	19.3	21.6	0.2374
5	6	0.0274	-0.0350	0.0535	0.0193	0.0216	0.0223	7	5	0.0214	0.0426	19.4	21.6	0.0951
6	0	0.0048	0.0186	-0.0316	-0.0196	0.0060	0.0079	7	6	0.0352	0.0182	19.4	19.8	0.0798

## E.5.2 Caudal: Rotation

----- Migration Results -----

Reference Axis: Automatic

=====

Available scenes:

-----

CREFX0M0R --- X-number: 0 --- Follow-up: Postoperative  
 C P RX1M0R --- X-number: 1 --- Follow-up: Postoperative  
 C P RX2M0R --- X-number: 2 --- Follow-up: Postoperative  
 C P RX3M0R --- X-number: 3 --- Follow-up: Postoperative  
 C P RX4M0R --- X-number: 4 --- Follow-up: Postoperative  
 C P RX5M0R --- X-number: 5 --- Follow-up: Postoperative  
 C P RX6M0R --- X-number: 6 --- Follow-up: Postoperative

-----

Xref	Xmig	X	Y	Z	Rx	Ry	Rz	#Matched Markers	#Matched Reference Markers	Rigid Body Error	Rigid Body Error Reference	Condition Number	Condition Number Reference Model	Maximum Total Point Motion	
-----															
Model: T4															
Reference: L1															
0	1	-0.0872	-0.0115	0.0371	-0.0104	0.0084	0.0240	7	4	0.1528	0.0207	18.5	22.0	0.2440	
1	2	0.0516	0.0101	0.1895	0.0860	0.0379	-0.0046	7	3	0.1663	0.0218	19.5	27.8	0.4691	
2	3	Not possible to calculate migration: No Reference Match													
2	4	-0.3837	-0.0006	0.2000	0.1342	0.0940	0.1015	7	3	0.1511	0.0370	18.9	82.3	0.5227	
4	5	0.0929	-0.0027	-0.1020	0.1486	0.1876	0.0887	5	3	0.1072	0.0422	30.1	80.7	0.2814	
5	6	Not possible to calculate migration: No Reference Match													
5	0	0.1201	0.0134	-0.1213	-0.2400	-0.2719	-0.1589	5	5	0.1262	0.0127	32.3	31.4	0.3610	
-----															
Model: T8															
Reference: L1															
0	1	-0.0312	-0.0332	0.0452	0.2047	0.0895	-0.0525	5	4	0.0495	0.0207	32.5	22.0	0.1314	
1	2	0.0074	0.0430	0.0778	-0.0698	-0.0916	0.0319	5	3	0.0306	0.0218	31.9	27.8	0.1391	
2	3	Not possible to calculate migration: No Reference Match													
2	4	-0.2644	-0.0371	0.1497	0.0444	0.0602	0.0891	6	3	0.0422	0.0370	22.1	82.3	0.3512	
4	5	0.0582	0.0129	-0.1124	-0.0118	-0.1644	0.0297	6	3	0.0503	0.0422	21.6	80.7	0.2603	
5	6	Not possible to calculate migration: No Reference Match													
5	0	0.0581	0.0423	-0.0282	-0.0225	0.0285	-0.0231	6	5	0.0359	0.0127	21.4	31.4	0.1373	

### E.5.3 Apex Superior Translation

----- Migration Results -----

Reference Axis: Automatic

=====

Available scenes:

-----

TREFX0M0R --- X-number: 0 --- Follow-up: Postoperative  
 T P TX1M0R --- X-number: 1 --- Follow-up: Postoperative  
 T P TX2M0R --- X-number: 2 --- Follow-up: Postoperative  
 T P TX3M0R --- X-number: 3 --- Follow-up: Postoperative  
 T P TX4M0R --- X-number: 4 --- Follow-up: Postoperative  
 T P TX5M0R --- X-number: 5 --- Follow-up: Postoperative  
 T P TX6M0R --- X-number: 6 --- Follow-up: Postoperative

-----

Xref	Xmig	X	Y	Z	Rx	Ry	Rz	#Matched Markers	#Matched Reference Markers	Rigid Body Error	Rigid Body Error Reference	Condition Number	Condition Number Reference Model	Maximum Total Point Motion
-----														
Model: T4														
Reference: T8														
0	1	0.1391	-0.0085	-0.0230	0.0246	-0.0069	-0.0100	7	7	0.0666	0.0400	19.7	20.5	0.1949
1	2	-0.0172	0.0124	-0.0199	-0.0235	-0.0339	-0.0628	7	7	0.0509	0.0300	19.8	20.4	0.1165
2	3	0.0323	0.0176	-0.0510	0.0210	0.0456	0.0810	7	7	0.0500	0.0328	19.7	20.4	0.1366
3	4	-0.0285	-0.0203	0.1024	0.0285	-0.1130	0.0214	7	7	0.1219	0.0340	19.8	20.6	0.3567
4	5	0.0369	0.0014	-0.0678	-0.0470	0.1122	-0.0905	7	7	0.1938	0.0295	19.8	20.6	0.5254
5	6	-0.0496	0.0038	0.0102	0.0120	0.0292	0.0402	7	7	0.0416	0.0271	19.9	20.5	0.0986
6	0	-0.1132	-0.0067	0.0490	-0.0156	-0.0329	0.0209	7	7	0.0418	0.0497	19.7	20.4	0.1612

## E.5.4 Apex Inferior Translation

----- Migration Results -----

Reference Axis: Automatic

Available scenes:

-----  
 BREFX0M0R --- X-number: 0 --- Follow-up: Postoperative  
 B P TX1M0R --- X-number: 1 --- Follow-up: Postoperative  
 B P TX2M0R --- X-number: 2 --- Follow-up: Postoperative  
 B P TX3M0R --- X-number: 3 --- Follow-up: Postoperative  
 B P TX4M0R --- X-number: 4 --- Follow-up: Postoperative  
 B P TX5M0R --- X-number: 5 --- Follow-up: Postoperative  
 B P TX6M0R --- X-number: 6 --- Follow-up: Postoperative  
 -----

Xref	Xmig	X	Y	Z	Rx	Ry	Rz	#Matched Markers	#Matched Reference Markers	Rigid Body Error	Rigid Body Error Reference	Condition Number	Condition Number Reference Model	Maximum Total Point Motion
-----														
Model: L1														
Reference: T8														
0	1	-0.0798	-0.0266	-0.0202	0.0451	0.0718	-0.0444	6	7	0.0328	0.0362	20.2	19.7	0.1134
1	2	0.1289	0.0252	-0.0096	-0.0704	-0.0223	0.0418	6	7	0.0538	0.0475	20.2	19.7	0.1594
2	3	-0.1156	-0.0237	0.0962	-0.0103	0.0771	-0.0296	6	7	0.0468	0.0780	20.3	19.6	0.2236
3	4	-0.069	-0.0037	-0.0552	0.0645	0.0049	-0.0412	6	7	0.0247	0.0332	20.2	19.8	0.1168
4	5	0.1943	0.0120	-0.0699	0.0456	-0.0698	0.0780	6	7	0.0185	0.0907	20.3	19.8	0.2526
5	6	0.0594	0.01270	0.1041	-0.0707	-0.0048	0.0337	6	7	0.0211	0.0365	20.2	19.8	0.1477
6	0	-0.1185	0.0046	-0.0451	-0.0036	-0.0569	-0.0385	6	7	0.0225	0.0771	20.2	19.7	0.1692

## E.5.5 Apex Superior Rotation

----- Migration Results -----

Reference Axis: Automatic

=====

Available scenes:

-----

TREFX0M0R --- X-number: 0 --- Follow-up: Postoperative  
 T P RX1M0R --- X-number: 1 --- Follow-up: Postoperative  
 T P RX2M0R --- X-number: 2 --- Follow-up: Postoperative  
 T P RX3M0R --- X-number: 3 --- Follow-up: Postoperative  
 T P RX4M0R --- X-number: 4 --- Follow-up: Postoperative  
 T P RX5M0R --- X-number: 5 --- Follow-up: Postoperative  
 T P RX6M0R --- X-number: 6 --- Follow-up: Postoperative

-----

Xref	Xmig	X	Y	Z	Rx	Ry	Rz	#Matched Markers	#Matched Reference Markers	Rigid Body Error	Rigid Body Error Reference	Condition Number	Condition Number Reference Model	Maximum Total Point Motion
-----														
Model: T4														
Reference: T8														
0	1	0.1135	0.0183	0.1039	0.1284	0.0796	-0.0969	7	7	0.1576	0.0526	19.7	20.5	0.4692
1	2	0.0245	-0.0481	0.0479	-0.0921	-0.1164	-0.1959	7	7	0.1649	0.1018	18.8	19.7	0.3967
2	3	-0.0002	0.0036	-0.0743	0.0485	0.0630	0.1483	7	7	0.1973	0.1072	20.3	21.4	0.3911
3	4	-0.0192	-0.0331	0.1111	0.0150	0.1493	-0.0590	7	6	0.0676	0.0890	20.4	26.5	0.2830
4	5	0.1418	0.0201	-0.1413	0.0602	-0.0645	-0.0418	7	6	0.1390	0.1219	20.9	28.0	0.3398
5	6	-0.1293	0.0010	-0.0720	-0.1384	-0.0733	0.1226	7	6	0.1797	0.1158	19.2	23.6	0.3914
6	0	-0.1497	0.0145	0.0554	-0.0384	-0.0524	0.0744	7	7	0.0915	0.0676	19.3	20.4	0.2283

## E.5.6 Apex Inferior Rotation

----- Migration Results -----

Reference Axis: Automatic

=====

Available scenes:

-----

BREFX0M0R --- X-number: 0 --- Follow-up: Postoperative  
 B P RX1M0R --- X-number: 1 --- Follow-up: Postoperative  
 B P RX2M0R --- X-number: 2 --- Follow-up: Postoperative  
 B P RX3M0R --- X-number: 3 --- Follow-up: Postoperative  
 B P RX4M0R --- X-number: 4 --- Follow-up: Postoperative  
 B P RX5M0R --- X-number: 5 --- Follow-up: Postoperative  
 B P RX6M0R --- X-number: 6 --- Follow-up: Postoperative

Xref	Xmig	X	Y	Z	Rx	Ry	Rz	#Matched Markers	#Matched Reference Markers	Rigid Body Error	Rigid Body Error Reference	Condition Number	Condition Number Reference Model	Maximum Total Point Motion
-----														
Model: L1														
Reference: T8														
0	1	0.0415	0.0142	0.1860	-0.2147	0.0572	0.0155	5	7	0.0326	0.0822	25.1	19.7	0.2640
1	2	-0.0338	-0.0282	-0.0588	0.1590	-0.0261	-0.0586	5	6	0.0322	0.0761	26.7	21.0	0.1332
2	3	0.4099	0.0607	-0.1228	0.0131	0.0365	0.1867	6	6	0.1147	0.0349	20.3	22.0	0.5392
3	4	-0.1614	-0.0410	-0.0324	-0.0128	0.1672	-0.1033	7	6	0.0255	0.2001	17.0	25.1	0.2634
4	5	0.2020	0.0161	-0.0222	-0.0990	-0.2043	0.1294	5	6	0.0203	0.1660	23.7	27.3	0.2644
5	6	-0.1155	-0.0232	0.0063	0.1348	-0.1539	-0.0065	5	4	0.0299	0.0661	28.7	42.2	0.1824
6	0	-0.1844	-0.0063	-0.4408	0.1873	0.2610	-0.0761	5	4	0.0216	0.0584	24.1	38.1	0.6048

## E.5.7 Dual Superior Translation

----- Migration Results -----

Reference Axis: Automatic

=====

Available scenes:

-----

TREFX0M0R --- X-number: 0 --- Follow-up: Postoperative  
 T P TX1M0R --- X-number: 1 --- Follow-up: Postoperative  
 T P TX2M0R --- X-number: 2 --- Follow-up: Postoperative  
 T P TX3M0R --- X-number: 3 --- Follow-up: Postoperative  
 T P TX4M0R --- X-number: 4 --- Follow-up: Postoperative  
 T P TX5M0R --- X-number: 5 --- Follow-up: Postoperative  
 T P TX6M0R --- X-number: 6 --- Follow-up: Postoperative

-----

Xref	Xmig	X	Y	Z	Rx	Ry	Rz	#Matched Markers	#Matched Reference Markers	Rigid Body Error	Rigid Body Error Reference	Condition Number	Condition Number Reference Model	Maximum Total Point Motion
-----														
Model: T8														
Reference: T4														
0	1	-0.1217	-0.0026	0.0736	-0.0247	0.0069	0.0100	7	7	0.0400	0.0666	20.5	19.7	0.1880
1	2	0.1298	-0.0211	-0.0176	0.0235	0.0340	0.0628	7	7	0.0300	0.0509	20.4	19.8	0.1519
2	3	-0.1772	-0.0030	0.0804	-0.0211	-0.0455	-0.0810	7	7	0.0328	0.0500	20.4	19.7	0.2535
3	4	-0.0523	0.0163	-0.0159	-0.0284	0.1130	-0.0213	7	7	0.0340	0.1219	20.6	19.8	0.1230
4	5	0.1805	-0.0095	-0.0551	0.0471	-0.1121	0.0906	7	7	0.0295	0.1938	20.6	19.8	0.2437
5	6	-0.0200	0.0028	0.0058	-0.0120	-0.0292	-0.0402	7	7	0.0271	0.0416	20.5	19.9	0.0678
6	0	0.0606	0.0176	-0.0711	0.0156	0.0329	-0.0209	7	7	0.0497	0.0418	20.4	19.7	0.1970

## E.5.8 Dual Inferior Translation

----- Migration Results -----

Reference Axis: Automatic

=====

Available scenes:

-----

BREFX0M0R --- X-number: 0 --- Follow-up: Postoperative  
 B P TX1M0R --- X-number: 1 --- Follow-up: Postoperative  
 B P TX2M0R --- X-number: 2 --- Follow-up: Postoperative  
 B P TX3M0R --- X-number: 3 --- Follow-up: Postoperative  
 B P TX4M0R --- X-number: 4 --- Follow-up: Postoperative  
 B P TX5M0R --- X-number: 5 --- Follow-up: Postoperative  
 B P TX6M0R --- X-number: 6 --- Follow-up: Postoperative

Xref	Xmig	X	Y	Z	Rx	Ry	Rz	#Matched Markers	#Matched Reference Markers	Rigid Body Error	Rigid Body Error Reference	Condition Number	Condition Number Reference Model	Maximum Total Point Motion
-----														
Model: T8														
Reference: L1														
0	1	-0.0406	0.0149	-0.1209	-0.0450	-0.0718	0.0444	7	6	0.0362	0.0328	19.7	20.2	0.1922
1	2	-0.0135	-0.0131	0.2105	0.0705	0.0222	-0.0418	7	6	0.0475	0.0538	19.7	20.2	0.2577
2	3	0.0367	0.0177	-0.0843	0.0103	-0.0771	0.0296	7	6	0.0780	0.0468	19.6	20.3	0.1449
3	4	-0.0453	-0.0082	-0.1254	-0.0645	-0.0049	0.0411	7	6	0.0332	0.0247	19.8	20.2	0.1815
4	5	0.0198	0.0033	-0.0414	-0.0455	0.0699	-0.0780	7	6	0.0907	0.0185	19.8	20.3	0.2736
5	6	0.0342	-0.0022	0.0938	0.0707	0.0048	-0.0337	7	6	0.0365	0.0211	19.8	20.2	0.1592
6	0	0.0089	-0.0129	0.0674	0.0035	0.0569	0.0385	7	6	0.0771	0.0225	19.7	20.2	0.1308



## E.5.9 Dual Superior Rotation

----- Migration Results -----

Reference Axis: Automatic

=====

Available scenes:

-----

TREFX0M0R --- X-number: 0 --- Follow-up: Postoperative  
 T P RX1M0R --- X-number: 1 --- Follow-up: Postoperative  
 T P RX2M0R --- X-number: 2 --- Follow-up: Postoperative  
 T P RX3M0R --- X-number: 3 --- Follow-up: Postoperative  
 T P RX4M0R --- X-number: 4 --- Follow-up: Postoperative  
 T P RX5M0R --- X-number: 5 --- Follow-up: Postoperative  
 T P RX6M0R --- X-number: 6 --- Follow-up: Postoperative

-----

Xref	Xmig	X	Y	Z	Rx	Ry	Rz	#Matched Markers	#Matched Reference Markers	Rigid Body Error	Rigid Body Error Reference	Condition Number	Condition Number Reference Model	Maximum Total Point Motion
-----														
Model: T8														
Reference: T4														
0	1	0.1052	-0.0878	0.1290	-0.1283	-0.0798	0.0967	7	7	0.0526	0.1576	20.5	19.7	0.2415
1	2	0.2658	0.0590	-0.1907	0.0917	0.1167	0.1957	7	7	0.1018	0.1649	19.7	18.8	0.5557
2	3	-0.2750	0.0304	0.1501	-0.0487	-0.0629	-0.1484	7	7	0.1072	0.1973	21.4	20.3	0.5034
3	4	0.1859	0.0287	-0.0803	-0.0148	-0.1493	0.0590	6	7	0.0890	0.0676	26.5	20.4	0.3612
4	5	-0.0548	-0.0323	0.2855	-0.0602	0.0644	0.0418	6	7	0.1219	0.1390	28.0	20.9	0.4198
5	6	-0.1429	0.0859	-0.1832	0.1385	0.0730	-0.1228	6	7	0.1158	0.1797	23.6	19.2	0.3896
6	0	-0.0098	0.0437	-0.0967	0.0385	0.0524	-0.0745	7	7	0.0676	0.0915	20.4	19.3	0.2513

## E.5.10 Dual Inferior Rotation

----- Migration Results -----

Reference Axis: Automatic

=====

Available scenes:

-----

BREFX0MOR --- X-number: 0 --- Follow-up: Postoperative  
 B P RX1MOR --- X-number: 1 --- Follow-up: Postoperative  
 B P RX2MOR --- X-number: 2 --- Follow-up: Postoperative  
 B P RX3MOR --- X-number: 3 --- Follow-up: Postoperative  
 B P RX4MOR --- X-number: 4 --- Follow-up: Postoperative  
 B P RX5MOR --- X-number: 5 --- Follow-up: Postoperative  
 B P RX6MOR --- X-number: 6 --- Follow-up: Postoperative

-----

Xref	Xmig	X	Y	Z	Rx	Ry	Rz	#Matched Markers	#Matched Reference Markers	Rigid Body Error	Rigid Body Error Reference	Condition Number	Condition Number Reference Model	Maximum Total Point Motion
-----														
Model: T8														
Reference: L1														
0	1	-0.0045	-0.0350	0.4075	0.2147	-0.0572	-0.0153	7	5	0.0822	0.0326	19.7	25.1	0.5844
1	2	-0.1156	0.0967	-0.3768	-0.1590	0.0259	0.0586	6	5	0.0761	0.0322	21.0	26.7	0.5771
2	3	0.1129	-0.0169	0.0773	-0.0133	-0.0364	-0.1868	6	6	0.0349	0.1147	22.0	20.3	0.2284
3	4	-0.0935	-0.0359	-0.0602	0.0131	-0.1672	0.1033	6	7	0.2001	0.0255	25.1	17.0	0.4662
4	5	0.0875	0.0570	0.3588	0.0994	0.2040	-0.1298	6	5	0.1660	0.0203	27.3	23.7	0.6663
5	6	0.0691	-0.0032	-0.3382	-0.1348	0.1539	0.0068	4	5	0.0661	0.0299	42.2	28.7	0.4855
6	0	0.0018	-0.0159	-0.0403	-0.1870	-0.2612	0.0759	4	5	0.0584	0.0216	38.1	24.1	0.2006

## E.6 Precision Calculations

### E.6.1 Caudal Precision

<b>Superior Precision</b>	X	Y	Z	Rx	Ry	Rz	MTPM
Translation	-0.0194	-0.021	0.0611	0.0039	-0.0416	0.0627	0.1764
	-0.0242	0.0333	0.0745	0.046	0.0136	0.0111	0.1405
	0.0368	-0.0218	-0.1871	-0.0514	0.0144	-0.0081	0.2458
	0.0006	-0.0419	0.3005	0.0668	-0.0133	-0.0159	0.3797
	-0.0667	0.0939	-0.35	-0.0573	-0.0515	0.0469	0.4062
	0.0677	-0.0832	0.1202	-0.0185	0.0366	-0.0207	0.1953
	0.0142	0.0417	-0.072	-0.0016	0.0411	-0.0781	0.119
Rotation	-0.0872	-0.0115	0.0371	-0.0104	0.0084	0.024	0.244
	0.0516	0.0101	0.1895	0.086	0.0379	-0.0046	0.4691
	-0.3837	-0.0006	0.2	0.1342	0.094	0.1015	0.5227
	0.0929	-0.0027	-0.102	0.1486	0.1876	0.0887	0.2814
	0.1201	0.0134	-0.1213	-0.24	-0.2719	-0.1589	0.361
Standard Deviation	0.1310	0.0444	0.1852	0.1032	0.1075	0.0719	0.1315
Precision	<b>0.2804</b>	<b>0.0950</b>	<b>0.3963</b>	<b>0.2208</b>	<b>0.2301</b>	<b>0.1539</b>	<b>0.2813</b>

<b>Inferior Precision</b>	X	Y	Z	Rx	Ry	Rz	MTPM
Translation	0.0067	-0.0082	0.0496	0.0274	0.0125	-0.0324	0.1758
	-0.0229	0.0287	0.0243	-0.0006	-0.0054	0.0009	0.0701
	0.0259	-0.0131	-0.0829	-0.0273	-0.0113	0.0061	0.1321
	-0.0049	-0.0123	0.1653	0.0747	0.0061	0.0063	0.1992
	-0.0318	0.0189	-0.2072	-0.0862	-0.0303	-0.0131	0.2374
	0.0274	-0.035	0.0535	0.0193	0.0216	0.0223	0.0951
	0.0048	0.0186	-0.0316	-0.0196	0.006	0.0079	0.0798
Rotation	-0.0312	-0.0332	0.0452	0.2047	0.0895	-0.0525	0.1314
	0.0074	0.043	0.0778	-0.0698	-0.0916	0.0319	0.1391
	-0.2644	-0.0371	0.1497	0.0444	0.0602	0.0891	0.3512
	0.0582	0.0129	-0.1124	-0.0118	-0.1644	0.0297	0.2603
	0.0581	0.0423	-0.0282	-0.0225	0.0285	-0.0231	0.1373
Standard Deviation	0.0844	0.0292	0.1075	0.0758	0.0668	0.0364	0.0826
Precision	<b>0.1807</b>	<b>0.0625</b>	<b>0.2300</b>	<b>0.1622</b>	<b>0.1430</b>	<b>0.0778</b>	<b>0.1767</b>

## E.6.2 Apex Precision

<b>Superior Precision</b>	X	Y	Z	Rx	Ry	Rz	MTPM
Translation	0.1391	-0.0085	-0.023	0.0246	-0.0069	-0.01	0.1949
	-0.0172	0.0124	-0.0199	-0.0235	-0.0339	-0.0628	0.1165
	0.0323	0.0176	-0.051	0.021	0.0456	0.081	0.1366
	-0.0285	-0.0203	0.1024	0.0285	-0.113	0.0214	0.3567
	0.0369	0.0014	-0.0678	-0.047	0.1122	-0.0905	0.5254
	-0.0496	0.0038	0.0102	0.012	0.0292	0.0402	0.0986
	-0.1132	-0.0067	0.049	-0.0156	-0.0329	0.0209	0.1612
Rotation	0.1135	0.0183	0.1039	0.1284	0.0796	-0.0969	0.4692
	0.0245	-0.0481	0.0479	-0.0921	-0.1164	-0.1959	0.3967
	-0.0002	0.0036	-0.0743	0.0485	0.063	0.1483	0.3911
	-0.0192	-0.0331	0.1111	0.015	0.1493	-0.059	0.283
	0.1418	0.0201	-0.1413	0.0602	-0.0645	-0.0418	0.3398
	-0.1293	0.001	-0.072	-0.1384	-0.0733	0.1226	0.3914
	-0.1497	0.0145	0.0554	-0.0384	-0.0524	0.0744	0.2283
Standard Deviation	0.0925	0.0203	0.0786	0.0661	0.0827	0.0947	0.1376
Precision	<b>0.1979</b>	<b>0.0434</b>	<b>0.1681</b>	<b>0.1414</b>	<b>0.1770</b>	<b>0.2028</b>	<b>0.2944</b>

<b>Inferior Precision</b>	X	Y	Z	Rx	Ry	Rz	MTPM
Translation	-0.0798	-0.0266	-0.0202	0.0451	0.0718	-0.0444	0.1134
	0.1289	0.0252	-0.0096	-0.0704	-0.0223	0.0418	0.1594
	-0.1156	-0.0237	0.0962	-0.0103	0.0771	-0.0296	0.2236
	-0.069	-0.0037	-0.0552	0.0645	0.0049	-0.0412	0.1168
	0.1943	0.012	-0.0699	0.0456	-0.0698	0.078	0.2526
	0.0594	0.0127	0.1041	-0.0707	-0.0048	0.0337	0.1477
	-0.1185	0.0046	-0.0451	-0.0036	-0.0569	-0.0385	0.1692
Rotation	0.0415	0.0142	0.1860	-0.2147	0.0572	0.0155	0.2640
	-0.0338	-0.0282	-0.0588	0.1590	-0.0261	-0.0586	0.1332
	0.4099	0.0607	-0.1228	0.0131	0.0365	0.1867	0.5392
	-0.1614	-0.0410	-0.0324	-0.0128	0.1672	-0.1033	0.2634
	0.2020	0.0161	-0.0222	-0.0990	-0.2043	0.1294	0.2644
	-0.1155	-0.0232	0.0063	0.1348	-0.1539	-0.0065	0.2266
	-0.1844	-0.0063	-0.4408	0.1873	0.2610	-0.0767	0.6048
Standard Deviation	0.1709	0.0269	0.1422	0.1078	0.1194	0.0815	0.1485
Precision	<b>0.3657</b>	<b>0.0577</b>	<b>0.3043</b>	<b>0.2307</b>	<b>0.2554</b>	<b>0.1744</b>	<b>0.3177</b>

### E.6.3 Dual Precision

Superior Precision	X	Y	Z	Rx	Ry	Rz	MTPM
Translation	-0.1217	-0.0026	0.0736	-0.0247	0.0069	0.01	0.188
	0.1298	-0.0211	-0.0176	0.0235	0.034	0.0628	0.1519
	-0.1772	-0.003	0.0804	-0.0211	-0.0455	-0.081	0.2535
	-0.0523	0.0163	-0.0159	-0.0284	0.113	-0.0213	0.123
	0.1805	-0.0095	-0.0551	0.0471	-0.1121	0.0906	0.2437
	-0.02	0.0028	0.0058	-0.012	-0.0292	-0.0402	0.0678
	0.0606	0.0176	-0.0711	0.0156	0.0329	-0.0209	0.197
Rotation	0.1052	-0.0878	0.129	-0.1283	-0.0798	0.0967	0.2415
	0.2658	0.059	-0.1907	0.0917	0.1167	0.1957	0.5557
	-0.275	0.0304	0.1501	-0.0487	-0.0629	-0.1484	0.5034
	0.1859	0.0287	-0.0803	-0.0148	-0.1493	0.059	0.3612
	-0.0548	-0.0323	0.2855	-0.0602	0.0644	0.0418	0.4198
	-0.1429	0.0859	-0.1832	0.1385	0.073	-0.1228	0.3896
	-0.0098	0.0437	-0.0967	0.0385	0.0524	-0.0745	0.2513
Standard Deviation	0.1563	0.0423	0.1321	0.0661	0.0827	0.0947	0.1441
Precision	<b>0.3344</b>	<b>0.0905</b>	<b>0.2828</b>	<b>0.1414</b>	<b>0.1771</b>	<b>0.2027</b>	<b>0.3083</b>
Inferior Precision	X	Y	Z	Rx	Ry	Rz	MTPM
Translation	-0.0406	0.0149	-0.1209	-0.045	-0.0718	0.0444	0.1922
	-0.0135	-0.0131	0.2105	0.0705	0.0222	-0.0418	0.2577
	0.0367	0.0177	-0.0843	0.0103	-0.0771	0.0296	0.1449
	-0.0453	-0.0082	-0.1254	-0.0645	-0.0049	0.0411	0.1815
	0.0198	0.0033	-0.0414	-0.0455	0.0699	-0.078	0.2736
	0.0342	-0.0022	0.0938	0.0707	0.0048	-0.0337	0.1592
	0.0089	-0.0129	0.0674	0.0035	0.0569	0.0385	0.1308
Rotation	-0.0045	-0.0350	0.4075	0.2147	-0.0572	-0.0153	0.5844
	-0.1156	0.0967	-0.3768	-0.1590	0.0259	0.0586	0.5771
	0.1129	-0.0169	0.0773	-0.0133	-0.0364	-0.1868	0.2284
	-0.0935	-0.0359	-0.0602	0.0131	-0.1672	0.1033	0.4662
	0.0875	0.0570	0.3588	0.0994	0.2040	-0.1298	0.6663
	0.0691	-0.0032	-0.3382	-0.1348	0.1539	0.0068	0.4855
	0.0018	-0.0159	-0.0403	-0.1870	-0.2612	0.0759	0.2006
Standard Deviation	0.0644	0.0356	0.2252	0.1078	0.1193	0.0815	0.1883
Precision	<b>0.1378</b>	<b>0.0762</b>	<b>0.4819</b>	<b>0.2307</b>	<b>0.2554</b>	<b>0.1744</b>	<b>0.4029</b>

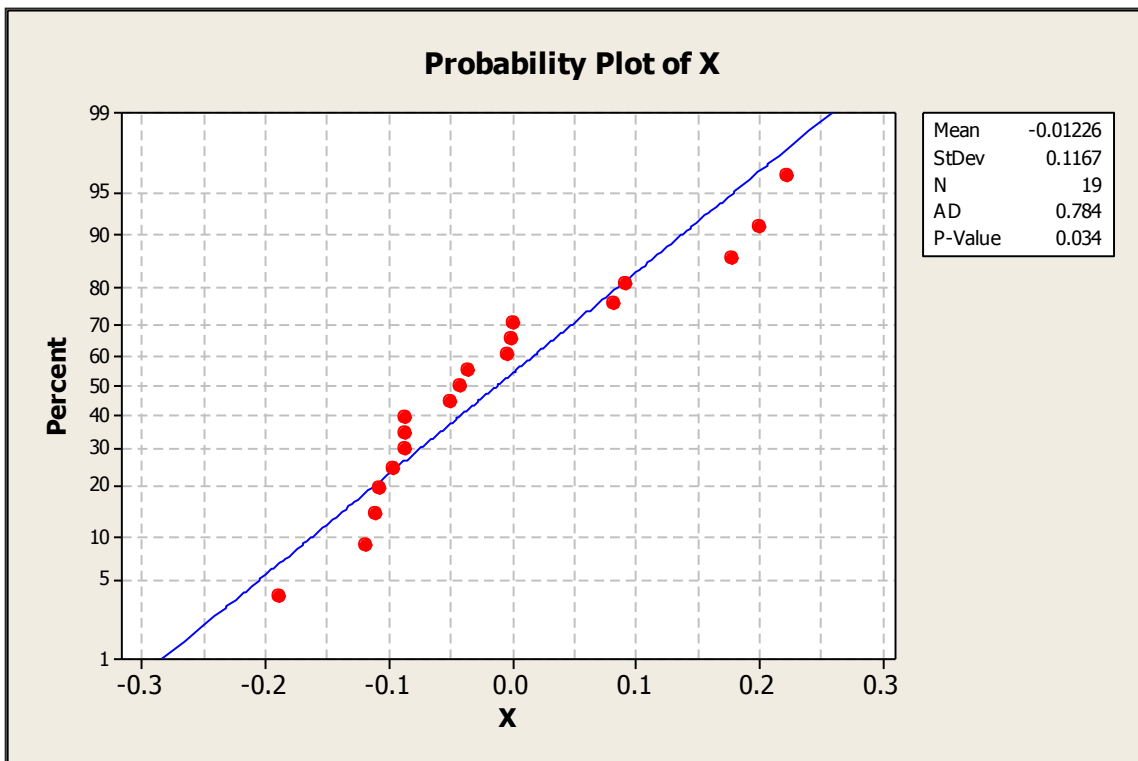
# Appendix F - Plots

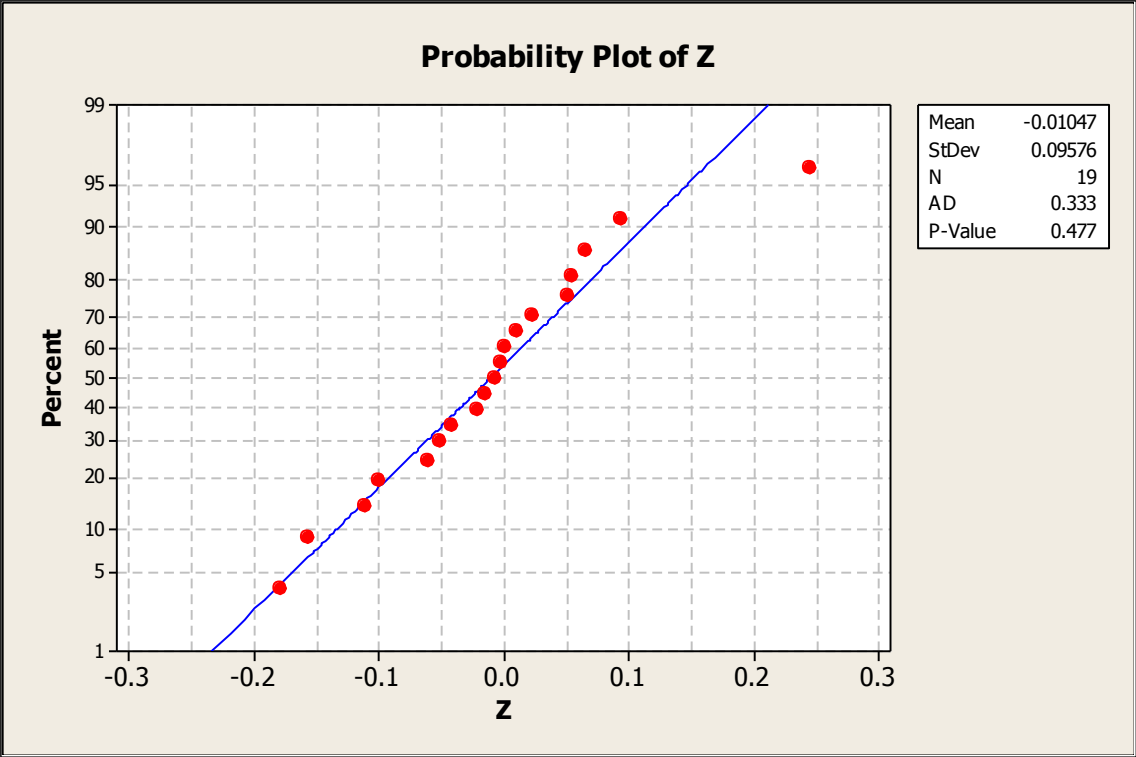
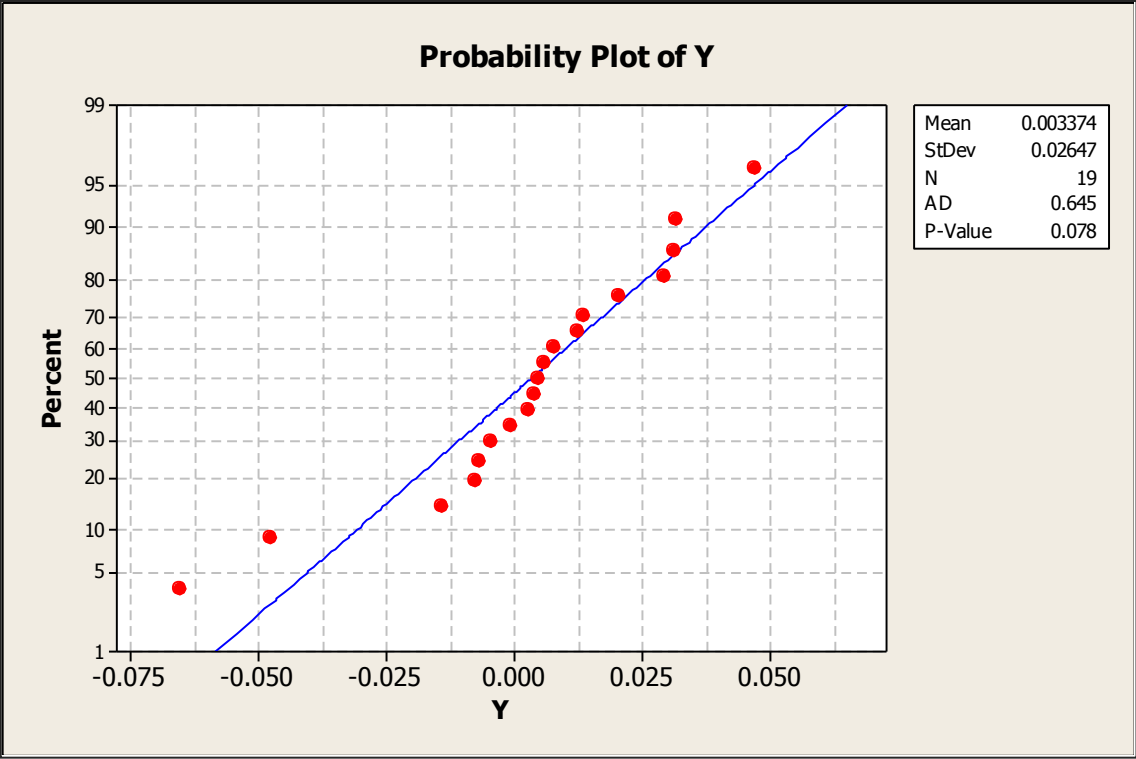
## F.1 Simulation Validation

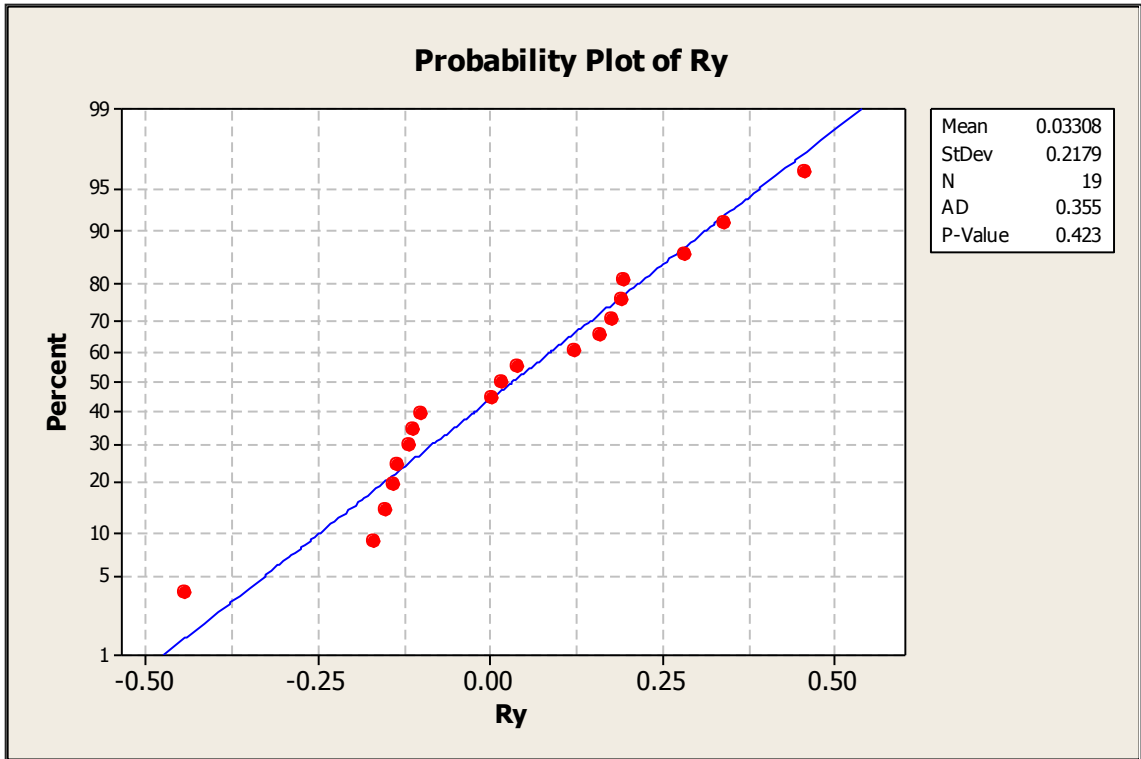
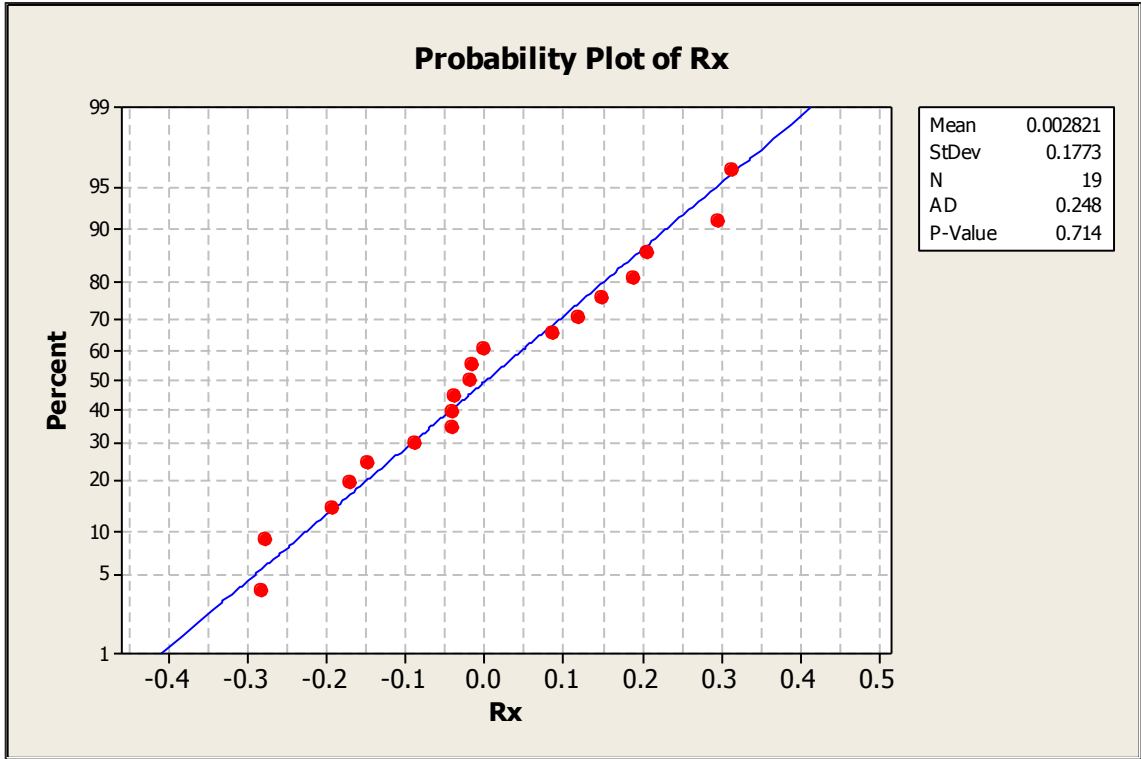
### F.1.1 Check for Normalcy

The plots in this section assess the distribution of the precision data sets. P-values less than **0.05** indicate non-parametric datasets.

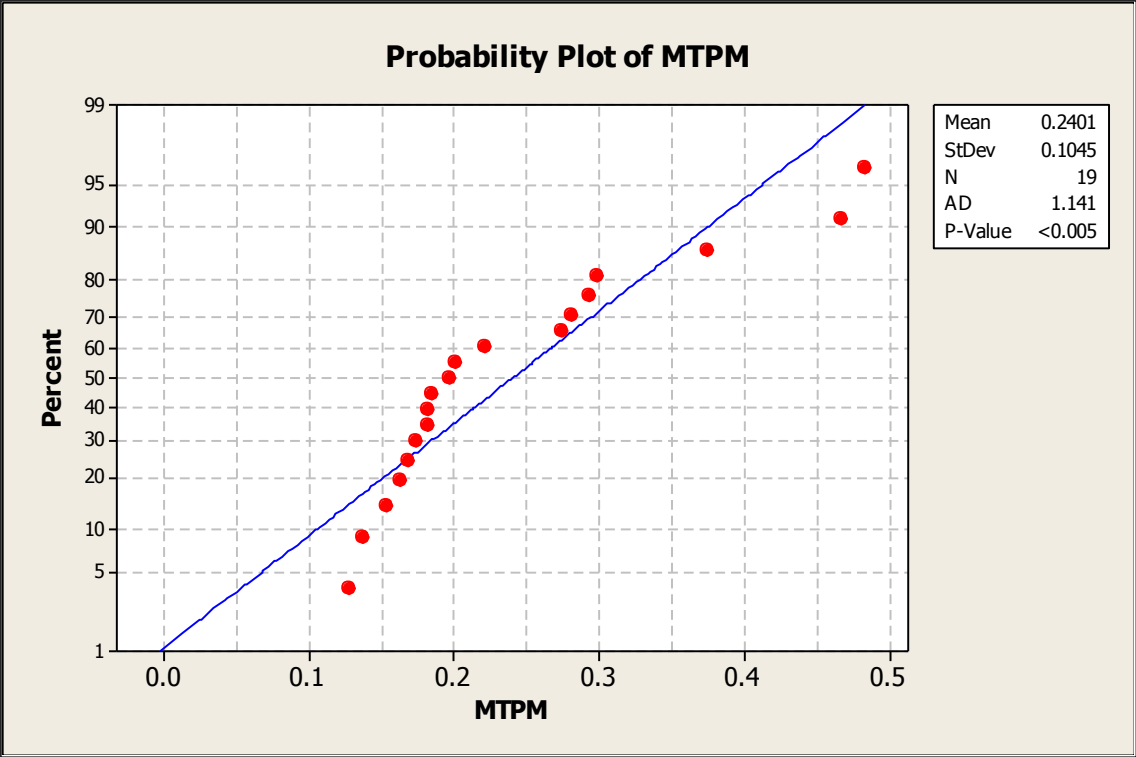
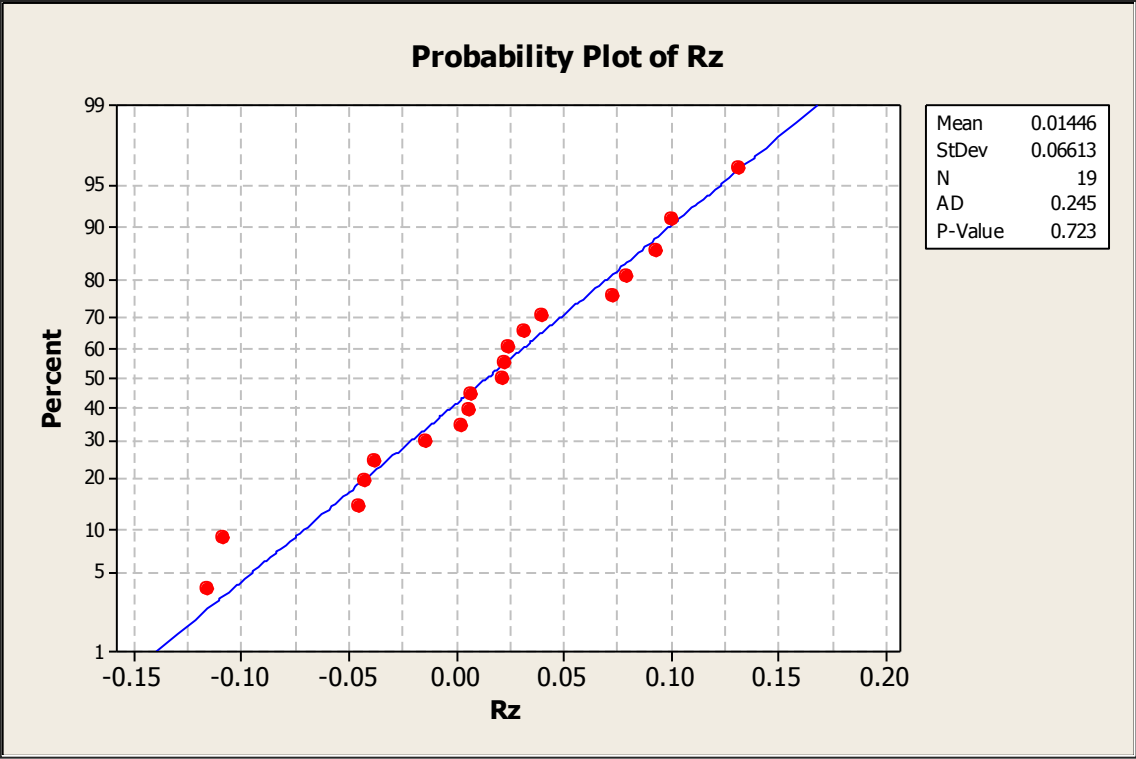
#### F.1.1.1 Phantom - Superior



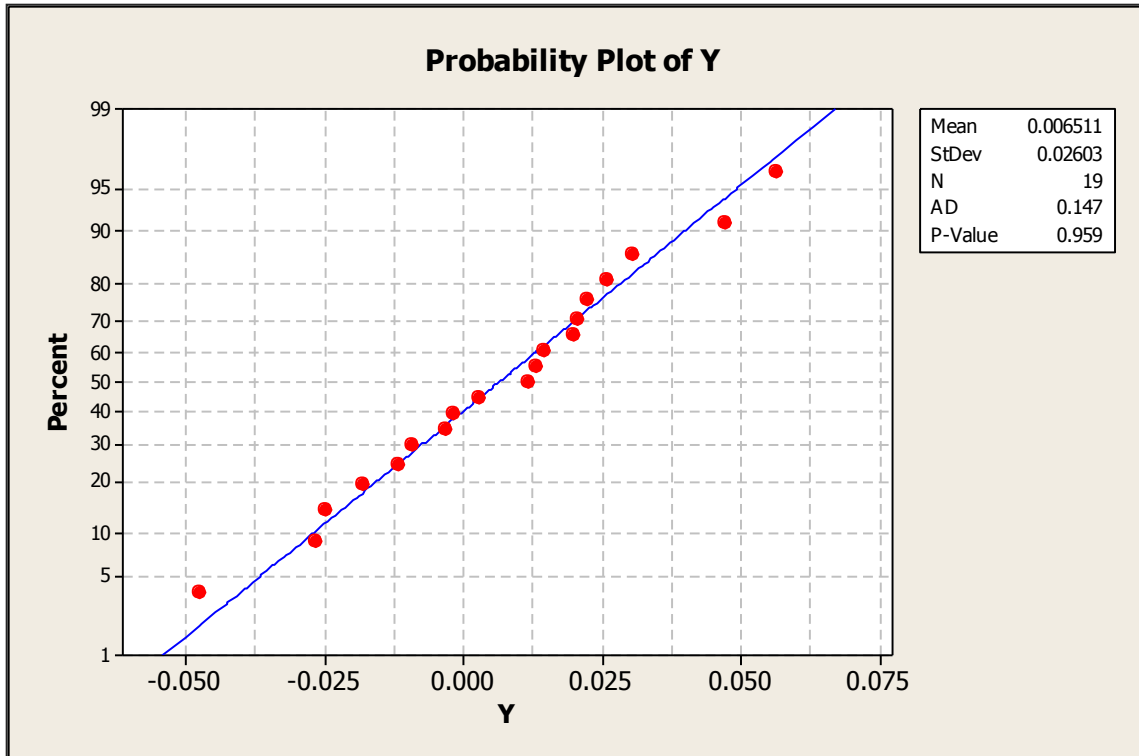
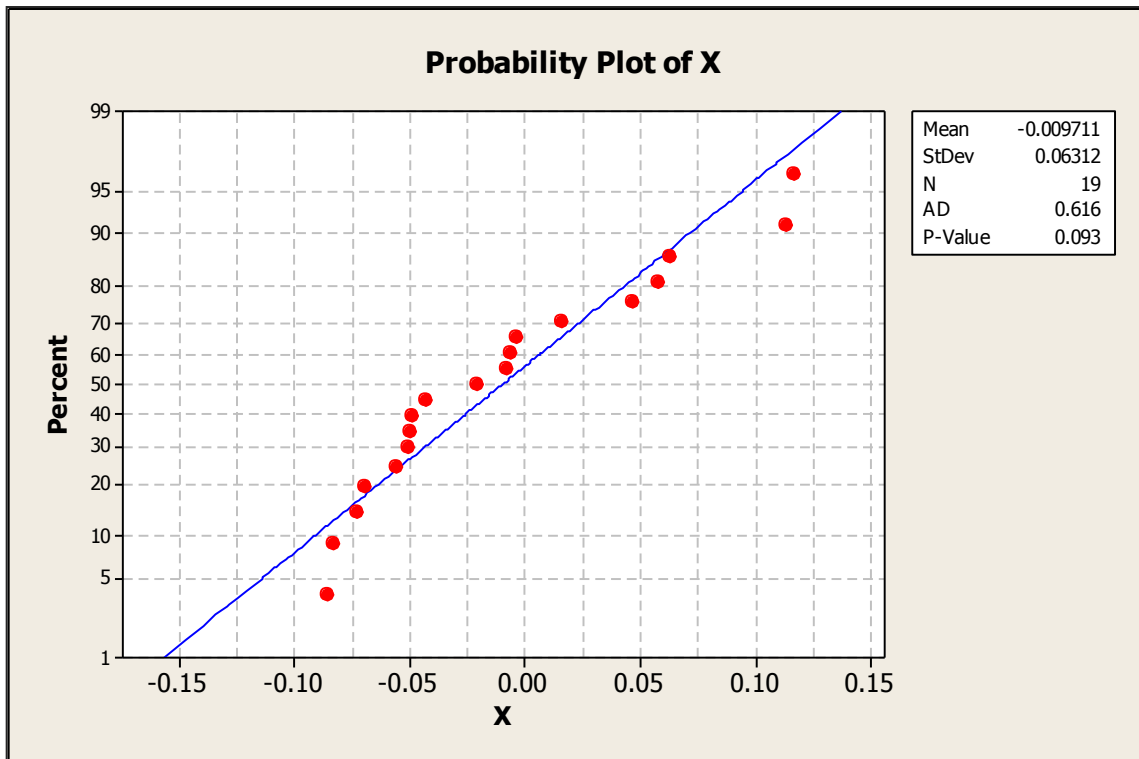


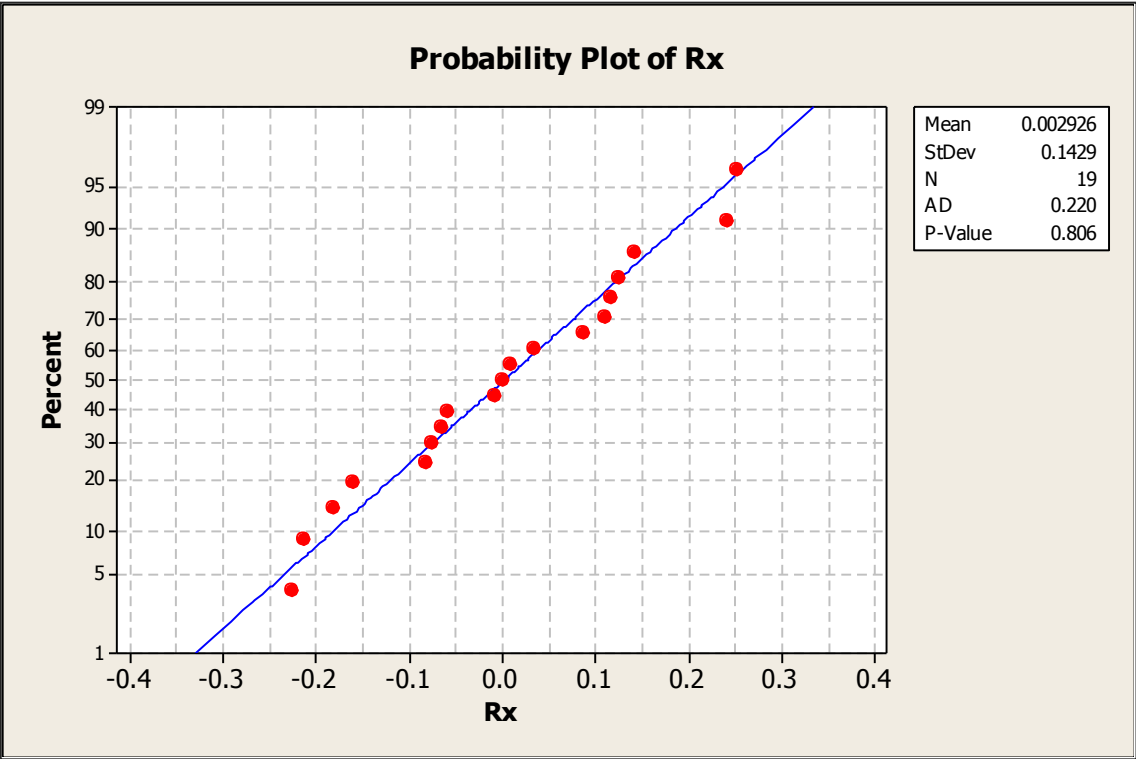
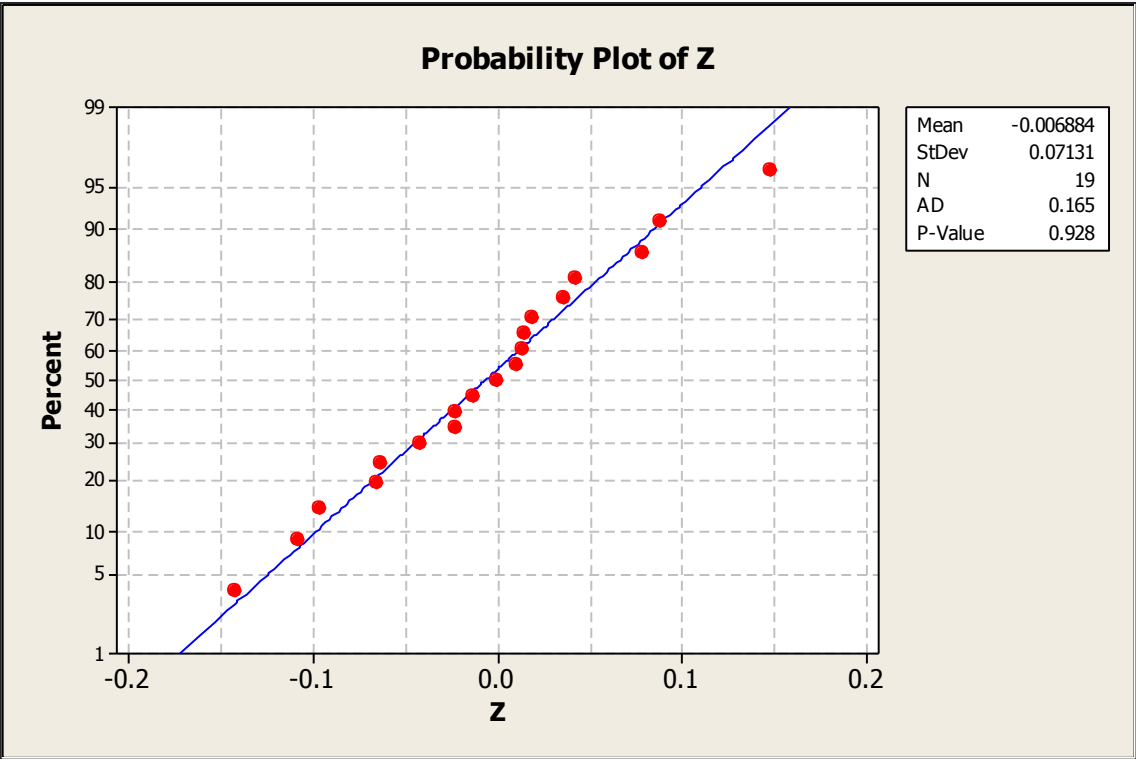


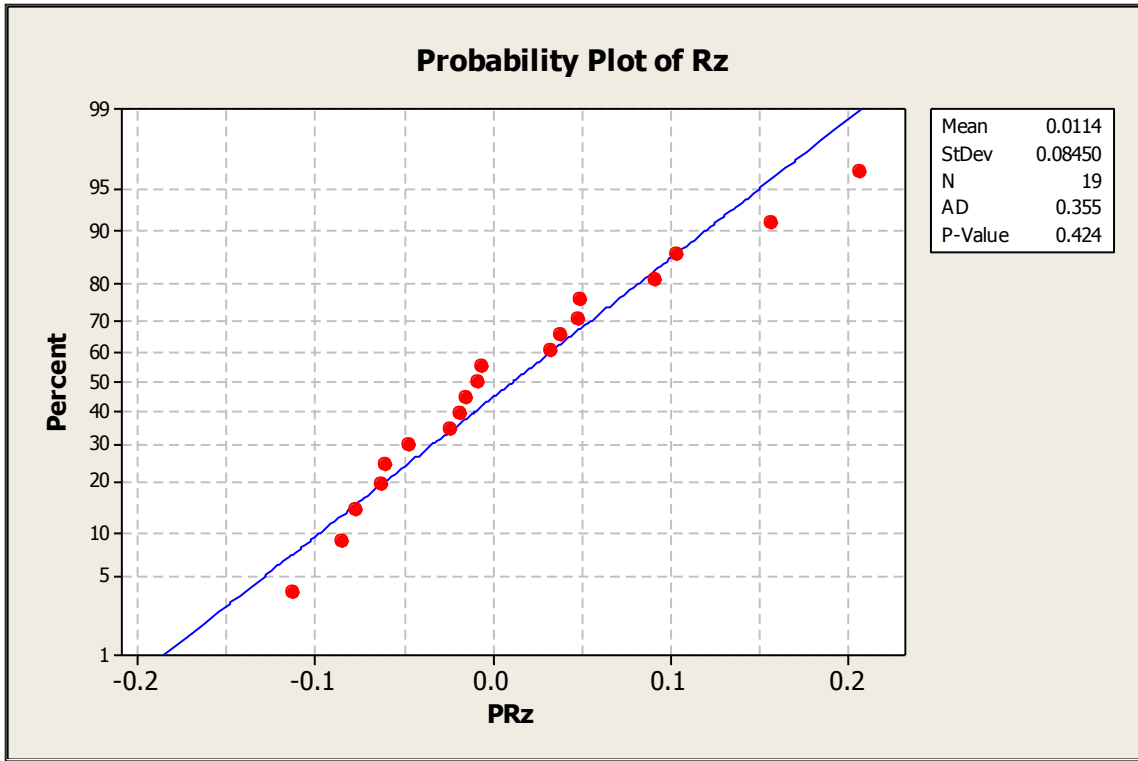
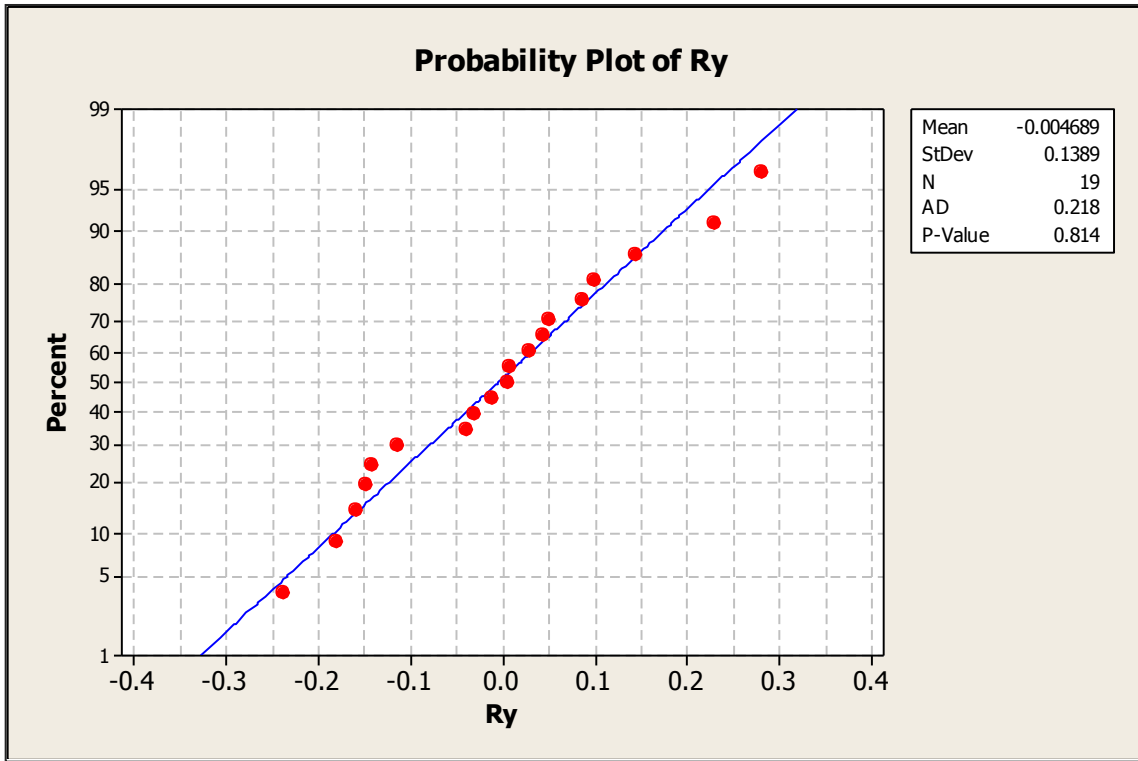




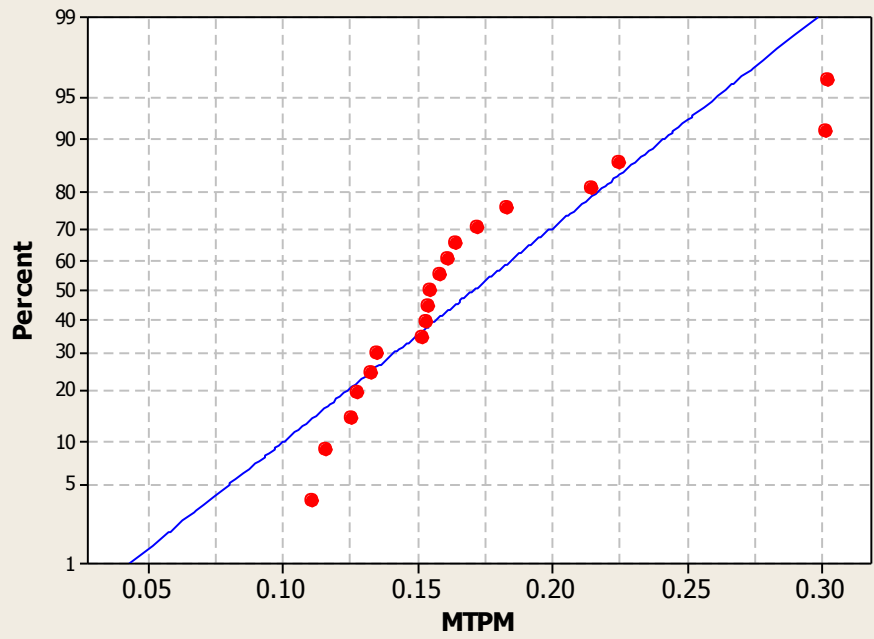
F.1.1.2 Phantom - Inferior





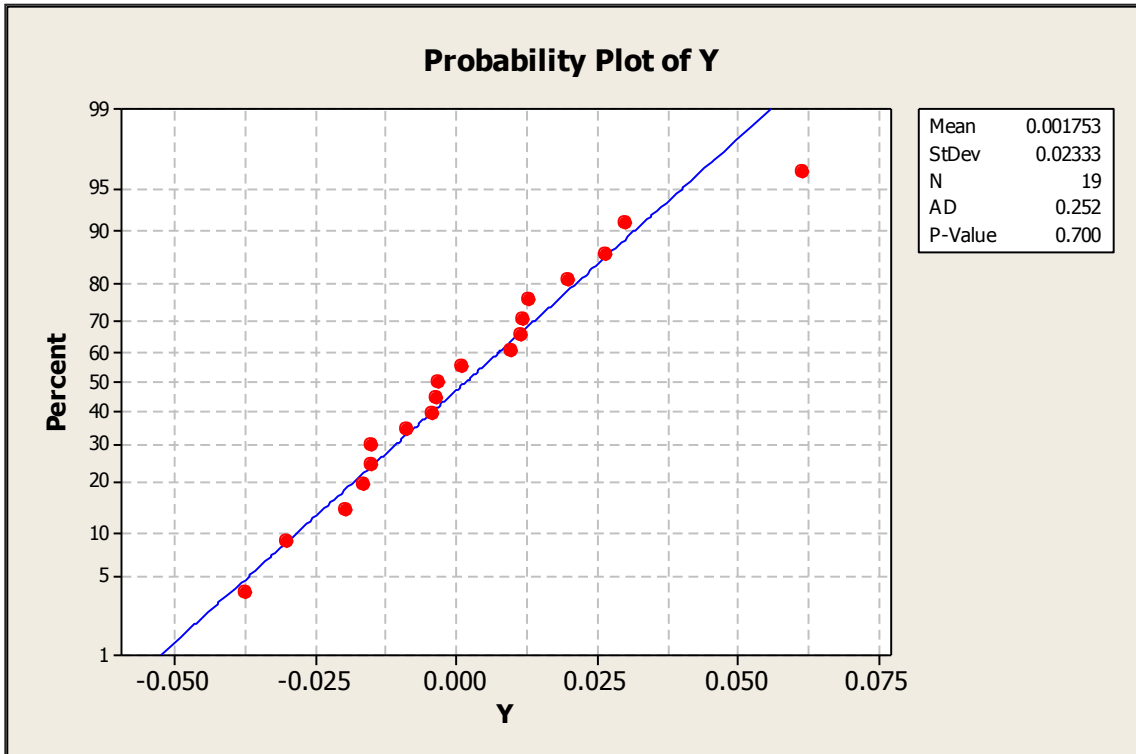
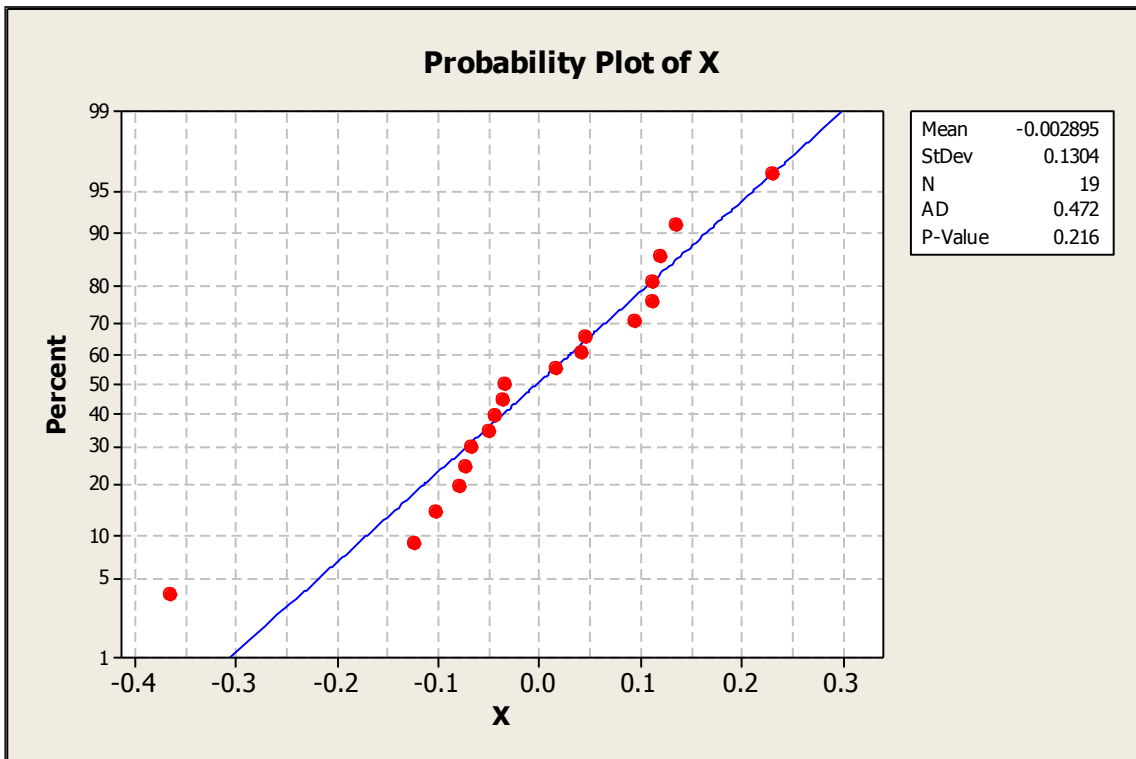


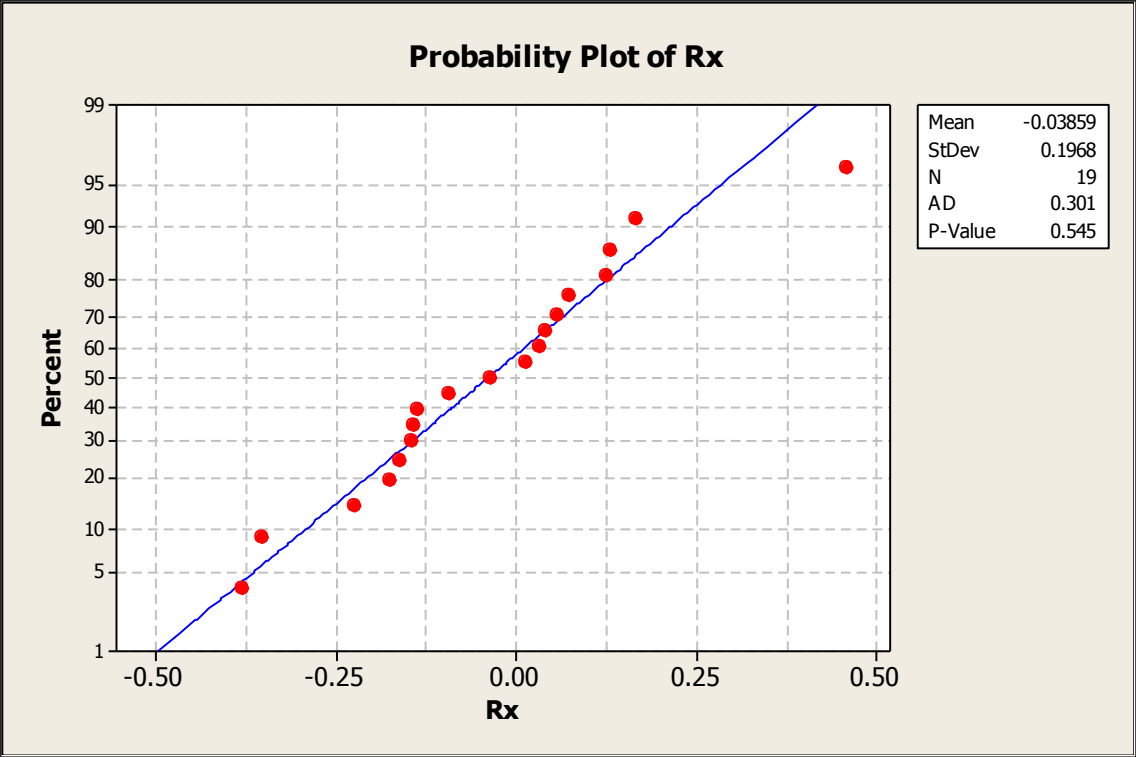
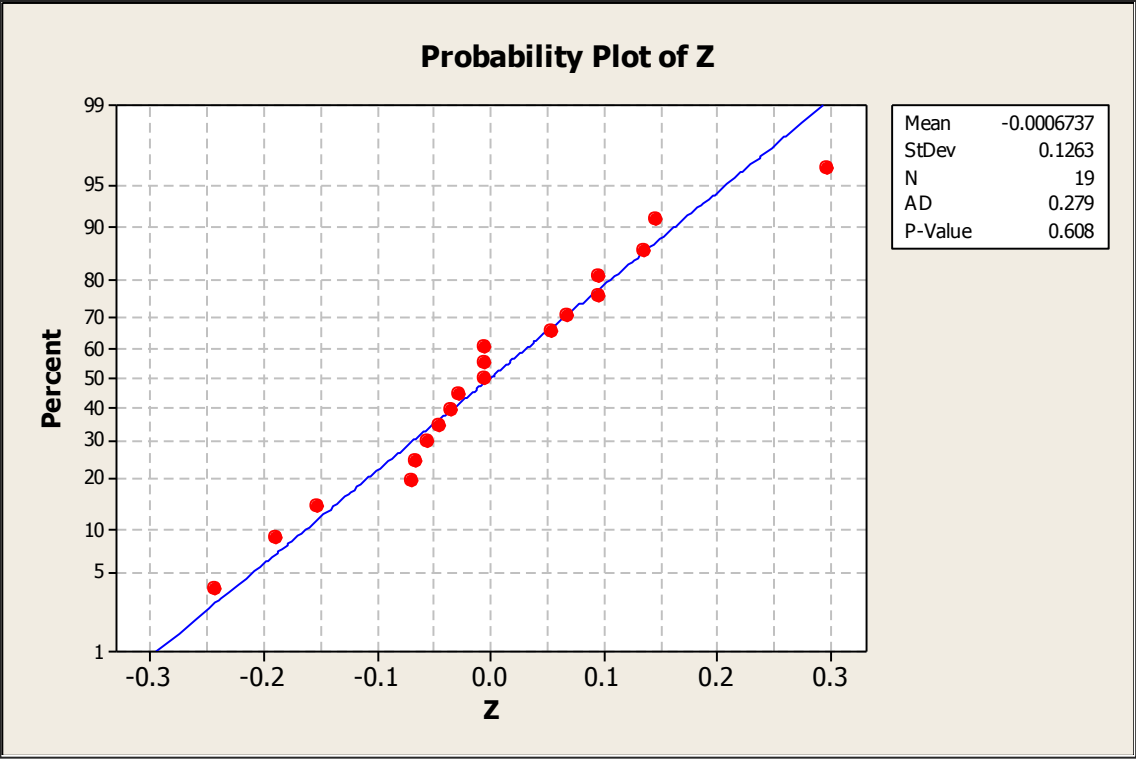
**Probability Plot of MTPM**

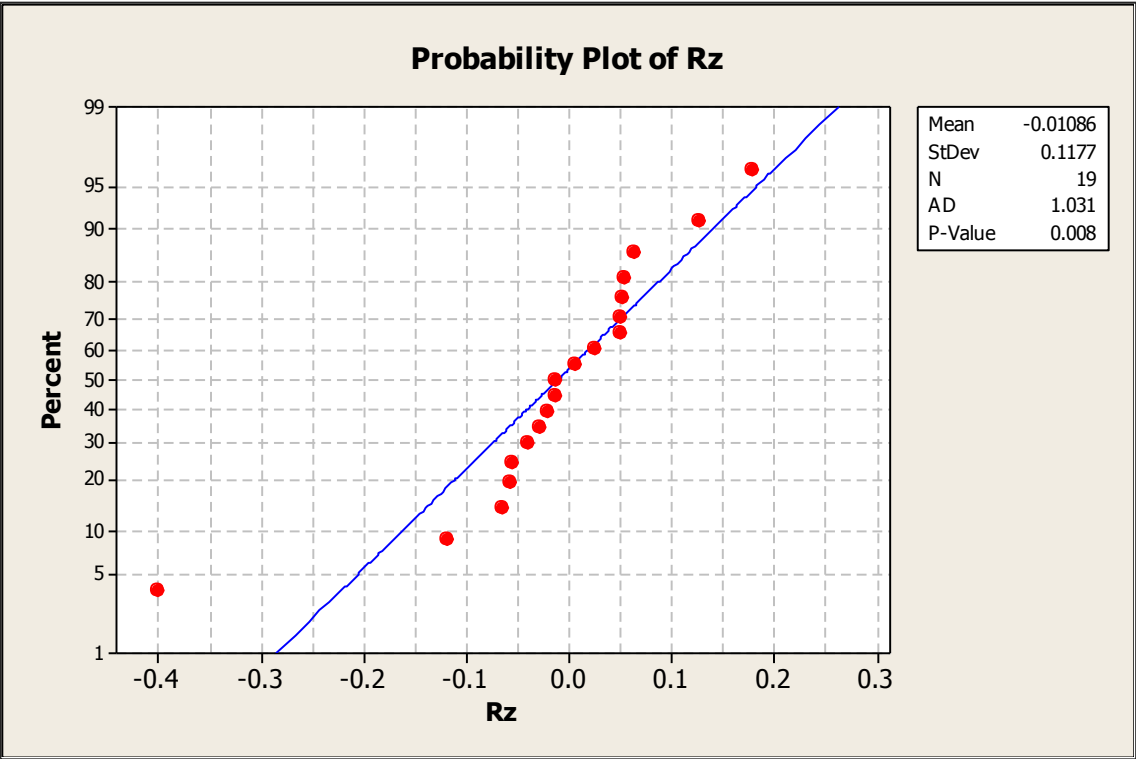
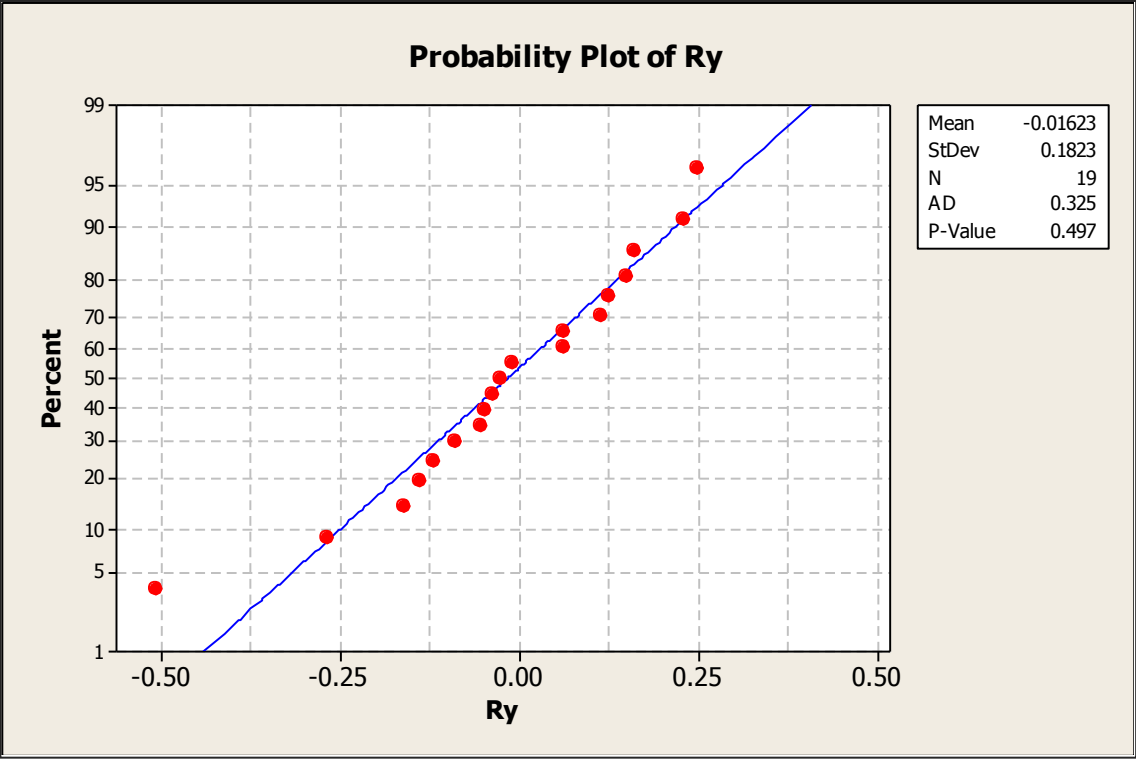


Mean	0.1710
StDev	0.05486
N	19
AD	1.286
P-Value	<0.005

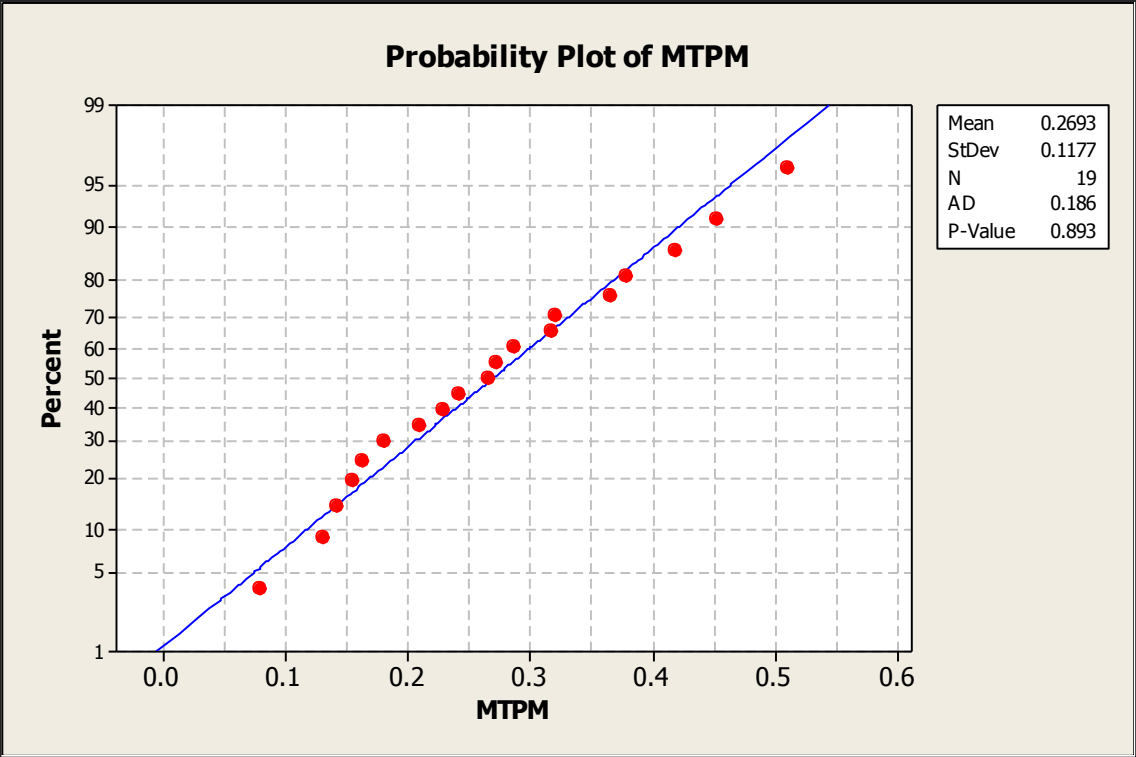
### F.1.1.3 Simulation - Superior



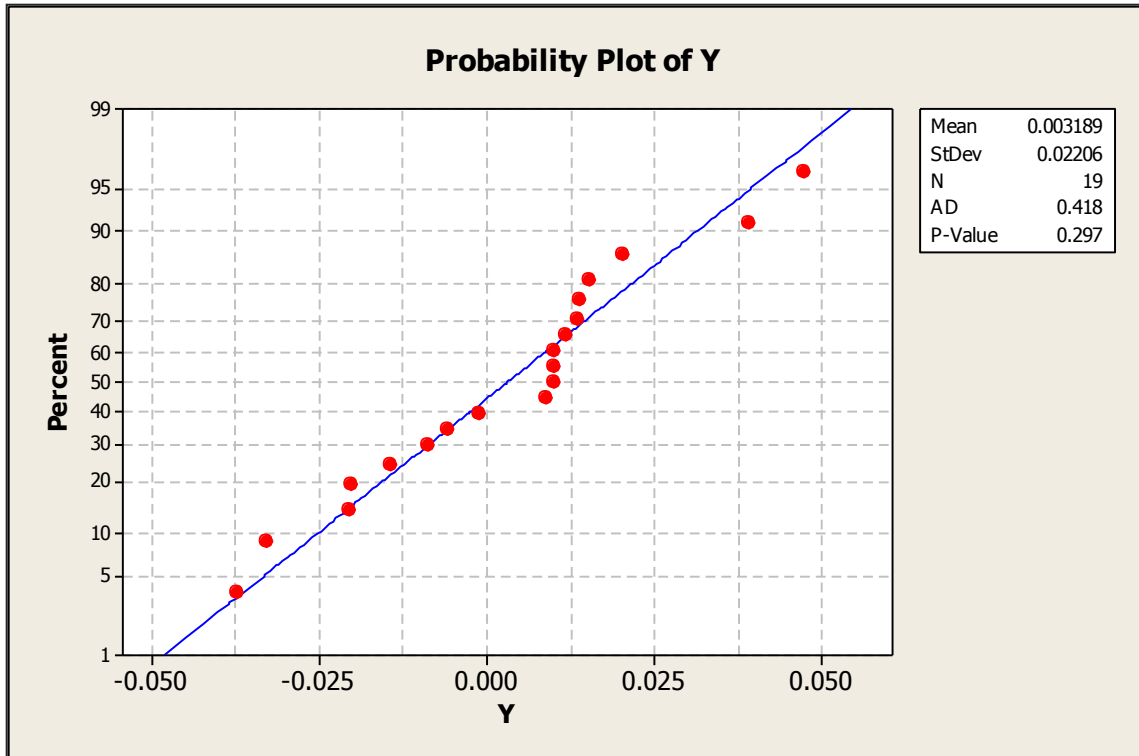
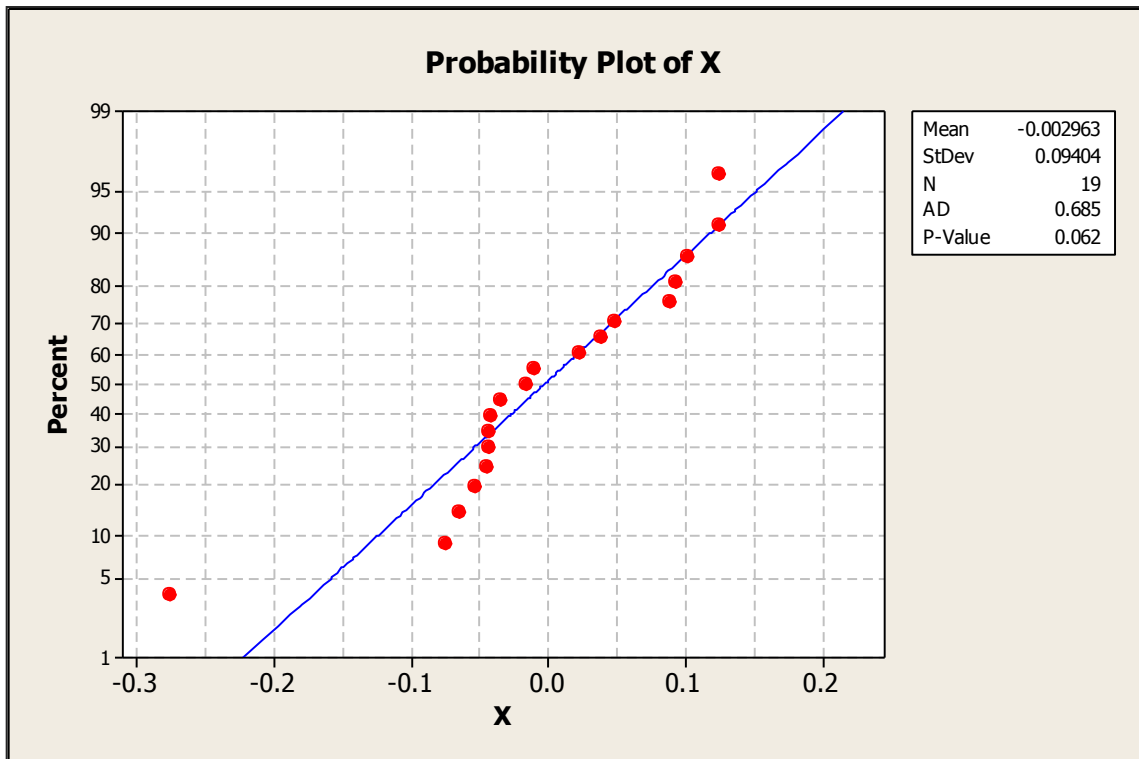


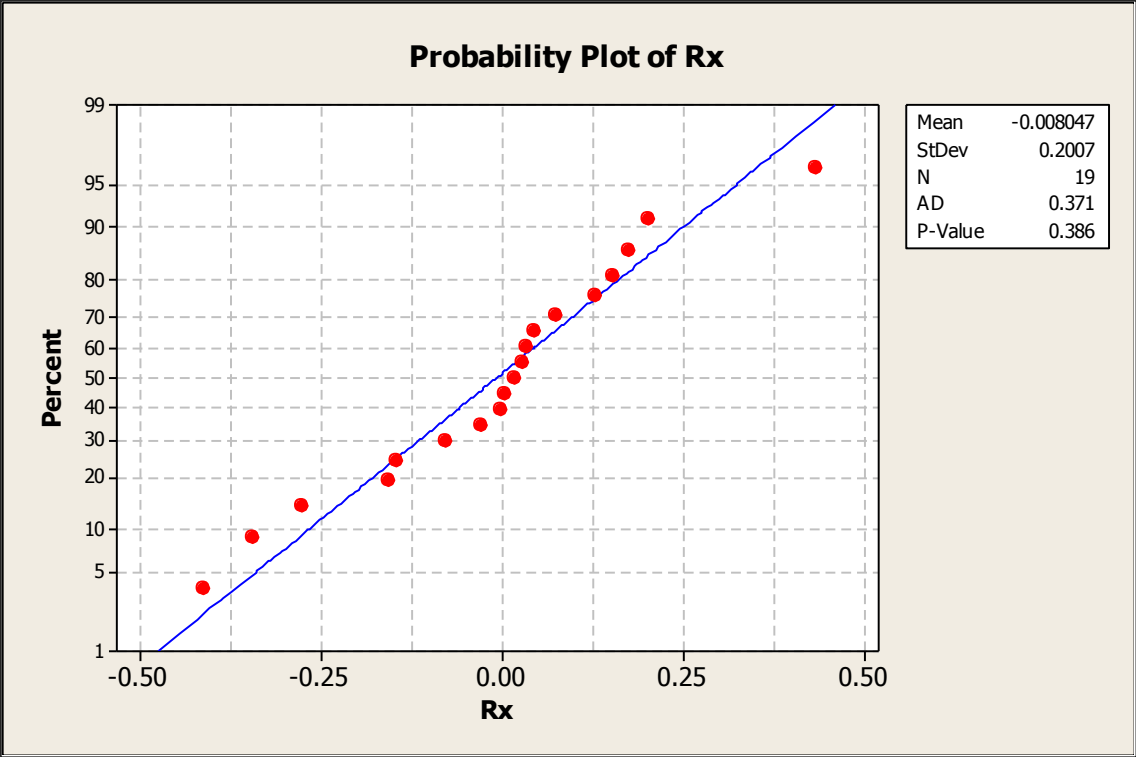
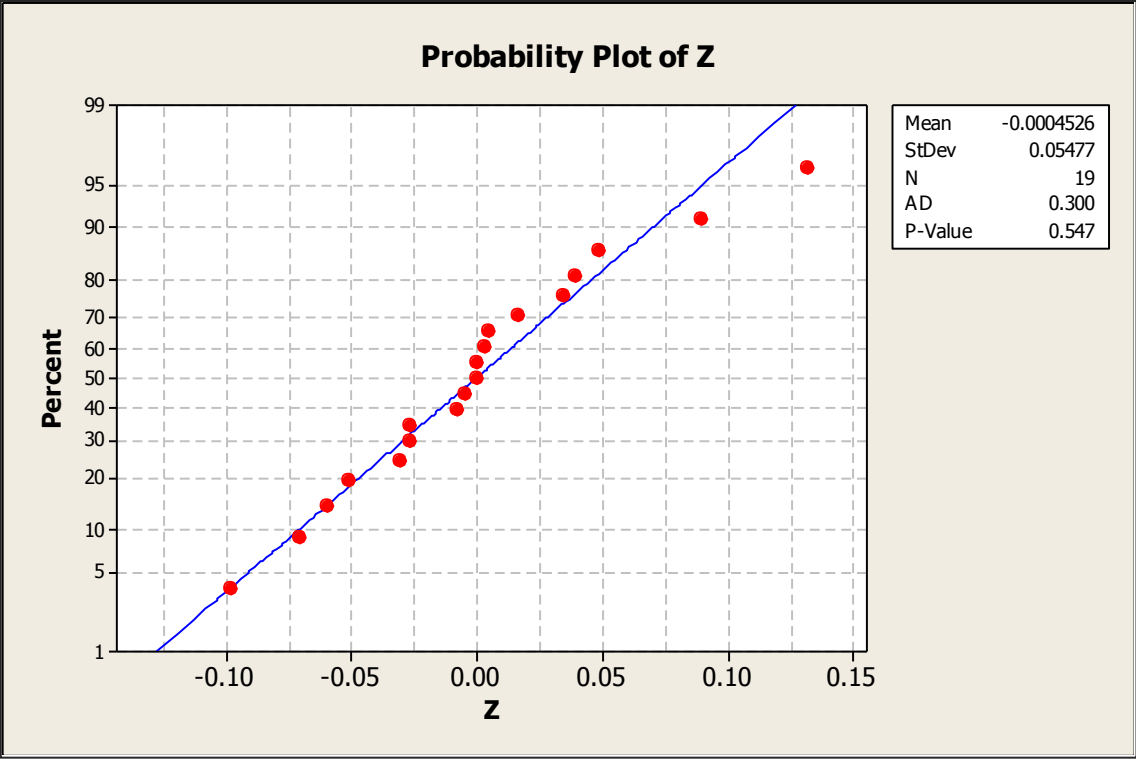


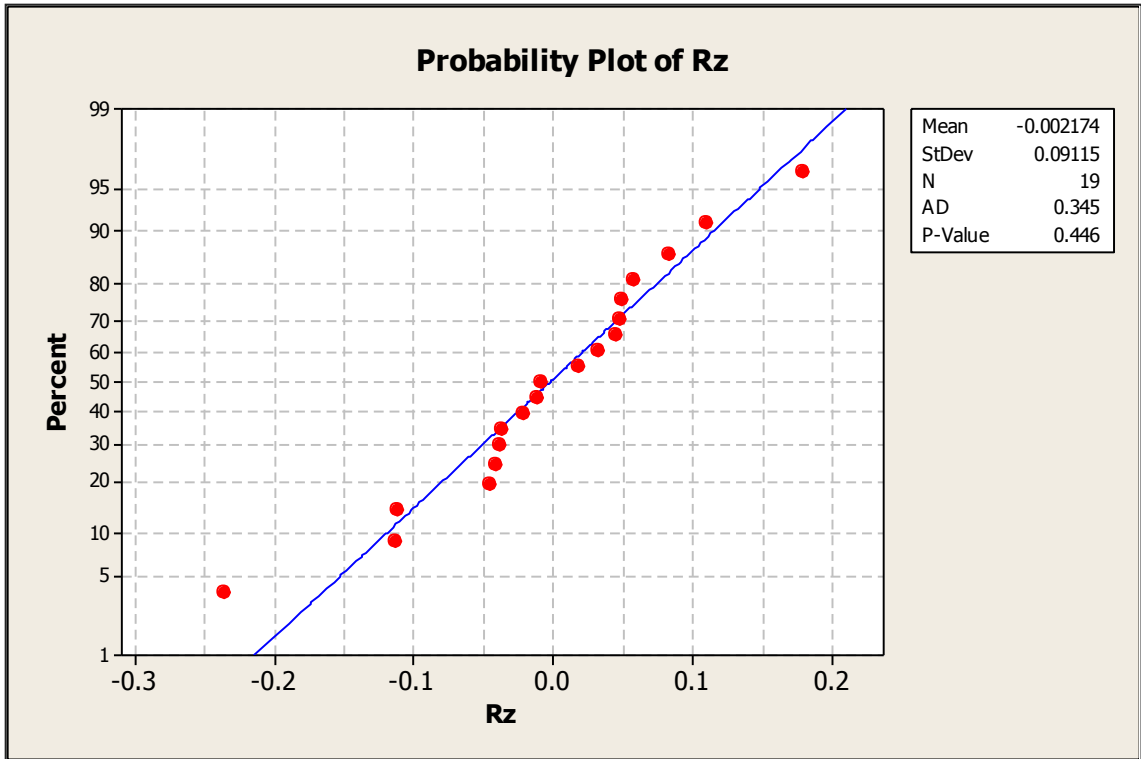
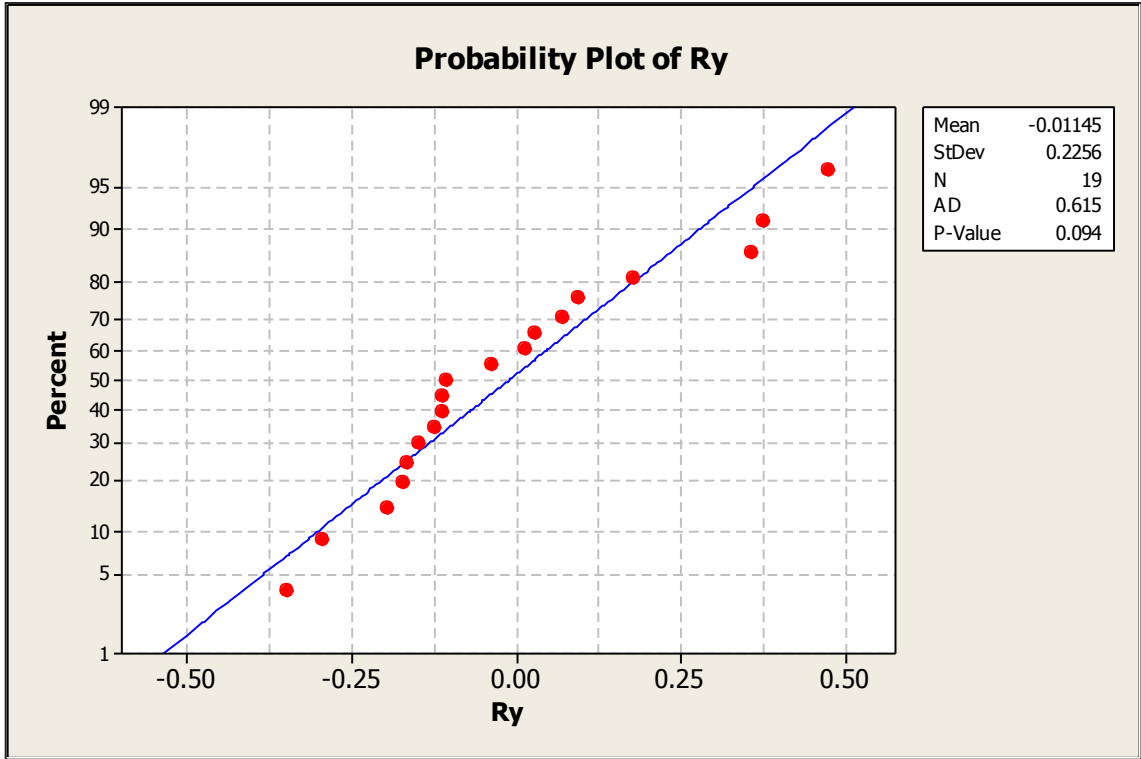




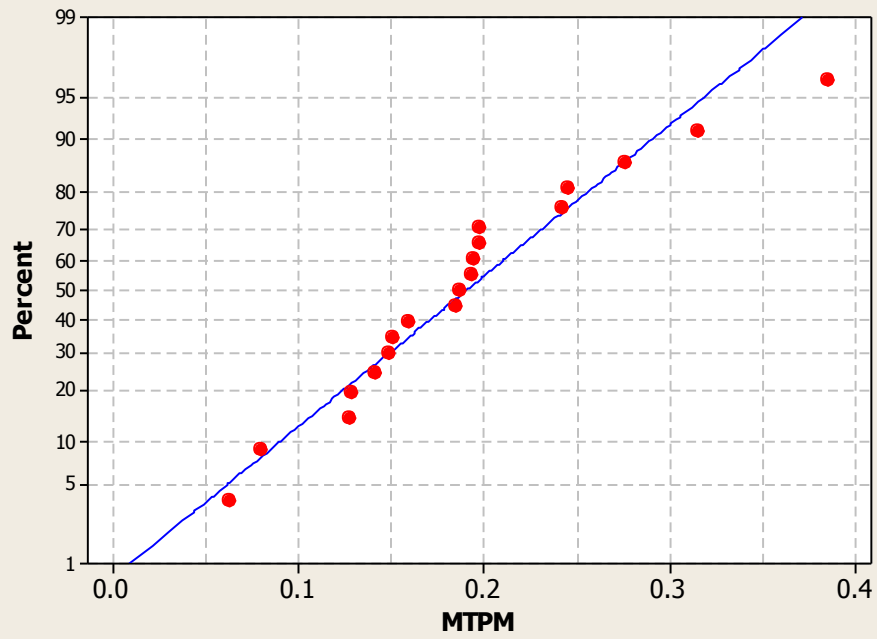
F.1.1.4 Simulation - Inferior







**Probability Plot of MTPM**

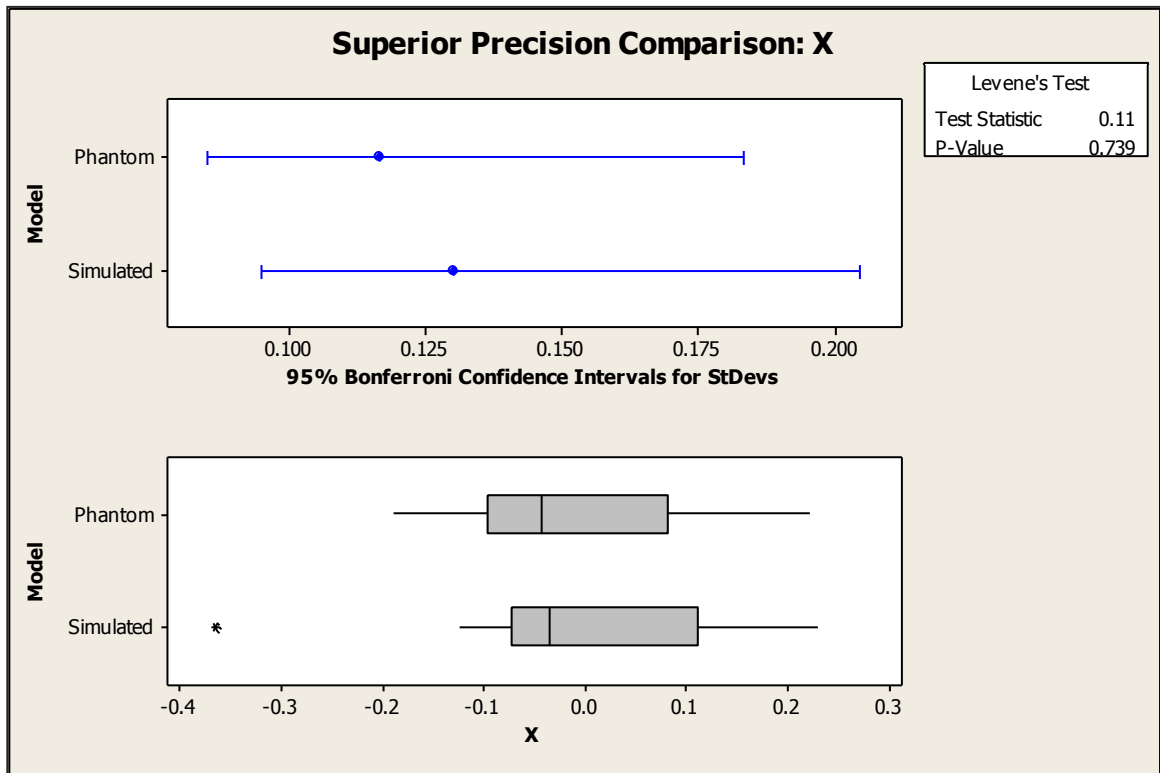


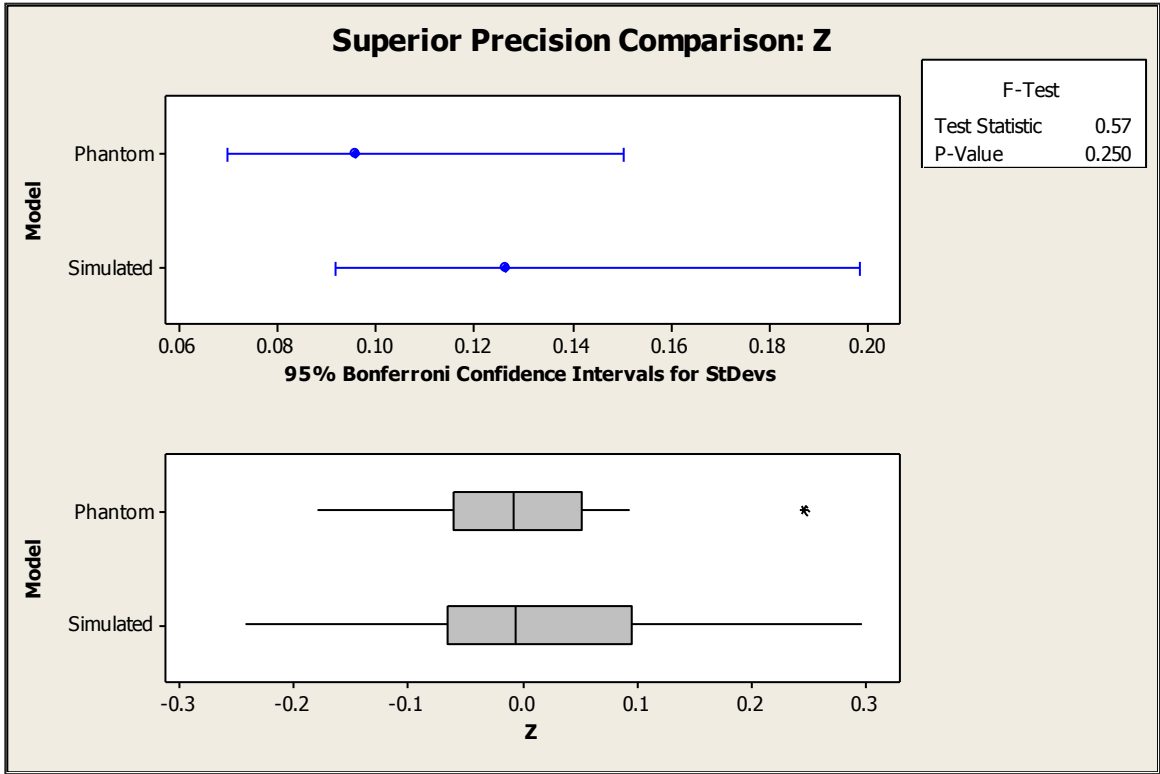
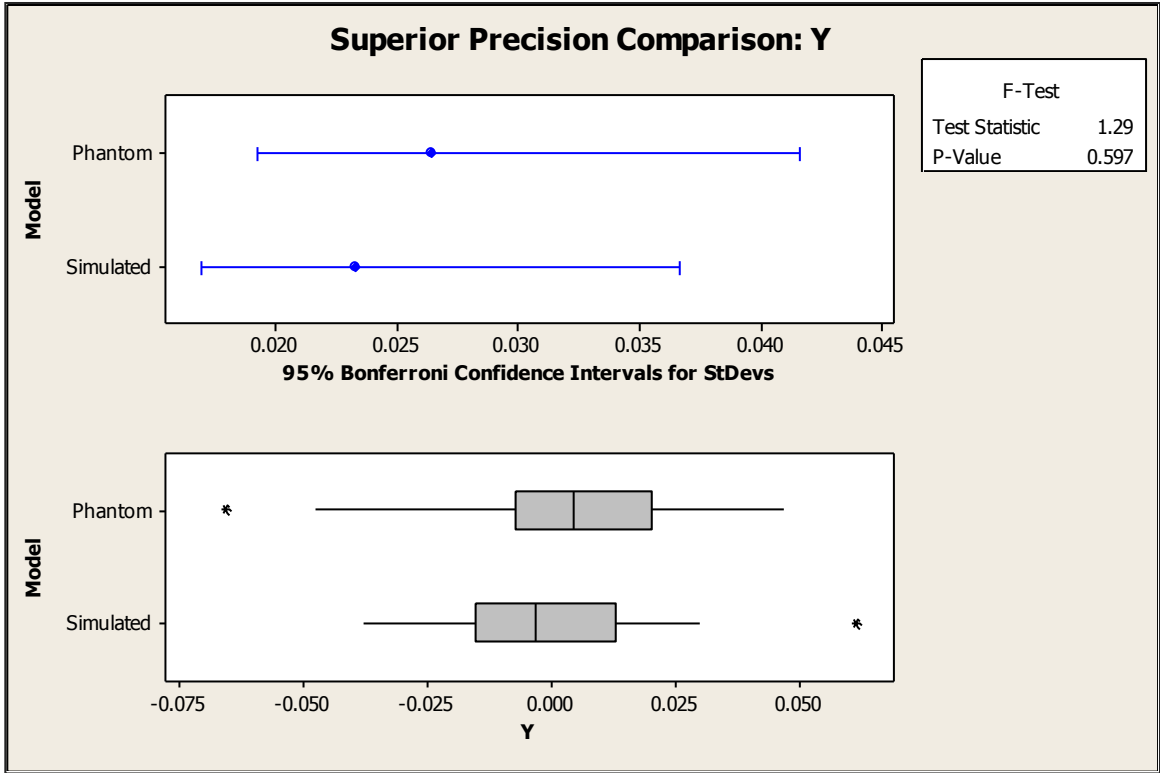
Mean	0.1908
StDev	0.07797
N	19
AD	0.425
P-Value	0.285

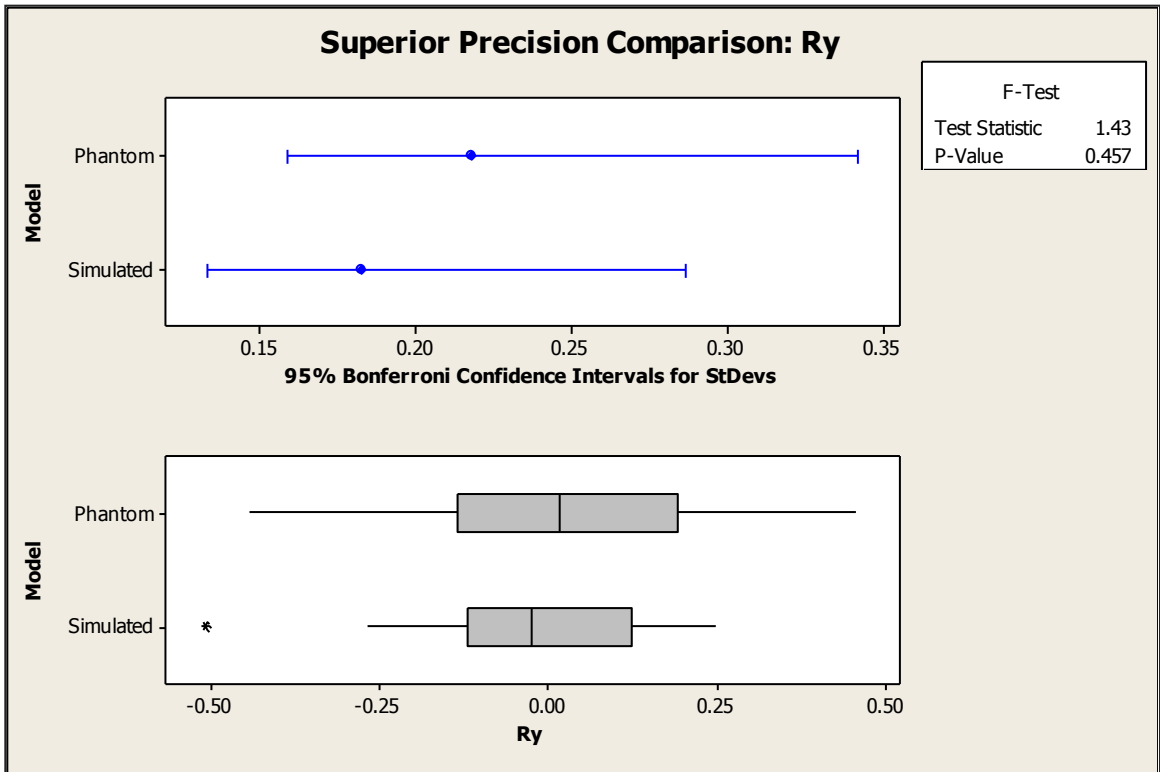
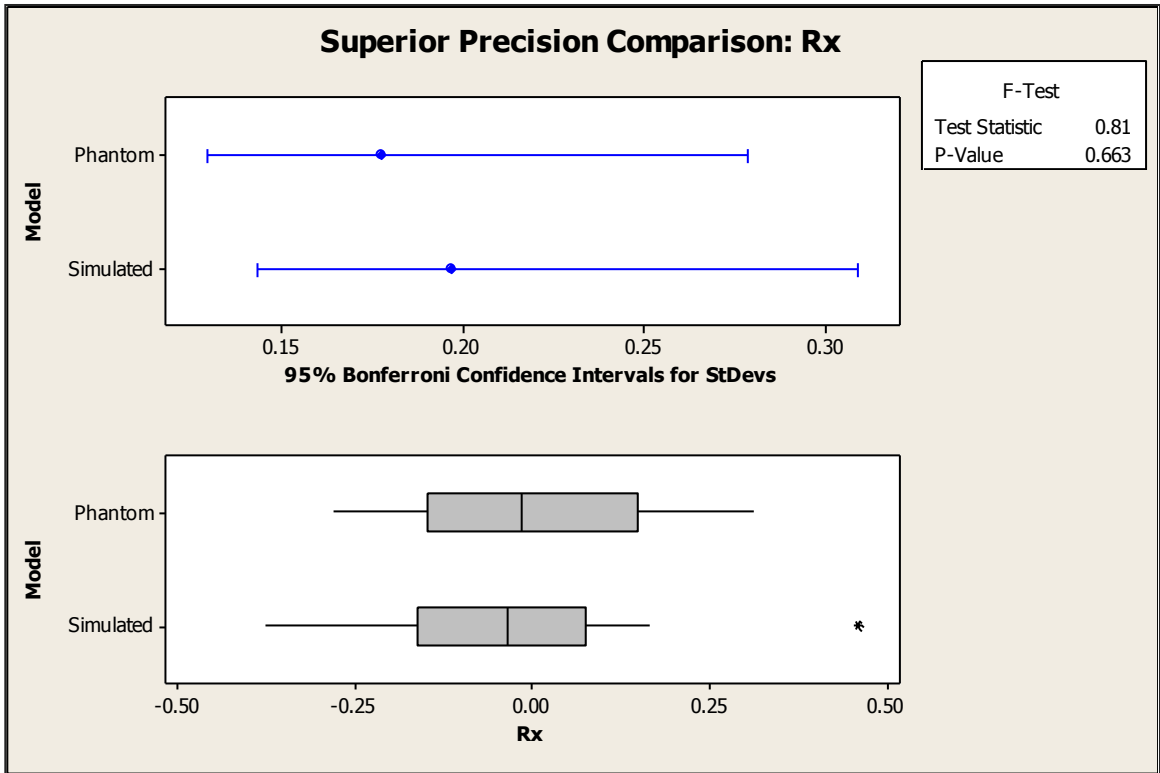
### F.1.2 Variance Comparison

The comparison of the origin style was done using either the F-Test or Levene test. The use of the F-Test was reserved for cases where the data sets for both the phantom and simulated models were normally distributed. If one or both data sets were non-parametrically distributed the Levene test was used. For each of the following plots the utilized test is indicated. P-values above **0.05** indicate no statistically significant differences between the two models.

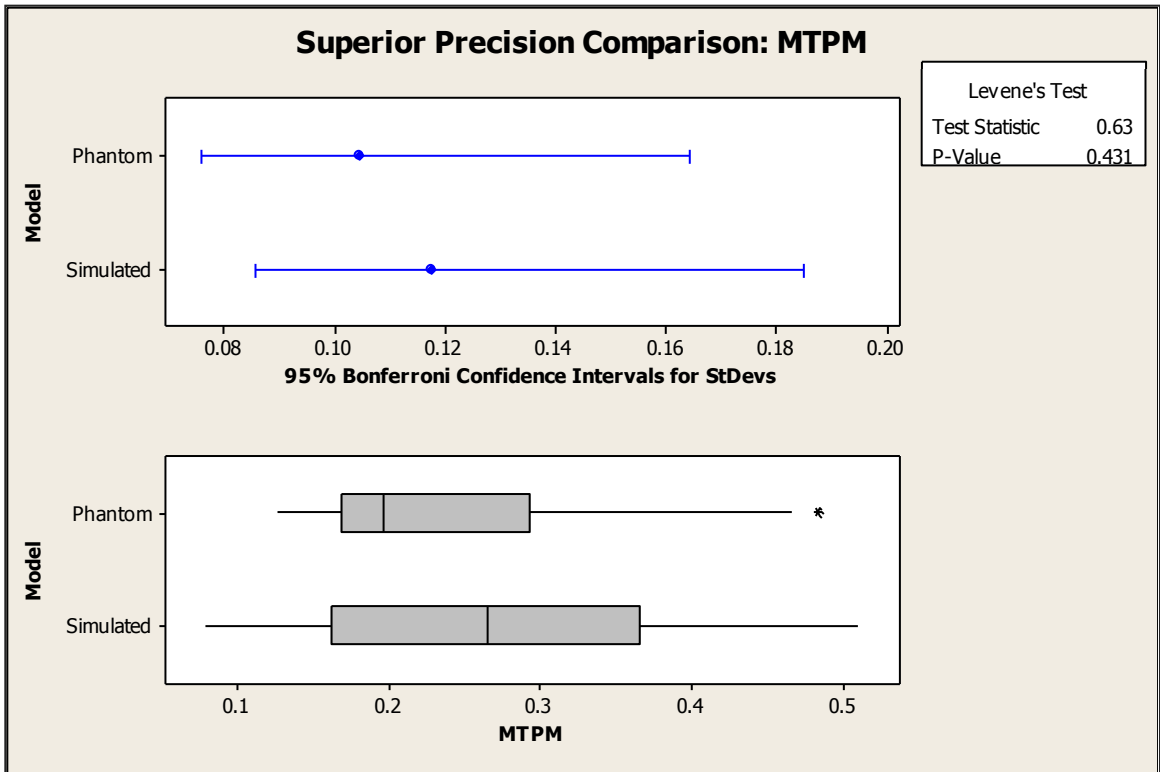
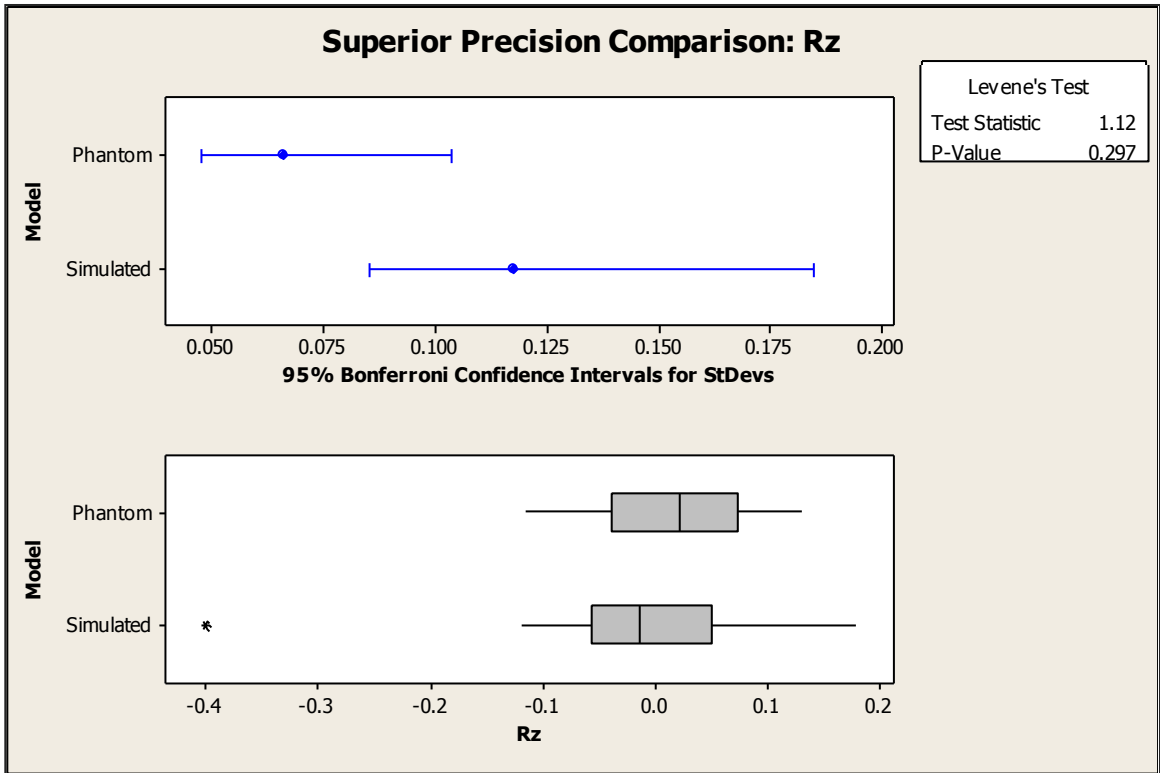
#### F.1.2.1 Superior Assessment



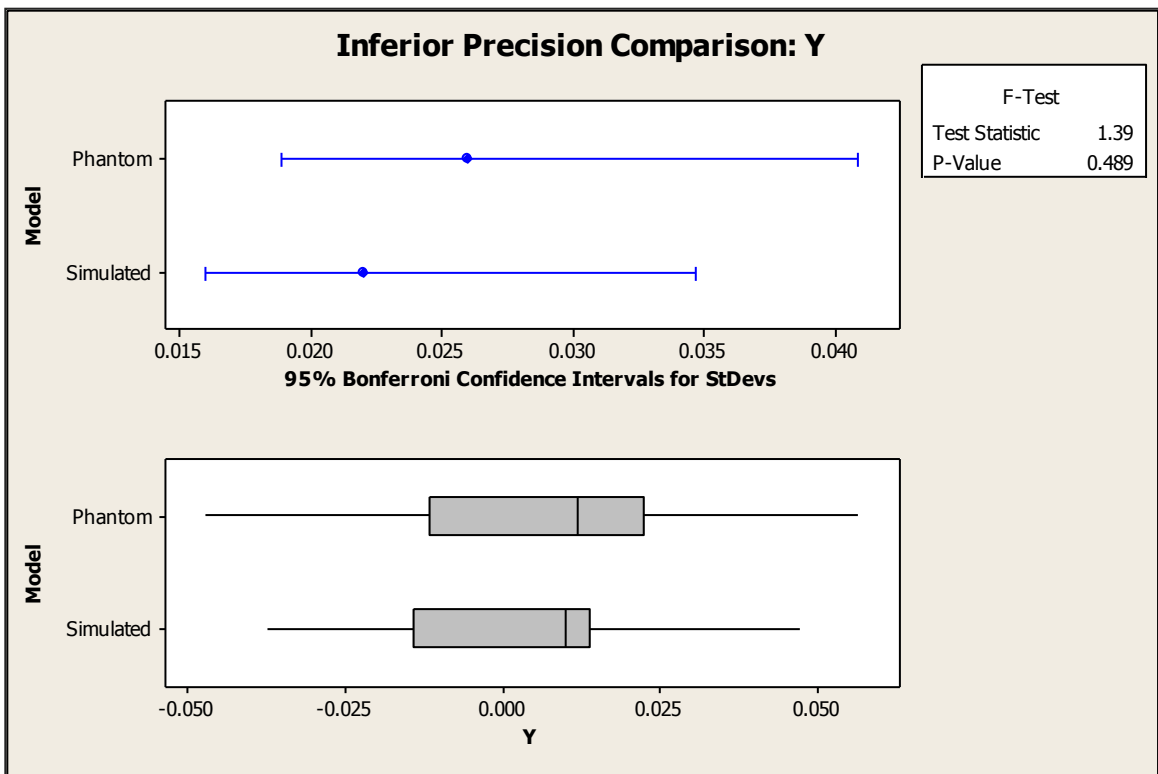
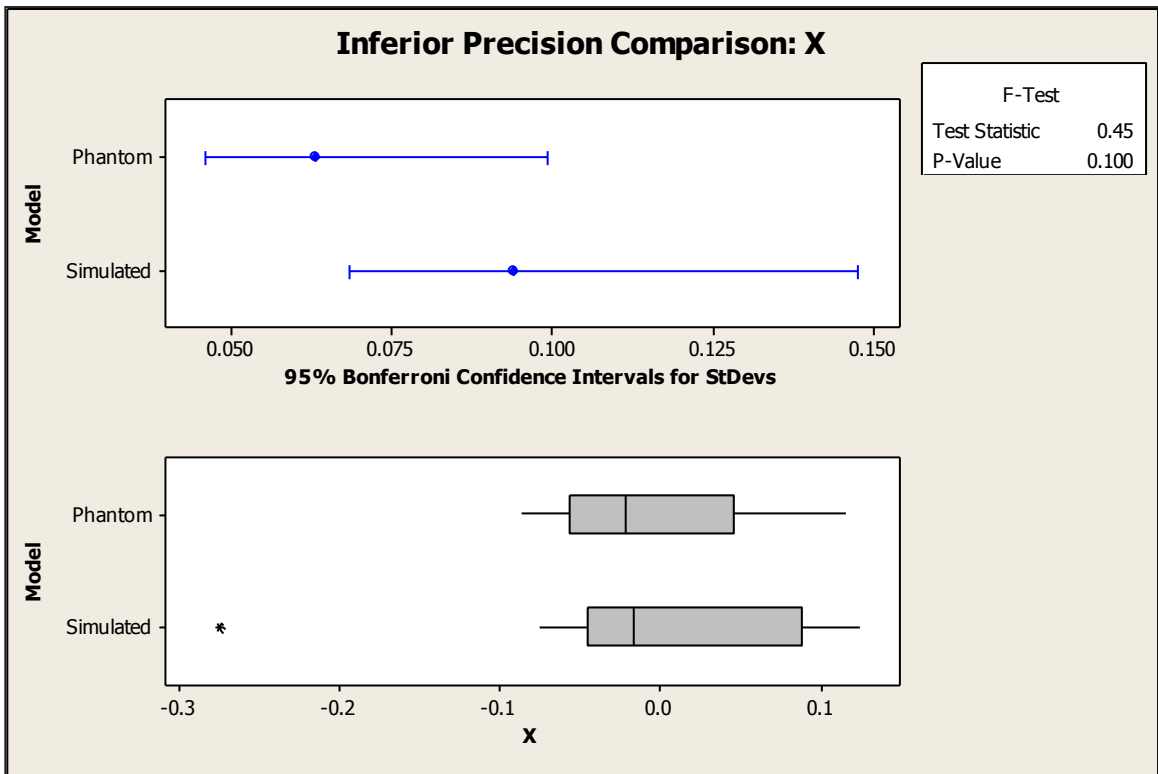


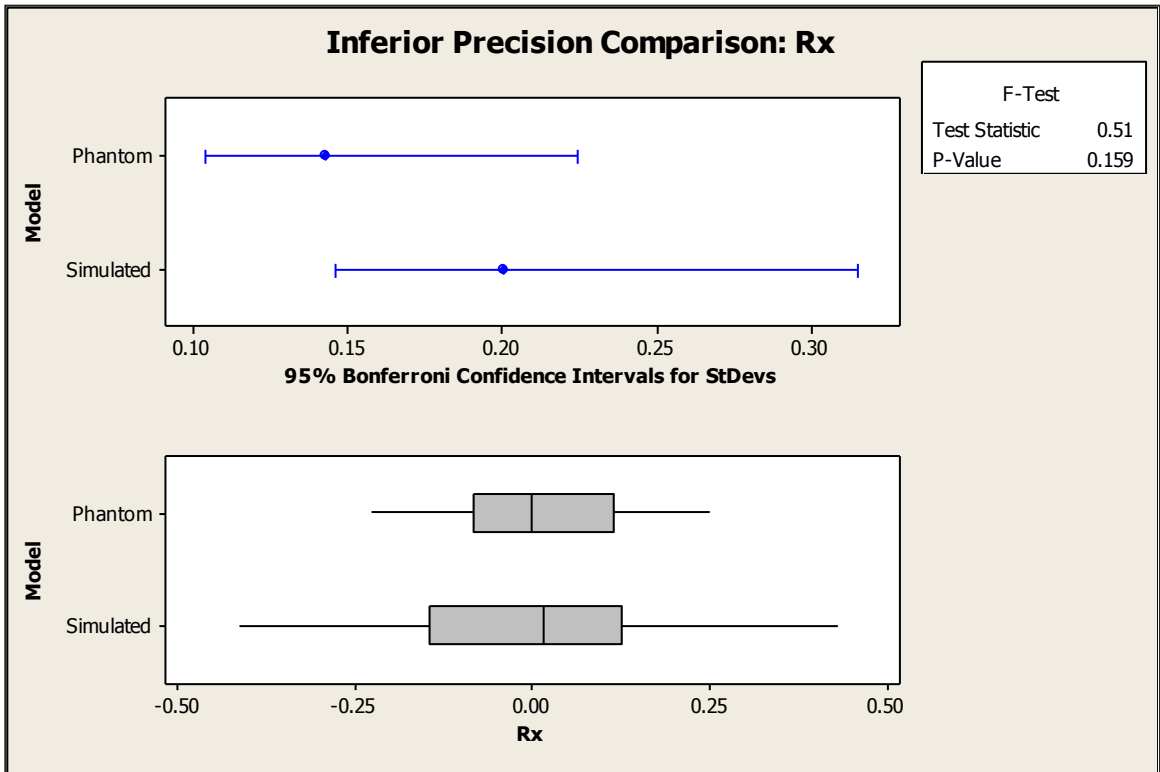
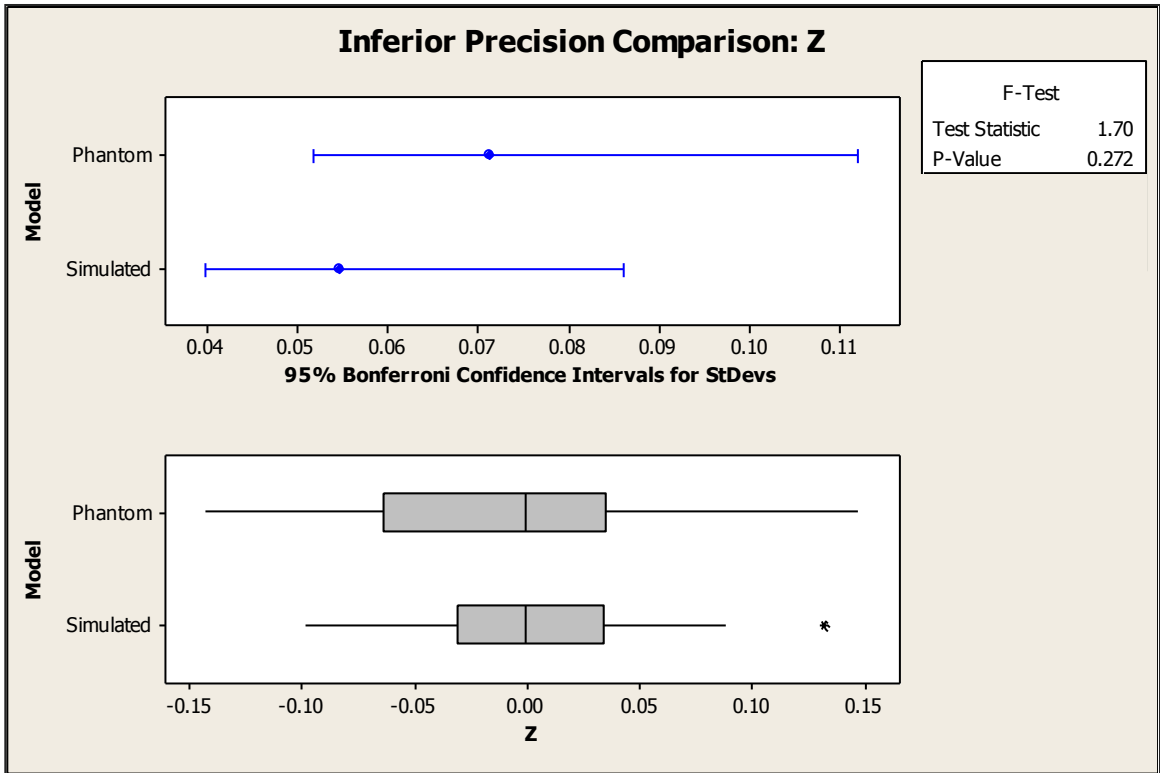


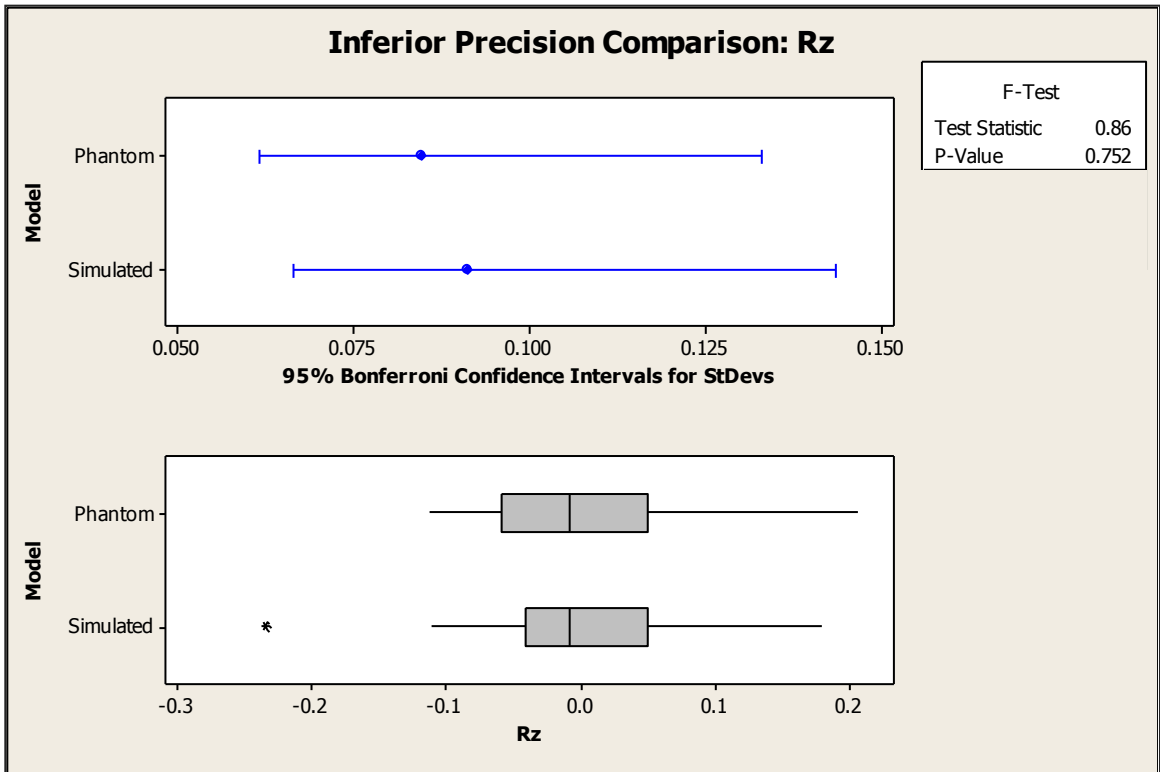
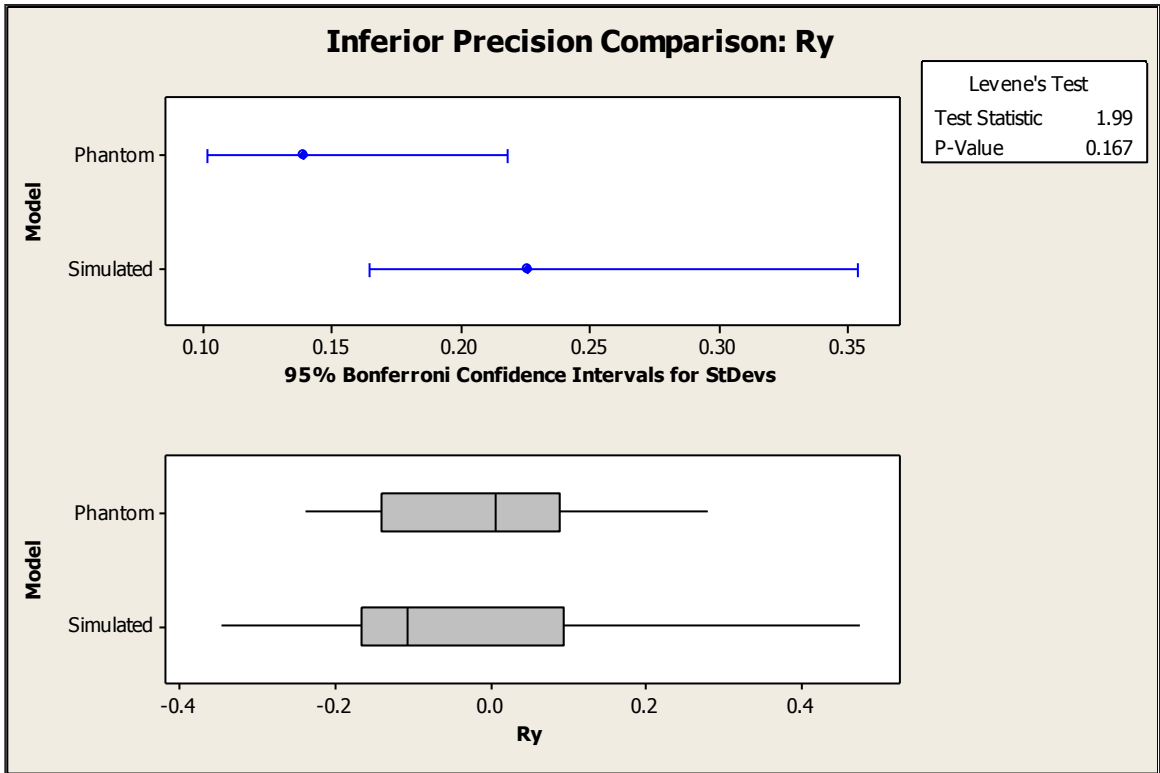




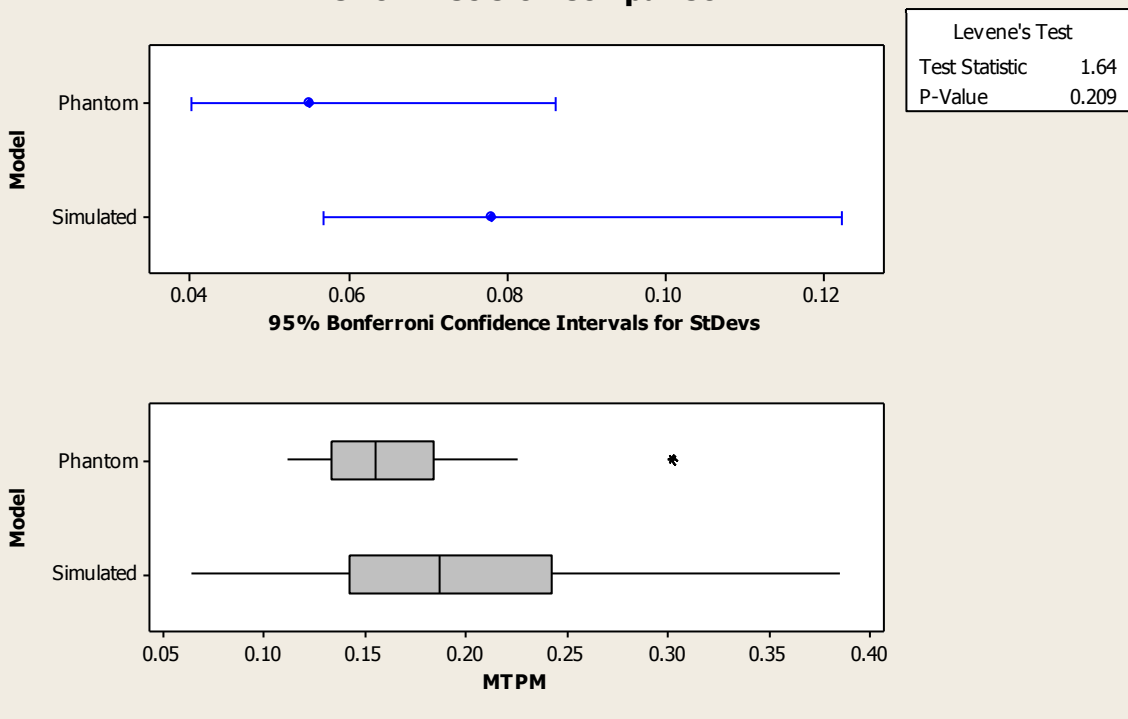
### F.1.2.2 Inferior Assessment







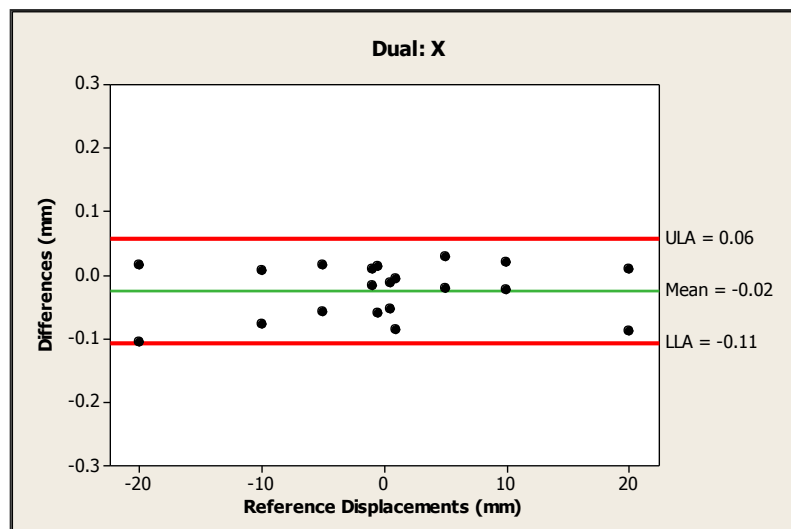
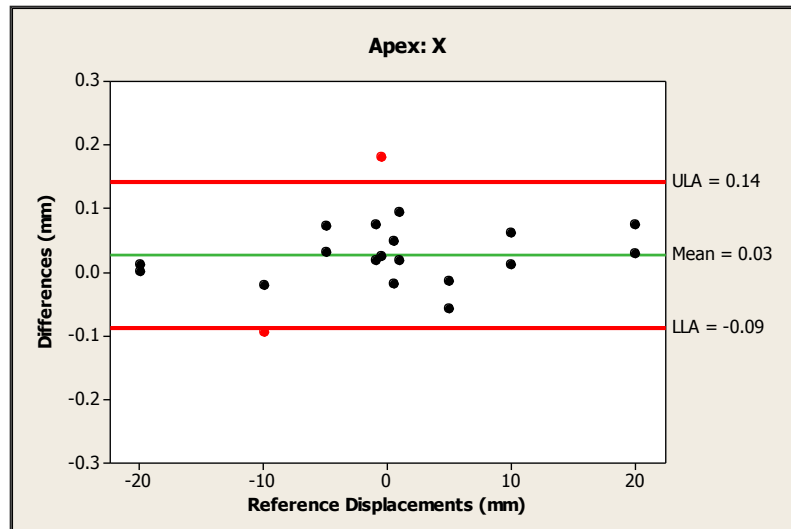
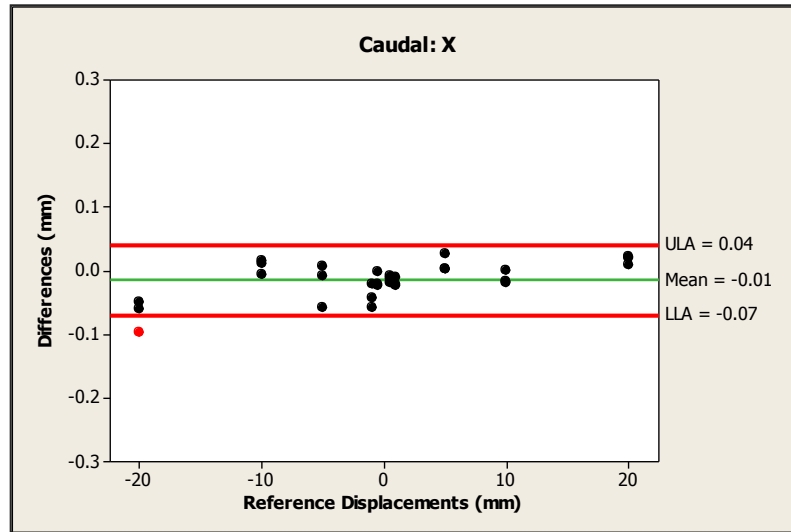
### Inferior Precision Comparison: MTPM



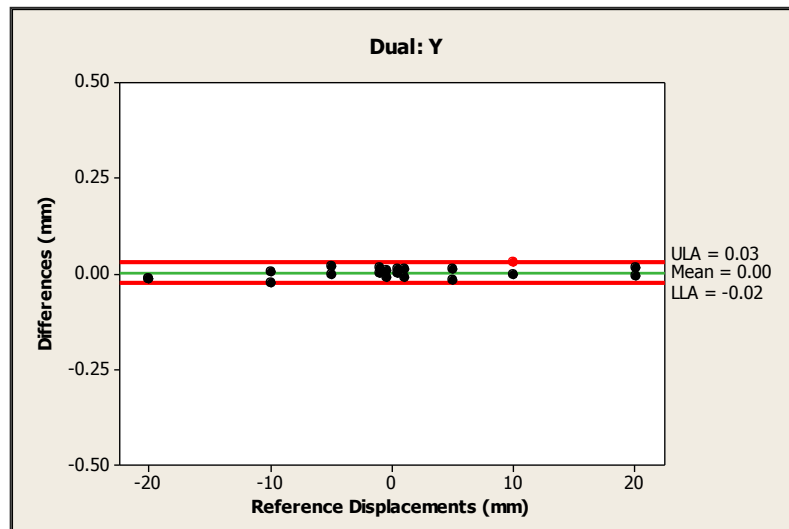
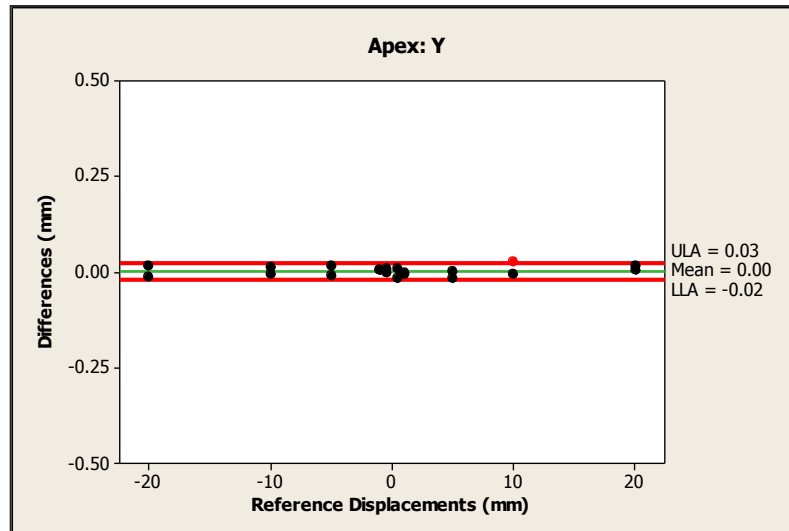
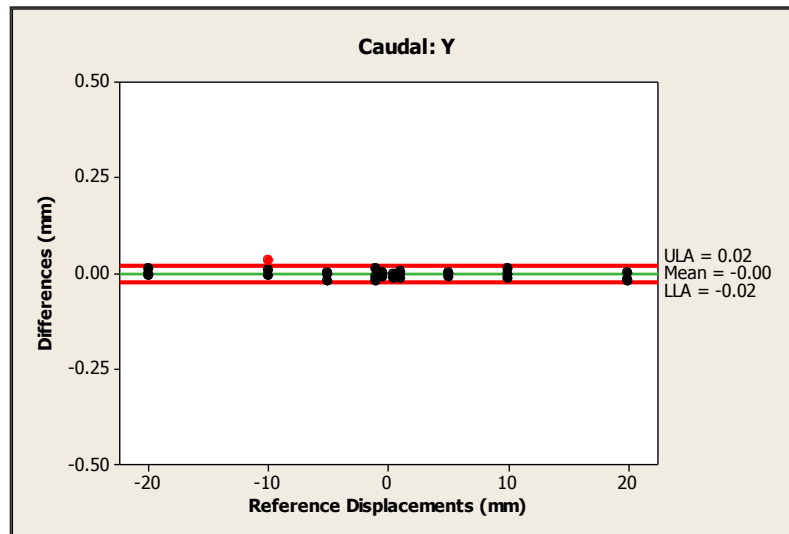
## F.2 Accuracy Plots

These are Bland-Altman plots comparing the measured values of each origin style to the reference inputted displacement. Each plot shows the mean for the set of data. This is the green horizontal line. For each plot the Limits of Clinical Significance are the maximum and minimum of the ordinate axis. For a measurement technique to agree with the true value the limits of agreement must be within the Limits of Clinical Significance. The Limits of Clinical Significance are the maxima and minima of the ordinate axis of each BA plot. The limits of agreement are shown by the red lines labeled ULA and LLA representing the Upper Limit of Agreement and Lower Limit of Agreement respectively. These limits are located  $\pm 1.96 * SD$  from the mean and show 95% confidence. The black data points are those which fall within the limits of agreement while the red data points are ones which fall outside these limits.

## F.2.1 X Accuracy – Translation along the X Axis

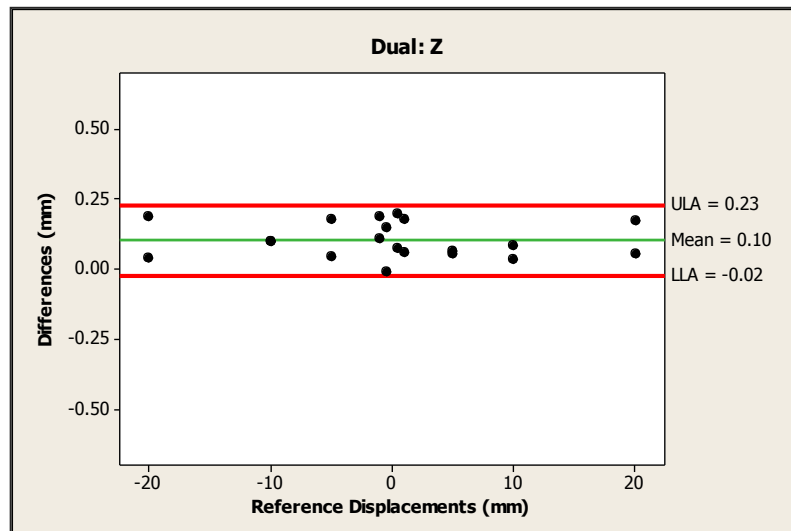
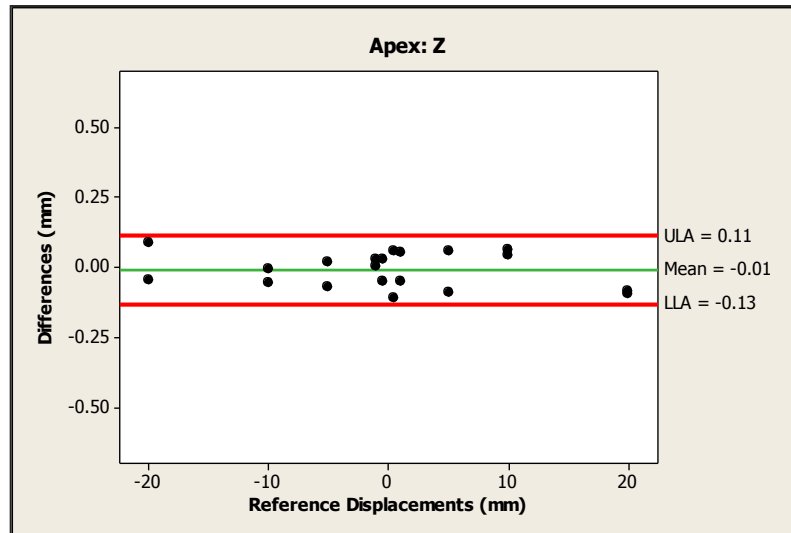
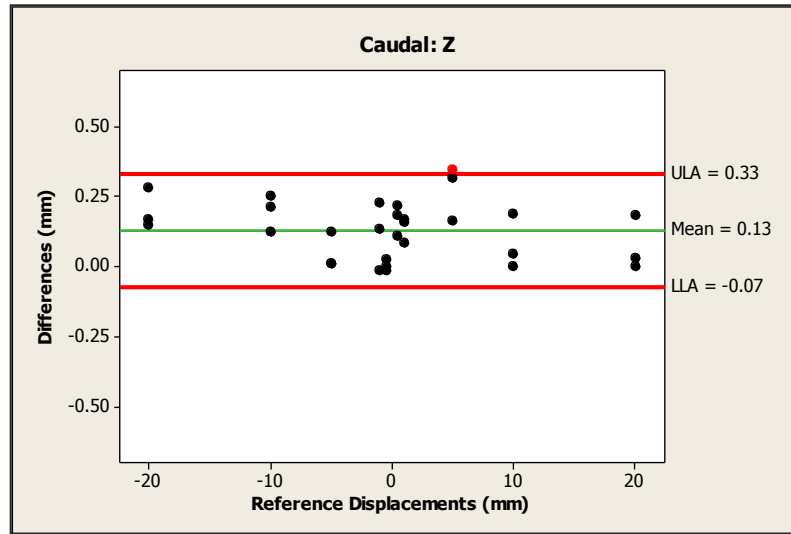


## F.2.2 Y Accuracy - Translation along the Y Axis

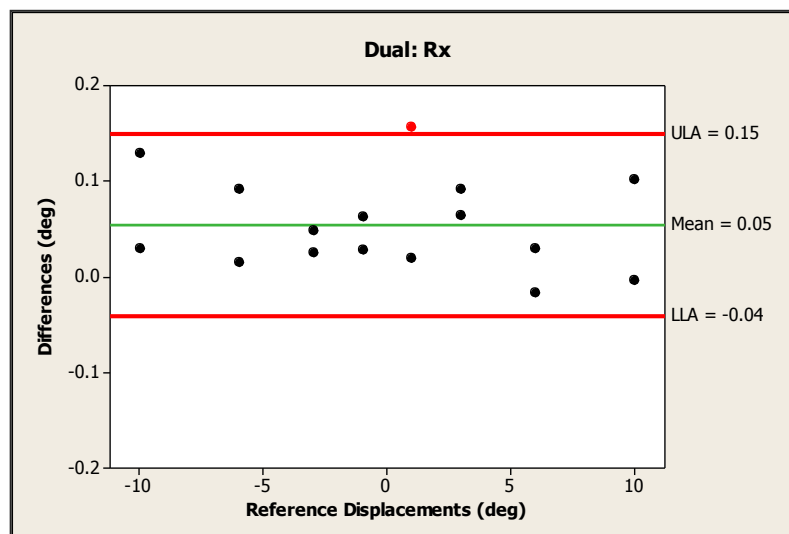
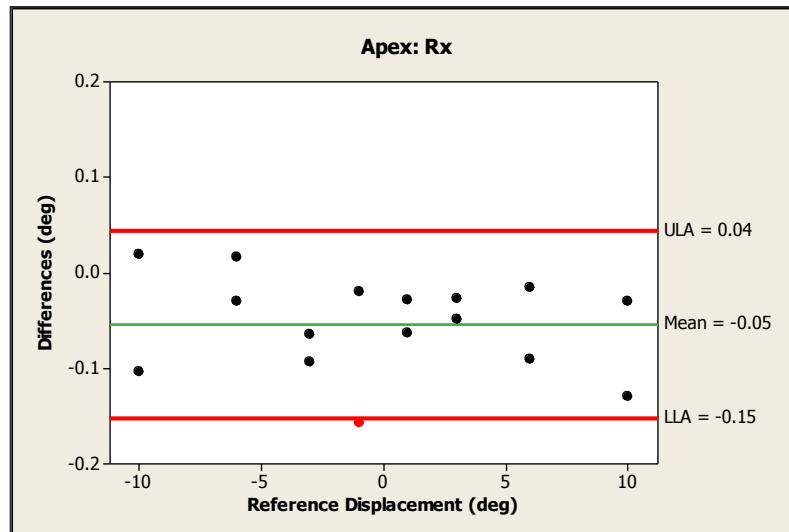
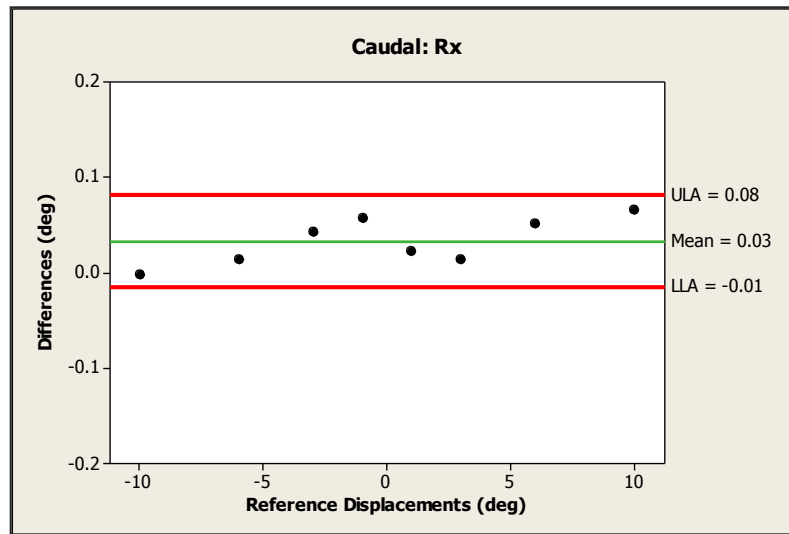




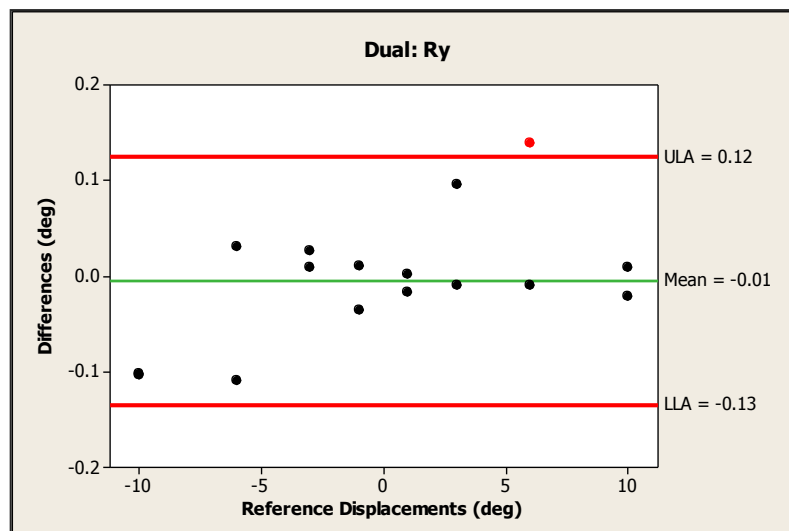
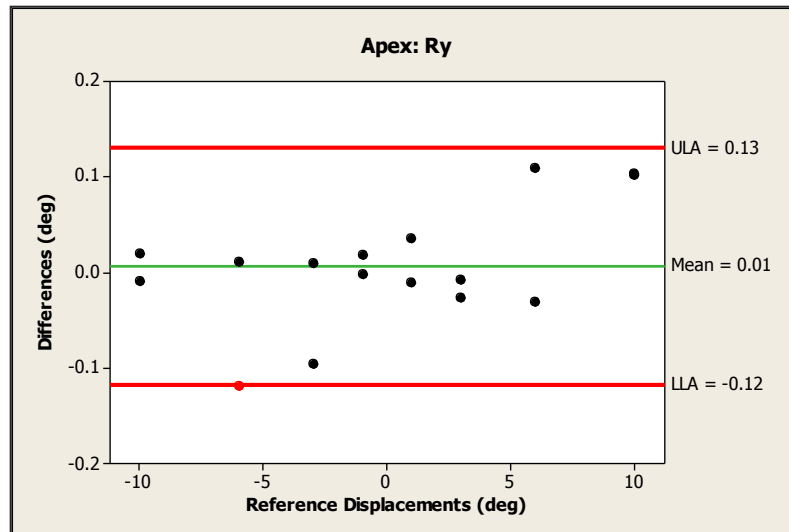
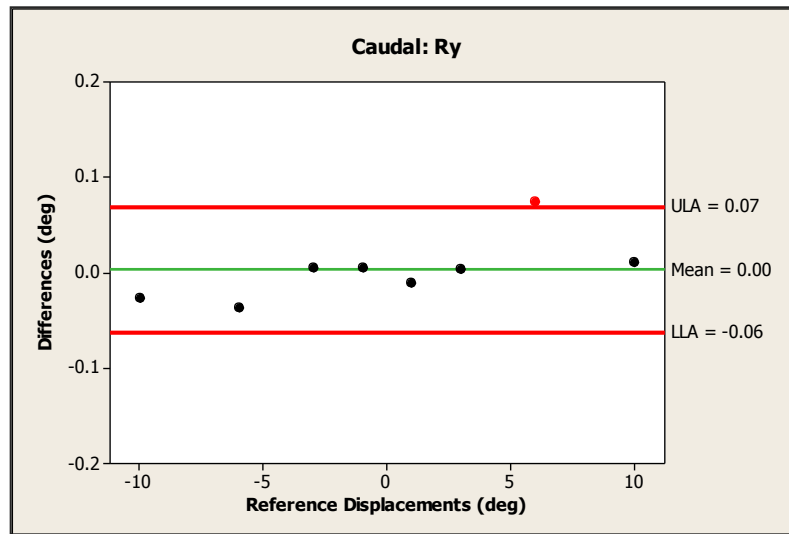
### F.2.3 Z Accuracy – Translation along the Z Axis



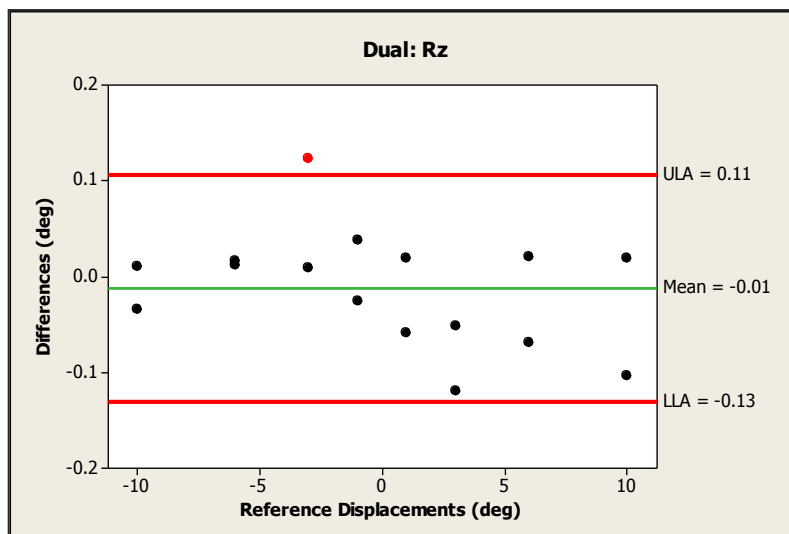
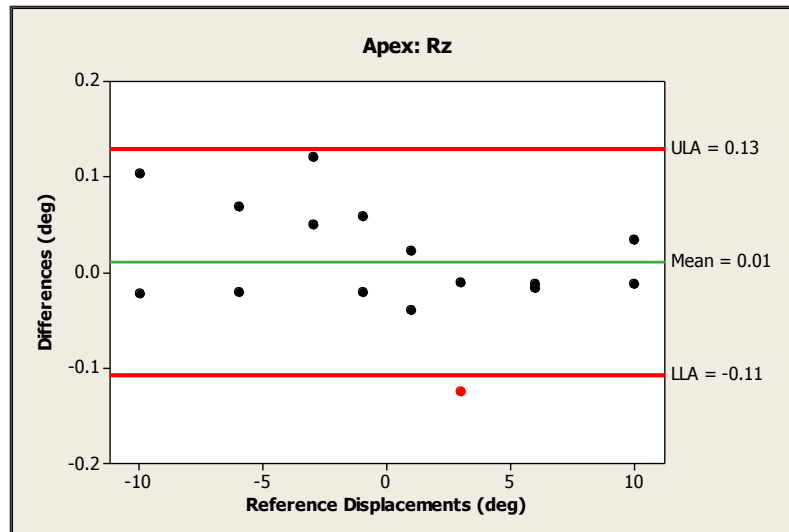
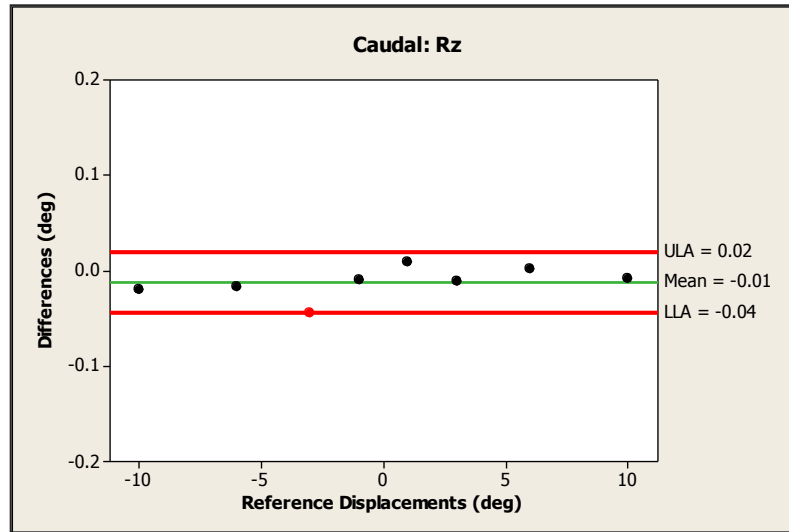
## F.2.4 Rx Accuracy - Rotation around the X Axis



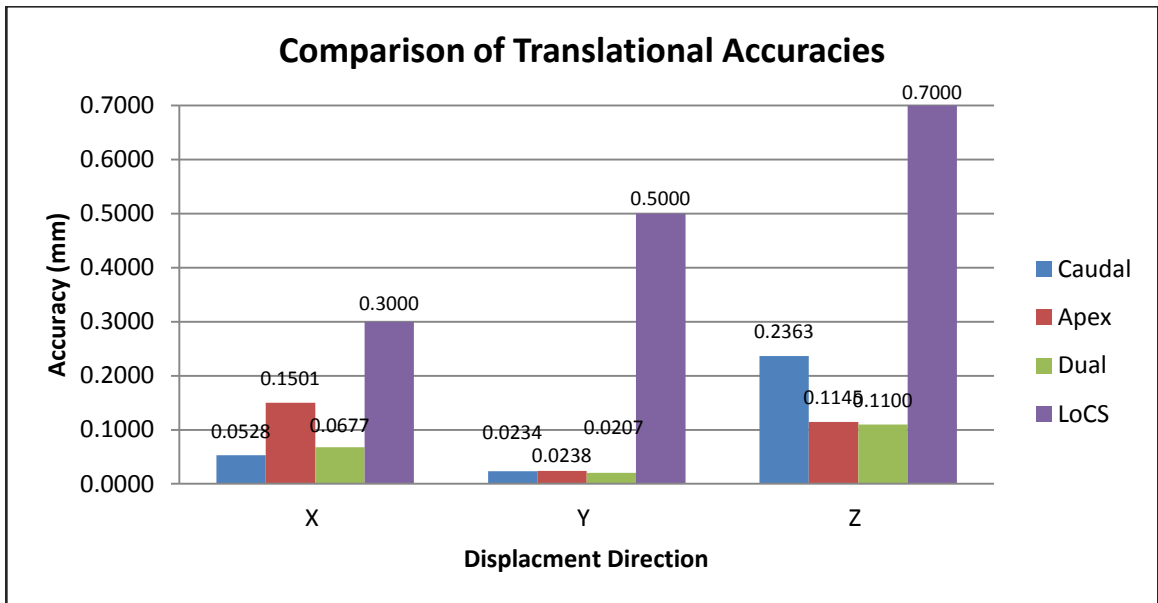
## F.2.5 Ry Accuracy - Rotation around the Y Axis



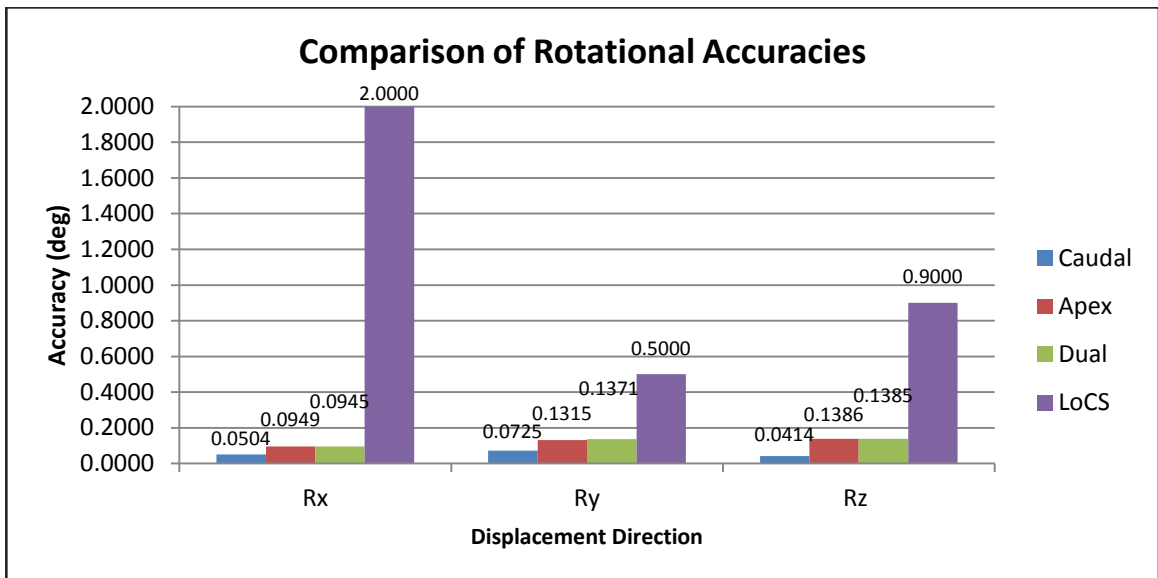
## F.2.6 Rz Accuracy - Rotation around the Z Axis



## F.2.7 Translational Accuracy Comparison



## F.2.8 Rotational Accuracy Comparison

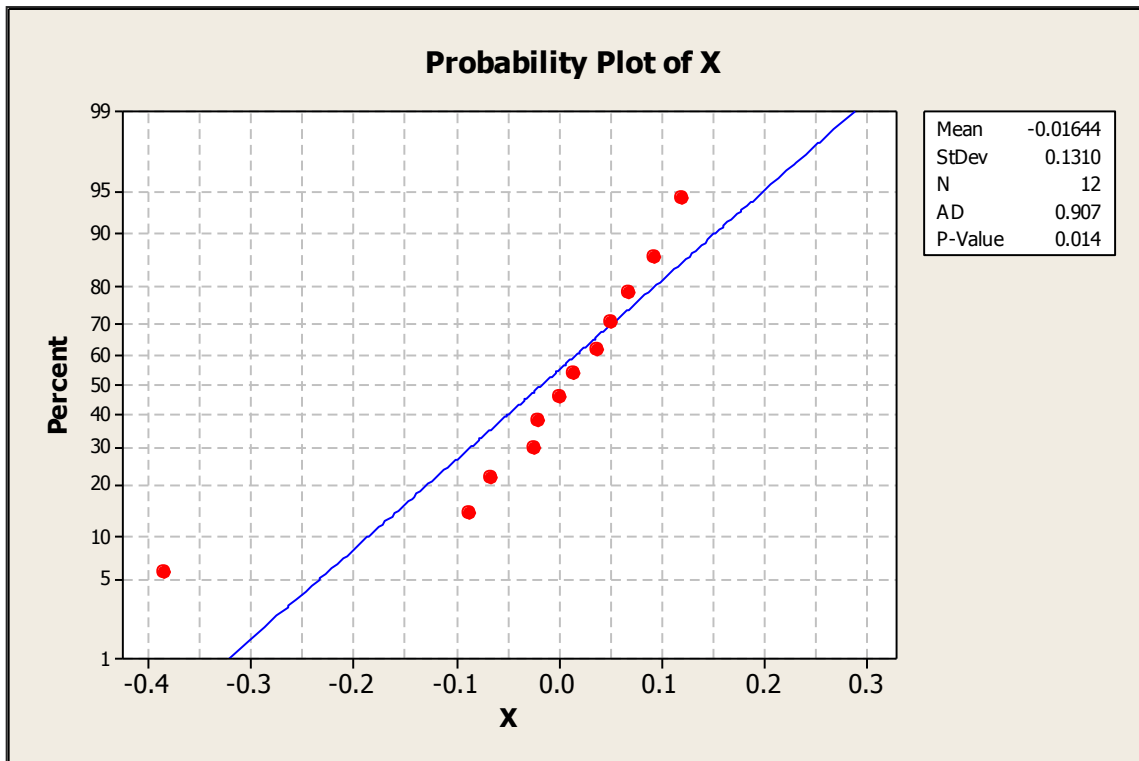


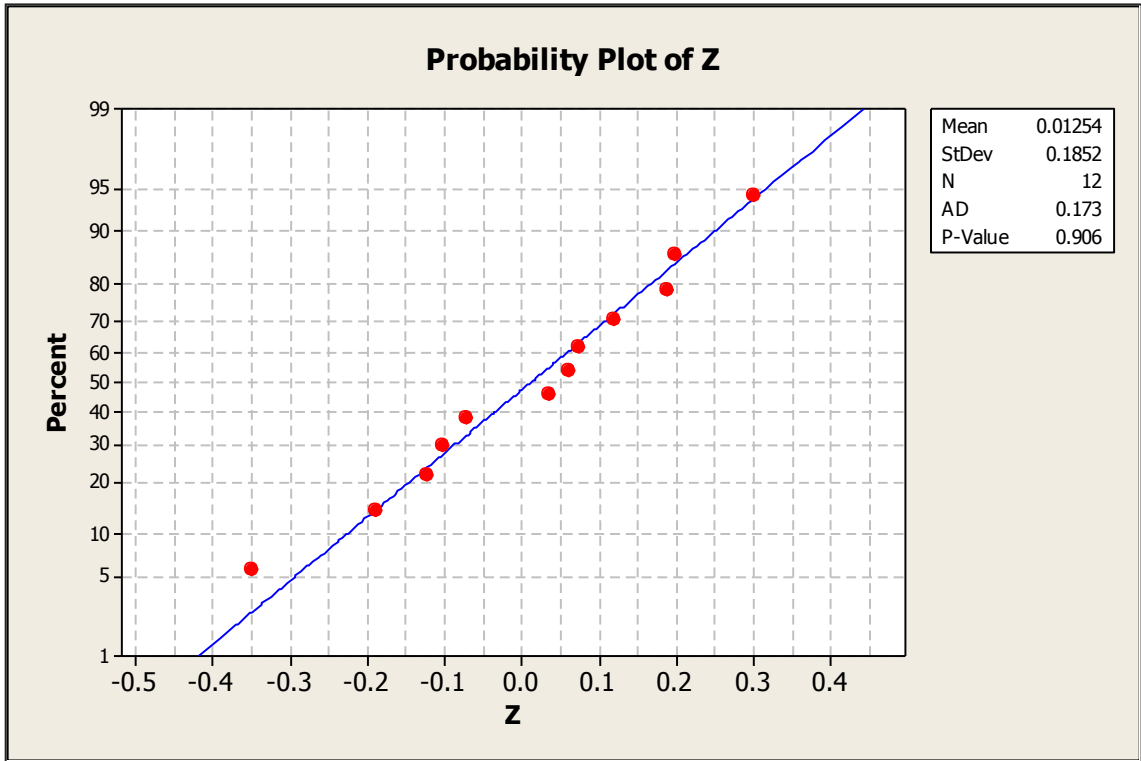
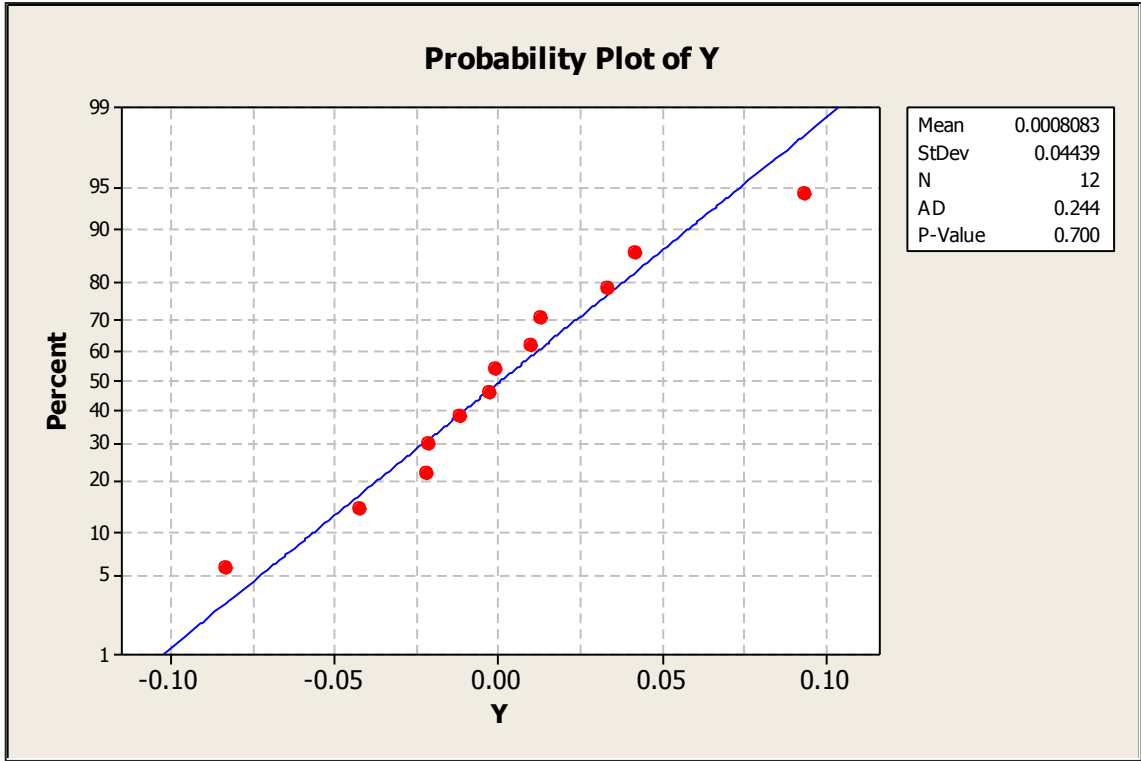
## F.3 Precision Plots

### F.3.1 Check for Normalcy

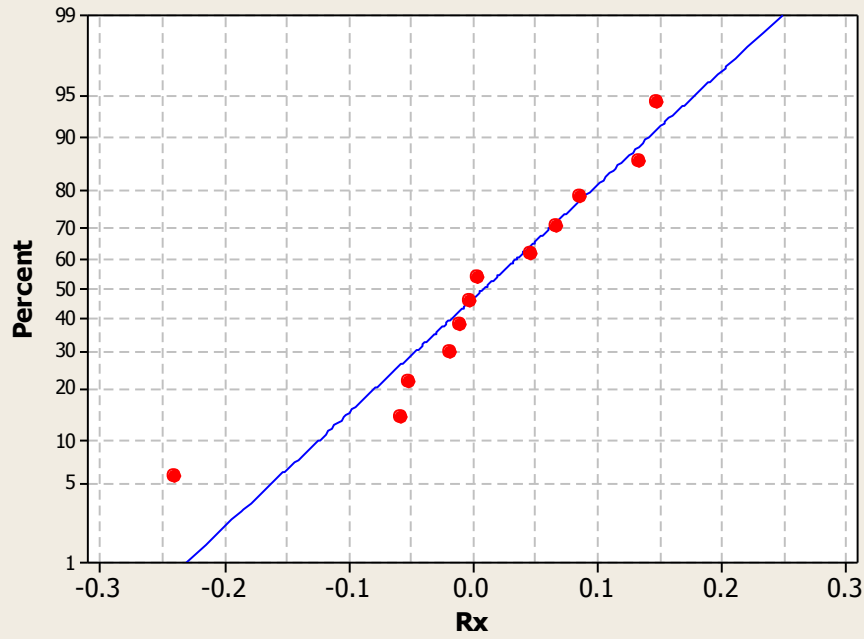
The plots in this section assess the distribution of the precision data sets. P-values less than **0.05** indicate non-parametric datasets.

#### F.3.1.1 Superior - Caudal



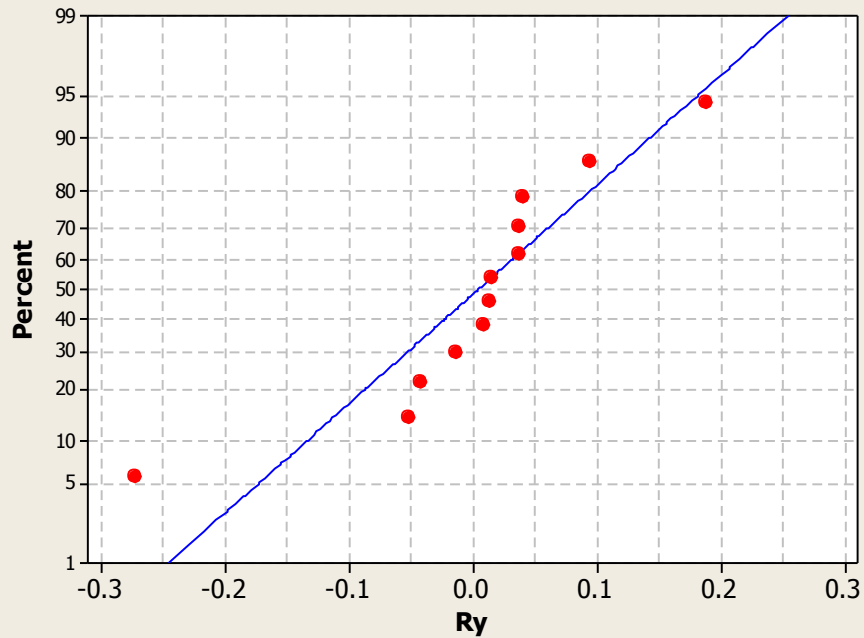


Probability Plot of Rx



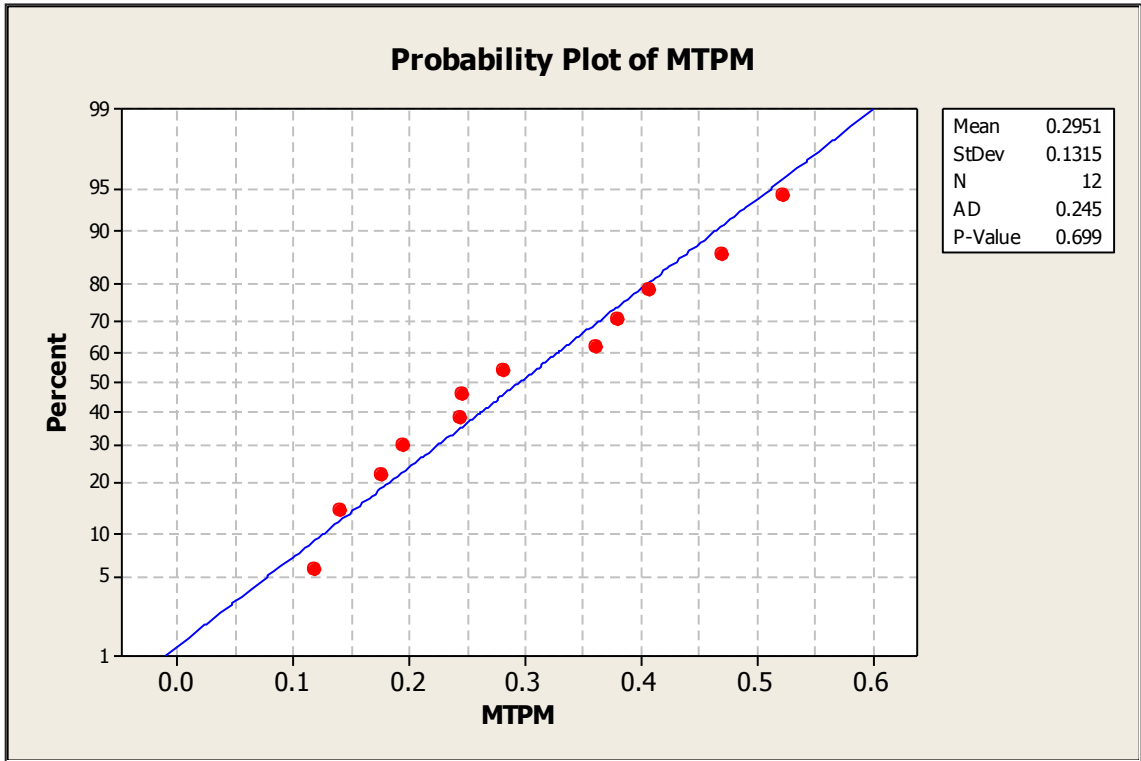
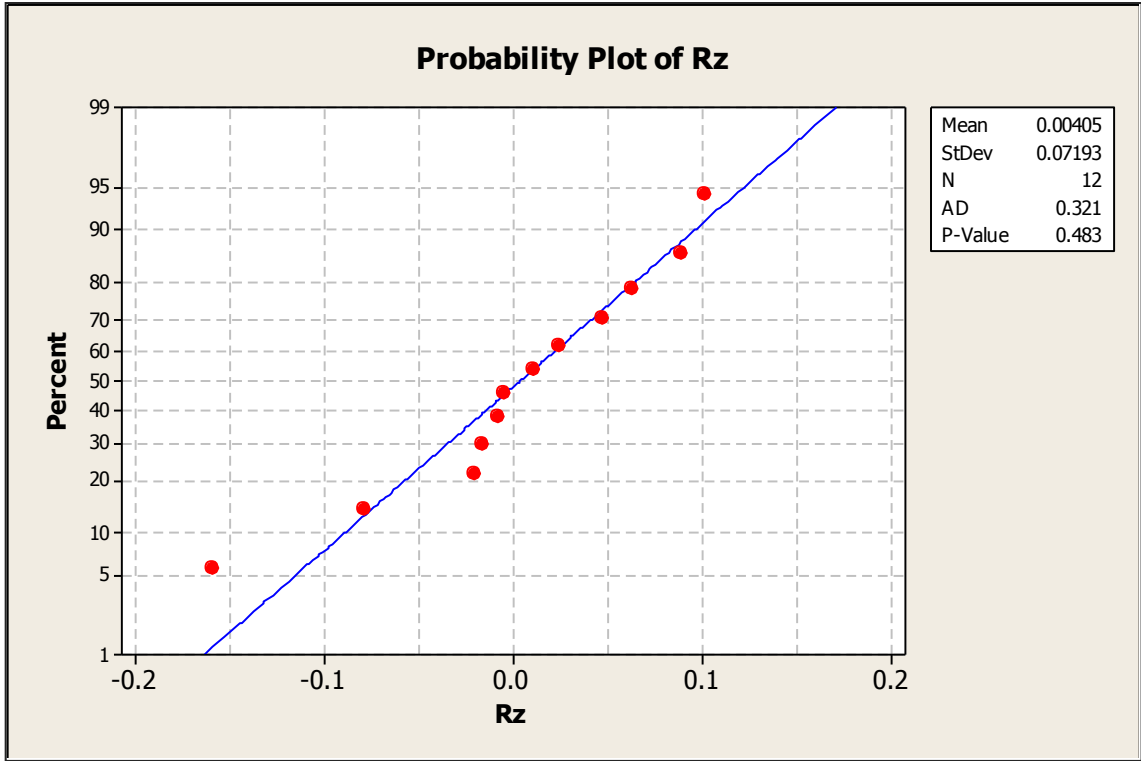
Mean	0.008858
StDev	0.1032
N	12
AD	0.386
P-Value	0.332

Probability Plot of Ry

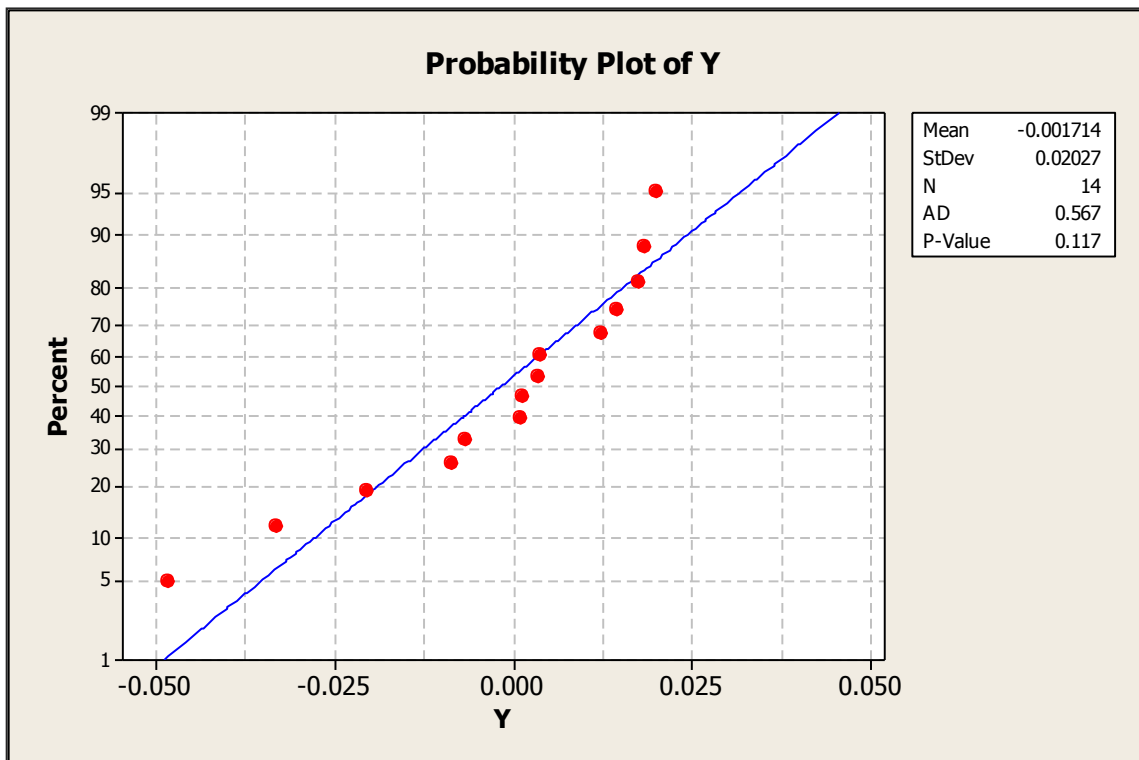
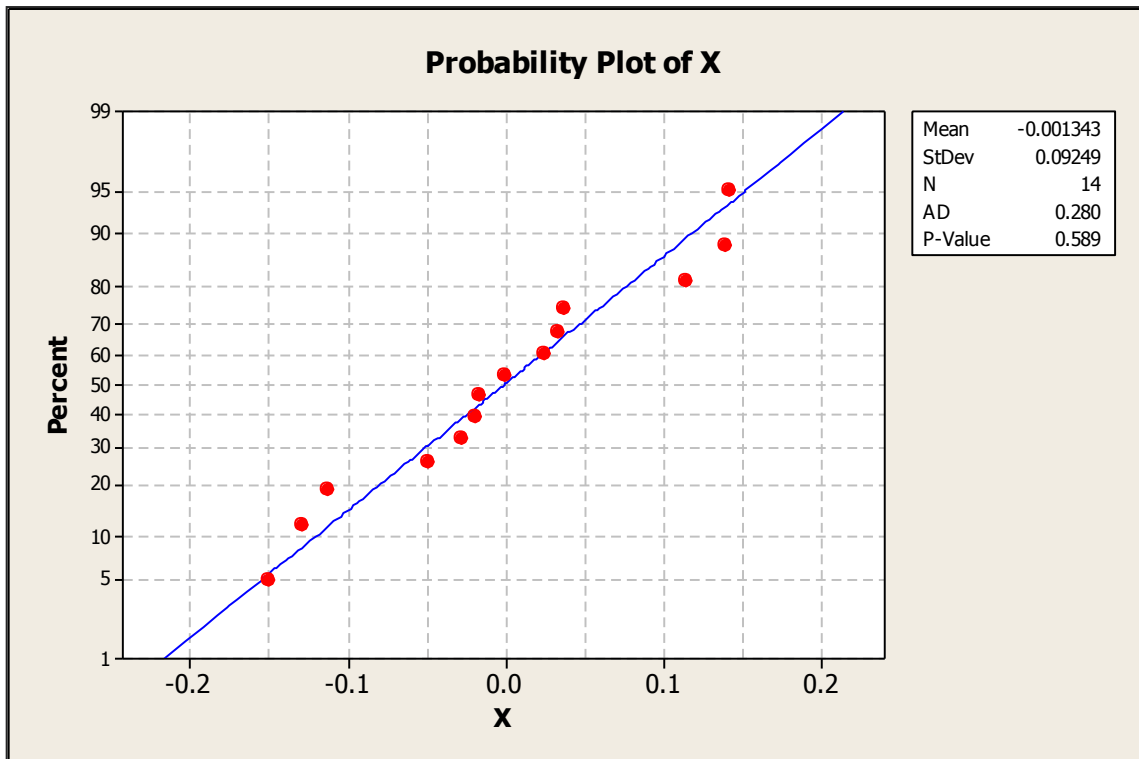


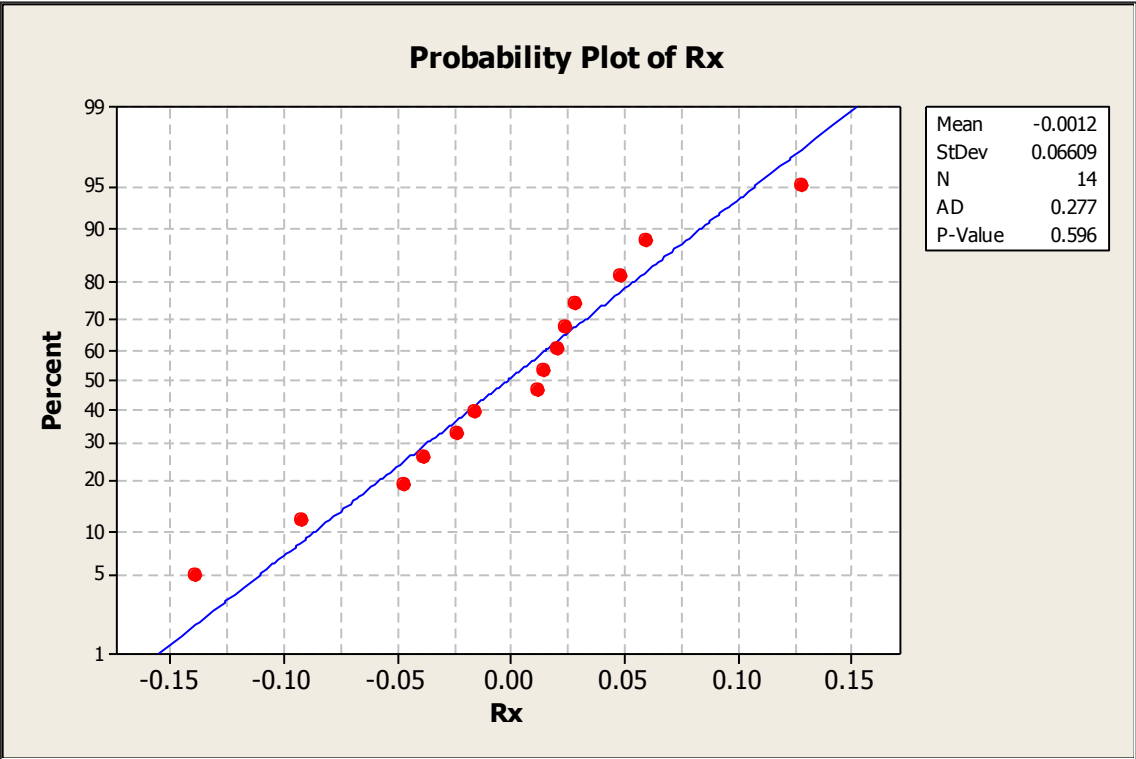
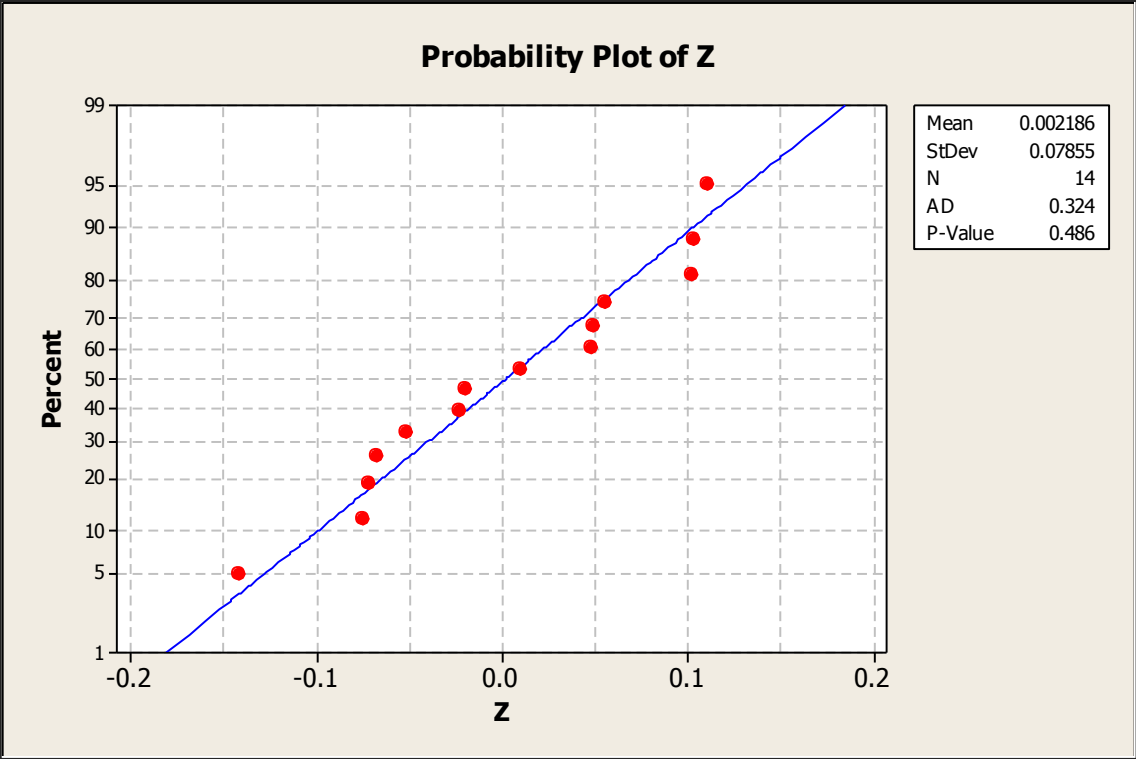
Mean	0.004608
StDev	0.1075
N	12
AD	0.801
P-Value	0.027

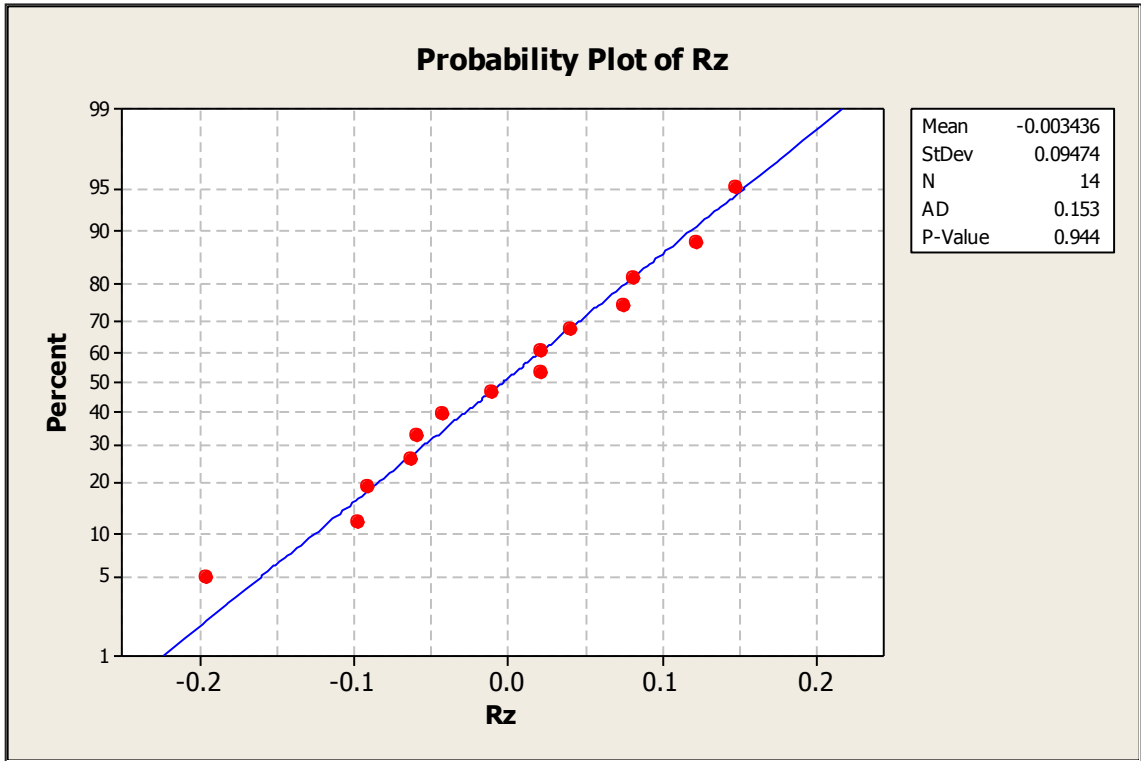
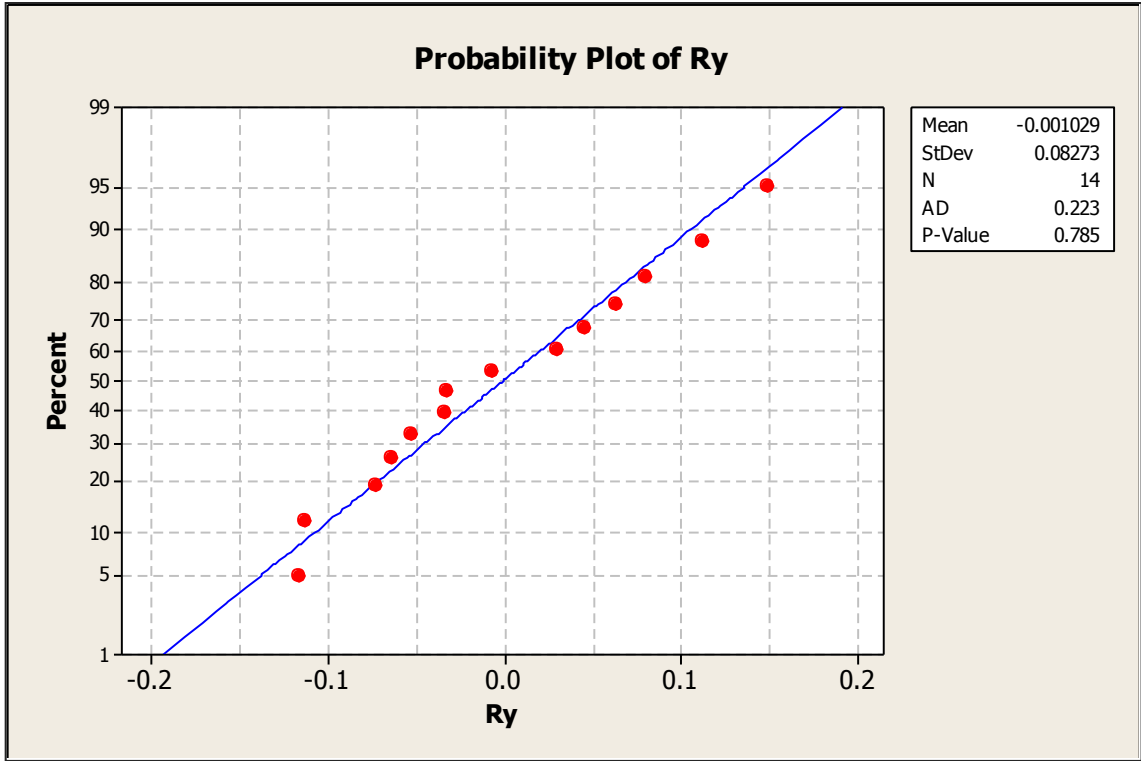




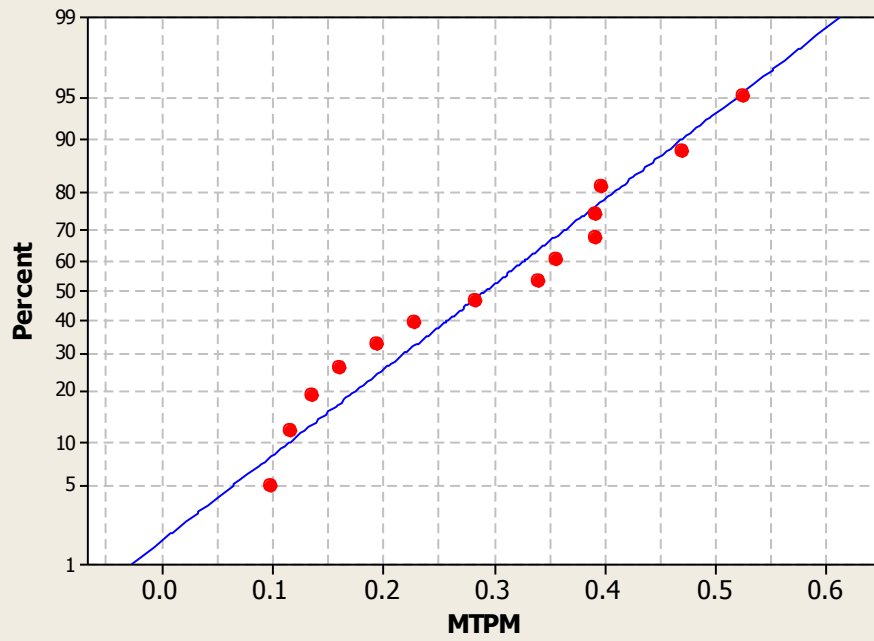
### F.3.1.2 Superior - Apex





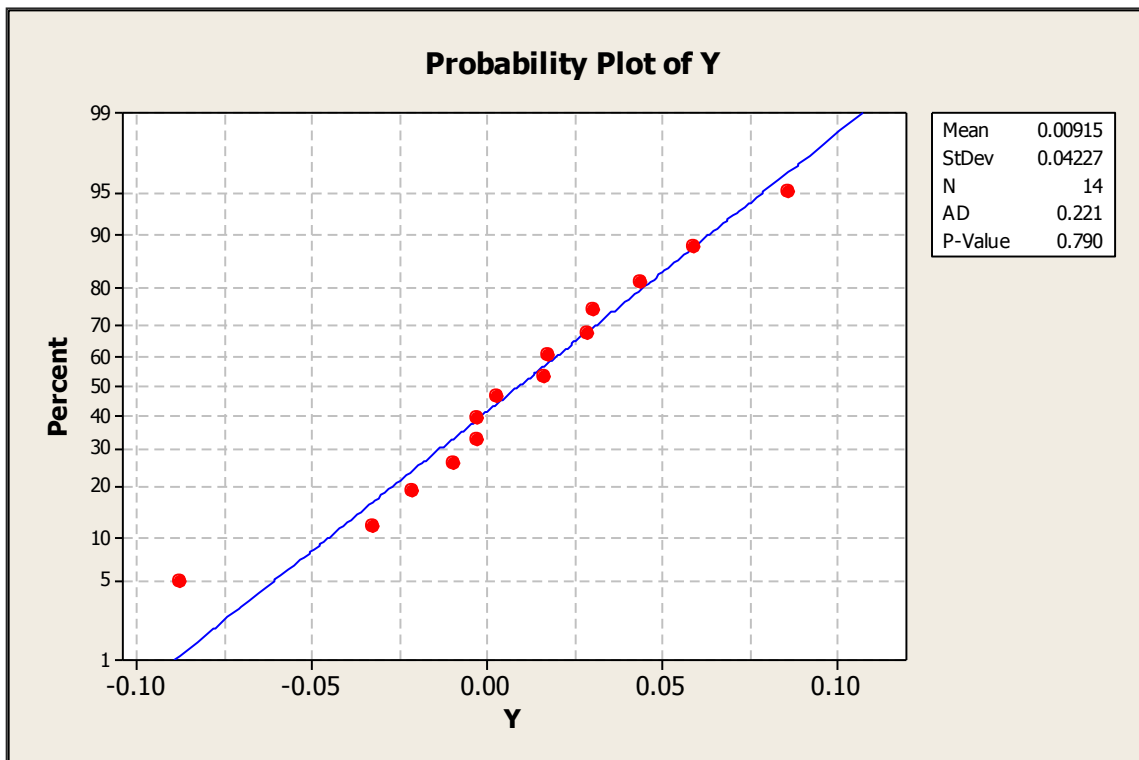
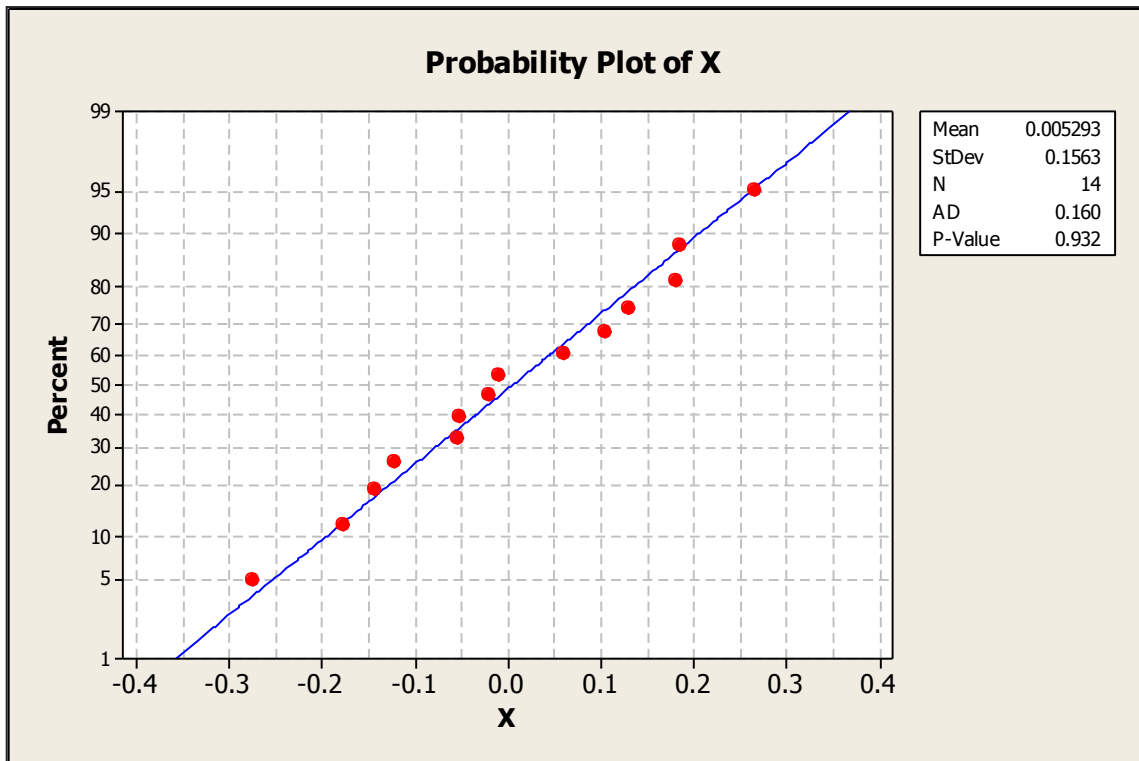


**Probability Plot of MTPM**

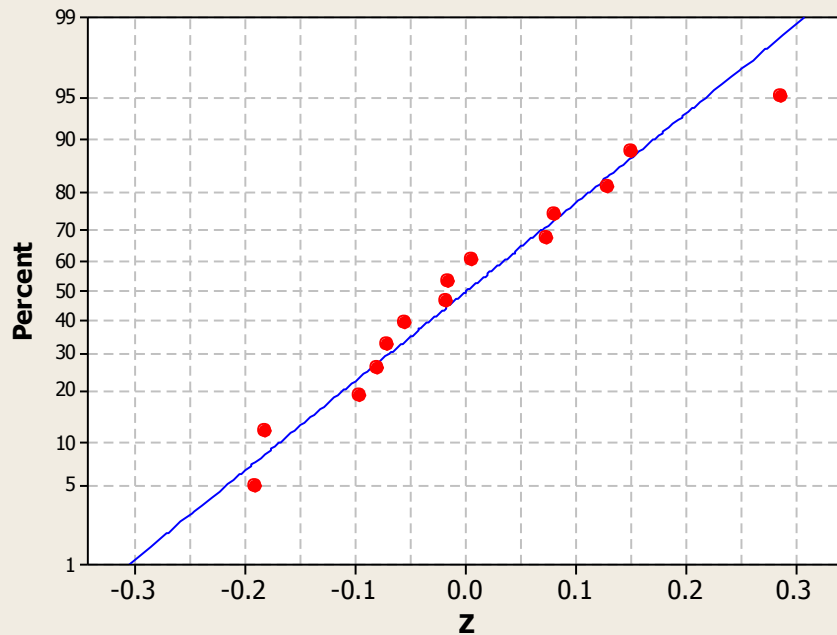


Mean	0.2921
StDev	0.1376
N	14
AD	0.329
P-Value	0.473

### F.3.1.3 Superior - Dual

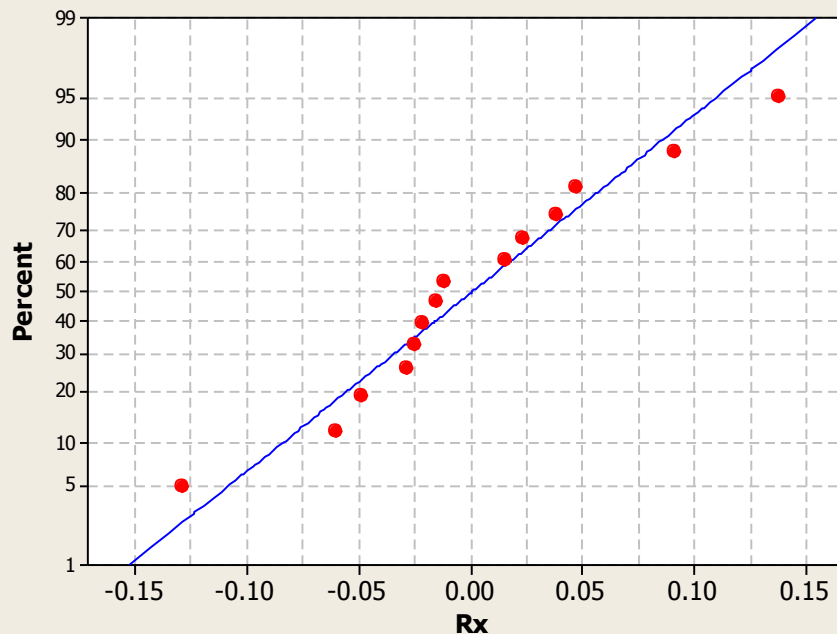


Probability Plot of Z

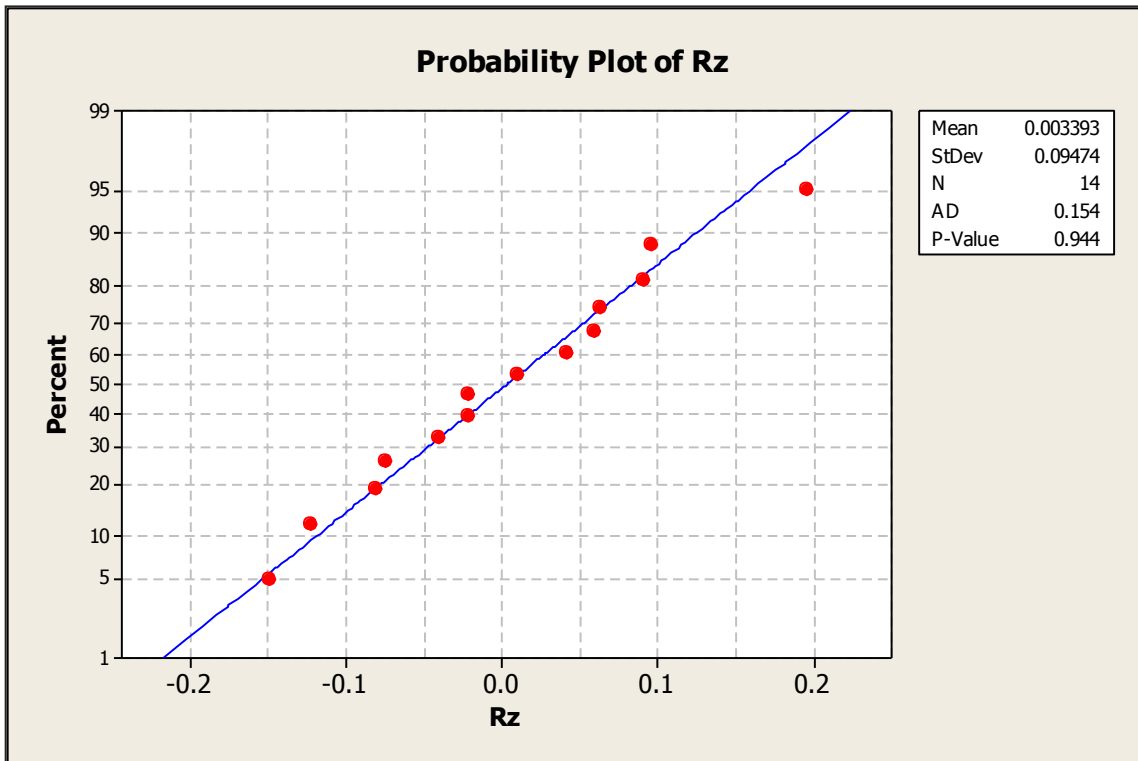
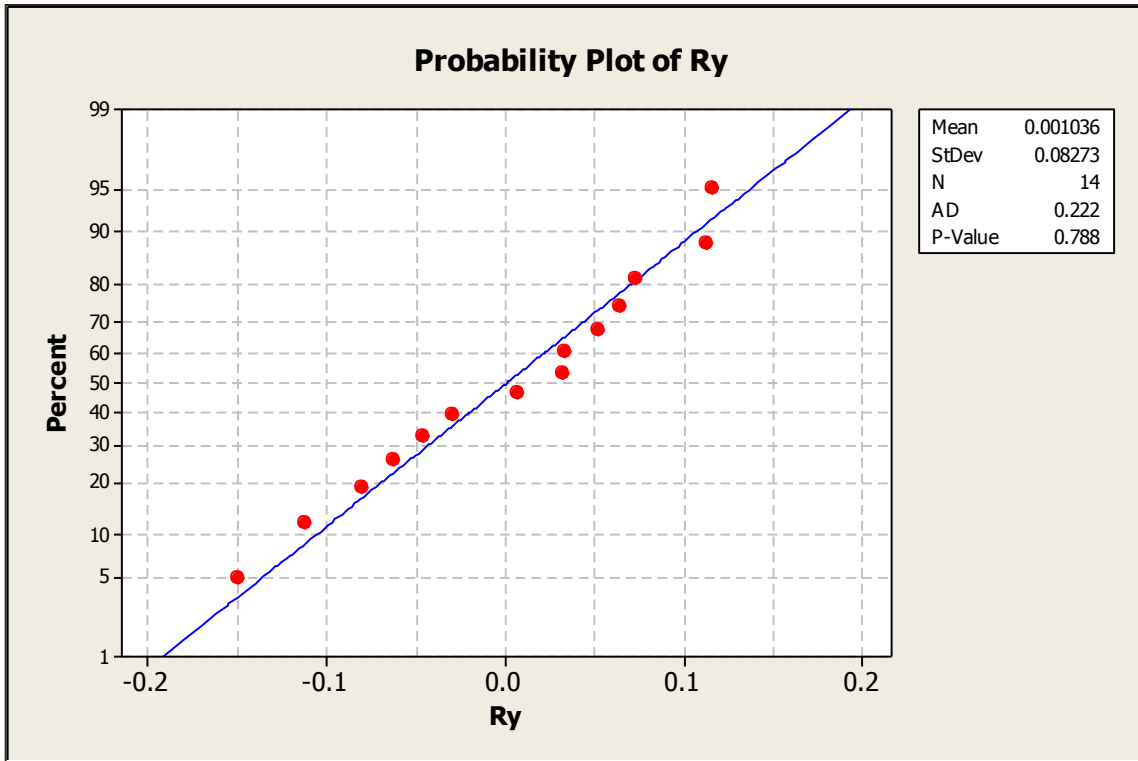


Mean	0.0009857
StDev	0.1321
N	14
AD	0.227
P-Value	0.772

Probability Plot of Rx

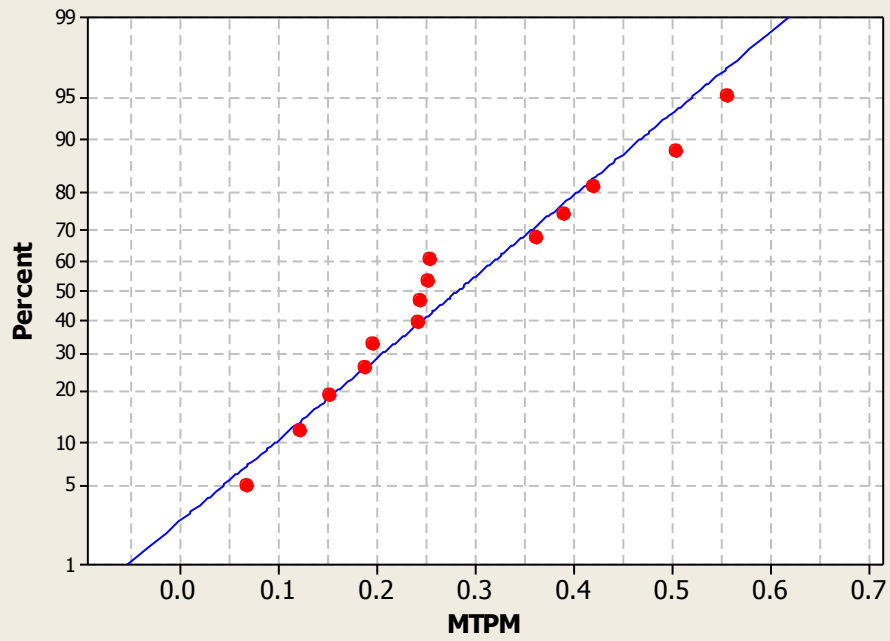


Mean	0.001193
StDev	0.06607
N	14
AD	0.276
P-Value	0.602



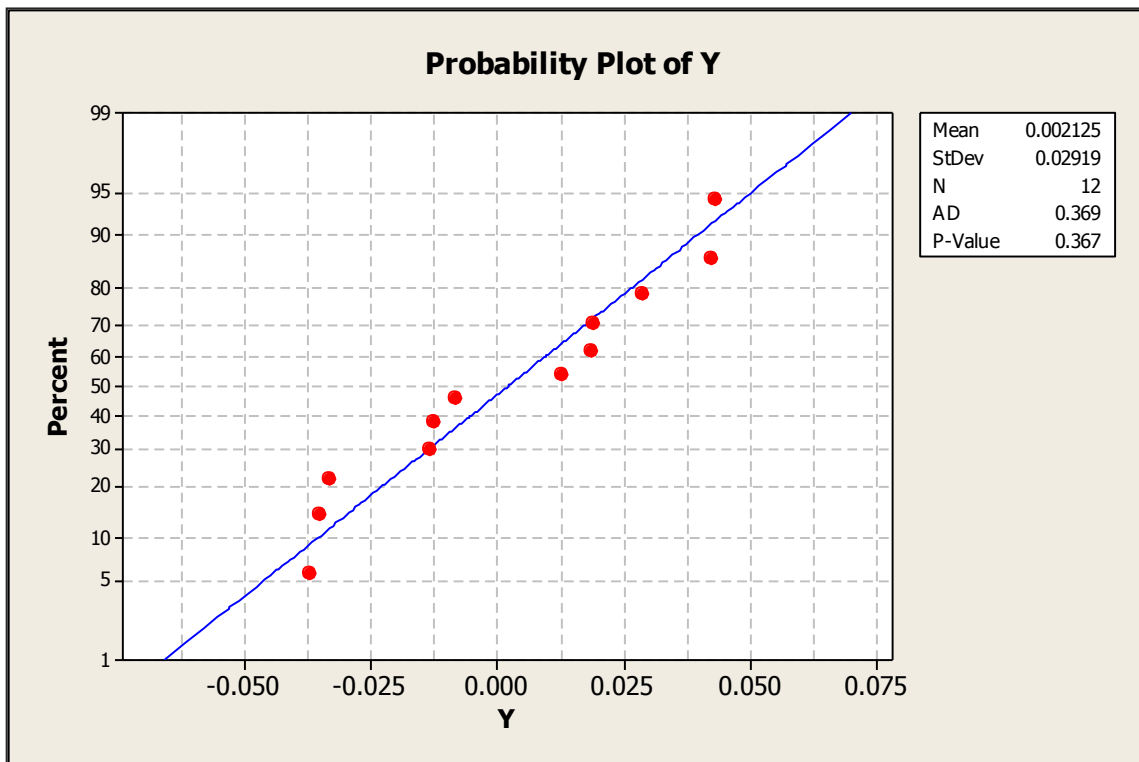
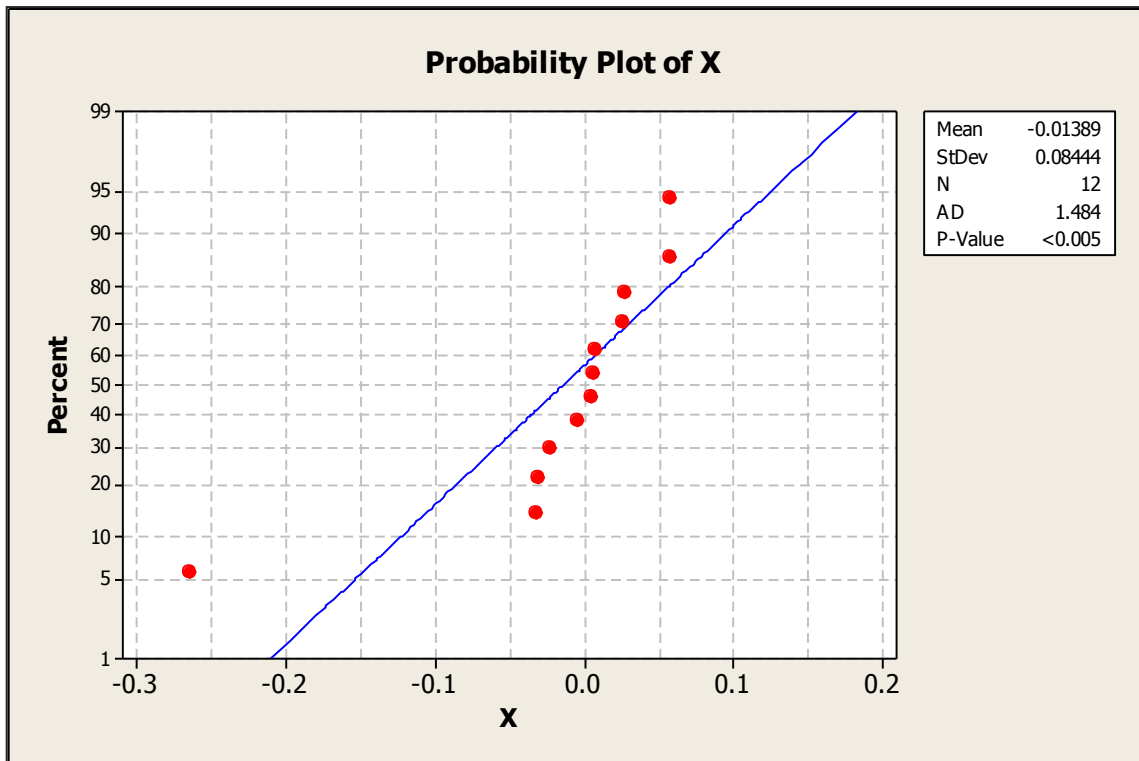


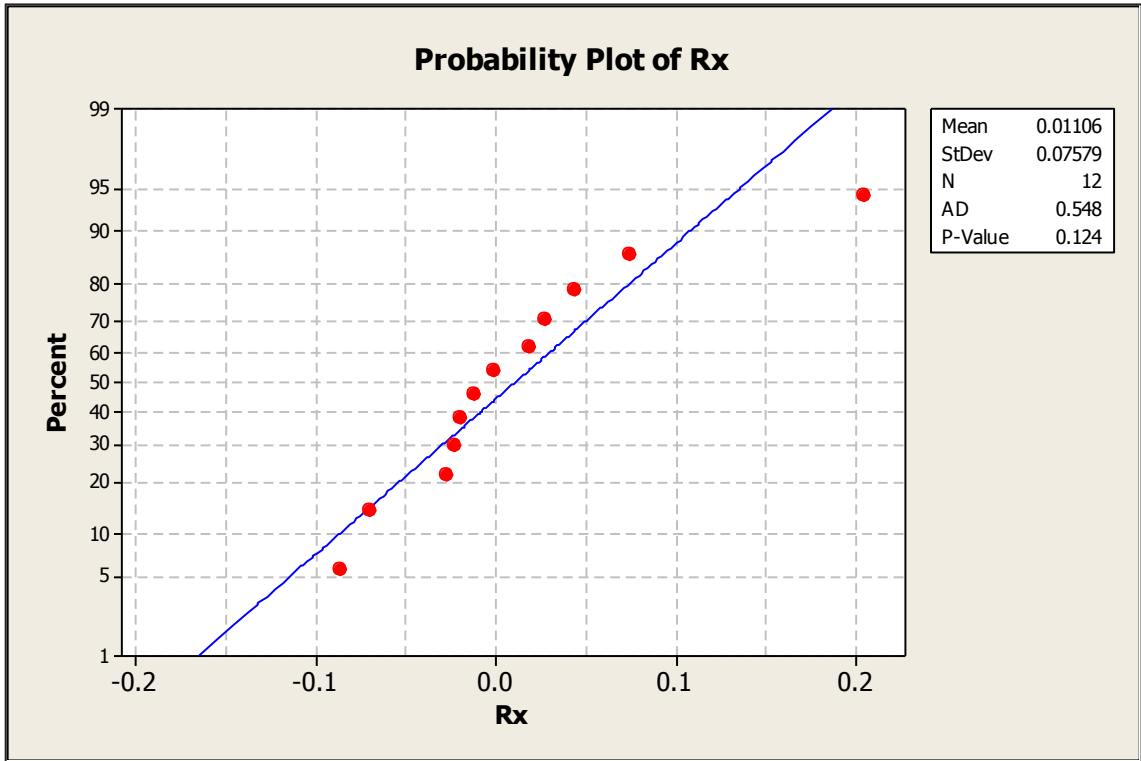
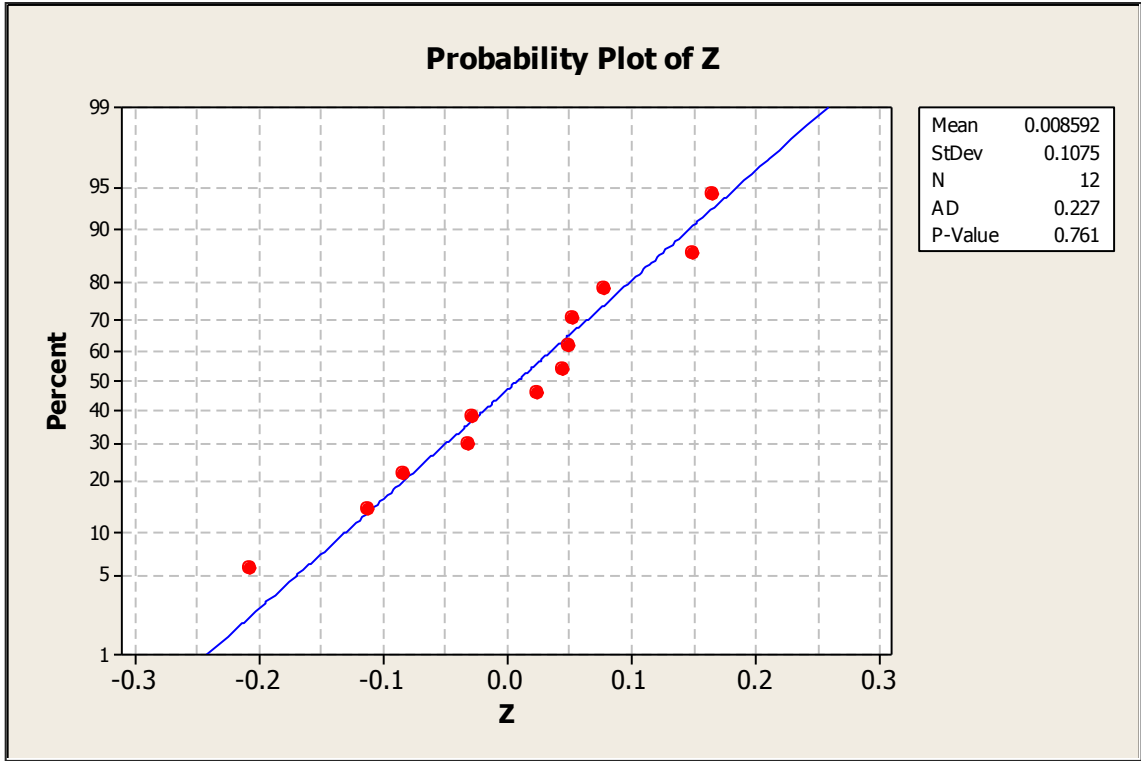
**Probability Plot of MTPM**



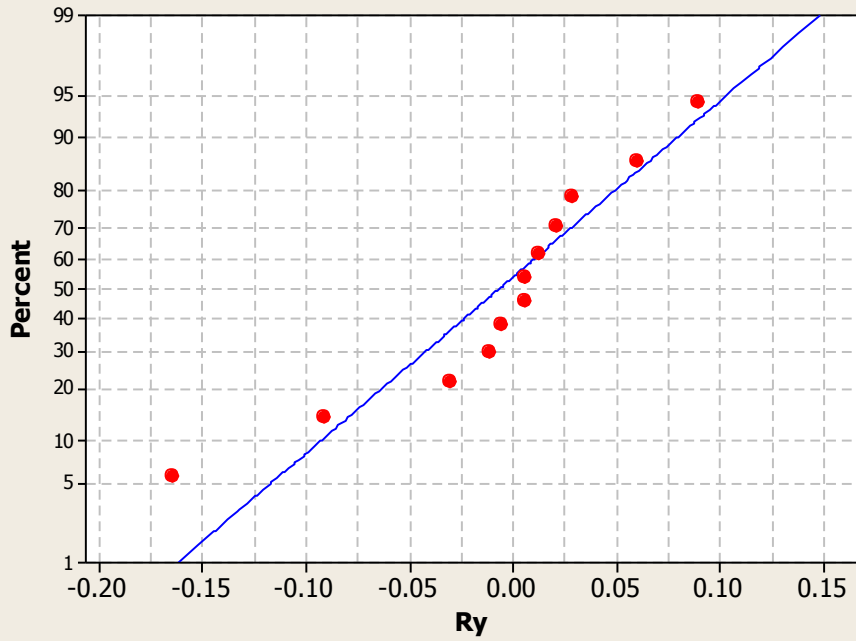
Mean	0.2820
StDev	0.1441
N	14
AD	0.351
P-Value	0.418

**F.3.1.4 Inferior - Caudal**



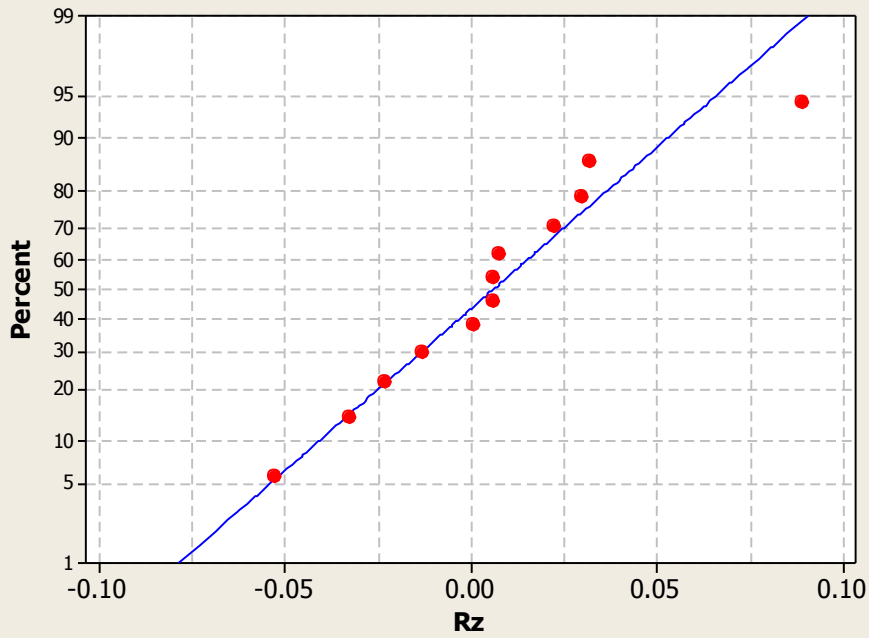


**Probability Plot of Ry**



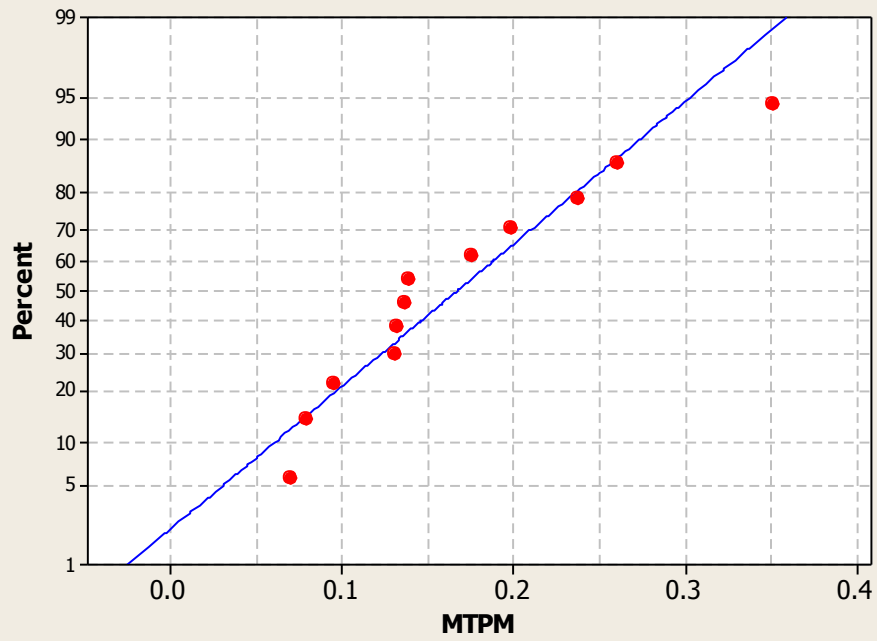
Mean	-0.00655
StDev	0.06682
N	12
AD	0.591
P-Value	0.097

**Probability Plot of Rz**



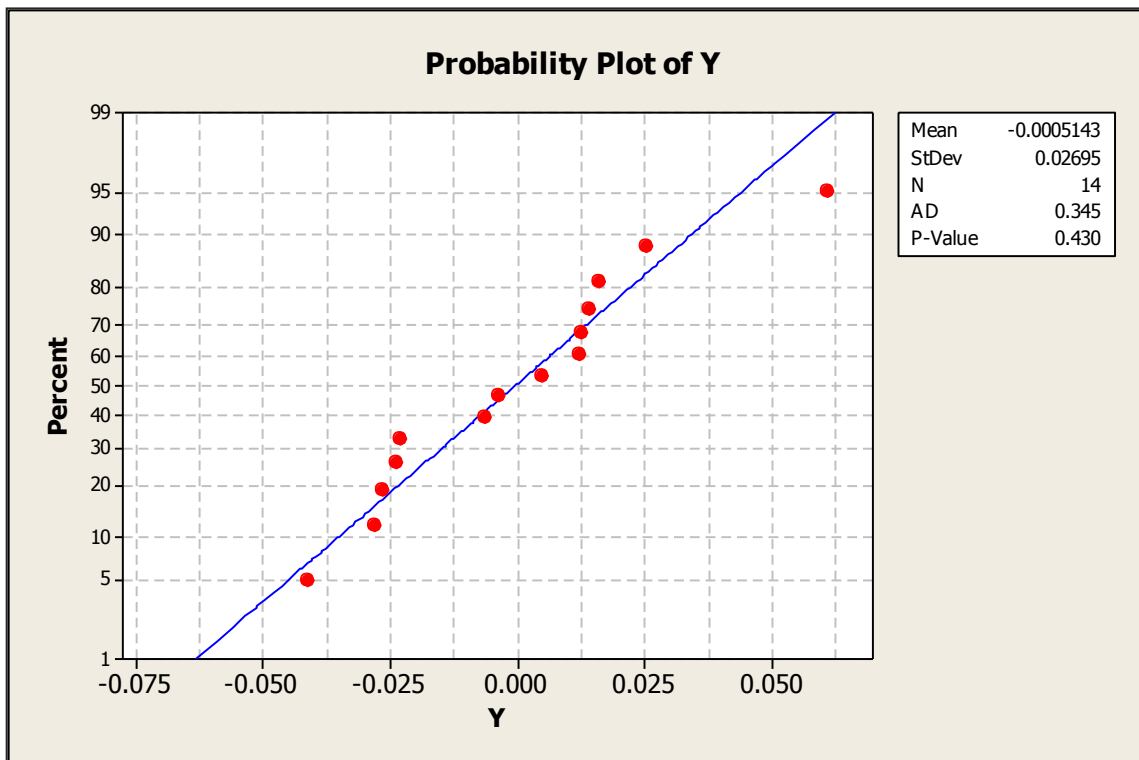
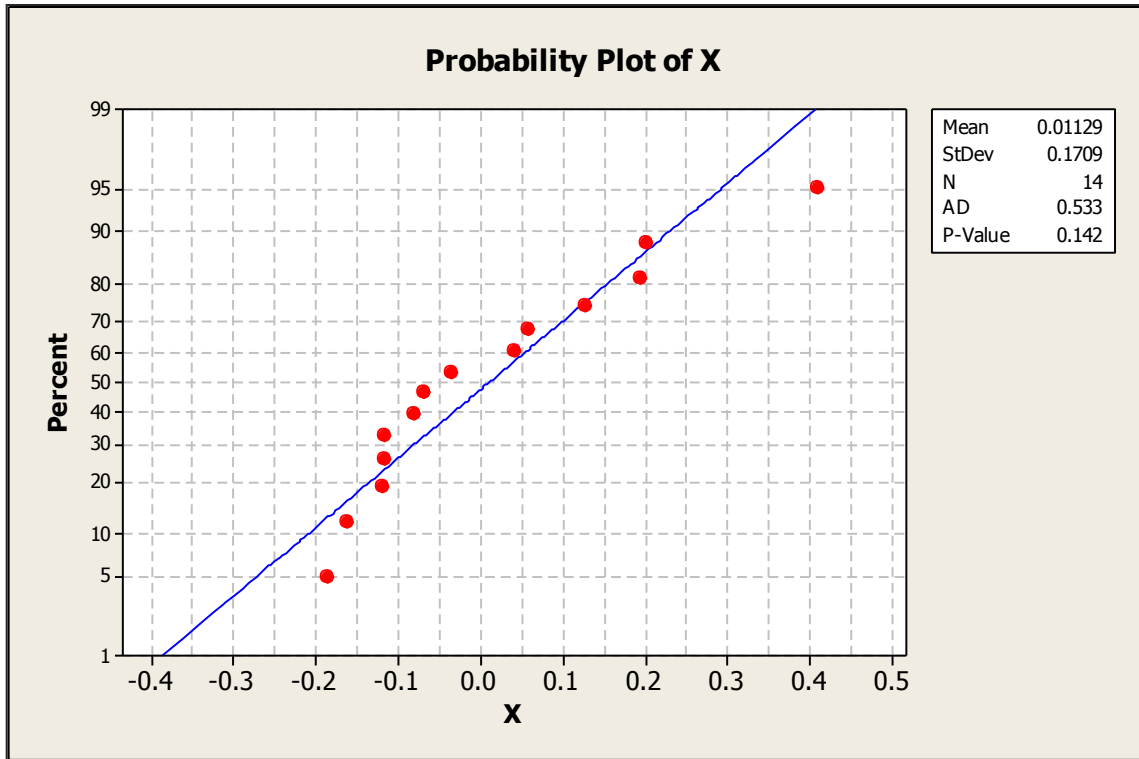
Mean	0.006092
StDev	0.03636
N	12
AD	0.301
P-Value	0.523

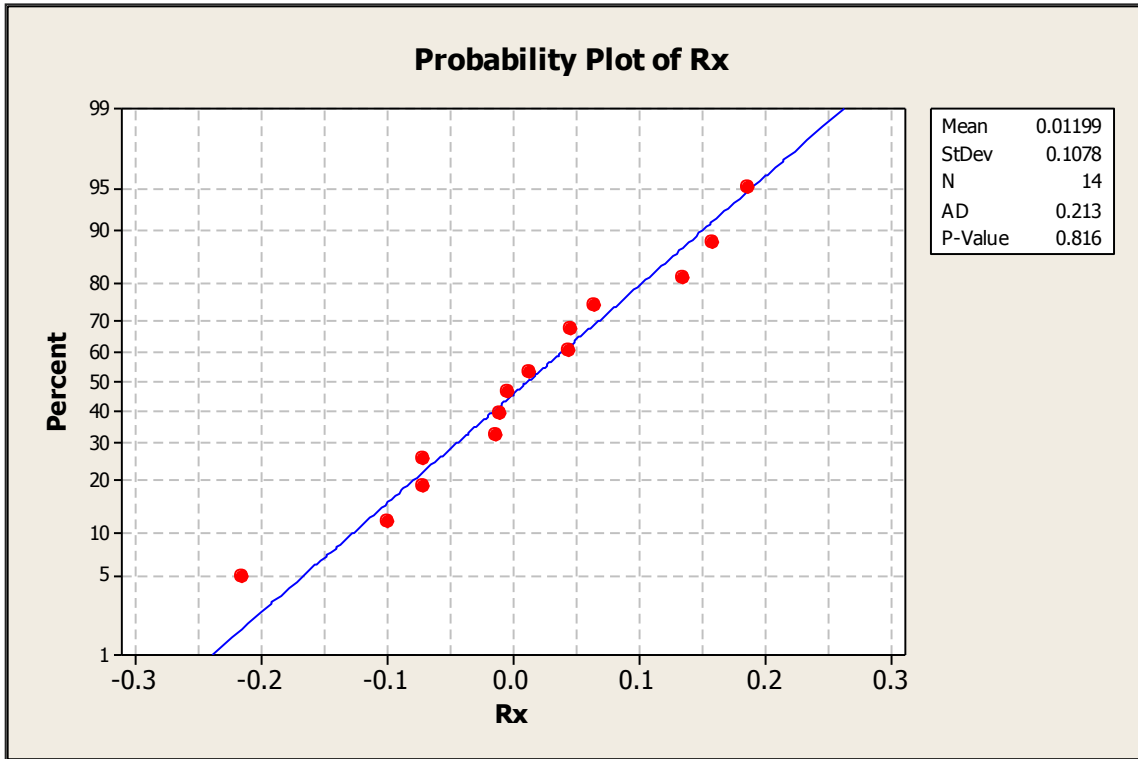
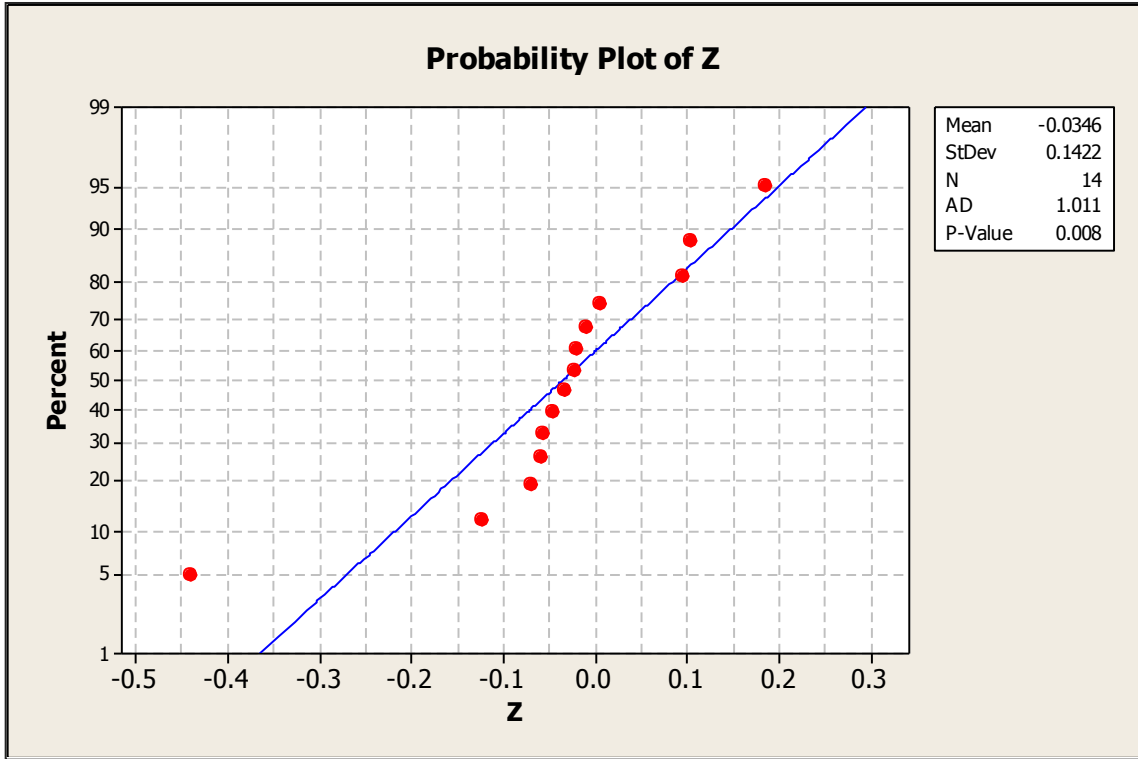
**Probability Plot of MTPM**



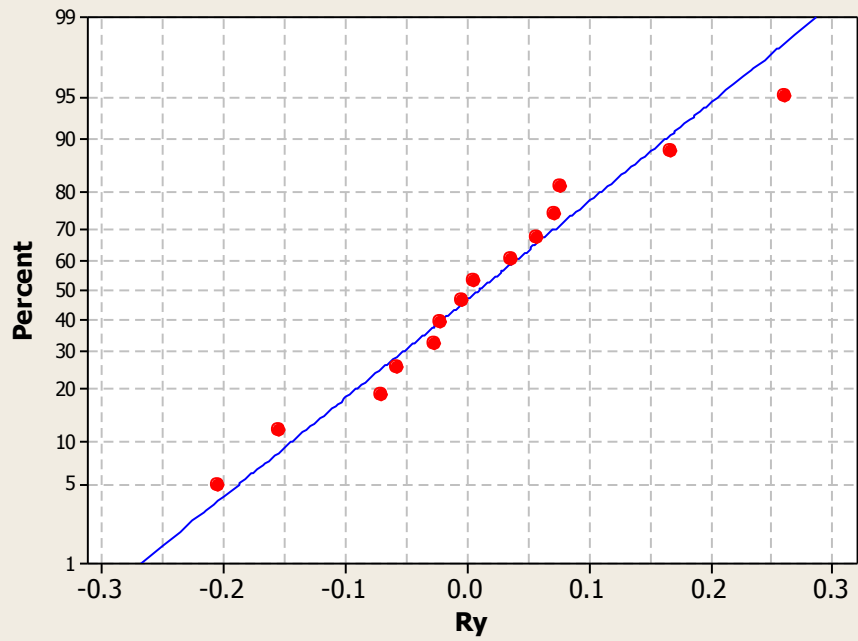
Mean	0.1674
StDev	0.08258
N	12
AD	0.416
P-Value	0.278

**F.3.1.5 Inferior - Apex**



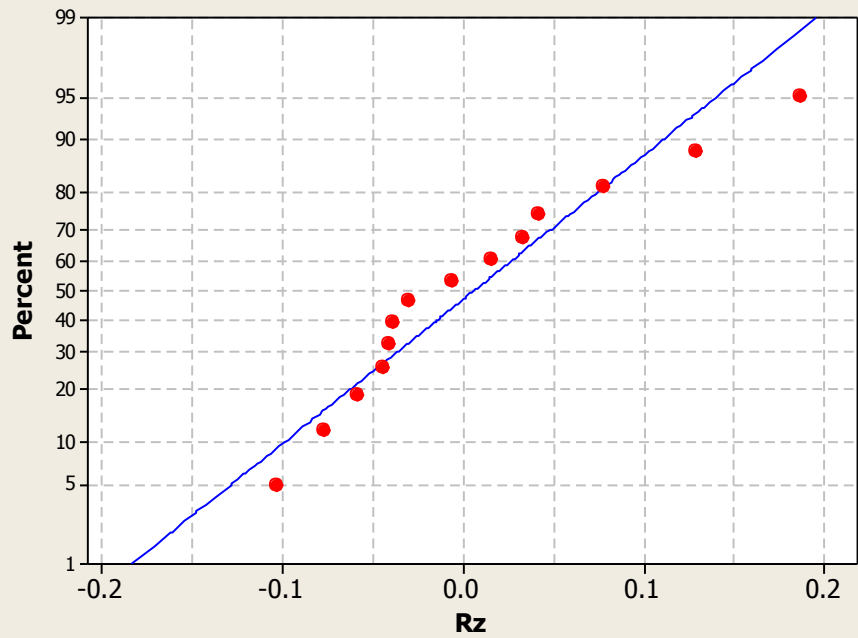


**Probability Plot of Ry**



Mean	0.009829
StDev	0.1194
N	14
AD	0.227
P-Value	0.772

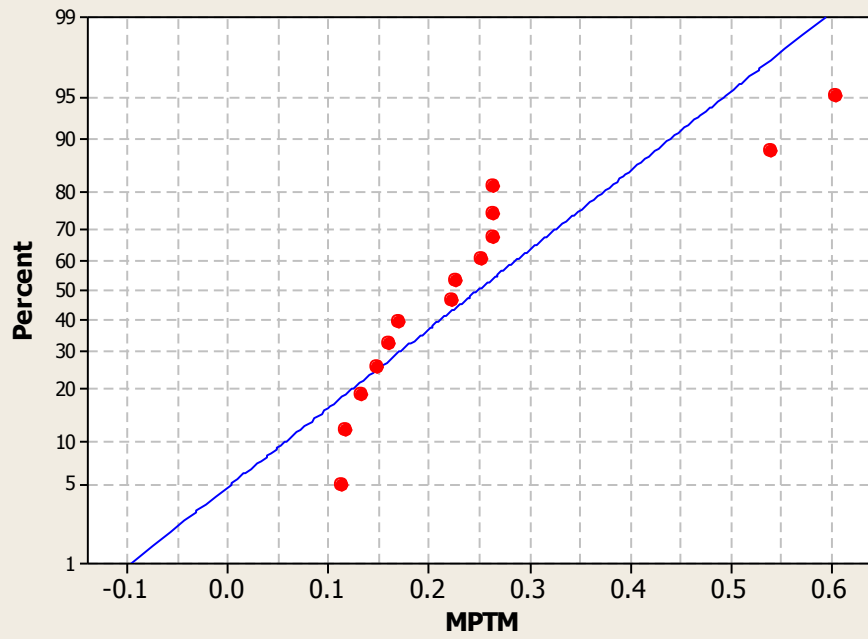
**Probability Plot of Rz**



Mean	0.006164
StDev	0.08149
N	14
AD	0.409
P-Value	0.299

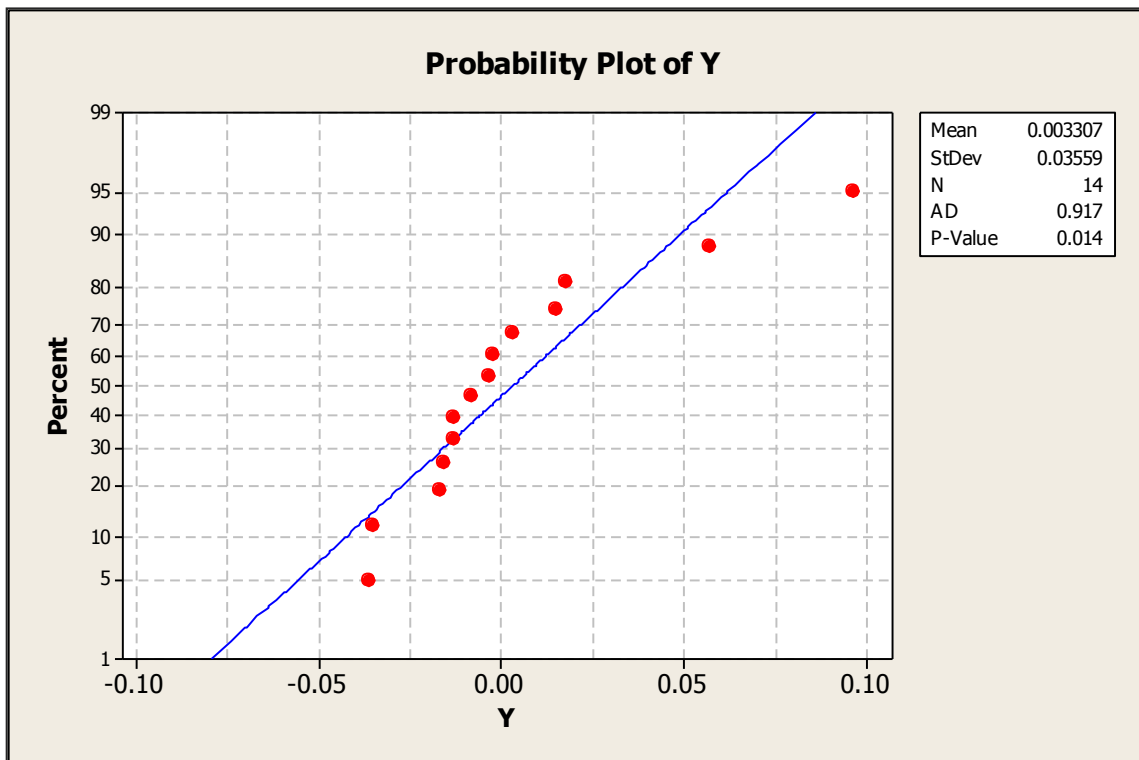
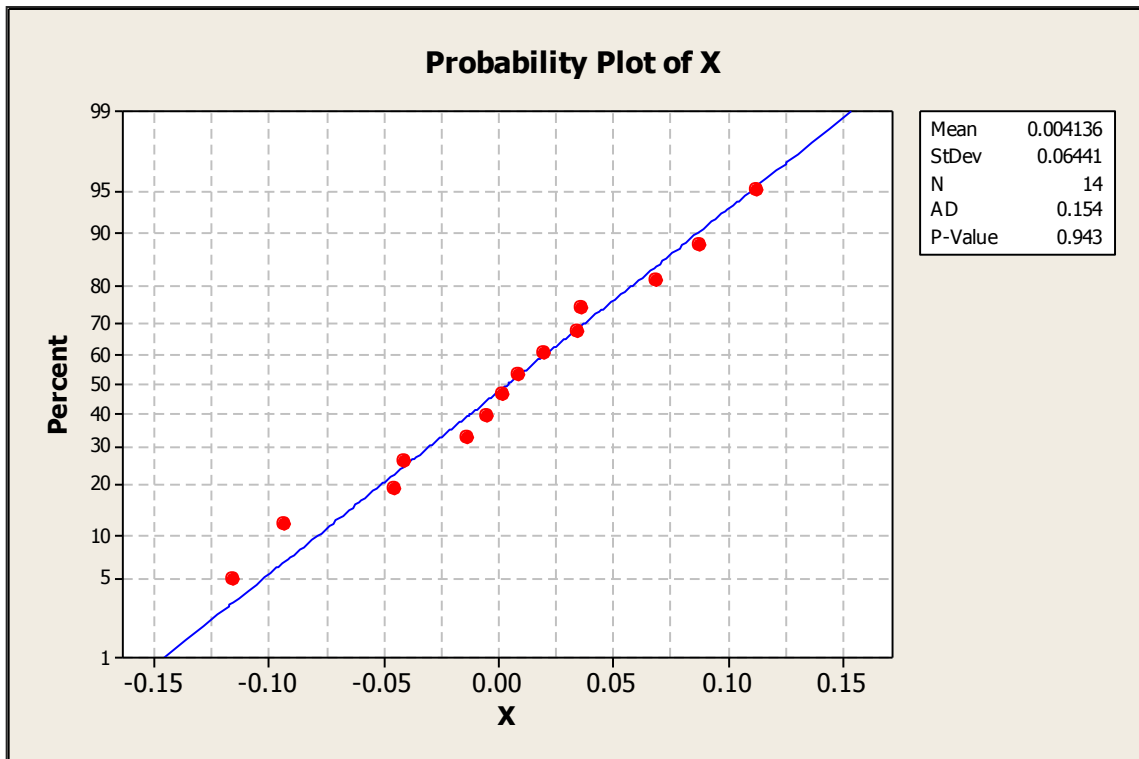


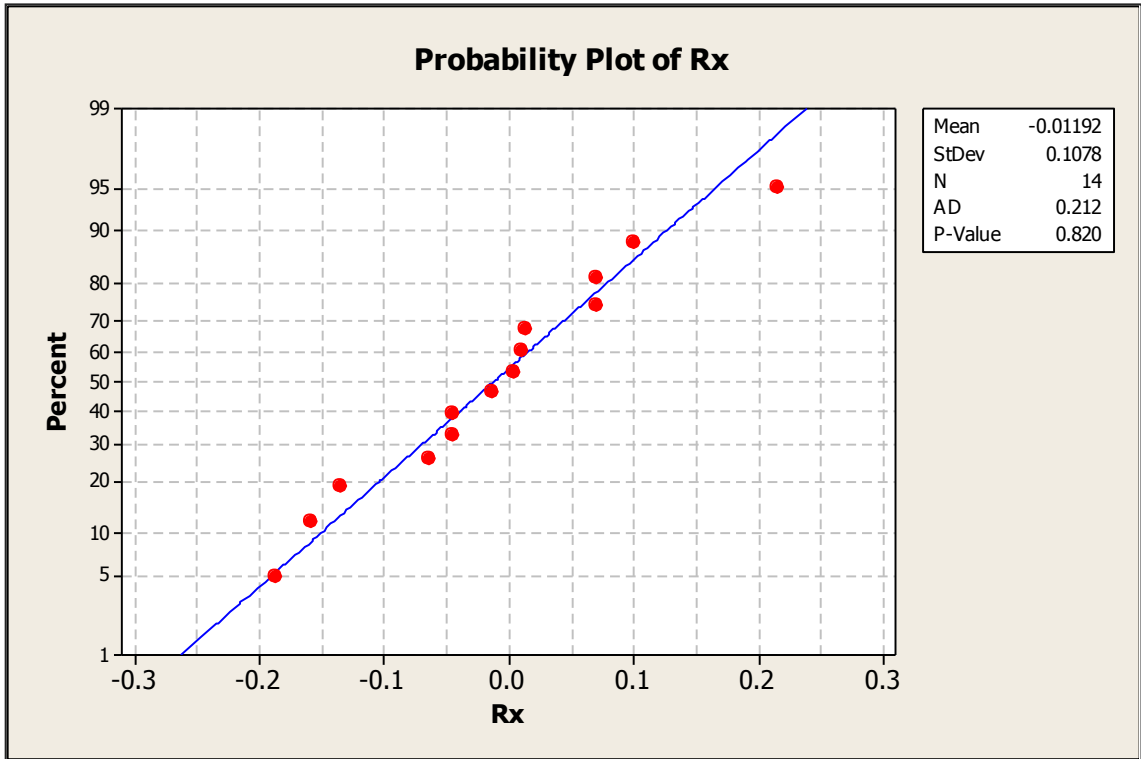
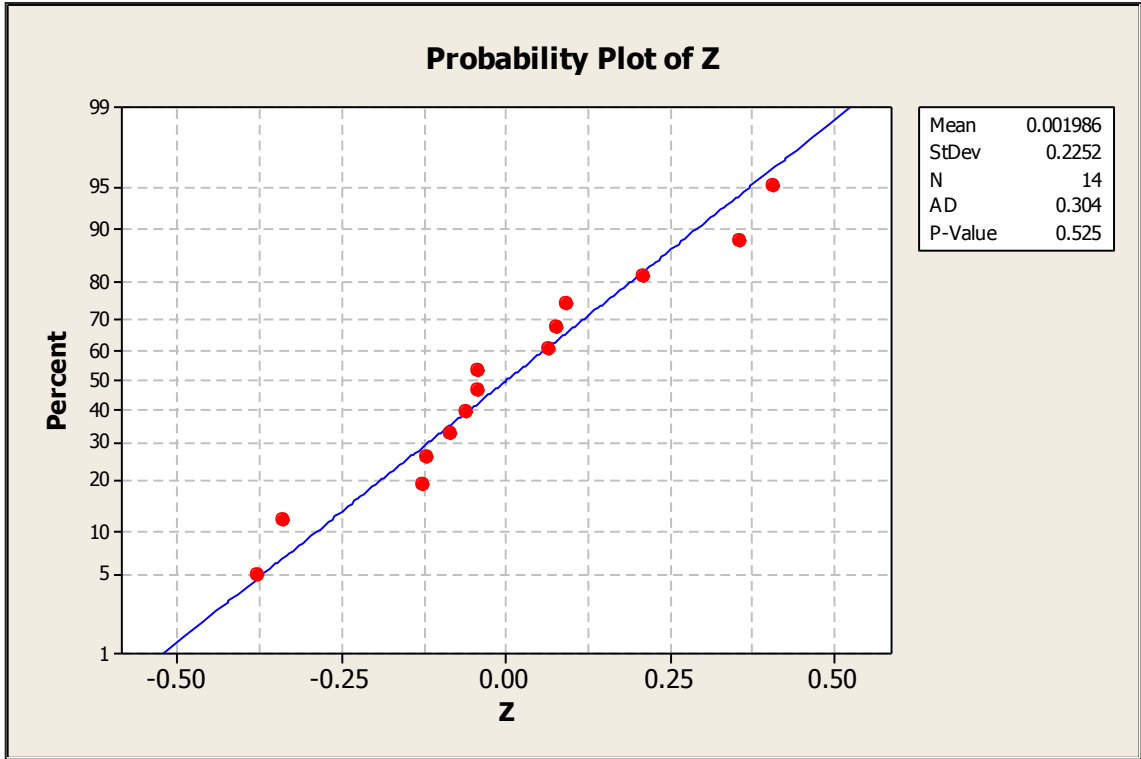
Probability Plot of MPTM

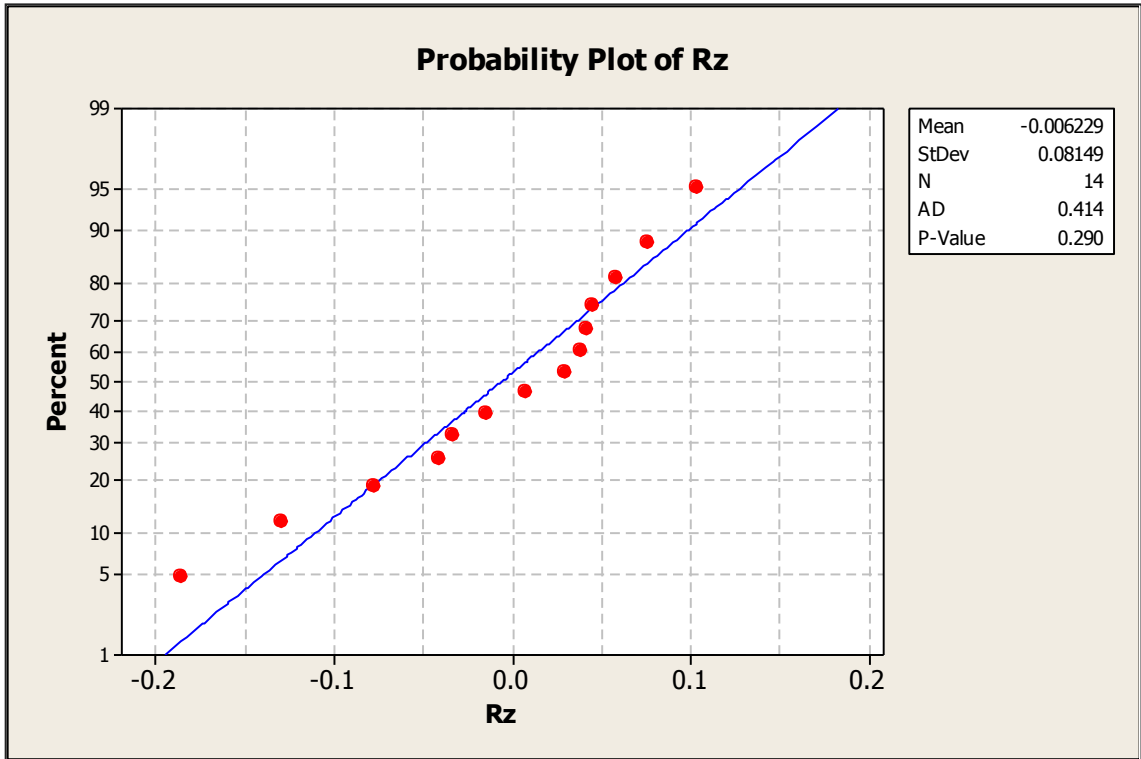
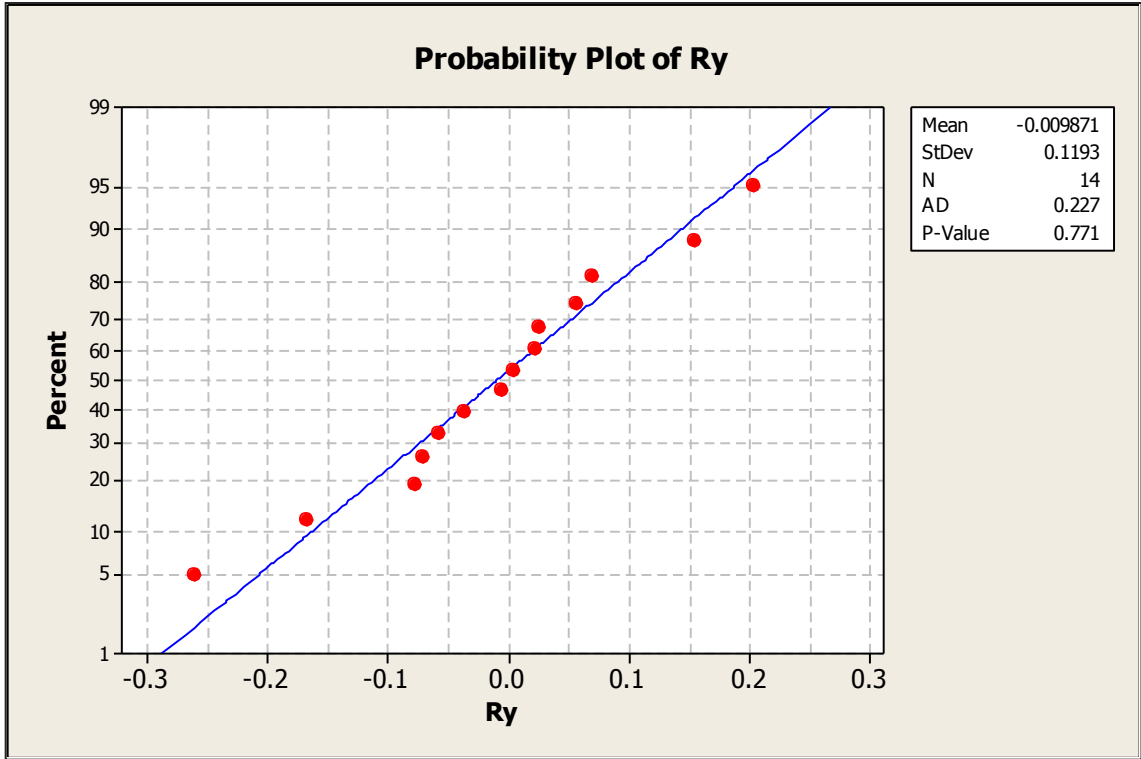


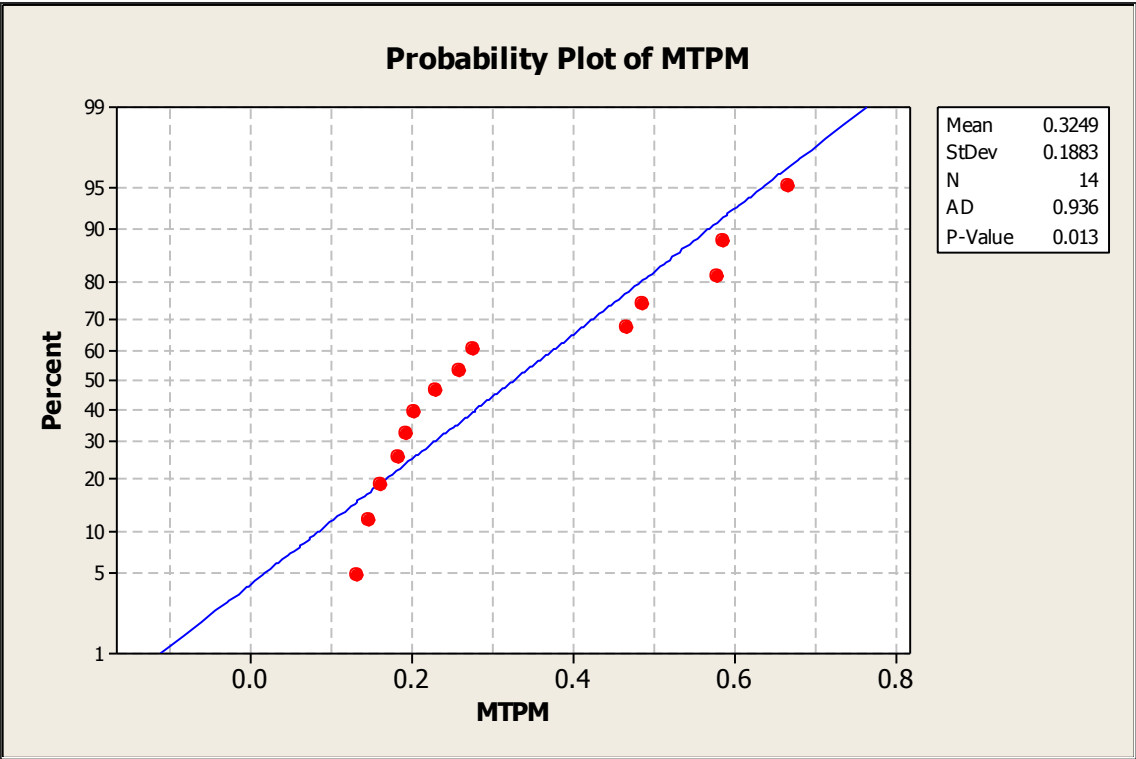
Mean	0.2484
StDev	0.1485
N	14
AD	1.261
P-Value	<0.005

### F.3.1.6 Inferior - Dual





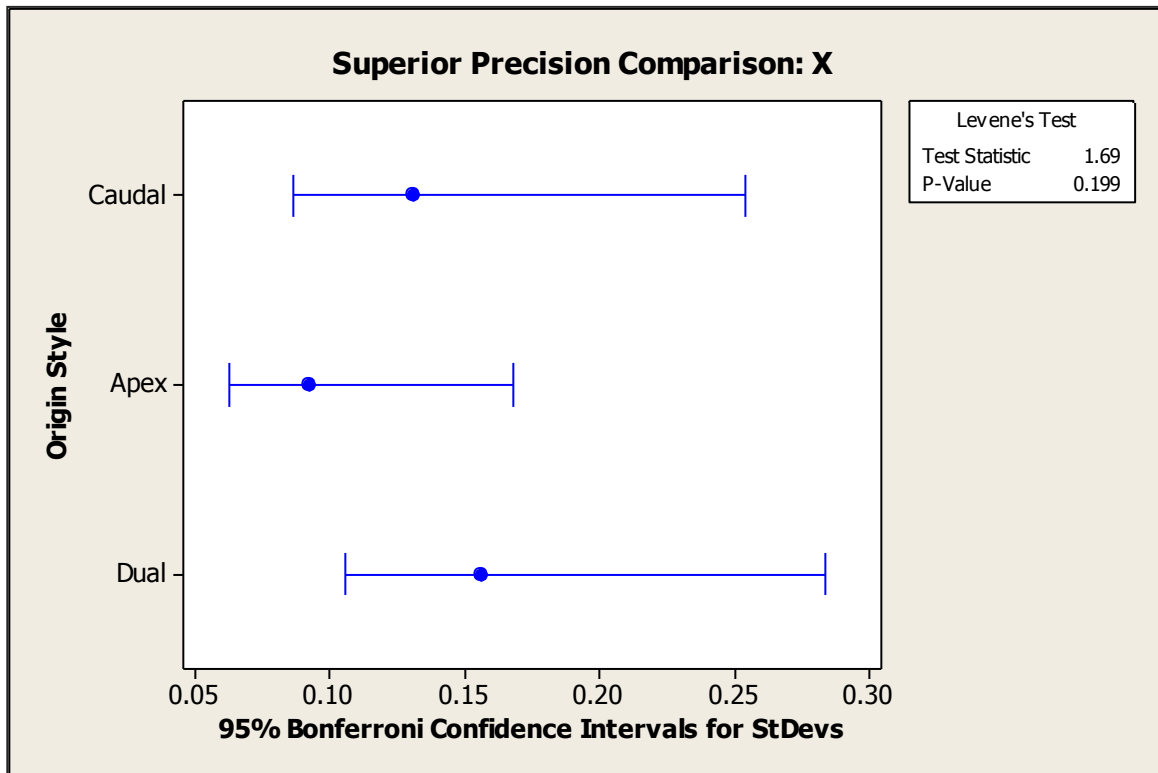


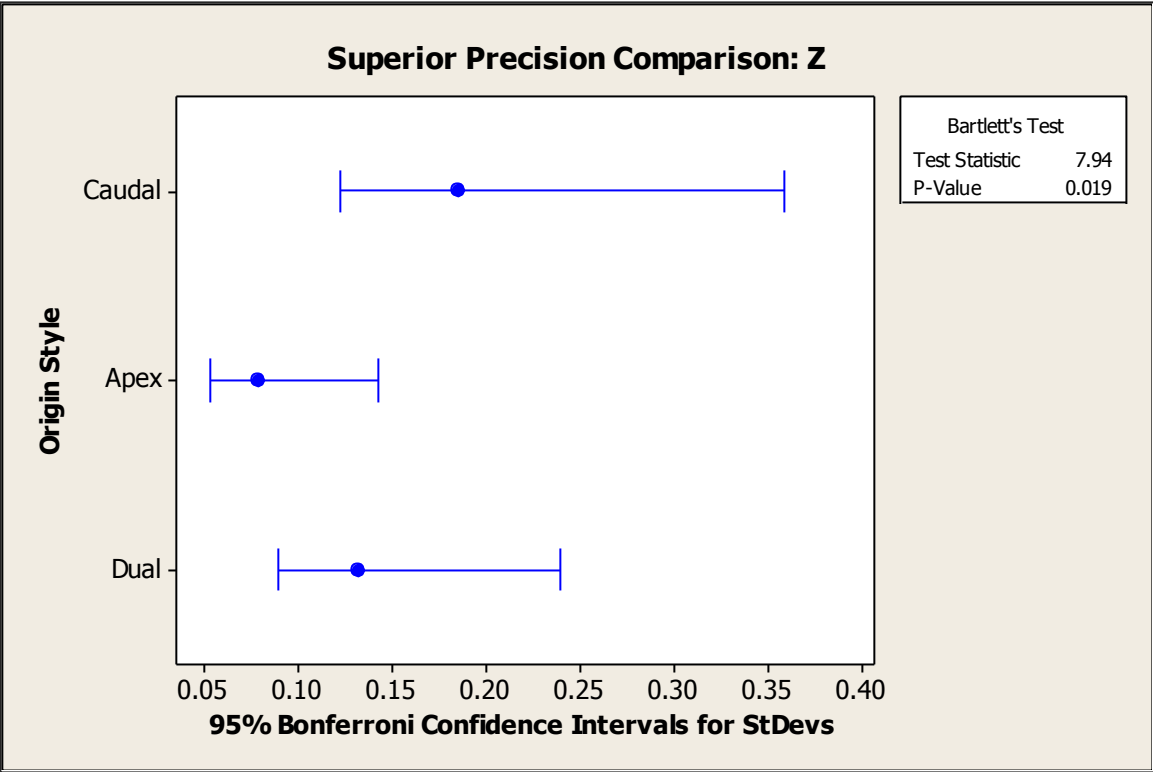
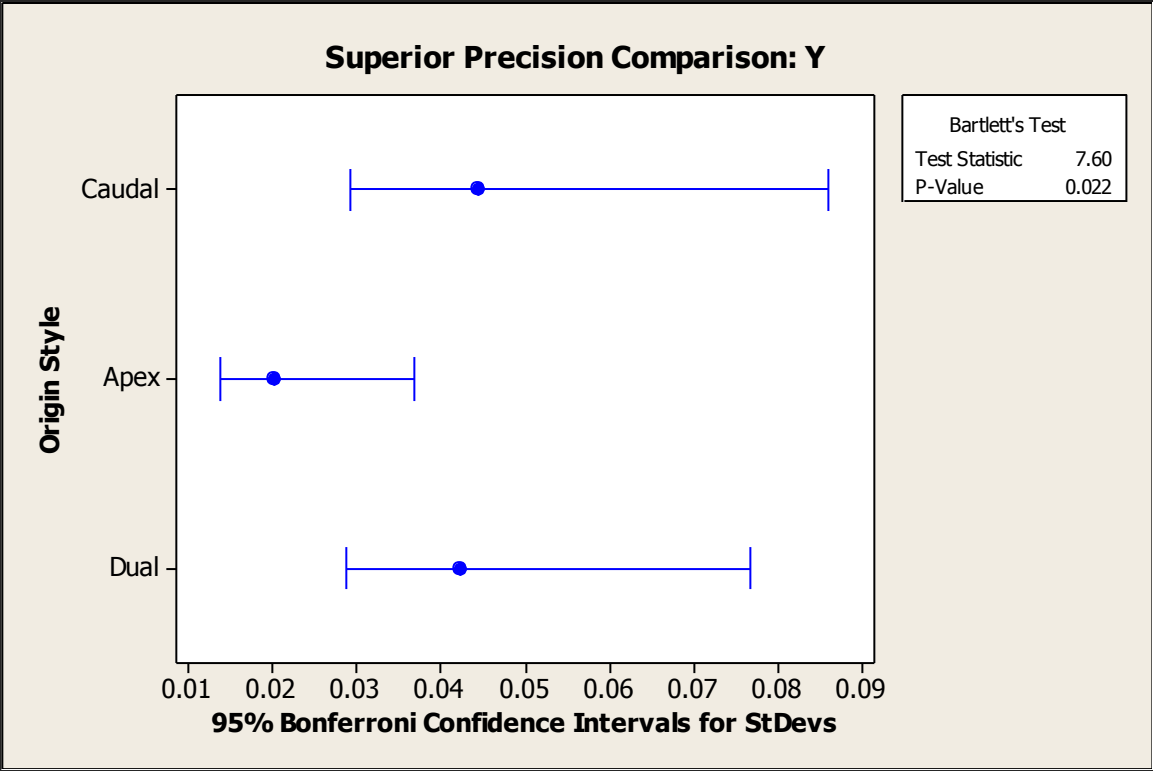


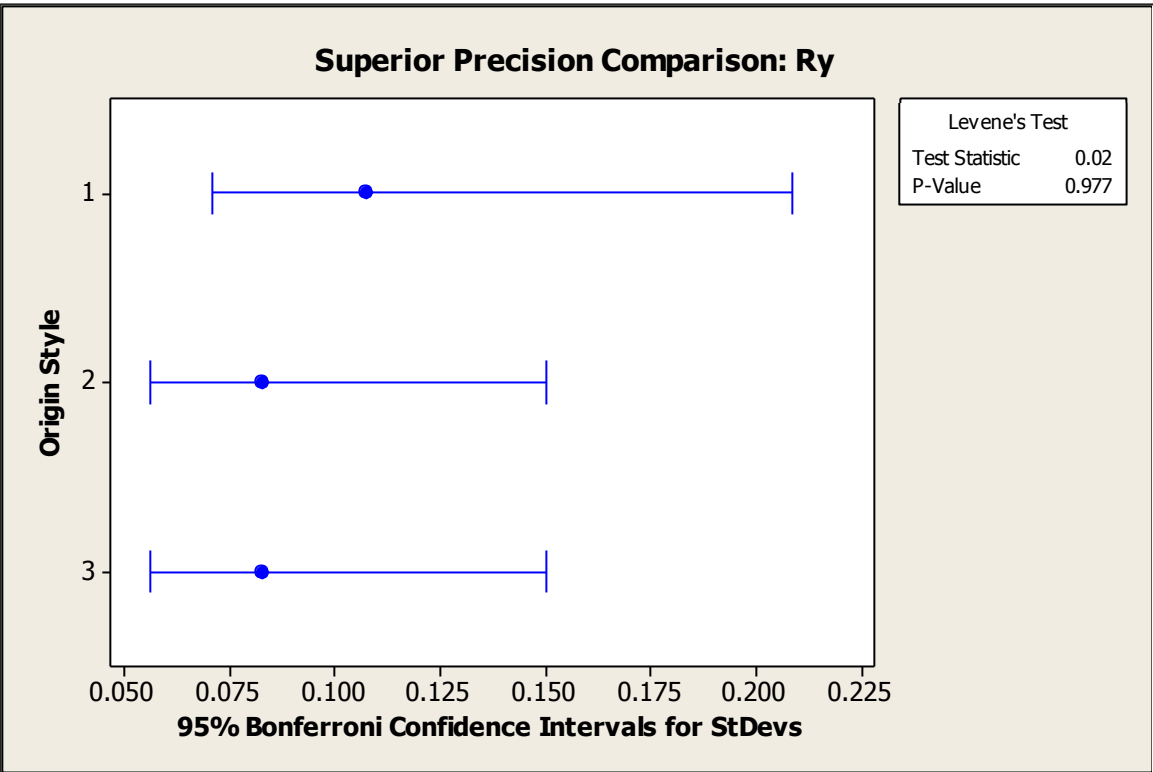
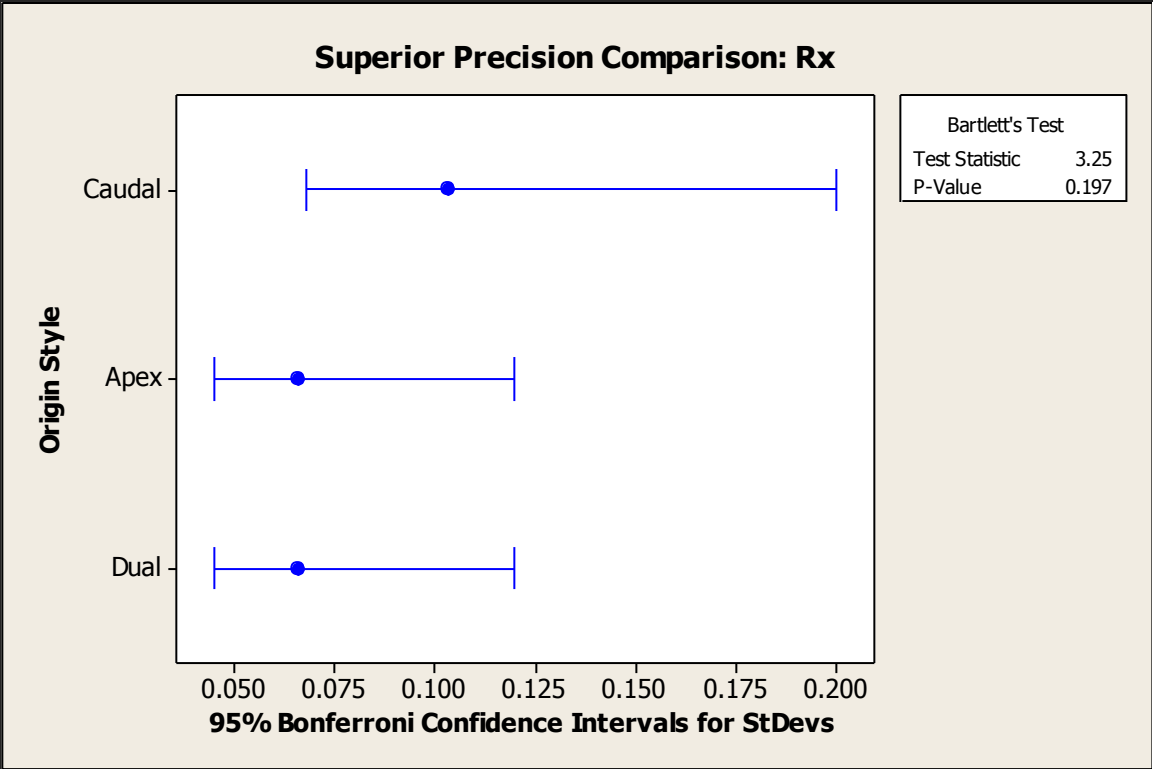
### F.3.2 Variance Comparison

The comparison of the origin style was done using either a Bartlett or Levene test. The use of the Bartlett test was reserved for cases where the data sets for all three origin styles were normally distributed. If one or more data sets were non-parametrically distributed the Levene test was used. For each of the following plots the utilized test is indicated. P-values above **0.05** indicate no statistically significant differences between the three origin styles.

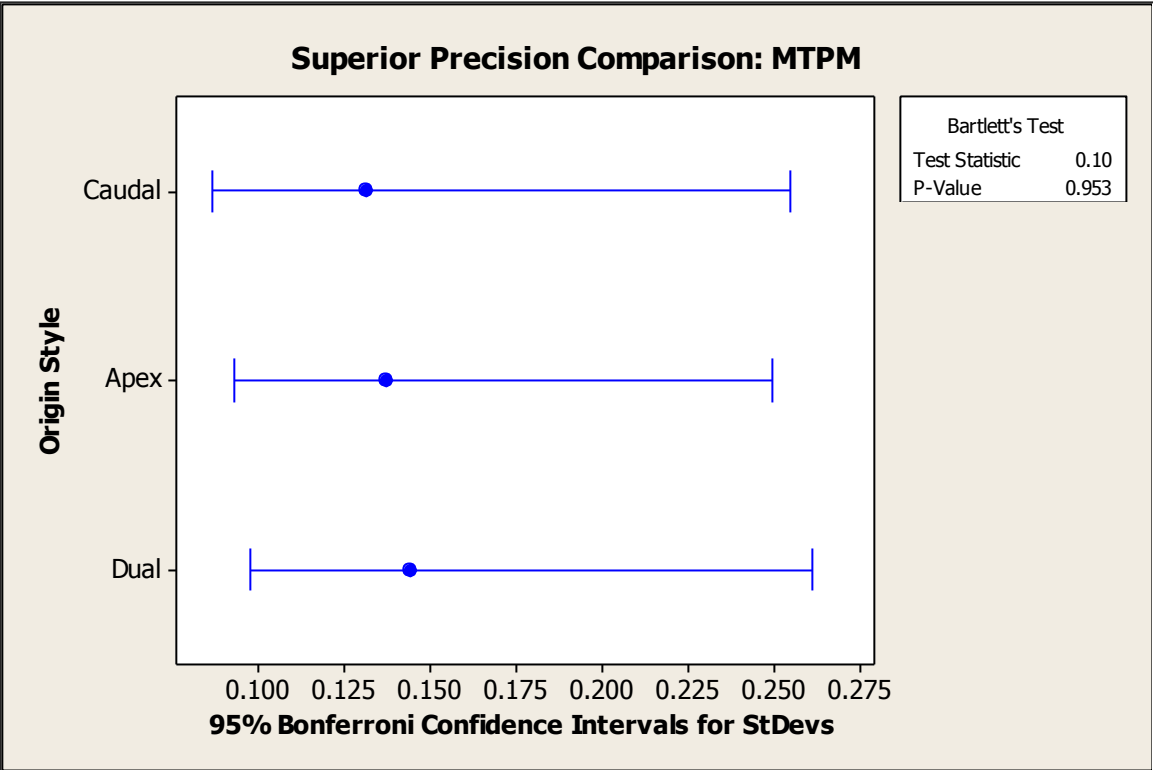
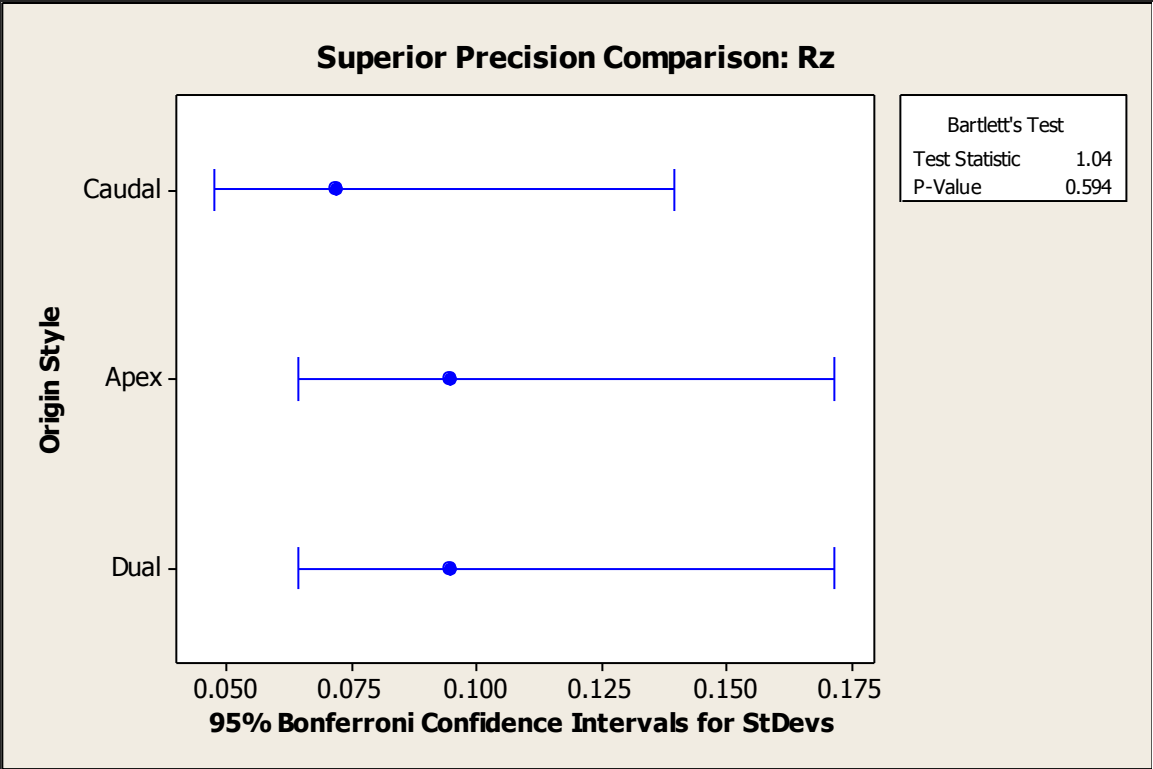
#### F.3.2.1 Superior Assessment



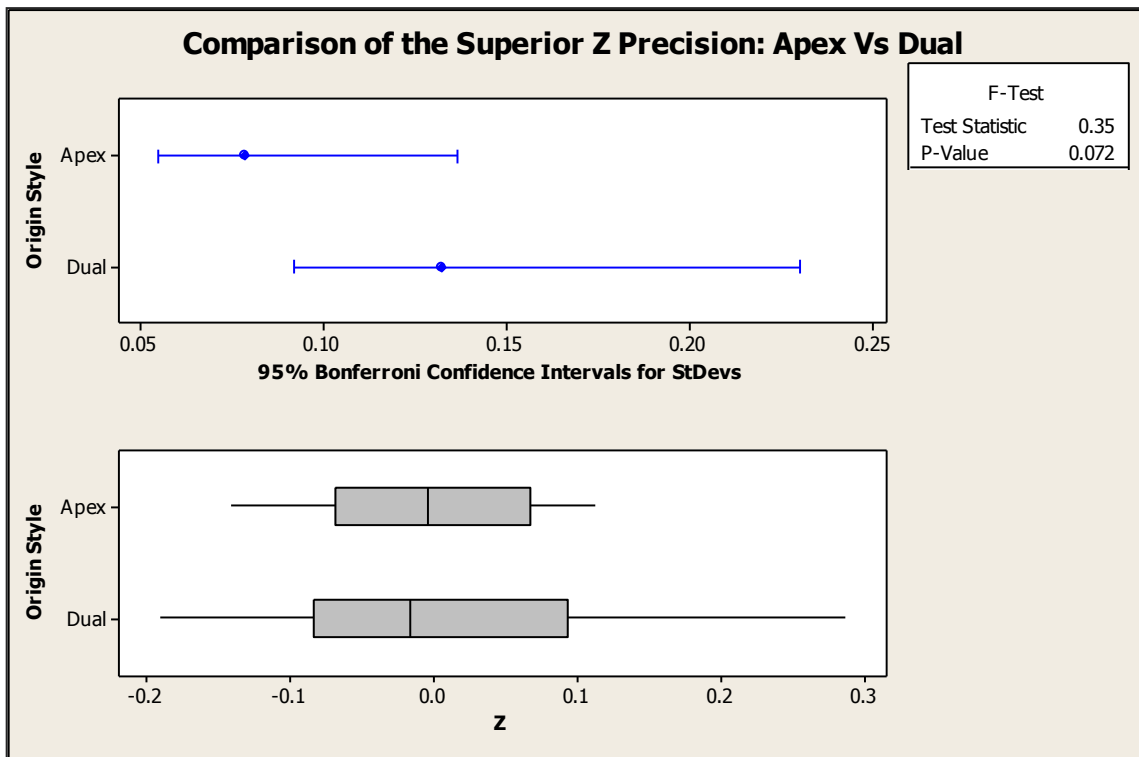
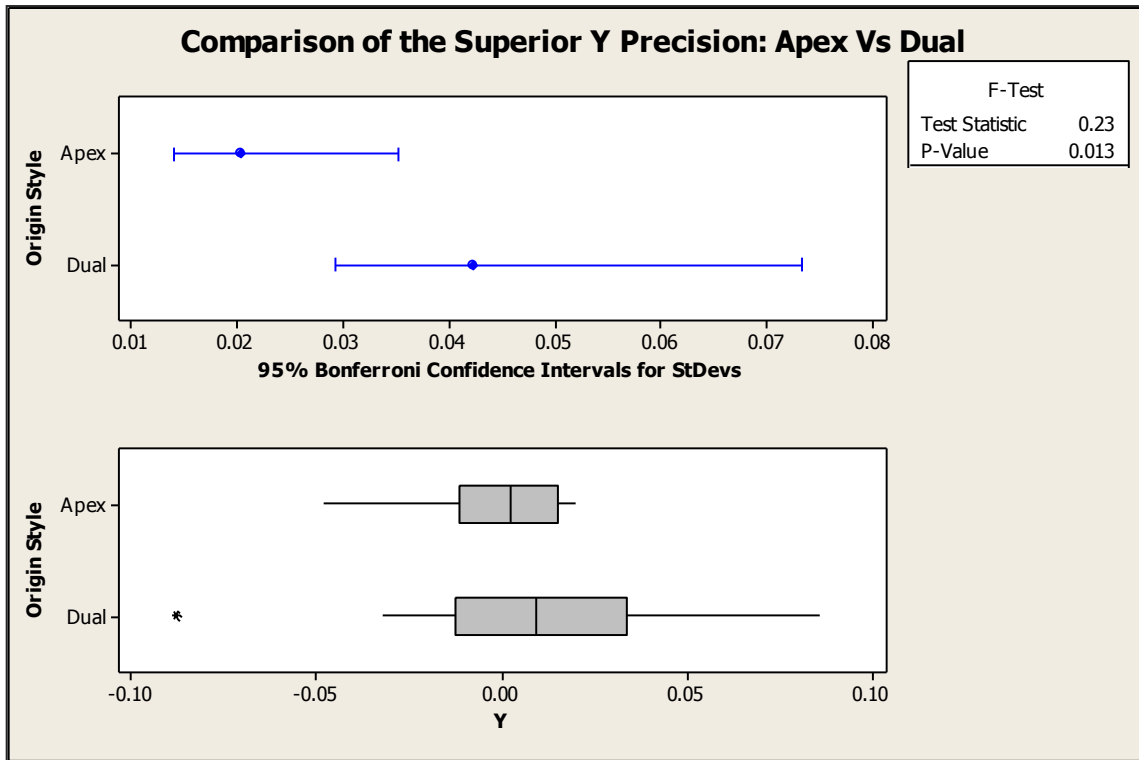




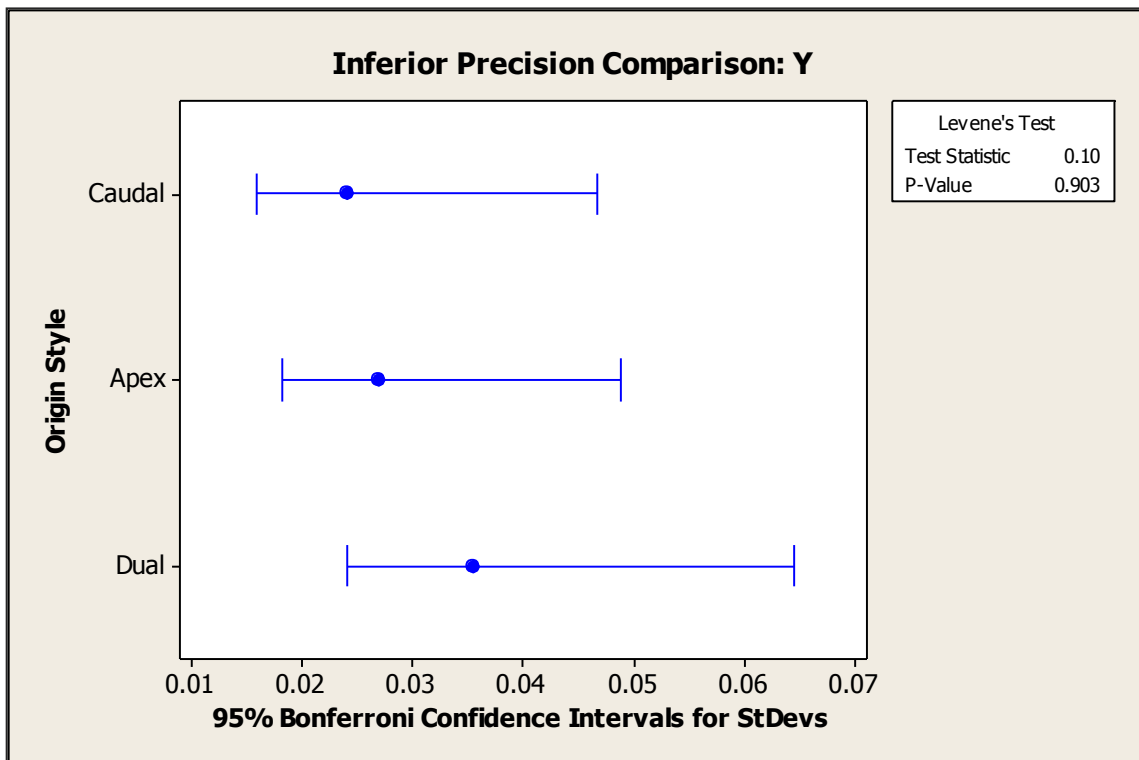
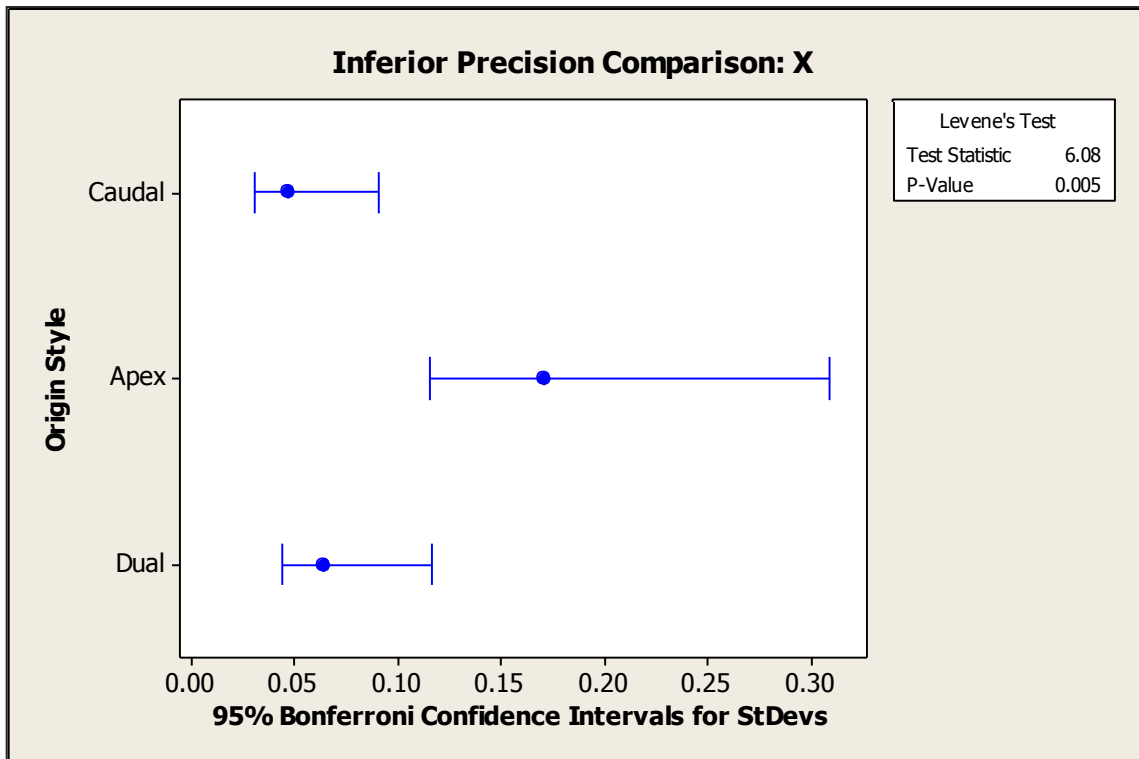


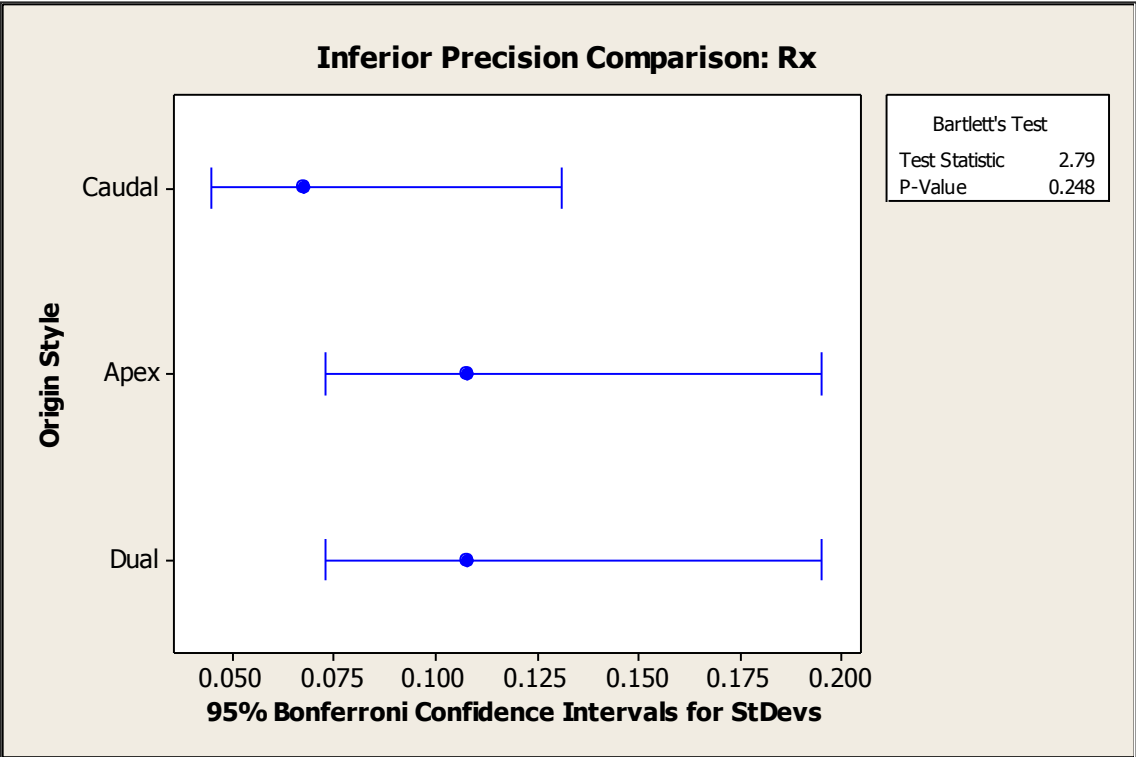
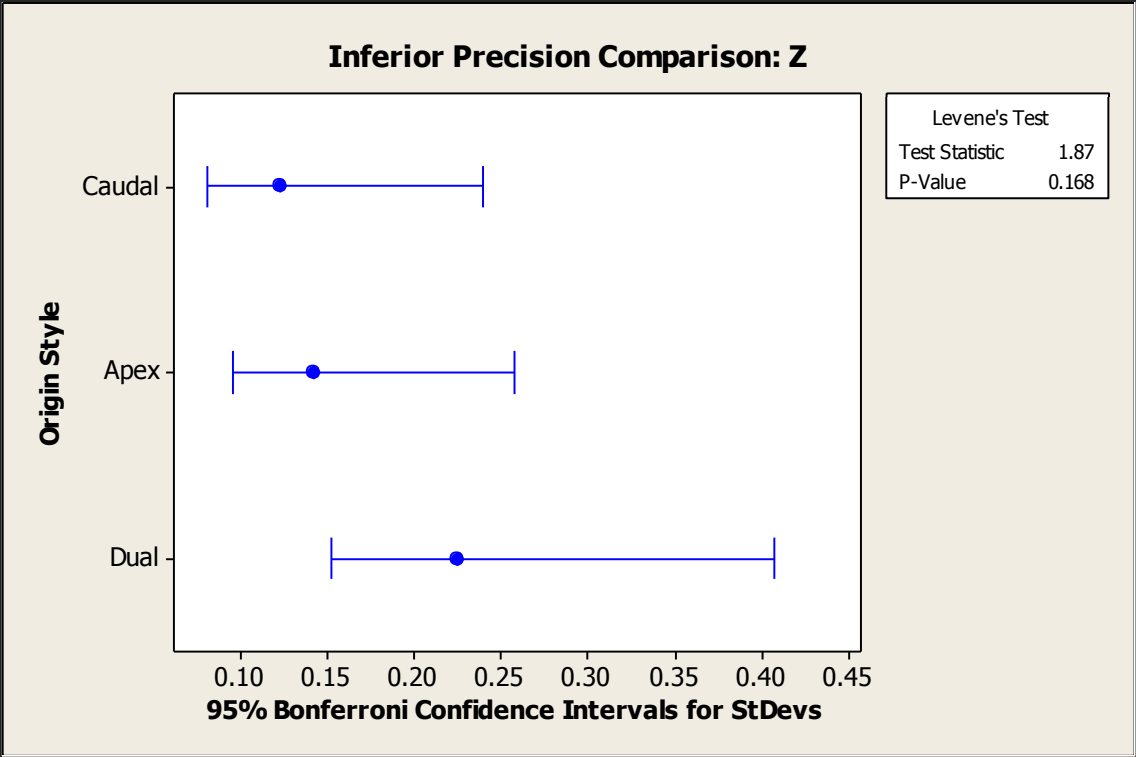


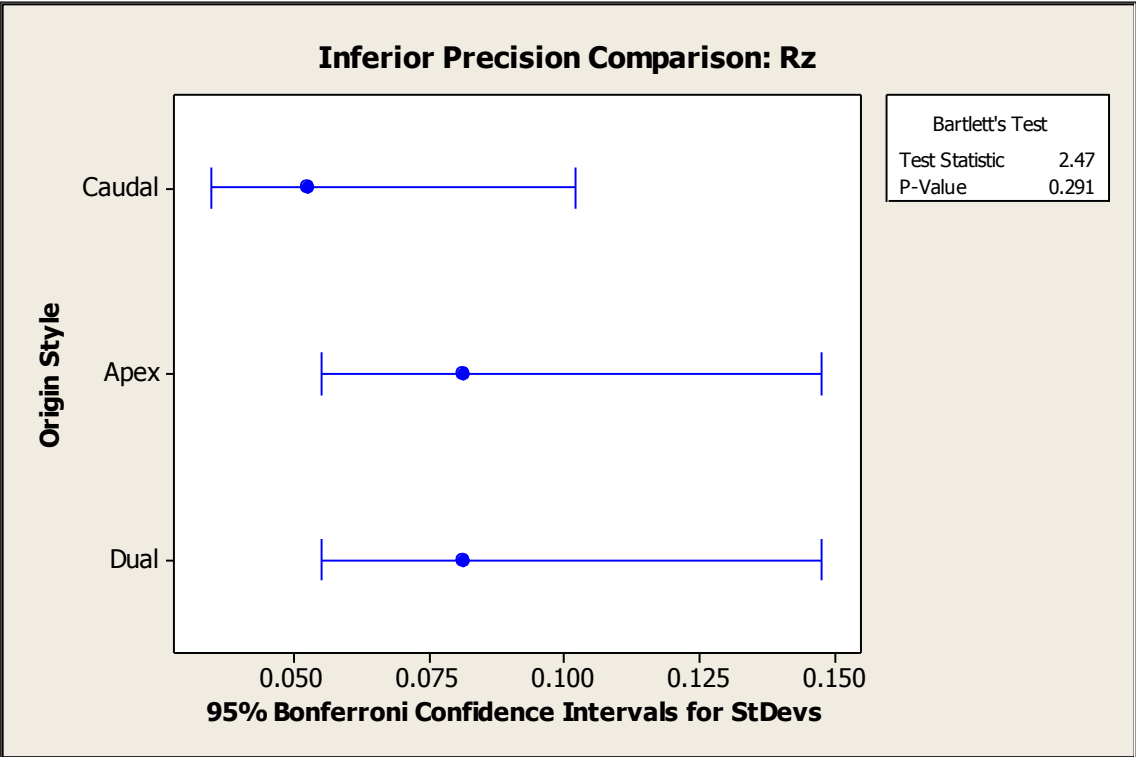
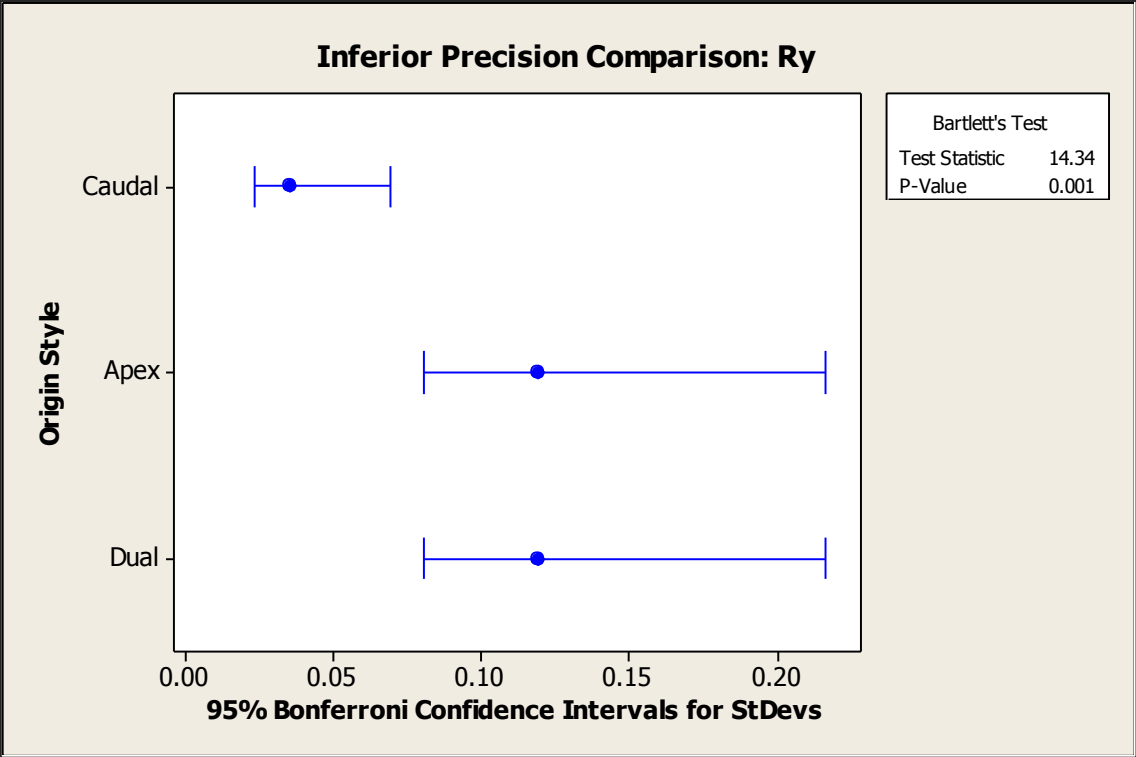
**F.3.2.2 Assessment of Apex Vs. Dual for Statistically Different Superior Precision**



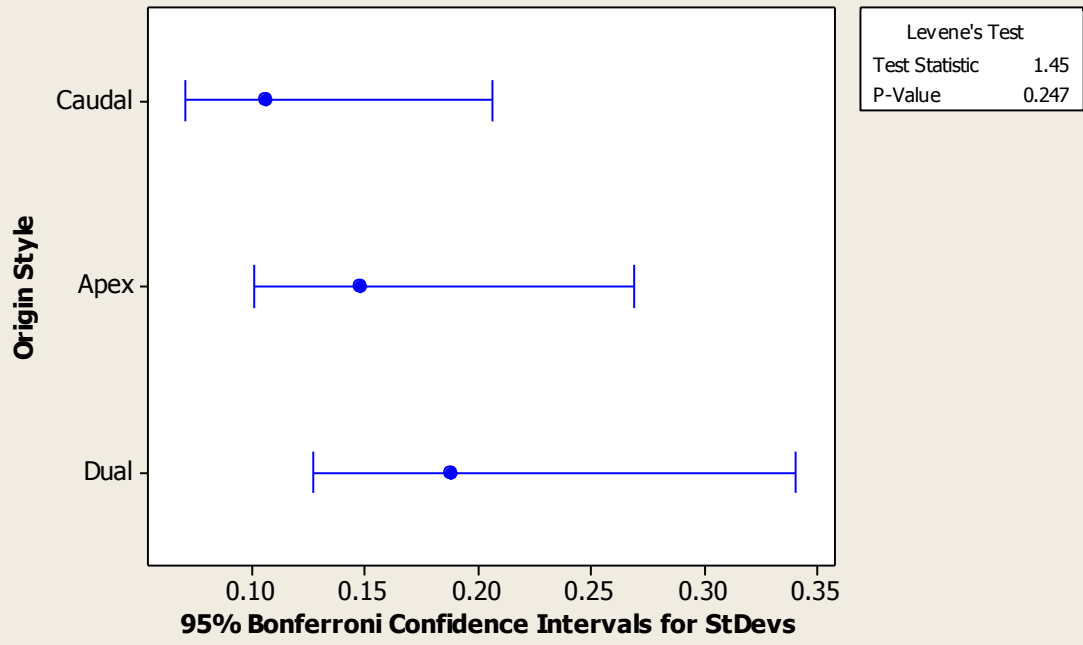
### F.3.2.3 Inferior Assessment





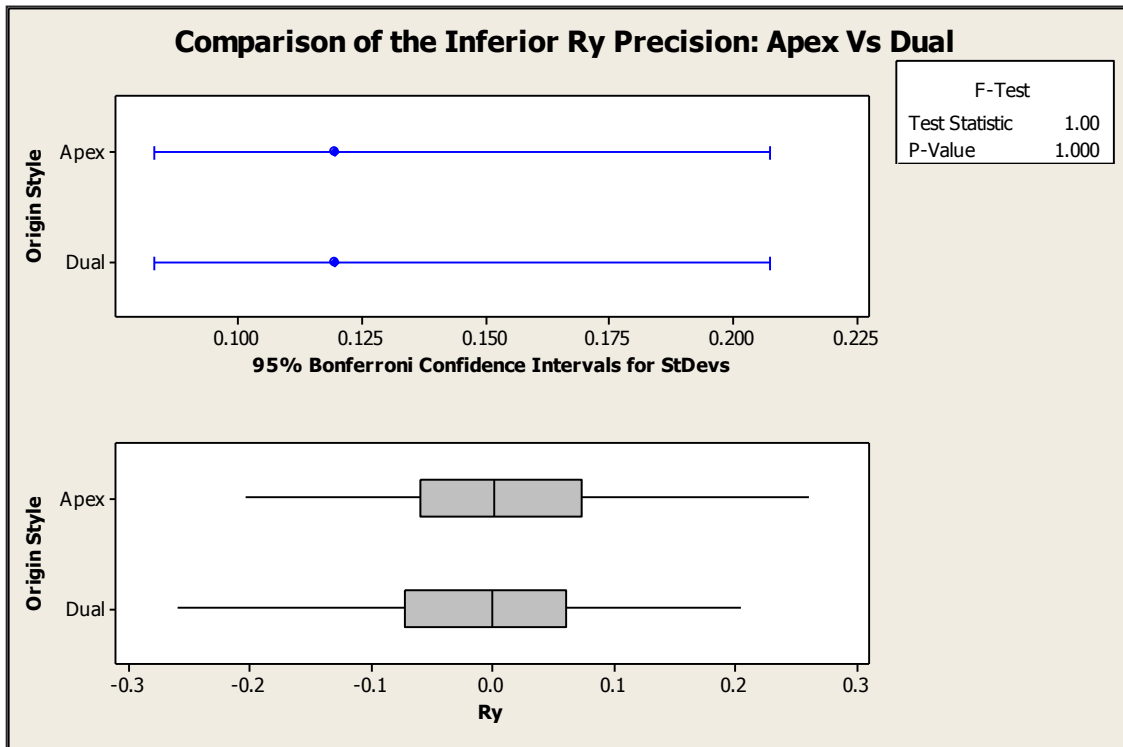
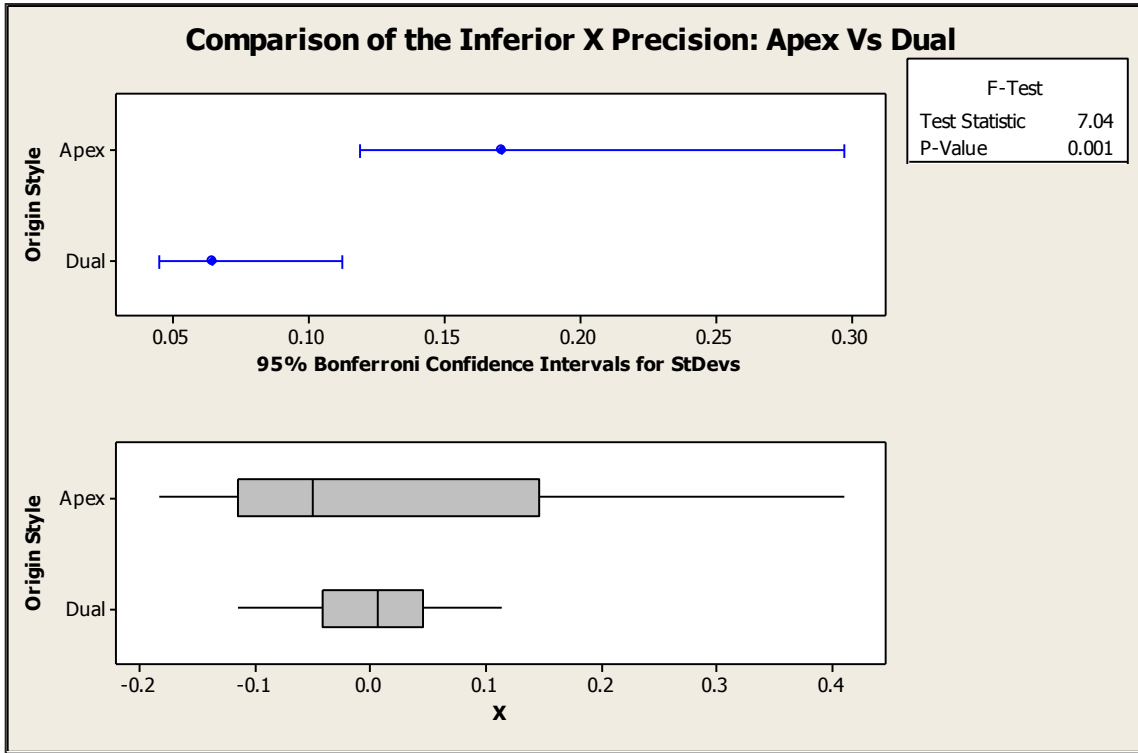


### Inferior Precision Comparison: MTPM



**F.3.2.4 Assessment of Apex Vs. Dual for Statistically Different Inferior**

**Precision**



## Appendix G - Original Thesis Work

This thesis work has been a continuation of the project started with this research group by A. Francis in 2009 [27]. During the course of this project there has been significant advancements made to the simulation process as well as a simulation validation component and an accuracy and precision assessment component. The original work conducted during the course of creating this thesis has been listed here. All of the following changes, improvements and additions had the potential to significantly impact the results of the project.

- i. Refining the marker placement protocol to use anatomical measurements available to surgeons during operations. This is a change from the precise (sub-millimetre) placement dimensions published by Francis (2009) [27]. This refinement affects the marker placement options and thus potentially affects the accuracy and precision of the RSA measurements.
- ii. Significant modifications to the simulation process originally developed at this institution by Francis (2009) [27]. The significant modifications include:
  - a. The use of a linear attenuation factor to produce image contrast. This is a significant improvement over the previous method surface attenuation method. The implementation of this new process greatly effects image spatial resolution and better simulates the physical RSA environment.
  - b. Created a calibration box native to the simulation environment which eliminated the errors associated with previously used CAD created calibration box. The previous simulated calibration box used the nominal



positions of the calibration markers instead of actual positions defined by HBI and used by the RSA software. This change impacts the accuracy of the RSA measurements.

**iii.** Validation of the Simulated RSA Environment

- a. Construction and imaging of a new phantom model used to assess the validity of the simulated environment.
- b. Construction of and imaging of a new simulated model developed from a CT scan of the physical phantom to match marker placement in both environments.
- c. Parallel precision studies of the two models to assess the validity of the simulated RSA environment. This included 35 RSA image pairs: 18 image sets of the physical phantom and 17 image sets of the simulated model. Each study produced 19 data points to assess system precision. Analysis of equal variance and was used to assess simulation validity.

**iv.** Creation of two novel origin styles, the Apex and Dual Origin Styles, to compensate for the limited imaging area present in the Halifax RSA suite. These origin styles are unique to this thesis alone.

**v.** Assessment of the Accuracy and Precision of three origin styles (Caudal, Apex and Dual)

- a. Changed the methodology from the previous project work of how accuracy and precision was calculated compared to the methods used by the previous project. The new methods used are based on those described in the literature by Madanat et al (2005, 2007), Laende et al (2009),

Bragdon et al (2002), Önsten et al (2001) and Allen et al (2004) [26], [34], [59–61], [63].

- b. Creation and analysis of approximately 300 original simulated RSA image sets (approximately 460 data points as the RSA exams are used twice for the Apex and Dual Origin Styles) for the assessment of the accuracy and precision of the Caudal, Apex and Dual Origin Styles.
- c. Statistical methods to assess the agreement of the three origin styles not previously used in this project. To compare accuracy measurements Bland-Altman plots were used and analysis of equal variance was used to assess the agreement between precision measurements. The use of these statistics is based on their use by Bland and Altman (1986) and their use in RSA by Laende et al (2009) [4], [61].

Along with the major original material, additional minor improvements were made to the simulation.

- i. Complete reconstruction of the vertebral and spinal models to better reflect the recorded measurements published by Panjabi et al (1991, 1992) [67], [68]. The models are now entirely based on the measurements reported in these two papers.
- ii. Additional refinements were made to the simulation process:
  - a. Refined how the simulated images are created using a different file structure method to improve coding and usability.
  - b. Improved the ease of use of model placement in the CAD RSA environment increasing usability of the simulation process.

## Appendix H - Permission for Publication

This thesis contains work not originally created by this researcher. I would like to thank Elise Laende and Antony Francis for their assistance and their permission to publicise their works.

Images Figure 1.12 and Figure 1.14 located on pages 41 and 44 were originally created by Antony Francis in his Master's thesis entitled: "*Simulation of a Standardized Bead Placement Protocol for Radiostereometric Analysis of Thoracic Spinal Fusion*" published in 2009 [27]. These images show the image simulation process and marker placement protocol developed over the course of his project.

The matrix mathematical equations presented in Section 3.2.4.1, starting on page 74, were originally developed by Elise Laende for her Master's thesis entitled: "*Radiostereometric Analysis of Migration and Inducible Displacement for the Evaluation of Total Knee Replacement Fixation*" published in 2006 [29]. I would also like to thank Elise for the use of her *LocalMigration Function* for MatLab. The code for this function, with her permission, has been included in Section D.2.3, starting on page 244.

February 22, 2012

**Antony Bou Francis,**

Marie Curie Research Fellow / PhD Student  
School of Mechanical Engineering  
University of Leeds  
Leeds, UK  
LS2 9JT

I am preparing my M.A.Sc. thesis for submission to the Faculty of Graduate Studies at Dalhousie University, Halifax, Nova Scotia, Canada. I am seeking your permission to include images produced for your thesis entitled:

*Simulation of a Standardized Bead Placement Protocol for Radiostereometric Analysis of Thoracic Spinal Fusion*

Canadian graduate theses are reproduced by the Library and Archives of Canada (formerly National Library of Canada) through a non-exclusive, world-wide license to reproduce, loan, distribute, or sell theses. I am also seeking your permission for the material described above to be reproduced and distributed by the LAC (NLC). Further details about the LAC (NLC) thesis program are available on the LAC (NLC) website ([www.nlc-bnc.ca](http://www.nlc-bnc.ca))

Full Publication details and a copy of this permission letter will be included in the thesis.

Sincerely,

Alan Spurway

---

Permission is granted for:

- a) The inclusion of the material described above in A. Spurway's thesis.
- b) For the material described above to be included in the copy of A. Spurway's thesis that is sent to the Library and Archives of Canada (formerly National Library of Canada) for reproduction and distribution.

Name: \_\_\_\_\_

Title: \_\_\_\_\_

Signature: \_\_\_\_\_

Date: \_\_\_\_\_

March 08, 2012

**Elise Laende**

6068 Cherry St.

Halifax, NS

B3H 2K3

I am preparing my M.A.Sc. thesis for submission to the Faculty of Graduate Studies at Dalhousie University, Halifax, Nova Scotia, Canada. I am seeking your permission to include the mathematical equations published in the *Mathematical Steps of Micromotion Calculations for RSA* Appendix produced for your thesis entitled:

*Radiostereometric Analysis of Migration and Inducible Displacement for the Evaluation of Total Knee Replacement Fixation*

I am also seeking your permission to include the coding to your Matlab Program:

*LocalMigration Function*

Canadian graduate theses are reproduced by the Library and Archives of Canada (formerly National Library of Canada) through a non-exclusive, world-wide license to reproduce, loan, distribute, or sell theses. I am also seeking your permission for the material described above to be reproduced and distributed by the LAC(NLC). Further details about the LAC(NLC) thesis program are available on the LAC(NLC) website ([www.nlc-bnc.ca](http://www.nlc-bnc.ca))

Full Publication details and a copy of this permission letter will be included in the thesis.

Sincerely,

Alan Spurway

---

Permission is granted for:

- a) The inclusion of the material described above in A. Spurway's thesis.
- b) For the material described above to be included in the copy of A. Spurway's thesis that is sent to the Library and Archives of Canada (formerly National Library of Canada) for reproduction and distribution.

Name: \_\_\_\_\_

Title: \_\_\_\_\_

Signature: \_\_\_\_\_

Date: \_\_\_\_\_

# PERMISSION LICENSE AGREEMENT

P3607.JBJSInc.JBJS Am.Lenke.887.Dalhousie University.Spurway

JBJSInc.JBJS Am.Lenke.887

4/3/2012

Mr. Alan J. Spurway

INVOICE  
ATTACHED

Dalhousie University

,

Dear Mr. Spurway,

Thank you for your interest in JBJS [Am] material. Please note: This permission does not apply to any figure or other material that is credited to any source other than JBJS. It is your responsibility to validate that the material is in fact owned by JBJS. If material within JBJS material is credited to another source (in a figure legend, for example) then any permission extended by JBJS is invalid. We encourage you to view the actual material at [www.ejbjs.org](http://www.ejbjs.org) or a library or other source. Information provided by third parties as to credits that may or may not be associated with the material may be unreliable.

We are pleased to grant you non-exclusive, nontransferable permission, limited to the format described below, and provided you meet the criteria below. Such permission is for one-time use and does not include permission for future editions, revisions, additional printings, updates, ancillaries, customized forms, any electronic forms, Braille editions, translations or promotional pieces unless otherwise specified below. We must be contacted for permission each time such use is planned. This permission does not include the right to modify the material. Use of the material must not imply any endorsement by the copyright owner. This permission is not valid for the use of JBJS logos or other collateral material.

Abstracts or collections of abstracts and all translations must be approved by publisher's agent in advance, and in the case of translations, before printing. No financial liability for the project will devolve upon JBJS, Inc. or on Rockwater, Inc.. All expenses for translation, validation of translation accuracy, publication costs and reproduction costs are the sole responsibility of the foreign language sponsor. The new work must be reprinted and delivered as a stand-alone piece and may not be integrated or bound with other material. JBJS does not supply photos or artwork; these may be downloaded from the JBJS website, scanned, or (if available) obtained from the author of the article.

## **PERMISSION IS VALID FOR THE FOLLOWING MATERIAL ONLY:**

### **Figure 3**

Journal of Bone and Joint Surgery American, , 2001, 83, 8, Adolescent idiopathic scoliosis: a new classification to determine extent of spinal arthrodesis, Lenke, 1169-1181

## **IN THE FOLLOWING WORK ONLY:**

electronic and/or print copies of "radiostereometric analysis origin styles: their impact on accuracy and precision in the assessment of spinal fusion success" to be published in English by Dalhousie University, with no commercial use

CREDIT LINE(S) must be published next to any figure, and/or if permission is granted for electronic form, visible at the same time as the content republished with a hyperlink to the publisher's home page.

WITH PAYMENT OF PERMISSIONS FEE. License, once paid, is good for one year from your anticipated publication date unless otherwise specified above. Failure to pay the fee(s) or to follow instructions here upon use of the work as described here, will result in automatic termination of the license or permission granted. All information is required. Payment should be made to Rockwater, Inc. by check or credit card, via mail

Please contact Beth Ann Rocheleau at [jbjs@rockwaterinc.com](mailto:jbjs@rockwaterinc.com) or 1-803-359-4578 with questions.

**WOLTERS KLUWER HEALTH LICENSE  
TERMS AND CONDITIONS**

Apr 13, 2012

---

This is a License Agreement between Alan J Spurway ("You") and Wolters Kluwer Health ("Wolters Kluwer Health") provided by Copyright Clearance Center ("CCC"). The license consists of your order details, the terms and conditions provided by Wolters Kluwer Health, and the payment terms and conditions.

**All payments must be made in full to CCC. For payment instructions, please see information listed at the bottom of this form.**

License Number	2887080997767
License date	Apr 13, 2012
Licensed content publisher	Wolters Kluwer Health
Licensed content publication	Spine
Licensed content title	Thoracic Human Vertebrae Quantitative Three-Dimensional Anatomy
Licensed content author	MANOHAR PANJABI, KOICHIRO TAKATA, VIJAY GOEL, et al
Licensed content date	Jan 1, 1991
Volume Number	16
Issue Number	8
Type of Use	Dissertation/Thesis
Requestor type	Individual
Title of your thesis / dissertation	Radiostereometric Analysis Origin Styles: Their Impact on Accuracy and Precision in the Assessment of Spinal Fusion Success
Expected completion date	Apr 2012
Estimated size(pages)	412
Billing Type	Invoice
Billing address	School of Biomedical Engineering Dalhousie University Halifax, NS B3H3J5 Canada
Customer reference info	
Total	0.00 USD